FRACTAL AND MULTIFRACTAL FACETS IN THE STRUCTURE AND DYNAMICS OF PHYSIOLOGICAL SYSTEMS AND APPLICATIONS TO HOMEOSTATIC CONTROL, DISEASE DIAGNOSIS AND INTEGRATED CYBER-PHYSICAL PLATFORMS

EDITED BY: Paul Bogdan, Plamen Ch. Ivanov and Andras Eke

PUBLISHED IN: Frontiers in Physiology

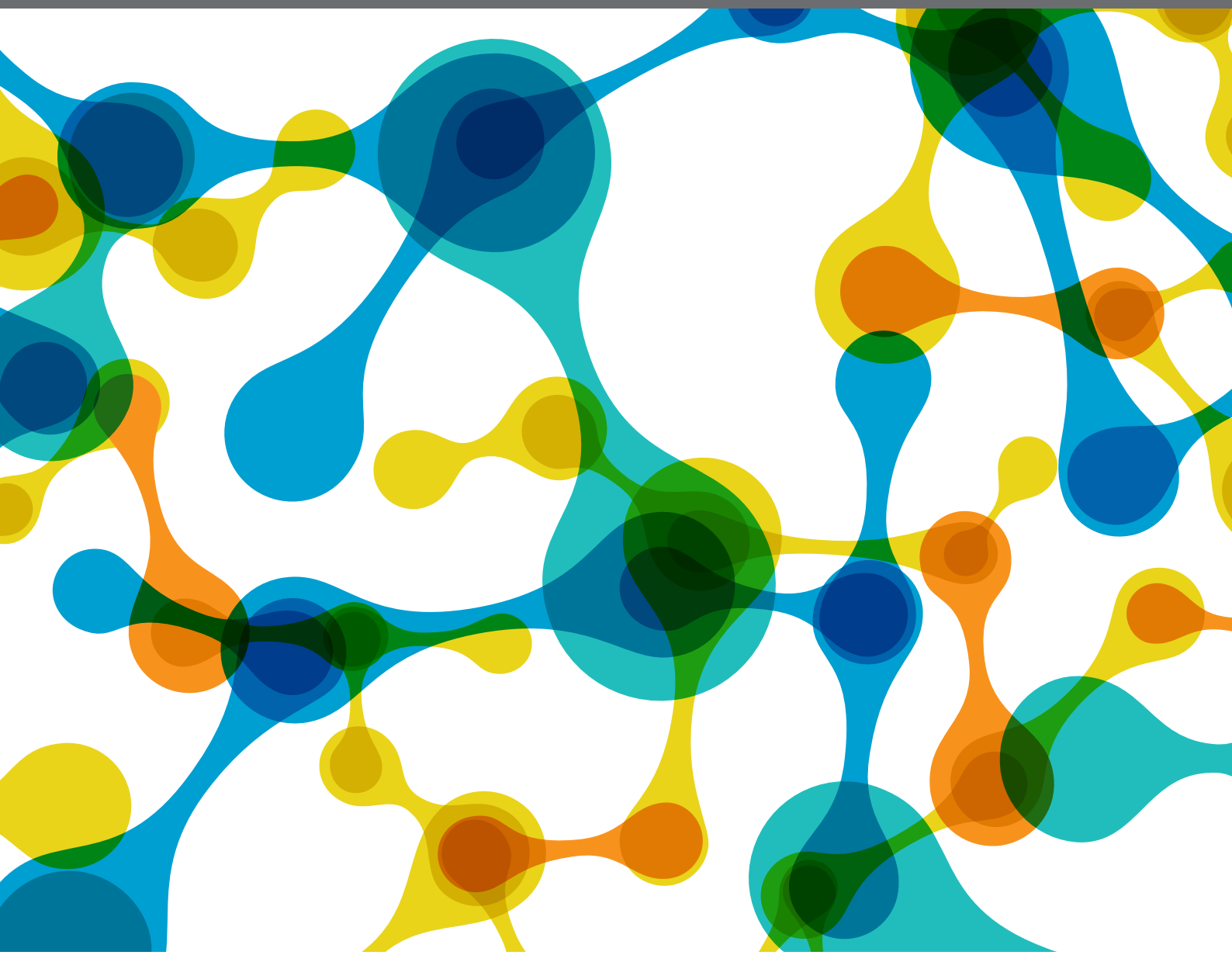

frontiers Research Topics

frontiers

ISSN 1664-8714
ISBN 978-2-88963-531-3
DOI 10.3389/978-2-88963-531-3

About Frontiers

Frontiers is more than just an open-access publisher of scholarly articles: it is a pioneering approach to the world of academia, radically improving the way scholarly research is managed. The grand vision of Frontiers is a world where all people have an equal opportunity to seek, share and generate knowledge. Frontiers provides immediate and permanent online open access to all its publications, but this alone is not enough to realize our grand goals.

Frontiers Journal Series

The Frontiers Journal Series is a multi-tier and interdisciplinary set of open-access, online journals, promising a paradigm shift from the current review, selection and dissemination processes in academic publishing. All Frontiers journals are driven by researchers for researchers; therefore, they constitute a service to the scholarly community. At the same time, the Frontiers Journal Series operates on a revolutionary invention, the tiered publishing system, initially addressing specific communities of scholars, and gradually climbing up to broader public understanding, thus serving the interests of the lay society, too.

Dedication to Quality

Each Frontiers article is a landmark of the highest quality, thanks to genuinely collaborative interactions between authors and review editors, who include some of the world's best academicians. Research must be certified by peers before entering a stream of knowledge that may eventually reach the public - and shape society; therefore, Frontiers only applies the most rigorous and unbiased reviews.
Frontiers revolutionizes research publishing by freely delivering the most outstanding research, evaluated with no bias from both the academic and social point of view. By applying the most advanced information technologies, Frontiers is catapulting scholarly publishing into a new generation.

What are Frontiers Research Topics?

Frontiers Research Topics are very popular trademarks of the Frontiers Journals Series: they are collections of at least ten articles, all centered on a particular subject. With their unique mix of varied contributions from Original Research to Review Articles, Frontiers Research Topics unify the most influential researchers, the latest key findings and historical advances in a hot research area! Find out more on how to host your own Frontiers Research Topic or contribute to one as an author by contacting the Frontiers Editorial Office: researchtopics@frontiersin.org

FRACTAL AND MULTIFRACTAL FACETS IN THE STRUCTURE AND DYNAMICS OF PHYSIOLOGICAL SYSTEMS AND APPLICATIONS TO HOMEOSTATIC CONTROL, DISEASE DIAGNOSIS AND INTEGRATED CYBER-PHYSICAL PLATFORMS

Topic Editors:
Paul Bogdan, University of Southern California, United States
Plamen Ch. Ivanov, Boston University, United States
Andras Eke, Semmelweis University, Hungary

Widespread chronic diseases (e.g., heart diseases, diabetes and its complications, stroke, cancer, brain diseases) constitute a significant cause of rising healthcare costs and pose a significant burden on quality-of-life for many individuals. Despite the increased need for smart healthcare sensing systems that monitor / measure patients' body balance, there is no coherent theory that facilitates the modeling of human physiological processes and the design and optimization of future healthcare cyber-physical systems (HCPS). The HCPS are expected to mine the patient's physiological state based on available continuous sensing, quantify risk indices corresponding to the onset of abnormality, signal the need for critical medical intervention in real-time by communicating patient's medical information via a network from individual to hospital, and most importantly control (actuate) vital health signals (e.g., cardiac pacing, insulin level, blood pressure) within personalized homeostasis.

To prevent health complications, maintain good health and/or avoid fatal conditions calls for a cross-disciplinary approach to HCPS design where recent statistical-physics inspired discoveries done by collaborations between physicists and physicians are shared and enriched by applied mathematicians, control theorists and bioengineers. This critical and urgent multi-disciplinary approach has to unify the current state of knowledge and address the following fundamental challenges: One fundamental challenge is represented by the need to mine and understand the complexity of the structure and dynamics of the physiological systems in healthy homeostasis and associated with a disease (such as diabetes). Along the same lines, we need rigorous mathematical techniques for identifying the interactions between integrated physiologic systems and understanding their role within the overall networking architecture of healthy dynamics. Another fundamental challenge calls for a deeper understanding of stochastic feedback and variability in biological systems and physiological processes, in particular, and for deciphering their implications not only on how to mathematically characterize homeostasis, but also on defining new control strategies that are accounting for intra- and inter-patient specificity – a truly mathematical approach to personalized medicine.

Numerous recent studies have demonstrated that heart rate variability, blood glucose, neural signals and other interdependent physiological processes demonstrate fractal and non-stationary characteristics. Exploiting statistical physics concepts, numerous recent research studies demonstrated that healthy human physiological processes exhibit complex critical phenomena with deep implications for how

homeostasis should be defined and how control strategies should be developed when prolonged abnormal deviations are observed. In addition, several efforts have tried to connect these fractal characteristics with new optimal control strategies that implemented in medical devices such as pacemakers and artificial pancreas could improve the efficiency of medical therapies and the quality-of-life of patients but neglecting the overall networking architecture of human physiology. Consequently, rigorously analyzing the complexity and dynamics of physiological processes (e.g., blood glucose and its associated implications and interdependencies with other physiological processes) represents a fundamental step towards providing a quantifiable (mathematical) definition of homeostasis in the context of critical phenomena, understanding the onset of chronic diseases, predicting deviations from healthy homeostasis and developing new more efficient medical therapies that carefully account for the physiological complexity, intra- and inter-patient variability, rather than ignoring it.

This Research Topic aims to open a synergetic and timely effort between physicians, physicists, applied mathematicians, signal processing, bioengineering and biomedical experts to organize the state of knowledge in mining the complexity of physiological systems and their implications for constructing more accurate mathematical models and designing QoL-aware control strategies implemented in the new generation of HCPS devices. By bringing together multi-disciplinary researchers seeking to understand the many aspects of human physiology and its complexity, we aim at enabling a paradigm shift in designing future medical devices that translates mathematical characteristics in predictable mathematical models quantifying not only the degree of homeostasis, but also providing fundamentally new control strategies within the personalized medicine era.

Citation: Bogdan, P., Ivanov, P. C., Eke, A., eds. (2020). Fractal and Multifractal Facets in the Structure and Dynamics of Physiological Systems and Applications to Homeostatic Control, Disease Diagnosis and Integrated Cyber-Physical Platforms. Lausanne: Frontiers Media SA. doi: 10.3389/978-2-88963-531-3

Table of Contents

frontiers in Physiology

EDITORIAL
published: 13 May 2020
doi: 10.3389/fphys.2020.00447

Editorial: Fractal and Multifractal Facets in the Structure and Dynamics of Physiological Systems and Applications to Homeostatic Control, Disease Diagnosis and Integrated Cyber-Physical Platforms

Paul Bogdan[1]*, *András Eke*[2,3] and *Plamen Ch. Ivanov*[4,5,6]

[1] *Ming-Hsieh Department of Electrical and Computer Engineering, University of Southern California, Los Angeles, CA, United States,* [2] *Department of Physiology, School of Medicine, Semmelweis University, Budapest, Hungary,* [3] *Department of Radiology and Biomedical Imaging, Yale University School of Medicine, New Haven, CT, United States,* [4] *Keck Laboratory for Network Physiology, Department of Physics, Boston University, Boston, MA, United States,* [5] *Harvard Medical School and Division of Sleep Medicine, Brigham and Women's Hospital, Boston, MA, United States,* [6] *Institute of Solid State Physics, Bulgarian Academy of Sciences, Sofia, Bulgaria*

Keywords: multifractals, physiological systems, control, disease diagnosis and analysis, cyber-physical systems (CPS)

OPEN ACCESS

Edited and reviewed by:
Zbigniew R. Struzik,
The University of Tokyo, Japan

***Correspondence:**
Paul Bogdan
pbogdan@usc.edu

Specialty section:
This article was submitted to Fractal and Network Physiology, a section of the journal Frontiers in Physiology

Received: *20 February 2020*
Accepted: *09 April 2020*
Published: *13 May 2020*

Citation:
Bogdan P, Eke A and Ivanov PC (2020) Editorial: Fractal and Multifractal Facets in the Structure and Dynamics of Physiological Systems and Applications to Homeostatic Control, Disease Diagnosis and Integrated Cyber-Physical Platforms. Front. Physiol. 11:447. doi: 10.3389/fphys.2020.00447

Editorial on the Research Topic

Fractal and Multifractal Facets in the Structure and Dynamics of Physiological Systems and Applications to Homeostatic Control, Disease Diagnosis and Integrated Cyber-Physical Platforms

A fundamental problem in biology, physiology, and medicine is understanding how complexity in the structure and dynamics of biological and physiological systems emerges from multicomponent regulatory mechanisms, where non-linear feedback loops across scales lead to efficient homeostatic control in the presence of continuous temporal variability in systems outputs. Addressing this problem requires (i) comprehensive analyses of systems dynamics based on multifractal formalism and methodology (Ivanov et al., 1999, 2001, 2002; Mukli et al., 2015) to probe feedback interactions underlying biological and physiological systems by quantifying the temporal organization of physiological fluctuations and their cascades across scales, and (ii) a general network physiology framework (Bashan et al., 2012; Ivanov and Bartsch, 2014; Bartsch et al., 2015; Ivanov et al., 2016) to investigate networks of interactions among diverse physiological systems and subsystems across space and time scales that lead to emergent complex behaviors at the organism level. An entire new class of diagnostic and prognostic biomarkers has resulted from pioneering studies in these new directions, especially needed now when witnessing a pandemic of chronic diseases (e.g., heart diseases, diabetes, and its complications, stroke, cancer, brain diseases) which constitute a significant cause of rising healthcare costs and a reduced quality-of-life (QoL).

Despite the increased need for smart healthcare sensing systems that monitor patients' body balance, there is no coherent theory that facilitates the modeling of human physiological processes and the design and optimization of future healthcare cyber-physical systems (HCPSs) (Bogdan and Marculescu, 2011; Xue and Bogdan, 2017; Bogdan, 2019). The HCPSs are expected to measure and mine the patient's physiological state based on available continuous sensing, quantify risk indices

corresponding to the onset of abnormality, signal the need for critical medical intervention in real-time by communicating patient's medical information via a network from individual to hospital, and most importantly control (actuate) vital health signals (e.g., cardiac pacing, insulin level, blood pressure) within personalized homeostasis.

To maintain good health, prevent health complications, and/or avoid fatal conditions calls for a cross-disciplinary approach to HCPS design that rely on recent advances in statistical physics, non-linear dynamics, machine learning, and artificial intelligence. There is a palpable need for a multi-disciplinary approach to consolidate the current state of art in order to respond to the following fundamental challenges. First and foremost, the fundamental properties (e.g., non-stationarity, fractality) of human physiology in terms of mathematical formalism needs to be characterized in order to facilitate the understanding of its complexity (West, 1991; Bassingthwaighte et al., 1994; Stanley et al., 1999; Amaral et al., 2001; Eke et al., 2002; Ivanov et al., 2009; Xue and Bogdan, 2019) in healthy homeostasis, as well as in conditions associated with aging and diseases (Mietus et al., 2000; Ashkenazy et al., 2001; Bernaola-Galvan et al., 2001; Schulte-Frohlinde et al., 2001; Goldberger et al., 2002; Schmitt and Ivanov, 2007).

Indeed, defining the trajectory of the healthy aging process in terms of its complexity metrics (Goldberger et al., 2002) seems essential to keep the health care system on target. At this end, Mukli et al. demonstrated the utility of multifractal metrics of cerebral hemodynamics as biomarkers of the healthy aging process. In particular, these authors—by applying a novel adaptive bimodal multifractal analysis (Mukli et al., 2015; Nagy et al., 2017) to enhanced human cerebrocortical functional Near Infrared Spectroscopy (fNIRS) data—disentangled the neurogenic from vasogenic components in brain dynamics that were then shown being attenuated in the course of healthy aging. Racz et al. applied multifractal time series analysis (Mukli et al., 2015) to investigate dynamic functional connectivity (DFC) reconstructed from resting-state electroencephalography (EEG) measurements. This work demonstrated that metrics of DFC as captured in the temporal evolution of graph theoretical measures—even under resting-state conditions—dynamically fluctuated according to region-specific true multifractal temporal patterns. Mono- and multifractal measures of the generalized Hurst exponent for individual functional connections exhibited a spatial pattern well in sink with the overall functional organization of the brain. The authors propose that multifractal analysis can provide further details in the description of DFC to most methods currently applied in the field, and could serve as a valuable tool for a better characterization of healthy and pathological brain functions. Akhrif et al. performed an adaptive monofractal analysis of functional magnetic resonance (fMRI) data and estimated the Hurst exponent of the impulsivity network. This study not only demonstrates that the Hurst exponent can be used as a biomarker to quantify deviations in network functions at early stages, but also serve as a control knob in therapeutic strategies aimed at delaying the onset and improving treatment of disorders. França et al. demonstrated that multifractal analysis can provide important relevant information for mining the intracranially recorded EEG data and extracting features that can be used for machine learning-based diagnosis outperforming other techniques like signal variance or power spectrum. In particular, they demonstrated that there may exist an optimal time scale between the sampling frequency and epoch length that can best influence the detection accuracy of temporal changes in multifractality associated with epileptic seizures. While this study has identified that multifractal algorithms perform well on EEG and simulated data alike, it also brought attention to the issue of optimal time scales at which machine learning-based diagnosis should be done.

With the goal of mathematical characterization of blood glucose variability, initially scrutinized in Ghorbani and Bogdan (2013). Kohnert et al. provided a cross-sectional investigation and compared the relationships between indices of non-linear dynamics and traditional glycemic variability, as well as their potential application in diabetes control. Although this analysis showed that the Poincaré plot measures the multiscale entropy (MSE) index, and the detrended fluctuation analysis exponents can help to discriminate between the type 1 and type 2 diabetes (e.g., the MSE index decreased consistently from the non-diabetic to the type 1 diabetic group), it also highlighted the need to develop more advanced complexity measures in order to better characterize the glycemia. These fractal-based observations can have a significant impact on the development of efficacious artificial pancreas with increased patient's QoL.

In order to extract the multifractal characteristics and determine disease signatures, Reyes-Manzano et al. investigated the multifractal behavior of the beat-to-beat heart dynamics captured in RR-interval fluctuations in fibromyalgia patients (FM) via the multifractal detrended fluctuation analysis (Kantelhardt et al., 2002). The multifractal and non-linear behavior exhibited a decrease in patients with fibromyalgia. Consequently, this investigation not only highlights the role of the dysfunctional autonomic control in the pathogenesis of fibromyalgia, but it can also provide a theoretical and algorithmic foundation for HCPS. With the goal of analyzing the cardiac abnormalities observed in heart failure disease, Platiša et al. exploited the short-term and long-term scaling exponents obtained via the detrended fluctuation analysis (DFA) (Peng et al., 1995; Hu et al., 2001; Chen et al., 2002, 2005; Xu et al., 2005; Ma et al., 2010) for discriminating the deterioration in cardiac autonomic nervous system control. Their study demonstrated that the heart failure patients exhibited a more pronounced heart rate asymmetry and a higher long-term scaling exponent. Moreover, a ratio between the DFA short-term and long-term scaling exponents can help at discriminating between various types of heart failure disease states.

To provide a deeper understanding of atrial fibrillation disease, Attuel et al. described a model of cardiac excitable cell network which is capable to reproduce the experimentally observed multifractal intermittent nature of the cardiac impulse energy. In order to investigate the cardiac electrophysiological and arrhythmogenic properties, Tse et al. studied the beat-to-beat variability in action potential duration data and concluded

that the atrial monophasic action potential recordings (MAPs) exhibits greater degree of variability than the ventricular MAPs. Along the same lines of exploiting non-linear metrics in various disease states, Ghita et al. investigated the tissue heterogeneity and dynamic non-linearity in respiratory impedance data and quantified the sensitivity of the forced oscillation technique to various degrees of obstruction in patients suffering from chronic obstructive pulmonary disease (COPD). They showed that the degree of non-linearity correlates well with various degrees of COPD.

We need rigorous mathematical techniques and a general theoretical framework to characterize the interactions between integrated physiologic systems with different output dynamics (Bartsch et al., 2012; Liu et al., 2015; Lin et al., 2016; Ivanov et al., 2017), as well as other related processes (e.g., metabolic, proteomic, genomic), and understand their role within the overall network physiology of healthy dynamics (Ivanov et al., 2016). Along the lines of characterizing the interactions across scales, Ghorbani et al. investigated the individual gene expression dynamics and the cross-dependency among genes and transcription factors in the context of gene regulatory networks corresponding to *Escherichia coli* and *Saccharomyces cerevisiae* bacteria. This initial study demonstrated that the interaction between genes and linked transcription factors exhibit multifractal and long-range cross-correlated characteristics with implications for understanding genome-level dynamics.

Finally, there is a fundamental need for deeper understanding of the mechanisms of stochastic feedback and variability in biological systems and physiological processes (Ivanov et al., 1998; Ashkenazy et al., 2002; Lo et al., 2002). This is essential for developing adequate approaches to mathematically characterize homeostasis as well as for defining new control strategies accounting for intra- and inter-patient specificity—a truly mathematical approach to personalized medicine (Xue and Bogdan, 2017; Bogdan, 2019; Yang and Bogdan, 2020). For example, the multi-scale interactions and feedback among cognitive events may play an essential role in information processing in the prefrontal cortex (Racz et al., 2017). Hu et al. demonstrated that the optimal performance of the working memory is concurrent with the critical dynamics at the network level and the excitatory and inhibitory balance at the neuron level. Moreover, this study suggests the existence of a unified multi-scale optimal state for the prefrontal cortex, which further can be modulated by dopamine opening new therapeutic strategies in HCPS.

The works presented in this Research Topic collection as well as current advances in the field of fractal and multi-fractal investigations of physiological systems structure and dynamics, and their applications to homeostatic control, clinical diagnosis, and the development of cyber-physical systems in healthcare outline a new horizon of multidisciplinary cooperation with new challenges. There is an urgent need for adopting a cross-scale perspective and a corresponding theoretical framework to investigate the multi-scale regulatory mechanisms underlying the overall network physiology and its relation to physiological states and functions emerging at the organism level in health and disease. When dealing with the heterogeneity, multi-modality and complexity of physiological processes, we need rigorous mathematical and algorithmic techniques that can extract causal interdependencies between systems across different scales while overcoming various noise sources. For example, obtaining high-frequency genomic and proteomic sensing data over large spatial and temporal dimensions can open new frontiers and lead to the discovery of basic laws of regulation with broad clinical applications. Consequently, progress in this direction will require new algorithmic strategies to quantify time-varying information flow among diverse physiological processes across scales, and determine how it influences the global dynamics of complex physiological networks. Intrinsically related with future efforts on quantifying causal dependencies and control principles in biological and physiological networks, it will be essential to develop robust optimization algorithms capable to reconstruct or infer the structure and dynamics of complex interdependent networks while overcoming partial observability, noise induced defects and adversarial interventions caused by bacterial or viral infections. Lastly, the biomedical and engineering communities need to develop new control methodologies that do not seek to only enforce a specific reference value (that proved beneficial for some patients), but rather ensure that the physiological complexity and multifractality are restored to the healthy profiles when abnormalities are detected—e.g., a mathematical strategy to abstract the complexity of brain network through an approximate transfer function and a new minimal control strategy allows one to efficiently enforce a healthy fractal profile when frailty is early detected.

Toward this end, with these challenges also unique opportunities arise for interdisciplinary research. From the interactions of statistical physics, non-linear dynamics, information theory, probability and stochastic processes, artificial intelligence, machine learning, control theory and optimization, basic physiology and medicine new theoretical and algorithmic foundations will emerge for mining, analyzing, and controlling the network physiology. Ultimately, such efforts would lead to a new class of network-physiology-derived diagnostic and prognostic markers with innovative applications in cyber-physical systems and clinical practice.

AUTHOR CONTRIBUTIONS

All authors listed have made a substantial, direct and intellectual contribution to the work, and approved it for publication.

ACKNOWLEDGMENTS

We acknowledge support from several funding agencies: PB acknowledges the support by the National Science Foundation (NSF) under the Career Award CPS/CNS-1453860, CCF-1837131, MCB-1936775, CNS-1932620, and CMMI-1936624, the U.S. Army Defense Advanced Research Projects Agency (DARPA) under grant number W911NF-17-1-0076, and the DARPA Young Faculty Award and Director's Fellowship Award under grant number N66001-17-1-4044; AE acknowledges

the support by the Department of Physiology, Semmelweis University; PChI thanks the W. M. Keck Foundation, National Institutes of Health Grant 1R01-HL098437, Office of Naval Research Grant 000141010078, US-Israel Binational Science Foundation Grant 2012219 for support. The funders had no role in decision to publish or preparation of the manuscript.

REFERENCES

Amaral, L. A. N., Ivanov, P. Ch., Aoyagi, N., Hidaka, I., Tomono, S., Goldberger, A. L., et al. (2001). Behavioral-independent features of complex heartbeat dynamics. *Phys. Rev. Lett.* 86:6026. doi: 10.1103/PhysRevLett.86.6026

Ashkenazy, Y., Hausdorff, J. M., Ivanov, P. Ch., and Stanley, H. E. (2002). A stochastic model of human gait dynamics. *Physica A* 316, 662–670. doi: 10.1016/S0378-4371(02)01453-X

Ashkenazy, Y., Ivanov, P. Ch., Havlin, S., Peng, C.-K., Goldberger, A. L., and Stanley, H. E. (2001). Magnitude and sign correlations in heartbeat fluctuations. *Phys. Rev. Lett.* 86, 1900–1903. doi: 10.1103/PhysRevLett.86.1900

Bartsch, R. P., Liu, K. K., Bashan, A., and Ivanov, P. Ch. (2015). Network physiology: how organ dynamically interact. *PLoS ONE* 10:e0142143. doi: 10.1371/journal.pone.0142143

Bartsch, R. P., Schumann, A. Y., Kantelhardt, J. W., Penzel, T., and Ivanov, P. Ch. (2012). Phase transitions in physiologic coupling. *Proc. Natl. Acad. Sci. U.S.A.* 109, 10181–10186. doi: 10.1073/pnas.1204568109

Bashan, A., Bartsch, R. P., Kantelhardt, J. W., Havlin, S., and Ivanov, P. Ch. (2012). Network physiology reveals relations between network topology and physiologic function. *Nat. Commun.* 3:702. doi: 10.1038/ncomms1705

Bassingthwaighte, J. B., Liebovitch, L. S., and West, B. J. (1994). *Fractal Physiology*. Oxford:American Physiological Society.

Bernaola-Galvan, P., Ivanov, P. Ch., Amaral, L. A. N., and Stanley, H. E. (2001). Scale invariance in the nonstationarity of human heart rate. *Phys. Rev. Lett.* 87:168105. doi: 10.1103/PhysRevLett.87.168105

Bogdan, P. (2019). Taming the unknown unknowns in complex systems: challenges and opportunities for modeling, analysis and control of complex (Biological) collectives. *Front. Physiol.* 10:1452. doi: 10.3389/fphys.2019.01452

Bogdan, P., and Marculescu, R. (2011). "Towards a science of cyber-physical systems design," in *Proceedings of the 2011 IEEE/ACM Second International Conference on Cyber-Physical Systems* (ICCPS) (Chicago, IL), 99–108.

Chen, Z., Hu, K., Carpena, P., Bernaola-Galvan, P., Stanley, H. E., and Ivanov, P. Ch. (2005). Effect of nonlinear filters on detrended fluctuation analysis. *Phys. Rev. E* 71:011104. doi: 10.1103/PhysRevE.71.011104

Chen, Z., Ivanov, P. Ch., Hu, K., and Stanley, H. E. (2002). Effect of nonstationarities on detrended fluctuation analysis. *Phys. Rev. E* 65:041107. doi: 10.1103/PhysRevE.65.041107

Eke, A., Herman, P., Kocsis, L., and Kozak, L. R. (2002). Fractal characterization of complexity in temporal physiological signals. *Physiol. Meas.* 23, R1–R38. doi: 10.1088/0967-3334/23/1/201

Ghorbani, M., and Bogdan, P. (2013). "A cyber-physical system approach to artificial pancreas design," in *Proceedings of the Ninth IEEE/ACM/IFIP International Conference on Hardware/Software Codesign and System Synthesis* (Montreal, QC: CODES+ISSS), 1–10.

Goldberger, A. L., Amaral, L. A. N., Hausdorff, J. M., Ivanov, P. Ch., Peng, C.-K. H., and Eugene Stanley, H. E. (2002). Fractal dynamics in physiology: alterations with disease and aging. *Proc. Natl. Acad. Sci. U.S.A.* 99, 2466–2472. doi: 10.1073/pnas.012579499

Hu, K., Ivanov, P. Ch., Chen, Z., Carpena, P., and Stanley, H. E. (2001). Effect of trends on detrended fluctuation analysis. *Phys. Rev. E* 64:011114. doi: 10.1103/PhysRevE.64.011114

Ivanov, P. Ch., Amaral, L. A. N., Goldberger, A. L., Havlin, S., Rosenblum, M. G., Stanley, H. E., et al. (2001). From 1/f noise to multifractal cascades in heartbeat dynamics. *Chaos* 11, 641–652. doi: 10.1063/1.1395631

Ivanov, P. Ch., Amaral, L. A. N., Goldberger, A. L., Havlin, S., Rosenblum, M. G., Struzik, Z. R., et al. (1999). Multifractality in human heartbeat dynamics. *Nature* 399, 461–465. doi: 10.1038/20924

Ivanov, P. Ch., Amaral, L. A. N., Goldberger, A. L., and Stanley, H. E. (1998). Stochastic feedback and the regulation of biological rhythms. *Europhys. Lett.* 43, 363–368. doi: 10.1209/epl/i1998-00366-3

Ivanov, P. Ch., and Bartsch, R. P. (2014). "Network physiology: mapping interactions between networks of physiologic networks," in *Networks of Networks: The Last Frontier of Complexity. Understanding Complex Systems,* eds G. D'Agostino and A. Scala (Cham: Springer). doi: 10.1007/978-3-319-03518-5_10

Ivanov, P. Ch., Goldberger, A. L., and Stanley, H. E. (2002). "Fractal and multifractal approaches in physiology," in *The Science of Disasters: Climate Disruptions, Heart Attacks and Market Crashes,* eds A. Bunde, J. Kropp, and H.-J. Schellnhuber H-J (Berlin: Springer Verlag), 219–257.

Ivanov, P. Ch., Liu, K. K. L., and Bartsch, R. P. (2016). Focus on the emerging new fields of network physiology and network medicine. *New J. Phys.* 18:100201. doi: 10.1088/1367-2630/18/10/100201

Ivanov, P. Ch., Liu, K. K. L., Lin, A., and Bartsch, R. P. (2017). "Network physiology: from neural plasticity to organ network interactions," in *Emergent Complexity from Nonlinearity, in Physics, Engineering and the Life Sciences. Springer Proceedings in Physics, Vol. 191* eds G. Mantica, R. Stoop, and S. Stramaglia (Cham: Springer), 145–165.

Ivanov, P. Ch., Ma, Q. D. Y., Bartsch, R. P., Hausdorff, J. M., Amaral, L. A. N., Schulte-Frohlinde, V., et al. (2009). Levels of complexity in scale-invariant neural signals. *Phys. Rev. E* 79:041920. doi: 10.1103/PhysRevE.79.041920

Kantelhardt, J. W., Zschiegner, S. A., Koscielny-Bunde, E., Havlin, S., Bunde, A., and Stanley, H. E. (2002). Multifractal detrended fluctuation analysis of nonstationary time series. *Phys. A Stat. Mech. Appl.* 316, 87–114. doi: 10.1016/S0378-4371(02)01383-3

Lin, A., Liu, K. K. L., Bartsch, R. P., and Ivanov, P. Ch. (2016). Delay-correlation landscape reveals characteristic time delays of brain rhythms and heart interactions. *Philos. Trans. R. Soc. A* 374:20150182. doi: 10.1098/rsta.2015.0182

Liu, K. K. L., Bartsch, R. P., Ma, Q. D. Y., and Ivanov, P. Ch. (2015). Major component analysis of dynamic networks of physiologic organ interactions. *J. Phys. Conf. Ser.* 640:012013. doi: 10.1088/1742-6596/640/1/012013

Lo, C.-C., Amaral, L. A. N., Havlin, S., Ivanov, P. Ch., Penzel, T., Peter, J.-H., et al. (2002). Dynamics of sleep-wake transitions during sleep. *Europhys. Lett.* 57, 625–631. doi: 10.1209/epl/i2002-00508-7

Ma, Q. D. Y., Bartsch, R. P., Bernaola-Galvan, P., Yoneyama, M., and Ivanov, P. Ch. (2010). Effects of extreme data loss on long-range correlated and anticorrelated signals quantified by detrended fluctuation analysis. *Phys. Rev. E* 81:031101. doi: 10.1103/PhysRevE.81.031101

Mietus, J. E., Peng, C. K., Ivanov, P. Ch., and Goldberger, A. L. (2000). "Detection of obstructive sleep apnea from cardiac interbeat interval time series," in *Computers in Cardiology, Vol.27 (Cat. 00CH37163)* (Cambridge, MA), 753–756.

Mukli, P., Nagy, Z., and Eke, A. (2015). Multifractal formalism by enforcing the universal behavior of scaling functions. *Phys. A Stat. Mech. Appl.* 417, 150–167. doi: 10.1016/j.physa.2014.09.002

Nagy, Z., Mukli, P., Herman, P., and Eke, A. (2017). Decomposing multifractal crossovers. *Front. Physiol.* 8:533. doi: 10.3389/fphys.2017.00533

Peng, C.-K., Havlin, S., Stanley, H. E., and Goldberger, A. L. (1995). Quantification of scaling exponents and crossover phenomena in nonstationary heartbeat time series. *Chaos* 5, 82–87. doi: 10.1063/1.166141

Racz, F. S., Mukli, P., Nagy, Z., and Eke, A. (2017). Increased prefrontal cortex connectivity during cognitive challenge assessed by fNIRS imaging. *Biomed. Opt. Express* 8, 3842–3855. doi: 10.1364/BOE.8.003842

Schmitt, D. T., and Ivanov, P. Ch. (2007). Fractal scale-invariant and nonlinear properties of cardiac dynamics remain stable with advanced age: a new

mechanistic picture of cardiac control in healthy elderly. *Am. J. Physiol. Regul. Integr. Comp. Physiol.* 293, R1923–R1937. doi: 10.1152/ajpregu.00372.2007

Schulte-Frohlinde, V., Ashkenazy, Y., Ivanov, P. Ch., Glass, L., Goldberger, A. L., and Stanley, H. E. (2001). Noise effects on the complex patterns of abnormal heartbeats. *Phys. Rev. Lett.* 87:068104. doi: 10.1103/PhysRevLett.87.068104

Stanley, H. E., Amaral, L. A. N., Goldberger, A. L., Havlin, S., Ivanov, P. Ch., and Peng, C. K. (1999). Statistical physics and physiology: monofractal and multifractal approaches. *Phys. A Stat. Mech. Appl.* 270, 309–324. doi: 10.1016/S0378-4371(99)00230-7

West, B. (1991). *Fractal Physiology and Chaos in Medicine*. Singapore: World Scientific Pub. Co. Inc.

Xu, L., Ivanov, P. Ch., Hu, K., Chen, Z., Carbone, A., and Stanley, H. E. (2005). Quantifying signals with power-law correlations: a comparative study of detrended fluctuation analysis and detrended moving average techniques. *Phys. Rev. E* 71:051101. doi: 10.1103/PhysRevE.71.051101

Xue, Y., and Bogdan, P. (2017). "Constructing compact causal mathematical models for complex dynamics," in *Proceedings of 8th ACM/IEEE International Conference on Cyber-Physical System (ICCPS), Cyber-Physical Systems Week* (Pittsburgh, PA).

Xue, Y., and Bogdan, P. (2019). Reconstructing missing complex networks against adversarial interventions. *Nat. Commun.* 10:1738. doi: 10.1038/s41467-019-09774-x

Yang, R., and Bogdan, P. (2020). Controlling the multifractal generating measures of complex networks. *Nat. Sci. Rep.* 10:5541. doi: 10.1038/s41598-020-62380-6

Conflict of Interest: The authors declare that the research was conducted in the absence of any commercial or financial relationships that could be construed as a potential conflict of interest.

frontiers in Physiology

ORIGINAL RESEARCH
published: 10 August 2018
doi: 10.3389/fphys.2018.01072

Impact of Healthy Aging on Multifractal Hemodynamic Fluctuations in the Human Prefrontal Cortex

Peter Mukli[1,2], *Zoltan Nagy*[1†], *Frigyes S. Racz*[2†], *Peter Herman*[3] *and Andras Eke*[1,2*]

[1] *Institute of Clinical Experimental Research, Semmelweis University, Budapest, Hungary,* [2] *Department of Physiology, Semmelweis University, Budapest, Hungary,* [3] *Department of Radiology and Biomedical Imaging, Yale University, New Haven, CT, United States*

OPEN ACCESS

Edited by:
Plamen Ch. Ivanov, Boston University, United States

Reviewed by:
Hussein M. Yahia, Institut National de Recherche en Informatique et en Automatique (INRIA), France
Danuta Makowiec, University of Gdansk, Poland

***Correspondence:**
Andras Eke
eke.andras@med.semmelweis-univ.hu

[†] *These authors have contributed equally to this work*

Specialty section:
This article was submitted to Fractal Physiology, a section of the journal Frontiers in Physiology

Received: *25 April 2018*
Accepted: *17 July 2018*
Published: *10 August 2018*

Citation:
Mukli P, Nagy Z, Racz FS, Herman P and Eke A (2018) Impact of Healthy Aging on Multifractal Hemodynamic Fluctuations in the Human Prefrontal Cortex. Front. Physiol. 9:1072. doi: 10.3389/fphys.2018.01072

Fluctuations in resting-state cerebral hemodynamics show scale-free behavior over two distinct scaling ranges. Changes in such bimodal (multi) fractal pattern give insight to altered cerebrovascular or neural function. Our main goal was to assess the distribution of local scale-free properties characterizing cerebral hemodynamics and to disentangle the influence of aging on these multifractal parameters. To this end, we obtained extended resting-state records ($N = 2^{14}$) of oxyhemoglobin (HbO), deoxyhemoglobin (HbR) and total hemoglobin (HbT) concentration time series with continuous-wave near-infrared spectroscopy technology from the brain cortex. 52 healthy volunteers were enrolled in this study: 24 young (30.6 ± 8.2 years), and 28 elderly (60.5 ± 12.0 years) subjects. Using screening tests on power-law, multifractal noise, and shuffled data sets we evaluated the presence of true multifractal hemodynamics reflecting long-range correlation (LRC). Subsequently, scaling-range adaptive bimodal signal summation conversion (SSC) was performed based on standard deviation (σ) of signal windows across a range of temporal scales (s). Building on moments of different order (q) of the measure, $\sigma(s)$, multifractal SSC yielded generalized Hurst exponent function, $H(q)$, and singularity spectrum, $D(h)$ separately for a fast and slow component (the latter dominating the highest temporal scales). Parameters were calculated reflecting the estimated measure at $s = N$ (focus), degree of LRC [Hurst exponent, $H(2)$ and maximal Hölder exponent, h_{max}] and measuring strength of multifractality [full-width-half-maximum of $D(h)$ and $\Delta H_{15} = H(-15) - H(15)$]. Correlation-based signal improvement (CBSI) enhanced our signal in terms of interpreting changes due to neural activity or local/systemic hemodynamic influences. We characterized the HbO-HbR relationship with the aid of fractal scale-wise correlation coefficient, $r_\sigma(s)$ and SSC-based multifractal covariance analysis. In the majority of subjects, cerebral hemodynamic fluctuations proved bimodal multifractal. In case of slow component of raw HbT, h_{max}, and $\hat{H}(2)$ were lower in the young group explained by a significantly increased $r_\sigma(s)$ among elderly at high temporal scales. Regarding the fast component of CBSI-pretreated HbT and that of HbO-HbR covariance,

h_{max}, and focus were decreased in the elderly group. These observations suggest an attenuation of neurovascular coupling reflected by a decreased autocorrelation of the neuronal component concomitant with an accompanying increased autocorrelation of the non-neuronal component in the elderly group.

Keywords: aging, cerebral hemodynamics, neurovascular coupling, near-infrared spectroscopy (NIRS), correlation-based signal improvement, multifractality, multifractal analysis, signal summation conversion

INTRODUCTION

Scale-free dynamics is an ubiquitous property of physiological processes (West, 1991; Eke et al., 2000; Ivanov et al., 2001) such as low frequency fluctuations of cerebral hemodynamics (Fox and Raichle, 2007; Herman et al., 2009; Pierro et al., 2012) and neural activity (Linkenkaer-Hansen et al., 2001; Ivanov et al., 2009; He, 2014). Scale-free dynamics is a hallmark of *complexity* viewed as an emergent property of biological systems composed of numerous elements with a network of stochastic (typically weak) connections amongst them (Csermely, 2006). Several human studies investigated the scale-free phenomenon of functional brain imaging signals by using mono-(Eke and Hermán, 1999; Thurner et al., 2003; Maxim et al., 2005; Eke et al., 2006; Khoa and Nakagawa, 2008; Bullmore et al., 2009; He et al., 2010; He, 2011; Herman et al., 2011) and multifractal analysis (Shimizu et al., 2004; Wink et al., 2008; Ciuciu et al., 2012; Quang Dang Khoa and Van Toi, 2012). Monofractal analysis reveals *global*, long-range correlation (LRC) structuring in terms of the influence of past events in the process on future ones (Bassingthwaighte et al., 1994; Eke et al., 2000, 2002). Multifractal analysis yields a distribution of fractality measures (Barabási et al., 1991; Stanley et al., 1999; Kantelhardt et al., 2002; Ihlen and Vereijken, 2010; Mukli et al., 2015) that enables a more detailed characterization of *local* temporal scaling behavior provided that fluctuations at wide range of temporal scales are sufficiently represented in the sampled physiological process (Eke et al., 2012). The estimation of these *complexity parameters* is essentially based on a power-law model fitted to the appropriate statistics of the data, which is reliable only if sample size is large enough [at the order of hundreds, Eke et al., 2002; Clauset et al., 2009]. Such statistics usually shows power-law scaling—indicating LRC—within a bounded interval of temporal scales usually termed as scaling range (SR; Caccia et al., 1997). In addition to the finite representation of the dynamics the lower and upper boundary of SR are determined by the signal genesis of the underlying physiological process. Nevertheless, numerous examples of empirical data exhibit multiple SR indicating *multimodal scaling*, see examples cited in Nagy et al. (2017). Multimodality has also been of concern in case of cerebral hemodynamics and typically present itself with two (case of bimodality) or even more apparent SRs in which the statistical measure of fractal analysis scales with a different exponent (Nagy et al., 2017).

Application of a possible bimodal scale-free model on resting-state hemodynamic signals requires a measurement technology, which assures that the process is sampled at high enough rate in long enough records. Near-infrared spectroscopy (NIRS) is an emergent imaging technology which readily captures cerebrocortical resting-state hemodynamic fluctuations at a cm spatial resolution and at high sampling frequency with no particular limitations on signal length (Jöbsis, 1977; Chance et al., 2007; Fox and Raichle, 2007). In case of continuous wave near-infrared spectroscopy (cwNIRS), the measured intensity signals are determined by the relative tissue concentration of total hemoglobin (HbT) and its constituents: oxy- and deoxyhemoglobin (HbO and HbR, respectively; Cope et al., 1988).

By now the physiological underpinnings of the functional NIRS (fNIRS) signal has been elucidated (Jöbsis, 1977; Kocsis et al., 2006a; Tachtsidis et al., 2008). As to its dynamics, oscillations of cerebral hemodynamics has been characterized by spectral analysis of NIRS signals (Elwell et al., 1999). Monofractal pattern of NIRS spectral data was first reported by Eke and Herman for the human brain cortex (Eke and Hermán, 1999). Later, multifractal properties of fNIRS were also demonstrated (Quang Dang Khoa and Van Toi, 2012). These pioneering reports understandably focused on signal analysis and not making an attempt to identify the underlying physiological mechanisms shaping the observed complex patterns. As to the nature of local hemodynamic fluctuations, they are primarily elicited by neural activity via neurovascular coupling (NVC; Devor et al., 2003; Drake and Iadecola, 2007) but the hemodynamic response is also modulated by endothelial mechanism (Li et al., 2013; Chen et al., 2014). In addition, systemic hemodynamic effects should be considered (Yamada et al., 2012; Scholkmann et al., 2014) for an enhanced interpretation of results obtained from resting-state records from subjects with similar age. Apart from non-biological noise and motion artifacts, resting-state NIRS (rsNIRS) signal bears the fingerprint about systemic hemodynamics such as cardiac cycle and respiration (Tian

Abbreviations: BOLD, blood oxygen level dependent; CBSI, correlation based signal improvement; ΔH_{15}, the difference between the $H(-15)$ and $H(15)$ values; ^{f}, measure describing the fast signal component dominating over the low-frequency region; FMF, focus-based multifractal formalism (an approach using focus-based regression scheme); *fwhm*, full-width of the singularity spectrum, $D(h)$, at half of its maximum; h_{max}, maximal Hölder exponent at which singularity strength (D) is equal to 1; LRC, long-range correlation; N_s, number of non-overlapping segments; PSD, power spectral density; rsNIRS, resting-state near-infrared spectroscopy; $r_\sigma(s)$, scale-wise fractal correlation coefficient; ^{s}, measure describing the slow signal component dominant over the lower scales; s', scaling boundary (possible breakpoint); ${}^{X}S_\sigma(q, s)$, scaling function value at a given moment order (q) and temporal scale (s), calculated from signal X, with σ as measure; $\ln({}^{X}\hat{S}(N))$, the focus of the scaling function for signal X; SR, scaling range; SSC, signal summation conversion (method); SSE, sum of squared error; v, the order of non-overlapping segments $v = 1, \ldots, N_s$; (V)LFO, (very) low-frequency oscillation.

et al., 2009; Li et al., 2013). Separation of the functional and the systemic components became of considerable interest and various approaches have been developed to address this issue (Scholkmann et al., 2014). Correlation between the fluctuations of oxy- and deoxyhemoglobin concentration is the basis of signal improvement presented by Cui et al. (2010) and the technique proposed by Yamada et al. (2012). Under certain assumptions—that usually hold in resting state, neural activity renders the relationship between HbO and HbR fluctuations more anticorrelated while fluctuations of systemic origin in the resting state (Cui et al., 2010; Scholkmann et al., 2014) has a correlated influence on hemoglobin chromophores.

The nonstationary fractal character of HbT (Eke et al., 2006) implies that its constituents, HbO, and HbR, also exhibit non-stationary dynamics. Consequently, their relationship should be explored in terms of a non-stationary characterization of correlation. Therefore, the HbO-HbR relationship was studied with the aid of scale-wise fractal cross-correlation coefficient and a novel adaptation of multifractal covariance analysis. The former is essentially a measure applicable to nonstationary time series building on the correlation of scale-wise mean variances obtained separately for HbO and HbR signal (Podobnik and Stanley, 2008; Zhou, 2008), while the latter is a multifractal approach examining the scaling properties—and its moments of various order—of HbO-HbR covariance similarly to the analyses described in Refs (Kristoufek, 2011; Jiang et al., 2016; Zhao et al., 2017).

It has been shown that aging (Goldberger et al., 2002; Lipsitz, 2003) and various diseases (Ivanov et al., 1999; Goldberger et al., 2002; Maxim et al., 2005) affect complexity parameters and the impact of other factors, such as gender (Ni et al., 2014), have also been recognized. This study contributes to this accumulating body of knowledge on the influence of aging on the complexity of physiological processes. In general, the contraction of homeodynamic space is an essential attribute of an aging biological system meaning that the dynamics of physiological processes in an elderly person is typically confined to a restricted state space (Rattan, 2014). Taking the cardiovascular system as an example the well-known dependence of heart rate variability (Beckers et al., 2006; Vandeput et al., 2012) on age can be attributed to a decline in autonomic modulation (Nunes Amaral et al., 2001; Lipsitz, 2003; Tulppo et al., 2005; Silva et al., 2017) reducing the adaptational reserve of regulatory mechanisms (Goldberger et al., 2002). Such reports on aging and altered complexity parameters are typically based on demonstrating coincidences, while there is a palpable need to establish a causal relationship for the changing complexity.

Accordingly, our goal was to provide plausible explanation for the physiological mechanism of observed age-related alterations based on parameters of complexity obtained from measures of brain hemodynamics captured by rsNIRS. Firstly, the measured signals were evaluated for the presence of true LRC-type multifractality. Multifractal parameters obtained for young and elderly volunteers were compared to assess the impact of aging on the complexity of cerebral hemodynamics. In addition, we extended our analysis incorporating the oxy- and deoxyhemoglobin signals in order to explore the age-dependent alterations in their relationship. The influence of age was characterized by exploring the strength of causal link between these measures of the coupled fluctuations of oxy- and deoxyhemoglobin and multifractal parameters of cerebral hemodynamics.

METHODS

Extended records of fluctuating rsNIRS signals from the human brain prefrontal cortex (PFC) analyzed for their multifractality in this work have been collected in a previous study of the group reporting on the monofractal serial correlation in these signals (Eke et al., 2006).

Near Infrared Spectroscopy

According to the principle of cwNIRS, backscattered light intensities were measured at wavelengths of 775, 830, 849, and 907 nm by a NIRO 500 Cerebral Oxygen Monitor (Hamamatsu Photonics, Hersching, Germany), a single-channel instrument. The mean penetration depth of near infrared photons for the 4 cm interoptode distance of this device can be estimated at approximately 2 cm (Firbank et al., 1998), thus our NIRS optode sampled the brain cortex (Chance, 1994). Based on the modified Beer-Lambert law (Kocsis et al., 2006b) the relative tissue concentrations of HbO and HbR were calculated along with HbT obtained as their sum. While the fluctuation of HbT reflects on cerebral blood volume (CBV) dynamics, that of the other two chromophores and their relationship are dependent on oxygenation, too.

Data Collection

HbO, HbR, and HbT data were dumped via the RS232 port of the NIRO instrument into a computer file at a rate of 2 Hz. Extended records of HbO, HbR, and HbT samples were created and processed for each subject in length of $N = 2^{14}$ proven to be adequate for fractal analysis (Eke et al., 2002). The source and detector fibers were secured in a rubber pad. The optode was mounted just under the hairline over the forehead. The cranium was shielded from ambient light. Instrument noise was determined by placing the optode over a slab of "mock" brain, whose scattering ($\mu_s = 10.96$ 1/mm) and absorption ($\mu_a = 0.099$ 1/mm) coefficients were matched to that of the human brain (courtesy of Prof. Britton Chance, University of Pennsylvania, Philadelphia, U.S.A.). The power of instrument noise was found negligible when compared to the power of resting-state fluctuations *in vivo* (Eke et al., 2006).

Subjects

Following approval by the Local Research Ethics Committee of Semmelweis University and having obtained informed written consent, 52 healthy volunteers with no neurological disorders (28 women, 24 men) participated in the study. To evaluate the effect of age and gender, subjects were assigned into groups of young females (Y_F, $n = 9$, age<45 years), young males (Y_M, $n = 13$, age<45 years) elderly females (E_F, $n = 19$, age≥45

years) and elderly males (E_M, $n = 10$, age≥45 years). The rsNIRS measurements were carried out in a comfortable sitting position in a session slightly exceeding 2.5 h as previously described in (Eke et al., 2006).

Data Preprocessing

Multifractal analyses were performed on raw signals and following correlation-based signal improvement (CBSI; Cui et al., 2010; Scholkmann et al., 2014), the latter designed to remove correlated (systemic) influences (e.g., head movement). Specifically, this preprocessing step incorporate a standard deviation ratio of HbO and HbR that is used in their subsequent linear combination yielding: ${}^{CBSI}HbT = \frac{1}{2}\cdot\left(HbR - \left({}^{O}\sigma\,(N)/{}^{R}\sigma\,(N)\right)\cdot HbR\right) + \frac{1}{2}\cdot\left(HbO - \left({}^{R}\sigma\,(N)/{}^{O}\sigma\,(N)\right)\cdot HbO\right)$. The improved HbT signal is regarded as a representation of anticorrelated hemodynamics attributable to local hemodynamic influences and oxygen consumption accompanying neuronal activity.

Multifractal Analyses

Multifractal Scaling Analysis

Signal summation conversion (SSC) method

The multifractal scaling functions of HbT, HbO, and HbR were calculated by the multifractal SSC method (Mukli et al., 2015) as the basis of our approach to evaluate the multifractality of our bimodal rsNIRS signals (**Figure 1**). For detailed description of the MF-SSC method the reader is referred to Refs. (Mukli et al., 2015; Nagy et al., 2017). Briefly, multifractal SSC uses a measure depending on the temporal scale (s) of signal window—bridge-detrended variance $\sigma(s)$, see Ref. (Eke et al., 2000)—and a set of q-order statistical moments, to create corresponding moment-wise generalized variance profiles, $S_\sigma(q, s)$ of Equation 1, spanning across a range of temporal scales within the chosen analytical SR.

$$S_\sigma(q,s) = \left[\frac{1}{N_s}\sum_{v=1}^{N_s}\mu_v^q(s)\right]^{1/q} \propto s^{H(q)} \qquad (1)$$

Specifically, 60 logarithmically spaced time scales were chosen between $s_{min} = 16$ and $s_{max} = 8192$ for computing $\sigma_v(s)$ in each non-overlapping time window [$v = 1, 2, ..., N_s = \mathrm{int}(N/s)$] of cumulatively summed signal. The low temporal scales dominated by fast fluctuations with weak, non-fractal autocorrelation (Eke et al., 2006) were excluded and the fairly high scales (Nagy et al., 2017) with well-manifested scale-free processes were secured. The selected moment orders ranging from −15 to 15 were adequate[1] to capture both large- and small-variance dynamics in a fluctuating rsNIRS signal; the former being emphasized by variance profiles corresponding to positive moments, the latter by those corresponding to negative moments (Grech and Pamuła, 2012; Mukli et al., 2015). Please note that statistical estimates obtained at $q = 2$ obey rules of *linearity*, while in fact, those for $q \neq 2$ capture *non-linearity* in system dynamics (Gómez-Extremera et al., 2016; Bernaola-Galván et al., 2017).

[1] q takes all integer values in this interval.

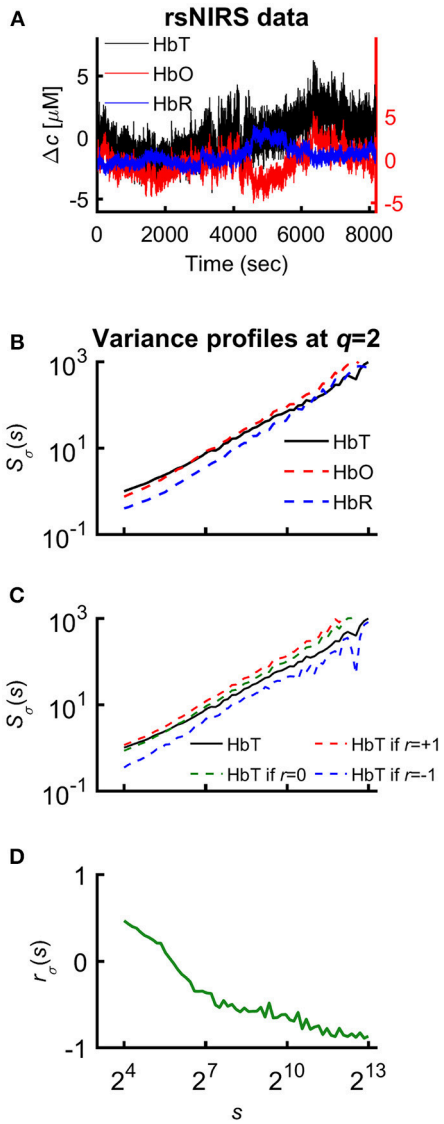

FIGURE 1 | Various representations of the measured NIRS signals. **(A)** Resting-state raw NIRS signal components. **(B)** Variance profiles of different signal components. **(C)** Variance profiles of HbT calculated at different set cross-correlation levels. **(D)** Fractal correlation coefficient between HbO and HbR as a function of scale. In this paper multifractal scaling function values are actually given by $S_\sigma(q, s)$ [or by $S_\sigma(s)$ for $q = 2$], where the subscript σ refers to the measure of the chosen multifractal method (SSC).

Relationship between variance profiles of hemoglobin chromophores

Since HbT = HbO+HbR, it is the generalized Bienaymé formula (Equation 2) which describes the relationship between their variance profiles[2]: ${}^{T}S_\sigma(2, s)$, ${}^{O}S_\sigma(2, s)$, and ${}^{R}S_\sigma(2, s)$ in an exact form[3] (Nagy et al., 2017).

[2] Different signal types (T – HbT; O – HbO; R – HbR; OR – relationship of oxy- and deoxyhemoglobin) are indicated by a left superscript to the variable of multifractal analysis.

[3] Note that the Bienaymé formula is not specific to fractal time series.

$$ {}^{T}S_{\sigma}(2,s)^{2} = {}^{O}S_{\sigma}(2,s)^{2} + {}^{R}S_{\sigma}(2,s)^{2} + 2r_{\sigma}(s)\cdot {}^{O}S_{\sigma}(2,s)\cdot {}^{R}S_{\sigma}(2,s). \quad (2) $$

The unknown factor is the scale-wise fractal correlation coefficient, $r_{\sigma}(s)$; all the others are scaling function values directly calculated from the measured signal.

Focus-Based Scaling-Range Adaptive Analyses

Focus-based multifractal analysis (FMF-SSC) were carried out (Mukli et al., 2015) to estimate the generalized Hurst exponent, $H(q)$, which is essentially a set of slopes of the scaling function profiles fitted in the analytical SR, as expressed by

$$ S_{\sigma}(q,s) \propto s^{H(q)}. \quad (3) $$

$H(q)$ describes the moment-wise or *global* distribution of fractal correlation (essentially that of the fractal dimension) in the signal, thereby generalizing $H(2)$, the usual outcome of monofractal time series analysis. Taking $H(q)$ as its input, the multifractal formalism (Frisch and Parisi, 1985; Barabási and Vicsek, 1991; Muzy et al., 1993; Eke et al., 2012) via the multiscaling exponent, $\tau(q)=qH(q)-1$, and Legendre transformation will yield $D(h)$, the *local* distribution of the fractal dimension or singularity strength, D, as a function of roughness or Hölder exponent, h.

$$ h = \frac{d\tau(q)}{dq}, \quad (4) $$

$$ D(h) = \inf_{q}\left(qh - \tau(q)\right). \quad (5) $$

Incorporating the focus—obtained as a fitted intersection of scaling function profiles at $s = N$–ensures monotonously decreasing $\hat{H}(q)$ and thus stable, uncorrupted $D(h)$. Enforcing the focus of scaling function, $\ln(\hat{S}_{\sigma}(N))$, when regressing for $\hat{H}(q)$ was recognized as a prerequisite to obtain stable results of multifractal analysis (Mukli et al., 2015).

In an attempt to find the best fitting model for the observed scaling functions we adapted the concept of bimodality originally described in the frequency domain (Eke et al., 2006). This pattern can be recognized as two scale-free processes separated by moment-wise breakpoint scales ($s'(q)$) (Nagy et al., 2017). The less correlated ("fast") component dominates the lower range of scales while a more correlated ("slow") component is characteristic in the higher scales (**Figure 2A**). A breakpoint-based bilinear regression model (denoted as moment-wise SR adaptive) was implemented as described in Ref. (Nagy et al., 2017). Briefly, it is an iterative process by estimating breakpoint scales that minimize sum of squared error (SSE) of the residuals for each and every moment as

$$ SSE(s'(q)) = \sum_{q=-15}^{15}\left[\sum_{s=s_{\min}}^{s'(q)}\left({}^{f}\widehat{H}(q)\cdot(\ln s - \ln N) + \ln {}^{f}\hat{S}_{\sigma}(N) - \ln S_{\sigma}(q,s)\right)^{2} + \left({}^{s}\widehat{H}(q)\cdot(\ln s - \ln N) + \ln {}^{s}\hat{S}_{\sigma}(N) - \ln S_{\sigma}(q,s)\right)^{2}\right], \quad (6) $$

where $\ln({}^{s}\hat{S}_{\sigma}(N))$ and $\ln({}^{f}\hat{S}_{\sigma}(N))$ are the moment-independent foci (**Figure 2B**) associated with the slow and fast components, respectively. ${}^{s}\hat{H}(q)$, ${}^{f}\hat{H}(q)$ are the slopes (**Figure 2C**) of the fitted two lines of regression[4] (i.e., the generalized Hurst exponent functions of the two components). This iteration thus adaptively yields the best segregation of scaling ranges. $\hat{H}(q)$ and $D(h)$ (**Figure 2D**) are obtained for the fast and the slow component, respectively.

We calculated global multifractal endpoint parameters to characterize the degree of autocorrelation [maximal Hölder exponent, $h_{\max}$ and monofractal Hurst exponent, $\hat{H}(2)$] and multifractality [$\Delta H_{15} = H(-15)$–$H(15)$, and full-width at half maximum (*fwhm*) of $D(h)$ (Wink et al., 2008; Grech and Pamuła, 2012)] in the measured cerebral hemodynamic signals as illustrated in lower panels of **Figure 2**.

Evaluating True Multifractality

Since multifractal tools—including FMF-SSC—readily produce seemingly realistic values for multifractal measures such as $D(h)$ even in the absence of true multifractality (Kantelhardt et al., 2002; Clauset et al., 2009; Grech and Pamuła, 2012); it is mandatory to evaluate our empirical signals in this regard using the following framework. Accordingly, because our FMF-SSC method always produces uncorrupted $D(h)$ irrespective whether the signal is a true multifractal or not, this property needs to be tested separately (**Figure A1**). Verification of true multifractality consists of three subsequent steps: (*i*) identifying general scale-free behavior with power spectral density (PSD) analysis, (*ii*) distinguishing true multifractality from multifractal noise, and (*iii*) determining the origin of the expressed multifractal scaling. Therefore, in these tests, true, long-range correlated multifractals are to be distinguished from processes lacking scale-free properties or not showing autocorrelation. Failing to pass in any of the aforementioned tests resulted in the exclusion of the subject in question from further analysis. Details of this framework are explained in the Appendix (**Supplementary Material**) and in Ref. (Racz et al., 2018).

Characterizing HbO-HbR Relationship

Scale-wise fractal cross-correlation coefficient

One approach to assess the relationship of HbO and HbR fluctuations is to calculate a measure of cross-correlation by using variance profiles. After rearrangement of Equation 2 it is possible to express $r_{\sigma}(s)$:

$$ r_{\sigma}(s) = \frac{{}^{T}S_{\sigma}(2,s)^{2} - {}^{O}S_{\sigma}(2,s)^{2} - {}^{R}S_{\sigma}(2,s)^{2}}{2\cdot {}^{O}S_{\sigma}(2,s)\cdot {}^{R}S_{\sigma}(2,s)}. \quad (7) $$

This measure indicates whether the fluctuations at a given scale are enhanced ($r_{\sigma}(s)>0$), diminished ($r_{\sigma}(s)<0$) by coupling HbO and HbR signal or their relationship is insensitive to coupling between them ($r_{\sigma}(s) = 0$).

The fractal cross-correlation analysis yielding $r_{\sigma}(s)$ is strikingly similar—in terms of calculation steps and order—to the detrended cross correlation analysis, the major difference of these methods concerns their measure (Podobnik and

[4]Parameters obtianed directly from multifractal regression analysis are denoted as estimates with a hat: $H(q)$ and $\ln(\hat{S}_{\sigma}(N))$.

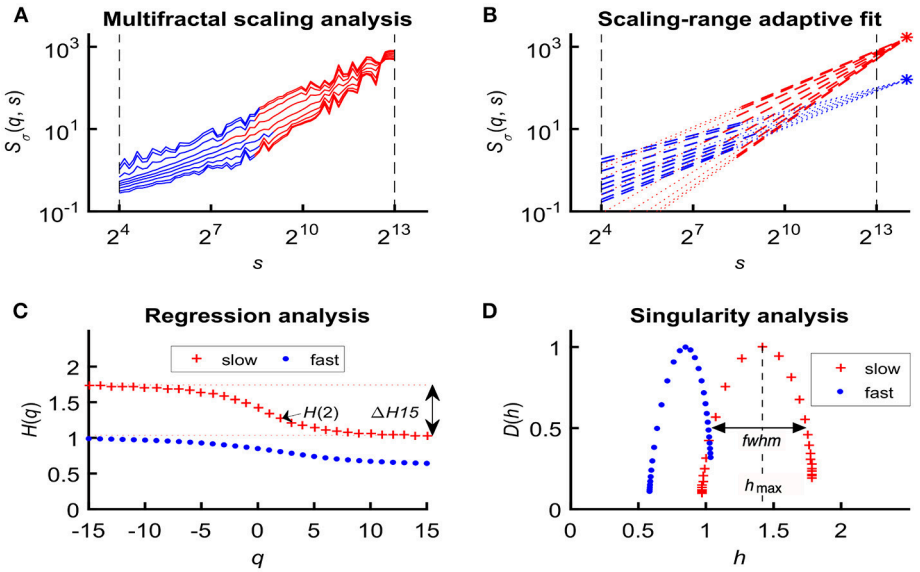

FIGURE 2 | Steps of bimodal multifractal SSC analysis. **(A)** Scaling function of SSC as moment-wise generalization of variance profiles. Separate components are marked in blue (fast) and red (slow). **(B)** The sets of power-law functions fitted separately for the two components with focus-based regression. **(C)** Generalized Hurst exponent functions, $H(q)$s of the two components as functions of moment order q. The focus point and $H(q)$ for both components (f, fast; s, slow) were iterated for finding the scale with minimum SSE($s'(q)$) as the true breakpoint at a given moment, which process finally yields ln $({}^{s}\hat{S}_{\sigma}(N))$, ln $({}^{f}\hat{S}_{\sigma}(N))$, ${}^{s}\hat{H}(q)$, and ${}^{f}\hat{H}(q)$ with the best fit. **(D)** Singularity spectra of the two components. *Multifractal endpoint parameters*: the highest singularity strength ($D = 1$) is associated with the maximal Hölder exponent (h_{max}), which usually correlates well with $H(2)$, a measure of global LRC in the signal. Distribution of local scale-free behavior is captured in $\Delta H_{15} = H(-15) - H(15)$ and in full-width at half maximum (*fwhm*) of $D(h)$ respectively, reflecting degree of multifractality.

Stanley, 2008). The cited approach uses fluctuation while ours calculates bridge-detrended variance to assess correlation of coupled non-stationary time series. When comparing the above scale-wise approaches with the standard means of calculating cross-correlation (i.e., Pearson and Spearman), the first major difference is that the prerequisite of stationarity applies to the latter methods. Furthermore, the sequence of calculation steps is critical, too: because when the standard cross-correlation is calculated it is followed by a step of averaging effectively abolishing the scale-wise information. It is worth of noting that Spearman proved a more robust standard measure of correlation than the Pearson coefficient as the latter assumes not only stationarity but linearity, too (Zimeo Morais et al., 2018).

Multifractal covariance analysis

The other approach is based on the extension of FMF-SSC in order to analyze the scaling of long-range cross-correlation. This method assesses the multifractality emerging genuinely from coupled oxy- and deoxyhemoglobin fluctuations. Scale- and moment-wise bridge-detrended covariances ($_{Cov}$) were calculated of HbO and HbR signals to yield an estimate of bivariate generalized Hurst exponent function, ${}^{OR}H(q)$.

$$ {}^{OR}S_{Cov}(q,s) = \left[\frac{1}{N_s}\sum_{v=1}^{N_s} {}^{OR}|Cov|_v^q(s)\right]^{1/q} \propto s^{{}^{OR}H(q)} \qquad (8) $$

Now applying Equations 3–5 yields the corresponding singularity spectrum and multifractal endpoint parameters. Covariance truly scales only if the ${}^{OR}\hat{H}(q)$ function differs from the average of ${}^{R}\hat{H}(q)$ and ${}^{O}\hat{H}(q)$. Therefore this comparison must be carried out after obtaining the distribution of scaling exponents and output parameters of multifractal analysis. Prior to that, moment-wise bimodal regression analysis had been performed on the q-wise (generalized) variance profiles of HbO, HbR, and HbT and on the HbO-HbR covariance profile in the same manner.

Descriptive Statistical Analyses

Normal distributions in each independent sample were checked by Shapiro-Wilk's test. Difference between group means or medians were considered significant in case of $p < \alpha_s$, $\alpha_s = 0.05$ (level of significance). Homogeneity of variances was confirmed by Levene's test.

Assessing the Effect of Age and Gender

Two-way univariate ANOVA were performed treating multifractal endpoint parameters and $r_\sigma(s)$ as dependent variables and assuming that there was an interaction between age and gender (categorical factors). Most of the results presented in this paper are based on the output of two-way ANOVA with Tukey's *post hoc* test. Had the prerequisites of ANOVA been not met, group means were compared with two-sample t-test (with Welch's correction for inhomogeneous variances in case of significant Levene's test). In the absence of normal distribution, the comparison

of group medians was performed by Mann-Whitney U test.

Multivariate ANOVA (MANOVA) was performed to detect age- and gender-related differences between direct descriptors of the scaling function: ${}^{s}\hat{H}(2)$, ${}^{f}\hat{H}(2)$, $\ln({}^{s}\hat{S}_{\sigma}(N))$, $\ln({}^{f}\hat{S}_{\sigma}(N))$. As changes occurring by coincidence is of concern, MANOVA tests were used taking $\hat{H}(2)$, $\ln({}^{s}\hat{S}_{\sigma}(N))$, $\ln({}^{f}\hat{S}_{\sigma}(N))$ and $r_{\sigma}(s)$ (at scales corresponding to the slow component s = 4,344, 4,828, 5,367, and 5,965) as dependent variables. The $p < 0.05$ of Wilks's test suggests that the same subjects are responsible for each of the between-group differences. Finally, examining the degree of correlation of dependent variables (expressed as r^2) enables to identify the most relevant endpoint parameters of multifractal analysis.

Explaining the Variance Profiles of HbT

In order to identify a link between the altered scale-wise fractal cross-correlation coefficient and the altered multifractal endpoint parameters, the influence of $r_{\sigma}(s)$ as an independent variable were evaluated on ${}^{T}S_{\sigma}(2, s)$ in a general linear model (GLM). The Bienaymé formula expresses an explicit relationship between ${}^{T}S_{\sigma}(2, s)$ and the scaling function values obtained for HbO, HbR, and $r_{\sigma}(s)$ (Equation 7). Accordingly, the variability of ${}^{T}S_{\sigma}(2, s)$ were explained with the aid of multiple regression tests that were performed for each temporal scales. The regressors of this model were ${}^{O}S_{\sigma}(2, s)$, ${}^{R}S_{\sigma}(2, s)$, and $r_{\sigma}(s)$ but categorical predictors (age and gender) were not included.

Subsequently, – in addition to the regressors of the previously described test—we took into account the effect of age and gender by applying scale-wise covariance analysis (AnCova). Specifically, age and gender were treated as categorical factors and ${}^{O}S_{\sigma}(2, s)$, ${}^{R}S_{\sigma}(2, s)$, and $r_{\sigma}(s)$ as covariates. Before AnCova, homogeneity of slopes model was evaluated for each s, significant result of this test means that AnCova is inapplicable due to an interaction between categorical predictors and covariates. In these cases the separate slopes model was used which include these interaction terms.

Software

For a more detailed description of our analytical flowchart as a guide for the FMF-SSC analysis, see (Eke et al., 2000, 2012; Mukli et al., 2015; Nagy et al., 2017). The above aspects of multifractal analyses of rsNIRS time series have been implemented in Matlab 2012 (The MathWorks, Inc., Natick, MA, U.S.A.) by custom scripts written by the authors based on the recently published "MultiFracTool" software (Mukli et al., 2015; Nagy et al., 2017; Racz et al., 2018). The toolbox can be requested from the corresponding author. Statistical analyses were performed with StatSoft Statistica 13.2.

RESULTS

The Presence of True Bimodal Multifractality

All measured signals showed an apparent bimodal scaling function. True multifractality was confirmed in 44 subjects, two of them with an unacceptable fit of the bimodal model. For further details, see Appendix in **Supplementary Material**.

Impact of Age-and Gender on Multifractal Endpoint Parameters

In case of raw HbT signals, the degree of autocorrelation for the slow component, marked by ${}^{s}\hat{H}(2)$, significantly increased with age unlike for the fast component (**Figure 3A**). Conversely, the neural component obtained with CBSI significantly decreased with age for the fast, but not for the slow component (**Figure 3B**). In the elderly group, the $h_{\max}$ of the slow component of the raw signal, ${}^{s}h_{\max}$, was found increased (**Figure 3C**), while it did not change with the CBSI-treated signal. These changes were the opposite—similarly to Hurst exponent—regarding ${}^{f}h_{\max}$ in the young group (**Figure 3D**). Regarding the foci, for the raw HbT signals they were statistically the same in both age groups (**Figure 3E**), while for the fast component of the CBSI-enhanced HbT signal they were lower in elderly subjects (**Figure 3F**). Given that the (SD(HbO)/SD(HbR) ratios—the key element in CBSI model—did not differ between young and elderly groups ($p = 0.543$), the above significant differences should be regarded as real.

Age-related differences remained significant when the slow and fast components were compared. Specifically, component-wise contrast – defined as $\ln({}^{s}\hat{S}_{\sigma}(N))/\ln({}^{f}\hat{S}_{\sigma}(N))$—turned out to be significantly different between the age groups ($p = 0.03$). A concomitant—albeit non-significant—decrease characterizing the fast component ($p = 0.405$) for focus contributed to an overall increased ratio of foci ($p = 0.067$).

Comparing the multifractal parameters of cerebral hemodynamic fluctuations of female and male subjects, the only significant difference was observed for their HbO slow component. Incorporating age groups rendered the gender-related differences non-significant.

In order to prove that the significant differences in endpoint parameters seen in **Figure 3** attribute to alterations in a single subject, endpoint parameters related to slow and fast component were statistically evaluated in combination as dependent variables in multivariate analysis. When scale-free endpoint parameters of the same kind [$\hat{H}(2)$, $h_{\max}$] were combined, MANOVA revealed a strong correlation ($r^2 > 0.7$). Furthermore, significant multifractal endpoint parameters of slow component of raw HbT and fast component of CBSI HbT showed joint significance in a multivariate analysis ($p = 0.045$, Wilk's test) suggesting the coincident change of both components. Taken it together, these findings indicate that the observed alterations in the multifractal endpoint parameters resulted from subject-wise aging. As to the key geometrical parameters of the multifractal scaling functions, p-values obtained from Wilk's test indicated an overall non-significant influence of age. Of note the two main estimates of the analysis – $\hat{H}(2)$ and $\ln(\hat{S}_{\sigma}(N)$ – showed positive correlation for the fast component of the CBSI-pretreated ($r^2 = 0.46$) and the slow component of the raw HbT signal ($r^2 = 0.58$). The p-values of the statistical analyses are summarized **Table 1**.

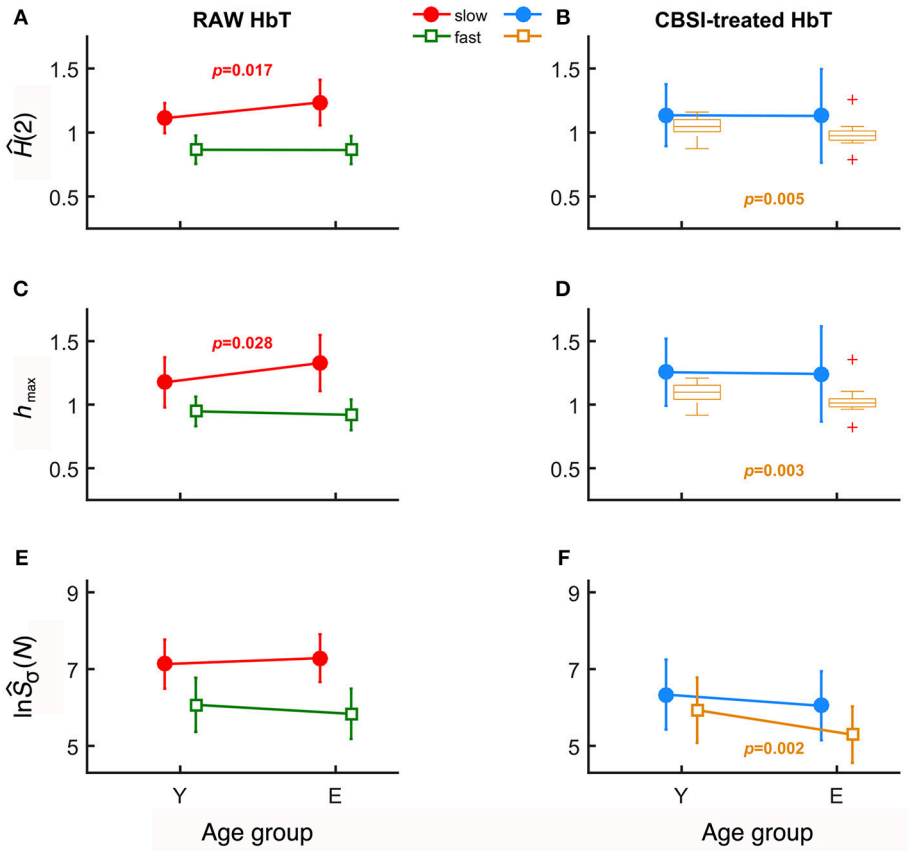

FIGURE 3 | Results of univariate statistical analysis of multifractal endpoint parameters. $\hat{H}(2)$ of slow and fast components in the two age groups calculated from raw **(A)** and on CBSI-pretreated **(B)** HbT signals. h_{max} obtained from raw **(C)** and CBSI-treated **(D)** HbT signals. Focus of raw **(E)** and CBSI-pretreated **(F)** HbT signals. Recall that the raw HbT signal represents neuronal and non-neuronal events combined, while the CBSI-pretreated signal is a enhanced representation of the underlying neurodynamics. Accordingly, the fact that we found significant differences in the slow component for the raw HbT signal and in the fast component for the CBSI-pretreated signals identifies the slow component emerging dominantly from vascular events, while the fast component attributed mainly to neurodynamics.

Influence of Age and Gender on the HbO-HbR Relationship

Scale-Wise Fractal Cross-Correlation

The mean fractal scale-wise cross-correlation coefficient was found higher at all scales in the elderly group (**Figure 4A**). Importantly, this decrease in $\overline{r_\sigma(s)}$was more pronounced in young participants at higher values of s achieving significance (two-way ANOVA, confirmed by Tukey's *post-hoc* test) at a cluster of the corresponding high temporal scales (see the probability profile on **Figure 4A**). Based on this parameter calculated at these large scales, the oxy- and deoxyhemoglobin fluctuations are uncorrelated (random) among the elderly and were found anticorrelated in the young group. MANOVA revealed a statistical coincidence between the age-related increase in $r_\sigma(s)$ at specific high scales (corresponding to 2,172, 2,414, 2,683, and 2,982 s) and the same alteration observed for each multifractal endpoint parameters [${}^{s}h_{max}$, ${}^{s}\hat{H}(2)$ of the raw HbT and ${}^{f}h_{max}$, ${}^{f}\hat{H}(2)$ of CBSI-treated HbT]. In addition, concerning $r_\sigma(s)$ and ${}^{T}S_\sigma(2,s)$ as dependent variables their close relationship specifically appears at some of these aforementioned temporal scales. Since $r_\sigma(s)$ is determined by the dynamics of oxygen delivery and its extraction in the brain (i.e., supply and demand), these are key results for discussing the impact of aging on cerebral oxygenation.

Multifractal Covariance

In contrast to scale-wise fractal correlation analysis when covariance is normalized by $\sigma(s)$, the multifractal covariance analysis allows for a moment-wise characterization of the scaling properties of HbO-HbR coupling extending also for $q \neq 2$. This method revealed a statistically significant age-related difference concerning the fast component [see ${}^{f}h_{max}$ and $\ln({}^{f}\hat{S}_{Cov}(N))$, **Figure 4B**], which is markedly correlated with ${}^{f}h_{max}$ ($r^2 = 0.55$) and $\ln({}^{f}\hat{S}_{Cov}(N))$ ($r^2 = 0.69$) obtained for CBSI-pretreated HbT signals across age groups.

Power-law scaling of the multifractal HbO-HbR covariance function may either originate from the independent scale-free variance profiles of HbO and HbR or as from the coupled fluctuations of the two. In case of the fast component, the significant contribution from the latter is confirmed for the whole

TABLE 1 | Significance of gender-related differences (*p*-values).

	Parameter	HbO–raw	HbR–raw	HbT–raw	HbT–CBSI	HbO vs. HbR
Slow component	$\hat{H}(2)$	0.938	0.086	0.559	0.437	0.673
	h_{max}	0.600	0.273	0.849	0.416	0.656
	ΔH_{15}	0.828	0.671	0.305	0.591	0.852
	fwhm	0.823	0.731	0.456	0.581	0.861
	$\ln({}^{s}\hat{S}_{\sigma}(N))$	0.408	0.539	0.273	0.296	0.494
Fast component	$\hat{H}(2)$	0.845	0.442	0.503	0.205	0.378
	h_{max}	0.115	0.060	0.140	0.141	0.049
	ΔH_{15}	0.028	0.189	0.196	0.066	0.140
	fwhm	0.014	0.220	0.247	0.071	0.138
	$\ln({}^{f}\hat{S}_{\sigma}(N))$	0.053	0.302	0.082	0.119	0.044

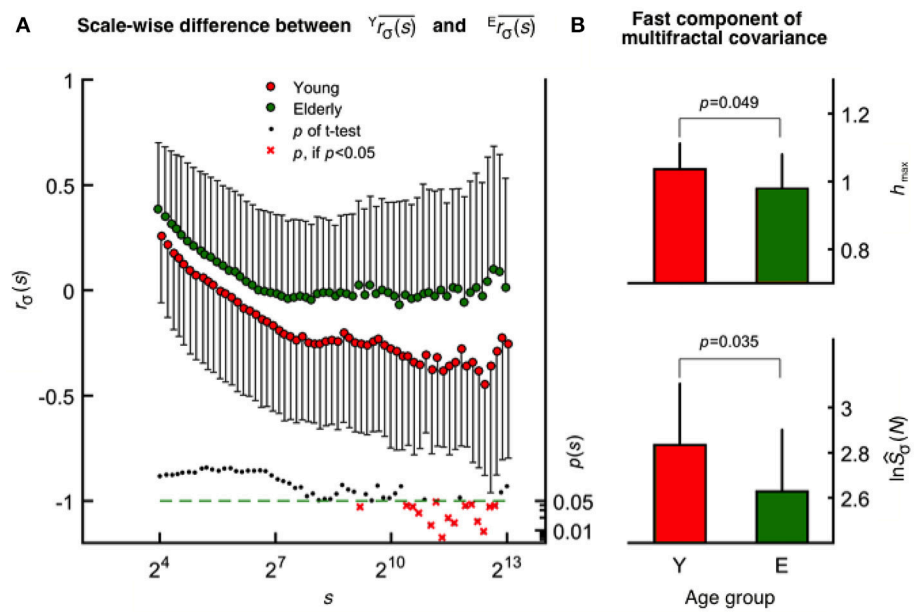

FIGURE 4 | Age-related differences revealed by scale-wise and scale-free analysis of oxy- and deoxyhemoglobin relationship. **(A)** Fractal correlation coefficient of HbO and HbR as functions of scale in the elderly (upper) and young (middle) groups with the corresponding *p*-values (lower). At s_{min}, these were above 0 and decreased gradually toward-1 as *s* approached s_{max} in both age groups. **(B)** Multifractal covariance of ${}^{f}h_{max}$ (upper) and $\ln({}^{f}\hat{S}_{\sigma}(N)$; lower) of the fast component in the young and elderly groups.

study population, given that ${}^{OR}H(q)$ derived from scale-wise covariances differed from $({}^{O}H(q)+{}^{R}H(q))/2$ both obtained at $q = 2$ ($p = 0.003$, Wilcoxon matched pairs test). Moreover this pattern was absent in the elderly group ($p = 0.116$), but not in the young group ($p = 0.006$).

The correlation (r^2) between dependent variables (i.e., multifractal endpoint parameters) captures the percentage of mutual variance of multifractal HbO-HbR covariance profiles and those obtained by SSC for the variance of CBSI-pretreated HbT signals. The percentage of mutual variance was the highest for $\ln({}^{f}\hat{S}_{Cov}(N))$ ($r^2 = 0.81$), and there was a strong relationship between their focus ratios ($r^2 = 0.72$). However, the correlation was moderate for ${}^{f}h_{max}$ ($r^2 = 0.56$). To sum it up, results of multifractal covariance analysis seems rather consistent with an altered fast component of the CBSI-pretreated HbT signals.

Significance of Fractal Scale-Wise Cross-Correlation

For the sake of comparison, we calculated fractal scale-wise cross-correlation and averaged running Pearson and Spearman correlation coefficients at the same time scales (**Figure 5**).

Variability of the HbT scaling function profiles at $q = 2$ and for all scales was explained as related to the independent variables–$r_{\sigma}(s)$, ${}^{O}S_{\sigma}(2, s)$, and ${}^{R}S_{\sigma}(2, s)$—based on the Bienaymé-formula given in Equation 2 (**Figure 6 top**). First, a series of multiple regression tests—not yet accounting for the effect of

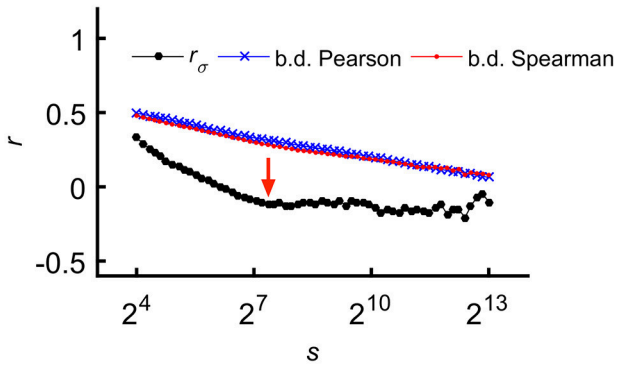

FIGURE 5 | Comparing means of different correlation coefficients between HbO and HbR calculated for all subjects. We explain the less correlated values observed for $r_\sigma(s)$ with the effect of calculation order on trends in the signal. In case of the mean Pearson- and Spearman-coefficients, detrending and averaging step come after calculating the correlation effectively neglecting the fundamentally scale-free character of the processes. However, considering fractal scale-wise correlation coefficient, this latter step is the last preceded by averaging of bridge-detrended variances at a given scale. Please also note the characteristic transient—indicated by red arrow—only appearing in $r_\sigma(s)$.

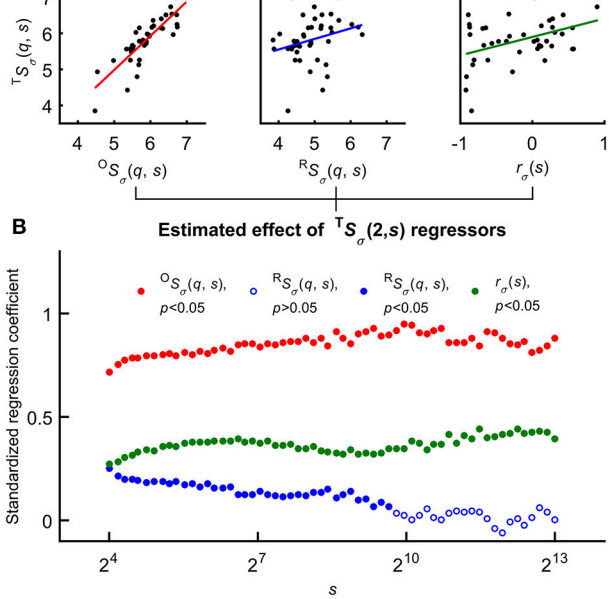

FIGURE 6 | Significance of multiple regression tests. **(A)** Scaling function value of HbT as a function of ${}^{O}S(q, s)$ (left), ${}^{R}S(q, s)$ (middle) and scale-wise fractal cross-correlation coefficient (right) acquired at equal scale and moment (exemplary case at $q = 2$ and $s = 4828$). **(B)** Regression coefficients and their significance (closed circle for cases of $p < 0.05$) related to scaling function values of HbO, HbR; and r_σ as functions of scale s. The estimated effect were significant for all s values in case of ${}^{O}S(q$ and $r_\sigma(s)$, and the lower standardized regression coefficients indicated the weak (not significant for all scales) effect of ${}^{R}S(q, s)$. For further details, see main text.

age and gender—were performed across all temporal scales that yielded positive correlation between each regressors and ${}^{T}S_\sigma(2, s)$. Importantly, the standardized regression coefficients proved to be significant for $r_\sigma(s)$ in case of all temporal scales. The highest estimated effects were observed in case of ${}^{O}S_\sigma(2, s)$ while this test revealed the weakest effect of ${}^{R}S_\sigma(2, s)$ being a non-significant regressor of ${}^{T}S_\sigma(2, s)$ at high scales (note the empty blue circles on **Figure 6 bottom**).

Subsequently gender and age were incorporated in the multiple regression model as categorical predictors to evaluate their influence on the p-value of correlation between the covariates and variance profiles related to CBV fluctuations (${}^{T}S_\sigma(2, s)$). In the GLM framework the appropriate choice was AnCova or separate slopes model depending on the prerequisites of each approach. Age in of itself turned out to be not determinant of scale-wise hemodynamic fluctuations captured by ${}^{T}S_\sigma(2, s)$. It is the scale-wise cross-correlation on the basis of which the impact of aging could be explained (**Table 2**). These results confirm the outcome of multiple regression analysis showing a significant and strong relationship between ${}^{T}S_\sigma(2, s)$ and ${}^{O}S_\sigma(2, s)$ and a less steep but still significant relationship between the dependent variable and the fractal scale-wise cross-correlation coefficient.

DISCUSSION

In this study, we found that hemodynamics in the human brain cortex captured by NIRS technology in most of the cases exhibited a bimodal multifractal scaling emerging from a range of low and high temporal scales (slow and fast components, respectively). We suggest relating the slow component of the raw HbT signal to dominantly vascular (vasogenic, i.e., non-neural) dynamics, while we consider the fast component primarily resulting from neurovascular coupling (i.e., neurogenic component). In order to demonstrate the impact of healthy aging, CBSI pretreatment of the raw HbT signal was necessary to enhance the neurovascular contribution in the fast component. Our main result is two-fold: first, we demonstrate that the vasogenic hemodynamics (CBV fluctuations proportional to HbT concentration changes) show increased long-range autocorrelation in the elderly group compared to the young group which is in agreement with what we had found previously applying monofractal analysis (${}^{low}PSD_{w,e}$ method[5]) within comparable scaling ranges (Eke et al., 2006). Second, we show that the fluctuations of the neural component are less correlated in the elderly group. This opposite influence of healthy aging on the slow vasogenic and the fast neurogenic fluctuations is consistent with an attenuated NVC. In support of this notion, we evidence that age-dependent alterations in HbO-HbR relationship is a manifestation of altered neurovascular coupling and also a determinant of scaling properties of CBV dynamics. Specifically, in *in silico* experiments we substantiated

[5]low – right half (high frequencies) of the spectrum is excluded, w – windowing, e – endmatching.

TABLE 2 | Homogeneity of Slopes Model/Separate Slopes Model/Covariance analysis results.

Effect	Significance of the effect
Gender or Age (*per se*)	Non-significant for any scale
Gender or Age (with interaction)	*Significant for 444 sec (Gender x Age x* $^{O}S_{\sigma}$ *x* $^{R}S_{\sigma}$*), Significant for 1758 sec (see below)*
$^{O}S_{\sigma}$ (*per se*)	*Significant for all scales*
$^{R}S_{\sigma}$ (*per se*)	*Significant for time scales between 8 and 400 sec*, non-significant for all time scales above 400 sec
$^{O}S_{\sigma}$ or $^{R}S_{\sigma}$ (with interaction)	*Significant for 444 sec (see above), significant for 610 sec (*$^{O}S_{\sigma}$ *x* $^{R}S_{\sigma}$ *x* r_{σ}*), significant for 1758 sec (see below)*
r_{σ} (*per se*)	Significant for all scales
r_{σ} (with interaction)	*Significant for 444 sec (see above), significant for 1758 sec (for all interactions, with the exception of Gender x* r_{σ}*)*

Interaction effects are denoted as "x".

that (i) a decreased correlation in neurogenic fluctuations is attributed to decreased incoming signaling, (ii) HbO-HbR relationship became more correlated due to aging either as a result of decreased incoming signaling concomitant to lesser hemodynamic response or from increased vascular stiffening. These alterations do indicate that linear CBV dynamics is susceptible to aging. In contrast, non-linear CBV dynamics is spared by aging as demonstrated in unaltered degree of multifractality.

Multifractality of cerebral hemodynamics has been investigated extensively in case of blood oxygen level dependent (BOLD) signals using functional magnetic resonance imaging (fMRI). The influence of brain activity was demonstrated in the pioneering work of Shimizu et al. (2004). Later, findings on the topology of multifractal parameters and methodological refinements were reported (Wink et al., 2008; Ciuciu et al., 2012). On data from a publicly available imaging repository (Biswal et al., 2010), the effect of age and gender on multifractal spectrum was shown for resting-state fMRI-BOLD signals (Ni et al., 2014). While rsNIRS signals have been made subject to multifractal analysis in an earlier feasibility study (Dzung, 2010; Quang Dang Khoa and Van Toi, 2012), our study—to the best of our knowledge—is the first reporting on it elucidating some of the key underlying mechanisms using a scrutinized dataset with proven true multifractality.

Multifractal CBV Dynamics

CBV dynamics in the human brain cortex was shown to follow a complex, scale-free temporal pattern in the frequency domain that could be captured in the $1/f^{\beta}$ model, where β is spectral index (Eke et al., 2006). The variance profile at $q = 2$ is analogous to the power spectrum, thus their apparent similarity can be readily shown (**Figure 7**). The estimated β obtained by $^{low}PSD_{w,e}$ method is directly related to $\hat{H}(2)$, given the explicit relation of $H(2)=(\beta+1)/2$ (Eke et al., 2000). In fact, the power spectrum is equivalent to the Fourier transform of the signal's autocorrelation function according to Wiener-Khinchin theorem (He et al., 2010)[6]. Since its decay follows a power law with $2\hat{H}(2)-1$ as its exponent, $\hat{H}(2)$ and $\hat{\beta}$ are interpreted as equivalent measures of LRC in the fractional Gaussian noise / fractional Brownian motion framework (Eke et al., 2002).

It should be recalled that Fourier transform builds on independency of frequency components. As multifractality can emerge from interactions between multiple time scales (Ihlen and Vereijken, 2010), it cannot be captured in the power spectrum alone. Nevertheless, its presence still could be detected in the form of phase-amplitude coupling [nested frequency, see Ref. (He et al., 2010)]. Thus capturing multifractality in the time domain can reveal the underlying multiplicative interactions between the temporal scales of the observation with ΔH_{15} and *fwhm* as the measures of these cross-scale interactions (Ihlen and Vereijken, 2010).

Separation of Neurogenic and Vasogenic Multifractal Dynamics: CBSI-Pretreatment

In pursuit of the physiological origin of hemodynamic fluctuations, the analyses were performed both on raw and CBSI-pretreated (Cui et al., 2010) data. In addition, we carried out *in silico* experiments to substantiate the need of this preprocessing step to identify components dominated by vasogenic and neurogenic influences, respectively (see **Supplementary Material**). CBSI method builds on the assumption that maximally correlated fluctuations of HbO and HbR are not related to neural activity. Given our recent demonstration of CBSI pretreatment enhancing the neuronal component in the signal (Racz et al., 2017) our two-teared approach of signal processing allows for a distinction between influences of neuronal and non-neuronal nature in this study; aspects of particular interest in the aging process. Accordingly, the age-related differences of the calculated multifractal measures revealed for the fast component of the pretreated signal should reflect altered neurogenic fluctuations. Vice versa, we found that the significant age-related differences in the multifractal indices obtained for the slow component of raw NIRS signals disappeared after applying CBSI. This indicated that the slow component was non-neural, referred to as vasogenic.

Some authors pointed out specific limitations of CBSI to isolate the neural component in the signal in fNIRS studies using various stimulus response paradigms (Scholkmann et al., 2014). Although the neural activity readily and always induces anticorrelated dynamics in HbO and HbR—as postulated in CBSI –, the response to a specific task may elicit systemic confounding effects, too. In this regard, CBSI cannot be considered to be immune to global effects (Tachtsidis et al., 2008). Nevertheless, as we present results based on the analysis of resting-state NIRS observations we do not need to deal with such confounding influences in task.

In principle, we could not *a priori* exclude that CBSI-pretreatment would not distort the signal. The formulation of

[6]Since Wiener-Khinchin theorem only applies to wide-sense stationary processes, the autocorrelation function of the increment process is considered according to the fGn6fBm framework.

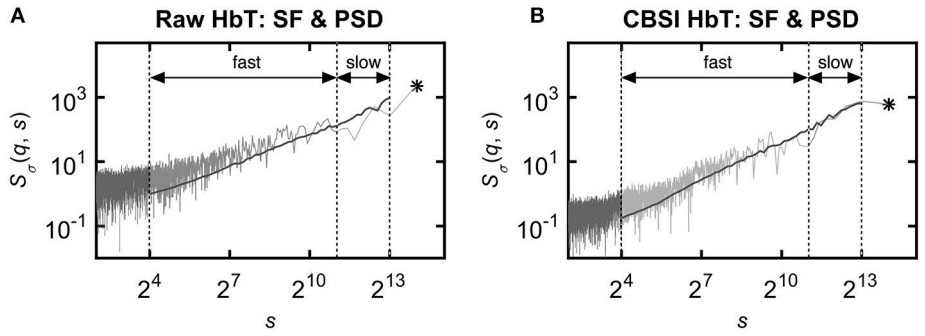

FIGURE 7 | Relationship between power spectrum and scaling function profiles obtained by the FMF-SSC method. Although multifractal analyses were performed in the time domain, its design and results can be interpreted in the frequency domain as well owing to the explicit relationship between representation of dynamics in the temporal and the spectral domains both for the raw **(A)** and CBSI-pretreated **(B)** signal. The ordinate shows both frequency and temporal scale. It is the variance profile at $q = 2$ that corresponds well with the mean spectral estimates. The range of spectral estimates fall in between $S(q, s)$ profiles for $q = 15$ and $q = -15$. The fractal scaling range emerges from the (non-fractal) noise (of biological origin) dominating the low temporal scales. It contains a breakpoint, which separates $S(2, s)$ into a slow (associated with high temporal scales) and a fast (associated with intermediate temporal scales) scale-free component. This appears as a low- and a very-low frequency spectral band in the frequency domain. For further details, see text. Component-based focus is indicated by asterisk (*) as $\ln(\hat{S}_\sigma(N))$ for the raw **(A)** and $\ln(\hat{S}_\sigma(N))$ for the CBSI-pretreated HbT signal **(B)**.

the pretreatment algorithm allows for analytical considerations about the influence of CBSI on multifractal parameters, which in cases of other pretreatment algorithms would be more difficult to make. In particular, the above step in the algorithm can be shown to affect only the scale-dependent measures such as $\ln(\hat{S}_\sigma(N))$ and breakpoint scales but not the scale-free parameters ($\hat{H}(2)$, $h_{\max}$, ΔH_{15}, and *fwhm*), unlike with various filtering methods (Valencia et al., 2008). Nevertheless, these scale-dependent influences spared the impact of age on scale-free parameters because mean ${}^{O}\sigma(N)/{}^{R}\sigma(N)$ were found very similar in all measurement groups.

Origin of Multifractality in Resting-State Hemodynamic Fluctuations

Fluctuations of rsNIRS signal related to neural activity should be viewed as a sampled representation of an interim stage from intrinsic signal generation throughout the brain to the region of interest (ROI), where it is transformed into hemodynamic fluctuations. The regionally recorded rsNIRS signal—aside from systemic influences—is produced by the NVC driven by incoming signaling. Directly, it represents the hemodynamics within a population of vessels behaving like viscoelastic balloons in the ROI. As to the non-neural component of the rsNIRS signal, a likely origin of scale-free behavior is the numerous weekly coupled vascular source (diameter-dependent segmental oscillations along the arterial tree) blending into a fractally correlated pattern (Colantuoni et al., 1994).

Signal generation also raises questions about the spatial dynamics and resting-state functional connectivity. Regarding the incoming neural activity, electrocorticography records captured across various locations in the brain cortex have been shown scale-free temporal structuring (He et al., 2010; He, 2011). Moreover, the power spectral density of cortical EEG exhibits scale-free structuring not only in the temporal but—in an interrelated manner—in the spatial domain, too, (Freeman et al., 2003). Specifically, as demonstrated by these authors, fluctuations spanning from high-frequency/low-power bands to the low-frequency/high-power ranges reflect upon neural events propagating across the micro-meso-macro scales representing contributions from ion channels, across gyri all the way to those of lobes, respectively. Hence a PSD and scaling function representations of neurodynamics and coupled hemodynamics could be viewed as capturing the information flow within the system from its sources via inhomogeneous network routes eventually converging onto the signaling input of the monitored ROI (Buzsaki, 2006). The sampled representation of this process will typically show inhomogeneously distributed fluctuations, visible as intermittent periods of small and large variability; genuine properties of multifractal processes (Ihlen and Vereijken, 2010).

When the multiplicative cascading process was extended into the spatial domain, a description was obtained comparable to the one by the self-organizing branching process (Zapperi et al., 1995); a refined extension of the SOC model (Bak et al., 1987). The inference is that the intermittent in essence multifractal temporal patterns and the inhomogeneous incoming network connections are manifestations of the same phenomenon: emergence of intermittent regional activity from multiple sites of the brain converging via multiplicative interactions between spatiotemporal scales as integrated incoming signaling in the ROI.

Indeed, our findings related to fractal dynamics could potentially reflect the presence of SOC (Bak et al., 1987) in the observed physiological subsystems shaping cerebral hemodynamics in the ROI. SOC, substantiating the $1/f$ noise-type neurodynamics of the human brain, builds on the notion that the brain dissipates the local low-frequency perturbation elicited by external or internal stimuli without any particular spatial or temporal scales (Stam, 2005; Bullmore et al., 2009; Chialvo, 2010; Sporns, 2011). When interactions between scales

occur, multifractality can readily emerge in systems showing properties of SOC (Tebaldi et al., 1999; Lima et al., 2017). Of relevance, in a recent rsNIRS study using 16 channels sampling of resting-state hemodynamics in the PFC, it has been evidenced that the presence of critical state in resting-state dynamic functional connectivity (Racz et al., 2018). In sum, the measured signals are considered as a composite of hemodynamic fluctuations of vasogenic and those elicited by incoming signaling of neurogenic origins with NVC as the link between the two.

Interpretation of Multifractal Endpoint Parameters

The vasogenic component of the rsNIRS signal in terms of its observed multifractal temporal patterns can be interpreted as a consequence of attenuated neurovascular coupling—reflected by an anticorrelated → random shift in the fractal cross-correlation of HbO and HbR. As to the neurogenic fluctuations here we explain the altered multifractal endpoint parameters resulting from interactions between multiple time scales along functional connections (Ihlen and Vereijken, 2010). Along with our focus-based multifractal formalism (Mukli et al., 2015) and a small world implementation (Watts and Strogatz, 1998) of the concept of self-organized criticality (Mandelbrot, 1974; Ihlen and Vereijken, 2010) offer a concise framework for the interpretation of the results obtained in this study the way outlined in the followings. Further details are provided below and please also see the **Supplementary Material**.

Linear dynamics: H(2) vs. $h_{\max}$

Since the degree of global LRC is quantified by $H(2)$, its changes can be interpreted as increased or decreased persistence, meaning correlation of a non-stationary process (Eke et al., 2000; Herman et al., 2011). Furthermore, Deligniéres et al. established a relationship between network *degeneracy*—meaning partial overlap in heterogeneous functional connections—and output signal correlation (Delignières and Marmelat, 2013). Accordingly, the Hurst exponent does not only reflect upon global scale-free properties emerging from a network, but its degree of degeneracy, too.

While LRC—and thus $H(2)$—reflects global scale-free properties, the Hölder trajectory is a local scale-free measure varying along the signal. Although multifractal analysis of physiological data usually shows tightly correlating changes of $h_{\max}$ and $\hat{H}(2)$, the interpretation of $h_{\max}$ as a measure of correlation within the signal is only approximate, since it is associated with $q = 0$, not $q = 2$.

Non-linear dynamics: ΔH_{15} *and fwhm*

Though ΔH_{15} is defined on $H(q)$ and *fwhm* is derived from $D(h)$, their excellent correlation – owing to the deterministic formalism established by Equations 3–5 – offers a rationale to interpret them together. The applications of q-order statistics reveals non-linear properties in scaling of the signal (Ashkenazy et al., 2003). Thus these two multifractal endpoints are indeed equivalent measures of multiplicative interaction between temporal scales of the observed dynamics process (Ihlen and Vereijken, 2010). Importantly, ΔH_{15} and *fwhm* should be regarded as indicators of non-linear dynamics (Gómez-Extremera et al., 2016; Bernaola-Galván et al., 2017).

Asymmetry of $D(h)$—an occasionally observed phenomenon—could be incorporated in the analysis of multifractality in terms of $W{=}W{+}/W{-}$ where *fwhm* is equal to the sum of $W+$ and $W-$ (Wink et al., 2008), corresponding to the width of left and right-half of the singularity spectrum. We calculated the W and found the shape of our singularity spectra symmetric and not affected by age and gender. We stress that testing for true multifractality based on ΔH_{15} statistics (for details see Appendix in **Supplementary Material**) is an essential prerequisite when it comes to evaluating changes in these endpoint parameters in regard of multifractal CBV dynamics.

A scale-dependent measure of hemodynamic power: focus

The focus of the scaling function is a key element of our regression scheme for obtaining $H(q)$ thus securing a robust estimate of $D(h)$ free of inversion (Mukli et al., 2015). Importantly, it is also a robust scale-dependent statistics estimated at signal length as a point of convergence for the scaling function profiles. Since our analysis is based on the SSC method using bridge-detrended variance, $\hat{S}_\sigma(N)$ is essentially the variance associated with the whole signal. Given that the coefficient of variance for our rsNIRS signals were the same, $\hat{S}_\sigma(N)$ is also the measure of the signal mean, which is consistent with our SOC-simulations (**Figure S3**). In the frequency domain, it is analogous with the power of the DC-component of the signal (see the behavior of spectra and scaling functions on **Figure 7** as $f \rightarrow 0$).

Since its value is influenced by numerous other variables, conclusions regarding hemodynamic alterations can be drawn if focus is interpreted together with $\hat{H}(2)$. Given their analogous frequency domain parameter the hemodynamic power corresponding to a spectral band can be estimated. The separated components of the rsNIRS signal have distinct scaling ranges, and the area under the scaling function corresponding to such SRs is an approximation of summed logarithmic variance of the given component. This area can be explicitly calculated as it is proportional with $\ln(\hat{S}_\sigma(N))$ and width of SR, and it also increases with decreased $\hat{H}(2)$. Given the straightforward relationship between summed variance and total hemodynamic power in a given temporal/frequency range, the obtained results for the area should be viewed as power of hemodynamic fluctuations associated with the isolated components.

The Inference of Bimodality

The majority of the measured rsNIRS signal showed bimodal scaling that was statistically confirmed by comparing the errors of fits for the bimodal and unimodal models. We used a scaling-range adaptive method to assess scaling exponents and multifractal endpoint parameters of the two components, which approach has already been used in our previous study (Nagy et al., 2017) and in other studies as well (Ge and Leung, 2012; Kuznetsov et al., 2013). The apparent structural heterogeneity in the scaling functions of our dataset (convex and/or concave transient range) prompted us to choose the robust moment-wise

SR-adaptive method instead of an alternative (decomposition of scaling function) that was specifically designed to assess additive properties of bimodal scaling.

The bimodal analysis is an adaptive tool that separates two fractal SRs within an overall range of scales between the lowest temporal scale of 8 seconds ($s_{min} = 16$) and 4096 seconds ($s_{max} = 8192$). Although the Fourier transform does not assume an exact relationship between temporal scales and frequencies, we can still assign the non-fractal "noise" component below s_{min} to a spectral range from 0.125 to 1 Hz (i.e., Nyquist frequency). It is known that this band is dominated by fluctuations of systemic origin such as cardiac pulsation and respiration (Tian et al., 2009; Sassaroli et al., 2012), which is corroboratory regarding the exclusion of time scales shorter than 8 s.

Earlier we introduced the slow and fast components as dominantly neurogenic and vasogenic, in the followings the reader is taken through arguments substantiating this division. The fast and slow components were identified in the time domain within their respective analytical scaling ranges in the time domain. In a frequency domain representation, they correspond to the low- and very low-frequency oscillations (LFO and VLFO, respectively; **Figure 7**). The LFO/VLFO classification was used by authors evaluating fundamental spectral aspects of NIRS dynamics (Obrig et al., 2000; Schroeter et al., 2004; Li et al., 2013; Vermeij et al., 2014). LFO is generally regarded of neural origin and thus is a commonly investigated in NIRS studies of cognition (Chance et al., 1993) and functional connectivity (Sasai et al., 2011). Also, it substantiated the concept of fMRI-based functional connectivity ever since Biswal et al. (1995) analyzed cross-correlations in paired signals by clipping their power spectra to zero above 0.1 Hz in order to identify temporal coincidences in local activities thus excluding the global influences. It seems reasonable to separate the VLFO component since its dynamics is dominated by non-neural (Schroeter et al., 2004; Li et al., 2013; Vermeij et al., 2014), particularly endothelium-related mechanisms (Li et al., 2013; Chen et al., 2014). VLFO would manifest as the slow, vasogenic component in our study within the breakpoints and s_{max}, while the range down to s_{min} corresponds to LFO (**Figure 7**). Nevertheless, the debate is still ongoing over further contributors to CBV dynamics such as vasomotion (Elwell et al., 1999) and Mayer-waves (Sassaroli et al., 2012); effectively being excluded from our analyses by setting s_{min} to 8 s corresponding to 0.125 Hz. In fact, vasomotion may show up, but within a narrow range of scales and at low fluctuation amplitudes thus having a weak effect if any on our scaling analysis. Please note that the assessment of bimodality and scale-free properties of both LFO and VLFO were only possible because the analyses were performed with a high-enough s_{max} as recommended by Nagy et al. (2017). The consequent statistical instability is compensated by our focus-based regression model.

Healthy Aging Is Associated With Altered Complexity of Cerebral Hemodynamics

In the present study, decreased $\hat{H}(2)$, h_{max}, and $\ln(\hat{S}_\sigma(N))$ were seen in the fast—neurogenic—component of the CBSI-pretreated NIRS signals of the elderly participants. In addition, we found an increased $\hat{H}(2)$ and h_{max} in the elderly group for the slow—vasogenic—component of the raw rsNIRS signal (**Figure 3**) with spared $\ln(\hat{S}_\sigma(N))$ and multifractality (i.e., no difference in ΔH_{15} and *fwhm*). These changes in the multifractal endpoint parameters are consistent with attenuated neurovascular coupling concomitant to declining incoming signaling and impaired vascular responses.

Altered Neurogenic Component Due to Declining Neurodynamics

Multifractal measures of the fast component ($\sim$ LFO) of the CBSI-pretreated NIRS signal revealed a difference between young and elderly subjects. Specifically, $\hat{H}(2)$, h_{max}, and $\ln({}^f\hat{S}_\sigma(N))$—a key parameter characterizing the overall decline in the neurogenic component—was found decreased among the elderly participants. In principle, a decrease of $\hat{H}(2)$ and h_{max} could have resulted from the contribution of biological noise. The decreased $\ln({}^f\hat{S}_\sigma(N))$ can be directly interpreted as a decreased power in LF oscillations which was concluded by other studies, too (Schroeter et al., 2004; Li et al., 2013; Vermeij et al., 2014). Although the decline in power appears at all frequencies, a disproportionate decrease could still manifest from biological noise present across the lower frequencies first seen in our previous study (Eke et al., 2006). A recent numerical study clearly showed that varying signal/noise ratio by adding white noise yielded underestimation of $H(q)$ (Ludescher et al., 2011). Hence our decreased $\hat{H}(q)$ and h_{max} of the fast component can at least in part be explained by the relative impact of biological noise progressively dominating the higher temporal scales. Although our choice of s_{min} exceeds this range of temporal scales, this factor must be taken into account in our interpretation of the observed alterations of the neurogenic component associated with the LFO range in our rsNIRS signals. In spite of the spurious estimates of $\hat{H}(q)$ attributable to the increased relative impact of biological noise, the conclusion of an overall decline in the neurogenic component can be still held. Nevertheless, please note that CBSI-pretreatment of raw HbT signal effectively removes the impact of non-anticorrelated dynamics in the signal. Therefore the impact of biological noise is unlikely and the observed changes should be regarded as real.

This allows us to interpret the decreased focus as a sign of decreased incoming signaling in line with the dominantly neurogenic origin of the LFO and the aforementioned *in silico* observations (**Supplementary Material**). As multifractality can be viewed as resulting from cross-scale spatiotemporal interactions (Monto, 2012), unchanged ΔH_{15} and *fwhm* suggest that healthy aging spared these interactions within the incoming networks.

As to the multiple mechanisms involved in neurogenic aspects of the aging process, based on our results we argue that even healthy aging leads to progressive attenuation in incoming signaling that to some unknown extent could be masked by impaired neurovascular coupling. The aging process is known leading to gray matter atrophy associated with dropping neuronal count (McGeer et al., 1984) and lower gray matter density (Sowell et al., 2003) along with impaired synaptic activity. The latter is known to be prevailing in postmenopausal women due to lower levels of estrogen (Gibbs and Aggarwal, 1998; Khan et al., 2013). In addition, an age-related decrease in the hemodynamic response elicited by cognitive task has been

observed in the human prefrontal cortex by NIRS (Schroeter et al., 2004). Several studies have evidenced that significant changes in resting state functional connectivity take place in the aging brain at large and small spatial scales alike with inference to temporal dynamics (Ferreira and Busatto, 2013). For example, the structural changes occurring in the aging brain imply changes in its functional connectivity readily manifesting in altered parameters of complexity parameters (Sun et al., 2012). Specifically, global deleterious effects of older age has been reported on functional networks (Achard and Bullmore, 2007) mounting to "topological marginalization" like that of the prefrontal cortex due to segregation in the global network. It was suggested that even healthy aging disrupts the underlying networks by severing the long-range connections, especially in higher-function areas like the prefrontal cortex (Ferreira and Busatto, 2013). In a sample of subjects (19–80 years) a linear effect of age associated with impaired resting-state functional connectivity has been demonstrated (Mevel et al., 2013).

Indeed, when eliminating the multiplicative neural interactions across spatial scales in an interaction-dominant model of human cognition (Ihlen and Vereijken, 2010), more aggregated, focal activities remain. Putatively, this model behavior (global → focal shift in intrinsic activities of the brain) is capable of explaining the loss of complexity in our rsNIRS signal as the sign of decreased incoming signaling. Nevertheless, this takes place in the PFC during healthy aging to such an extent that would still not interfere with the cross-scale spatiotemporal interactions in the observed dynamics captured in unaltered parameters of multifractality.

A further theory suggests the role of dedifferentiation in the aging of physiological subsystems like the brain function (Sleimen-Malkoun et al., 2014). Experiment using a motor task paradigm indeed demonstrated that in addition to stronger activation in dedicated regions to a motor task, older adults generally exhibit activation of additional areas of the brain not or only marginally involved in young participants (Sleimen-Malkoun et al., 2014). Approaches relying on fMRI-based connectivity studies accounting for the difference in task and connectivity paradigms demonstrated that higher levels of activity coexists with disrupted connectivity (Sala-Llonch et al., 2015).

Altered Vasogenic Component Due to Impaired Vascular Responses

The observations regarding the vasogenic component are compatible with those of our previous monofractal study using raw rsNIRS signals reporting on an increased spectral index β in the elderly suggesting the impact of age-related vascular sclerosis on CBV dynamics (Eke et al., 2006). The increased $\hat{H}(2)$ and focus indicate a more correlated vascular dynamics with decreased hemodynamic power in the elderly group. The mean singularity spectrum for the vasogenic component was found shifted to the right (reflected by $h_{\max}$) with maintained shape and width (**Figure 8**). Consistent with this view, we hypothesize that healthy aging leads to this increased correlation pattern in the vasogenic (VLF) component as a result of vessel stiffening and a decline in the endothelium-mediated (metabolic) regulation of cerebrovascular smooth muscle tone. Our evidence to this hypothesis is indirect, though: the result of CBSI-pretreatment and the temporal scales characterizing VLF hemodynamics. Nevertheless, this interpretation of our results is in agreement with several studies on this component of cerebral hemodynamics. In an rsNIRS study investigating the effect of age, Li et al. demonstrated (Li et al., 2013) decreased average amplitudes of spontaneous oscillations in the elderly. The latter authors assumed that the oscillations in the 0.005–0.02 Hz range originated from the endothelium. Aging has also been shown decreasing the responsiveness of distal segments of the arterial tree due to endothelial dysfunction (Toda, 2012) and increasing wall stiffness (Schroeter et al., 2004; Zhu et al., 2011; Wardlaw et al., 2013; Vermeij et al., 2014). The functional hyperemia studied by selectively interrupting endothelial signaling in the somatosensory cortex of rats confirmed its key role in mediating the very slow—maintained—hemodynamic response brought about by NVC (Chen et al., 2014). The vascular decline in the elderly thus may attenuate the local hemodynamic response, too.

As to the attenuation in local vascular dynamics, indeed, the local hemodynamic response elicited by *incoming* neural activity is known to be driven *locally* by fast glutamate-mediated signaling, and more *globally* by amine- and ACh-mediated neural systems (Attwell and Iadecola, 2002). Both have been shown declining with age (McGeer et al., 1984; Gibbs and Aggarwal, 1998; Attwell and Iadecola, 2002). The above scenario may indicate that an impaired neurovascular coupling (Fabiani et al., 2014; Tarantini et al., 2017) could to some degree mask the effects of deterioration of connectivity on neurogenic signal complexity.

Implications of HbO-HbR Relationship

Age-related physiological dysregulation is essentially a gradual and typically irreversible loss of regulatory control originating from structural instabilities in regulatory systems (Cohen, 2016). We shall discuss this phenomenon concerning parameters reflecting neurovascular coupling with coupled HbO-HbR dynamics in its focus. We used multifaceted approach for its characterization: (i) scale-wise fractal cross-correlation, (ii) multifractal covariance and (iii) statistical analysis of Bienaymé-formulation of the HbO-HbR relationship. At this end, we interpret our results as the impact of age on the output of an integrated system of neurodynamics, coupled HbO-HbR dynamics and hemodynamics as genuinely interrelated aspects of neurovascular coupling.

Age-Related Increase in Scale-Wise Fractal Cross-Correlation

In elderly participants, the higher $r_\sigma(s)$ capturing HbO-HbR relationship indicate the relatively larger contribution of correlating systemic hemodynamics to the recorded NIRS signal (which) is also consistent with declining neurodynamics. Furthermore, scale-wise correlation coefficients were found significantly elevated for rather high temporal scales directly influencing this domain of the variance profiles associated with the vasogenic component (**Figure 4A**). In a certain range of scales characterizing VLFO, the increase in $r_\sigma(s)$ values were

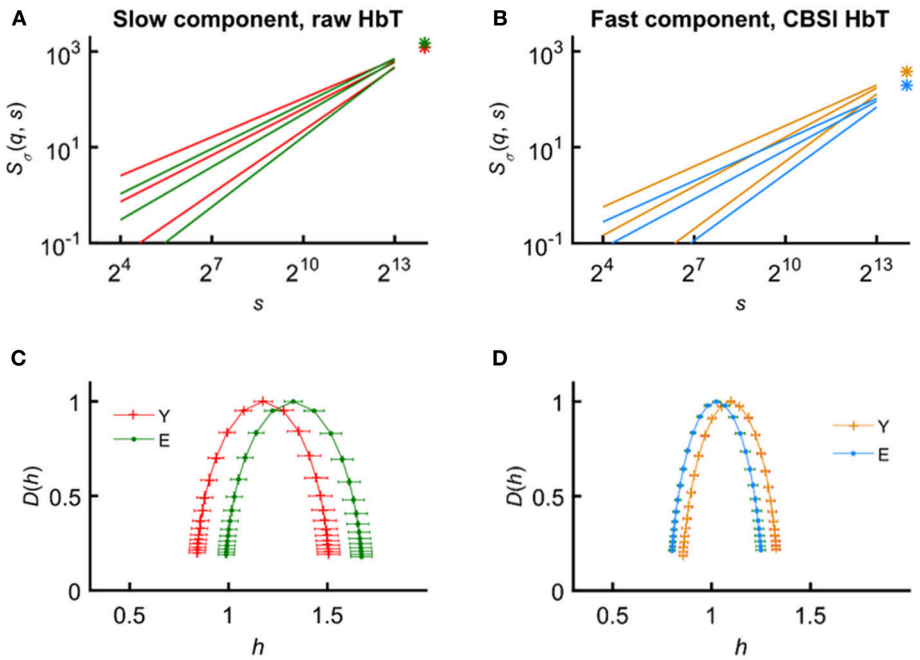

FIGURE 8 | Input and output parameters of the focus-based multifractal formalism in the young and elderly groups for the slow (vasogenic) and fast (neurogenic) components of CBV fluctuations. Average scaling functions **(A,B)** and average singularity spectra **(C,D)** obtained for the raw and CBSI-pretreated HbT signal. Age coding: young—red **(A,C)**, blue **(C,D)**; elderly—green **(A,C)**, orange **(B,D)**. Preserved focus and increased correlation characterize the age-related changes of the vasogenic component **(A)**. Conversely, these parameters of the neurogenic component indicate a decline apparent in the average scaling functions **(B)**. The alteration of h_{max} is a good indicator of the right-ward shift of *D(h)* for the vasogenic **(C)** and a left-ward shift for the neurogenic component **(D)**. It also reveals altered correlation properties if the shape and distribution of singular behavior is not much affected, which happens to be the case in this study as the distribution of Hölder exponents was found symmetrical around h_{max} irrespective of age and gender.

significantly associated with the ${}^{s}h_{\max}$ and ${}^{s}\hat{H}(2)$ of the raw HbT. Given the demonstrated association between endothelial-mediated responses and VLFO (Stefanovska et al., 1999), the pattern found in our study should be regarded as evidence supporting the endothelial contribution to the age-related increase in ${}^{s}h_{\max}$ and ${}^{s}\hat{H}(2)$.

Analyzing the coupled fluctuations of oxy- and deoxyhemoglobin has been used to assess cerebral oxygenation changes and the underlying processes (Reinhard et al., 2006; Wylie et al., 2009; Pierro et al., 2012). There is scarce evidence to determine the effects of aging on their relationship and the rationale behind the utilized parameters is also debatable. Please note the difference in the scale-wise pattern of $r_\sigma(s)$ only showing a clear gradual decrease below ≈50–100 s (see the red arrow on **Figure 5**). It is reasonable to assume that such pattern reflects the relative contribution of mechanisms eliciting correlated or anticorrelated chromophore dynamics. Supposing the origin of the anticorrelated dynamics within the local balloons, and regarding the correlated dynamics mainly of systemic origin, this pattern may be informative of a relative impact of local and systemic hemodynamics on our measured rsNIRS signals. Specifically, local determinants of oxygen supply and extraction dominate the correlation across wide range of frequencies below 0.01 Hz (Stefanovska et al., 1999) emphasizing the potential contribution of spatiotemporally sustained response mediated by astrocyte-endothelial signaling (Iadecola and Nedergaard, 2007).

The Significance of Non-linear Relationship Revealed by Multifractal Covariance Analysis

While scale-wise cross-correlation analysis does not reveal scale-free properties, multifractal covariance analysis is specifically designed to characterize LRCs and multifractality in the coupled HbO-HbR dynamics. The covarying fluctuations of HbO and HbR originate from their respective individual fluctuations and the directly coupled dynamics of the exchange between the two compartments. Following the approach of Kristoufek (2011) the deviation of ${}^{\mathrm{OR}}\hat{H}(2)$ from $({}^{\mathrm{O}}\hat{H}(2)+{}^{\mathrm{R}}\hat{H}(2))/2$ indicates oxygen exchange within the hemoglobin pool. We found a clearly significant decrease of $\ln({}^{f}\hat{S}_{Cov}(N))$ in the elderly (**Figure 4B**) indicating weakening of the coupled fluctuation of HbO and HbR. Indeed, the inference is an upset balance between oxygen demand and supply. Given the strong association between the foci of the fast component of the covariance scaling function and of CBSI-pretreated signal scaling function, this change supposedly can be attributed to the age-related decline in neurodynamics. Although at a weaker significance and lower correlation with the corresponding multifractal endpoint parameter (obtained for multifractal covariance analysis and multifractal analysis of CBSI-pretreated signals, respectively), the decreased ${}^{f}h_{\max}$ of HbO-HbR covariance in the elderly participants besides its similar pattern with ${}^{f}h_{\max}$ of neurogenic fluctuations supports this notion. Clearly, more evidence is needed coming from measurements and synthesized datasets

to elaborate and consolidate physiological models for this interpretation.

Although our approach is essentially similar to the multifractal detrended- (Zhou, 2008), height cross-correlation (Kristoufek, 2011) analyses and cross-wavelet analysis (Ciuciu et al., 2014; Jiang et al., 2016), this is the first paper describing and utilizing the bivariate adaptation of multifractal SSC analysis. Owing to the similarities between our implementation and other time domain algorithms a reliable parameter estimation was expected. A performance characterization of multifractal covariance analysis on synthetic signals with known degree of correlation, while is certainly desirable, but is beyond the scope of the present study.

The Importance of Coupled HbO-HbR Fluctuations Driving Cerebral Hemodynamics

Physiologically, oxygen consumption related to neural activity is not blood flow-limited, but rather neural activity controls the $CMRO_2$ and cerebral hemodynamics (Raichle and Mintun, 2006). Consequently, it is plausible to explain variations of CBV fluctuations (proportional to the measured HbT signal) as a function of HbO-HbR relationship providing insight in variations in cerebral oxygenation. The explicit deterministic, quantitative relationship between key variables of the study established by Bienaymé-formula (Equation 2) offers an explicit way assigned by GLM to evaluate their role with special emphasis on $r_\sigma(s)$.

Scale-wise cross-correlation is a robustly significant determinant of HbT fluctuations at all temporal scales within the framework of GLM. Omitting either age and gender from the statistical analyses (i.e., multiple regression, **Figure 6**) or incorporating these categorical variables in it (AnCova/separate slopes) yields essentially the same outcome on the role of $r_\sigma(s)$. Considering the impact of age on $r_\sigma(s)$ and the age-corrected dependence of $r_\sigma(s)$ CBV fluctuations (see **Table 2**) it can be concluded that age exerts its effect on ${}^{T}S_\sigma(2, s)$ in part via $r_\sigma(s)$ shifting toward uncorrelated chromophore dynamics. The impact of weakened HbO-HbR coupling in the elderly—supposedly due to declining neurodynamics—is clearly seen in the age-related changes of multifractal endpoint parameters characterizing cerebral hemodynamics.

Limitations and Future Perspectives

Acquiring additional modalities would have allowed for a more straightforward physiological interpretation of the signal. Specifically, transcranial Doppler measurement (capturing blood flow velocity in the middle cerebral artery) or continuous blood pressure records offer measures on systemic influences that could have been regressed out. To compensate, we applied CBSI to remove these influences from the signal. Further development and testing of robust pre-processing methods are in place to further enhance the interpretation of multifractal measures of physiological processes.

The intimate relationship between multifractal hemodynamic fluctuations and functional connectivity has been demonstrated and characterized on intrinsic fMRI networks (Ciuciu et al., 2014) and by revealing scale-free network dynamics in the prefrontal cortex captured by NIRS (Racz et al., 2018). In this comparison, our single-region measurement measurement appears like a limitation (Novi et al., 2016). However, in fact, we present an analytical framework which is capable of integrating aspects on incoming signaling with those of regional hemodynamics elicited by neurovascular coupling.

The tools developed for characterizing the coupled HbO-HbR dynamics have potentials in other applications, too. The fractal scale-wise correlation analysis captures linear aspects while the multifractal covariance analysis adds a non-linear dimension to the assessment of coupling between non-stationary time series. These methods open new ways in uni- and multimodal applications to investigate functional connectivity or neurovascular coupling, respectively.

CONCLUSIONS

Mono- and multifractal approaches have greatly enriched our insight of biological complexity in particular that of the brain (Bullmore and Sporns, 2009; Herman et al., 2009; Ihlen and Vereijken, 2010; Nagy et al., 2017; Racz et al., 2018). To the best of our knowledge, this study is the first using consolidated datasets with tested and proven correlation-type multifractality for an in-depth characterization of resting-state NIRS fluctuations. Here we interpret the multifractality of single-region cerebral hemodynamics as resulting from neurogenic oscillations via cross-scale interactions blending into a scale-free intermittent arrhythmic pattern via neurovascular coupling. However, the intrinsic and endothelium-evoked heterogeneous oscillations of the vascular smooth muscle tone give rise to multifractality of vasogenic fluctuations. The multifractal endpoint parameters obtained from raw and pre-processed signal attest to the impact of healthy aging on cerebral hemodynamic fluctuations in the human prefrontal cortex. Specifically, we report that the total power of very-low frequency—vasogenic—oscillations of CBV decreased due to a preserved value of focus and an increase of LRC, $({}^{s}\hat{H}(2))$; the latter is concomitant to the right-shifting singularity spectra $[D(h)$ along with its ${}^{s}h_{\max}]$. As to the hemodynamic fluctuations elicited by neural activity—related to low-frequency oscillations—we show a general decline indicated by decreased $\hat{H}(2)$, $h_{\max}$, and focus of the neurogenic component. On the contrary, parameters reflecting degree of multifractality are the same in the group of young and elderly subjects which demonstrates non-pathological aging spares non-linear hemodynamics. In case of the elderly participants, the anticorrelation of HbO and HbR fluctuations were barely present at high temporal scales, while an attenuated cross-correlation was revealed by multifractal covariance analysis. We show that the impact of age on the parameters of neuro- and vasogenic components must have resulted from the age-related alterations in HbO-HbR coupling. In our study, the HbO-HbR relationship appears as a key element directly influenced by the neuronal activity and directly coupled to CBV dynamics via neurovascular coupling which seems like sensitive to aging. We suggest that decreased

incoming signaling and the prevalence of an altered pattern of moment-to-moment HbO-HbR coupling could contribute to the mismatch between oxygen demand and supply. Together with vascular dysfunction could well be considered as factors behind the observed age-dependent alterations of cerebral hemodynamics.

AUTHOR CONTRIBUTIONS

PM adapted the multifractal analytical framework to resting-state NIRS signals, performed the analysis on measured data and wrote the manuscript. ZN developed methods and helped writing the manuscript. FR implemented a testing framework and assessed true multifractality of the measured data. PH carried out the measurements. AE helped developing and writing the manuscript and provided conceptual guidance in the study.

ACKNOWLEDGMENTS

The authors acknowledge the support from the Hungarian Scientific Research Found OTKA grant T 034122 awarded to AE.

SUPPLEMENTARY MATERIAL

The Supplementary Material for this article can be found online at: https://www.frontiersin.org/articles/10.3389/fphys.2018.01072/full#supplementary-material

REFERENCES

Achard, S., and Bullmore, E. (2007). Efficiency and cost of economical brain functional networks. *PLoS Comput Biol.* 3:e17. doi: 10.1371/journal.pcbi.0030017

Ashkenazy, Y., Havlin, S., Ivanov, P. C., Peng, C. K., Schulte-Frohlinde, V., and Stanley, H. E. (2003). Magnitude and sign scaling in power-law correlated time series. *Phys. A Statist. Mech. Appl.* 323, 19–41. doi: 10.1016/S0378-4371(03)00008-6

Attwell, D., and Iadecola, C. (2002). The neural basis of functional brain imaging signals. *Trends Neurosci.* 25, 621–625. doi: 10.1016/S0166-2236(02)02264-6

Bak, P., Tang, C., and Wiesenfeld, K. (1987). Self-organized criticality: an explanation of the 1/f noise. *Phys. Rev. Lett.* 59, 381–384. doi: 10.1103/PhysRevLett.59.381

Barabási, A. L., and Vicsek, T. (1991). Multifractality of self-affine fractals. *Phys. Rev. A* 44, 2730–2733. doi: 10.1103/PhysRevA.44.2730

Barabási, A. L., Szépfalusy, P., and Vicsek, T. (1991). Multifractal spectra of multi-affine functions. *Physica A* 178, 17–28. doi: 10.1016/0378-4371(91)90072-K

Bassingthwaighte, J. B., Liebovitch, L. S., and West, B. J. (1994). *Fractal Physiology*. New York, NY: Oxford University Press.

Beckers, F., Verheyden, B., and Aubert, A. E. (2006). Aging and nonlinear heart rate control in a healthy population. *Am. J. Physiol. Heart Circ. Physiol.* 290, H2560–H2570. doi: 10.1152/ajpheart.00903.2005

Bernaola-Galván, P. A., Gómez-Extremera, M., Romance, A. R., and Carpena, P. (2017). Correlations in magnitude series to assess nonlinearities: Application to multifractal models and heartbeat fluctuations. *Phys. Rev. E* 96:032218. doi: 10.1103/PhysRevE.96.032218

Biswal, B. B., Mennes, M., Zuo, X. N., Gohel, S., Kelly, C., Smith, S. M., et al. (2010). Toward discovery science of human brain function. *Proc. Natl. Acad. Sci. U.S.A.* 107, 4734–4739. doi: 10.1073/pnas.0911855107

Biswal, B., Yetkin F. Z., Haughton, V. M., and Hyde, J. S. (1995). Functional connectivity in the motor cortex of resting human brain using echo-planar mri. *Magn. Reson. Med.* 34, 537–541. doi: 10.1002/mrm.1910340409

Bullmore, E., and Sporns, O. (2009). Complex brain networks: graph theoretical analysis of structural and functional systems. *Nat. Rev. Neurosci.* 10, 186–198. doi: 10.1038/nrn2575

Bullmore, E., Barnes, A., Bassett, D. S., Fornito, A., Kitzbichler, M., Meunier, D., et al. (2009). Generic aspects of complexity in brain imaging data and other biological systems. *NeuroImage* 47, 1125–1134. doi: 10.1016/j.neuroimage.2009.05.032

Buzsaki, G. (2006). *Rhythms of the Brain.* New York, NY: Oxford University Press.

Caccia, D. C., Percival, D., Cannon, M. J., Raymond, G., and Bassingthwaighte, J. B. (1997). Analyzing exact fractal time series: evaluating dispersional analysis and rescaled range methods. *Phys. A Statist. Mech. Appl.* 246, 609–632. doi: 10.1016/S0378-4371(97)00363-4

Chance, B. (1994). Current state of methodology on hemoglobin oximetry in tissues. *Adv. Exp. Med. Biol.* 345, 23–32.

Chance, B., Nioka, S., and Zhao, Z. (2007). A wearable brain imager. *IEEE Eng. Med. Biol. Mag.* 26, 30–37. doi: 10.1109/MEMB.2007.384093

Chance, B., Zhuang, Z., UnAh, C., Alter, C., and Lipton, L. (1993). Cognition-activated low-frequency modulation of light absorption in human brain. *Proc. Natl. Acad. Sci. U.S.A.* 90, 3770–3774. doi: 10.1073/pnas.90.8.3770

Chen, B. R., Kozberg, M. G., Bouchard, M. B., Shaik, M. A., and Hillman, E. M. (2014). A critical role for the vascular endothelium in functional neurovascular coupling in the brain. *J. Am. Heart Assoc.* 3:e000787. doi: 10.1161/JAHA.114.000787

Chialvo, D. R. (2010). Emergent complex neural dynamics. *Nat. Phys.* 6, 744–750. doi: 10.1038/Nphys1803

Ciuciu, P., Abry, P., and He, B. J. (2014). Interplay between functional connectivity and scale-free dynamics in intrinsic fMRI networks. *Neuroimage* 95, 248–263. doi: 10.1016/j.neuroimage.2014.03.047

Ciuciu, P., Varoquaux, G., Abry, P., Sadaghiani, S., and Kleinschmidt, A. (2012). Scale-free and multifractal time dynamics of fmri signals during rest and task. *Front. Physiol.* 3:186. doi: 10.3389/fphys.2012.00186

Clauset, A., Shalizi, C. R., and Newman, M. E. J. (2009). Power-law distributions in empirical data. *SIAM Rev.* 51, 661–703. doi: 10.1137/070710111

Cohen, A. A. (2016). Complex systems dynamics in aging: new evidence, continuing questions. *Biogerontology* 17, 205–220. doi: 10.1007/s10522-015-9584-x

Colantuoni, A., Bertuglia, S., and Intaglietta, M. (1994). Microvascular vasomotion: origin of laser Doppler flux motion. *Int. J. Microcirc. Clin. Exp.* 14, 151–158.

Cope, M., Delpy, D. T., Reynolds, E. O., Wray, S., Wyatt, J., and van der Zee, P. (1988). Methods of quantitating cerebral near infrared spectroscopy data. *Adv. Exp. Med. Biol.* 222, 183–189. doi: 10.1007/978-1-4615-9510-6_21

Csermely, P. (2006). *Weak* Links: The universal key to the stability of networks and complex systems. Berlin; Heidelberg: Springer.

Cui, X., Bray, S., and Reiss, A. L. (2010). Functional near infrared spectroscopy (NIRS) signal improvement based on negative correlation between oxygenated and deoxygenated hemoglobin dynamics. *Neuroimage* 49, 3039–3046. doi: 10.1016/j.neuroimage.2009.11.050

Davies, R. B., and Harte, D. S. (1987). Tests for hurst effect. *Biometrika* 74, 95–101. doi: 10.1093/biomet/74.1.95

Delignières, D., and Marmelat, V. (2013). Degeneracy and long-range correlations. *Chaos* 23:043109. doi: 10.1063/1.4825250

Devor, A., Dunn, A. K., Andermann, M. L., Ulbert, I., Boas, D. A., and Dale, A. M. (2003). Coupling of total hemoglobin concentration, oxygenation, and neural activity in rat somatosensory cortex. *Neuron* 39, 353–359. doi: 10.1016/S0896-6273(03)00403-3

Drake, C. T., and Iadecola, C. (2007). The role of neuronal signaling in controlling cerebral blood flow. *Brain Lang.* 102, 141–152. doi: 10.1016/j.bandl.2006.08.002

Dutta, S. (2010). Eeg pattern of normal and epileptic rats: monofractal or multifractal? *Fractals* 18, 425–431. doi: 10.1142/S0218348x10005081

Dzung, N. T. (2010). "Multifractality in NIRS data of brain activity," in *IFMBE Proceedings* (Ho Chi Minh City), 80–83.

Eke, A., and Hermán, P. (1999). Fractal analysis of spontaneous fluctuations in human cerebral hemoglobin content and its oxygenation level recorded by NIRS. *Adv. Exp. Med. Biol.* 471, 49–55. doi: 10.1007/978-1-4615-4717-4_7

Eke, A., Hermán, P., and Hajnal, M. (2006). Fractal and noisy CBV dynamics in humans: influence of age and gender. *J. Cereb. Blood Flow Metab.* 26, 891–898. doi: 10.1038/sj.jcbfm.9600243

Eke, A., Hermán, P., Bassingthwaighte, J. B., Raymond, G. M., Percival, D. M., Cannon, M., et al. (2000). Physiological time series: distinguishing fractal noises from motions. *Pflügers Archiv. Eur. J. Physiol.* 439, 403–415. doi: 10.1007/s004249900135

Eke, A., Herman, P., Kocsis, L., and Kozak, L. R. (2002). Fractal characterization of complexity in temporal physiological signals. *Physiol. Meas.* 23, R1–R38. doi: 10.1088/0967-3334/23/1/201

Eke, A., Herman, P., Sanganahalli, B. G., Hyder, F., Mukli, P., and Nagy, Z. (2012). Pitfalls in fractal time series analysis: Fmri BOLD as an exemplary case. *Front. Physiol.* 3:417. doi: 10.3389/fphys.2012.00417

Elwell, C. E., Springett, R., Hillman, E., and Delpy, D. T. (1999). Oscillations in cerebral haemodynamics. Implications for functional activation studies. *Adv. Exp. Med. Biol.* 471, 57–65.

Fabiani, M., Gordon, B. A., Maclin, E. L., Pearson, M. A., Brumback-Peltz, C. R., Low, K. A., et al. (2014). Neurovascular coupling in normal aging: a combined optical, ERP and fMRI study. *Neuroimage* 85 (Pt 1), 592–607. doi: 10.1016/j.neuroimage.2013.04.113

Ferreira, L. K., and Busatto, G. F. (2013). Resting-state functional connectivity in normal brain aging. *Neurosci. Biobehav. Rev.* 37, 384–400. doi: 10.1016/j.neubiorev.2013.01.017

Firbank, M., Okada, E., and Delpy, D. T. (1998). A theoretical study of the signal contribution of regions of the adult head to near-infrared spectroscopy studies of visual evoked responses. *Neuroimage* 8, 69–78. doi: 10.1006/nimg.1998.0348

Fox, M. D., and Raichle, M. E. (2007). Spontaneous fluctuations in brain activity observed with functional magnetic resonance imaging. *Nat. Rev. Neurosci.* 8, 700–711. doi: 10.1038/nrn2201

Freeman, W. J., Holmes, M. D., Burke, B. C., and Vanhatalo, S. (2003). Spatial spectra of scalp EEG and EMG from awake humans. *Clin. Neurophysiol.* 114, 1053–1068. doi: 10.1016/s1388-2457(03)00045-2

Frisch, U., and Parisi, G. (1985). "Turbulence and predictability in geophysical fluid dynamics and climate dynamics," in *Fully Developed Turbulence and Intermittency Appendix: On the Singularity Structure of Fully Developed Structure*, eds M. Ghil, R. Benzi, and G. Parisi (Amsterdam: North-Holland), 823.

Ge, E., and Leung, Y. (2012). Detection of crossover time scales in multifractal detrended fluctuation analysis. *J. Geogr. Syst.* 15, 115–147. doi: 10.1007/s10109-012-0169-9

Gibbs, R. B., and Aggarwal, P. (1998). Estrogen and basal forebrain cholinergic neurons: implications for brain aging and Alzheimer's disease-related cognitive decline. *Horm. Behav.* 34, 98–111. doi: 10.1006/hbeh.1998.1451

Goldberger, A. L., Amaral, L. A., Hausdorff, J. M., Ivanov, P. C. h., Peng, C. K., and Stanley, H. E. (2002). Fractal dynamics in physiology: alterations with disease and aging. *Proc. Natl. Acad. Sci. U.S.A.* 99 (Suppl. 1), 2466–2472. doi: 10.1073/pnas.012579499

Gómez-Extremera, M., Carpena, P., Ivanov, P. c. h., and Bernaola-Galván, P. A. (2016). Magnitude and sign of long-range correlated time series: Decomposition and surrogate signal generation. *Phys. Rev. E* 93:042201. doi: 10.1103/PhysRevE.93.042201

Grech, D., and Pamuła, G. (2012). Multifractal background noise of monofractal signals. *Acta Phys. Pol.* 121(2 B), B34–B39. doi: 10.12693/APhysPolA.121.B-34

He, B. J. (2011). Scale-free properties of the functional magnetic resonance imaging signal during rest and task. *J. Neurosci.* 31, 13786–13795. doi: 10.1523/JNEUROSCI.2111-11.2011

He, B. J. (2014). Scale-free brain activity: past, present, and future. *Trends Cogn. Sci.* 18, 480–487. doi: 10.1016/j.tics.2014.04.003

He, B. J., Zempel, J. M., Snyder, A. Z., and Raichle, M. E. (2010). The temporal structures and functional significance of scale-free brain activity. *Neuron* 66, 353–369. doi: 10.1016/j.neuron.2010.04.020

Herman, P., Kocsis, L., and Eke, A. (2009). Fractal characterization of complexity in dynamic signals: application to cerebral hemodynamics. *Methods Mol. Biol.* 489, 23–40. doi: 10.1007/978-1-59745-543-5_2

Herman, P., Sanganahalli, B. G., Hyder, F., and Eke, A. (2011). Fractal analysis of spontaneous fluctuations of the BOLD signal in rat brain. *NeuroImage* 58, 1060–1069. doi: 10.1016/j.neuroimage.2011.06.082

Iadecola, C., and Nedergaard, M. (2007). Glial regulation of the cerebral microvasculature. *Nat. Neurosci.* 10, 1369–1376. doi: 10.1038/nn2003

Ihlen, E. A., and Vereijken, B. (2010). Interaction-dominant dynamics in human cognition: beyond 1/f(alpha) fluctuation. *J. Exp. Psychol. Gen.* 139, 436–463. doi: 10.1037/a0019098

Ihlen, E. A., and Vereijken, B. (2013). Multifractal formalisms of human behavior. *Hum. Mov. Sci.* 32, 633–651. doi: 10.1016/j.humov.2013.01.008

Ivanov, P. C. h., Ma, Q. D., Bartsch, R. P., Hausdorff, J. M., Amaral, L. A., Schulte-Frohlinde, V., et al. (2009). Levels of complexity in scale-invariant neural signals. *Phys. Rev. E* 79 (4 Pt 1):041920. doi: 10.1103/PhysRevE.79.041920

Ivanov, P. C., Nunes Amaral, L. A., Goldberger, A. L., Havlin, S., Rosenblum, M. G., Stanley, H. E., et al. (2001). From 1/f noise to multifractal cascades in heartbeat dynamics. *Chaos* 11, 641–652. doi: 10.1063/1.1395631

Ivanov, P. C., Amaral, L. A., Goldberger, A. L., Havlin, S., Rosenblum, M. G., Struzik, Z. R., et al. (1999). Multifractality in human heartbeat dynamics. *Nature* 399, 461–465. doi: 10.1038/20924

Jiang, Z. Q., Gao, X. L., Zhou, W.-X., and Stanley, H. E. (2016). Multifractal cross wavelet analysis. *Fractals* 25:1750054. doi: 10.1142/S0218348X17500542

Jöbsis, F. F. (1977). Noninvasive, infrared monitoring of cerebral and myocardial oxygen sufficiency and circulatory parameters. *Science* 198, 1264–1267. doi: 10.1126/science.929199

Kantelhardt, J. W., Zschiegner, S. A., Koscielny-Bunde, E., Havlin, S., Bunde, A., and Stanley, H. E. (2002). Multifractal detrended fluctuation analysis of nonstationary time series. *Physica A* 316, 87–114. doi: 10.1016/S0378-4371(02)01383-3

Khan, M. M., Dhandapani, K. M., Zhang, Q. G., and Brann, D. W. (2013). Estrogen regulation of spine density and excitatory synapses in rat prefrontal and somatosensory cerebral cortex. *Steroids* 78, 614–623. doi: 10.1016/j.steroids.2012.12.005

Khoa, T. Q., and Nakagawa, M. (2008). Recognizing brain activities by functional near-infrared spectroscope signal analysis. *Nonlinear Biomed. Phys.* 2:3. doi: 10.1186/1753-4631-2-3

Kocsis, L., Herman, P., and Eke, A. (2006a). Mathematical model for the estimation of hemodynamic and oxygenation variables by tissue spectroscopy. *J. Theor. Biol.* 241, 262–275. doi: 10.1016/j.jtbi.2005.11.033

Kocsis, L., Herman, P., and Eke, A. (2006b). The modified Beer-Lambert law revisited. *Phys. Med. Biol.* 51, N91–N98. doi: 10.1088/0031-9155/51/5/N02

Kristoufek, L. (2011). Multifractal height cross-correlation analysis: a new method for analyzing long-range cross-correlations. *Epl* 95:6. doi: 10.1209/0295-5075/95/68001

Kuznetsov, N., Bonnette, S., Gao, J., and Riley, M. A. (2013). Adaptive fractal analysis reveals limits to fractal scaling in center of pressure trajectories. *Ann. Biomed. Eng.* 41, 1646–1660. doi: 10.1007/s10439-012-0646-9

Li, Z., Zhang, M., Xin, Q., Luo, S., Cui, R., Zhou, W., et al. (2013). Age-related changes in spontaneous oscillations assessed by wavelet transform of cerebral oxygenation and arterial blood pressure signals. *J. Cereb. Blood Flow Metab.* 33, 692–699. doi: 10.1038/jcbfm.2013.4

Lima, G. Z. d. S., Corso, G., Correa, M. A., Sommer, R. L., Ivanov, P. C., and Bohn, F. (2017). Universal temporal characteristics and vanishing of multifractality in Barkhausen avalanches. *Phys. Rev. E* 96:022159. doi: 10.1103/PhysRevE.96.022159

Linkenkaer-Hansen, K., Nikouline, V. V., Palva, J. M., and Ilmoniemi, R. J. (2001). Long-range temporal correlations and scaling behavior in human brain oscillations. *J. Neurosci.* 21, 1370–1377. doi: 10.1523/JNEUROSCI.21-04-01370.2001

Lipsitz, L. A. (2003). "Aging as a process of complexity loss," in *Complex Systems Science in Biomedicine*, eds T. S. Deisboeck, D. Kresh, and J. K. Kepler (Boston, MA: Springer), 641–654.

Lo, C. C., Amaral, L. A. N., Havlin, S., Ivanov, P. C., Penzel, T., Peter, J. H., et al. (2002). Dynamics of sleep-wake transitions during sleep. *Europhys. Lett.* 57, 625–631. doi: 10.1209/epl/i2002-00508-7

Ludescher, J., Bogachev, M. I., Kantelhardt, J. W., Schumann, A. Y., and Bunde, A. (2011). On spurious and corrupted multifractality: the effects of additive

noise, short-term memory and periodic trends. *Physica A* 390, 2480–2490. doi: 10.1016/j.physa.2011.03.008

Mandelbrot, B. B. (1974). Intermittent turbulence in self-similar cascades: divergence of high moments and dimension of the carrier. *J. Fluid Mech.* 62, 331–358. doi: 10.1017/S0022112074000711

Maxim, V., Sendur, L., Fadili, J., Suckling, J., Gould, R., Howard, R., et al. (2005). Fractional Gaussian noise, functional MRI and Alzheimer's disease. *NeuroImage* 25, 141–158. doi: 10.1016/j.neuroimage.2004.10.044

McGeer, P. L., McGeer, E. G., Suzuki, J., Dolman, C. E., and Nagai, T. (1984). Aging, Alzheimer's disease, and the cholinergic system of the basal forebrain. *Neurology* 34, 741–745. doi: 10.1212/WNL.34.6.741

Mevel, K., Landeau, B., Fouquet, M., La Joie, R., Villain, N., Mezengé, F., et al. (2013). Age effect on the default mode network, inner thoughts, and cognitive abilities. *Neurobiol. Aging* 34, 1292–1301. doi: 10.1016/j.neurobiolaging.2012.08.018

Monto, S. (2012). Nested synchrony-a novel cross-scale interaction among neuronal oscillations. *Front. Physiol.* 3:384. doi: 10.3389/fphys.2012.00384

Mukli, P., Nagy, Z., and Eke, A. (2015). Multifractal formalism by enforcing the universal behavior of scaling functions. *Physica A* 417, 150–167. doi: 10.1016/j.physa.2014.09.002

Muzy, J. F., Bacry, E., and Arneodo, A. (1993). Multifractal formalism for fractal signals: the structure-function approach versus the wavelet-transform modulus-maxima method. *Phys. Rev. E Stat. Nonlin. Soft. Matter. Phys.* 47, 875–884. doi: 10.1103/PhysRevE.47.875

Nagy, Z., Mukli, P., Herman, P., and Eke, A. (2017). Decomposing multifractal crossovers. *Front. Physiol.* 8:00533. doi: 10.3389/fphys.2017.00533

Ni, H. J., Huang, X. L., Ning, X. B., Huo, C. Y., Liu, T. B., and Ben, D. (2014). Multifractal analysis of resting state fMRI series in default mode network: age and gender effects. *Chinese Sci. Bull.* 59, 3107–3113. doi: 10.1007/s11434-014-0355-x

Novi, S. L., Rodrigues, R. B., and Mesquita, R. C. (2016). Resting state connectivity patterns with near-infrared spectroscopy data of the whole head. *Biomed. Optics Express* 7, 2524–2537. doi: 10.1364/BOE.7.002524

Nunes Amaral, L. A., Ivanov, P. C., Aoyagi, N., Hidaka, I., Tomono, S., Goldberger, A. L., et al. (2001). Behavioral-independent features of complex heartbeat dynamics. *Phys. Rev. Lett.* 86(26 Pt 1), 6026–6029. doi: 10.1103/PhysRevLett.86.6026

Obrig, H., Neufang, M., Wenzel, R., Kohl, M., Steinbrink, J., Einhäupl, K., et al. (2000). Spontaneous low frequency oscillations of cerebral hemodynamics and metabolism in human adults. *Neuroimage* 12, 623–639. doi: 10.1006/nimg.2000.0657

Pierro, M. L., Sassaroli, A., Bergethon, P. R., Ehrenberg, B. L., and Fantini, S. (2012). Phase-amplitude investigation of spontaneous low-frequency oscillations of cerebral hemodynamics with near-infrared spectroscopy: a sleep study in human subjects. *Neuroimage* 63, 1571–1584. doi: 10.1016/j.neuroimage.2012.07.015

Podobnik, B., and Stanley, H. E. (2008). Detrended cross-correlation analysis: a new method for analyzing two nonstationary time series. *Phys. Rev. Lett.* 100:084102. doi: 10.1103/PhysRevLett.100.084102

Quang Dang Khoa, T., and Van Toi, V. (2012). Multifractals Properties on the Near Infrared Spectroscopy of Human Brain Hemodynamic. *Math. Probl. Eng.* 2012, 1–12. doi: 10.1155/2012/670761

Racz, F. S., Mukli, P., Nagy, Z., and Eke, A. (2017). Increased prefrontal cortex connectivity during cognitive challenge assessed by fNIRS imaging. *Biomed. Optics Express* 8, 3842–3855. doi: 10.1364/BOE.8.003842

Racz, F. S., Mukli, P., Nagy, Z., and Eke, A. (2018). Multifractal dynamics of resting-state functional connectivity in the prefrontal cortex. *Physiol. Meas.* 39:024003. doi: 10.1088/1361-6579/aaa916

Raichle, M. E., and Mintun, M. A. (2006). Brain work and brain imaging. *Annu. Rev. Neurosci.* 29, 449–476. doi: 10.1146/annurev.neuro.29.051605.112819

Rattan, S. I. S. (2014). Aging is not a disease: implications for intervention. *Aging Disease* 5, 196–202. doi: 10.14336/AD.2014.0500196

Reinhard, M., Wehrle-Wieland, E., Grabiak, D., Roth, M., Guschlbauer, B., Timmer, J., et al. (2006). Oscillatory cerebral hemodynamics–the macro- vs. microvascular level. *J. Neurol. Sci.* 250, 103–109. doi: 10.1016/j.jns.2006.07.011

Roux, S. G., Venugopal, V., Fienberg, K., Arneodo, A., and Foufoula-Georgiou, E. (2009). Evidence for inherent nonlinearity in temporal rainfall. *Adv. Water Resour.* 32, 41–48. doi: 10.1016/j.advwatres.2008.09.007

Sala-Llonch, R., Bartrés-Faz, D., and Junqué, C. (2015). Reorganization of brain networks in aging: a review of functional connectivity studies. *Front. Psychol.* 6:663. doi: 10.3389/fpsyg.2015.00663

Sasai, S., Homae, F., Watanabe, H., and Taga, G. (2011). Frequency-specific functional connectivity in the brain during resting state revealed by NIRS. *Neuroimage* 56, 252–257. doi: 10.1016/j.neuroimage.2010.12.075

Sassaroli, A., Pierro, M., Bergethon, P. R., and Fantini, S. (2012). Low-frequency spontaneous oscillations of cerebral hemodynamics investigated with near-infrared spectroscopy: a review. *IEEE J. Sel. Topics Quant. Elect.* 18, 1478–1492. doi: 10.1109/jstqe.2012.2183581

Saupe, D. (1988). "Algorithms for random fractals," in *The Science of Fractal Images*, eds H. O. Peitgen and D. Saupe. (New York, NY: Springer-Verlag), 71–136.

Scholkmann, F., Kleiser, S., Metz, A. J., Zimmermann, R., Mata Pavia, J., Wolf, U., et al. (2014). A review on continuous wave functional near-infrared spectroscopy and imaging instrumentation and methodology. *NeuroImage* 85, 6–27. doi: 10.1016/j.neuroimage.2013.05.004

Schroeter, M. L., Schmiedel, O., and Von Cramon, D. Y. (2004). Spontaneous low-frequency oscillations decline in the aging brain. *J. Cereb. Blood Flow Metab.* 24, 1183–1191. doi: 10.1097/01.WCB.0000135231.90164.40

Schumann, A. Y., and Kantelhardt, J. W. (2011). Multifractal moving average analysis and test of multifractal model with tuned correlations. *Phys. A* 390, 2637–2654. doi: 10.1016/j.physa.2011.03.002

Shimizu, Y., Barth, M., Windischberger, C., Moser, E., and Thurner, S. (2004). Wavelet-based multifractal analysis of fMRI time series. *Neuroimage* 22, 1195–1202. doi: 10.1016/j.neuroimage.2004.03.007

Silva, L. E., Silva, C. A., Salgado, H. C., and Fazan, R. (2017). The role of sympathetic and vagal cardiac control on complexity of heart rate dynamics. *Am. J. Physiol. Heart Circ. Physiol.* 312, H469–H477. doi: 10.1152/ajpheart.00507.2016

Sleimen-Malkoun, R., Temprado, J. J., and Hong, S. L. (2014). Aging induced loss of complexity and dedifferentiation: consequences for coordination dynamics within and between brain, muscular and behavioral levels. *Front. Aging Neurosci.* 6:140. doi: 10.3389/fnagi.2014.00140

Sowell, E. R., Peterson, B. S., Thompson, P. M., Welcome, S. E., Henkenius, A. L., and Toga, A. W. (2003). Mapping cortical change across the human life span. *Nat. Neurosci.* 6, 309–315. doi: 10.1038/nn1008

Sporns, O. (2011). The human connectome: a complex network. *Ann. N. Y. Acad. Sci.* 1224, 109–25. doi: 10.1111/j.1749-6632.2010.05888.x

Stam, C. J. (2005). Nonlinear dynamical analysis of EEG and MEG: review of an emerging field. *Clin. Neurophysiol.* 116, 2266–2301. doi: 10.1016/j.clinph.2005.06.011

Stanley, H. E., Amaral, L. A., Goldberger, A. L., Havlin, S., Ivanov, P. C. h., and Peng, C. K. (1999). Statistical physics and physiology: monofractal and multifractal approaches. *Phys. A* 270, 309–324. doi: 10.1016/S0378-4371(99)00230-7

Stefanovska, A., Bracic, M., and Kvernmo, H. D. (1999). Wavelet analysis of oscillations in the peripheral blood circulation measured by laser Doppler technique. *IEEE Trans. Biomed. Eng.* 46, 1230–1239.

Sun, J., Tong, S., and Yang, G. Y. (2012). Reorganization of brain networks in aging and age-related diseases. *Aging Dis.* 3, 181–193.

Tachtsidis, I., Leung, T. S., Devoto, L., Delpy, D. T., and Elwell, C. E. (2008). Measurement of frontal lobe functional activation and related systemic effects: a near-infrared spectroscopy investigation. *Adv. Exp. Med. Biol.* 614, 397–403. doi: 10.1007/978-0-387-74911-2_44

Tarantini, S., Tran, C. H. T., Gordon, G. R., Ungvari, Z., and Csiszar, A. (2017). Impaired neurovascular coupling in aging and Alzheimer's disease: contribution of astrocyte dysfunction and endothelial impairment to cognitive decline. *Exp. Gerontol.* 94, 52–58. doi: 10.1016/j.exger.2016.11.004

Tebaldi, C., De Menech, M., and Stella, A. L. (1999). Multifractal scaling in the Bak-Tang-Wiesenfeld sandpile and edge events. *Phys. Rev. Lett.* 83, 3952–3955.doi: 10.1103/PhysRevLett.83.3952

Thurner, S., Windischberger, C., Moser, E., Walla, P., and Barth, M. (2003). Scaling laws and persistence in human brain activity. *Phys. A* 326, 511–521. doi: 10.1016/S0378-4371(03)00279-6

Tian, F., Chance, B., and Liu, H. (2009). Investigation of the prefrontal cortex in response to duration-variable anagram tasks using functional near-infrared spectroscopy. *J. Biomed. Opt.* 14:054016. doi: 10.1117/1.3241984

Toda, N. (2012). Age-related changes in endothelial function and blood flow regulation. *Pharmacol Ther.* 133, 159–176. doi: 10.1016/j.pharmthera.2011.10.004

Tulppo, M. P., Kiviniemi, A. M., Hautala, A. J., Kallio, M., Seppänen, T., Mäkikallio, T. H., et al. (2005). Physiological background of the loss of fractal heart rate dynamics. *Circulation* 112, 314–319. doi: 10.1161/CIRCULATIONAHA.104.523712

Valencia, M., Artieda, J., Alegre, M., and Maza, D. (2008). Influence of filters in the detrended fluctuation analysis of digital electroencephalographic data. *J. Neurosci. Methods* 170, 310–316. doi: 10.1016/j.jneumeth.2008.01.010

Vandeput, S., Verheyden, B., Aubert, A. E., and Van Huffel, S. (2012). Nonlinear heart rate dynamics: circadian profile and influence of age and gender. *Med. Eng. Phys.* 34, 108–117. doi: 10.1016/j.medengphy.2011.07.004

Vermeij, A., Meel-van den Abeelen, A. S., Kessels, R. P., van Beek, A. H., and Claassen, J. A. (2014). Very-low-frequency oscillations of cerebral hemodynamics and blood pressure are affected by aging and cognitive load. *Neuroimage* 85 (Pt 1), 608–615. doi: 10.1016/j.neuroimage.2013.04.107

Wardlaw, J. M., Smith, C., and Dichgans, M. (2013). Mechanisms of sporadic cerebral small vessel disease: insights from neuroimaging. *Lancet Neurol.* 12, 483–497. doi: 10.1016/s1474-4422(13)70060-7

Watts, D. J., and Strogatz, S. H. (1998). Collective dynamics of "small-world" networks. *Nature* 393, 440–442. doi: 10.1038/30918

West, B. J. (1991). *Fractal Physiology and Chaos in Medicine.* World Scientific Pub. Co. Inc.

Wink, A. M., Bullmore, E., Barnes, A., Bernard, F., and Suckling, J. (2008). Monofractal and multifractal dynamics of low frequency endogenous brain oscillations in functional MRI. *Hum. Brain Mapp.* 29, 791–801. doi: 10.1002/hbm.20593

Wylie, G. R., Graber, H. L., Voelbel, G. T., Kohl, A. D., DeLuca, J., Pei, Y., et al. (2009). Using co-variations in the Hb signal to detect visual activation: a near infrared spectroscopic imaging study. *Neuroimage* 47, 473–481. doi: 10.1016/j.neuroimage.2009.04.056

Yamada, T., Umeyama, S., and Matsuda, K. (2012). Separation of fNIRS Signals into Functional and Systemic Components Based on Differences in Hemodynamic Modalities. *PLoS ONE* 7:0050271. doi: 10.1371/journal.pone.0050271

Zapperi, S., Bækgaard Lauritsen K., and Stanley, H. E. (1995). Self-organized branching processes: mean-field theory for avalanches. *Phys. Rev. Lett.* 75, 4071–4074.

Zhao, L., Li, W., Fenu, A., Podobnik, B., Wang, Y., and Stanley, H. E. (2017). The q-dependent detrended cross-correlation analysis of stock market. *arXiv preprint arXiv:*1705.01406. doi: 10.1088/1742-5468/aa9db0

Zhou, W. X. (2008). Multifractal detrended cross-correlation analysis for two nonstationary signals. *Phys. Rev. E Stat. Nonlin. Soft. Matter Phys.* 77(6 Pt 2), 066211. doi: 10.1103/PhysRevE.77.066211

Zhu, Y. S., Tseng, B. Y., Shibata, S., Levine, B. D., and Zhang, R. (2011). Increases in cerebrovascular impedance in older adults. *J. Appl. Physiol.* 111, 376–381. doi: 10.1152/japplphysiol.01418.2010

Zimeo Morais, G. A., Scholkmann, F., Balardin, J. B., Furucho, R. A., de Paula, R. C. V., Biazoli, C. E. Jr., et al. (2018). Non-neuronal evoked and spontaneous hemodynamic changes in the anterior temporal region of the human head may lead to misinterpretations of functional near-infrared spectroscopy signals. *Neurophotonics* 5:011002. doi: 10.1117/1.NPh.5.1.011002

Conflict of Interest Statement: The authors declare that the research was conducted in the absence of any commercial or financial relationships that could be construed as a potential conflict of interest.

frontiers in Physiology

ORIGINAL RESEARCH
published: 17 August 2018
doi: 10.3389/fphys.2018.01118

Multifractal Analysis Reveals Decreased Non-linearity and Stronger Anticorrelations in Heart Period Fluctuations of Fibromyalgia Patients

*Cesar F. Reyes-Manzano[1], Claudia Lerma[2], Juan C. Echeverría[3], Manuel Martínez-Lavin[4], Laura A. Martínez-Martínez[4], Oscar Infante[2] and Lev Guzmán-Vargas[1]**

[1] Unidad Profesional Interdisciplinaria en Ingeniería y Tecnologías Avanzadas, Instituto Politécnico Nacional, Ciudad de Mexico, Mexico, [2] Departamento de Instrumentación Electromecánica, Instituto Nacional de Cardiología Ignacio Chávez, Ciudad de Mexico, Mexico, [3] Departamento de Ingeniería Eléctrica, Universidad Autónoma Metropolitana Unidad Iztapalapa, Ciudad de Mexico, Mexico, [4] Departamento de Reumatología, Instituto Nacional de Cardiología Ignacio Chávez, Ciudad de Mexico, Mexico

OPEN ACCESS

Edited by:
Plamen Ch. Ivanov,
Boston University, United States

Reviewed by:
Luis F. Ciria,
Universidad de Granada, Spain
Pandelis Perakakis,
Universidad Loyola Andalucía, Spain

***Correspondence:**
Lev Guzmán-Vargas
lguzmanv@ipn.mx

Specialty section:
This article was submitted to Fractal Physiology, a section of the journal Frontiers in Physiology

Received: *05 April 2018*
Accepted: *25 July 2018*
Published: *17 August 2018*

Citation:
Reyes-Manzano CF, Lerma C, Echeverría JC, Martínez-Lavin M, Martínez-Martínez LA, Infante O and Guzmán-Vargas L (2018) Multifractal Analysis Reveals Decreased Non-linearity and Stronger Anticorrelations in Heart Period Fluctuations of Fibromyalgia Patients. Front. Physiol. 9:1118. doi: 10.3389/fphys.2018.01118

Objective: To characterize the multifractal behavior of the beat to beat heart-period or RR fluctuations in fibromyalgia patients (FM) in comparison with healthy-matched subjects.

Methods: Multifractral detrended fluctuation analysis (MDFA) was used to study multifractality in heartbeat times-series from 30 female healthy subjects and 30 female patients with fibromyalgia during day and night periods.The multifractal changes as derived from the magnitude and sign analysis of these RR fluctuations were also assessed.

Results: The RR fluctuations dynamics of healthy subjects showed a broad multifractal spectrum. By contrast, a noticeable decrease in multifractality and non-linearity was observed for patients with fibromyalgia. In addition, the spectra corresponding to FM subjects were located on the average to the right of the spectra of healthy individuals, indicating that the local scaling exponents reflect a smoother behavior compared to healthy dynamics. Moreover, the multifractal analysis as applied to the magnitude and sign heartbeat series confirmed that, in addition to a decreased nonlinearity, fibromyalgia patients presented stronger anticorrelation in directionality, which did not remain invariant for small or rather larger fluctuations as it occurred in healthy subjects.

Conclusion: When compared to healthy controls, fibromyalgia patients display decreased nonlinearity and stronger anticorrelations in heart period fluctuations. These findings reinforce the hypothesis of the potential role of the dysfunctional autonomic nervous system in the pathogenesis of fibromyalgia.

Keywords: heart rate variability, scaling, magnitude and sign analysis, complexity theory, dysautonomia, multifractaility, fibromyalgia

1. INTRODUCTION

Diverse methods derived from non-linear dynamics and statistical physics have been used to characterize the spatiotemporal organization displayed by complex signals from different living systems (Ashkenazy et al., 2002; Hu et al., 2004; Ivanov et al., 2001, 2009; Bassingthwaighte et al., 2013). Frequently, many of these signals exhibit power law scaling when analyzed by techniques which are capable to detect a single scaling exponent; but for other signals, a better description is given in terms of a set of local exponents as it is the case of multifractals (Goldberger et al., 2002; Bunde et al., 2012). The multifractal formalism was introduced in the context of turbulence studies (Kolmogorov, 1941; Frisch, 1995) and velocity fluctuations (Frisch and Parisi, 1985). Since Mandelbrot (1974) introduced the concept of multifractality in the context of geometric objects; many different systems have been described using a broad multifractal spectrum, indicating that a wide range of local exponent values are needed to characterize the irregularity in the original signal (Mandelbrot, 1977; Ivanov et al., 1999a, 2001; Feder, 2013). The traditional procedure to perform a multifractal analysis is derived from the construction of a standard partition function, and only applies to normalized stationary signals (Wang et al., 2014). At the beginning of the 90s, the wavelet transform modulus maxima (WTMM) method was introduced to determine the multifractal spectrum based on wavelet transform over different scales (Daubechies, 1992; Bacry et al., 1993; Muzy et al., 1993, 1994; Arneodo et al., 1995a,b; Ivanov et al., 1996).

Later, in 2002 Kantelhardt et al. (2002) introduced the multifractral detrended fluctuation analysis (MDFA), as an extension of the monofractal detrended fluctuation analysis (DFA) method (Peng et al., 1994). One of the advantages of the MDFA is that it provides a stable spectrum of a range of multifractal signals, with a reliable estimation of the set of local Hurst exponents. Besides, the MDFA has been tested to extract a reliable multifractal spectrum when it is applied within time scales corresponding to low frequencies (Galaska et al., 2008).

On the other hand, the RR fluctuations or heart rate variability has been the object of study by means of nonlinear methods during past decades (Nunes Amaral et al., 2001; Ivanov et al., 2001, 2009; Peña et al., 2009; Hernández-Pérez et al., 2011). One of the most important features extracted by means of these methods is the presence of power-law fractal organization under healthy circumstances, while a degradation of the fractal scaling is frequently observed for pathologic conditions (Guzmán-Vargas et al., 2003). A more detailed assessment of the complex RR fluctuations have revealed that healthy interbeat dynamics is well described by a broad mutifractal spectrum, and a reduction in the multifractality was detected for patients with congestive heart failure (Ivanov et al., 1996; Guzmán-Vargas and Angulo-Brown, 2003; Guzmán-Vargas et al., 2005; Bojorges-Valdez et al., 2007; Galaska et al., 2008).

Given the need to elucidate the etiology of fibromyalgia (FM), identifying alterations in its RR fluctuations complexity has gained particular interest. In this pathology, chronic pain and other symptoms affect multiple systems extensively (Martinez-Lavin et al., 2008). The pathophysiology of FM remains uncertain, and no specific mechanisms can be pinpointed to explain the dynamical changes observed in the heart rate variability of these patients. However, there is strong evidence about the involvement of the autonomic nervous system both, in the etiology and the multifaceted alterations of this disease. The main affliction of the syndrome (chronic pain) seems to be maintained by the chronic sympathetic hyperactivity that is associated with altered connections between the sensory neurons and the sympathetic nervous system (Martinez-Lavin, 2004). In addition, the fact of having defective catecholamine clearing enzymes appears to increase the susceptibility to pain (Diatchenko et al., 2004). We have previously hypothesized that the understanding of FM requires an approach in which the autonomic nervous system is considered as a complex adaptive system, which in itself constitutes the main element of the stress response system (Martinez-Lavin et al., 2008). From this point of view, we would expect that the alterations in this complex adaptive system become manifested in the dynamical properties of the physiological variables that such system regulates (such as the beat to beat heart-period or RR fluctuations). The first evidence of an altered complexity of RR fluctuations in FM was the observation of a larger monofractal short-term scaling exponent in FM patients compared to healthy subjects (Lerma et al., 2016). Yet, it is not known if the multifractal spectrum of these patients also shows a reduction or other alterations. Here, we studied RR time series of patients with FM during day and night periods. Our aim was to characterize the multifractal behavior of the RR fluctuations in FM patients and in carefully selected healthy-matched subjects, using the MDFA method. In addition, the multifractal changes as derived from the magnitude and sign analysis of these RR fluctuations were also assessed.

2. METHODS AND DATA

2.1. Multifractal Detrended Fluctuation Analysis (MFDFA)

The multifractal detrended fluctuation analysis was introduced by Kantelhardt et al., which is a robust method to detect the scaling properties of the fluctuactions related with multifractilty of a given signal. We briefly explain the main steps of the multifractal detrended fluctuation analysis (Kantelhardt et al., 2002):

- Step 1: Given the time series x_k of length N. First, we determine the profile

$$Y(i) \equiv \sum_{k=1}^{i} [x_k - \langle x \rangle], \qquad i = 1, ..., N, \tag{1}$$

  where $\langle x \rangle$ represents the mean value.
- Step 2: Next, the profile $Y(i)$ is divided into $N_s \equiv int(N/s)$ segments of size s. To make more robust the statistics, the same procedure is applied but starting from the end of the time series, and in this way, $2N_s$ segments are considered for the calculations.

- Step 3: A least-square fit is applied to the $2N_s$ segments of the integrated data. Then the variance is calculated,

$$F^2(v,s) \equiv \frac{1}{s}\sum_{i=1}^{s}\{Y[(v-1)s+i] - y_v(i)\}^2, \quad (2)$$

for, $v = 1, ..., N_s$, where y_v represents the fitting polynomial, which can be linear, quadratic, or a higher order polynomial.

- Step 4: Now the qth-values are considered in the fluctuation function

$$F_q(s) \equiv \left\{\frac{1}{2N_s}\sum_{v=1}^{2N_s}[F^2(v,s)]^{\frac{q}{2}}\right\}^{\frac{1}{q}} \quad (3)$$

with q a parameter that modifies the behavior of $F_q(s)$. Particularly, the cases of $q < 0$ characterize small fluctuations whereas $q > 0$ refer to larger ones (Kantelhardt et al., 2002). The steps 2–4 are repeated for different time scales s in order to construct the log-log plot of $F_q(s)$ vs. s.

- Step 5: Finally, the scaling behavior is described by,

$$F_q(s) \sim s^{h(q)}, \quad (4)$$

where $h(q)$ is an exponent that may depend on q and it is called the generalized Hurst exponent. For instance, when $q = 2$, $h(2)$ is related to the standard Hurst exponent. For monofractal time series, it is expected that $h(q)$ remains constant as the value of q is changed.

The use of different moments (q-values) permits to stablish a relationship between the generalized Hurst exponent $h(q)$ and the scaling exponent $\tau(q)$, which is defined via an appropriate partition function in the standard multifractal formalism (Feder, 1988; Kantelhardt et al., 2002). This relationship is given by,

$$\tau(q) = qh(q) - 1. \quad (5)$$

The singularity spectrum $f(\alpha)$ can be constructed to characterize the multifractal properties of the time series. Specifically, $f(\alpha)$ can obtained from $\tau(q)$ via the Legendre transform, by taking

$$\alpha = \tau'(q) \qquad \text{and} \qquad F(\alpha) = q\alpha - \tau(q), \quad (6)$$

where α represents the singularity strength of Holder exponent and $F(\alpha)$ is the dimension of the subset of the time series that is characterized by α. We also recall that sometimes the multifractal properties are described in terms of the generalized dimensions:

$$D(q) = \frac{\tau(q)}{q-1}. \quad (7)$$

In order to characterize the multifractal spectrum $f(\alpha)$, we resort to the following quantities (Makowiec et al., 2006; Galaska et al., 2008):

- **Width of the spectrum:** distance between the maximum and minimum Holder exponents,

$$\Delta\alpha = \alpha_{max} - \alpha_{min}. \quad (8)$$

- **Left-side width of the spectrum:** distance between α^* [which corresponds to $F_{max}(\alpha^*)$] and minimum α value

$$\Delta\alpha^{left} = \alpha_{F_{max}} - \alpha_{min}. \quad (9)$$

- **Right-side width of the spectrum:** distance between maximum α and α^*

$$\Delta\alpha^{rigth} = \alpha_{max} - \alpha_{F_{max}}. \quad (10)$$

- **Global Hurst exponent:**

$$H_G = \frac{1}{2}(1 + \tau(2)), \quad (11)$$

where $\tau(2)$ represents the value of the scaling exponent for $q = 2$.

- **Left-slope and right-slope in τ:** linear approximation to the behavior of τ for negative (left) and positive (right) moments q.

To further explore the multifractal changes in healthy and FM conditions, we also resort to the magnitude and sign analysis of the RR sequences. Ashkenazy et al. (2001) have reported that scaling properties of the magnitude series are related to the multifractal structure of the origial signal (non-linear properties), whereas scaling sign analysis reveal mostly information about linear correlation of the time series. Briefly, from the increment ΔRR series, two new series are constructed: the magnitude series $|\Delta RR|$ and sign(ΔRR), where the function sign(ΔRR) is defined to be $+1$ for $\Delta RR > 0$, -1 for $\Delta RR < 0$ and 0 for $\Delta RR = 0$. The magnitude and sign analysis of heart rate variability have been proved to be useful to deferentiate between pathological changes and certain clinical conditions (Ashkenazy et al., 2001; Schmitt and Ivanov, 2007; Reyes-Lagos et al., 2016).

2.2. Patients and Data

As previously described (Lerma et al., 2016), we studied 30 women with fibromyalgia. Eligibility criteria for patients were the following: (1) to have fibromyalgia according to the 1990 American College of Rheumatology guidelines; (2) to be free of any medication that could affect autonomic performance including tranquilizers or antidepressants; (3) to be 18–50 years old; (4) to be in the fertile period of their lives with active menstrual cycles, but not to be in their menstrual period the day of the study; (5) to have no comorbid conditions; and (6) to freely agree to participate in the study. Patients were sourced from different rheumatology private practices in Mexico City. For each patient, a control of similar age ($\pm$2 years) was recruited. Eligibility criteria for controls were the following: (1) to consider themselves healthy and to have five or fewer fibromyalgia tender points; and (2) Not to be in their menstrual period the day of the study. Controls were medical or paramedical personnel. A rheumatologist examined all prospective participants to ascertain the diagnosis of FM or the healthy status of controls. All participants filled out validated spanish questionnaires for a systematic and comprehensive assessment of their symptoms, including the Fibromyalgia Impact Questionnaire (FIQ) and

the Composite Autonomic Symptom Scale (COMPASS). The fibromyalgia group had higher scores of the symptoms than the control group (total FIQ score: 63 ± 16 vs. 10 ± 10, $p < 0.0001$; total COMPASS score: 55 ± 16 vs. 15 ± 11, $p < 0.0001$). A detailed description of all symptoms is described elsewhere (Lerma et al., 2016). FM patients had similar age and body mass index (age = 31 ± 8 years old, body mass index = 23.8 ± 4.4 Kg/m^2) than healthy participants (31 ± 8 years old, and body mass index (24.4 ± 3.2 Kg/m^2). All participants signed a written consent form. The study was approved by the Research Committee and by the Bioethics Committee of the Instituto de Cardiología de Mexico.

The RR fluctuations time series of each participant were obtained from an ambulatory 24 h electrocardiogram recording with a Holter monitor (model DMS-307, DMS Inc.). An automated computer program was used to identify the time of occurrence of each heartbeat. Then the difference in time between consecutive heartbeats was calculated (RR interval), and an adaptive filtering method was used to identify and replace the RR intervals that were not originated during normal sinus rhythm (Wessel et al., 2000). The RR fluctuations time series had a mean RR interval of 0.806 ± 0.082 in the FM group and 0.770 ± 0.074 s in the healthy group ($p = 0.070$).

2.3. Statistical Analysis

Kolmogorov–Smirnov tests were applied to all variables to assess their normal distributions. Variables with normal distribution were compared between groups by Student t-tests; variables with no normal distributions were compared by Mann–Withney U-tests. Regression analyses of $h(q)$ vs. q were performed to compare values of $h(q)$ between FM and control groups. For each group, the 95% confidence intervals of each model parameter were estimated in a second order polynomial model [$h(q) = \beta_0 + \beta_1 q + \beta_2 q^2$]. The statistical analysis was performed with SPSS version 21.0.

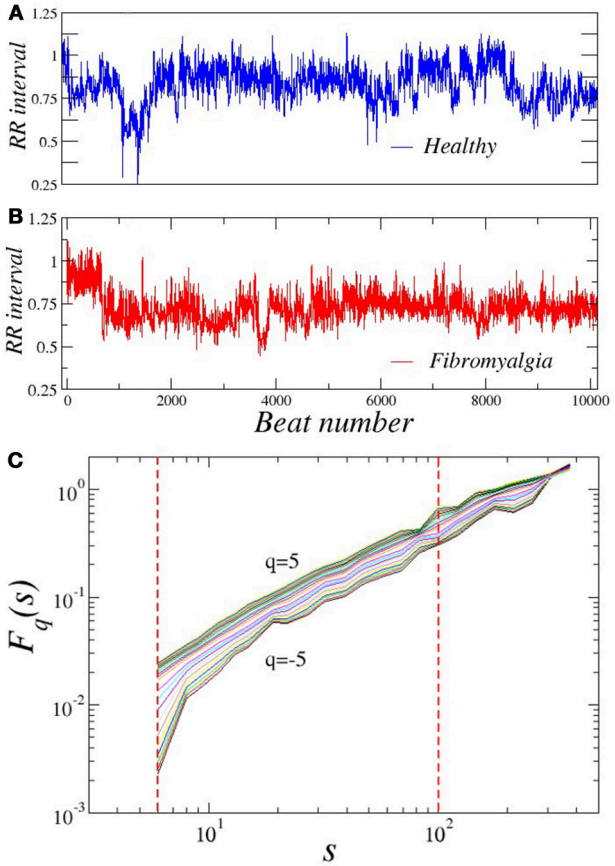

FIGURE 1 | Representative RR time series during timeday of a **(A)** healthy subject and **(B)** patient with FM. Plot of **(C)** $F_q(s)$ vs. q of a RR sequence (healthy subject) for several values of q.

3. RESULTS

For both, healthy and FM patients, we performed the multifractal analysis of RR time series from two 5-h segments of the ECG recordings: nighttime (0.00 p.m.–5:00 a.m.) and daytime (2:00 p.m.–7:00 p.m.). These series are illustrated in the **Figures 1A,B**. First, we explored the behavior of the fluctuactions in the plane $F_q(s)$ vs. s for different values of q and for different segment lenghts (from 30 min to 5 h) as shown in the **Figure 1C**. It is very important to consider the proper range selection of scales s, for which the fittings in the fluctuactions $F_q(s)$ are calculated. In our case, we selected the scale range $6 < s < 100$ and the length of the segment $\Delta t = 1,500 \approx 30$ min to apply MFDFA. The values of the local scaling exponents of all subjects are averaged over all segments of the 5 h interval (either at daytime or nighttime). The behavior of $h(q)$ vs. q was determined for q-values within the interval $[-5, 5]$, and the multifractal spectrum was then constructed. **Figure 2** shows the results of the MFDFA for the healthy and FM groups for daytime records. We observe that the Hurst exponent $h(q)$ is not independent of q, i.e., a similar variation in the average scaling-exponent values as a function of q is observed for both groups (the confidence intervals of β_1 and β_2 from both groups are overlapped). This is a manifestation of multifractal properties in the time series (**Figure 2A**). However, the confidence intervals of β_0 from both groups do not overlap, indicating that the $h(q)$ values from FM data are consistently higher (i.e., smoother) than the corresponding values of the healthy group. These results are in good concordance with a previous report about monofractal estimation of the scaling exponent [$h(2)$] based on the standard two-point correlation DFA method (Lerma et al., 2016). For healthy subjects, we observe that the behavior of $\tau(q)$ vs. q exhibits slightly more nonlinearity (**Figure 2B**) than the FM patients, which show more linear $\tau(q)$ behavior. This indicates that under healthy conditions the dynamics seems to show more multifractal features (**Table 1**). We find significant differences in Right-slope in τ ($p < 0.05$) between healthy and FM groups, but not significant differences were found for Left-slope in τ ($p > 0.5$). **Figure 2C** shows the spectra of both groups. We observe that, for healthy subjects, the local Holder exponents cover the range $1 < \alpha < 1.62$, while for FM patients the dominant exponents fall within the interval $1.1 < \alpha < 1.7$. These results indicate that FM signals are similar to Brownian-type fluctuactions because the interval of the dominant exponents are closer to the 1.5 value.

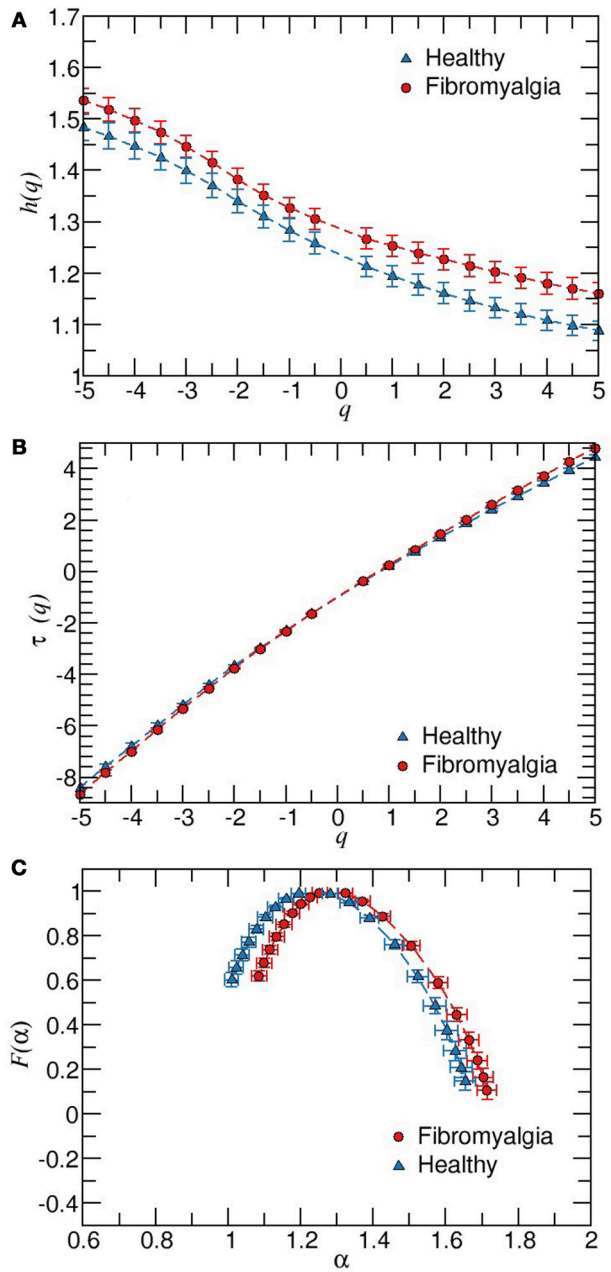

FIGURE 2 | Results of the MFDFA for all healthy and FM subjects. **(A)** Plot of $h(q)$ vs. q. The values of $h(q)$ are derived from fittings within the interval $6 < s < 100$ and a time window of 1,500 RR values during daytime. The estimated regression models were $h(q) = 1.295 - 0.039q + 0.003q^2$ (for FM patients), and $h(q) = 1.261 - 0.042q + 0.002q^2$ (for healthy group). In both models, β_0, β_1, and $\beta_2 \neq 0$ with $p < 0.001$ and $R^2 > 0.55$. The confidence intervals of β_1 and β_2 are overlapped in both groups, while there was no overlap in β_0 of the FM group (1.281, 1.309) with the healthy group (1.226, 1.256). **(B)** Behavior of $\tau(q)$ for data showed in **(A)**. **(C)** Multifractal spectrum $F(\alpha)$ *vs* α. Error bars represent the standard error of the mean.

TABLE 1 | Characteristics of the multifractal spectrum in patients with FM and healthy subjects during daytime.

Parameters	Healthy	Fibromyalgia	*p*-value
$\Delta\alpha$	0.6324 ± 0.1809	0.6136 ± 0.1291	0.6565
$\Delta\alpha^{left}$	0.4317 ± 0.1567	0.4320 ± 0.1150	0.9947
$\Delta\alpha^{rigth}$	0.2006 ± 0.1095	0.1816 ± 0.0813	0.4638
H_G	1.1595 ± 0.1108	1.2302 ± 0.1089	0.01947
Left-slope in τ	1.5389 ± 0.2122	1.6031 ± 0.2871	0.3459
Right-slope in τ	1.0904 ± 0.1515	1.1770 ± 0.1257	0.0236

The values of the parameters (mean ± SD) were obtained from fittings within the interval $6 < s < 100$ *in the* $\log F_q(s)$ *vs.* $\log s$ *plane.* H_G *stands for global Hurst exponent.*

Next, we also repeated the calculations for nighttime periods. We find that during this period, there are not significant differences between healthy and FM groups regarding the multifractal properties (data not shown). To endorse our findings, we also performed the same analysis on two surrogate data sets derived from each group. First, we shuffled the RR intervals to destroy temporal correlations while preserving the probability distribution. Second, the Fourier transform is applied to the RR intervals sequences, then we randomize the Fourier phases and the inverse Fourier transform is performed to get the surrogate time series. This process preserves the linear properties of the signal (the same power spectrum) but changes the probability distribution of the RR intervals (see **Figure 3**). We observe that when the temporal two-point correlations are destroyed, the dominant local scaling exponents are close to the 0.5 value for both groups (**Figures 3A,C**). For phase-randomized data, we found that the width of the multifractal spectrum of the healthy group is narrower than the width corresponding to FM patients (**Figures 3B,D**), confirming that the contribution of phase correlations to the multifractality is more important in healthy subjects compared to FM patients where the multifractal spectrum suffered a small change, as described above.

Next, we apply the MDFA to the magnitude and sign series derived from the daytime or nighttime intervals. As it is shown in **Figure 4A**, the average values of $h(q)$ of magnitudes series are higher for healthy subjects compared to the FM group. Moreover, the width of the multifractal sprectrum of healthy data is slightly larger than the width of the FM case, confirming that the contribution of nonlinearities is more important under healthy dynamics compared to the FM dynamics (**Figure 4B**). **Figure 5** shows the results of the sign series. We observe that, unlike the previous cases, here FM data lead to a wider multifractal spectrum compared to healthy group. We also remark that the FM group is characterized by a more anticorrelated scaling exponents while the dominant exponents for healthy subjetcs are less anticorrelated. For a better comparison of both groups, the above description of the differences in the multifractal structure between healthy subjects and FM patiens allow us to construct a scatter plot of the generalized Hurst exponent $h_{RR}(q)$ of the original RR time series vs. the corresponding Hurst exponent of magnitude $h_{mag}(q)$ [or $h_{RR}(q)$ vs. sign $h_{sign}(q)$] (**Figure 6**). We find that, for $h_{RR}(q)$ vs. $h_{mag}(q)$, two different tendencies are observed for positive and negative moments with a steeper slope in the case of negative moments and both groups are clearly differentiated (**Figure 6A**). For $h_{RR}(q)$ vs. $h_{sign}(q)$, sign scaling

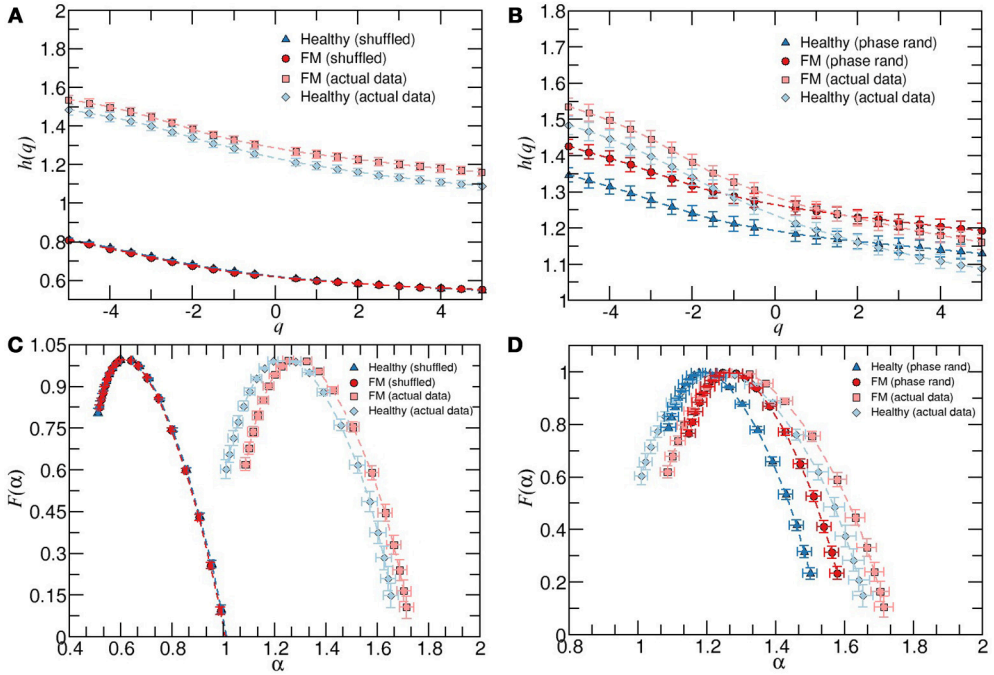

FIGURE 3 | (A) Average behavior of $h(q)$ vs. q for healthy subjects, patients with FM and their corresponding shuffled version. **(B)** As in **(A)** but for the phase randomized data. The exponents were calculated for the scaling region $6 < s < 100$. **(C)** Multifractal spectrum $F(\alpha)$ *vs* α for healthy and FM groups and their corresponding shuffled version. **(D)** As in **(C)** but for the phase randomized data, all during timeday. Error bars represent the standard error of the mean.

exponents of healthy data are almost constant for both negative and positive moments while FM patients exhibit variations in both type of scaling exponents and again both groups are separated, specially for positive moments (**Figure 6B**).

4. DISCUSSION

This work presents a thorough exploration of the dynamic behavior of heart rate variability in FM patients from the point of view of multifractality, nonlinearity and directionality. Our main findings are decreased multifractality and non-linearity as well as stronger anticorrelation in FM patients during daytime compared to matched-healthy subjects.

The differences during daytime between groups were mainly identified in two characteristics of the multifractal spectrum (H_G and the right slope in τ) as well as in a larger effect of the phase randomization that provoked a narrower width of the resulting multifractal spectrum for the healthy group. This implied a reduced nonlinearity of heart rate variability in FM patients, which was also confirmed by the multifractal structure of the magnitude series because the generalized $h_{mag}(q)$ values of the healthy group were consistently larger for all qth values. Moreover, the generalized $h_{sign}(q)$ showed consistently smaller values in FM patients, which implies a stronger anticorrelated behavior for all qth values ($q > -4$). The multrifractal approach also exhibited that in FM patients, the value of $h_{sign}(q)$ changes at different qth values, while this variation does not occur in healthy subjects. From a dynamical point of view, whereas a narrower and shifted multifractal spectrum in FM patients reveals smoother Brownian-like fluctuations, in accordance with previous results based on a monofractal analysis (Lerma et al., 2016), their stronger anticorrelated behavior indicates that the fluctuations in heart rate variability tend to alternate the increments and decrements of the RR interval at several scales. Given the well-known effects of periodic trends on the scaling properties (Hu et al., 2004; Schmitt and Ivanov, 2007; Perakakis et al., 2009), such smoother fluctuations in FM patients may arise, among other factors, from the occurrence of periodic breathing patterns that have been observed in FM (Sergi et al., 1999). Future studies are required to asses the potential influence of periodic breathing patterns upon multifractality HRV properties in FM. FM is characterized by a wide range of symptoms and inter-subject variability is usually very high. A strength of our study is the carefully selected patient and control groups. All patients had well-established fibromyalgia, without comorbid conditions and were free of any medication that could affect autonomic nervous system performance. Expert rheumatologists examined all prospective participants to ascertain the diagnosis of FM or the healthy status of controls according to the American College of Rheumatology. Further studies with large samples are needed to assess the generalization of the present findings in more heterogeneous samples of patients

Previous studies have used both time domain and frequency domain heart rate variability analysis. The majority of studies

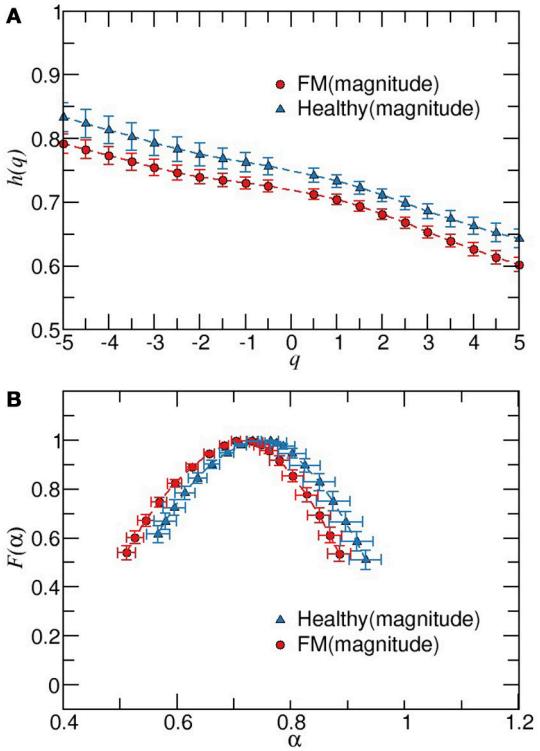

FIGURE 4 | Multifractal detrended fluctuation analysis of magnitude increment sequences of healthy and FM patients during timeday. **(A)** Behavior of $h(q)$ vs. q for scaling exponents obtained from fittings in the scaling region $15 < s < 100$. $F(\alpha)$ vs. α for data showed in **(B)**. Error bars represent the standard error of the mean.

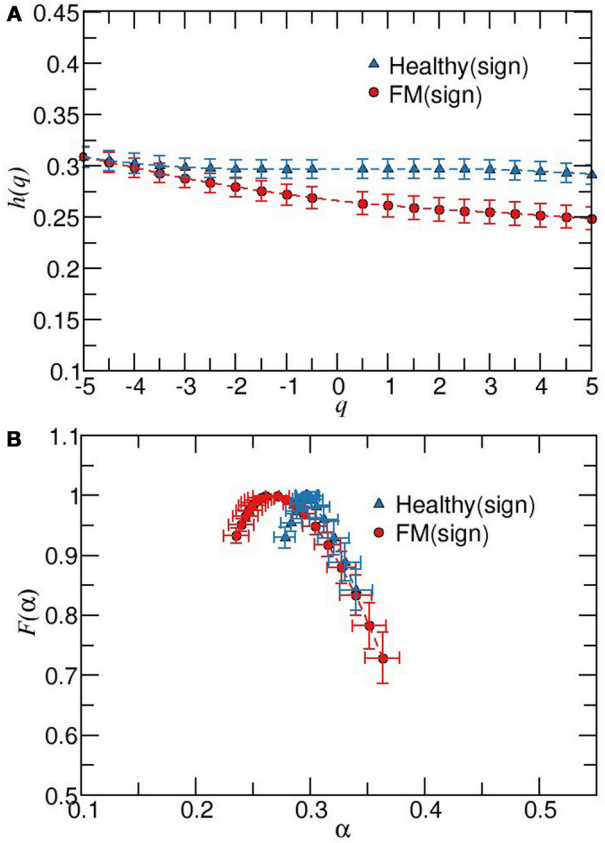

FIGURE 5 | Multifractal detrended fluctuation analysis of sign time series from healthy and patients with FM during timeday.**(A)** Plot of $h(q)$ vs. q for scaling exponents obtained from fittings in the scaling region $15 < s < 100$. **(B)** $F(\alpha)$ vs. α for data showed in **(A)**. Error bars represent the standard error of the mean.

observed lower heart rate variability in FM patients compared to healthy control persons, as well as increased sympathetic activity and a blunted autonomic response to stressors (Meeus et al., 2013). The power spectral analysis of heart rate variability in FM patients have actually shown a sympathetic predominance during all phases of the circadian cycle (Martínez-Lavín et al., 1998), and the time domain analysis indicated a decreased overall variability, which correlated with some FM symptoms (Lerma et al., 2011). In our study, representative multifractality indexes were different between patients and controls during daytime but not at night. A hypothetical explanation for this finding could be that the blunted response to stressors of fibromyalgia patients degrade the multifractal dynamics exhibited by heart rate variability when confronted to the daytime chores. Concerning patients with congestive heart failure, a disease that compromise the cardiovascular dynamics more severely than FM, a monofractal analysis of healthy dynamics vs. patients with congestive heart failure showed scaling exponents of both groups that are closer to each other during sleep phases with a noticeably similar irregular behavior compared to daytime periods (Ivanov et al., 1999b). Far from the reductionist vision of FM as a disease solely caused by chronic sympathetic hyperactivity, we consider that FM and related conditions may result from an overall degraded performance of the autonomic nervous system, which is a complex adaptive system that constitutes the main orchestrator of the stress response system (Martinez-Lavin et al., 2008). From this point of view, previous findings of smoother heart rate variability are consistent with the hypothesis of an altered and more "rigid" autonomic response to stress (Lerma et al., 2016). The current work provides further evidence of this decreased complexity in the autonomic nervous system because the multifractal analysis showed less nonlinearity in FM patients than in healthy subjects. This was observed by a larger H_G and larger right slope in τ (**Table 1**), which was also confirmed by the surrogate analysis and multifractal analysis of the magnitude series as explained above. Moreover, the multifractal analysis of the sign series showed that FM patients have an increased anticorrelated behavior, which is consistent with the sympathetic predominance of FM according to the stochastic feedback model for random walks (Ivanov et al., 1998). In this model, an increment of anticorrelations is achieved by introducing a dominant attracting factor to set the main heart rate (i.e., instead of concurrent influences from several factors, one modulating factor becomes predominant).

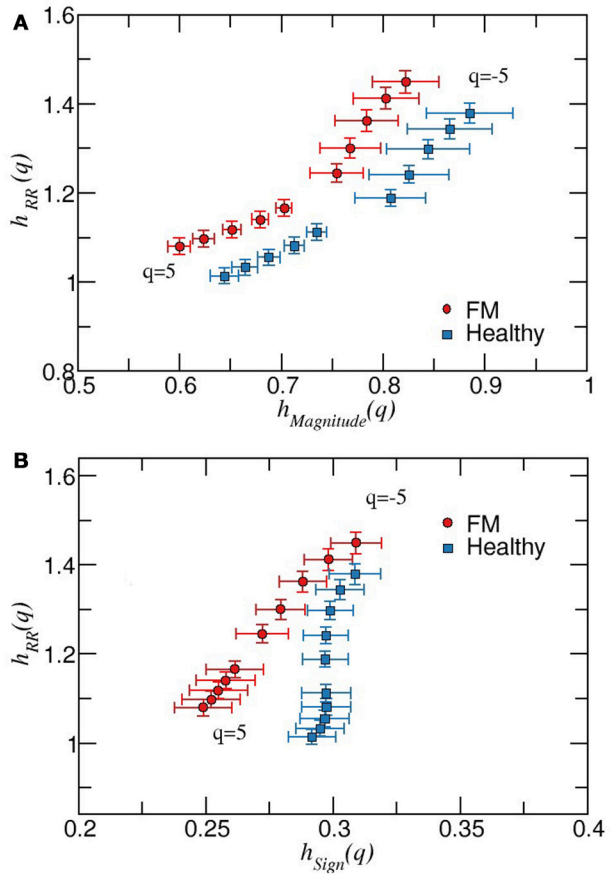

FIGURE 6 | (A) Scatter plot of the generalized Hurst exponents $h_{RR}(q)$ vs. $h_{mag}(q)$, for healthy and FM groups during daytime periods. For both groups, symbols with error bars represent the mean value, and the error bars the corresponding standard error of the mean. We observe that both groups are well separated for the different values of q. **(B)** As in **(A)** but for the generalized Hurst exponents $h_{RR}(q)$ vs. $h_{sign}(q)$, for healthy and FM groups during daytime periods. In this case, both groups are close each other for negative moments while tend to be more separated as q increases.

There are other hypotheses beyond the autonomic modulation that have motivated the exploration of changes in the anatomical or functional complexity, which both could be associated with the hyperactivity of the nociceptive system in FM patients. For example, morphometric analysis of different subcortical brain regions in FM patients showed a reduction in the total brainstem volume, which was significantly correlated with the clinical score of tender points (Fallon et al., 2013). From a functional point of view, the interaction between brain areas of FM patients has been assessed through network sensitivity analysis of electroencephalogram data. Two properties of such networks (node degree and frequency) showed significant correlation with chronic intensity pain, suggesting that the central nervous system of these patients has an altered network configuration that may increase hypersensitivity to pain (Lee et al., 2018). However, it remains uncertain if such changes of the central nervous system participate in functional alterations of other regulatory systems, and if this participation modifies effector variables such as the heart rate period.

The multifractal detrended analysis as applied here to magnitude and sign heart rate variability sequences indicated a potential route to evaluate the impairment of the regulatory adaptability because, regardless of characterizing the directionality in small ($q < 0$) or rather large fluctuations ($q > 0$), the level of anticorrelation remained invariant for healthy subjects. Given that our healthy subjects were carefully selected (see section 2), this finding could then imply that such invariance reveals stability because the interplay of different attracting factors (Ivanov et al., 1998) are similar manifested during the course of small or large fluctuations. The current work provides further evidence of this decreased complexity in the autonomic nervous system because the multifractal analysis showed less nonlinearity in FM patients than in healthy subjects. Future studies associating the severity of the disease will determine if this new information has clinical implications and additional analyses remain to be performed to assess this consideration.

5. CONCLUSIONS

The multifractal analysis of heart rate variability revealed a loss of complexity (i.e., less nonlinearity) and increased anticorrelated dynamical behavior in FM patients, which reinforces the hypothesis of the crucial role of the impaired autonomic nervous systems in the etiology and diverse alterations of FM.

AUTHOR CONTRIBUTIONS

CR-M participated in the study design, data analysis and interpretation, statistical analysis, and drafting of the article. CL participated in the study design, data collection, data interpretation, and drafting of the article. JE participated in the study design, data interpretation, and drafting of the article. MM-L contributed to the study design, enrollment of patients, and data interpretation. LM-M participated in the study design, enrollment of patients, data collection, and data interpretation. OI contributed to the study design and data interpretation. LG-V contributed to the conception and design of the study, data analysis, data interpretation, and drafting of the article. All the authors did a critical revision and gave their approval to the article.

FUNDING

This work was partially supported by COFAA-IPN, EDI-IPN, SNI-Conacyt, Mexico.

REFERENCES

Arneodo, A., Bacry, E., Graves, P., and Muzy, J.-F. (1995a). Characterizing long-range correlations in dna sequences from wavelet analysis. *Phys. Rev. Lett.* 74, 3293–3296. doi: 10.1103/PhysRevLett.74.3293

Arneodo, A., Bacry, E., and Muzy, J. (1995b). The thermodynamics of fractals revisited with wavelets. *Phys. A* 213, 232–275.

Ashkenazy, Y., Hausdorff, J. M., Ivanov, P. C., and Stanley, H. E. (2002). A stochastic model of human gait dynamics. *Phys. A* 316, 662–670. doi: 10.1016/S0378-4371(02)01453-X

Ashkenazy, Y., Ivanov, P. C., Havlin, S., Peng, C.-K., Goldberger, A. L., and Stanley, H. E. (2001). Magnitude and sign correlations in heartbeat fluctuations. *Phys. Rev. Lett.* 86, 1900–1903. doi: 10.1103/PhysRevLett.86.1900

Bacry, E., Muzy, J., and Arnéodo, A. (1993). Singularity spectrum of fractal signals from wavelet analysis: exact results. *J. Stat. Phys.* 70, 635–674.

Bassingthwaighte, J. B., Liebovitch, L. S., and West, B. J. (2013). *Fractal Physiology*. New York, NY: Springer.

Bojorges-Valdez, E. R., Echeverría, J. C., Valdés-Cristerna, R., and Peña, M. A. (2007). Scaling patterns of heart rate variability data. *Physiol. Meas.* 28, 721–730. doi: 10.1088/0967-3334/28/6/010

Bunde, A., Kropp, J., and Schellnhuber, H. J. (2012). *The Science of Disasters: Climate Disruptions, Heart Attacks, and Market Crashes*. Berlin: Springer Science & Business Media.

Daubechies, I. (1992). *Ten Lectures on Wavelets*. Philadelphia, PA: SIAM.

Diatchenko, L., Slade, G. D., Nackley, A. G., Bhalang, K., Sigurdsson, A., Belfer, I., et al. (2004). Genetic basis for individual variations in pain perception and the development of a chronic pain condition. *Hum. Mol. Genet.* 14, 135–143. doi: 10.1093/hmg/ddi013

Fallon, N., Alghamdi, J., Chiu, Y., Sluming, V., Nurmikko, T., and Stancak, A. (2013). Structural alterations in brainstem of fibromyalgia syndrome patients correlate with sensitivity to mechanical pressure. *Neuroimage Clin.* 3, 163–170. doi: 10.1016/j.nicl.2013.07.011

Feder, J. (1988). *Fractals (Physics of Solids and Liquids)*. New York, NY: Plennum.

Feder, J. (2013). *Fractals*. Oslo: Springer Science & Business Media.

Frisch, U. (1995). *Turbulence: The Legacy of AN Kolmogorov*. Cambridge: Cambridge University Press.

Frisch, U., and Parisi, G. (1985). "Fully developed turbulence and intermittency," in *Turbulence and Predictability in Geophysical Fluid Dynamics Climate Dynamics,* eds M. Ghil, R. Benzi and G. Parisi (Amsterdam: North-Holland Publisher), 71–88.

Galaska, R., Makowiec, D., Dudkowska, A., Koprowski, A., Chlebus, K., Wdowczyk-Szulc, J., et al. (2008). Comparison of wavelet transform modulus maxima and multifractal detrended fluctuation analysis of heart rate in patients with systolic dysfunction of left ventricle. *Ann. Noninvasive Electrocardiol.* 13, 155–164. doi: 10.1111/j.1542-474X.2008.00215.x

Goldberger, A. L., Nunes Amaral, L. A., Hausdorff, J. M., Ivanov, P. C., Peng, C.-K., and Stanley, H. E. (2002). Fractal dynamics in physiology: alterations with disease and aging. *Proc. Natl. Acad. Sci. U.S.A.* 99(Suppl. 1), 2466–2472. doi: 10.1073/pnas.012579499

Guzmán-Vargas, L., and Angulo-Brown, F. (2003). Simple model of the aging effect in heart interbeat time series. *Phys. Rev. E Stat. Nonlin. Soft Matter Phys.* 67:052901. doi: 10.1103/PhysRevE.67.052901

Guzmán-Vargas, L., Calleja-Quevedo, E., and Angulo-Brown, F. (2003). "On fractal analysis of cardiac interbeat time series," in *AIP Conference Proceedings*, 226–231.

Guzmán-Vargas, L., Munoz-Diosdado, A., and Angulo-Brown, F. (2005). Influence of the loss of time-constants repertoire in pathologic heartbeat dynamics. *Phys. A Stat. Mech. Appl.* 348, 304–316. doi: 10.1016/j.physa.2004.09.019

Hernández-Pérez, R., Guzmán-Vargas, L., Reyes-Ramirez, I., and Angulo-Brown, F. (2011). Differences in the stability of the heart interbeat rate during wake and sleep periods. *Fluct. Noise Lett.* 10, 405–416. doi: 10.1142/S0219477511000661

Hu, K., Ivanov, P. C., Chen, Z., Hilton, M. F., Stanley, H. E., and Shea, S. A. (2004). Non-random fluctuations and multi-scale dynamics regulation of human activity. *Phys. A Stat. Mech. Appl.* 337, 307–318. doi: 10.1016/j.physa.2004.01.042

Ivanov, P. C., Nunes Amaral, L. A., Goldberger, A. L., Havlin, S., Rosenblum, M. G., Struzik, Z. R., et al. (1999a). Multifractality in human heartbeat dynamics. *Nature* 399, 461–465.

Ivanov, P. C., Nunes Amaral, L. A., Goldberger, A. L., Havlin, S., Rosenblum, M. G., Stanley, H. E., et al. (2001). From 1/f noise to multifractal cascades in heartbeat dynamics. *Chaos* 11, 641–652. doi: 10.1063/1.1395631

Ivanov, P. C., Nunes Amaral, L. A., Goldberger, A. L., and Stanley, H. E. (1998). Stochastic feedback and the regulation of biological rhythms. *Europhys. Lett.* 43, 363–368.

Ivanov, P. C., Bunde, A., Nunes Amaral, L. A., Havlin, S., Fritsch-Yelle, J., Baevsky, R. M., et al. (1999b). Sleep-wake differences in scaling behavior of the human heartbeat: analysis of terrestrial and long-term space flight data. *Europhys. Lett.* 48, 594–600.

Ivanov, P. C., Ma, Q. D., Bartsch, R. P., Hausdorff, J. M., Nunes Amaral, L. A., Schulte-Frohlinde, V., et al. (2009). Levels of complexity in scale-invariant neural signals. *Phys. Rev. E Stat. Nonlin. Soft Matter Phys.* 79:041920. doi: 10.1103/PhysRevE.79.041920

Ivanov, P. C., Rosenblum, M. G., Peng, C.-K., Mietus, J., Havlin, S., Stanley, H. E., et al. (1996). Scaling behaviour of heartbeat intervals obtained by wavelet-based time-series analysis. *Nature* 383, 323–327.

Kantelhardt, J. W., Zschiegner, S. A., Koscielny-Bunde, E., Havlin, S., Bunde, A., and Stanley, H. E. (2002). Multifractal detrended fluctuation analysis of nonstationary time series. *Phys. A Stat. Mech. Appl.* 316, 87–114. doi: 10.1016/S0378-4371(02)01383-3

Kolmogorov, A. N. (1941). *The Local Structure of Turbulence in Incompressible Viscous Fluid for Very Large Reynolds Numbers.* London: Doklady Akademiia Nauk SSSR.

Lee, U., Kim, M., Lee, K., Kaplan, C. M., Clauw, D. J., Kim, S., et al. (2018). Functional brain network mechanism of hypersensitivity in chronic pain. *Sci. Rep.* 8:243. doi: 10.1038/s41598-017-18657-4

Lerma, C., Martinez, A., Ruiz, N., Vargas, A., Infante, O., and Martinez-Lavin, M. (2011). Nocturnal heart rate variability parameters as potential fibromyalgia biomarker: correlation with symptoms severity. *Arthritis Res. Ther.* 13:R185. doi: 10.1186/ar3513

Lerma, C., Martinez-Martinez, L.-A., Ruiz, N., Vargas, A., Infante, O., and Martinez-Lavin, M. (2016). Fibromyalgia beyond reductionism. Heart rhythm fractal analysis to assess autonomic nervous system resilience. *Scand. J. Rheumatol.* 45, 151–157. doi: 10.3109/03009742.2015.1055299

Makowiec, D., Gała, R., Dudkowska, A., Rynkiewicz, A., and Zwierz, M. (2006). Long-range dependencies in heart rate signals-revisited. *Phys. A Stat. Mech. Appl.* 369, 632–644. doi: 10.1016/j.physa.2006.02.038

Mandelbrot, B. B. (1974). Intermittent turbulence in self-similar cascades: divergence of high moments and dimension of the carrier. *J. Fluid Mech.* 62, 331–358.

Mandelbrot, B. B. (1977). *Fractals*. San Francisco, CA: Wiley Online Library.

Martinez-Lavin, M. (2004). Fibromyalgia as a sympathetically maintained pain syndrome. *Curr. Pain Headache Rep.* 8, 385–389. doi: 10.1007/s11916-996-0012-4

Martínez-Lavín, M., Hermosillo, A. G., Rosas, M., and Soto, M. E. (1998). Circadian studies of autonomic nervous balance in patients with fibromyalgia: a heart rate variability analysis. *Arthritis Rheumatol.* 41, 1966–1971. doi: 10.1002/1529-0131(199811)41:11h1966::AID-ART11i3.0.CO;2-O

Martinez-Lavin, M., Infante, O., and Lerma, C. (2008). Hypothesis: the chaos and complexity theory may help our understanding of fibromyalgia and similar maladies. *Semin. Arthritis Rheum.* 37, 260–264. doi: 10.1016/j.semarthrit.2007.04.003

Meeus, M., Goubert, D., De Backer, F., Struyf, F., Hermans, L., Coppieters, I., et al. (2013). "Heart rate variability in patients with fibromyalgia and patients with chronic fatigue syndrome: a systematic review," in *Seminars in Arthritis and Rheumatism, Vol. 43* (Elsevier), 279–287. doi: 10.1016/j.semarthrit.2013.03.004

Muzy, J.-F., Bacry, E., and Arneodo, A. (1993). Multifractal formalism for fractal signals: the structure-function approach versus the wavelet-transform modulus-maxima method. *Phys. Rev. E* 47:875. doi: 10.1103/PhysRevE.47.875

Muzy, J.-F., Bacry, E., and Arneodo, A. (1994). The multifractal formalism revisited with wavelets. *Int. J. Bifurcat. Chaos* 4, 245–302.

Nunes Amaral, L. A., Ivanov, P. C., Aoyagi, N., Hidaka, I., Tomono, S., Goldberger, A. L., et al. (2001). Behavioral-independent features of complex heartbeat dynamics. *Phys. Rev. Lett.* 86, 6026–6029. doi: 10.1103/PhysRevLett.86.6026

Peña, M., Echeverría, J. C., Garcia, M., and González-Camarena, R. (2009). Applying fractal analysis to short sets of heart rate variability data. *Med. Biol. Eng. Comput.* 47, 709–717. doi: 10.1007/s11517-009-0436-1

Peng, C.-K., Buldyrev, S. V., Havlin, S., Simons, M., Stanley, H. E., and Goldberger, A. L. (1994). Mosaic organization of dna nucleotides. *Phys. Rev. E* 49:1685.

Perakakis, P., Taylor, M., Martinez-Nieto, E., Revithi, I., and Vila, J. (2009). Breathing frequency bias in fractal analysis of heart rate variability. *Biol. Psychol.* 82, 82–88. doi: 10.1016/j.biopsycho.2009.06.004

Reyes-Lagos, J. J., Hadamitzky, M., Peña-Castillo, M. Á., Echeverría, J. C., Bösche, K., Lückemann, L., et al. (2016). Exogenous oxytocin reduces signs of sickness behavior and modifies heart rate fluctuations of endotoxemic rats. *Physiol. Behav.* 165, 223–230. doi: 10.1016/j.physbeh.2016.07.013

Schmitt, D. T., and Ivanov, P. C. (2007). Fractal scale-invariant and nonlinear properties of cardiac dynamics remain stable with advanced age: a new mechanistic picture of cardiac control in healthy elderly. *Am. J. Physiol. Regul. Integr. Compar. Physiol.* 293, R1923–R1937. doi: 10.1152/ajpregu.00372.2007

Sergi, M., Rizzi, M., Braghiroli, A., Sarzi Puttini, P., Greco, M., Cazzola, M., et al. (1999). Periodic breathing during sleep in patients affected by fibromyalgia syndrome. *Eur. Respir. J.* 14, 203–208.

Wang, J., Shang, P., and Cui, X. (2014). Multiscale multifractal analysis of traffic signals to uncover richer structures. *Phys. Rev. E Stat. Nonlin. Soft Matter Phys.* 89:032916. doi: 10.1103/PhysRevE.89.032916

Wessel, N., Voss, A., Malberg, H., Ziehmann, C., Voss, H. U., Schirdewan, A., et al. (2000). Nonlinear analysis of complex phenomena in cardiological data. *Herzschrittmacherther. Elektrophysiol.* 11, 159–173. doi: 10.1007/s003990070035

Conflict of Interest Statement: The authors declare that the research was conducted in the absence of any commercial or financial relationships that could be construed as a potential conflict of interest.

frontiers in Physiology

ORIGINAL RESEARCH
published: 06 September 2018
doi: 10.3389/fphys.2018.01257

Applications of Variability Analysis Techniques for Continuous Glucose Monitoring Derived Time Series in Diabetic Patients

Klaus-Dieter Kohnert[1], Peter Heinke[1], Lutz Vogt[2], Petra Augstein[1,3] and Eckhard Salzsieder[1]*

[1] Institute of Diabetes "Gerhardt Katsch", Karlsburg, Germany, [2] Diabetes Service Center, Karlsburg, Germany, [3] Heart and Diabetes Medical Center, Karlsburg, Germany

Methods from non-linear dynamics have enhanced understanding of functional dysregulation in various diseases but received less attention in diabetes. This retrospective cross-sectional study evaluates and compares relationships between indices of non-linear dynamics and traditional glycemic variability, and their potential application in diabetes control. Continuous glucose monitoring provided data for 177 subjects with type 1 (n = 22), type 2 diabetes (n = 143), and 12 non-diabetic subjects. Each time series comprised 576 glucose values. We calculated Poincaré plot measures (SD1, SD2), shape (SFE) and area of the fitting ellipse (AFE), multiscale entropy (MSE) index, and detrended fluctuation exponents ($\alpha 1$, $\alpha 2$). The glycemic variability metrics were the coefficient of variation (%CV) and standard deviation. Time of glucose readings in the target range (TIR) defined the quality of glycemic control. The Poincaré plot indices and α exponents were higher ($p < 0.05$) in type 1 than in the type 2 diabetes; SD1 (mmol/l): 1.64 ± 0.39 vs. 0.94 ± 0.35, SD2 (mmol/l): 4.06 ± 0.99 vs. 2.12 ± 1.04, AFE ($mmol^2/l^2$): 21.71 ± 9.82 vs. 7.25 ± 5.92, and $\alpha 1$: 1.94 ± 0.12 vs. 1.75 ± 0.12, $\alpha 2$: 1.38 ± 0.11 vs. 1.30 ± 0.15. The MSE index decreased consistently from the non-diabetic to the type 1 diabetic group (5.31 ± 1.10 vs. 3.29 ± 0.83, $p < 0.001$); higher indices correlated with lower %CV values ($r = -0.313$, $p < 0.001$). In a subgroup of type 1 diabetes patients, insulin pump therapy significantly decreased SD1 (−0.85 mmol/l), SD2 (−1.90 mmol/l), and AFE (−16.59 $mmol^2/l^2$), concomitantly with %CV (−15.60). The MSE index declined from 3.09 ± 0.94 to 1.93 ± 0.40 (p = 0.001), whereas the exponents $\alpha 1$ and $\alpha 2$ did not. On multivariate regression analyses, SD1, SD2, SFE, and AFE emerged as dominant predictors of TIR (β = −0.78, −1.00, −0.29, and −0.58) but %CV as a minor one, though $\alpha 1$ and MSE failed. In the regression models, including SFE, AFE, and $\alpha 2$ (β = −0.32), %CV was not a significant predictor. Poincaré plot descriptors provide additional information to conventional variability metrics and may complement assessment of glycemia, but complexity measures produce mixed results.

Keywords: variability analysis techniques, continuous glucose monitoring, glucose time series, indices of non-linear and fractal dynamics, multiscale entropy, Poincaré plots, detrended fluctuation analysis, glycemic control of diabetes

OPEN ACCESS

Edited by:
Zbigniew R. Struzik,
The University of Tokyo, Japan

Reviewed by:
Michal Javorka,
Comenius University in Bratislava, Slovakia
Dirk Cysarz,
Universität Witten/Herdecke, Germany

****Correspondence:***
Klaus-Dieter Kohnert
kohnert@diabetes-karlsburg.de

Specialty section:
This article was submitted to Fractal Physiology, a section of the journal Frontiers in Physiology

Received: *27 April 2018*
Accepted: *20 August 2018*
Published: *06 September 2018*

Citation:
Kohnert K-D, Heinke P, Vogt L, Augstein P and Salzsieder E (2018) Applications of Variability Analysis Techniques for Continuous Glucose Monitoring Derived Time Series in Diabetic Patients. Front. Physiol. 9:1257. doi: 10.3389/fphys.2018.01257

INTRODUCTION

Glucose variability (GV), as based on the amplitude of continuously recorded glycemic profiles, is an essential factor in the clinical control of diabetes, and high amplitudes in glucose excursions represent an independent predictor of hypoglycemia (Monnier et al., 2011). Moreover, GV may be a risk factor for the development of chronic diabetes complications (Nalysnyk et al., 2010). Several indices were introduced to measure GV (Rodbard, 2009), but these classical indices only consider the amplitude of the glucose signal, i.e., the global variability, and neglect any time component (Kovatchev and Cobelli, 2016). A few GV metrics, containing a time component are known. For example mean of daily differences (Molnar et al., 1972), mean absolute glucose change (Hermanides et al., 2010; Kohnert et al., 2013), and continuous overlapping net glycemic action (McDonnel et al., 2005), but they firmly correlate to the amplitude-only-based indices. A new metric, glycemic variability percentage, recently introduced by Peyser et al. (2018), gives weight to the amplitude as well as the frequency of glucose fluctuations. However, the limitation of all these indices is that they emanate from linear analyses methods and thus fail to measure the complexity or structural variability of glucose time series. The theory of non-linear dynamics provides the basis for analysis of structural variability in complex systems (Schubert, 2013). Consequently, variability analysis of physiological signals may either comprise evaluation by metrics from linear or non-linear methods. However, only non-linear analysis techniques provide access to the dynamics of regulatory systems.

Several researchers developed multiple measures of variability to assess the degree and patterns of physiological signal variation over time intervals in health and disease. Voss et al. (2009) and Bravi et al. (2011) have identified several domains of variability including geometric, information, and fractal scaling domains. We selected measures of non-linear dynamics from three different variability domains proposed by Bravi et al., 2011). These include Poincaré plots (Kovatchev et al., 2005; Crenier, 2014), multiscale entropy (Chen et al., 2014; Costa et al., 2002, 2014), and detrended fluctuation analysis (Yamamoto et al., 2010; Ogata et al., 2012; Khovanova et al., 2013; Thomas et al., 2015) for the variability analysis of glucose time series (**Table 1**). These techniques have recently found application in analyzing the dynamics of glucose time series from patients with diabetes mellitus. The results of these studies collectively showed reduced dynamics of blood glucose variations in patients with diabetes as compared with non-diabetic subjects (Ogata et al., 2012; Chen et al., 2014; Crenier, 2014; Costa et al., 2014; Khovanova et al., 2013; Kohnert et al., 2017).

Beyond traditional estimates of glycemia and glycemic variability, dynamical measures may enable assessment of several extrinsic factors and treatment modalities that can modify the intrinsic dynamics of the glucoregulatory system. However, whether such factors affect glucose dynamics or which, if any, of the dynamical measures, could complement traditional clinical measures of glycemic variability in the assessment of diabetes control is not known.

Herein, we address these problems by examining glucose dynamics in type 1 and type 2 diabetes. We compare classical measures of glycemic variability with indices from different domains of variability and investigate their interrelationships. Finally, we evaluate their contribution to the quality of glycemic control and potential clinical significance.

MATERIALS AND METHODS

Study Design

The present study is a cross-sectional investigation that used historical data. We conducted a retrospective analysis of ambulatory continuous glucose monitoring (CGM) profiles recorded with the second-generation MiniMed CGM system (Northridge, CA, United States) set at a sampling rate of one glucose measurement every 5 min. We analyzed the CGM data using the MiniMed Solution Software (Version 2b, Medtronic MiniMed) and utilized established measures of glucose dynamics, glycemic variability, and glycemic control. Study participants had received glucose sensors placed on their abdomen. We used a minimum of four blood glucose meter calibrations per day and a mean duration of 69-h continuous monitoring. We excluded data not meeting the validity criteria of the manufacturer ($\geq$three paired sensor/meter readings and mean absolute difference $\leq$ 28%).

Study Subjects and Collection of CGM Data

The CGM data were collected for a total of 177 study participants: Twenty-two patients with type 1 diabetes (T1D), 143 with type 2 diabetes (T2D), and 12 non-diabetic control subjects (ND). All subjects participated in the Diabetiva Program (Augstein et al., 2010), an integrated national diabetes care network. The study participants entered the type and amount of food consumed into their logbooks during CGM. The entrance of consumed food enabled calculation of carbohydrate intake per day, according to standard tables containing the nutrient composition with carbohydrate exchange units (Metternich, 2008). Of the T2D patients 42 had diet alone and of those assigned to oral therapy 63 had received common oral agents only or combinations thereof.

TABLE 1 | Techniques of variability analysis of glucose time series.

Domain	Features	Indices	Feature assumptions
Geometric	Poincaré plots features	SD1, SD2, SFE, AFE	Low dimensional representation of the dynamical attractor
Information	Multiscale entropy	MSE	The complexity changes depend on the window length used
Fractal scaling	Detrended fluctuation analysis	$\alpha 1$, $\alpha 2$	The SD of the detrended cumulative time series has scale-invariant properties

Based on the classification of analysis techniques by Bravi et al. (2011).

Eighteen patients had insulin plus oral antidiabetes agents, and 20 patients received insulin alone. T1D patients (n = 22) had been treated with multiple daily insulin injections (MDI) of short- and long-acting insulin. A subgroup of these patients (n = 10) switched to continuous subcutaneous insulin injections (CSII). Patients after CSII are not included in the characteristics of the total study cohort. Eighty-five percent of all patients had taken blood pressure lowering medication. Data were not included in this evaluation if patients had severe diabetes complications or decompensated glycemic control with glycated hemoglobin (HbA1c) values > 10% (86 mmol/mol).

The original study had obtained ethical approval and required no further approval for this retrospective data analysis.

Linear Analysis

As the primary measures of GV, we computed the percentage of coefficient of variation of glucose (%CV) and standard deviation (SD) from the data obtained and averaged the data over a 48-h CGM period (Rodbard, 2011). The glucose exposure metrics included mean glucose and glycosylated hemoglobin (HbA1c). To assess the quality of glycemic control, we computed the time (h/day) in the target range (Rodbard, 2018) and defined a range of 3.9–8.9 mmol/l as acceptable for clinical practice (Bergenstal et al., 2013).

Non-linear Analysis

Forty-eight hour CGM profiles obtained during recordings were used for calculation of dynamical parameters. We applied the standard Poincaré plot (PCP), which is a scattergram constructed by locating data points from the CGM time series on the coordinate plane according to the pairing $G_{(t)}$, $G_{(t)}+\Delta t$. $G_{(t)}$ is the glucose level at time t, and Δt is the time delay, which is a multiple of the sampling time of the signal. We probed Δt values of 30, 60, and 120 min but found Δt = 60 min most suitable to represent the PCP geometry characteristics for our study groups and used the code created by Crenier (2014) to compute the pairs of coordinates defining the PCPs. *SD1* and *SD2* statistics (Brennan et al., 2001), enabled quantification of the plots. The PCP measures included the minor axis of the fitting-ellipse (SD1) defined as the dispersion of data perpendicular to the line of identity and along the major axis (SD2) of the ellipse. Further PCP-derived metrics were the shape (SFE) and area (AFE) of the fitting ellipse calculated as $SFE = SD2/SD1$ and $AFE = \pi * SD1 * SD2$ (Crenier, 2014). Of note, although SD1 and SD2 quantify more or less linear rather than non-linear features (Brennan et al., 2001; Schulz and Voss, 2017), we formally include these indices here in differentiating them from traditional measures of global GV.

The analysis of multiscale entropy (MSE) for the CGM sequences utilized the previously described procedure (Chen et al., 2014; Costa et al., 2014). This procedure comprised: (1) derivation of a set of time series from the original glucose signal on different time scales using the coarse-graining technique, (2) computation of sample entropy (SampEn) with standard parameter values for each coarse-grained time series. We chose the window length m = 2, the sensitivity criterion r = 0.15 times the SD, and the data length N = 576 within the entire coarse-grained sequence with the broadest scale factor set at M = 5. Thus, the length of the coarse-grained data (Humeau-Heurtier, 2015) at this scale factor contained 115 glucose samples. We calculated SampEn for the scales 1 to 5, using the mse.c program available at https://www.physionet.org/physiotools/mse/tutorial/.

The complexity index was defined as the sum of these SampEn values.

We also analyzed the CGM time series by calculating the detrended fluctuation analysis (DFA) according to the standard method, as described by (Yamamoto et al., 2010), which involves the integration of the time series and dividing it into intervals of equal size n. Integration of the time series was performed as follows:

$$y(k) = \sum_{t-1}^{k} [B(i) - B_{ave}]$$

F(n) is the calculated detrended fluctuation represented as the root-mean-square fluctuation from the trend summed up for all boxes (B) with *B(i)* as each point in the time series and B_{ave} as the average of the whole series.

$$F(n) = \sqrt{\frac{1}{N} \sum_{k=1}^{N} [y(k) - y_n(k)]^2}$$

n: size of the time segments (windows) of the integrated curve
F(n): the measure of the difference between the integrated curve and the regression lines
y(k): the value at each individual point of the integrated curve
$y_n(k)$: the value of the regression line at the point
N: the total number of data points

Plots drawn with *log F(n)* on the y-axis and *log(time window)* permitted computation of the α exponents and constructing the slope of the line relating *F(n)* to *log(time window)*. Because of the crossover phenomenon observed in the regression line α (Peng et al., 1995), we split the regression line into two regions, the short-term (α*1*) and long-term (α*2*) range. Alpha 1 represents the slope of the regression within 1.25 h calculated as n = 2–16 points and α*2* the slope of the regression over 1.25 h from 16 to 144 data points.

Statistical Analysis

We categorized the patients into type 1 and type 2 diabetes and included a control group of healthy participants. We used one-way analysis of variance (ANOVA) and the t-test with Bonferroni–Holm correction for control of multiple pairwise comparisons. The two-tailed paired Student's t-test permitted comparison between MDI and CSII data. Variables are presented as means ± SD and their statistical significance by a two-tailed test. Diabetes duration is given as median (25th – 75th) percentile. Spearman's correlation revealed the strength of associations between dynamical indices and linear regression analyses and their associations with conventional GV measures. Multiple linear regression analysis used a

core model (standardized regression coefficient denoted by β) that consisted of the following covariates: age, sex, diabetes duration, body mass index, carbohydrate intake, and antidiabetic therapy (CORE MODEL). Antidiabetic therapy was coded: 1 = none, 2 = diet with/without oral agents, 3 = oral agents with/without insulin and 4 = insulin alone. Stepwise forward selection identified confounding variables (McNamee, 2005). The variance inflation factor (VIF) and Durbin-Watson statistic ensured the absence of confounding effects. Results at $p < 0.05$ were statistically significant. We applied the Statistical Package for the Social Sciences software package (version 17.0; SPSS, Chicago, IL, United States) for statistical analyses.

RESULTS

Characteristics of Study Subjects

The summary of demographic and clinical characteristics of the study cohort in **Table 2** shows that patients with T2D were significantly older (65.4 ± 8.2 years) than those with T1D (43.3 ± 15.2 years) or the ND control subjects (44.3 ± 12.4 years), but the age difference between the T1D and ND group was not statistically significant. Diabetes duration (years) was shorter in T2D [7.0 (3.0 – 12.0)] than in T1D [20.5 (14.8 – 29.0)], and body mass index was higher in T2D than in T1D patients (30.3 ± 4.8 vs. 25.3 ± 3.9 kg/m^2). However, carbohydrate intake and hemoglobin A1c (HbA1c %) were lower in T2D patients than in patients with T1D; HbA1c (6.8 ± 1.0 vs. 7.7 ± 0.9), whereas mean glucose levels did not significantly differ ($p = 0.37$) between these two diabetes groups. As expected, the global GV measured by %CV was markedly higher ($p < 0.001$) in the group of T1D patients than in the T2D (36.9 ± 8.6 vs. 20.2 ± 7.4) and ND (15.7 ± 3.5) groups. Likewise, SD was significantly higher in the T1D than in the T2D and ND group. Consistent with the data on glucose exposure and GV, the time spent in target range was significantly longer ($p < 0.001$) in the ND than in the T2D and T1D group (23.4 ± 1.0 vs. 17.4 ± 6.2 vs. 13.2 ± 3.8).

The Dynamics of CGM Tracings in the Study Groups

Comparison of sample CGM tracings (**Figure 1**) obtained from a non-diabetic control subject (**Figure 1A**) a patient with T2D (**Figure 1B**), and T1D patient (**Figure 1C**) exemplified that the selected dynamical indices are capable of expressing differences in glucose dynamics between individual patients. Despite well-controlled diabetes, as reflected by HbA1c < 7.0% and mean glucose values < 9.4 mmol/l, significant glycemic fluctuations in the CGM time series were evident in the two diabetic patients. There SD2, AFE, α exponents increased, and MSE values decreased, indicating altered glucose dynamics as compared with that of the non-diabetic sample. Note, high PCP metrics and low MSE index values correlated with large glycemic fluctuations and loss of the information content of the glucose signal.

Dynamical Indices in Diabetic Patients and Non-diabetic Control Subjects

Figure 2 shows that the selected non-linear GV indices in diabetic patients are significantly different ($p < 0.05$) from those in non-diabetic subjects (ND). Moreover, except for SFE, all other metrics of PCP geometry were higher in T1D than in patients with T2D (**Figures 2A,B**). The SFE index did not differ between the T1D and T2D group 2.51 ± 0.58 vs. 2.26 ± 0.64, $p = 0.08$). On the contrary, the MSE index values (**Figure 2C**) increased significantly ($p < 0.001$) between groups when moving from T1D (3.29 ± 0.83) to T2D (3.89 ± 1.19) and finally to the ND group (5.31 ± 1.10). Lower MSE indices correlated with higher %CV values (−0.313, $p < 0.001$). These changes indicate a loss of complexity in the glucose time series of diabetic patients. The two DFA α exponents in **Figure 2D** were higher in diabetes compared to non-diabetes, but among both diabetes groups, were higher in patients with T1D than in those with T2D: $\alpha 1$ (1.95 ± 0.12 vs. 1.75 ± 0.12, $p < 0.001$) and $\alpha 2$ (1.38 ± 0.11 vs. 1.30 ± 0.15, $p = 0.017$).

Correlations Among Indices From Different Variability Domains

When we investigated the associations between the classical PCP indices by Spearman's correlation analysis (**Table 3**), we found strong correlations of SD1 and SD2 with the AFE index ($r = 0.776$–0.805, $p < 0.001$ for all). We noticed weak negative associations between SD1 and SFE ($r = -0.167$, $p = 0.026$), whereas those with SD2 (0.604, $p < 0.001$ were stronger. The associations among MSE and the PCP indices were moderate but inverse for SD1, SD2, SFE, and AFE, ($r = -0.432$ to -0.564, $p < 0.001$), and with the exponent $\alpha 1$ ($r = -0.401$, $p < 0.001$) and $\alpha 2$ ($r = -0.385$, $p < 0.001$).

Relationships Between Dynamical Indices and Conventional Measures of Global Glucose Variability

Linear regression analysis of dynamical variables against conventional metrics of glycemic variability (**Table 4**) indicated that the PCP descriptors SD1, SD2, and AFE, with the exception of SFE, have a consistently closer and positive relationship with %CV (β = 0.78–0.82, $p < 0.001$) than the DFA α exponents (β = 0.47 and 0.41, $p < 0.001$). In contrast, the complexity index, MSE, has a weak, negative relationship (β = −0.36 and −0.38, $p < 0.001$) with %CV and SD. These results clearly show that numerically higher PCP metrics and DFA exponents relate to larger glucose fluctuations, whereas lower complexity index values correlate with higher glycemic variability.

Dynamical Indices as Determinants of the Quality of Glucose Control

We performed multiple regression analyses to assess the independent effects of glucose dynamics on TIR as the quality measure of glycemic control. We included %CV as the conventional, linear measure of GV and the covariates age, sex

TABLE 2 | Demographic and metabolic characteristics of diabetic patients and control subjects.

Characteristic	Type 1 Diabetes	Type 2 Diabetes	Non-diabetes	*P*- value
Patients (*n*)	22	143	12	
Sex (male/female)	11/11	91/52	5/7	
Age (years)	43.3 ± 15.2	65.4 ± 8.2$^{***,+++}$	44.3 ± 12.4	<0.001
Diabetes duration (years)	20.5 (14.8 – 29.0)	7.0 (3.0 – 12.0)*	NA	<0.001
Body mass index (kg/m^2)	25.3 ± 3.9	30.3 ± 4.8***	27.1 ± 4.1	<0.001
Carbohydrate intake (g/day)	211.8 ± 46.6	138.8 ± 50.7$^{**,+++}$	185.6 ± 35.3	<0.001
Glucose exposure				
Hemoglobin A1C (%)	7.7 ± 0.9^{+++}	6.8 ± 1.0$^{***,+++}$	5.0 ± 0.3	< 0.001
Hemoglobin A1C (mmol/mol)	61	51	31	
Mean glucose (mmol/l)	8.0 ± 1.7^{+++}	7.8 ± 2.0^{+++}	5.4 ± 0.5	<0.001
Glucose variability				
Coefficient of variation (%)	36.9 ± 8.6^{+++}	20.2 ± 7.4$^{***,+}$	15.7 ± 3.5	<0.001
Standard deviation (mmol/l)	2.9 ± 0.7^{+++}	1.6 ± 0.7$^{***,+++}$	0.9 ± 0.2	<0.001
Quality of glycemic control				
Time in target range (h/day)	13.2 ± 3.8^{+}	17.4 ± 6.2$^{*,+}$	23.4 ± 1.0	<0.001

*Data are mean ± SD or median (25th – 75th percentile) values. (NA), not applicable. The groups were compared using analysis of variance (ANOVA) and t-test with Bonferroni–Holm correction. Differences between the groups: **$p < 0.01$, ***$p < 0.001$ vs. type 1 diabetes and $^{+}p < 0.05$, $^{+++}p < 0.001$vs. non-diabetes.*

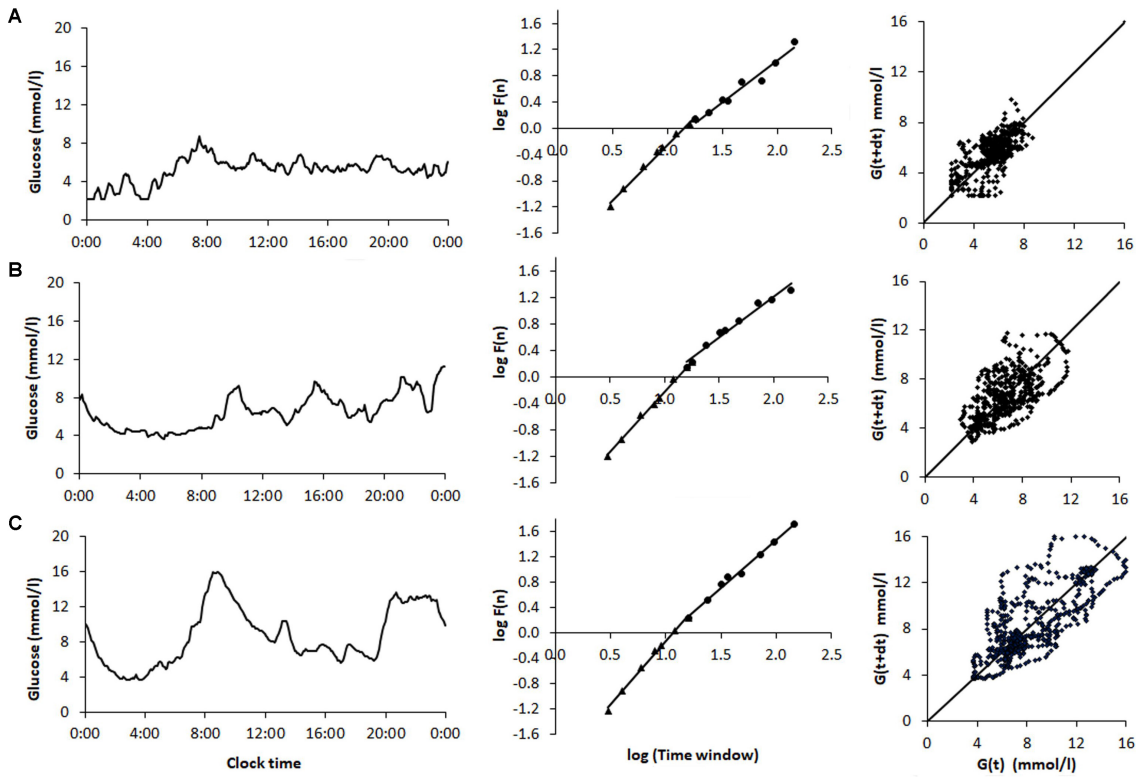

FIGURE 1 | Analysis of samples of 48-h continuous glucose monitoring tracings obtained from **(A)** a non-diabetic control subject (ND), **(B)** a patient with type 2 diabetes (T2D) on sulfonylurea treatment, and **(C)** a type 1 diabetic (T1D) patient treated with multiple insulin injections. The columns (from left to right) show the CGM profiles, detrended fluctuation analysis, and Poincaré plots. The glycemic characteristics and the dynamical indices derived from the glucose time series are shown in **Table 6**. Note the increase in the Poincaré indices SD1, SD2, and AFE, the decrease in MSE as well as the increasing short- ($\alpha 1$) and long-term ($\alpha 2$) fractal scaling exponent when moving from the non-diabetic subject down to the T1D patient.

diabetes duration, body mass index, carbohydrate intake, and antidiabetic therapy (**Supplementary Table 1**, see link on this article). In the fully adjusted regression models (model 2–5, 8) the dynamical indices were associated with TIR. Out of these, models 2, 3, and 5 achieved an adjusted R^2 of 0.39, 0.50, and 0.31 with SD1 ($\beta = -0.78$), SD2 ($\beta = -1.00$), and AFE ($\beta = -0.58$); %CV

β = 0.34, 0.47, and 0.11, respectively. The statistical significance for SD1, SD2, and AFE was $p < 0.001$. These regression analyses revealed that SD1, SD2, and AFE were the most powerful predictor variables of the quality of glycemic control presented as TIR. SFE (β = −0.29) and α*2* (β = −0.32) were also significant (both $p < 0.001$) but weaker predictors. The covariates age, sex, diabetes duration, body mass index, carbohydrate intake, and antidiabetic therapy, except for carbohydrate intake in model 4 and 8, failed to contribute significantly. MSE (model 6) was not a significant predictor. In the regression models integrating the variables AFE, SFE, and α*2*, %CV failed to contribute to TIR. The variance inflation factors (≤3.5) and the Durban-Watson statistic (1.8 – 2.1) confirmed the absence of significant collinearity.

Glucose Dynamics Before and After Switching From Multiple Daily Insulin Injections to Continuous Subcutaneous Insulin Infusions

The transition from multiple daily insulin injections (MDI) to continuous subcutaneous insulin infusions (CSII) in a subgroup of 10 patients with T1D, reduced SD1, SD2, and the AFE index except for SFE (**Table 5**). The significant reduction by roughly 50% in SD1, SD2, and AFE indicates an overall improvement in PCP geometry. Whereas the MSE index decreased (3.09 ± 0.94 vs. 1.93 ± 0.40, $p = 0.001$), the DFA scaling exponents α*1* (2.04 ± 0.06 vs. 2.09 ± 0.02, $p = 0.05$) and α*2* (1.43 ± 0.11 vs. 1.57 ± 0.36, $p = 0.16$) did not significantly vary. These latter results suggest a further loss of complexity and a non-significant change in fractal-like behavior of the glucose time series after initiation of insulin pump therapy. HbA1c (range 7.3 – 10.3% at baseline) and the mean glucose levels (range 6.2 – 12.1 mmol/l at baseline) did not significantly change. As **Table 5** further shows, the amplitude-based glucose fluctuations, measured as %CV and SD, declined markedly ($p = 0.003$ and 0.010, respectively). Likewise, the quality of diabetes control ameliorated, as TIR increased from 13.0 to 17.7 h/day ($p = 0.021$). This result is consistent with the CGM profiles in **Figure 3**, demonstrating lower glycemic amplitudes and better glycemic control after the commencement of CSII therapy (**Figure 3B**).

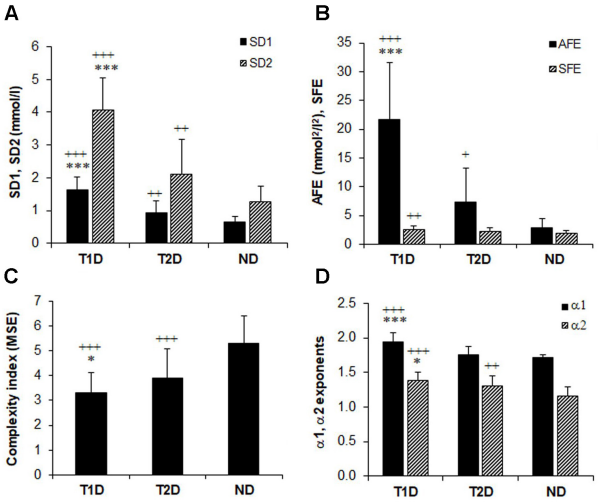

FIGURE 2 | Comparison of glucose variability indices in non-diabetes (ND), type 2 (T2D), and type 1 diabetes (TD1) from the geometric, information, and fractal scaling domains. Analysis of variance (*ANOVA*) and *t*-test with Bonferroni–Holm correction gave the between-group differences as indicated: $^{*}p < 0.05$, $^{***}p < 0.001$ vs. type 2 diabetes and $^{++}p < 0.01$, $^{+++}p < 0.001$ vs. non-diabetes.

DISCUSSION

Glucose time series may differ in individual diabetic patients despite comparable HbA1c and mean glucose levels because such clinical, linear measures are not appropriate to reveal the inherent dynamics of the glucoregulatory system.

We demonstrate that several indices derived from the geometric, information, and fractal scaling domains of variability techniques can characterize the variability of glucose time series in health and diabetes. Previous studies in the literature (Yamamoto et al., 2010; Khovanova et al., 2013; Chen et al., 2014; Costa et al., 2014; Weissman and Binah, 2014), using various non-linear signal processing techniques, reported that glucose dynamics appears reduced in patients with diabetes compared with non-diabetic subjects. However, it is not known whether the type and severity of diabetes or factors such as age, diabetes

TABLE 3 | Spearman correlation coefficients among measures of glucose dynamics.

		Poincaré plot				Multiscale entropy	Detrended fluctuation analysis	
		SD1	**SD2**	**SFE**	**AFE**	**MSE**	**α*1***	**α*2***
Poincaré plot	SD1 (short term)	1						
	SD2 (long term)	**0.872**	1					
	SFE (shape)	−0.167	**0.604**	1				
	AFE (area)	**0.776**	**0.805**	**0.365**	1			
Multiscale entropy	MSE	**−0.432**	**−0.549**	**−0.437**	**−0.564**	1		
Detrended fluctuation analysis	α1 (short term)	**0.468**	**0.454**	0.160	**0.489**	**−0.401**	1	
	α2 (long term)	0.270	**0.600**	**0.780**	**0.433**	**−0.385**	0.236	1

Correlations at the significance level of $p < 0.001$ are given in bold face; those at $p < 0.05$ (two-tailed) in regular type face.

TABLE 4 | Linear regression analysis of indices of glucose dynamics against conventional measures of glycemic variability Coefficient of Variation (%CV) and Standard deviation (SD).

		%CV			SD		
		β	R^2_{adj}	*P-value*	β	R^2_{adj}	*P-value*
Poincaré plot	SD1	0.82	0.67	<0.001	0.90	0.81	<0.001
	SD2	0.82	0.67	<0.001	0.94	0.88	<0.001
	SFE	−0.34	0.11	<0.001	−0.44	0.19	<0.001
	AFE	0.78	0.60	<0.001	0.86	0.74	<0.001
Multiscale entropy	MSE	−0.36	0.13	<0.001	−0.38	0.14	<0.001
Detrended	α1	0.47	0.22	<0.001	0.43	0.14	<0.001
fluctuation analysis	α2	0.41	0.16	<0.001	0.47	0.22	< 0.001

duration, BMI, and carbohydrate intake or antihyperglycemic therapy may affect the dynamical behavior of glucose time series. Regarding the natural history of diabetes, immune-mediated destruction of the pancreatic β-cells leading to an irreversible loss of the β-cell mass characterizes T1D, whereas in T2D a progressive decline of β-cell function over time occurs with rising insulin resistance and deterioration of glucose regulation. Because of the diverse pathogenic mechanisms, T1D needs insulin and is difficult to control, but those patients with T2D are able to manage their disease mostly with a variety of oral antihyperglycemic agents.

The indices derived from PCP and DFA analysis in the present study provided qualitatively similar results with respect to the differentiation of the glucose time series dynamics between the two types of diabetes, i.e., the values for these indices be significantly lower in the T2D than in the T1D group but were lowest in the ND group. In contrast, the complexity index calculated from MSE is highest in the ND group and lowest in the T1D group. These data are also compatible with the increase in glucose fluctuations (reduced non-linear autocorrelation) and thus with the diminished glycemic stability observed in the glucose profile structure of our T1D and T2D patient samples (**Figure 1**). In so far PCP descriptors in T1D and healthy control subjects are concerned, this is in agreement with a report by Crenier (2014). Regarding the ratio of long-term to short-term glucose time series variability, SFE was correspondingly higher in patients with T1D than in the non-diabetic subjects. Numerically high PCP indices unequivocally point toward dynamical instability in the glucoregulation. Nevertheless, the indices SD1, SD2, and AFE of PCP analysis quantify linear rather than non-linear features of the underlying time series (Brennan et al., 2001; Fishman et al., 2012). Consistent with the changes that occurred in the PCP geometry, the decreased MSE, and the altered DFA plots with increased α*1* and α2 exponents observed in the T1D group further indicate significant alterations in the feedback mechanism that is less able to diminish glucose fluctuations in patients with T1D than in those with T2D.

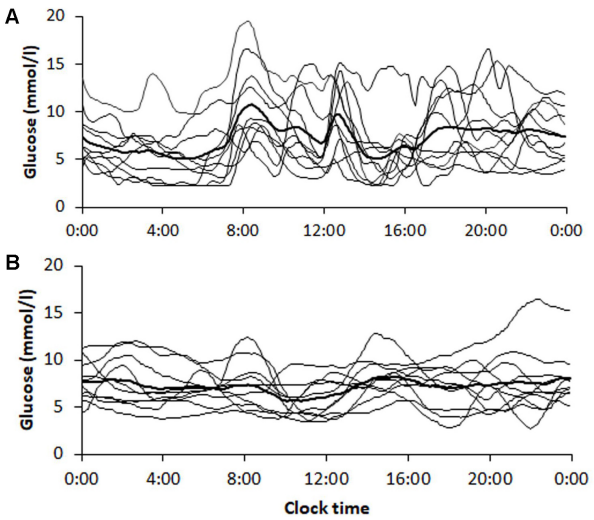

FIGURE 3 | Continuous glucose monitoring tracings obtained from patients (n = 10) with type 1 diabetes **(A)** before and **(B)** 6 months after initiation of insulin pump therapy. Tracings are shown for each patient with the average curve in bold. The corresponding dynamic and glycemic measures are shown in **Table 5**.

TABLE 5 | Comparison of dynamic and glycemic measures in type 1 diabetic patients before and after initiation of continuous subcutaneous insulin infusion therapy.

	Before CSII	At 6 months after initiation of CSII	*P*-value
Dynamic measures			
SD1 (mmol/l)	1.66 ± 0.37	0.81 ± 0.19	<0.001
SD2 (mmol/l)	4.37 ± 0.74	2.47 ± 0.90	<0.001
SFE	2.75 ± 0.74	3.07 ± 0.86	0.17
AFE ($mmol^2/l^2$)	23.07 ± 7.18	6.48 ± 3.32	<0.001
MSE	3.09 ± 0.94	1.93 ± 0.40	0.001
α1	2.04 ± 0.06	2.09 ± 0.02	0.05
α2	1.43 ± 0.11	1.57 ± 0.36	0.16
Glycemic measures			
HbA1c (%)	8.2 ± 0.85	7.7 ± 0.51	0.07
Mean glucose (mmol/l)	7.4 ± 1.2	7.5 ± 1.6	0.83
CV (%)	39.9 ± 8.5	24.3 ± 6.8	0.003
SD (mmol/l)	2.9 ± 0.6	1.8 ± 0.7	0.010
Time in range (h/day)	13.0 ± 3.0	17.7 ± 5.3	0.021

The number of patients was n = 10. Data are mean ± SD values. P-values are two-tailed.

TABLE 6 | Summary of characteristics and metrics of the continuous glucose monitoring profiles shown in **Figure 1** for a non-diabetic control subject (ND), a patient with type 2 diabetes (T2D), and a type 1 diabetic patient (T1D).

ID	Group	Diabetes duration (years)	HbA1c (%)	Mean glucose (mmol/l)	CV (%)	SD1 (mmol/l)	SD2 (mmol/l)	AFE ($mmol^2/l^2$)	MSE	α1	α2
777773	ND	NA	5.1	5.6	23.42	0.81	2.00	5.08	5.47	1.81	1.32
128701	T2D	13	6.1	6.1	26.27	1.11	2.39	8.31	4.66	1.83	1.24
125264	T1D	29	6.8	8.7	32.37	1.48	3.67	17.06	2.86	2.02	1.53

Our previous results demonstrated that the β-cell function is an independent predictor of glucose time series dynamics as measured by the DFA alpha exponents (Kohnert et al., 2014). Thus, the reduced glucose dynamics in the T1D versus the T2D patient group allows the assumption that worsening of the glucoregulation is partly due to the loss of the β-cell secretory capacity, whereas the remaining β-cell reserve prevents such derailment in T2D. The variability indices from the different domains correlated weakly or moderately to one another. As one could expect, the strongest correlations existed between the PCP indices within the geometric domain. The unexpectedly weak correlation across the variability domains suggests that the indices are not interchangeable. These correlations are in a way comparable with those found for the cardiac interbeat time series (Bassi et al., 2015) because the information retrieved from PCP and from DFA analysis show structural correlations of the underlying dynamics. By the multivariate regression analyses, we disclosed that the measures of glucose profile dynamics are independent predictors of the quality of glucose control, as defined by the time spent in target range (TIR). The analyses showed that the PCP indices SD1, SD2, and AFE along with %CV were independent determinants of TIR (**Supplementary Table 1**). Sex, age, diabetes duration, BMI, carbohydrate intake, and antidiabetic treatment had, if any, no substantial influence. Of note, we found that SD1, SD2, and AFE explained 35, 44, and 29%, respectively, of the interindividual variance in TIR compared to an additional 3–8% defined by the %CV. The variables SFE and α*2*, even significant in the regression models, were weaker predictors, explaining 17 and 21% of TIR. Moreover, the regression models (4, 5, and 8) including SFE, AFE, and α*2* demonstrate that these measures predicted the quality of glycemic control, whereas the overall glycemic variability as measured by %CV was not a significant predictor. The MSE did not determine TIR which indicates that this index is not useful in the assessment of the quality of glycemic control. Therefore, the evaluated indices do not reflect purely the global GV, although they relate to conventional measures of GV. Methods analyzing the fluctuation of glucose time series are not detecting the same phenomena as those methods that identify amplitude-based glycemic variability. Indeed, a loss in glucose time series dynamics gives rise to increased overall glycemic variability (Garcia Maset et al., 2016). Although strongly correlated with SD (in our study $r = 0.876$, $p < 0.0001$), we chose %CV for our regression models as the standard metric of GV in clinical research (Rodbard, 2018) to compare its effect on TIR with those indices from the different variability domains. We used TIR as an established and clinically useful indicator of the quality of glycemic control, reflecting the time in predefined target ranges (Bergenstal et al., 2013 and Rodbard, 2018).

Finally, we investigated the dynamics of glucose time series in a cohort of T1D patients in response to insulin pump therapy. CSII yielded a marked improvement in the PCP geometry–consistent with the report by Crenier (2014), except for the SFE descriptor, with a corresponding decrease in glycemic variability (calculated as %CV and SD) and increased quality of glycemic control as evaluated using TIR. Although HbA1c did not significantly change and mean glucose not markedly drop (Vogt et al., 2016), one may conclude that overall glycemia improved because of reduced glycemic variability and increased TIR. Of note, however, the MSE index decreased, whereas the DFA long-term exponent α*2* tended to increase. This is an unexpected result, and we do not have any plausible explanation, because healthier glycemic dynamics are associated both with higher MSE values and lower α exponents (see **Figures 2C,D**). Nevertheless, these finding suggests that even 6 months of CSII could not halt the loss of glucose time series complexity and fractal structure in glucose dynamics. In other words, CSII therapy is inappropriate to reverse glucose dynamics to those of non-diabetic subjects. We assume that owing to the absolute β-cell insulin deficiency in T1D, the glucoregulatory system remains insufficient to correct defective glucose dynamics. Islet transplantation rather than insulin pump therapy would offer restoration of the β-cell function (Vantyghem et al., 2014). Whether such therapy can restore glucose complexity and the fractal structure is not known and requires appropriate clinical studies.

This study has limitations in as much as it is retrospective in nature, and the number of subjects in the T1D and ND group is relatively small. Furthermore, the follow-up time in the patients after insulin pump therapy appears too short to allow restitution of glucose complexity and the fractal structure of glucose time series. In patients with T2D, for example, β-cell function began to increase not until after 12 months of CSII therapy (Choi et al., 2013). The strength of the investigation is the use of indices from different variability domains and classical GV measures as well as the inclusion of both patients with T1D and T2D to enable comparison of glucose dynamics between distinct types of diabetes.

In summary, this study provides evidence that glucose time series dynamics differ between the two primary forms of diabetes. The loss of complexity is more pronounced in T1D than in T2D, which we anticipate is due to differences in the β-cell pathology. Insulin pump therapy for 6 months can not reverse multiscale dynamics toward those of non-diabetic subjects because of the failure to mimic healthy patterns of insulinemia. Our findings,

which corroborate and extend previous work by others, also emphasize the need for using an ensemble of indices from various variability domains to characterize glucose time series more specifically. Moreover, we show that a combination of several dynamical metrics and classical GV measures has the potential to assess both the natural glucoregulatory system and quality of blood glucose control which may help in approaching diabetes treatment on a personalized basis.

AUTHOR CONTRIBUTIONS

K-DK contributed to the study conception, data analysis, interpretation, statistical analyses, and wrote the manuscript, added to the revision of the manuscript for intellectual content and approval. PH contributed to the data collection, review, interpretation, revision of the manuscript for intellectual content, and support of the paper. LV and PA devoted to the study conception, design, and approval of the document. ES is the guarantor of this work and, as such, took responsibility for the integrity of data and the accuracy of the data analysis.

SUPPLEMENTARY MATERIAL

The Supplementary Material for this article can be found online at: https://www.frontiersin.org/articles/10.3389/fphys.2018.01257/full#supplementary-material

REFERENCES

Augstein, P., Vogt, L., Kohnert, K. D., Heinke, P., and Salzsieder, E. (2010). Translation of personalized decision support into routine diabetes care. *J. Diabetes Sci. Technol.* 4, 1532–1539. doi: 10.1177/19322681000400631

Bassi, D., Arakelian, V. M., Goncalves Mendes, R., Rossi Caruso, F. C., Bonjorno Junior, J. C., Lopes Zangrando, K. T., et al. (2015). Poor glycemic control impacts linear and non-linear dynamics of heart rate in dm type 2. *Rev. Bras. Med. Esporte* 21, 313–317. doi: 10.1590/1517-869220152104150003

Bergenstal, R. M., Ahmann, A. J., Bailey, T., Beck, R. W., Bissen, J., Buckingham, B., et al. (2013). Recommendations for standardizing glucose reporting and analysis to optimize clinical decision making in diabetes: the ambulatory glucose profile. *Diabetes Technol. Ther.* 15, 198–211. doi: 10.1089/dia.2013.0051

Bravi, A., Longtin, A., and Seely, J. E. (2011). Review and classification of variability analysis techniques with clinical applications. *Biomed. Eng. Online* 10:90. doi: 10.1186/1475-925X-10-90

Brennan, M., Palaniswami, M., and Kamen, P. (2001). Do existing measures of Poincaré plot geometry reflect nonlinear features of heart rate variability? *IEEE Trans. Biomed. Eng.* 48, 1342–1347. doi: 10.1109/10.959330

Chen, J. L., Chen, P. F., and Wang, H. M. (2014). Decreased complexity of glucose dynamics in diabetes: evidence from multiscale entropy analysis of continuous glucose monitoring system data. *Am. J. Physiol. Regul. Integr. Comp. Physiol.* 307, R179–R183. doi: 10.1152/ajpregu.00108.2014

Choi, S.-B., Lee, J.-H., Lee, J.-H., Kim, S., Han, S.-D., Kim, I.-H., et al. (2013). Improvement of ß-cell function after achievement of optimal glycaemic control via long-term continuous subcutaneous insulin infusion therapy in non-newly diagnosed type 2 diabetic patients with suboptimal glycaemic control. *Diabetes Metab. Res. Rev.* 29, 473–482. doi: 10.1002/dmrr.2416

Costa, M., Goldberger, A. L., and Peng, C. K. (2002).). Multiscale entropy analysis of complex physiologic time series. *Phys. Rev. Lett.* 89:068102. doi: 10.1103/PhysRevLett.89068102

Costa, M. D., Henriques, T., Munshi, M. N., Segal, A. R., and Goldberger, A. L. (2014). Dynamical glucometry: use of multiscale entropy analysis in diabetes. *Chaos* 24:033139. doi: 10.1063/1.4894537

Crenier, L. (2014). Poincaré plot quantification for assessing glucose variability from continuous glucose monitoring systems and a new risk marker for hypoglycemia: application to type 1 diabetes patients switching to continuous subcutaneous insulin infusion. *Diabetes Technol. Ther.* 16, 247–254. doi: 10.1089/dia.2013.0241

Fishman, M., Jacono, F. J., Park, S., Jamasebi, R., Thungtong, A., Loparo, K. A., et al. (2012). A method for analyzing temporal patterns of variabilityof a time series from Poincaré plots. *J. Appl. Physiol.* 113, 297–306. doi: 10.1152/japplphysiol.01377.2010

Garcia Maset, L., Blasco Gonzales, L., Llop Furquet, G., Montes Suay, F., and Hernandes Marco, R. (2016). Study of glycemic variability through time series analyses (detrended fluctuation analysis and Poincaré plot) in children and adolescents with type 1 diabetes. *Diabetes Technol. Ther.* 18, 719–724. doi: 10.1089/dia.2016.0208

Hermanides, J., Vriesendorp, T. M., Bosman, R. J., Zandstra, D. F., Hoekstra, J. B., and DeVries, J. H. (2010). Glucose variability is associated with intensive care unit mortality. *Crit. Care Med.* 38, 838–842. doi: 10.1097/CCM.0b013e3181cc4be9

Humeau-Heurtier, A. (2015). The multiscale entropy algorithm and its variants: a review. *Entropy* 17, 3110–3123. doi: 10.3390/e17053110

Khovanova, N. A., Khovanov, I. A., Shabno, L., Griffiths, F., and Holt, T. A. (2013). Characterisation of linear predictability and non- stationarity of subcutaneous glucose profiles. *Comput. Methods Programs Biomed.* 110, 260267. doi: 10.1016/j.cmpb.2012.11.009

Kohnert, K. D., Heinke, P., Fritzsche, G., Vogt, L., Augstein, P., and Salzsieder, E. (2013). Evaluation of the mean absolute glucose change as a measure of glycemic variability using continuous glucose monitoring. *Diabetes Technol. Ther.* 6, 448–454. doi: 10.1089/dia.2012.0303

Kohnert, K. D., Heinke, P., Vogt, L., Augstein, P., and Salzsieder, E. (2014). Decling ß-cell function is associated with the lack of long-range negative correlations in glucose dynamics and increased glycemic variability: a retrospective analysis in patients with type 2 diabetes. *J. Clin. Transl. Endocrinol.* 1, 192–199. doi: 10.1016/j.jcte.2014.09.003

Kohnert, K. D., Heinke, P., Vogt, L., Augstein, P., Thomas, A., and Salzsieder, E. (2017). Association of blood glucose dynamics with antihyperglycemic treatment and glycemic variability in type 1 and type 2 diabetes. *J. Endocrinol. Invest.* 40, 1201–1207. doi: 10.007/s40618-017-0682-2

Kovatchev, B., and Cobelli, C. (2016). Glucose variability: timing, risk analysis, and relationship to hypoglycemia in diabetes. *Diabetes Care* 39, 502–510. doi: 10.2337/dc16-0841

Kovatchev, B. P., Clarke, W. L., Breton, M., Brayman, K., and McCall, A. (2005). Quantifying temporal glucose variability in diabetes via continuous glucose monitoring: mathematical methods and clinical application. *Diabetes Technol. Ther.* 7, 849–862. doi: 10.1089/dia.2005.7.849

McDonnel, C. M., Donath, S. M., Vidmar, S. I., Werther, G. A., and Cameron, F. J. (2005). A novel approach to continuous glucose analysis utilizing glycemic variation. *Diabetes Technol. Ther.* 7, 253–263. doi: 10.1089/dia.2005.7.253

McNamee, R. (2005). Regression modelling and other methods to control confounding. *Occup. Environ. Med.* 62, 500–506. doi: 10.1136/oem.2002.001115

Metternich, K. (2008). *Die Diabetes-Journal-Naehrwert-Tabelle: BE, KE und Kalorien auf einen Blick*. Mainz: Verlag Kirchheim+CoGmbH.

Molnar, G. D., Taylor, W. F., and Ho, M. M. (1972). Day-to-day variation of continuously monitored glycaemia: a further measure of diabetes instability. *Diabetologia* 8, 342–348. doi: 10.1007/BF01218495

Monnier, L., Wojtuscizyn, A., Colette, C., and Owens, D. (2011). The contribution of glucose variability to asymptomatic hypoglycemia in persons with type 2 diabetes. *Diabetes Technol. Ther.* 13, 813–818. doi: 10.1089/dia.2011.0049

Nalysnyk, L., Hernandez-Medina, M., and Krishnarajah, G. (2010). Glycaemic variability and complications in patients with diabetes mellitus: evidence from a systematic review of the literature. *Diabetes Obes. Metab.* 12, 288–298. doi: 10.1111/j.1463-1326.2009.01160.x

Ogata, H., Tokuyama, K., Nagasaka, S., Tsuchita, T., Kusaka, I., Ishibashi, S., et al. (2012). The lack of long-range negative correlations in glucose dynamics is associated with worse glucose control in patients with diabetes mellitus. *Metabolism* 61, 1041–1050. doi: 10.1016/j.metabol.2011.12.007

Peng, C. K., Havlin, S., Stanley, H. E., and Goldberger, A. L. (1995). Quantification of scaling exponents and crossover phenomena in nonstationary heartbeat time series. *Chaos* 5, 82–87. doi: 10.1063/1.166141

Peyser, T. A., Balo, A. K., Buckingham, B. A., Hirsch, I. B., and Garcia, A. (2018). Glycemic variability percentage: a novel method for assessing glycemic variability from continuous glucose monitor data. *Diabetes Technol. Ther.* 20, 6–16. doi: 10.1089/dia.2017.0187

Rodbard, D. (2009). Interpretation of continuous glucose monitoring data: glycemic variability and quality of glycemic control. *Diabetes Technol. Ther.* 11(Suppl. 1), S55–S67. doi: 10.1089/dia.2008.0132

Rodbard, D. (2011). Glycemic variability: measurement and utility in clinical medicine and research-one viewpoint. *Diabetes Technol. Ther.* 11, 1077–1080. doi: 10.1089/dia.2011.0104

Rodbard, D. (2018). Metrics to evaluate quality of glycemic control: comparison of time in target range, hypoglycemic, and hyperglycemic ranges with "risk indices". *Diabetes Technol. Ther.* 20, 325–334. doi: 10.1089/dia.2018.0092

Schubert, P. (2013). The application of nonlinear methods to characterize human variability from time series. *Ger. J. Sports Med.* 64, 132–140. doi: 10.5960/dzsm.2012.064

Schulz, S., and Voss, A. (2017). "Symbolic dynamics, Poincaré plot analysis and compression entropy estimate complexity in biological time series," in *Complexity and Nonlinearity in Cardiovascular Signals*, ed. G. Valenza (Berlin: Springer International Publishing), 45–85.

Thomas, F., Signal, M., and Chase, J. G. (2015). Using contiuous glucose monitoring data and detrended fluctuation analysis to determine patient condition: a review. *J. Diabetes Sci. Technol.* 9, 1327–1335. doi: 10.1177/1932296815592410

Vantyghem, M. C., Raverdy, V., Belavoine, A. S., Defrance, F., Caiazzo, R., Arnalsteen, L., et al. (2014). Continuous glucose monitoring after islet transplantation in type 1 diabetes: an excellent graft function (ß-score greater than 7) is required to abrogate hyperglycemia, whereas a minimal function is necessary to supress severe hypoglycemia (ß-score greater than 3). *J. Clin. Endocrinol. Metab.* 97, E3–E6. doi: 10.1210/jc.2012-2115

Vogt, L., Kohnert, K. D., Heinke, P., Thomas, A., and Salzsieder, E. (2016). Use of the KADIS-CSII PROGRAM for adjusting insulin pump therapy in type 1 diabetes. Bulletin of the Karaganda University. *Biol. Med. Geogr. Ser.* 4, 25–33.

Voss, A., Schulz, S., Schroeder, R., Baumert, M., and Caminal, P. (2009). Methods derived from nonlinear dynamics for analysing heart rate variability. *Phil. Trans. R. Soc. A* 367, 277–296. doi: 10.1098/rsta.2008.0232

Weissman, A., and Binah, O. (2014). The fractal nature of blood glucose fluctuations. *J. Diabetes Complications* 28, 646–651. doi: 10.1016/j.jdiacomp.2014.05.009

Yamamoto, N., Kubo, Y., Ishizawa, K., Kim, G., Moriya, T., Yamanouchi, T., et al. (2010). Detrended fluctuation analysis is considered to be useful as a new indicator for short-term glucose complexity. *Diabetes Technol. Ther.* 12, 775–783. doi: 10.1089/dia.2010.0059

Conflict of Interest Statement: The authors declare that the research was conducted in the absence of any commercial or financial relationships that could be construed as a potential conflict of interest.

frontiers in Physiology

ORIGINAL RESEARCH
published: 04 October 2018
doi: 10.3389/fphys.2018.01378

Fractal Analysis of BOLD Time Series in a Network Associated With Waiting Impulsivity

Atae Akhrif[1], Marcel Romanos[1], Katharina Domschke[2], Angelika Schmitt-Boehrer[3] and Susanne Neufang[1†]*

[1] Center of Mental Health, Department of Child and Adolescent Psychiatry, University of Wuerzburg, Wuerzburg, Germany, [2] Department of Psychiatry and Psychotherapy, Faculty of Medicine, Medical Centre - University of Freiburg, Freiburg, Germany, [3] Center of Mental Health, Department of Psychiatry, Psychosomatics and Psychotherapy, University of Wuerzburg, Wuerzburg, Germany

OPEN ACCESS

Edited by:
Plamen Ch. Ivanov, Boston University, United States

Reviewed by:
John G. Holden, University of Cincinnati, United States
Andras Eke, Semmelweis University, Hungary

***Correspondence:**
Susanne Neufang
Susanne.Neufang@hhu.de

†Present Address:
Susanne Neufang, Department of Psychiatry and Psychotherapy, Medical Faculty Heinrich-Heine University, Duesseldorf, Germany

Specialty section:
This article was submitted to Fractal Physiology, a section of the journal Frontiers in Physiology

Received: *07 February 2018*
Accepted: *11 September 2018*
Published: *04 October 2018*

Citation:
Akhrif A, Romanos M, Domschke K, Schmitt-Boehrer A and Neufang S (2018) Fractal Analysis of BOLD Time Series in a Network Associated With Waiting Impulsivity. Front. Physiol. 9:1378. doi: 10.3389/fphys.2018.01378

Fractal phenomena can be found in numerous scientific areas including neuroscience. Fractals are structures, in which the whole has the same shape as its parts. A specific structure known as *pink noise* (also called fractal or 1/f noise) is one key fractal manifestation, exhibits both stability and adaptability, and can be addressed via the Hurst exponent (*H*). FMRI studies using *H* on regional fMRI time courses used fractality as an important characteristic to unravel neural networks from artificial noise. In this fMRI-study, we examined 103 healthy male students at rest and while performing the 5-choice serial reaction time task. We addressed fractality in a network associated with waiting impulsivity using the adaptive fractal analysis (AFA) approach to determine *H*. We revealed the fractal nature of the impulsivity network. Furthermore, fractality was influenced by individual impulsivity in terms of decreasing fractality with higher impulsivity in regions of top-down control (left middle frontal gyrus) as well as reward processing (nucleus accumbens and anterior cingulate cortex). We conclude that fractality as determined via *H* is a promising marker to quantify deviations in network functions at an early stage and, thus, to be able to inform preventive interventions before the manifestation of a disorder.

Keywords: fMRI, Hurst Exponent, frontal cortex, nucleus accumbens, biomarker, impulse control disorders

INTRODUCTION

Fractal structures possess the property that the whole structure consists of parts, which have the same pattern composition but at different scales and/or in different sizes [e.g., broccoli, the Koch snowflake (Koch, 1904, 1906; Mandelbrot, 1967, 1983)]. Fractals can be found not only in static objects but also dynamic processes. This property of *self-similarity*, or in the temporal domain *scale invariance* (Suckling et al., 2008; Ivanov et al., 2009; Nagy et al., 2017) means that both, rapidly occurring changes and slowly proceeding dynamics follow the same structure, or better, that measures of the patterns are independent of the sampling rate, used during data acquisition (Riley et al., 2012).

For time series, this property is mathematically expressed as follows:

$$S(f) = \frac{C_f}{|f|^{\beta}} \quad (1)$$

$$\beta = 2H - 1 \quad (2)$$

$S(f)$ represents the power spectrum density of the analyzed fluctuations, f the frequency, C_f a constant and $0 < \beta < 2$. Furthermore, β is related to the Hurst Exponent (H) according to Equation 2 (see **Figure 1**). For more details on how to compute H refer to method section fractal analysis (AFA) as suggested by Riley et al. (2012).

Fractal patterns have been examined in many research fields including physiology and neuroscience. A specific phenomenon called *pink noise* (also called fractal or 1/f noise, with $\beta = 1$) is one of the key fractal manifestations. Pink noise is a stochastic process, used for the modeling of dynamic systems. Its power spectral density is inversely proportional to the sample frequency (Keshner, 1982; Eke et al., 2000, 2002). Because pink or 1/f noise lies between white noise ($\frac{1}{f^0}$, or random noise), and red/Brownian noise ($\frac{1}{f^2}$, power density decreases with increasing frequency), it has been proven to bring stability and adaptability into dynamic processes, thus, crucial properties of well-functioning complex systems (Bak et al., 1987). Pink noise has been documented in behavioral as well as physiological processes, for example in heartbeat dynamics (Ivanov et al., 1999, 2001), neural network organization (Lipsitz and Goldberger, 1992; Lipsitz, 2002) and cognitive processes (Ihlen and Vereijken, 2010; Wijnants et al., 2012). The manifold appearance of pink noise has led to the speculation, that "there exists some profound law of nature that applies to all non-equilibrium systems and results in such noise" (Sejdić and Lipsitz, 2013). Intuitively, one might assume that pink noise has a detrimental effect to a system's performance and accuracy. However, as pink noise arises from the interaction of multiple systems and operates over different scales, it has been shown to contribute to system resiliency and structural integrity if individual components were lost or interrupted for example by age or disease (Lipsitz and Goldberger, 1992; Lipsitz, 2002). Thus, a fractal network structure, thus, qualifies a system to cope with stress or disturbances by adjusting specific components and fine tuning its responses (for a review see Sejdić and Lipsitz, 2013).

Pink noise can be found in the fMRI signal (i.e., the Blood-Oxygen-Level-Dependent, BOLD response) (Bullmore et al., 2009; He, 2011; Herman et al., 2011; Ciuciu et al., 2012, 2014; Eke et al., 2012; Churchill et al., 2016; Nagy et al., 2017). H valued close to 1 in the fMRI signal has been associated with a higher predictability of time series (Gentili et al., 2017), greater low-frequency power and, therefore, higher persistence over time (Ball et al., 2011), as well as highly complex and well attuned dynamics in the underlying network (Lipsitz and Goldberger, 1992; Goldberger et al., 2002). Likewise, it has been shown that deviation from pink noise in relevant parameters, independent of whether the changes occurred in the direction of white or red noise, was associated with neurological as well as psychiatric disorders (resting-state fMRI in Alzheimer's disease: Maxim et al., 2005; e.g., reaction time sequences in attention deficit/hyperactivity disorder: Gilden and Hancock, 2007).

In addition, fractality seem to be more pronounced in low compared to high frequencies. For example, Fox et al. (2007) reported 1/f noise in the fMRI signal (Fox et al., 2007), emphasizing that "spontaneous BOLD follow a 1/f distribution, meaning that there is an increasing power in the low frequencies." (Fox and Raichle, 2007). In addition, Gentili et al. (2017) found brain regions where H as well as metrics of low-frequency oscillations (i.e., amplitude of low-frequency fluctuations, ALFF, fractional amplitude of low-frequency fluctuations, fALFF) had similar effects hinting toward strong relation between both measures (Gentili et al., 2017). In task-fMRI data, fractal noise of inactive voxels differed from those of active ones (Thurner et al., 2003). Recent resting-state fMRI-studies showed, that H correlated with personality traits such as anxiety (Gentili et al., 2015) and extraversion (Gentili et al., 2017) in regions of the default mode network, with response time in the inferior frontal gyrus (Wink et al., 2008) hinting toward an influence of personality traits and task performance on the persistence of network dynamics (Wink et al., 2008). Likewise, findings from task-fMRI studies reported that H decreased with task processing (Ciuciu et al., 2012) and cognitive effort (Barnes et al., 2009; Churchill et al., 2016) concluding that "task-related modulation of multifractality appears only significant in functional networks and thus can be considered as the key property disentangling functional networks from artifacts" (Ciuciu et al., 2012).

Impulsivity is a personality trait, which spans from normal manifestations, e.g., in life time situations where decision making under time pressure is required (Burnett Heyes et al., 2012), to pathological presentations, mirroring the psychiatric symptoms of "loss of control" and "impulse control disorder" associated for example with ADHD (e.g., Sebastian et al., 2013; for a recent review see Hinshaw, 2017). Waiting impulsivity (WI) is one form of impulsivity and is operationally defined as the tendency to premature responding, i.e., to respond before target onset. Thus, it involves the aspects of response inhibition and top-down control, mediated by motivational aspects and reward processing (Robinson et al., 2009; Voon et al., 2014). Its associated functional network consists of the dlPFC and the vmPFC representing impulse control (Mechelmans et al., 2017), the reward-perception-related NAcc, the ACC for the cognitive evaluation of the reward and hippocampus (HC) and amygdala (AMY) responsible for reward-based learning (Dalley et al., 2011). Impulsivity has been documented to affect on the behavioral performance of attentional functions, working memory, motor speed, and language processing (Hinshaw et al.,

Abbreviations: BOLD, Blood-Oxygen-Level-Dependent; AFA, adaptive fractal analysis; dlPFC, dorsolateral prefrontal cortex; fMRI, functional magnetic resonance imaging; highImp, high impulsive; HFC, high frequency components; HC, hippocampus; H, Hurst Exponent; LFC, low frequency components; lowImp, low impulsive subjects; MFG, middle frontal gyrus; NAcc, nucleus accumbens; PSD, power spectrum density; rs-fMRI, resting-state fMRI; ROI, Regions of Interest; vmPFC, ventromedial prefrontal cortex.

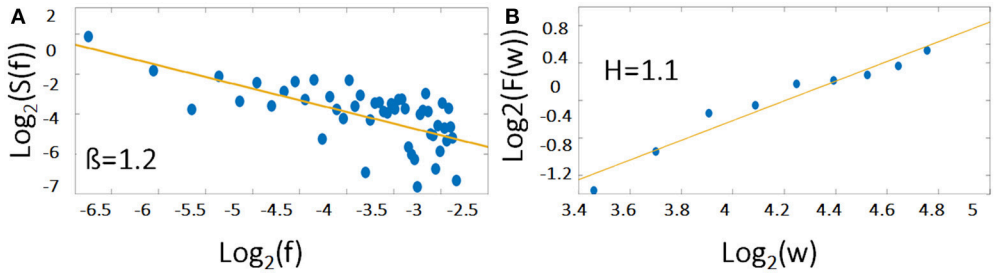

FIGURE 1 | The 1/f noise pattern in a power spectrum (Equation 1) of an exemplary time course is shown on logarithmic scales while the scale invariance relation (Equation 3) is indicated by the slope H. Please note, that the relationship between β and H is according to Equation (2) $\beta = 2H - 1$. For demonstration, the example of a representative individual time course of the right MFG during task has been used.

2002; Huang-Pollock et al., 2006; Solanto et al., 2007). In brain activation, high impulsive healthy subjects showed reduced activation in right dorsolateral prefrontal cortex (dlPFC) while performing a descision making task (Deserno et al., 2015), bilaterally in the ventral prefrontal cortex (vmPFC) during motor inhibition (Goya-Maldonado et al., 2010) as well as in the dlPFC and the hippocampus in aggressive impulsive subjects (Sala et al., 2011). At rest, impulsivity affected functional connectivity from resting-state fMRI in terms of less elaborated neural network architecture, e.g., lateral and medial prefrontal regions were isolated from reward associated regions such as the nucleus accumbens (NAcc) (Davis et al., 2013), connectivity between the NAcc and the anterior cingulate cortex (ACC) as well as the ACC and the amygdala (Li et al., 2013). A first study addressing the influence of impulsivity on H revealed that impulsivity correlated negatively with H in the orbito-frontal cortex (i.e., the vmPFC) and NAcc (Hahn et al., 2012) the way that the higher impulsive the subjects the smaller the H.

In this study, we examined the fractal nature of a brain network associated with WI using the AFA approach. H was determined for all network regions at rest and while performing a WI task. To define, whether a subject is high (highImp) or low impulsive (lowImp), the number of premature responses has been used (Feja et al., 2014; e.g., Donnelly et al., 2014). A permutation test was performed to insure the validity of using the number of premature responses as grouping criteria (see Supplement permutation.xlsx—**Supplementary Datasheet 1**). Based on the introduced findings we were intrigued to address the existence of pink noise in our network, thus, we expected to find

(a) a fractal nature of the impulsivity network and that fractality consists of pink noise, i.e., H values of all network regions were close to 1.
(b) smaller H at task compared to rest (Barnes et al., 2009; Ciuciu et al., 2012; Churchill et al., 2016).
(c) significant influence of impulsivity on H predominantly in the PFC and the NAcc (Wink et al., 2008; Hahn et al., 2012). In line with the previous studies (Gilden and Hancock, 2007; Hausdorff, 2007) we expected to find deviation from 1/f noise pronounced in highImp compared to lowImp subjects.

MATERIALS AND METHODS

Subjects

In this study, data of the same sample of 103 students was used as described by Neufang et al. (2016). Students were between 19 and 28 years old (24.0 ± 2.6 years), and were recruited at the University of Wuerzburg, Germany. From all subjects, measures for impulsivity were collected, using the Wender-Reimherr-Interview and Attention-Deficit/Hyperactivity Disorder checklist (subscales "impulsivity" and "hyperactivity and impulse control") (Rösler et al., 2008). The examination was conducted in accordance with the Declaration of Helsinki in its latest version from 2008 and was approved by the ethics committee of the Faculty of Medicine, University of Wuerzburg, and written informed consent was obtained from all subjects.

Experimental Paradigm

The used paradigm was an fMRI-adaptation of the four-choice serial reaction time task by Voon et al. (2014) and has been described in detail by Neufang et al. (2016), Voon et al. (2014), and Neufang et al. (2016). The task entailed the detection of a brief visual target (a green dot) after a certain waiting period. Depending on the subject's task performance, a reward of 1 Euro or 1 Cent was given, or better the punishment of 1 Euro was subtracted. In detail, a trial implied three phases/experimental conditions: the "cue" presentation, indicating the start of the waiting period; the "target" onset, in terms of a green circle in one of the choices. Subjects were instructed to indicate the correct choice by pressing the corresponding button as fast and as correct as possible; the reward feedback, showing the amount of recently earned/lost money in combination with the overall amount of earned money (see **Figure 2**).

The task consisted of one baseline run outside the scanner and five experimental runs within the scanner. During the five runs in the scanner, WI was experimentally manipulated by (i) implementing a monetary reward (blocs 1, 3, 4, 5), (ii) varying the duration of the target presentation (blocs 3, 4, 5), (c) extending the waiting period (cue-target interval) (blocs 4 and 5) and (d) presenting additional distractor taget before the actual target presentation, i.e., circles in different colors (bloc 5). Task scanning was of a total duration of 14 min.

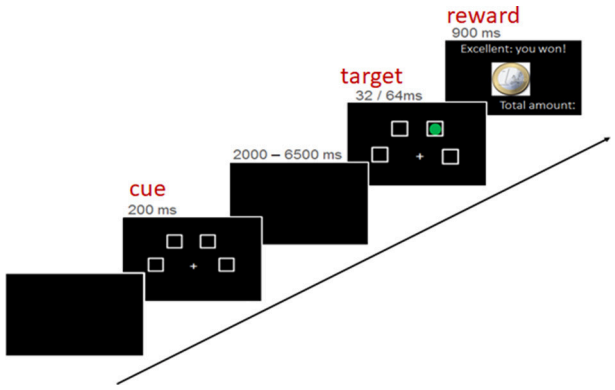

FIGURE 2 | Structure of an experimental trial.

Before task-fMRI, all subjects were scanned at rest for 12 min. During the rs-fMRI, subjects kept their eyes open and were instructed not to think of something specific. Eyes were controlled by the examiner via an eye tracking camera outside the MR scanner.

fMRI—Data Acquisition

The fMRI scanner was a 3 Tesla TIM Trio Scanner (Siemens, Erlangen, Germany). Functional MRI included a T2*-weighted gradient echo-planar imaging sequence with the following sequence parameters: repetition time (TR) = 2000 ms, echo time (TE) = 30 ms, 36 slices, 3 mm thickness, field of view (FoV) = 192 mm, flip angle = 90°, number of volumes in task-fMRI = 425, number of volumes in rs-fMRI = 350).

fMRI—Data Processing

Data preprocessing was performed using the Statistical Parametric Mapping Software Package (SPM12). Preprocessing followed the standard routine including temporal and spatial alignment, i.e., slice time correction and realignment and unwarp, spatial normalization [standard space: Montreal Neurological Institute (MNI) space] including a resampling of the data to an isotropic voxel size of $2 \times 2 \times 2$ mm^3, spatial smoothing with a Gaussian kernel of 8 mm full width at half maximum (FWHM), and linear trend removal [using the matlab routine detrend (y)] (see **Supplementary Presentation 1**) (Bai et al., 2008; Zhang et al., 2008; Fox et al., 2009; Qiu et al., 2011). Pre-processing did not include high-pass filtering or global mean correction.

fMRI Time Course Extraction

Regions of Interest (ROI) were defined based on the significantly activated brain regions while performing the waiting impulsivity task. In detail, for the identification of global activation maxima, the contrasts *target* > *baseline* and *reward* > *baseline* were defined on a single subject level and analyzed on group level using a one sample *t*-test. The local maxima of each significantly activated regions were identified and coordinates were then used as the centere of a 10 mm spheric ROI using MarsBar [24]. ROIs were built and used for the extraction of the time course for each subject. Time course extraction was performed using the routine as suggested by Brett et al. (2002) (see MarsBar manual, http://marsbar.sourceforge.net/marsbar.pdf) from preprocessed fMRI data (i.e., smoothed files resulting from the pre-processing procedure) (Brett et al., 2002).

AFA

Fractal analysis of time series is based on quantifying the degree of fluctuation around the overall trend of the data over time, to measure the scale invariance quantified by the value of H (Equation 3, see below). In this paper, we split the fMRI signal in its two components: the low and the high frequency components (LFC, HFC) (see **Figure 3**).

LFC is the second order polynomial that is a smooth and global fit of the original time course (see **Figure 4**). HFC represents the residuals after subtracting the fitting curve from the original time course. For time series to be fractal, their power spectrum density (PSD) must be inversely proportional to frequency (see also **Figure 5**, legend).

After analyzing these two main components, we found, that the residuals were more likely to obscure the results with respect to the scale invariance analysis. HFC, in addition, could not be classified as fractal (see **Figure 5A**). The low frequency component of the signal on the other hand, held all the information concerning the fractal nature of the original signal. In line with earlier studies and to avoid inaccuracies and the reduction of H, we focused in our analyses on those parts of the signal/those regions, which showed power law scaling and fractal scaling was present (e.g., Cannon et al., 1997; Herman et al., 2011; Riley et al., 2012): only the LCF was taken into consideration for further analysis via AFA to compute H.

AFA is one of the existing mathematical methods that computes H, a factor that reflects in a scale law manner the relationship, that is intrinsic to fractal processes, between the variance of fluctuation computed around, in our case, a second order polynomial trend $v(i)$ fitted to time series within each segment w, and its size:

$$F(w) = \left[\frac{1}{N} \sum_{i=1}^{N} (u(i) - v(i))^2 \right]^{\frac{1}{2}} \sim w^H, \qquad (3)$$

N: length of the time series

$$w = 2n + 1,\ n = 5, 6 \ldots, 13$$

H is determined as the slope of the log-log diffusion plot $\log_2(F(w))$ as a function of $\log_2(w)$ (see **Figure 1B**).

Statistical Analysis

The factor *impulsive phenotype* was defined as high impulsive (highImp) versus low impulsive subjects (lowImp), based on the subjects' number of premature responses. If the number was ≥ 3 they were classified as highImp and if the number was <3 as lowImp. Threshold definition was adapted from Feja et al. (2014) in terms of the median value of premature responses across all subjects [range: 0–6 number of premature responses

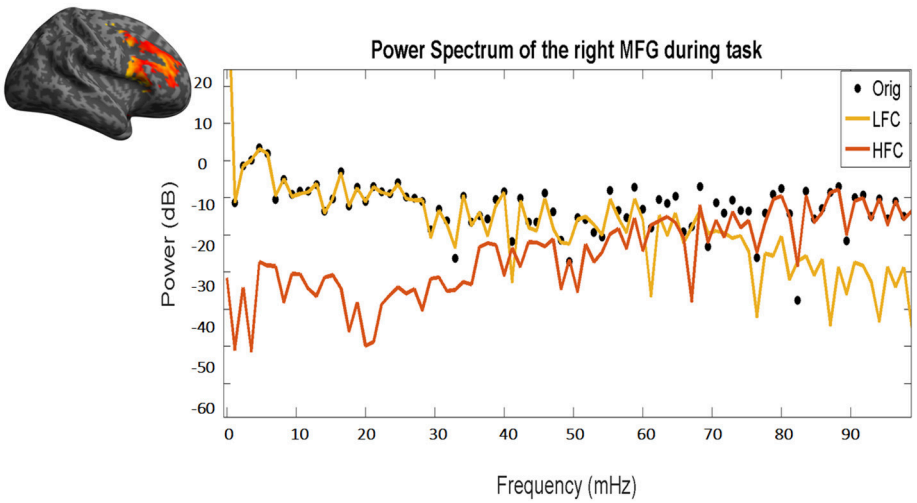

FIGURE 3 | Power frequency spectrum of the original time course (black dots), as well as of the resulting low (yellow line) and high frequency (red line) components. Please note the overlap between the black dots (original time course) and the yellow line (LFC) in low frequencies (left part of the x-axis) and between the black dots and the red line (HFC) in high frequencies (right part of the x-axis). The same time course of the right MFG during task of a representative subject has been used.

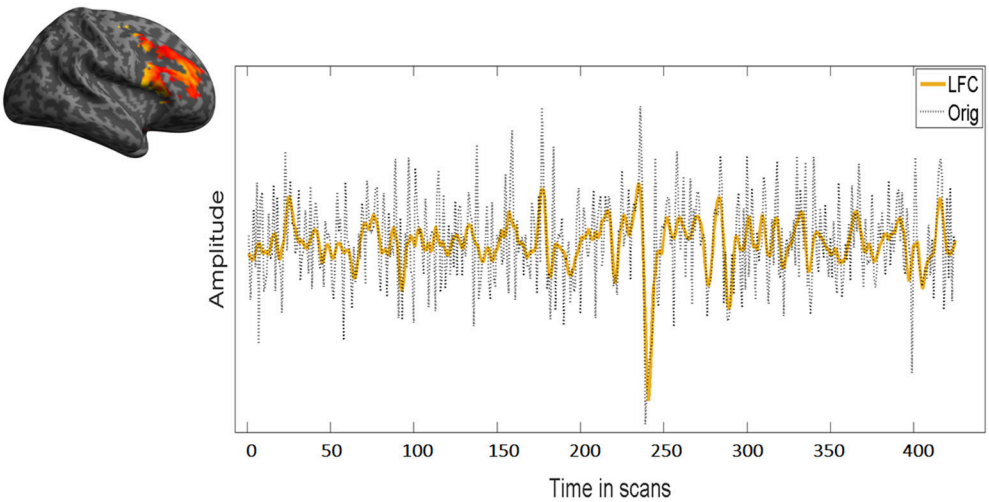

FIGURE 4 | Overlap between low frequency course (LFC) and the original time course. LFC fits well the data without overfitting leaving out unnecessary information for the fractal analysis. In this figure, the same time course of the right MFG during task of a representative subject has been used.

(adapted from Feja et al., 2014)]. The sample consisted of 66 lowImp subjects and 38 highImp. In addition, a permutation test was performed to insure the validity of using the number of premature responses as grouping criteria (see Supplement permutation.xlsx—**Supplementary Datasheet 1**).

On behavioral level, 1 × 2 ANOVA models were defined using the between-subject factor *impulsivity phenotype* (highImp vs. lowImp) as independent factor and the dependent variables the behavioral parameters *no. of premature responses*, *accuracy*, *reward (amount of total win)* and *reaction times*.

The question of the existence of pink noise was verified using a one sample Wilcoxon test with H of all network regions as test variables and 1 as hypothetical median.

To address the two aspects (a) changes in fractality at rest and while task processing and (b) the influence of impulsivity on fractality of the impulsivity network, the following statistical analyses were performed:

(a) To compare fractality at rest and while task processing, non-parametric tests of related samples were defined using the within-subject factor *condition* (task vs. rest), and H as dependent variable. To reveal the impact of the impulsive phenotype on differences between rest and task, the same analyses were performed phenotype-specifically.
(b) The influence of impulsivity on network fractality was performed using both, the factorial and the dimensional

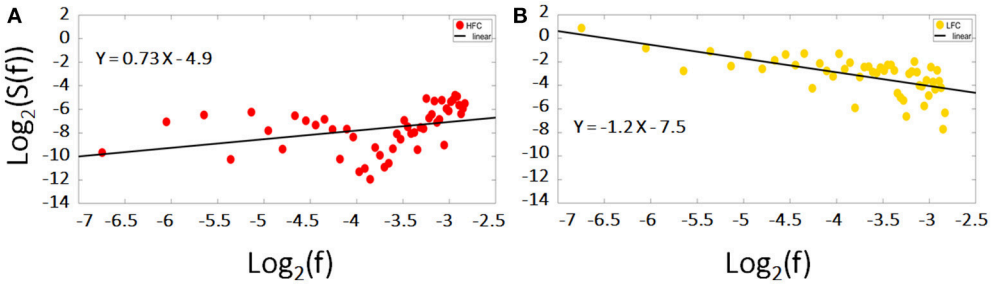

FIGURE 5 | Log-log diffusion plots of the power spectrum density (PSD) of the low and high frequency components (LFC, HFC): whereas the HFC (red dots) fails to fulfill the criteria of a fractal structure expressed by Equation 1, the PSD of the LFC (yellow dots) is clearly inversely proportional to frequency hinting toward a fractal nature. The data presented is the same time course of the right MFG during task of a representative subject.

approach. Impulsive phenotype differences of H were addressed using non-parametric Mann-Whitney-U-Test for 2 independent samples using the between-subject factor *impulsive phenotype* and dependent variables were H scores. In addition, correlations between WI (i.e., the number of premature responses, task accuracy, reward and reaction times) and H scores were performed.

For all statistical analyses a significance threshold of $p < 0.05$, corrected for multiple comparisons using the False-Discovery Rate (Benjamini and Hochberg, 1995), was applied. The number of test as well as q*-scores representing the FDR-corrected significance levels were provided for each analysis in the results section as well as in **Tables 1**, **2**.

RESULTS

post-hoc power analyses using G*Power (version 3.1.9.3, http://www.gpower.hhu.de/) revealed a power of 0.77 and a critical $Z = 1.6$.

Regarding behavioral differences only main effect of impulsive phenotype on the number of premature responses passed the threshold of significance ($Ml_{owImp} = 0.6 \pm 0.5$, $M_{highImp} = 2.5 \pm 0.9$, $F_{(102,2)} = 201.8$, $p = 0.000$, corrected for 4 comparisons with $q^* = 0.0125$). All other effects on any other dependent variable were not significant (for further results please see Neufang et al., 2016).

Performed fMRI analyses revealed that whereas activation bilaterally in the middle frontal gyrus (MFG) (right MFG: $x = 40$, $y = 0.8, 34$, $T = 19.7$; left MFG: $x = -44$, $y = 6, 28$, $T = 21.7$), the ACC ($x = 6$, $y = 30, 28$, $T = 18.6$) as well as the vmPFC ($x = 0$, $y = 48, -12$, $T = 6.5$) was associated with impulse control, bilaterally the HC (right HC: $x = 24$, $y = -28, -6$, $T = 21.9$; left HC: $x = -22$, $y = -28, -6$, $T = 17.7$), the right NAcc ($x = 8$, $y = 12, -10$, $T = 14.6$), and the left amygdala ($x = -22$, $y = 0, -12$, $T = 6.0$) were active while reward processing (see **Figure 6**).

Via AFA we found that at rest (a) across all subjects, H was similar to 1 in the following network regions (rHC: $M = 0.93 \pm 0.13$, $p = 0.000$; lHC: $M = 0.96 \pm 0.12$, $p = 0.000$; lMFG: $M = 1.01 \pm 0.12$, $p = 0.156$; rMFG: $M = 1.00 \pm 0.12$, $p = 0.577$; ACC: $M = 1.01 \pm 0.12$, $p = 0.414$; rNAcc: $M = 1.03 \pm 0.10$, $p = 0.060$; lAMY: $M = 1.00 \pm 0.11$, $p = 0.928$; vmPFC: $M = 1.01 \pm 0.12$, $p = 0.087$, corrected for 8 comparisons with $q^* = .006$) proving a stable fractal nature of this network for confidence intervals from bootstrap see **Supplementary Table 1**.

(a) Across all subjects (i.e., independent of the impulsive phenotype), H was significantly higher at rest compared to task in all regions. Group-specific analyses, however, revealed that in highImp subjects, fractality in the right HC did not differ at rest and during task processing (see **Table 1**). In lowImp subjects, H was significantly higher at rest compared to task in all regions.

(b) H during task-processing differed between impulsivity phenotypes in terms of reduced H in highImp subjects in the reward-associated NAcc and the impulse control-related ACC (see **Table 2**). Furthermore, H of the left HC varied trend-wisely between impulsivity groups across. At rest, there was no significant difference in any region. Correlations revealed a significant correlation between H of the left MFG and the number of premature responses ($r = -0.242$, $p = 0.013$, corrected for 16 comparisons with $q^* = 0.012$), whereas there was no significant relation between H and accuracy, reward and reaction times.

DISCUSSION

In this study, we addressed the fractal nature of a neural network associated with waiting impulsivity. We found that (a) pink noise in all network regions, proving the existence of a stable fractal nature within this network (Bak et al., 1987; Lipsitz and Goldberger, 1992; Lipsitz, 2002; Wijnants et al., 2012). Furthermore, (b) H was significantly higher at rest compared to task. This was the case in all regions and across all subjects. However, in high impulsive (highImp) subjects, H was comparable between both activation conditions in the right HC. (c) Finally, during task processing, fractality in impulse control related left MFG as well as reward-associated NAcc and ACC was influenced by impulsivity the way that in highImp subjects H was significantly smaller and, therefore, was a less adequate 1/f noise fit candidate compared to lowImp subjects.

TABLE 1 | Comparison of H between task and rest across all subjects.

	Across all subjects			lowImp			highImp		
	Task [M(SD)]	Rest [M(SD)]	Z	Task [M(SD)]	Rest [M(SD)]	Z	Task [M(SD)]	Rest [M(SD)]	Z
rHC	0.88 (0.11)	0.93 (0.13)	3.7**	0.88 (0.11)	0.94 (0.13)	3.4**	0.88 (0.11)	0.92 (0.12)	n.s.
lHC	0.90 (0.10)	0.96 (0.12)	3.8**	0.91 (0.10)	0.96 (0.13)	2.6**	0.88 (0.10)	0.95 (0.10)	2.8**
lMFG	0.93 (0.11)	1.01 (0.12)	5.4**	0.94 (0.11)	1.02 (0.11)	4.1**	0.90 (0.12)	1.00 (0.12)	3.5**
rMFG	0.92 (0.13)	1.00 (0.12)	4.4**	0.93 (0.14)	1.00 (0.13)	2.7**	0.90 (0.12)	1.00 (0.12)	3.6**
ACC	0.93 (0.12)	1.01 (0.12)	4.8**	0.96 (0.13)	1.02 (0.13)	2.8**	0.89 (0.09)	0.99 (0.10)	4.1**
rNAcc	.91 (0.13)	0.97 (0.13)	3.6**	0.93 (0.13)	0.98 (0.12)	2.3**	0.87 (0.13)	1.00 (0.12)	2.9**
lAMY	0.88 (0.11)	1.02 (0.12)	3.0**	0.89 (0.12)	0.92 (0.12)	n.s.	0.86 (0.11)	0.95 (0.14)	2.7**
vmPFC	0.98 (0.11)	1.07 (0.12)	5.4**	0.98 (0.11)	1.07 (0.12)	4.2***	0.97 (0.11)	0.91 (0.12)	3.3**

rHC, right hippocampus; lHC, left hippocampus; lMFG, left middle frontal gyrus; rMFG, right middle frontal gyrus; ACC, anterior cingulate cortex; Nacc, nucleus accumbens; lAMY, left amygdala; vmPFC, ventromedial prefrontal gyrus; lowImp, low impulsive subjects; highImp, high impulsive subjects; FDR-corrected was applied for 8 comparisons; corrected significance level were q^*(all subjects) = 0.05; q^*(highImp subjects) = 0.04; q^*(highImp subjects) = 0.04; $^{**}p < q^*$; n.s., not significant.

TABLE 2 | Comparison of H between high and low impulsive subjects.

	lowImp [M(SD)]	highImp [M(SD)]	Z
TASK			
rHC	0.87 (0.11)	0.88 (0.11)	0.2
lHC	0.91 (0.10)	0.88 (0.10)	1.9
lMFG	0.94 (0.11)	0.90 (0.11)	1.7
rMFG	0.93(14)	0.90 (0.11)	1.1
ACC	0.96 (0.13)	0.89 (0.09)	3.0**
rNAcc	0.93 (0.13)	0.87 (0.13)	2.4**
lAMY	0.89 (0.11)	0.86 (0.11)	1.4
vmPFC	0.98 (0.11)	0.97 (0.11)	0.6
REST			
All regions		n.s	.

*rHC, right hippocampus; lHC, left hippocampus; lMFG, left middle frontal gyrus; rMFG, right middle frontal gyrus; ACC, anterior cingulate cortex; Nacc, nucleus accumbens; lAMY, left amygdala; vmPFC, ventromedial prefrontal gyrus; $_{low}$, low impulsive subjects; $_{high}$, high impulsive subjects; FDR-corrected was applied for 16 comparisons; corrected significance level was $q^* = 0.007$; ** $p < q^*$; n.s., not significant.*

The Fractal Nature of the Waiting Impulsivity Network

As introduced we learned that a brain network follows a stable fractal patterns when H is close to 1 (e.g., Stadnitski, 2012), is decreased while cognitive activation (Barnes et al., 2009; Ciuciu et al., 2012; Churchill et al., 2016), and is sensitive to normal and abnormal alteration such as disease or age (Lipsitz and Goldberger, 1992; Lipsitz, 2002; Sejdić and Lipsitz, 2013). In our data, we could find all these aspects and, hence, assumed a fractal nature in the impulsivity network: (a) at rest, H varied around 1 across all subjects; during task processing, H was significantly reduced in all regions and, finally, when comparing H between high and low impulsive subjects, H was reduced in highImp subjects in some of the network regions. The network examined here has been introduced in a comprehensive review article by Dalley et al. (2011) and is based on relevant findings from humans and animal studies on impulsivity and cognitive top-down control (Dalley et al., 2011). The notion that the suggested network regions were indeed involved in the processes of waiting impulsivity as measured via the 5-CSRTT has been shown in recent studies (NAcc and ACC: Morris et al., 2016; e.g., NAcc and vmPFC: Neufang et al., 2016; dlPFC and ACC: Mechelmans et al., 2017). The characterization of this network as a "healthy and complex system" (Bak et al., 1987), however, has been demonstrated in this study for the first time.

Fractality During Task Processing and at Rest

Higher fractality at rest compared to task processing/cognitive effort is in line with earlier findings (He, 2011; Ciuciu et al., 2012; Churchill et al., 2016). In the context of the common knowledge, that neural networks are predominantly active after an external stimulation, e.g., of our senses or while cognitive processing (Penn and Shatz, 1999; Kandel et al., 2000), this finding seems counter-intuitive. However, the recent years of research on the brain at rest have accentuated the prominence of *endogenously* engendered brain responses as an important defining factor in modeling the topology of large-scale neuronal networks (for reviews see Linkenkaer-Hansen, 2002; Calhoun and De Lacy, 2017; Gorges et al., 2017; Liégeois et al., 2017; Smitha et al., 2017). The terms used most frequently to describe resting-state neural activity, such as "endogenous," "intrinsic" and "spontaneous," indicate that network function is created within the brain itself, and can, thus, be understood as "self-organized" (Linkenkaer-Hansen, 2002). Self-organized criticality, in return, has been described by Bak et al. (1987) as the origin of fractal objects. They demonstrated, that "dynamic systems naturally evolve into self-organized critical structures of states" and suggested, that "this self-organized criticality is the common underlying mechanism" behind those dynamic system (Bak et al., 1987). For an empirical example in the context of sleep dynamics, Lo et al. (2013) were able to identify two independent paths for the transition between sleep phases using power-law scaling on noctural EEG recordings (Lo et al., 2013). Thus, a task-induced stimulation operating as an involvement from the outside system may lead to a reduction of these dynamics, hence of fractality.

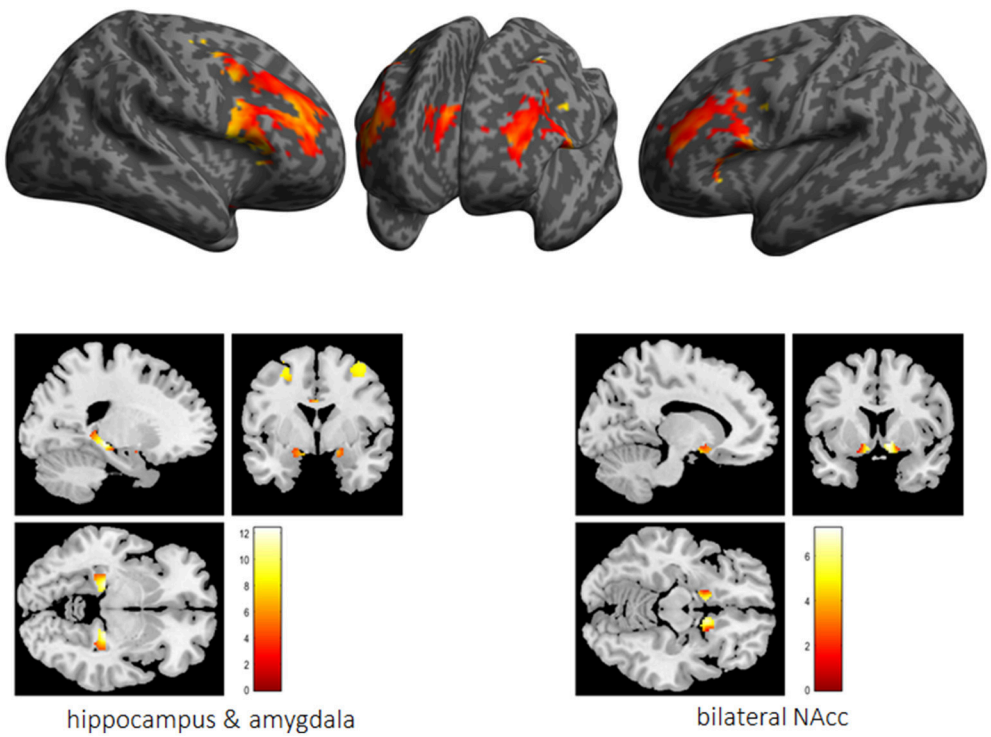

FIGURE 6 | The impulsivity network is presented in terms of significantly activated brain regions across all subjects while performing the 5-choice serial reaction time task. PFC, prefrontal cortex; ACC, anterior cingulate cortex; Nacc, nucleus accumbens.

In highImp subjects, however, *H* did not decrease significantly during task in the right HC. A generally small fractality in the hippocampus has been reported by He (2011, 2014). They found varying *H* across different cortical regions with lowest *H* in the HC, interpreting these findings in terms of regional differences in neurovascular coupling mechanisms (He, 2011, 2014;). Impaired hippocampal *H* has also been reported between patients with Alzheimer's disease and control subjects (Maxim et al., 2005) with the persistence of *H* being assumed to reflect neurodegenerative processes. The insignificant change of *H* during task processing in high impulsive subjects in our study, thus, might reflect a weaker recruitment of the right HC while performing the task and a more superficial learning (e.g., El-Gaby et al., 2015). In return, this finding can also be interpreted the way, that the right HC is less adaptive in high impulsive subjects, thus constantly following its own dynamics, leading to an impaired motivation- or reward-based learning of the task (Chantiluke et al., 2012; Moreno-López et al., 2012).

Fractality Differs in Function of Impulsivity

Our analyses revealed, that impulsivity modulated fractality only during task processing and predominantly in the fronto-striatal loop namely the ACC and the NAcc, as well as the left MFG. Morris et al. (2016) showed that functional connectivity in the ACC and the NAcc via the subthalamic nucleus varied in function of the number of premature responses (Morris et al., 2016) emphasizing the crucial and interacting role of these two structures on the key parameter of waiting impulsivity. The left MFG as part of the dorsolateral PFC, in return, reflects the counterpart, i.e., top-down control which decreases with higher reward processing (Mechelmans et al., 2017).

In the NAcc as well as in the ACC, in high impulsive subjects, *H* was significantly reduced compared to low impulsive subjects. A negative association between impulsivity/reward sensitivity and the ventral striatum has been reported by Hahn et al. (2012) before in the way that the higher impulsive/reward sensitive the subjects were, the smaller the *H* (Hahn et al., 2012). Reduced *H* in the NAcc and ACC in high impulsive subjects of our study, thus, reflects an altered reward processing.

In addition, significant correlations between impulsivity and fractality in the frontal cortex have been shown for the orbito-frontal cortex (Hahn et al., 2012) as well as for the lateral PFC (Ball et al., 2011). Similar to these findings, we found a significant (negative) correlation with the number of premature responses and *H* in the left MFG across all subjects as well as in the vmPFC in the highImp group. The MFG is strongly involved in response inhibition and cognitive control (Chambers et al., 2009; Boehler et al., 2010; Braver, 2012; Bari and Robbins, 2013), thus, a more random top-down control in highImp subjects reflects impaired control and more impulsive task performance. Taken together, the combination of impaired top-down control and altered reward processing is common and has been described for numerous impulse control disorders

such as attention-deficit/hyperactivity disorder (e.g., Scheres and Hamaker, 2010), eating disorders (for review Citrome, 2015), addiction (Weinstein, 2017), bipolar disorder, and depression (Carver et al., 2008).

In contrast to findings by Wink et al., H of network regions associated with waiting impulsivity did not correlate with reaction time (Wink et al., 2008). This, however, might be based on the different anatomical structures: Wink et al. reported a correlation of H and resting-state fMRI signals in the right inferior frontal cortex, which was not included in our network.

LIMITATION AND CONCLUSION

In this study, we chose a monofractal approach. The main reasons were the following: (1) This is a pilot study for a clinical project; thus, data acquisition was strongly determined by the factors (a) field strength (3T) (b) total scanning time (12 min/365 volumes during resting-state; 14 min/420 volumes during tast), (c) sample rate (TR was 2000 ms) to ensure the feasibility for patients to perform the scanning procedure successfully. All factors, however, play a crucial role in the analysis of fractal patterns in fMRI (Eke et al., 2012). For example, the field strength highly influences measurement sensitivity (Eke et al., 2006) and multi-fractal analysis is "known to require a much higher signal definition for an optimal performance" than monofractal (Ciuciu et al., 2012; Eke et al., 2012). Likewise, multi-fractal analyses need longer time series/higher sampling rates than those found for monofractal series (Eke et al., 2002, 2012). (2) In a previous step multi-fractality was addressed (using q from −2 to 2) and revealed, that our signals are, with no loss of information, to be approximated as monofractal (see **Figure S1**). The monofractal approximation, however, has been proven to be a robust assumption and, thus, an adequate tool to address similar signals.

In summary, we revealed that activity in the neural network associated with waiting impulsivity is of fractal nature. The use of fractal parameters to examine neural networks regarding to health or disorder has been described in earlier studies (e.g., Lipsitz, 2002; Maxim et al., 2005; Hahn et al., 2012; Lei et al., 2013; Sokunbi et al., 2014; El-Gaby et al., 2015; Dona et al., 2017; Gorges et al., 2017), introducing these parameters as exceptionally sensitive toward alterations. In our study, however, we performed analysis in a very homogenous sample of young adult male students. The classification into high and low impulsive subjects, therefore, is relative and does not represent samples with manifest impulse control disorders. The transfer of the present data to a clinical context therefore predominantly relies on the findings of earlier studies (e.g., Lipsitz, 2002; Maxim et al., 2005; Hahn et al., 2012; Lei et al., 2013; Sokunbi et al., 2014; El-Gaby et al., 2015; Dona et al., 2017; Gorges et al., 2017) and would be of high interest for future studies.

In contrast to earlier studies, in which H was determined on the whole brain level and in a data-driven manner (e.g., Suckling et al., 2008; Wink et al., 2008; Barnes et al., 2009; Gentili et al., 2015, 2017; Churchill et al., 2016), we chose to focus on an earlier described network. This way, we were able to *a priori* match cognition and neural structures, however, taking the risk of losing information, for example regarding the compensatory recruitment of additional structures. When examining a clinical sample, thus, a combined approach would be indicated.

Taken together, we would like to emphasize, that the use of fractality and H in particular, has two advantages which makes it a promising biomarker in the early detection of disease: (i) the reference score is a concrete number (e.g., 1) the difference can be interpreted as a measure of the deviation from this reference state, (ii) in principle the assessment of H can be integrated in the (f)MRI clinical routine protocol subject to the availability of sufficiently long fMRI-BOLD sequences. However, consistent with earlier observations with various fractal time series methods (Eke et al., 2000) -, as specifically stated by Riley et al. (2012), "AFA requires careful consideration of signal properties, parameter settings, and interpretation of results, and should not be applied blindly to unfamiliar signals." (Riley et al., 2012). In line with earlier studies, our data showed the potential of fractal parameters in the detection of altered brain function in the clinical context. For that reason, it is highly recommended to follow up on the development of methods to making fractal analysis accessible to a wider public and delivering unambiguous results.

AUTHOR CONTRIBUTIONS

SN, MR, and AS-B conceptualized and supervised the study, SN and AA acquired and analyzed the data. AS-B, MR, and KD supported the transfer of the findings into the current discussion of translational (AS-B) and clinical neuroscience (MR, KD). All authors contributed to and have approved the final manuscript.

FUNDING

This work was supported by grants from the Deutsche Forschungsgemeinschaft (DFG; SFB-TRR-58 project C02 and Z02 to KD, MR, and SN).

SUPPLEMENTARY MATERIAL

The Supplementary Material for this article can be found online at: https://www.frontiersin.org/articles/10.3389/fphys.2018.01378/full#supplementary-material

Figure S1 | The scaling function f and the corresponding regression line of the entire signal (left upper row) and for its LFC only (right upper row). Please note that data points in the case of the LFC are linearly fitted, whereas this is not the case in the entire signal. The diagramm in the lower row shows that the slopes H of the regression lines are q-indepenent (monofractal). For this diagramm, MFDFA has been used (Ihlen, 2012). For demonstration, the example of a representative individual time course has been used.

Supplementary Presentation 1 | Plots of raw BOLD series.

Supplementary Table 1 | Bootstrap.

Supplementary Datasheet 1 | Permutations.

REFERENCES

Bai, F., Zhang, Z., Yu, H., Shi, Y., Yuan, Y., Zhu, W., et al. (2008). Default-mode network activity distinguishes amnestic type mild cognitive impairment from healthy aging: a combined structural and resting-state functional MRI study. *Neurosci. Lett.* 438, 111–115. doi: 10.1016/j.neulet.2008.04.021

Bak, P., Tang, C., and Wiesenfeld, K. (1987). Self-organized criticality: An explanation of the 1/f noise. *Phys. Rev. Lett.* 59, 381–384. doi: 10.1103/PhysRevLett.59.381

Ball, G., Stokes, P. R., Rhodes, R. A., Bose, S. K., Rezek, I., Wink, A. M., et al. (2011). Executive functions and prefrontal cortex: a matter of persistence? *Front. Syst. Neurosci.* 5:3. doi: 10.3389/fnsys.2011.00003

Bari, A., and Robbins, T. W. (2013). Inhibition and impulsivity: behavioral and neural basis of response control. *Prog. Neurobiol.* 108, 44–79. doi: 10.1016/j.pneurobio.2013.06.005

Barnes, A., Bullmore, E. T., and Suckling, J. (2009). Endogenous human brain dynamics recover slowly following cognitive effort. *PLoS ONE* 4:e6626. doi: 10.1371/journal.pone.0006626

Benjamini, Y., and Hochberg, Y. (1995). Controlling the false discovery rate: a practical and powerful approach to multiple testing. *J. R. Stat. Soc. B* 57, 289–300.

Boehler, C. N., Appelbaum, L. G., Krebs, R. M., Hopf, J. M., and Woldorff, M. G. (2010). Pinning down response inhibition in the brain–conjunction analyses of the Stop-signal task. *Neuroimage* 52, 1621–1632. doi: 10.1016/j.neuroimage.2010.04.276

Braver, T. S. (2012). The variable nature of cognitive control: a dual mechanisms framework. *Trends Cogn. Sci.* 16, 106–113. doi: 10.1016/j.tics.2011.12.010

Brett, M., Anton, J.-L., Valabregue, R., and Poline, J.-P. (2002). "Region of interest analysis using an SPM toolbox [abstract]," in *Neuroimage International Conference on Functional Mapping of the Human Brain* (Sendai).

Bullmore, E., Barnes, A., Bassett, D. S., Fornito, A., Kitzbichler, M., Meunier, D., et al. (2009). Generic aspects of complexity in brain imaging data and other biological systems. *Neuroimage* 47:1125. doi: 10.1016/j.neuroimage.2009.05.032

Burnett Heyes, S., Adam, R. J., Urner, M., Van Der Leer, L., Bahrami, B., Bays, P. M., et al. (2012). Impulsivity and rapid decision-making for reward. *Front. Psychol.* 3:153. doi: 10.3389/fpsyg.2012.00153

Calhoun, V. D., and De Lacy, N. (2017). Ten key observations on the analysis of resting-state functional MR imaging data using independent component analysis. *Neuroimaging Clin. N. Am.* 27, 561–579. doi: 10.1016/j.nic.2017.06.012

Cannon, M. J., Percival, D. B., Caccia, D. C., Raymond, G. M., and Bassingthwaighte, J. B. (1997). Evaluating scaled windowed variance methods for estimating the Hurst coefficient of time series. *Phys. A* 241:606. doi: 10.1016/S0378-4371(97)00252-5

Carver, C. S., Johnson, S. L., and Joormann, J. (2008). Serotonergic function, two-mode models of self-regulation, and vulnerability to depression: what depression has in common with impulsive aggression. *Psychol. Bull.* 134, 912–943. doi: 10.1037/a0013740

Chambers, C. D., Garavan, H., and Bellgrove, M. A. (2009). Insights into the neural basis of response inhibition from cognitive and clinical neuroscience. *Neurosci. Biobehav. Rev.* 33, 631–646. doi: 10.1016/j.neubiorev.2008.08.016

Chantiluke, K., Halari, R., Simic, M., Pariante, C. M., Papadopoulos, A., Giampietro, V., et al. (2012). Fronto-striato-cerebellar dysregulation in adolescents with depression during motivated attention. *Biol. Psychiatry* 71, 59–67. doi: 10.1016/j.biopsych.2011.09.005

Churchill, N. W., Spring, R., Grady, C., Cimprich, B., Askren, M. K., Reuter-Lorenz, P. A., et al. (2016). The suppression of scale-free fMRI brain dynamics across three different sources of effort: aging, task novelty and task difficulty. *Sci. Rep.* 6:30895. doi: 10.1038/srep30895

Citrome, L. (2015). A primer on binge eating disorder diagnosis and management. *CNS Spectr.* 20(Suppl. 1), 44–50; quiz 51. doi: 10.1017/S1092852915000772

Ciuciu, P., Abry, P., and He, B. J. (2014). Interplay between functional connectivity and scale-free dynamics in intrinsic fMRI networks. *Neuroimage* 95, 248–263. doi: 10.1016/j.neuroimage.2014.03.047

Ciuciu, P., Varoquaux, G., Abry, P., Sadaghiani, S., and Kleinschmidt, A. (2012). Scale-free and multifractal time dynamics of fMRI signals during rest and task. *Front. Physiol.* 3:186. doi: 10.3389/fphys.2012.00186

Dalley, J. W., Everitt, B. J., and Robbins, T. W. (2011). Impulsivity, compulsivity, and top-down cognitive control. *Neuron* 69, 680–694. doi: 10.1016/j.neuron.2011.01.020

Davis, F. C., Knodt, A. R., Sporns, O., Lahey, B. B., Zald, D. H., Brigidi, B. D., et al. (2013). Impulsivity and the modular organization of resting-state neural networks. *Cereb. Cortex* 23, 1444–1452. doi: 10.1093/cercor/bhs126

Deserno, L., Wilbertz, T., Reiter, A., Horstmann, A., Neumann, J., Villringer, A., et al. (2015). Lateral prefrontal model-based signatures are reduced in healthy individuals with high trait impulsivity. *Transl. Psychiatry* 5:e659. doi: 10.1038/tp.2015.139

Dona, O., Noseworthy, M. D., Dematteo, C., and Connolly, J. F. (2017). Fractal Analysis of Brain Blood Oxygenation Level Dependent (BOLD) signals from children with mild traumatic brain injury (mTBI). *PLoS ONE* 12:e0169647. doi: 10.1371/journal.pone.0169647

Donnelly, N. A., Holtzman, T., Rich, P. D., Nevado-Holgado, A. J., Fernando, A. B., Van Dijck, G., et al. (2014). Oscillatory activity in the medial prefrontal cortex and nucleus accumbens correlates with impulsivity and reward outcome. *PLoS ONE* 9:e111300. doi: 10.1371/journal.pone.0111300

Eke, A., Herman, P., Bassingthwaighte, J. B., Raymond, G. M., Percival, D. B., Cannon, M., et al. (2000). Physiological time series: distinguishing fractal noises from motions. *Pflugers Arch.* 439, 403–415. doi: 10.1007/s004249900135

Eke, A., Herman, P., and Hajnal, M. (2006). Fractal and noisy CBV dynamics in humans: influence of age and gender. *J. Cereb. Blood Flow Metab.* 26, 891–898. doi: 10.1038/sj.jcbfm.9600243

Eke, A., Herman, P., Kocsis, L., and Kozak, L. R. (2002). Fractal characterization of complexity in temporal physiological signals. *Physiol. Meas.* 23, R1–38. doi: 10.1088/0967-3334/23/1/201

Eke, A., Herman, P., Sanganahalli, B. G., Hyder, F., Mukli, P., and Nagy, Z. (2012). Pitfalls in Fractal Time Series Analysis: fMRI BOLD as an Exemplary Case. *Front. Physiol.* 3:417. doi: 10.3389/fphys.2012.00417

El-Gaby, M., Shipton, O. A., and Paulsen, O. (2015). Synaptic plasticity and memory: new insights from hippocampal left-right asymmetries. *Neuroscientist* 21, 490–502. doi: 10.1177/1073858414550658

Feja, M., Hayn, L., and Koch, M. (2014). Nucleus accumbens core and shell inactivation differentially affects impulsive behaviours in rats. *Prog. Neuropsychopharmacol. Biol. Psychiatry* 54, 31–42. doi: 10.1016/j.pnpbp.2014.04.012

Fox, M. D., and Raichle, M. E. (2007). Spontaneous fluctuations in brain activity observed with functional magnetic resonance imaging. *Nat. Rev. Neurosci.* 8, 700–711. doi: 10.1038/nrn2201

Fox, M. D., Snyder, A. Z., Vincent, J. L., and Raichle, M. E. (2007). Intrinsic fluctuations within cortical systems account for intertrial variability in human behavior. *Neuron* 56, 171–184. doi: 10.1016/j.neuron.2007.08.023

Fox, M. D., Zhang, D., Snyder, A. Z., and Raichle, M. E. (2009). The global signal and observed anticorrelated resting state brain networks. *J. Neurophysiol.* 101, 3270–3283. doi: 10.1152/jn.90777.2008

Gentili, C., Cristea, I. A., Ricciardi, E., Vanello, N., Popita, C., David, D., et al. (2017). Not in one metric: Neuroticism modulates different resting state metrics within distinctive brain regions. *Behav. Brain Res.* 327, 34–43. doi: 10.1016/j.bbr.2017.03.031

Gentili, C., Vanello, N., Cristea, I., David, D., Ricciardi, E., and Pietrini, P. (2015). Proneness to social anxiety modulates neural complexity in the absence of exposure: a resting state fMRI study using Hurst exponent. *Psychiatry Res.* 232, 135–144. doi: 10.1016/j.pscychresns.2015.03.005

Gilden, D. L., and Hancock, H. (2007). Response variability in attention-deficit disorders. *Psychol. Sci.* 18, 796–802. doi: 10.1111/j.1467-9280.2007.01982.x

Goldberger, A. L., Amaral, L. A., Hausdorff, J. M., Ivanov, P., Peng, C. K., and Stanley, H. E. (2002). Fractal dynamics in physiology: alterations with disease and aging. *Proc. Natl. Acad. Sci. U.S.A.* 99(Suppl. 1), 2466–2472. doi: 10.1073/pnas.012579499

Gorges, M., Roselli, F., Muller, H. P., Ludolph, A. C., Rasche, V., and Kassubek, J. (2017). Functional connectivity mapping in the animal model: principles and applications of resting-state fMRI. *Front. Neurol.* 8:200. doi: 10.3389/fneur.2017.00200

Goya-Maldonado, R., Walther, S., Simon, J., Stippich, C., Weisbrod, M., and Kaiser, S. (2010). Motor impulsivity and the ventrolateral prefrontal cortex. *Psychiatry Res.* 183, 89–91. doi: 10.1016/j.pscychresns.2010.04.006

Hahn, T., Dresler, T., Ehlis, A. C., Pyka, M., Dieler, A. C., Saathoff, C., et al. (2012). Randomness of resting-state brain oscillations encodes Gray's personality trait. *Neuroimage* 59, 1842–1845. doi: 10.1016/j.neuroimage.2011.08.042

Hausdorff, J. M. (2007). Gait dynamics, fractals and falls: finding meaning in the stride-to-stride fluctuations of human walking. *Hum. Mov. Sci.* 26, 555–589. doi: 10.1016/j.humov.2007.05.003

He, B. J. (2011). Scale-free properties of the functional magnetic resonance imaging signal during rest and task. *J. Neurosci.* 31, 13786–13795. doi: 10.1523/JNEUROSCI.2111-11.2011

He, B. J. (2014). Scale-free brain activity: past, present, and future. *Trends Cogn. Sci.* 18, 480–487. doi: 10.1016/j.tics.2014.04.003

Herman, P., Sanganahalli, B. G., Hyder, F., and Eke, A. (2011). Fractal analysis of spontaneous fluctuations of the BOLD signal in rat brain. *Neuroimage* 58, 1060–1069. doi: 10.1016/j.neuroimage.2011.06.082

Hinshaw, S. P. (2017). Attention Deficit Hyperactivity Disorder (ADHD): controversy, developmental mechanisms, and multiple levels of analysis. *Annu Rev Clin Psychol.* 4:291–316. doi: 10.1146/annurev-clinpsy-050817-084917

Hinshaw, S. P., Carte, E. T., Sami, N., Treuting, J. J., and Zupan, B. A. (2002). Preadolescent girls with attention-deficit/hyperactivity disorder: II. Neuropsychological performance in relation to subtypes and individual classification. *J. Consult. Clin. Psychol.* 70, 1099–1111.

Huang-Pollock, C. L., Nigg, J. T., and Halperin, J. M. (2006). Single dissociation findings of ADHD deficits in vigilance but not anterior or posterior attention systems. *Neuropsychology* 20, 420–429. doi: 10.1037/0894-4105.20.4.420

Ihlen, E. A. (2012). Introduction to multifractal detrended fluctuation analysis in matlab. *Front. Physiol.* 3:141. doi: 10.3389/fphys.2012.00141

Ihlen, E. A., and Vereijken, B. (2010). Interaction-dominant dynamics in human cognition: beyond 1/fα fluctuation. *J. Exp. Psychol.* 139, 436–463. doi: 10.1037/a0019098

Ivanov, P., Ma, Q. D., Bartsch, R. P., Hausdorff, J. M., Nunes Amaral, L. A., Schulte-Frohlinde, V., et al. (2009). Levels of complexity in scale-invariant neural signals. *Phys. Rev. E Stat. Nonlin. Soft Matter Phys.* 79:041920. doi: 10.1103/PhysRevE.79.041920

Ivanov, P. C., Amaral, L. A. N., Goldberger, A. L., and Havlin, S. (1999). Multifractality in human heartbeat dynamics. *Nature* 399:461. doi: 10.1038/20924

Ivanov, P. C., Nunes Amaral, L. A., Goldberger, A. L., Havlin, S., Rosenblum, M. G., Stanley, H. E., et al. (2001). From 1/f noise to multifractal cascades in heartbeat dynamics. *Chaos* 11, 641–652. doi: 10.1063/1.1395631

Kandel, E. R., Schwartz, J. H., and Jessel, T. M. (2000). *Principles of Neuroscience, 4th Edn.* New York, NY: McGraw Hill.

Keshner, M. (1982). 1/f noise. *Proc. IEEE* 70, 212–218. doi: 10.1109/PROC.1982.12282

Koch, H. V. (1904). Sur une courbe continue sans tangente, obtenue par une construction géométrique élémentaire. *Astron. och Fys.* 1, 681–702.

Koch, H. V. (1906). Une méthode géométrique élémentaire pour l'étude de certaines questions de la théorie des courbes planes. *Acta Math.* 30, 145–174. doi: 10.1007/BF02418570

Lei, X., Zhao, Z., and Chen, H. (2013). Extraversion is encoded by scale-free dynamics of default mode network. *Neuroimage* 74, 52–57. doi: 10.1016/j.neuroimage.2013.02.020

Li, N., Ma, N., Liu, Y., He, X. S., Sun, D. L., Fu, X. M., et al. (2013). Resting-state functional connectivity predicts impulsivity in economic decision-making. *J. Neurosci.* 33, 4886–4895. doi: 10.1523/JNEUROSCI.1342-12.2013

Liégeois, R., Laumann, T. O., Snyder, A. Z., Zhou, J., and Yeo, B. T. T. (2017). Interpreting temporal fluctuations in resting-state functional connectivity MRI. *Neuroimage* doi: 10.1016/j.neuroimage.2017.09.012

Linkenkaer-Hansen, K. (2002). *Self Organized Criticality and Stochastic Resonance in the Human Brain Dept Of Engineering Physics and Mathematics.* Helsinki: Helsinki University of Technology.

Lipsitz, L. A. (2002). Dynamics of stabilitythe physiologic basis of functional health and frailty. *J. Gerontol.* 57, B115–B125. doi: 10.1093/gerona/57.3.B115

Lipsitz, L. A., and Goldberger, A. L. (1992). Loss of complexity and aging: potential applications of fractals and chaos theory to senescence. *JAMA* 267, 1806–1809. doi: 10.1001/jama.1992.03480130122036

Lo, C. C., Bartsch, R. P., and Ivanov, P. C. (2013). Asymmetry and basic pathways in sleep-stage transitions. *Europhys. Lett.* 102:10008. doi: 10.1209/0295-5075/102/10008

Mandelbrot, B. (1967). How long is the coast of britain? statistical self-similarity and fractional dimension. *Science* 156, 636–638. doi: 10.1126/science.156.3775.636

Mandelbrot, B. B. (1983). *The Fractal Geometry of Nature.* New York, NY: W. H. Freeman.

Maxim, V., Sendur, L., Fadili, J., Suckling, J., Gould, R., Howard, R., et al. (2005). Fractional gaussian noise, functional MRI and Alzheimer's disease. *Neuroimage* 25, 141–158. doi: 10.1016/j.neuroimage.2004.10.044

Mechelmans, D. J., Strelchuk, D., Donamayor-Alonso, N., Banca, P., Robbins, T. W., Baek, K., et al. (2017). Reward sensitivity and waiting impulsivity: shift towards reward valuation away from action control. *Int. J. Neuropsychopharmacol.* 20, 971–978. doi: 10.1093/ijnp/pyx072

Moreno-López, L., Soriano-Mas, C., Delgado-Rico, E., Rio-Valle, J. S., and Verdejo-Garcia, A. (2012). Brain structural correlates of reward sensitivity and impulsivity in adolescents with normal and excess weight. *PLoS ONE* 7:e49185. doi: 10.1371/journal.pone.0049185

Morris, L. S., Kundu, P., Baek, K., Irvine, M. A., Mechelmans, D. J., Wood, J., et al. (2016). Jumping the gun: mapping neural correlates of waiting impulsivity and relevance across alcohol misuse. *Biol. Psychiatry* 79, 499–507. doi: 10.1016/j.biopsych.2015.06.009

Nagy, Z., Mukli, P., Herman, P., and Eke, A. (2017). Decomposing multifractal crossovers. *Front. Physiol.* 8:533. doi: 10.3389/fphys.2017.00533

Neufang, S., Akhrif, A., Herrmann, C. G., Drepper, C., Homola, G. A., Nowak, J., et al. (2016). Serotonergic modulation of 'waiting impulsivity' is mediated by the impulsivity phenotype in humans. *Transl. Psychiatry* 6:e940. doi: 10.1038/tp.2016.210

Penn, A. A., and Shatz, C. J. (1999). Brain waves and brain wiring: the role of endogenous and sensory-driven neural activity in development. *Pediatr. Res.* 45, 447–458. doi: 10.1203/00006450-199904010-00001

Qiu, Y. W., Han, L. J., Lv, X. F., Jiang, G. H., Tian, J. Z., Zhuo, F. Z., et al. (2011). Regional homogeneity changes in heroin-dependent individuals: resting-state functional MR imaging study. *Radiology* 261, 551–559. doi: 10.1148/radiol.11102466

Riley, M. A., Bonnette, S., Kuznetsov, N., Wallot, S., and Gao, J. (2012). A tutorial introduction to adaptive fractal analysis. *Front. Physiol.* 3:371. doi: 10.3389/fphys.2012.00371

Robinson, E. S., Eagle, D. M., Economidou, D., Theobald, D. E., Mar, A. C., Murphy, E. R., et al. (2009). Behavioural characterisation of high impulsivity on the 5-choice serial reaction time task: specific deficits in 'waiting' versus 'stopping'. *Behav. Brain Res.* 196, 310–316. doi: 10.1016/j.bbr.2008.09.021

Rösler, M., Retz, W., Retz-Junginger, P., Stieglitz, R. D., Kessler, H., Reimherr, F., et al. (2008). ADHS-Diagnose bei Erwachsenen. *Nervenarzt* 79, 320–327. doi: 10.1007/s00115-007-2375-0

Sala, M., Caverzasi, E., Lazzaretti, M., Morandotti, N., De Vidovich, G., Marraffini, E., et al. (2011). Dorsolateral prefrontal cortex and hippocampus sustain impulsivity and aggressiveness in borderline personality disorder. *J. Affect. Disord.* 131, 417–421. doi: 10.1016/j.jad.2010.11.036

Scheres, A., and Hamaker, E. L. (2010). What we can and cannot conclude about the relationship between steep temporal reward discounting and hyperactivity-impulsivity symptoms in attention-deficit/hyperactivity disorder. *Biol. Psychiatry* 68, e17–e18. doi: 10.1016/j.biopsych.2010.05.021

Sebastian, A., Jacob, G., Lieb, K., and Tuscher, O. (2013). Impulsivity in borderline personality disorder: a matter of disturbed impulse control or a facet of emotional dysregulation? *Curr. Psychiatry Rep.* 15:339. doi: 10.1007/s11920-012-0339-y

Sejdić, E., and Lipsitz, L. A. (2013). Necessity of noise in physiology and medicine. *Comput. Methods Programs Biomed.* 111, 459–470. doi: 10.1016/j.cmpb.2013.03.014

Smitha, K. A., Akhil Raja, K., Arun, K. M., Rajesh, P. G., Thomas, B., Kapilamoorthy, T. R., et al. (2017). Resting state fMRI: A review on methods in resting state connectivity analysis and resting state networks. *Neuroradiol. J.* 30, 305–317. doi: 10.1177/1971400917697342

Sokunbi, M. O., Gradin, V. B., Waiter, G. D., Cameron, G. G., Ahearn, T. S., Murray, A. D., et al. (2014). Nonlinear complexity analysis of brain FMRI signals in schizophrenia. *PLoS ONE* 9:e95146. doi: 10.1371/journal.pone.0095146

Solanto, M. V., Gilbert, S. N., Raj, A., Zhu, J., Pope-Boyd, S., Stepak, B., et al. (2007). Neurocognitive functioning in AD/HD, predominantly

inattentive and combined subtypes. *J. Abnorm. Child Psychol.* 35, 729–744. doi: 10.1007/s10802-007-9123-6

Stadnitski, T. (2012). "Measuring fractality," in *Fractal Analyses: Statistical and Methodological Innovations and Best Practices*, eds J. G. Holden, M. A. Riley, J. Gao, and K. Torre (Lausanne, CH: Frontiers in Physiology), 22–34.

Suckling, J., Wink, A. M., Bernard, F. A., Barnes, A., and Bullmore, E. (2008). Endogenous multifractal brain dynamics are modulated by age, cholinergic blockade and cognitive performance. *J. Neurosci. Methods* 174, 292–300. doi: 10.1016/j.jneumeth.2008.06.037

Thurner, S., Windischberger, C., Moser, E., Walla, P., and Barth, M. (2003). Scaling laws and persistence in human brain activity. *Phys. A Statist. Mech. Appl.* 326, 511–521. doi: 10.1016/S0378-4371(03)00279-6

Voon, V., Irvine, M. A., Derbyshire, K., Worbe, Y., Lange, I., Abbott, S., et al. (2014). Measuring "waiting" impulsivity in substance addictions and binge eating disorder in a novel analogue of rodent serial reaction time task. *Biol. Psychiatry* 75, 148–155. doi: 10.1016/j.biopsych.2013.05.013

Weinstein, A. M. (2017). An update overview on brain imaging studies of internet gaming disorder. *Front. Psychiatry* 8:185. doi: 10.3389/fpsyt.2017.00185

Wijnants, M. L., Cox, R. F., Hasselman, F., Bosman, A. M., and Van Orden, G. (2012). Does sample rate introduce an artifact in spectral analysis of continuous processes? *Front. Physiol.* 3:495. doi: 10.3389/fphys.2012.00495

Wink, A. M., Bullmore, E., Barnes, A., Bernard, F., and Suckling, J. (2008). Monofractal and multifractal dynamics of low frequency endogenous brain oscillations in functional MRI. *Hum. Brain Mapp.* 29, 791–801. doi: 10.1002/hbm.20593

Zhang, D., Snyder, A. Z., Fox, M. D., Sansbury, M. W., Shimony, J. S., and Raichle, M. E. (2008). Intrinsic functional relations between human cerebral cortex and thalamus. *J. Neurophysiol.* 100, 1740–1748. doi: 10.1152/jn.90463.2008

Conflict of Interest Statement: The authors declare that the research was conducted in the absence of any commercial or financial relationships that could be construed as a potential conflict of interest.

The handling editor and reviewer AE declared their involvement as co-editors in the Research Topic, and confirm the absence of any other collaboration.

frontiers in Physiology

ORIGINAL RESEARCH
published: 22 October 2018
doi: 10.3389/fphys.2018.01446

Gene Expression Is Not Random: Scaling, Long-Range Cross-Dependence, and Fractal Characteristics of Gene Regulatory Networks

*Mahboobeh Ghorbani, Edmond A. Jonckheere and Paul Bogdan**

Electrical Engineering Department, University of Southern California, Los Angeles, CA, United States

Gene expression is a vital process through which cells react to the environment and express functional behavior. Understanding the dynamics of gene expression could prove crucial in unraveling the physical complexities involved in this process. Specifically, understanding the coherent complex structure of transcriptional dynamics is the goal of numerous computational studies aiming to study and finally control cellular processes. Here, we report the scaling properties of gene expression time series in *Escherichia coli* and *Saccharomyces cerevisiae*. Unlike previous studies, which report the fractal and long-range dependency of DNA structure, we investigate the individual gene expression dynamics as well as the cross-dependency between them in the context of gene regulatory network. Our results demonstrate that the gene expression time series display fractal and long-range dependence characteristics. In addition, the dynamics between genes and linked transcription factors in gene regulatory networks are also fractal and long-range cross-correlated. The cross-correlation exponents in gene regulatory networks are not unique. The distribution of the cross-correlation exponents of gene regulatory networks for several types of cells can be interpreted as a measure of the complexity of their functional behavior.

Keywords: gene expression, gene regulatory network, fractals, dynamics, entropy

OPEN ACCESS

Edited by:
Zbigniew R. Struzik,
The University of Tokyo, Japan

Reviewed by:
Alessandro Giuliani,
Istituto Superiore di Sanità (ISS), Italy
Ralf Metzler,
Universität Potsdam, Germany

***Correspondence:**
Paul Bogdan
pbogdan@usc.edu

Specialty section:
This article was submitted to Fractal Physiology, a section of the journal Frontiers in Physiology

Received: *29 November 2017*
Accepted: *24 September 2018*
Published: *22 October 2018*

Citation:
Ghorbani M, Jonckheere EA and Bogdan P (2018) Gene Expression Is Not Random: Scaling, Long-Range Cross-Dependence, and Fractal Characteristics of Gene Regulatory Networks. Front. Physiol. 9:1446. doi: 10.3389/fphys.2018.01446

INTRODUCTION

Protein synthesis is fundamental for biological systems to perform a variety of functions. They control the organism's shape or can function as enzymes catalyzing specific metabolic pathways to regulate specific cellular processes. These cellular functions include responding to stimuli, transporting molecules and catalyzing metabolic reactions. In order to program cells for performing the desired functionality, one should regulate the protein synthesizing process. The process of protein synthesis from the activation of a specific gene is called gene expression (Lockhart and Winzeler, 2000; Teichmann and Babu, 2004; Huang et al., 2005; Düvel et al., 2010).

Gene expression (briefly shown in **Figure 1a**) is the process in which the genetic information of a cell causes a cell to generate a functional gene product and, finally, perform specific cell functions (Niedenthal et al., 1996). In other words, it is the process by which genotype information gives rise to phenotype (observable characteristics). It is a vital process, which causes cellular differentiation, morphogenesis, and the versatility and adaptability of any organism (O'Connor et al., 2010). Controlling the production process of the desired gene expression product (e.g., a protein) refers

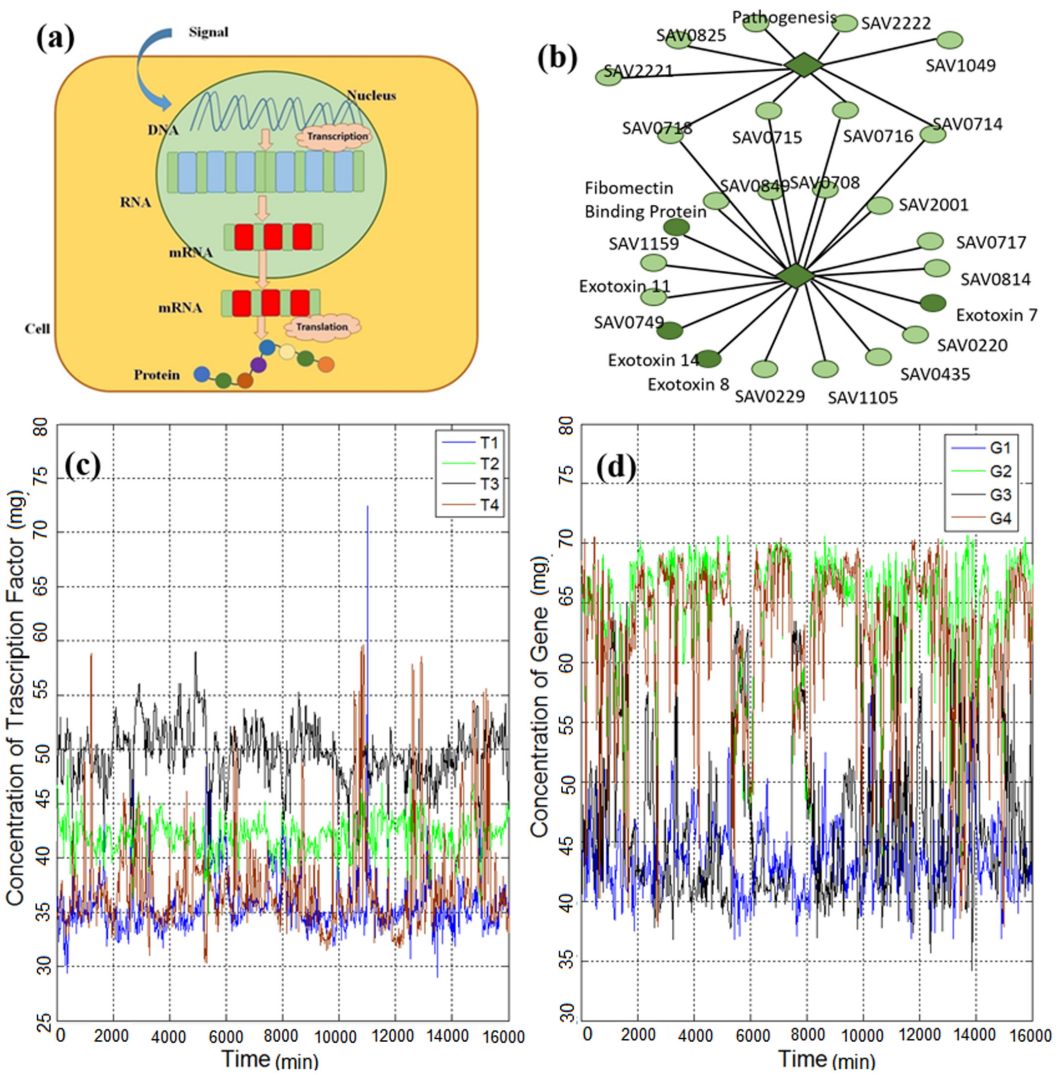

FIGURE 1 | (a) Gene expression process is initiated with the triggering of a gene in the DNA strand and continues with the generation of RNA, mRNA and, finally, the protein product. **(b)** Part of the gene regulatory network of *Escherichia coli* reported by Lockhart and Winzeler (2000), which consists of genes and transcription factors (TFs). The diamonds represent TFs and the circles represent genes. **(c)** Time series of TFs of *E. coli* obtained from Marbach et al. (2012) and explained in the methods section. **(d)** Time series of genes of *E. coli* obtained from Marbach et al. (2012) and explained in the methods section.

to the regulation of the gene expression process. The regulation of gene expression controls the amount and timing of production of target proteins (Malone et al., 2009). Hence, investigating the dynamics of gene expression enables to understand the mechanisms driving biological organisms. This knowledge helps us from both scientific and engineering perspectives. It can be exploited to detect an anomaly or disease or to engineer cells for performing specific tasks (e.g., drug delivery for cancer treatment) as it is the target of synthetic biology.

The biophysical mechanism affecting the regulation process has been actively studied (Elf et al., 2007; Kolesov et al., 2007; Kuhlman and Cox, 2012; Bauer and Metzler, 2013; Pulkkinen and Metzler, 2013). For instance, searching for the target gene by the transcription factors (TFs) is discussed in Kolesov et al. (2007); Pulkkinen and Metzler (2013) and the diffusion process of search for the target genes is studied in Elf et al. (2007); Bauer and Metzler (2013). Also, the spatial distribution of gene products is reported in Kuhlman and Cox (2012). However, these prior studies were not concerned with the mathematical characterization of the gene expression dynamics for several gene regulations in a network of genes. To identify the main mathematical characteristics of gene expression dynamics, we investigate individual and cross-dependent gene expression time series. First, we investigate the statistical properties of single (isolated) gene expression time series (shown in **Figures 1c,d**), and, then, we analyze the cross-correlation between pairs consisting of a gene and a TF in the gene regulatory network (**Figure 1b**). In contrast to the previous study (Tsuchiya et al., 2016) in which regulation of cell fate through genome-wide expression by temporal-spatial self-organization is considered,

here, we mainly analyze the temporal variability of individual genes. We then investigate the correlation of linked TF and genes. Moreover, we analyze the expression level of single cells without considering population effect (Tsuchyia et al., 2007).

The remaining of this paper is organized as follows: In the first part of the Results section, we present our findings on the individual and cross-dependence dynamics of gene expression time series. Then, we report the distribution of the cross-dependencies and a complexity quantification strategy for the gene expression networks. In the latest section of Results, we investigate whether the observed multifractality can be explained by a well-known model such as the Mandelbrot analytical cascade model. The Discussion section concludes our findings and outlines some future research directions. Lastly, the Methods section summarizes the mathematical strategies used for obtaining the findings reported here.

RESULTS

Gene Expression Dynamics Exhibits Long-Range Dependency and Multifractal Properties

We investigate the statistical properties of gene expression data and compute the Hurst exponents of gene expression time series in *Saccharomyces cerevisiae* (*S. cerevisiae*) and *Escherichia coli* (*E. coli*). **Figures 2a,b** show the log–log plot of the fluctuation function as a function of the scale for the time series of a TF (ynel) in *S. cerevisiae* and *E. coli*, respectively. In these plots, the slope of the curve represents the Hurst exponent. We observe that 95 and 98% of the time series of genes from the *S. cerevisiae* and the *E. coli* gene expression networks, respectively, exhibit a long-range dependency property. More precisely, their Hurst exponent was greater than 0.5. To demonstrate this important property, **Figures 2c,e** show the histogram of the Hurst exponent of gene expression time in *S. cerevisiae* and *E. coli*, respectively. Generally speaking, a Hurst exponent that exceeds the 0.5 threshold value denotes a persistent (positively correlated) behavior in the sense that a high value is likely to be followed by another high value with nonzero probability. In addition, because the Hurst exponent for most of the genes is significantly higher than 0.5, the gene and TF time series cannot be regarded as a random process and modeled through Markovian formalism (Kantelhardt et al., 2001). This mathematical characteristic provides a clue as to how to construct stochastic models for gene expression processes, but this is left for future work. We observe the same property in the time series of TFs in *S. cerevisiae and E. coli*. More precisely, 97% of the TFs in *S. cerevisiae and E. coli* possess the long-range dependence property. The histogram of the Hurst exponent of TFs in *S. cerevisiae* and *E. coli* are shown in **Figures 2d,f** respectively.

Employing fractal analysis is also helpful to gain insight into other interesting properties. Here, we see a bimodal characteristic in the Hurst exponent distribution, shown in **Figures 2c–f**. This feature is especially visible in **Figures 2c,e** where the histogram of genes in *S. cerevisiae* and *E. coli* is presented. This may be explained by a possible bimodal diffusion potential, as in Muzychuk (2006). Since gene expression includes a diffusion process with multiple diffusion potentials (inside and outside the nucleus), this bimodality can be explained by non-equilibrium Brownian motion with multiple potential profiles. However,

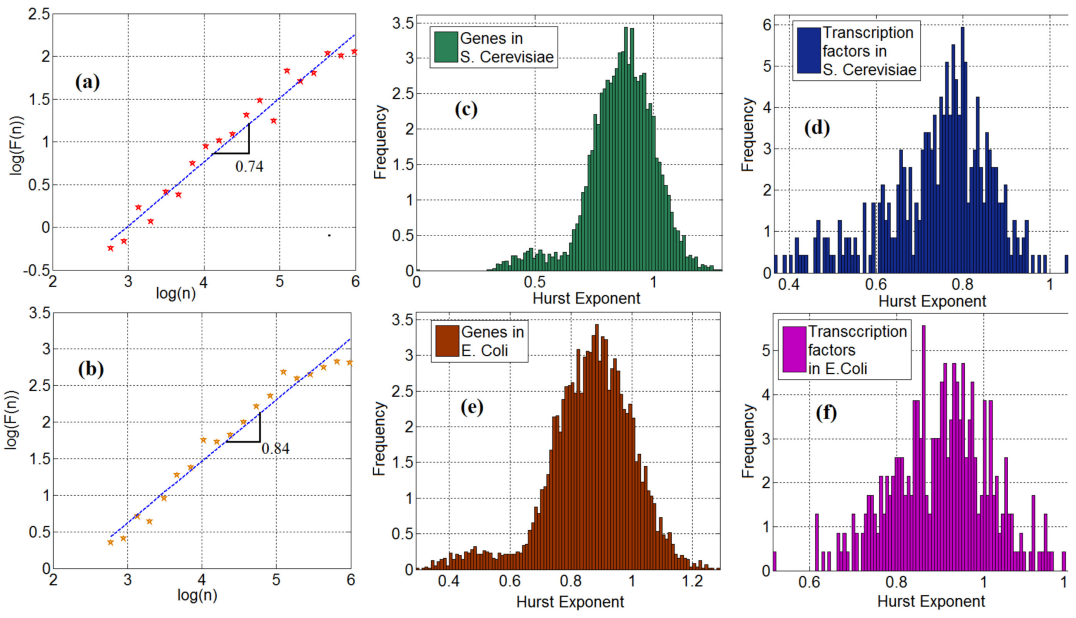

FIGURE 2 | (a) Scaling of fluctuation function of a gene time series in *Saccharomyces cerevisiae*, **(b)** Scaling of fluctuation function of ynel gene time series in *E. coli*, **(c)** Histogram of cross-correlation exponent of genes in *S. cerevisiae*, **(d)** Histogram of cross-correlation exponent of TFs in *S. cerevisiae*, **(e)** Histogram of cross-correlation exponent of genes in *E. coli*. **(f)** Histogram of cross-correlation exponent of TFs in *E. coli*.

further experimental studies are required to elucidate the nature and implications of these bimodal statistics.

By employing the multifractal detrended fluctuation analysis (MFDFA) (Kantelhardt et al., 2002) (see Materials and methods section) to examine the multifractal characteristics of gene expression time series, we observe that both genes and TFs have pronounced multifractal properties. For monofractal behavior, the generalized Hurst exponent displays a linear dependency with the order q of the cross moments. Instead, if the generalized Hurst exponent exhibits a nonlinear dependency (such as the S-shape displayed in **Figure 3b**) as a function of the order q of the cross-moments, then the stochastic interdependence is considered to possess multifractal characteristics.

To provide a more in-depth report, we use the bootstrapping technique (Efron, 1982) to investigate the existence of the long-range dependence property, considering the limitations related to the length of the experimental time series. For every gene expression time series, we have sampled 10 randomized subintervals of the gene expression time series, each containing 90% of the ordered piece of the original time series. Then, we calculate the Hurst exponents for all the randomized versions. The difference between the percentage of the long-range dependency for the gene expression time series and the randomized versions was approximately 0.006 for *E. coli* and 0.0001 *S. cerevisiae*. We also investigate whether the observed Hurst exponent varies in different conditions. We observed that for time series of *E. coli*, the Hurst exponent varies in different acidic levels and osmotic stress level and we have reported them in **Supplementary Material**.

Time Series of Interactions Within the Gene Regulatory Networks Demonstrate Long-Range Cross-Correlation and Multifractal Properties

We analyzed the cross-correlation between linked pairs of genes and TFs in gene regulatory networks. By computing the cross-correlation exponent (Podobnik and Stanley, 2008), we noticed that 98% of the linked pairs of genes and TFs in gene regulatory network for *E. coli* and *S. cerevisiae* possess the long-range dependence property. **Figure 3a** shows the scaling of the detrended covariance function for a pair of gene and TF (link) in *E. coli* (ihfB to ompR) and *S. cerevisiae* (YLR256W to YKL020C). We have applied the multifractal detrended cross-correlation analysis for pairs of genes and TFs (links) in the gene regulatory network of *E. coli* and *S. cerevisiae* and found that there is a pronounced multifractal cross-correlation signature in these gene regulatory network links. **Figure 3b** shows the

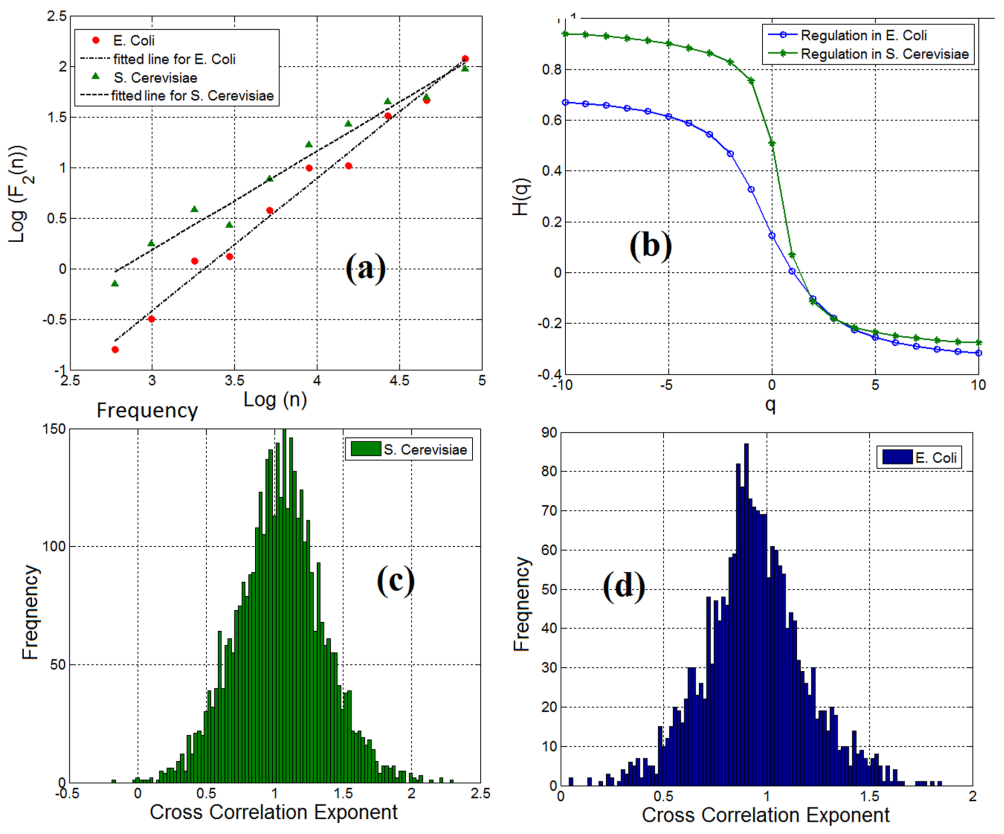

FIGURE 3 | (a) Scaling of detrended covariance function in a gene-TF link in *E. coli* (ihfB to ompR) and *S. cerevisiae* (YLR256W to YKL020C) regulatory network. **(b)** Generalized cross-correlation exponent of a gene-TF link in *E. coli* and *S. cerevisiae*. **(c)** Histogram of cross-correlation exponents of gene regulatory network links in *S. cerevisiae* and **(d)** Histogram of cross-correlation exponents of gene regulatory network links.

generalized Hurst exponent $H(q)$ as a function of the order of the cross moments q in **Figure 3a**. For a mono-fractal behavior, the generalized Hurst exponent displays a linear dependency with the order q of the cross-moments. Instead, if the generalized Hurst exponent exhibits a nonlinear dependency (such as the S-shape displayed in **Figure 3b**) on the order q of the cross-moments, then the stochastic interdependence is considered to possess multifractal characteristics. In conclusion, the causal relationship between TFs and genes in gene regulatory networks was mainly also long-range dependent. The concentration level of a gene not only depends on the current concentration level of the linked TF but also on the previous values of that gene. This dependency obeys a power-law-like relationship.

The Distribution of Cross-Correlation Exponents of Pairs of Genes and Transcription Factors of Gene Regulatory Networks Has a Wide Range of Variation

Although we observe the fractal and long-range cross-correlation in linked pairs of genes and TFs in the gene regulatory networks, the cross-correlation exponents were not the same in all the links. We have shown the distribution of the cross-correlation exponents for pairs of genes and TFs in the *S. cerevisiae* and *E. coli* gene regulatory networks in **Figures 3c,d** respectively. Inspired by Shannon entropy (Shannon, 2001), we use this histogram for measuring the entropy, and hence, the information content of a gene regulatory network across different cell types for quantitative analysis and specification of gene regulatory networks. The computed Shannon sample entropy for *S. cerevisiae* and *E. coli* was 4.18 and 5.29, respectively. Consequently, we conclude that the gene expression network of *E. coli* has more complex dynamics than that of *S. cerevisiae*. Also, considering a static gene regulatory network and having traces of gene expression time series for a cell at different times, we can compute the cross-correlation exponents for the links at a different time. This can be useful to compare statistical properties and complexity of dynamics. Similarly, by having different time series of gene expression dynamics, we can compare normal vs. disease affected (for example cancer typed) cells.

Multifractal Characteristics of Interactions Within the Gene Regulatory Network Can Be Modeled by Random Cascades on Wavelet Dyadic Trees

We analyzed the multifractal property of the cross-correlation of pairs of genes and TFs in a gene regulatory network. We investigated whether the observed multifractality can be explained by the known analytical cascade models including the Mandelbrot bimodal cascade model (Mandelbrot et al., 1997) (see Materials and methods section) and the random cascades on wavelet dyadic trees (Arneodo et al., 1998). We observe deviations of the empirical spectrums from the Mandelbrot model and an approximate agreement to the random cascades on wavelet dyadic trees model.

Based on the range of the Holder exponent values in the multifractal spectrum, we observe that only 0.04 of the links in a gene regulatory network of *S. cerevisiae* and none of the links in the network of *E. coli* can be modeled by the Mandelbrot cascade model for multifractal spectrums (see Materials and methods section). We observe that even for the few links that we could find a closest Mandelbrot model spectrum, the deviation from the Mandelbrot model and the data we had for gene regulatory network was significant. We show two such samples in **Figure 4**. **Figure 4a** shows several multifractal spectrums for the links in *E. coli* gene networks. Note that the peak of the multifractal spectrum for these spectrums was lower than the value 1, which does not fit with the Mandelbrot Binomial Cascade Model (Mandelbrot et al., 1997). **Figure 4b** shows several multifractal spectrums for the links in *S. cerevisiae*. **Figure 4c** shows the closest Mandelbrot Model we could fit for the links in the *S. cerevisiae* gene regulatory model. There is a significant deviation between the Mandelbrot model and the spectrum from gene regulatory network data.

We also investigated the agreement between the observed multifractality of the cross-dependencies in the gene regulatory network of S. cerevisiae and *E. coli*, respectively, and a few well-known multifractal models such as the random cascades on wavelet dyadic trees (Arneodo et al., 1998). We investigated whether the log-normal W-cascade model can be fitted to the cross-dependencies (links) in the two above-mentioned

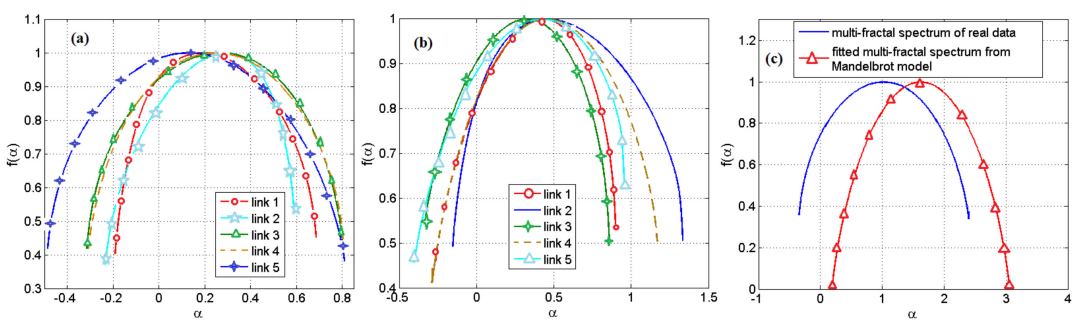

FIGURE 4 | (a) Multifractal spectrum of several randomly picked links of gene regulatory network of *E. coli*. **(b)** The multifractal spectrum of several randomly picked links of gene regulatory network of *S. cerevisiae*. **(c)** The multifractal spectrum of a link between the gene regulatory network of *S. cerevisiae* and the best spectrum from the Mandelbrot binomial model.

gene regulatory networks. We extracted the parameter of the estimated log-normal W-cascade model based on the peak of the empirical spectrum and the variation of the singularity spectrum (see the Methods section). We observed very similar spectrums for a significant number of links. We computed the overlapping area under the curve for both the estimated and the empirical multifractal spectrums. The ratio of the area of the overlapping fitted spectrum to the area of the empirical spectrum can be used to either accept or reject the postulated multifractal model as a good fitting for the empirically estimated multifractal spectrums. In this study, we used two threshold values of 70 and 75% for the ratio of mentioned areas. For the gene expression cross-dependencies in *E. coli*, we observed a 74 and 38% agreement between the postulated model and the empirically estimated multifractal spectrums when considering overlapping area ratio thresholds of 70 and 75, respectively. For the gene expression cross-dependencies in *S. cerevisiae*, we observed a 59 and 31% agreement between the postulated multifractal model and the empirically estimated multifractal spectrums when considering overlapping area thresholds of 70 and 75%, respectively. **Figures 5A,B** show a best fitting scenario between the postulated multifractal model and an empirically estimated spectrum for a cross-dependence in the gene regulatory network of *E. coli* and *S. cerevisiae*, respectively.

We also investigated the agreement between the empirical multifractal spectrums and the log-Poisson W-cascade model (Arneodo et al., 1998). We observed that the empirical multifractal spectrums could not be described by this cascade model since the second derivative of the mass exponent should follow a power law (see Methods section) while the empirical data has a significant deviation from a power law trend (see **Figure 6** in the Methods section).

DISCUSSION

A genome expression vector is the most informative descriptor of a cell state, as the functional state of an organism is determined largely by the pattern of expression of its genes (O'Connor et al., 2010). Gene expression is the process in which information from a gene is used to synthesize a functional gene product. It is the process in which the information flows within a complex biological system. As the search for patterns in nature and their interpretation is one of the main purposes of science, unveiling the DNA patterns in those sequences has become an exciting challenge to the present generation of biologists, statistical physicists, and information scientists. Toward this end, many researchers have studied the statistical properties of coding and non-coding segments of DNA sequences. They have reported interesting results showing fractal nature of coding DNA regions (Lockhart and Winzeler, 2000; Teichmann and Babu, 2004; Huang et al., 2005; Düvel et al., 2010). However, these studies fail to address the dynamical properties of the biological systems. Since biological systems are dynamic, their study requires monitoring their activity at multiple time points.

To investigate the causal relations in gene expression, numerous biophysical mechanisms affecting the regulation process were studied in Elf et al. (2007), Kolesov et al. (2007), Kuhlman and Cox (2012), Bauer and Metzler (2013), Pulkkinen and Metzler (2013). It is demonstrated by several simulations that rapid and reliable gene regulation requires that the TF be close to their target site on DNA (Kolesov et al., 2007). In Pulkkinen and Metzler (2013), the authors use an explicit model for numerical analysis. The authors report that the observed variations in regulation efficiency are linked to the magnitude of the variation of TF concentration peaks as a function of binding site distance from the source. In Bauer and Metzler (2013), the authors have presented a semi-analytical model for the *in vivo* target search of the TFs within a diffusion framework. They have shown that alternating between three-dimensional bulk diffusion and one-dimensional sliding along the DNA contour can provide a quantitative approach to gene regulation in living bacteria cells. Their proposed model agrees with experimental findings regarding the mean search time of lac repressor in a living *E. coli*. In Elf et al. (2007), the authors have reported their observation of kinetics of the gene expression process

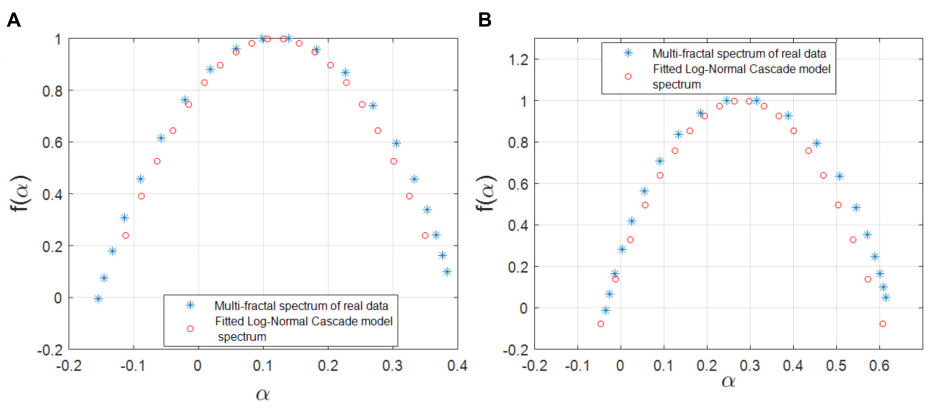

FIGURE 5 | (A) The multifractal spectrum of a cross-dependency (link) between the gene regulatory network of *E. coli* (soxR and soxS genes) that can best be fitted by the log-normal cascade multifractal model. **(B)** The multifractal spectrum of a cross-dependency (link) between the gene regulatory network of *S. cerevisiae* (YKL032C and YKL043W genes) that can best be fitted by the log-normal cascade multifractal model.

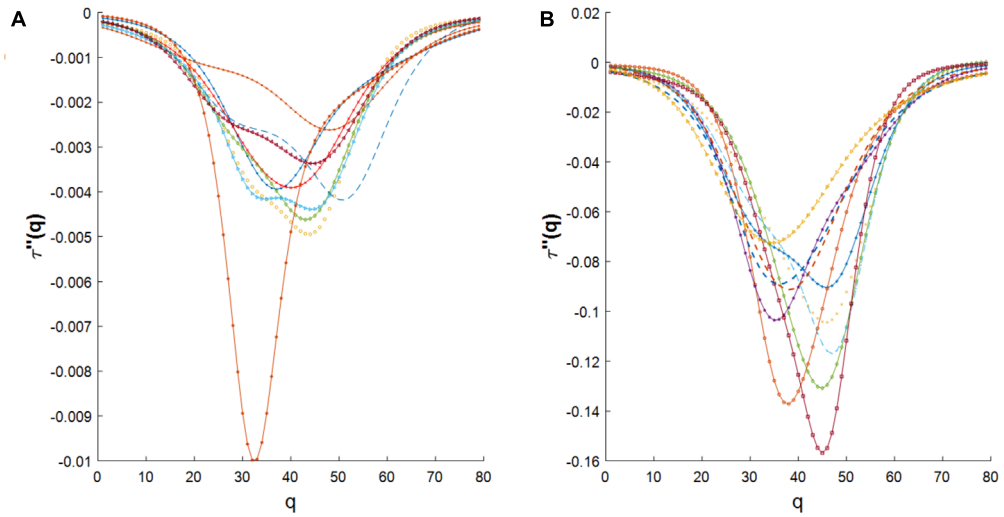

FIGURE 6 | (A) The second derivative of the mass exponent for cross-dependencies in *E. coli*. **(B)** The second derivative of the mass exponent for cross-dependencies in *S. cerevisiae*.

at the single-molecule level in living cells by labeling with a fluorescent protein, which agrees with 1D diffusion along DNA segments and 3D diffusion. In Kuhlman and Cox (2012), the authors test the expectation of previous theoretical models using high-throughput single-molecule microscopy to determine the average spatial distribution of lac repressor. Their finding shows inconsistency between expectations and experimental findings. They show that the gene products distribution is spatially inhomogeneous and dependent on the location of the repressor gene in bacteria and eukaryotes. However, they do not consider the gene expression dynamics from a network of genes perspective and do not account for cross-correlations and multiscale phenomena.

To study the dynamic nature of gene expression processes, researchers must monitor activity levels of genes and TFs at multiple time points. The most informative source of information regarding gene expression activity is the gene expression time-series. With advances in gene array technology, the level of gene expression of thousands of genes (by providing the concentration level of gene expression products) can be measured simultaneously. By accessing a high- throughput data collection, a wide range of insights, such as characterizing the functions of specific genes, the relationships among these genes, and their regulation and coordination can be gained. These insights can also be used to understand the gene regulatory network as a complex network. There are many studies which try to infer the underlying gene regulatory network from empirical time series (Marbach et al., 2012). However, little is known about the mathematical characteristics of the gene expression dynamics from a complex systems perspective.

In this paper, we investigated the scaling properties of gene expression dynamics. Unlike previous work that demonstrated the fractal properties in DNA sequences (Peng et al., 1994; Arneodo et al., 1996; Zhang et al., 2011; Marbach et al., 2012), we investigate the dynamics of cross-dependencies between genes and TFs within the gene regulatory networks. We show that the gene expression time series (which is the concentration of gene expression products in the process of gene expression) have fractal and long-range dependence properties in *E. coli* and *S. cerevisiae*. We also investigate the cross-correlation of gene-TFs, which are linked together in gene expression networks. We report the fractal and long-range cross-dependency of linked genes and TFs of gene expression networks in *E. coli* and *S. cerevisiae*. We also show that the multifractal nature of these cross-correlations cannot be modeled through a Mandelbrot binomial cascade model. In contrast, we found very good agreement between the empirical multifractal spectrum of the cross-dependencies in the gene regulatory networks and the log-normal W-cascade model. We suggest investigating more cascade models on empirical data (Bacry and Muzy, 2003; Chainais et al., 2005; Kiyono et al., 2007) as future work. In summary, there is a need for more advanced theoretical models that can capture the multifractality observed in this critical biological process. One possible method for modeling gene expression dynamics can exploit the multifractal Fokker-Planck formalism, as discussed in Xue and Bogdan (2017).

We also propose using the distribution of cross-correlation exponent of the links in gene regulatory network as a measure of the complexity for the regulatory networks. Having this complexity measure enables a quantitative descriptor for different cell types or to differentiate different cell fates when the system undergoes transitions. We report the distribution of cross-correlation exponent of links in regulatory networks of *E. coli* and *S. cerevisiae* as case studies. We suggest investigating this property on a wider range of biological systems when enough data sets are available. We also propose using this property as a network property in general. We propose using the distribution of cross-correlation exponents of gene-TF links in a complex network to measure the

complexity of the interactions in the network. Also, the computed cross-correlation exponents of a network can be used by other algorithms, such as those proposed in Anand and Bianconi (2009), Anand et al. (2011), Teschendorff and Enver (2017) for computing the entropy of a network. This has a variety of applications in distinguishing the different status of cells (e.g., healthy vs. disease affected states). This can reveal insightful results in many complex networks either in biology, social, financial and many other interesting examples of complex networks.

Our findings explain the inherent variability in gene expression processes, even among isogenic cells situated in an identical environment. Because of the long-range cross-dependency of a gene and its linked TF, the current concentration level of a gene depends both on current and previous values of its own and its linked TF. As explained in previous studies, this leads to phenotypic diversity, which can be helpful for surviving in an uncertain and fluctuating environment (Ji et al., 2013). Also, the endogenous cellular mechanism through positive and negative feedback controls variability in gene expression to prevent disruption from normal development. Hence, unlike the usual assumption about noise as a nuisance, variability in gene expression makes the population of cells more robust against environmental fluctuations. Interestingly, there are other examples in nature in which the presence of noise makes the system smarter. For example, in Maass (2014), they have shown how the presence of noise in a network of spiking neurons in the human brain enables probabilistic reasoning and creative problem-solving.

This study is the first to demonstrate the long-range dependency of gene expression dynamics. In contrast to previous studies (Bernaola-Galván et al., 1996), which have shown the long-range dependency for the structure of DNA, we investigate the dynamics of gene expression time series. Previous studies show that coding regions of DNA structure, which store the biological information for the gene expression process, possess the long-range dependency property (Bernaola-Galván et al., 1996). In contrast, our results report the same property in gene expression time series. Of note, these dynamics stem from the transformation of information from the structure to dynamics by producing gene products. This is an insightful empirical result that can trigger more studies on other examples from nature, as well as analytical and mathematical investigations. For example, investigating other processes that follow a rule from a static structure to generate dynamical products and process (such as the central dogma of biology) can be interesting. Lastly, mathematical and analytical investigation of the relation between structure and dynamics of processes are also fundamental in theory. It would be revealing to investigate how long-range dependency (and/or fractal/multifractal properties) evolves from structure to dynamics (and vice versa) in processes. Answering to the question of how long-range dependency transfers between structure and dynamics and how the degree of fractality/multifractality of structure and dynamics are like each other would have a huge impact on predicting the behavior of complex systems.

MATERIALS AND METHODS

We use the data set from the publicly available DREAM project[1] (Stolovitsky and Califano, 2007), which is for assessment of network inference methods. It is organized around annual challenges where the community of network inference experts is solicited to run their algorithms on benchmark data sets. The data is provided from Gene-expression microarray datasets for *E. coli* and *S. cerevisiae*[2]. A compendium of microarray data is compiled for *E. coli*, where all chips are on the same Affymetrix platform, the *E. coli* Antisense Genome Array. In total, 805 chips with available raw data Affymetrix files were compiled. Completion of microarray normalization and filtering resulted in a total of 4,297 genes over the 805 microarrays. Also, a compendium of microarray data was compiled for *S. cerevisiae*, where all chips are on the same Affymetrix platform, the Affymetrix Yeast Genome S98 Array. Chips were downloaded from GEO (Platform ID: GPL). In total, 536 chips with available raw data Affymetrix files were compiled. The completion of microarray normalization and filtering resulted in a total of 5,667 genes over the 536 microarrays. Transcriptional interactions and, hence, gene regulatory networks for *E. coli* and *S. cerevisiae* are collected from strong experimental supports in Marbach et al. (2012). Known transcriptional interactions for *E. coli* are collected from manually curated Ecocyc (Gama-Castro et al., 2010) and RegulonDB (Keseler et al., 2010) databases. A gene regulatory network for *E. coli* is constructed from RegulonDB Release 6.8. Only transcriptional interactions with at least one strong piece of evidence were included (2,066 interactions). For *S. cerevisiae*, we use the network based on the most stringent thresholds from MacIsaac et al. in MacIsaac et al. (2006) compared to other studies (Hu et al., 2007; Abdulrehman et al., 2010). By varying the thresholds required for binding and evolutionary conservation of motifs, different versions of the network were obtained. Based on the most stringent thresholds, which includes only interactions with strong evidence of binding and a strongly conserved motif, the interactions in the regulatory network are obtained. There are 5950 time-series, each having 536 data points for *S. cerevisiae*, and 4511 time-series, each having 805 data points for *E. coli* expression series.

Noise in Gene Expression Time Series

Since DNA, RNA, and proteins involved in the gene expression process can be present and active at a few copies per cell, this process is sensitive to stochastic fluctuations (Raser and O'shea, 2005). The four most important sources of variation in gene expression dynamics include (i) the inherent stochasticity of biochemical processes that are dependent on the small number of molecules, (ii) differences in the internal states of cells, (iii) subtle environmental differences, and (iv) genetic mutations (Raser and O'shea, 2005). The existence of this variation causes genetically

[1] http://wiki.c2b2.columbia.edu/dream

[2] https://www.synapse.org/#!Synapse:syn2787209/wiki/70349

identical organisms with identical environmental exposure to varying in behavior and shape. The fluctuation in the gene expression process is inevitable and does not follow the law of mass action. Hence, in this study, we have investigated the process independently of assuming stationarity and the MFDFA method explained below is used.

The Hurst Exponent and Multifractal Detrended Fluctuation Analysis (MFDFA)

In this paper, we have used the MFDFA method for analysis of gene expression time series. This method, which is the extension of detrended fluctuation analysis (DFA) to extract the Hurst exponent (Kantelhardt et al., 2002), is introduced in Kantelhardt et al. (2002) for analysis of multifractal properties of nonstationary time series. Since we do not have the stationarity assumption for gene expression time series, MFDFA method is a suitable one for studying them. Scaling properties and long-range dependency of time series can be obtained by the DFA method. However, for time series with multifractal properties and different scaling exponents on different scaling regimes or different time intervals, it is essential to exploit the multifractal detrended fluctuation method (MFDFA) to reveal the multifractal property.

The MFDFA method consists of five steps to estimate the multifractal spectrum of a nonstationary time series. Similar to the DFA method, the *profile* of the time series is obtained first, which is determined by the integration of the difference of the time series with its average value ($\hat{x}$):

$$y(i) = \sum_{i=1}^{k} (x(i) - \hat{x})$$

Second, it divides the profile into non-overlapping segments (or scales (n = N/s), where s is the scale). For each of these boxes, a least squared local trend is fitted.

Third, it calculates the local trend within each segment. For each of these boxes, a least squared local trend is fitted. The value of the fitted time series obtained for boxes of length (n) is denoted by y_{n}.

Fourth, it computes the average of the fluctuation function over all segments to obtain the qth order fluctuation function.

$$F(s)_q = \sum_{k=1}^{Ns} ((y(i) - y_{\mathrm{n}}(i))^2)^q / Ns$$

Finally, the Generalized Hurst exponent is estimated by fitting a linear line to the log-log plot of the $F(s)_{\mathrm{q}}$ with respect to scale (s), according to the following equation:

$$F(s)_{\mathrm{q}} = s^{H(q)}$$

The Hurst exponent is the value of the Generalized Hurst exponent (H(q = 2)), which is a special case and is used usually when one is interested only in analyzing the long-range dependency of a signal and not the multifractal chrematistics.

Finally, the multifractal spectrum of the multi-variable signal ($\alpha, f(\alpha)$) is estimated by the Legendre transform:

$$\tau(q) = H(q)^*(q-1)$$

$$\alpha(q) = d\tau(q)/dq$$

$$f(\alpha) = q\alpha - \tau(q)$$

Detrended Cross-Correlation Analysis (DCCA)

This method is designed to investigate the power law cross-correlation between two time-series (Podobnik and Stanley, 2008). Similar to the DFA (discussed in the previous sub-section), which computes the scaling behavior of the auto-correlation function, the DCCA method computes the scaling behavior of the cross-correlation function between two time-series and analyzes its scaling behavior.

DCCA method first computes the integrated *profile* of each time series:

$$y_1(i) = \sum_{i=1}^{k} (x_1(i) - \widehat{x_1})$$

$$y_2(i) = \sum_{i=1}^{k} (x_2(i) - \widehat{x_2})$$

Second, both the entire time series is divided into non-overlapping intervals. Third, it computes the local trend in each interval for each time series ($y_{1,n}(i)$, *and* $y_{2,n}(i)$). Fourth, it calculates the covariance of the residual of profiles from local trends. It calculates the detrended covariance (H(q)) by summing over all segments of the nonstationary time series:

$$\widehat{F}(s)_{\mathrm{q}} = \sum_{k=1}^{Ns} ((y_1(i) - y_{1,n}(i)^2 (y_2(i) - y_{2,n}(i))^2)^q / Ns$$

The cross-correlation exponent (λ) is estimated by fitting a linear line to the log-log plot of the $\widehat{F}(s)_{\mathrm{q}}$ with respect to scale (s):

$$\widehat{F}(s)_{\mathrm{q}} = s^{\lambda}$$

The Mandelbrot Binomial Cascade Model

This model is proposed by Mandelbrot et al. (1997) to better explain an alternative for probability distribution for the erratic or fractal appearance of a probability measure. It starts with a probability measure (μ), which is self-similar:

$$\mu([a,b]) = m_0\ \mu_{([2a,2b])} + m_1\ \mu_{([2a-1,2b-1])}$$

Once the unit interval [0,1] is divided into two subintervals, m_0 mass is assigned to the left subinterval and $m_1 = 1 - m_0$ is assigned to the right subinterval. Repeating this step for each of the subintervals for n times will result in the Mandelbrot model with n iterations. Mandelbrot has proved that the limit behavior of this model when n is infinitely large (∞) can be best illustrated

by multifractal formalism. He formulated the (α, f(α)) spectrum on the basis of the parameters of the Mandelbrot Cascade model. We have compared the observed multifractality spectrum in gene expression time series to the closest one obtained by Mandelbrot cascade model.

Random Cascades on Wavelet Dyadic Trees

This model (Arneodo et al., 1998) is proposed to model multifractal objects. The notion of cascade here refers to a self-similar process whose properties are defined multiplicatively in different scales. In summary, in this model, the wavelet coefficients of a function are self-similar at different scales. Two types of W-cascades are proposed: Log-Normal *W*-cascades and Log-Poisson *W*-cascades. For the log-normal cascade (with μ and σ for parameters of the normal random variable), the following equation holds for singularity spectrum:

$$F(\alpha) = -\frac{\ln 2}{2\sigma^2}(\alpha + \mu / \ln 2)^2$$

For the Log-Poisson *W*-cascades, the following equation holds for the mass exponent:

$$\tau(q) = \frac{1}{\ln 2}(\lambda(1-\delta^q)-\gamma q) - 1$$

As can be seen, the second derivative of the mass exponent for Log-Poisson *W*-cascade model has the following equation:

$$\tau'(q) = {}^{\lambda}/_{\ln 2}(-\ln \delta\, \delta^q) - {}^{\gamma}/_{\ln 2}$$

$$\tau''(q) = -{}^{\lambda}/_{\ln 2}(\ln \delta)^2 \delta^q$$

We have reported the similarity of the multifractal spectrum of cross-dependencies in gene expression time series to the log-normal *W*-cascades model. Also, we have reported the disagreement of the multifractal spectrum of cross-dependencies in gene expression time series to log-Poisson *W*-cascade model due to its deviation from power-law shape as shown in **Figure 6**.

Entropy and Entropy of a Network

Shannon entropy (Shannon, 2001) is a measure of *the unpredictability* of the state, or equivalently, of its *average information content*. Shannon defined the entropy of a discrete random variable X with possible values of $\{x_1, x_2, \ldots, x_k\}$ and probability mass function P(X) as:

$$H(X) = E[I(X)] = E[-\log P(X)]$$

More explicitly, entropy can be written as:

$$H(X) = -\sum_{i=1}^{n} P(x_i) \log P(x_i)$$

Entropy is a measure of the unpredictability of the state or its average containing information. One example to illustrate is when there is no uncertainty and the random variables take only one value in which the value of the entropy will be zero. As the number of possibilities increases, the entropy increases as well.

We have used the notion of entropy in the context of networks. We consider the weight of the links in the network as the random variable and we discuss entropy of the weight of the weighted links. Given an undirected binary graph of gene regulatory networks and time series of genes and TFs in the network (which are the nodes in the gene regulatory network), we construct a weighted network (shown in **Figure 7**). In the constructed weighted network, the weight of each link is the *cross-correlation exponent* of the time series of two time-series linked together in the gene regulatory network. Then, in the new constructed weighted network, we consider the distribution of the weights of the links and entropy of them as a measure of the entropy of the network. Also, this weighted network can be used for other algorithms measuring the entropy of complex networks proposed in Anand and Bianconi (2009), Anand et al. (2011). **Figure 7** illustrates this method by showing how the weights are assigned

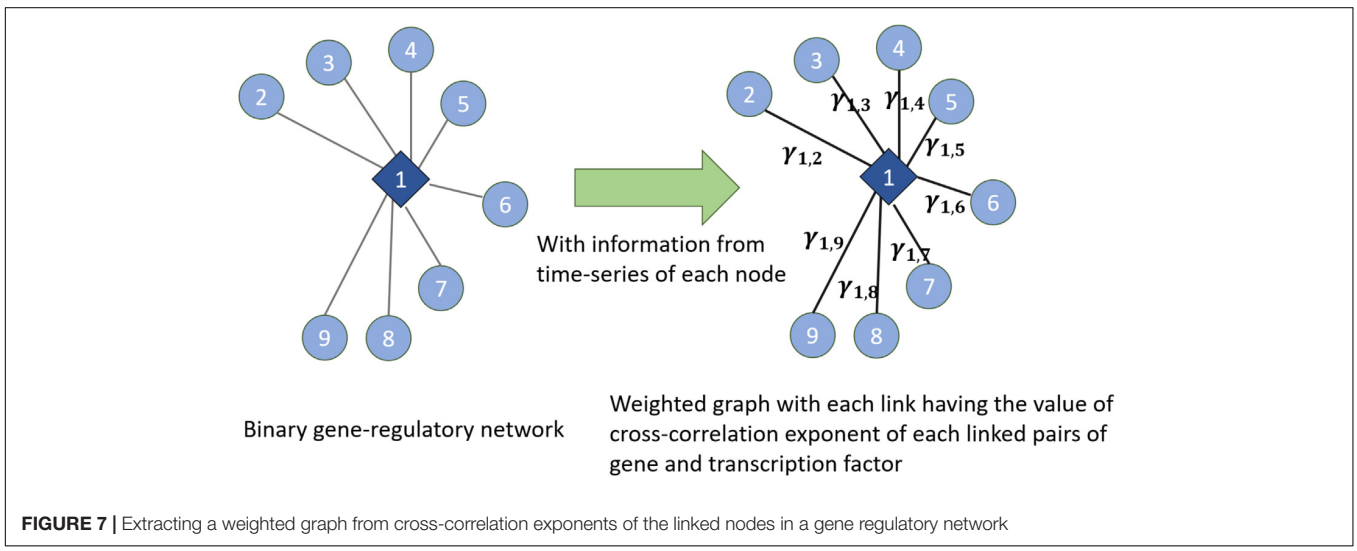

FIGURE 7 | Extracting a weighted graph from cross-correlation exponents of the linked nodes in a gene regulatory network

to each link. In this figure, $\gamma_{1,2}, \ldots, \gamma_{1,9}$ are the cross-corrections of the time series of the TF and genes which are linked together in the gene regulatory network in the left part of the figure. Hence, this shows how knowing the existing interactions in the network and having the time series of each node's dynamics can lead us to know cross-correlation exponents and then assigning the concept of entropy to the network dynamics.

AUTHOR CONTRIBUTIONS

All authors listed have made a substantial, direct and intellectual contribution to the work, and approved it for publication. PB conceived the idea. MG, EJ, and PB discussed the research problem and approaches, identified analytical challenges and solutions. MG implemented the research discussions and performed the research.

FUNDING

PB gratefully acknowledges the support by the U.S. Army Defense Advanced Research Projects Agency (DARPA) under grant no. W911NF-17-1-0076, the DARPA Young Faculty Award under grant no. N66001-17-1-4044 support, and the National Science Foundation Career award under grant no. CPS/CNS-1453860. The views, opinions, and/or findings contained in this article are those of the authors and should not be interpreted as representing the official views or policies, either expressed or implied by the Defense Advanced Research Projects Agency, the Department of Defense or the National Science Foundation.

ACKNOWLEDGMENTS

We thank our reviewers for extremely insightful comments and feedback on our work that contributed to the significant improvement of the manuscript.

SUPPLEMENTARY MATERIAL

The Supplementary Material for this article can be found online at: https://www.frontiersin.org/articles/10.3389/fphys.2018.01446/full#supplementary-material

REFERENCES

Abdulrehman, D., Monteiro, P. T., Teixeira, M. C., Mira, N. P., Lourenço, A. B., dos Santos, S. C., et al. (2010). YEASTRACT: providing a programmatic access to curated transcriptional regulatory associations in *Saccharomyces cerevisiae* through a web services interface. *Nucleic Acids Res.* 39(Suppl. 1), D136–D140. doi: 10.1093/nar/gkq964

Anand, K., and Bianconi, G. (2009). Entropy measures for networks: toward an information theory of complex topologies. *Phys. Rev. E* 80:045102.

Anand, K., Bianconi, G., and Severini, S. (2011). Shannon and von Neumann entropy of random networks with heterogeneous expected degree. *Phys. Rev. E* 83:036109.

Arneodo, A., Bacry, E., and Muzy, J. F. (1998). Random cascades on wavelet dyadic trees. *J. Math. Phys.* 39, 4142–4164. doi: 10.1063/1.532489

Arneodo, A., d'Aubenton-Carafa, Y., Bacry, E., Graves, P. V., Muzy, J. F., and Thermes, C. (1996). Wavelet based fractal analysis of DNA sequences. *Physica D* 96, 291–320. doi: 10.1023/B:JOBP.0000016438.86794.8e

Bacry, E., and Muzy, J. F. (2003). Log-infinitely divisible multifractal processes. *Commun. Math. Phys.* 236, 449–475. doi: 10.1007/s00220-003-0827-3

Bauer, M., and Metzler, R. (2013). In vivo facilitated diffusion model. *PloS One* 8:e53956. doi: 10.1371/journal.pone.0053956

Bernaola-Galván, P., Román-Roldán, R., and Oliver, J. L. (1996). Compositional segmentation and long-range fractal correlations in DNA sequences. *Phys. Rev. E* 53, 5181–5189. doi: 10.1103/PhysRevE.53.5181

Chainais, P., Riedi, R., and Abry, P. (2005). On non-scale-invariant infinitely divisible cascades. *IEEE Trans. Inf. Theory* 51, 1063–1083. doi: 10.1109/TIT.2004.842570

Düvel, K., Yecies, J. L., Menon, S., Raman, P., Lipovsky, A. I., Souza, A. L., et al. (2010). Activation of a metabolic gene regulatory network downstream of mTOR complex 1. *Mol. Cell* 39, 171–183. doi: 10.1016/j.molcel.2010.06.022

Efron, B. (1982). *The Jackknife, the Bootstrap and Other Resampling Plans*. Philadelphia, PA: Society for Industrial and Applied Mathematics. doi: 10.1137/1.9781611970319

Elf, J., Li, G.-W., and Xie, X. S. (2007). Probing transcription factor dynamics at the single-molecule level in a living cell. *Science* 316, 1191–1194. doi: 10.1126/science.1141967

Gama-Castro, S., Salgado, H., Peralta-Gil, M., Santos-Zavaleta, A., Muniz-Rascado, L., Solano-Lira, H., et al. (2010). RegulonDB version 7.0: transcriptional regulation of *Escherichia coli K*-12 integrated within genetic sensory response units (gensor units). *Nucleic Acids Res.* 39(Suppl. 1), D98–D105. doi: 10.1093/nar/gkq1110

Hu, Z., Killion, P. J., and Iyer, V. R. (2007). Genetic reconstruction of a functional transcriptional regulatory network. *Nat. Genet.* 39, 683–687. doi: 10.1038/ng2012

Huang, S., Eichler, G., Bar-Yam, Y., and Ingber, D. E. (2005). Cell fates as high-dimensional attractor states of a complex gene regulatory network. *Phys. Rev. Lett.* 94:128701. doi: 10.1103/PhysRevLett.94.128701

Ji, N., Middelkoop, T. C., Mentink, R. A., Betist, M. C., Tonegawa, S., Mooijman, D., et al. (2013). Feedback control of gene expression variability in the *Caenorhabditis elegans* wnt pathway. *Cell* 155, 869–880. doi: 10.1016/j.cell.2013.09.060

Kantelhardt, J. W., Koscielny-Bunde, E., Rego, H. H., Havlin, S., and Bunde, A. (2001). Detecting long-range correlations with detrended fluctuation analysis. *Physica A* 295, 441–454. doi: 10.1016/S0378-4371(01)00144-3

Kantelhardt, J. W., Zschiegner, S. A., Koscielny-Bunde, E., Havlin, S., Bunde, A., and Stanley, H. E. (2002). Multifractal detrended fluctuation analysis of nonstationary time series. *Physica A* 316, 87–114. doi: 10.1016/S0378-4371(02)01383-3

Keseler, I. M., Collado-Vides, J., Santos-Zavaleta, A., Peralta-Gil, M., Gama-Castro, S., Muñiz-Rascado, L., et al. (2010). EcoCyc: a comprehensive database of *Escherichia coli* biology. *Nucleic Acids Res.* 39(Suppl. 1), D583–D590. doi: 10.1093/nar/gkq1143

Kiyono, K., Struzik, Z. R., and Yamamoto, Y. (2007). Estimator of a non-gaussian parameter in multiplicative log-normal models. *Phys. Rev. E* 76:041113.

Kolesov, G., Wunderlich, Z., Laikova, O. N., Gelfand, M. S., and Mirny, L. A. (2007). How gene order is influenced by the biophysics of transcription regulation. *Proc. Natl. Acad. Sci.* 104, 13948–13953. doi: 10.1073/pnas.0700672104

Kuhlman, T. E., and Cox, E. C. (2012). Gene location and DNA density determine transcription factor distributions in *Escherichia coli*. *Mol. Syst. Biol.* 8:610. doi: 10.1038/msb.2012.42

Lockhart, D. J., and Winzeler, E. A. (2000). Genomics, gene expression and DNA arrays. *Nature* 405, 827–836. doi: 10.1038/35015701

Maass, W. (2014). Noise as a resource for computation and learning in networks of spiking neurons. *Proc. IEEE* 102, 860–880. doi: 10.1109/JPROC.2014.2310593

MacIsaac, K. D., Wang, T., Gordon, D. B., Gifford, D. K., Stormo, G. D., and Fraenkel, E. (2006). An improved map of conserved regulatory sites for *Saccharomyces cerevisiae*. *BMC Bioinformatics* 7:113. doi: 10.1186/1471-2105-7-113 NODOI doi: 10.1186/1471-2105-7-113

Malone, T. W., Laubacher, R., and Dellarocas, C. (2009). *Harnessing Crowds: Mapping the Genome of Collective Intelligence*. MIT Sloan Research Paper No. 4732-09. Available at: http://ssrn.com/abstract=1381502

Mandelbrot, B. B., Fisher, A. J., and Calvet, L. E. (1997). *A Multifractal Model of Asset Returns*. New Haven, CT: Cowles Foundation for Research in Economics.

Marbach, D., Costello, J. C., Küffner, R., Vega, N. M., Prill, R. J., Camacho, D. M., et al. (2012). DREAM5 consortium. wisdom of crowds for robust gene network inference. *Nat. Methods* 9, 796–804. doi: 10.1038/nmeth.2016

Muzychuk, O. V. (2006). Using bimodal probability distributions in the problems of Brownian diffusion. *Radiophys. Quantum Electron.* 49, 645–655. doi: 10.1007/s11141-006-0099-9

Niedenthal, R. K., Riles, L., Johnston, M., and Hegemann, J. H. (1996). Green fluorescent protein as a marker for gene expression and subcellular localization in budding yeast. *Yeast* 12, 773–786. doi: 10.1002/(SICI)1097-0061(19960630)12:8<773::AID-YEA972>3.0.CO;2-L

O'Connor, C. M., Adams, J. U., and Fairman, J. (2010). *Essentials of cell biology*. Cambridge: NPG Education.

Peng, C. K., Buldyrev, S. V., Havlin, S., Simons, M., Stanley, H. E., and Goldberger, A. L. (1994). Mosaic organization of DNA nucleotides. *Phys. Rev. E* 49, 1685–1689. doi: 10.1103/PhysRevE.49.1685

Podobnik, B., and Stanley, H. E. (2008). Detrended cross-correlation analysis: a new method for analyzing two nonstationary time series. *Phys. Rev. Lett.* 100:084102.

Pulkkinen, O., and Metzler, R. (2013). Distance matters: the impact of gene proximity in bacterial gene regulation. *Phys. Rev. Lett.* 110:198101.

Raser, J. M., and O'shea, E. K. (2005). Noise in gene expression: origins, consequences, and control. *Science* 309, 2010–2013. doi: 10.1126/science.1105891

Shannon, C. E. (2001). A mathematical theory of communication. *ACM SIGMOBILE Mobile Computing and Commun. Rev.* 5, 3–55. doi: 10.1145/584091.584093

Stolovitsky, G., and Califano, A. (2007)). "Reverse engineering biological networks," in *Workshop for Dialogue on Reverse Engineering Assessment and Methods*, eds G. Stolovitsky and A. Califano (Malden, MA: Wiley-Blackwell).

Teichmann, S. A., and Babu, M. M. (2004). Gene regulatory network growth by duplication. *Nat. Genet.* 36, 492–496. doi: 10.1038/ng1340

Teschendorff, A. E., and Enver, T. (2017). Single-cell entropy for accurate estimation of differentiation potency from a cell's transcriptome. *Nat. Commun.* 8:15599. doi: 10.1038/ncomms15599

Tsuchiya, M., Giuliani, A., Hashimoto, M., Erenpreisa, J., and Yoshikawa, K. (2016). Self-organizing global gene expression regulated through criticality: mechanism of the cell-fate change. *PloS One* 11:e0167912. doi: 10.1371/journal.pone.0167912

Tsuchyia, M., Wong, S. T., Yeo, Z. X., Colosimo, A., Palumbo, M. C., Farina, L., et al. (2007). Gene expression waves. *FEBS J.* 274, 2878–2886. doi: 10.1111/j.1742-4658.2007.05822.x

Xue, Y., and Bogdan, P. (2017). "Constructing compact causal mathematical models for complex dynamics," in *Proceedings of the Cyber-Physical Systems (IC), ACM/IEEE 8th International Conference* (New York, NY: IEEE), 97–108.

Zhang, Q., Zhou, S., and Wei, X. (2011). An efficient approach for DNA fractal-based image encryption. *Appl. Math. Inf. Sci.* 5, 445–459.

Conflict of Interest Statement: The authors declare that the research was conducted in the absence of any commercial or financial relationships that could be construed as a potential conflict of interest.

frontiers in Physiology

ORIGINAL RESEARCH
published: 27 November 2018
doi: 10.3389/fphys.2018.01578

Quantification of Beat-To-Beat Variability of Action Potential Durations in Langendorff-Perfused Mouse Hearts

Gary Tse[1,2,3], Yimei Du[4], Guoliang Hao[5], Ka Hou Christien Li[6], Fiona Yin Wah Chan[7], Tong Liu[8], Guangping Li[8], George Bazoukis[9], Konstantinos P. Letsas[9], William K. K. Wu[10], Shuk Han Cheng[11,12,13]* and Wing Tak Wong[14]**

[1] Department of Medicine and Therapeutics, Faculty of Medicine, Chinese University of Hong Kong, Hong Kong, China, [2] Li Ka Shing Institute of Health Sciences, Faculty of Medicine, Chinese University of Hong Kong, Hong Kong, China, [3] Shenzhen Research Institute, The Chinese University of Hong Kong, Shenzhen, China, [4] Research Center of Ion Channelopathy, Institute of Cardiology, Union Hospital, Tongji Medical College, Huazhong University of Science and Technology, Wuhan, China, [5] Department of Physiology, Anatomy and Genetics, University of Oxford, Oxford, United Kingdom, [6] Faculty of Medicine, Newcastle University, Newcastle, United Kingdom, [7] School of Biological Sciences, University of Cambridge, Cambridge, United Kingdom, [8] Tianjin Key Laboratory of Ionic-Molecular Function of Cardiovascular Disease, Department of Cardiology, Tianjin Institute of Cardiology, Second Hospital of Tianjin Medical University, Tianjin, China, [9] Laboratory of Cardiac Electrophysiology, Second Department of Cardiology, Evangelismos General Hospital of Athens, Athens, Greece, [10] State Key Laboratory of Digestive Disease, Department of anesthesia and Intensive Care, LKS Institute of Health Sciences, The Chinese University of Hong Kong, Hong Kong, China, [11] Department of Biomedical Sciences, College of Veterinary Medicine and Life Science, City University of Hong Kong, Hong Kong, China, [12] State Key Laboratory of Marine Pollution at City University of Hong Kong, Hong Kong, China, [13] Department of Materials Science and Engineering, College of Science and Engineering, City University of Hong Kong, Hong Kong, China, [14] State Key Laboratory of Agrobiotechnology, School of Life Sciences, Chinese University of Hong Kong, Hong Kong, China

OPEN ACCESS

Edited by:
Paul Bogdan,
University of Southern California,
United States

Reviewed by:
Siddharth Jain,
California Institute of Technology,
United States
Clara Ionescu,
Ghent University, Belgium

***Correspondence:**
Gary Tse
tseg@cuhk.edu.hk
Shuk Han Cheng
bhcheng@cityu.edu.hk
Wing Tak Wong
jack_wong@cuhk.edu.hk

Specialty section:
This article was submitted to Fractal Physiology, a section of the journal Frontiers in Physiology

Received: *25 March 2018*
Accepted: *22 October 2018*
Published: *27 November 2018*

Citation:
Tse G, Du Y, Hao G, Li KHC, Chan FYW, Liu T, Li G, Bazoukis G, Letsas KP, Wu WKK, Cheng SH and Wong WT (2018) Quantification of Beat-To-Beat Variability of Action Potential Durations in Langendorff-Perfused Mouse Hearts. Front. Physiol. 9:1578. doi: 10.3389/fphys.2018.01578

Background: Beat-to-beat variability in action potential duration (APD) is an intrinsic property of cardiac tissue and is altered in pro-arrhythmic states. However, it has never been examined in mice.

Methods: Left atrial or ventricular monophasic action potentials (MAPs) were recorded from Langendorff-perfused mouse hearts during regular 8 Hz pacing. Time-domain, frequency-domain and non-linear analyses were used to quantify APD variability.

Results: Mean atrial APD (90% repolarization) was 23.5 ± 6.3 ms and standard deviation (SD) was 0.9 ± 0.5 ms (n = 6 hearts). Coefficient of variation (CoV) was 4.0 ± 1.9% and root mean square (RMS) of successive differences in APDs was 0.3 ± 0.2 ms. The peaks for low- and high-frequency were 0.7 ± 0.5 and 2.7 ± 0.9 Hz, respectively, with percentage powers of 39.0 ± 20.5 and 59.3 ± 22.9%. Poincaré plots of APD_{n+1} against APD_n revealed ellipsoid shapes. The ratio of the SD along the line-of-identity (SD2) to the SD perpendicular to the line-of-identity (SD1) was 8.28 ± 4.78. Approximate and sample entropy were 0.57 ± 0.12 and 0.57 ± 0.15, respectively. Detrended fluctuation analysis revealed short- and long-term fluctuation slopes of 1.80 ± 0.15 and 0.85 ± 0.29, respectively. When compared to atrial APDs, ventricular APDs were longer (ANOVA, $P < 0.05$), showed lower mean SD and CoV but similar RMS of successive differences in APDs and showed lower SD2 ($P < 0.05$). No difference in the remaining parameters was observed.

Conclusion: Beat-to-beat variability in APD is observed in mouse hearts during regular pacing. Atrial MAPs showed greater degree of variability than ventricular MAPs. Non-linear techniques offer further insights on short-term and long-term variability and signal complexity.

Keywords: variability, repolarization, time, frequency, non-linear, entropy

INTRODUCTION

Beat-to-beat variations in the repolarization time-course represent an intrinsic property of cardiac electrophysiological function. This may be manifested as variability of action potential durations (APDs) at the cellular level (Nanasi et al., 2017), or of QT durations at the organism level (Niemeijer et al., 2014; Phadumdeo and Weinberg, 2018). This variability may be affected by distinct physiological states, such as the degree of intercellular coupling (Zaniboni et al., 2000), redox states (Kistamas et al., 2015a), altered intracellular calcium handling (Kistamas et al., 2015b) or APD itself (Abi-Gerges et al., 2010). Clinical studies have shown that higher variability in QT intervals can predict pro-arrhythmic outcomes in the context of non-ischemic heart failure (Hinterseer et al., 2010), as well as long QT syndrome (Hinterseer et al., 2009).

Mouse models are widely used to study cardiac electrophysiological and arrhythmogenic properties, owing to their amenability to pharmacological or genetic manipulation (Nerbonne, 2014; Choy et al., 2016). However, despite the importance of APD variability, it has never been examined in this species. In this study, we quantified beat-to-beat variability in APDs by applying time-domain and non-linear techniques for the first time to monophasic action potential recordings (MAPs) obtained from Langendorff-perfused mouse hearts during regular pacing.

MATERIALS AND METHODS

Solutions

Krebs-Henseleit solution (composition in mM: NaCl 119, $NaHCO_3$ 25, KCl 4, KH_2PO_4 1.2, $MgCl_2$ 1, $CaCl_2$ 1.8, glucose 10 and sodium pyruvate 2, pH 7.4), which has been bicarbonate-buffered and bubbled with 95% O_2-5% CO_2, was used in the experiments described in this study.

Preparation of Langendorff-Perfused Mouse Hearts

This study was approved by the Animal Welfare and Ethical Review Body at the University of Cambridge. Wild-type mice of 129 genetic background between 5 and 7 months of age were used. They were maintained at room temperature (21 ± 1°C) and were subjected to a 12:12 h light/dark cycle with free access to sterile rodent chow and water in an animal facility. Mice were terminated by dislocation of the cervical spine in accordance with Sections 1(c) and 2 of Schedule 1 of the UK Animals (Scientific Procedures) Act 1986. The technique for Langendorff perfusion has been used by our group and described previously (Tse et al., 2016a,d, 2017). After removal from their chest cavities, the hearts were submerged in ice-cold Krebs-Henseleit solution. The aortas were cannulated using a custom-made 21-gauge cannula prefilled with ice-cold buffer. A micro-aneurysm clip (Harvard Apparatus, UK) was used to secure the hearts onto the Langendorff perfusion system. Retrograde perfusion was carried out at a flow rate of 2 to 2.5 ml min^{-1} by use of a peristaltic pump (Watson–Marlow Bredel pumps model 505S, Falmouth, Cornwall, UK). The perfusate passed through successively 200 and 5 μm filters and warmed to 37°C using a water jacket and circulator before arriving at the aorta. Approximately 90% of the hearts regained their pink color and spontaneous rhythmic activity. These were therefore studied further. The remaining 10% did not and were discarded. The hearts were perfused for a further 20 min to minimize residual effects of endogenous catecholamine release, before their electrophysiology properties were characterized.

Stimulating Procedures

Paired platinum electrodes (1 mm interpole distance) were used to stimulate the right ventricular epicardium electrically. This took place at 8 Hz, using square wave pulses of 2 ms in duration, with a stimulation voltage set to three times the diastolic threshold (Grass S48 Stimulator, Grass-Telefactor, Slough, UK) immediately after the start of perfusion.

Atrial and Ventricular Map Recording Procedures

For atrial MAP recordings, the atrio-ventricular nodes of the Langendorff perfused hearts were first mechanically ablated as previously described (Tse et al., 2016b). This eliminated ventricular far-field activity at the recording electrode. The MAP electrode was placed at the left atrial or ventricular epicardium (Linton Instruments, Harvard Apparatus). The stimulating and recording electrodes were maintained at constant positions separated approximately by a distance of 3 mm. All recordings were performed using a baseline cycle length (BCL) of 125 ms (8 Hz) to exclude rate-dependent differences in action potential durations (APDs). MAPs were pre-amplified using a NL100AK head stage, amplified with a NL 104A amplifier and band pass filtered between 0.5 Hz and 1 kHz using a NL125/6 filter (Neurolog, Hertfordshire, UK) and then digitized (1401plus MKII, Cambridge Electronic Design, Cambridge, UK) at 5 kHz. Waveforms were analyzed using Spike2 software (Cambridge Electronic Design, UK). MAP waveforms that did not match established criteria for MAP signals were rejected (Knollmann et al., 2001; Tse et al., 2016c). They must have stable baselines, fast upstrokes, with no inflections or negative spikes, and a rapid first phase of repolarization. Zero Percent repolarization

was measured at the peak of the MAP and Hundred Percent repolarization was measured at the point of return of the potential to baseline (Gussak et al., 2000; Knollmann et al., 2001; Fabritz et al., 2003).

APD Variability Analysis

APD variability analysis was performed using Kubios HRV Standard software (Version 3.0.2) over a 60 s period. Time-domain analysis yielded the (1) standard deviation (SD) of APDs, which represents the overall (short-term and long-term) variability, and (2) root mean square (RMSSD) of successive differences of APDs, which represents the short-term variability:

$$\mathrm{SDAPD} = \sqrt{\frac{1}{N-1}\sum_{j=1}^{N}\left(\mathrm{APD}_j - \overline{\mathrm{APD}}\right)^2} \quad (1)$$

$$\mathrm{RMSSD} = \sqrt{\frac{1}{N-1}\sum_{j=1}^{N-1}\left(\mathrm{APD}_{j+1} - \mathrm{APD}_j\right)^2} \quad (2)$$

Frequency-domain analysis was conducted using the Fast Fourier Transform method. For frequency domain parameters, spectral analysis was performed by using fast-Fourier transform method. The sampling frequency was set to 8 Hz. The power in the repolarization spectrum between 0.04 and 4 Hz was defined as total power (TP). The power in the repolarization spectrum was divided into three different frequency bands: very low frequency power (VLF, 0 to 0.04 Hz), low frequency power (LF, 0.04 to 1.5 Hz) and high frequency power (HF, 1.5 to 4 Hz).

The above frequency analysis does not provide any information on the time evolution of the frequencies. To achieve, this, time-frequency analysis was conducted using two different techniques. Firstly, short-time Fourier transform (STFT) was used to break the signal into small time segments using an appropriate sliding-window function, and then apply a Fourier transformation to the successive sliding-window segments. The Hanning window with a Fast Fourier Transform length of 256 and overlap of 128 were selected.

Secondly, continuous wavelet transform (CWT) was used to divide a continuous-time function into wavelets given by:

$$\mathrm{CWT(a,b)} = \frac{1}{\sqrt{\mathrm{a}}}\int_{-\infty}^{+\infty} \mathrm{x}(\mathrm{t})\ .\ \psi^*\left(\frac{\mathrm{t}-\mathrm{b}}{\mathrm{a}}\right)\mathrm{dt} \quad (3)$$

Where the superscript, *, is the complex conjugate and $\psi_{a,b}{}^*$ represents a translated and scaled complex conjugated mother wavelet. The mother wavelet ψ is invertible when it verifies the condition of admissibility which is stated as:

$$\int_{-\infty}^{+\infty} \frac{\left|\widehat{\psi}(\omega)\right|}{\omega}\,\mathrm{d}\omega < \infty \quad (4)$$

The Morlet wavelet was selected, which uses a Gaussian-modulated sinusoid:

$$\psi(t) = \frac{1}{\sqrt[4]{\pi}}\left(\mathrm{e}^{\mathrm{i}\omega_o t} - \mathrm{e}^{-\frac{\omega_0^2}{2}}\right)\mathrm{e}^{-\frac{t^2}{2}} \quad (5)$$

where ω_o is the central frequency of the mother wavelet. The second term in the brackets corrects for the non-zero mean of the complex sinusoid of the first term. This becomes negligible for values of $\omega_o > 5$, which we selected in our case:

$$\psi(t) = \frac{1}{\sqrt[4]{\pi}}\mathrm{e}^{\mathrm{i}\omega_o t}\,\mathrm{e}^{-\frac{t^2}{2}} \quad (6)$$

Non-linear properties of APD variability were studied as follow. Poincaré plots are graphical representations of the correlation between successive APD values, in which $\mathrm{APD_{n+1}}$ is plotted against $\mathrm{APD_n}$. This enables determination of the SD of the points perpendicular to the line-of-identity (SD1). Different points along this perpendicular axis represent a beat-to-beat variation between the initial (n) and subsequent ($n + 1$) contraction, representing multiple two-beat "snapshots" with little correlation to a progressive time parameter. Therefore, SD1 is associated with instantaneous or short-term variability. As for the points along the line-of-identity (SD2), it shows beat-to-beat consistency between the initial (n) and subsequent ($n + 1$) RR interval. Hence, deviation of the clustered SD2 points away from the average RR interval, taken with reference to the centroid, represents long-term variability. The ratio SD2 to SD1 then gives an indication of the degree of long-term variability in relation to the short-term variability.

Coined in 1991 by Pincus et al., the concept of approximate entropy was introduced to provide approximations on the degree of regularity when applied to a short-duration epoch, which cannot be achieved with moment statistics such as mean and variance. This is applied to non-stationary biomedical data such as heart rate variability, which commonly presents with non-linearity and complexity. Logarithmically, the approximate entropy takes into account the imputed threshold "*r*" under which a recurrence is identified. With this it expresses the likelihood of repeated signals within the threshold for m and $m + 1$ points. It is computed as follows:

Firstly, a set of length m vectors $\mathrm{u_j}$ is formed:

$$\mathrm{u_j} = (\mathrm{APD_j}; \mathrm{APD_{j+1}}, \ldots, \mathrm{APD_{j+m-1}});\ \mathrm{j} = 1; 2; \ldots \mathrm{N} - \mathrm{m} + 1 \quad (7)$$

where, m is the embedding dimension and N is the number of measured APDs. The distance between these vectors is defined as the maximum absolute difference between the corresponding elements:

$$\mathrm{d(u_j, u_k)} = \max\{|\mathrm{APD_{j+n}} - \mathrm{APD_{k+n}}||\mathrm{n} = 0, \ldots, \mathrm{m} - 1\} \quad (8)$$

for each $\mathrm{u_j}$ the relative number of vectors $\mathrm{u_k}$ for which $\mathrm{d(u_j, u_k)} \leq \mathrm{r}$ is calculated. This index is denoted with Cmj (r) and can be written in the form

$$C_j^m(r) = \frac{\text{nbr of}\left\{u_k |\ d\left(u_j, u_k\right) \leq r\right\}}{N - m + 1}\ \forall k \quad (9)$$

Taking the natural logarithms gives:

$$\Phi^m(r) = \frac{1}{N - m + 1}\sum_{j=1}^{N-m+1} \ln C_j^m(r)\,. \quad (10)$$

The approximate entropy is then defined as:

$$\mathrm{ApEn}\,(m,\ r,\ N) = \ \Phi^{m}\,(r) - \ \Phi^{m+1}(r) \tag{11}$$

Approximate entropy measures the likelihood that certain patterns of observations are followed by different patterns of observations. As such, a lower approximate entropy values reflect a more regular signal, whereas higher values reflect a more irregular signal (Pincus, 1991; Mesin, 2018).

The sample entropy also provides a measure of signal irregularity but is less susceptible to bias than approximate entropy (Richman and Moorman, 2000; Nayak et al., 2018). This is done by eliminating the counting of self-matches; hence the count of the number of similar vector lengths is always one less than that of ApEn. Furthermore, sample entropy uses the logarithm of the sum of conditional properties rather than each conditional property individually, illustrated by the negative natural logarithm for conditional properties. Both sample entropy and approximate entropy are able to differentiate between experimental and theoretical data sets. However, it has been demonstrated that sample entropy yielded better relative consistency compared to approximate entropy, reflecting independence from data length and choice of m or r (Molina-Pico et al., 2011).

This is given by:

$$C_j^m\,(r) = \ \frac{\text{nbr of}\left\{u_k |\ d\left(u_j, u_k\right) \le r\right\}}{N-m}\ \forall k\ \neq j \tag{12}$$

Averaging then gives:

$$C^m\,(r) = \ \frac{1}{N-m+1}\ \sum_{j=1}^{N-m+1} C_j^m(r) \tag{13}$$

The sample entropy is then given by:

$$\mathrm{SampEn}\,(m,\ r,\ N) = \ \ln\left(\frac{C^m\,(r)}{C^{m+1}\,(r)}\right) \tag{14}$$

Finally, detrended fluctuation analysis (DFA) was performed to determine long-range correlations in non-stationary physiological time series (Peng et al., 1995), yielding both short-term fluctuation (α1) and long-term fluctuation (α2) slopes. The point at which the slopes α1 and α2 is the crossover point.

Statistical Analysis

All values were expressed as mean ± standard error of the mean (SEM). Numerical data were compared by one-way analysis of variance (ANOVA), a statistical technique that utilizes the F-distribution to compare the means or two or more samples. $P < 0.05$ was considered statistically significant and was denoted by * in the figures.

RESULTS

Atrial and Ventricular Action Potential Duration Variability Determined Using Time-Domain and Frequency-Domain Methods

Representative stable MAP recordings were obtained from the left atrial (**Figure 1A**) or ventricular (**Figure 1B**) epicardium of Langendorff-perfused mouse hearts during regular 8 Hz pacing. Typical time series of atrial and ventricular APDs at 90% repolarization (APD_{90}) are shown in **Figures 1C,D**, respectively and their corresponding histograms are shown in **Figures 1E,F**, respectively. Atrial APD_{90} took a mean value of 23.5 ± 6.3 ms (**Figure 2A**) with a mean standard deviation (SD) 0.9 ± 0.5 ms (**Figure 2B**) ($n = 6$ hearts). The coefficient of variation (CoV), a measure of relative variability calculated by dividing SD by the mean and subsequently multiplying by 100%, was 4.0 ± 1.9% (**Figure 2C**) and the root mean square (RMS) of successive differences in APDs was 0.3 ± 0.2 ms (**Figure 2D**). By contrast, ventricular APD_{90} ($n = 6$ hearts) were longer than atrial APD_{90} (44.0 ± 9.1 ms; ANOVA, $P < 0.05$), with lower mean SD (0.4 ± 0.2 ms, $P < 0.05$), CoV (0.8 ± 0.3%, $P < 0.01$) but similar RMS of successive differences in APD_{90} (0.2 ± 0.3%, $P > 0.05$).

An example of a frequency spectrum using the Fast Fourier Transform method is shown in **Figure 3A**. Frequency-domain analysis revealed that the peaks for very low-, low- and high-frequency for atrial MAPs were 0.04 ± 0.00, 0.7 ± 0.5 and 2.7 ± 0.9 Hz, respectively (**Figures 3B–D**), with percentage powers of 1.7 ± 2.6, 39.0 ± 20.5, and 59.3 ± 22.9% (**Figures 3E–G**). For the ventricles, similar peak frequencies (0.04 ± 0.00, 0.2 ± 0.0 and 3.0 ± 0.6%) and percentage powers (0.9 ± 1.1, 66.0 ± 27.8, and 32.5 ± 27.0) were observed (ANOVA, $P > 0.05$).

Simultaneous time-frequency analysis was subsequently performed using short-time Fourier transform (STFT) and continuous wavelet transform (CWT). Application of STFT yielded plots demonstrating frequency against time for atrial and ventricular APD_{90} (**Figures 4A,B**), and their corresponding three-dimensional representations (**Figures 4C,D**). CWT with Morlet wavelets as basis functions of atrial and ventricular APD_{90} yielded image plots shown in **Figures 4E,F**, respectively.

Action Potential Duration Variability Determined Using Non-linear Methods

Poincaré plots expressing APD_{n+1} as a function of APD_n were constructed for the atrial and ventricular MAPs (**Figures 5A,B**). In all of the hearts studied, ellipsoid shapes of the data points were evident. The SD perpendicular to the line-of-identity (SD1) and SD along the line-of-identity (SD2) are shown in **Figures 5C,D**, respectively. For atrial recordings, the mean SD1 and SD2 were 0.20 ± 0.15 and 1.26 ± 0.67, respectively. The SD2 to SD1 ratio took a mean value of 8.28 ± 4.78 (**Figure 5E**). The approximate and sample entropy took values of 0.57 ± 0.12 (**Figure 5F**) and 0.57 ± 0.15 (**Figure 5G**), respectively. For ventricular MAPs, Poincaré plots of APD_{n+1} against APD_n revealed similar ellipsoid shapes. They showed similar SD1 (0.15 ± 0.19, $P > 0.05$) and lower SD2 (0.49 ± 0.26, $P < 0.05$).

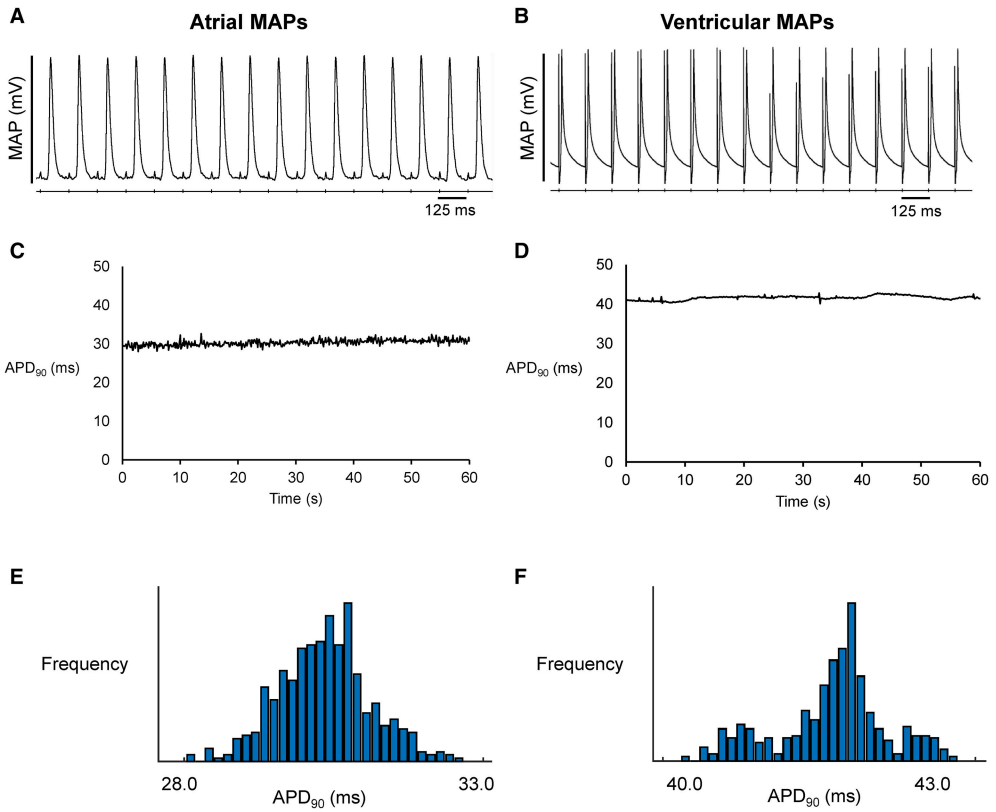

FIGURE 1 | Representative MAP traces from a single heart obtained over a ten-second period during regular 8 Hz pacing from the left atrium **(A)** or left ventricle **(B)**. The corresponding time-series **(C,D)** and histograms **(E,F)** for action potential duration at 90% repolarization (APD_{90}).

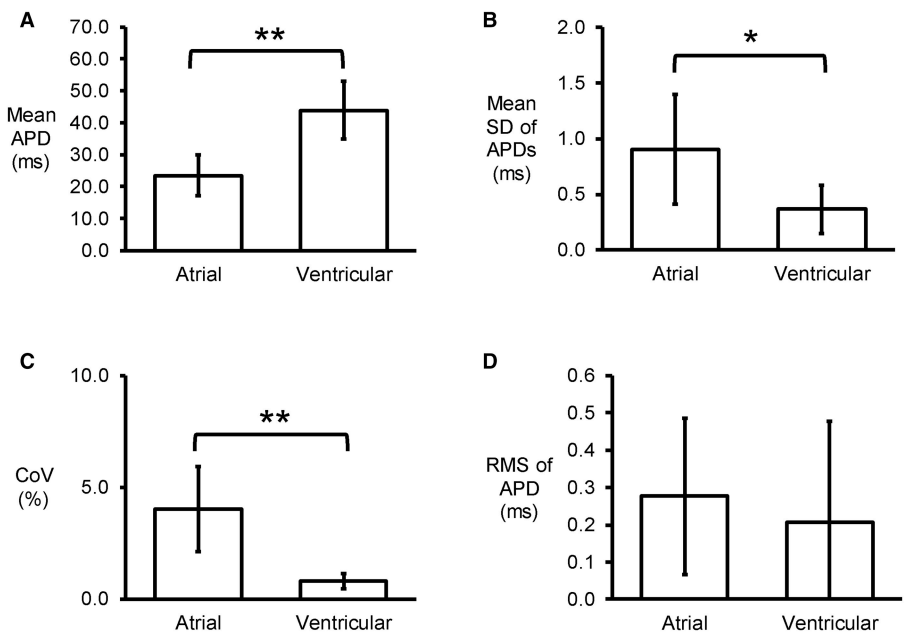

FIGURE 2 | Time-domain analysis yielding mean APD **(A)**, standard deviation (SD) of APDs **(B)**, coefficient of variation (CoV) **(C)**, and root mean square (RMS) of successive differences of APDs **(D)** ($n = 6$; $^{*}P < 0.05$; $^{**}P < 0.01$).

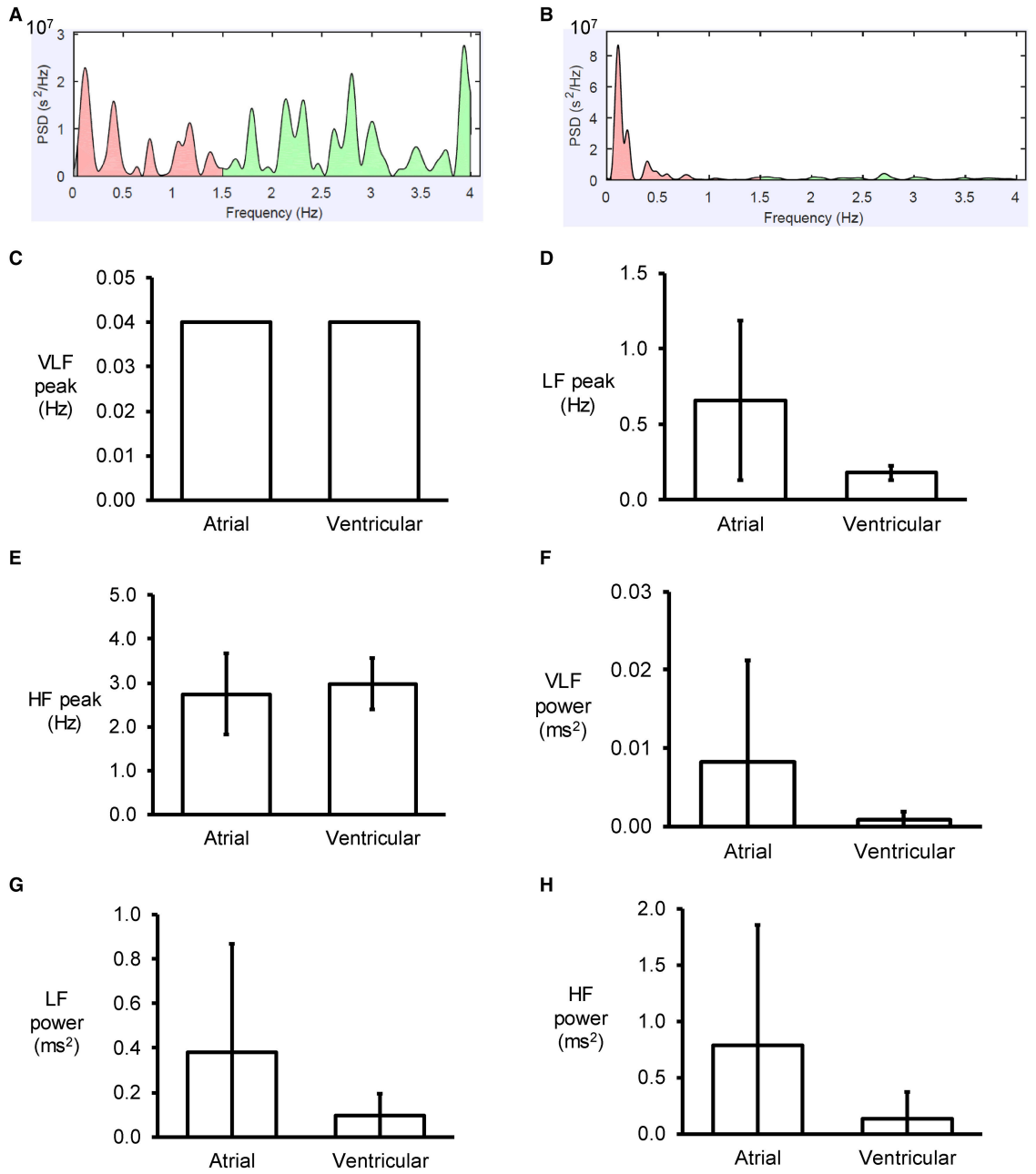

FIGURE 3 | Examples of frequency spectra using the Fast Fourier Transform method for atrial **(A)** and ventricular **(B)** MAP recordings. Peaks for very low- **(C)**, low- **(D)** and high-frequency **(E)** for atrial and ventricular MAPs, and their percentage powers **(F–H)**.

Nevertheless, there was no difference in SD2/SD1 ratio (6.19 ± 3.03, $P > 0.05$). Moreover, approximate entropy (0.69 ± 0.27, $P > 0.05$), and sample entropy (0.75 ± 0.54, $P > 0.05$) were statistically indistinguishable when compared to the atrial parameters.

Detrended fluctuation analysis plotting the detrended fluctuations F(n) as a function of n in a log-log scale was performed for the atrial and ventricular MAPs (**Figures 6A,B**). This revealed short- (α1) and long-term (α2) fluctuation slopes of 1.80 ± 0.15 (**Figure 6C**) and 0.85 ± 0.29 (**Figure 6D**), respectively for the atria, which were not significantly different from the values obtained from the ventricles (1.32 ± 0.49 and 1.15 ± 0.28, respectively, both $P > 0.05$). α1 was significantly larger than α2 in the atria (ANOVA, $P < 0.001$) but not in the ventricles (ANOVA, $P > 0.05$).

The variability data for APD_{70}, APD_{50}, and APD_{30} are shown in **Supplementary Appendices 1–3**, respectively.

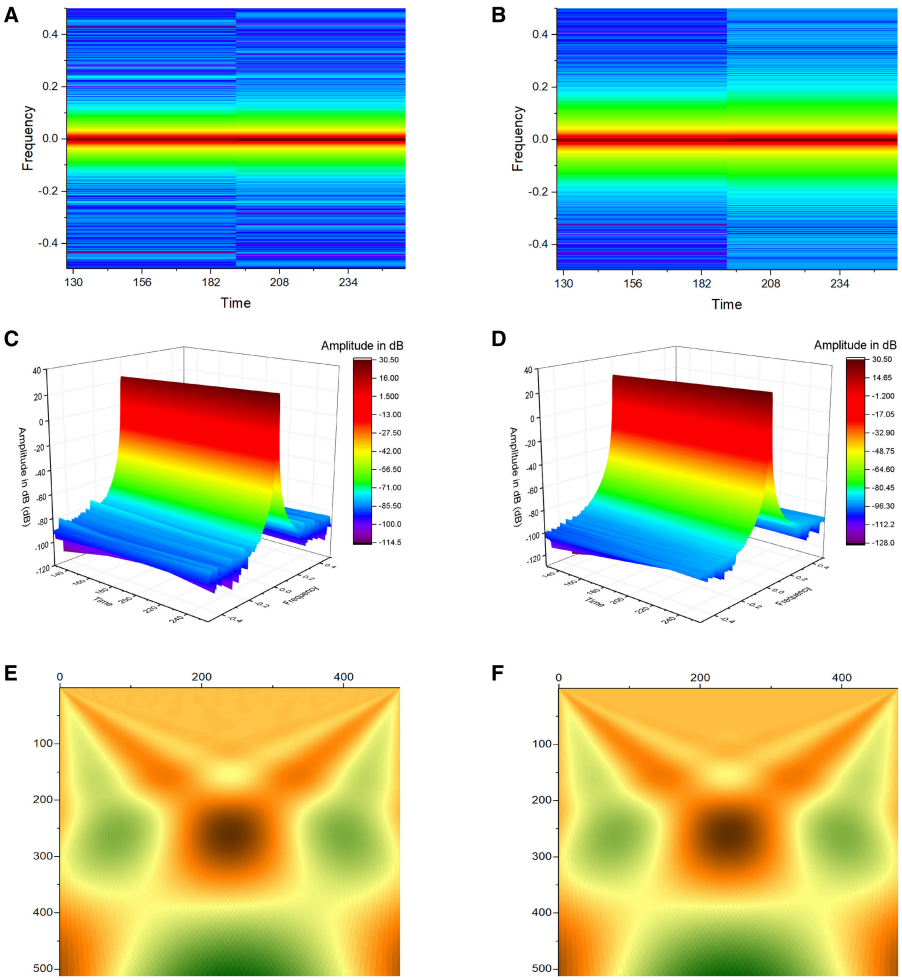

FIGURE 4 | Application of Short-Time Fourier Transform (STFT) yielded plots demonstrating frequency against time for atrial **(A)** and ventricular APD_{90} **(B)**, and their corresponding three-dimensional representations **(C,D)**. Continuous wavelet transform (CWT) with Morlet wavelets as basis functions of atrial **(E)** and ventricular APD_{90} **(F)**.

DISCUSSION

This is the first proof-of-concept study investigating the beat-to-beat variability in repolarization time-courses of atrial and ventricular MAP recordings in whole hearts of mice. The main findings are that (1) variability in APDs can be detected using time-domain, frequency-domain, combined time-frequency, and non-linear methods; (2) the atria and ventricles show similar low- and high-frequency peaks; (3) but the atria showed predominantly low-frequency components whereas the ventricles showed predominantly high-frequency components; (4) Poincaré plot showed ellipsoid shapes from all of the hearts; (5) the SD perpendicular to the line-of-identity (SD2) was significantly larger than the SD along the line-of-identity (SD1), leading to SD2/SD1 ratios greater than unity; (6) a degree of disorder was identified by approximate and sample entropy analyses, (7) short-term fluctuation slopes were steeper than long-term fluctuation slopes.

Variability in recorded signals is an intrinsic property of excitable media in biological systems. In the heart, heart rate variability (HRV) is normally observed in the healthy state (Shaffer and Ginsberg, 2017), whereas alterations in HRV have been associated with adverse outcomes such as arrhythmogenesis that may be mediated through generation of APD variability (Mcintyre et al., 2014). Similarly, beat-to-beat variability in the repolarization time-course can be present and can be observed electrocardiographically as QT interval variability (Baumert et al., 2016; Orini et al., 2016). Naturally occurring beat-to-beat variations in APDs have been observed in isolated cardiomyocytes (Kiyosue and Arita, 1989; Shryock et al., 2013), even when pacing rate and temperature are held constant (Zaniboni et al., 2000). It has been studied in detail in canine ventricular cardiomyocytes (Abi-Gerges et al., 2010; Kistamas et al., 2015a,b; Szentandrassy et al., 2015; Magyar et al., 2016), but never in mouse models whether in single cells or isolated hearts. Our study adds to the literature by demonstrating

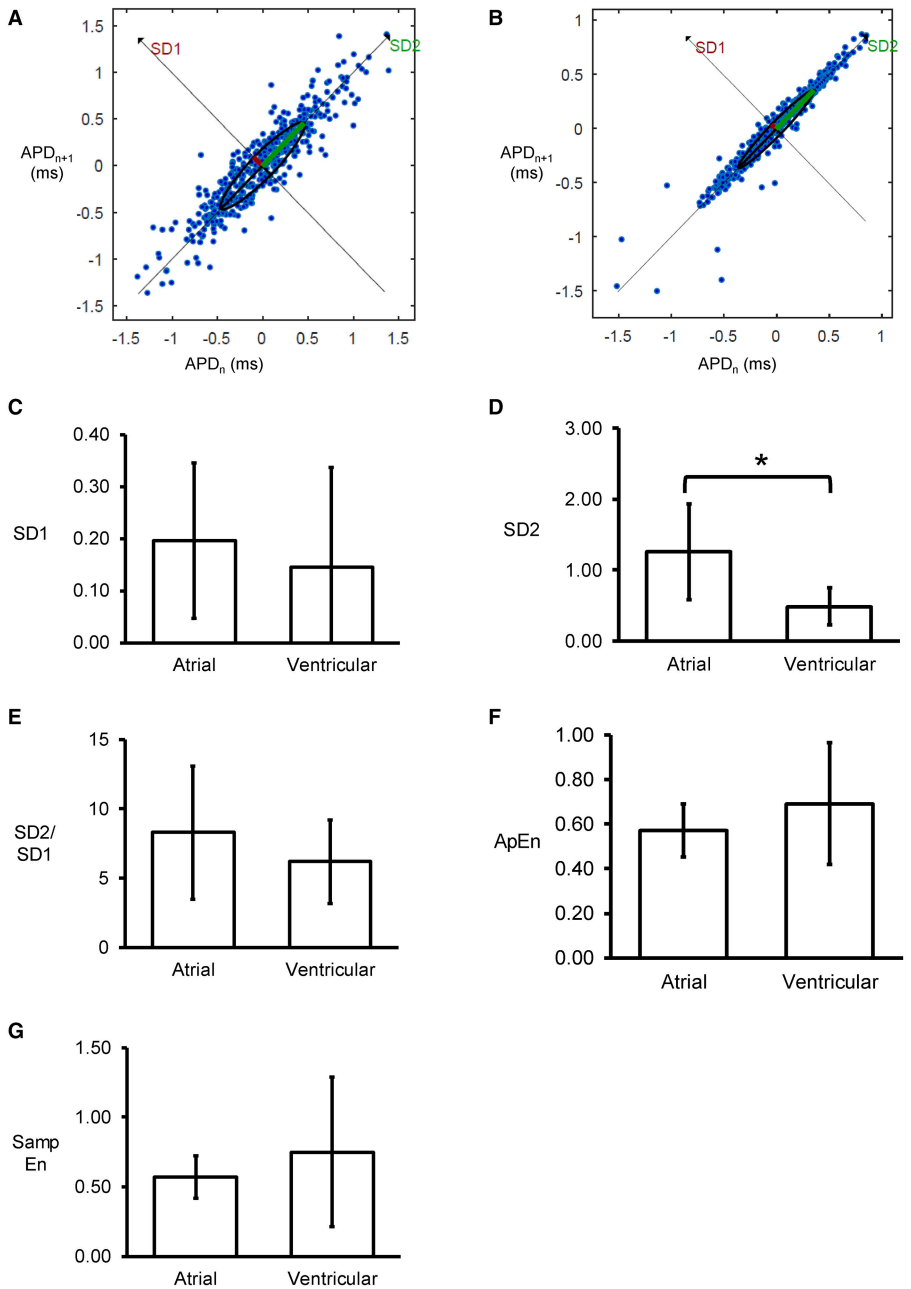

FIGURE 5 | Representative Poincaré plots of APD_{n+1} against APD_n from the left atrium **(A)** or left ventricle **(B)** from a single heart. SD along the line-of-identity (SD1) **(C)** and SD perpendicular to the line-of-identity (SD2) **(D)**, and the SD2/SD1 ratio **(E)**, approximate entropy **(F)**, and sample entropy **(G)** (*$P < 0.05$).

that such variabilities are also present in Langendorff-perfused mouse hearts under similar constant rate pacing conditions. Computational modeling has previously identified the molecular mechanisms underlying such beat-to-beat variability in APDs (Heijman et al., 2013). These include stochastic gating of ion channels, in particular that of sodium and delayed rectifier potassium channels. Although fluctuations in APDs was present in our experimental mouse model, the variability was very small, with standard deviation of around 1.4 ms for the atria and 0.2 ms for the ventricles. This may be due to the differing morphology of the cardiac action potentials in this species. Consistent with these findings, modeling studies suggests that variability is higher in species that have more pronounced plateau phase during repolarization, such as guinea pigs and rabbits (Heijman et al., 2013), than those with a triangular action potential morphology such as mice. Indeed, the standard deviation is around 10 ms in guinea pig ventricular cardiomyocytes (Zaniboni et al., 2000) and 7 ms in rabbit sinoatrial nodal cells (Wilders and Jongsma, 1993).

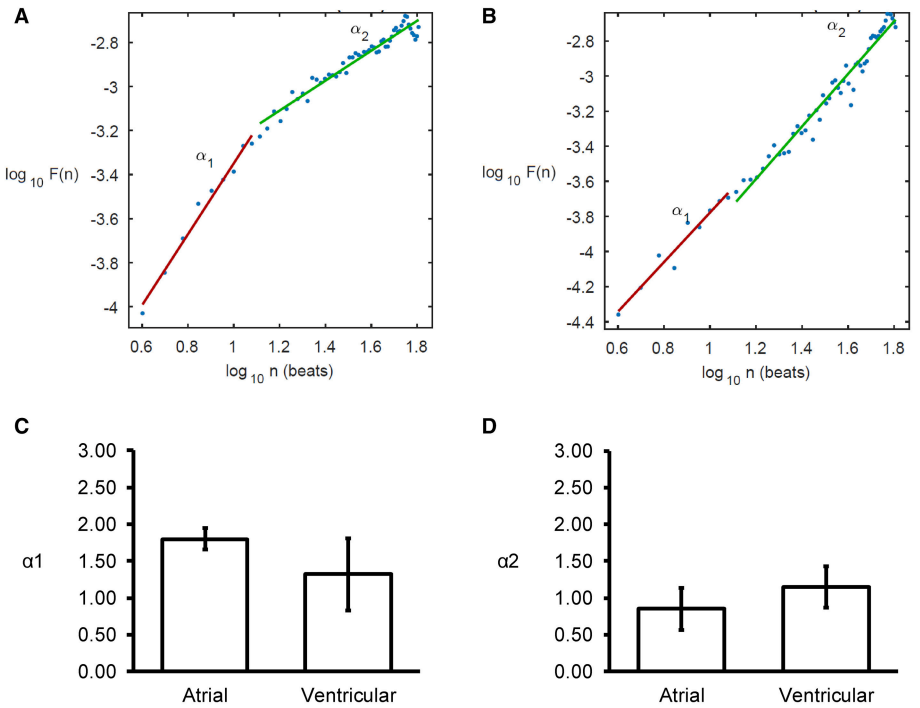

FIGURE 6 | Detrended fluctuation analysis (DFA) plots expressing detrended fluctuations F(n) as a function of n in a log-log scale for the atria **(A)** and ventricles **(B)**, yielding short-term **(C)**, and long-term **(D)** fluctuation slopes (α1 and α2, respectively).

This variability is dependent on the APD. Therefore, one way to express this is the coefficient of variation (CoV), given by the percentage of SD divided by the mean APD. The CoV is around 2% in both the guinea pig and the rabbit ventricles. From our study, we found CoV to be 4.0% in the atria and 0.8% in the ventricles. It should be noted that our model used intact hearts whereas single cells were used in the other studies. Multicellular preparations are known to show lower levels of variability than in single cells because of electrical coupling, which dampens the differences between cells (Magyar et al., 2015).

Time-domain analysis allowed the quantification of the variability using standard deviations, coefficients of variations and root mean squares of successive APDs in both the atria and ventricles. It was noted that atrial APDs were significantly shorter than ventricular APDs, in keeping with our previous findings (Tse et al., 2016a,b). Moreover, we report for the first time higher degrees of variability in the atria as reflected by higher mean SD, CoV and RMS of APDs when compared to the ventricles. Frequency-domain analysis using the Fast Fourier Transform-based method produced power spectrum density estimates for the APD_{90} time series. This provides the basic information on how power is distributed as a function of frequency. We observed that both atrial and ventricular MAPs were predominantly in the low-frequency domain. LF and HF rhythms in repolarization variability are important as they reflect QT rate adaptation (Merri et al., 1993). Variability assessed in the frequency domain represents an index of temporal dispersion of ventricular repolarization (Lombardi et al., 1998) which is an important determinant of arrhythmogenesis. However, the above frequency analysis does not provide any information on the time evolution of the frequencies. To achieve, this, time-frequency analysis was conducted using both short-time Fourier transform (STFT) and continuous wavelet transform (CWT). Previously, time-frequency analysis has been applied to electrograms to detect regional cardiac repolarization alternans that occur transiently (Orini et al., 2013, 2014).

Significantly, non-linear analyses of APDs yielded further insights. Thus, Poincaré plots of APDs showed ellipsoid shapes in all of the hearts studied, and together with a SD2/SD1 ratio > 1, indicated that variability in the long-term was greater than variability in the short-term. This ratio was around 6 to 8 and did not significantly differ between the atria and ventricles. In a canine model, higher short-term variability calculated from Poincaré plots being associated with the occurrence of drug-induced *torsade de pointes* (Thomsen et al., 2004). Furthermore, the present findings also found a degree of entropy present in the atria and ventricles. Entropy refers to the degree of disorder in a system and has been used to quantify the regularity or complexity of biological signals (Pincus, 1991; Pincus and Goldberger, 1994). These entropy calculations are based on the state space reconstruction of time series data (Richman and Moorman, 2000; Bandt and Pompe, 2002; Li et al., 2015). Our study quantified for the first time approximate entropy in the atria and ventricles. This is an appropriate method for time series with more than 50 points, a condition that we have satisfied (Pincus, 2001). Similar, this study determined sample entropy,

which is a refined version of approximate entropy. It can quantify the irregularity of APD time series without biasing (Richman and Moorman, 2000) and has the advantage of eliminating self-matches and being less dependent on time-series length (Li et al., 2009). Entropy has been identified as a pro-arrhythmic indicator (Cervigon et al., 2016). High entropy in repolarization was shown to predict arrhythmic or mortality outcomes in patients receiving implantable-cardioverter defibrillator for primary prevention of sudden cardiac death (Demazumder et al., 2016). Further studies are needed to confirm or refute the hypothesis that increased approximate or sample entropy predicts the onset of atrial or ventricular arrhythmias in mouse hearts. However, its use has some important limitations. For example, it should not be applied to long duration signals because more computations are required for real-time implementation (Tripathy et al., 2017).

Fractional calculus has been applied to investigate physiological time series such as heart rate variability (González et al., 2012; Sturmberg and West, 2013; Sturmberg et al., 2015). Some techniques assume stationary signals whilst others do not make such assumptions (Gao et al., 2013). This study applied for the first time detrended fluctuation analysis (DFA) to reveal complex fractal fluctuation patterns by delineating them into long- and short-term fluctuation for the first time in the mouse heart. DFA is a method for quantifying long-range correlations in non-stationary physiological time series (Peng et al., 1995). DFA enables correct estimation of the power law scaling, the Hurst exponent, in the presence of extrinsic non-stationaries while eliminating spurious detection of long-range dependence (West et al., 2008). The average fluctuation is plotted against the number of beats on a log-log scale, yielding short- and long-term fluctuation slopes, or scaling exponents (α1 and α2, respectively). α of 0.5 indicates uncorrelated data, and deviations from 0.5 indicates the presence of correlation. For example, in the atria, we found α1 to be around 1.7, suggesting the presence of short-term correlation, but α2 was around 0.7, suggesting the minimal long-term correlations. In the ventricles, α1 and α2 took similar values to those observed in the atria.

Previously, decreases in the short-term exponent of HRV, has been associated with arrhythmic and mortality outcomes in heart failure after acute myocardial infarction (Huikuri et al., 2000) and in end-stage renal failure patients receiving peritoneal dialysis (Chiang et al., 2016). Decreases in the short-term exponent have also been detected prior to the onset of atrial arrhythmias (Vikman et al., 1999). In a rabbit hypertrophic cardiomyopathy model, DFA of maximum QT intervals showed higher scaling exponent in diseased compared to control groups (Sanbe et al., 2005). In human induced pluripotent stem cell-derived cardiomyocytes, fractal correlations as determined by $\alpha 1$ was observed (Kuusela et al., 2016). In humans, a significant decrease in α1 was observed during sympathetic activation suggesting a breakdown of the short-term fractal organization of heart rate (Tulppo et al., 2005). Moreover, normal α1 but lower α2 was observed in patients with atrial fibrillation compared to those without AF (Kalisnik et al., 2015).

Previous work has demonstrated that HRV time series have a crossover phenomenon (Havlin et al., 1999; Penzel et al., 2003). In this study, DFA also found scaling trends with two distinct values. This is interesting because it may be related to bi-fractality, where fractal patterns can emerge from random fluctuations via allometric filtering mechanisms (Scafetta and West, 2007). Thus, APD time series are potentially crossover-fractals with two fractal dimensions. This could be validated by using empirical mode decomposition to construct crossover-fractals from two monofractals (Liaw and Chiu, 2010). However, although DFA is useful for exploring the structure of correlations in physiological time series, tracking the local evolution of the exponent by a recursive least-squares method can yield structures of correlations that can provide additional details on the dynamics of these series (Bojorges-Valdez et al., 2007). Our findings suggest that repolarization characteristics exhibit fractal behavior and may be better represented using concepts from fractional calculus, for example by using fractal dynamical equations (Marculescu and Bogdan, 2011). Such an approach has successfully been used to optimize control for implantable pacemakers (Bogdan et al., 2012, 2013).

Moreover, fractional differintegration was used to characterize HRV, allowing determination of the standard deviation of the fractionally differintegrated RR time series for a fractional differintegration of order α [SDFDINN(α)]. α_c, the order of the fractional differintegration that provide the minimum standard deviation of the fractionally differintegrated RR set, showed a linear correlation with the Hurst exponent. Interestingly this method for estimating the exponent showed less bias and lower variance when compared to DFA (García-González et al., 2013). Also, α_c was closely related to α_1 but they were not equal. Future studies are needed to explore the predictive values of these fluctuation exponents, and to evaluate the efficacy of fractal dynamical state equation to describe the spatial and temporal dependency structure of repolarization properties in mouse models of cardiac arrhythmias (Xue and Bogdan, 2017).

CONCLUSIONS

The present findings provide a proof-of-concept that APD variability is present at baseline conditions and can be detected using time-domain, frequency-domain and non-linear techniques. Atrial MAPs showed greater degree of variability than ventricular MAPs. Non-linear techniques offer further insights on short-term and long-term variability and signal complexity.

AUTHOR CONTRIBUTIONS

GT: study conception, data analysis and interpretation, manuscript drafting, critical revision of manuscript. YD, FC, TL, GH, KHCL, GL, GB, and SC: data interpretation, critical revision of manuscript. KL, WKW, and WTW: study supervision, data interpretation, critical revision of manuscript.

FUNDING

The Biotechnology and Biological Sciences Research Council (GT). Economic and Social Research Council (FC). The National

Nature Science Foundation of China (No. 81470421 and No. 81770328 to YD).

ACKNOWLEDGMENTS

GT received research funding from the BBSRC for this research and is currently supported by a Clinical Assistant Professorship from the Croucher Foundation of Hong Kong. WTW is supported by the Direct Grant for Research from the Research Committee of the Chinese University of Hong Kong, China. YD is supported by the National Nature Science Foundation of China (No. 81470421 and No. 81770328).

SUPPLEMENTARY MATERIAL

The Supplementary Material for this article can be found online at: https://www.frontiersin.org/articles/10.3389/fphys.2018.01578/full#supplementary-material

REFERENCES

Abi-Gerges, N., Valentin, J. P., and Pollard, C. E. (2010). Dog left ventricular midmyocardial myocytes for assessment of drug-induced delayed repolarization: short-term variability and proarrhythmic potential. *Br. J. Pharmacol.* 159, 77–92. doi: 10.1111/j.1476-5381.2009.00338.x

Bandt, C., and Pompe, B. (2002). Permutation entropy: a natural complexity measure for time series. *Phys. Rev. Lett.* 88:174102. doi: 10.1103/PhysRevLett.88.174102

Baumert, M., Porta, A., Vos, M. A., Malik, M., Couderc, J.-P., Laguna, P., et al. (2016). QT interval variability in body surface ECG: measurement, physiological basis, and clinical value: position statement and consensus guidance endorsed by the European Heart Rhythm Association jointly with the ESC working group on cardiac cellular electrophysiology. *Europace* 18, 925–944. doi: 10.1093/europace/euv405

Bogdan, P., Jain, S., Goyal, K., and Marculescu, R. (2012). "Implantable pacemakers control and optimization via fractional calculus approaches: a cyber-physical systems perspective," in 2012 *IEEE/ACM Third International Conference on Cyber-Physical Systems* (Beijing), 23–32. doi: 10.1109/ICCPS.2012.11

Bogdan, P., Jain, S., and Marculescu, R. (2013). Pacemaker control of heart rate variability: a cyber physical system perspective. *ACM Trans. Embed. Comput. Syst.* 12, 1–22. doi: 10.1145/2435227.2435246

Bojorges-Valdez, E. R., Echeverría, J. C., Valdés-Cristerna, R., and Peña, M. A. (2007). Scaling patterns of heart rate variability data. *Physiol. Meas.* 28, 721–730. doi: 10.1088/0967-3334/28/6/010

Cervigon, R., Moreno, J., Garcia-Quintanilla, J., Perez-Villacastin, J., and Castells, F. (2016). Entropy at the right atrium as a predictor of atrial fibrillation recurrence outcome after pulmonary vein ablation. *Biomed. Tech.* 61, 29–36. doi: 10.1515/bmt-2014-0172

Chiang, J.-Y., Huang, J.-W., Lin, L.-Y., Chang, C.-H., Chu, F.-Y., Lin, Y.-H., et al. (2016). Detrended fluctuation analysis of heart rate dynamics is an important prognostic factor in patients with end-stage renal disease receiving peritoneal dialysis. *PLoS ONE* 11:e0147282. doi: 10.1371/journal.pone.0147282

Choy, L., Yeo, J. M., Tse, V., Chan, S. P., and Tse, G. (2016). Cardiac disease and arrhythmogenesis: mechanistic insights from mouse models. *Int. J. Cardiol. Heart Vasc.* 12, 1–10. doi: 10.1016/j.ijcha.2016.05.005

Demazumder, D., Limpitikul, W. B., Dorante, M., Dey, S., Mukhopadhyay, B., Zhang, Y., et al. (2016). Entropy of cardiac repolarization predicts ventricular arrhythmias and mortality in patients receiving an implantable cardioverter-defibrillator for primary prevention of sudden death. *EP Europace* 18, 1818–1828. doi: 10.1093/europace/euv399

Fabritz, L., Kirchhof, P., Franz, M. R., Eckardt, L., Mönnig, G., Milberg, P., et al. (2003). Prolonged action potential durations, increased dispersion of repolarization, and polymorphic ventricular tachycardia in a mouse model of proarrhythmia. *Basic Res. Cardiol.* 98, 25–32. doi: 10.1007/s00395-003-0386-y

Gao, J., Gurbaxani, B., Hu, J., Heilman, K., Emauele, V., Lewis, G., et al. (2013). Multiscale analysis of heart rate variability in non-stationary environments. *Front. Physiol.* 4:119. doi: 10.3389/fphys.2013.00119

García-González, M. A., Fernández-Chimeno, M., Capdevila, L., Parrado, E., and Ramos-Castro, J. (2013). An application of fractional differintegration to heart rate variability time series. *Comput. Methods Programs Biomed.* 111, 33–40. doi: 10.1016/j.cmpb.2013.02.009

González, M. A. G., Castro, J. J. R., and Fernández-Chimeno, M. (2012). "A novel index based on fractional calculus to assess the dynamics of heart rate variability: changes due to Chi or Yoga meditations," in 2012 *Computing in Cardiology* (Krakow), 925–928.

Gussak, I., Chaitman, B. R., Kopecky, S. L., and Nerbonne, J. M. (2000). Rapid ventricular repolarization in rodents: electrocardiographic manifestations, molecular mechanisms, and clinical insights. *J. Electrocardiol.* 33, 159–170. doi: 10.1016/S0022-0736(00)80072-2

Havlin, S., Amaral, L. A. N., Ashkenazy, Y., Goldberger, A. L., Ivanov, P. C., and Stanley, H. E. (1999). Application of statistical physics to heartbeat diagnosis. *Physica A Stat. Mech. Appl.* 274, 99–110. doi: 10.1016/S0378-4371(99)00333-7

Heijman, J., Zaza, A., Johnson, D. M., Rudy, Y., Peeters, R. L., Volders, P. G., et al. (2013). Determinants of beat-to-beat variability of repolarization duration in the canine ventricular myocyte: a computational analysis. *PLoS Comput. Biol.* 9:e1003202. doi: 10.1371/journal.pcbi.1003202

Hinterseer, M., Beckmann, B. M., Thomsen, M. B., Pfeufer, A., Dalla Pozza, R., Loeff, M., et al. (2009). Relation of increased short-term variability of QT interval to congenital long-QT syndrome. *Am. J. Cardiol.* 103, 1244–1248. doi: 10.1016/j.amjcard.2009.01.011

Hinterseer, M., Beckmann, B. M., Thomsen, M. B., Pfeufer, A., Ulbrich, M., Sinner, M. F., et al. (2010). Usefulness of short-term variability of QT intervals as a predictor for electrical remodeling and proarrhythmia in patients with nonischemic heart failure. *Am. J. Cardiol.* 106, 216–220. doi: 10.1016/j.amjcard.2010.02.033

Huikuri, H. V., Makikallio, T. H., Peng, C. K., Goldberger, A. L., Hintze, U., and Moller, M. (2000). Fractal correlation properties of R-R interval dynamics and mortality in patients with depressed left ventricular function after an acute myocardial infarction. *Circulation* 101, 47–53. doi: 10.1161/01.CIR.101.1.47

Kalisnik, J. M., Hrovat, E., Hrastovec, A., Avbelj, V., Zibert, J., and Gersak, B. (2015). Severe cardiac autonomic derangement and altered ventricular repolarization pave the way to postoperative atrial fibrillation. *Innovations* 10, 398–405. doi: 10.1097/IMI.0000000000000203

Kistamas, K., Hegyi, B., Vaczi, K., Horvath, B., Banyasz, T., Magyar, J., et al. (2015a). Oxidative shift in tissue redox potential increases beat-to-beat variability of action potential duration. *Can. J. Physiol. Pharmacol.* 93, 563–568. doi: 10.1139/cjpp-2014-0531

Kistamas, K., Szentandrassy, N., Hegyi, B., Vaczi, K., Ruzsnavszky, F., Horvath, B., et al. (2015b). Changes in intracellular calcium concentration influence beat-to-beat variability of action potential duration in canine ventricular myocytes. *J. Physiol. Pharmacol.* 66, 73–81. Available online at: https://pdfs.semanticscholar.org/9776/967cc719dbcc52982ac82cc3f400074aa601.pdf

Kiyosue, T., and Arita, M. (1989). Late sodium current and its contribution to action potential configuration in guinea pig ventricular myocytes. *Circ. Res.* 64, 389–397. doi: 10.1161/01.RES.64.2.389

Knollmann, B. C., Katchman, A. N., and Franz, M. R. (2001). Monophasic action potential recordings from intact mouse heart: validation, regional heterogeneity, and relation to refractoriness. *J. Cardiovasc. Electrophysiol.* 12, 1286–1294. doi: 10.1046/j.1540-8167.2001.01286.x

Kuusela, J., Kim, J., Rasanen, E., and Aalto-Setala, K. (2016). The effects of pharmacological compounds on beat rate variations in human long QT-syndrome cardiomyocytes. *Stem Cell Rev.* 12, 698–707. doi: 10.1007/s12015-016-9686-0

Li, H., Han, W., Hu, C., and Meng, M. Q. H. (2009). "Detecting ventricular fibrillation by fast algorithm of dynamic sample entropy," in 2009 *IEEE International Conference on Robotics and Biomimetics (ROBIO)* (Guilin), 1105–1110.

Li, P., Liu, C., Li, K., Zheng, D., Liu, C., and Hou, Y. (2015). Assessing the complexity of short-term heartbeat interval series by distribution entropy. *Med. Biol. Eng. Comput.* 53, 77–87. doi: 10.1007/s11517-014-1216-0

Liaw, S.-S., and Chiu, F.-Y. (2010). Constructing crossover-fractals using intrinsic mode functions. *Adv. Adapt. Data Anal.* 2, 509–520. doi: 10.1142/S1793536910000598

Lombardi, F., Colombo, A., Porta, A., Baselli, G., Cerutti, S., and Fiorentini, C. (1998). Assessment of the coupling between RTapex and RR interval as an index of temporal dispersion of ventricular repolarization. *Pacing Clin. Electrophysiol.* 21, 2396–2400. doi: 10.1111/j.1540-8159.1998.tb01189.x

Magyar, J., Banyasz, T., Szentandrassy, N., Kistamas, K., Nanasi, P. P., and Satin, J. (2015). Role of gap junction channel in the development of beat-to-beat action potential repolarization variability and arrhythmias. *Curr. Pharm. Des.* 21, 1042–1052. doi: 10.2174/1381612820666141029102443

Magyar, J., Kistamas, K., Vaczi, K., Hegyi, B., Horvath, B., Banyasz, T., et al. (2016). Concept of relative variability of cardiac action potential duration and its test under various experimental conditions. *Gen. Physiol. Biophys.* 35, 55–62. doi: 10.4149/gpb_2015019

Marculescu, R., and Bogdan, P. (2011). Cyberphysical systems: workload modeling and design optimization. *IEEE Design Test Comput.* 28, 78–87. doi: 10.1109/MDT.2010.142

Mcintyre, S. D., Kakade, V., Mori, Y., and Tolkacheva, E. G. (2014). Heart rate variability and alternans formation in the heart: the role of feedback in cardiac dynamics. *J. Theor. Biol.* 350, 90–97. doi: 10.1016/j.jtbi.2014.02.015

Merri, M., Alberti, M., and Moss, A. J. (1993). Dynamic analysis of ventricular repolarization duration from 24-hour Holter recordings. *IEEE Trans. Biomed. Eng.* 40, 1219–1225. doi: 10.1109/10.250577

Mesin, L. (2018). Estimation of complexity of sampled biomedical continuous time signals using approximate entropy. *Front. Physiol.* 9:710. doi: 10.3389/fphys.2018.00710

Molina-Pico, A., Cuesta-Frau, D., Aboy, M., Crespo, C., Miro-Martinez, P., and Oltra-Crespo, S. (2011). Comparative study of approximate entropy and sample entropy robustness to spikes. *Artif. Intell. Med.* 53, 97–106. doi: 10.1016/j.artmed.2011.06.007

Nanasi, P. P., Magyar, J., Varro, A., and Ordog, B. (2017). Beat-to-beat variability of cardiac action potential duration: underlying mechanism and clinical implications. *Can. J. Physiol. Pharmacol.* 95, 1230–1235. doi: 10.1139/cjpp-2016-0597

Nayak, S. K., Bit, A., Dey, A., Mohapatra, B., and Pal, K. (2018). A review on the nonlinear dynamical system analysis of electrocardiogram signal. *J. Healthc. Eng.* 2018:6920420. doi: 10.1155/2018/6920420

Nerbonne, J. M. (2014). Mouse models of arrhythmogenic cardiovascular disease: challenges and opportunities. *Curr. Opin. Pharmacol.* 15, 107–114. doi: 10.1016/j.coph.2014.02.003

Niemeijer, M. N., Van Den Berg, M. E., Eijgelsheim, M., Van Herpen, G., Stricker, B. H., Kors, J. A., et al. (2014). Short-term QT variability markers for the prediction of ventricular arrhythmias and sudden cardiac death: a systematic review. *Heart* 100, 1831–1836. doi: 10.1136/heartjnl-2014-305671

Orini, M., Hanson, B., Monasterio, V., Martinez, J. P., Hayward, M., Taggart, P., et al. (2014). Comparative evaluation of methodologies for T-wave alternans mapping in electrograms. *IEEE Trans. Biomed. Eng.* 61, 308–316. doi: 10.1109/TBME.2013.2289304

Orini, M., Hanson, B., Taggart, P., and Lambiase, P. (2013). Detection of transient, regional cardiac repolarization alternans by time-frequency analysis of synthetic electrograms. *Conf. Proc. IEEE Eng. Med. Biol. Soc.* 2013, 3773–3776. doi: 10.1109/EMBC.2013.6610365

Orini, M., Taggart, P., and Lambiase, P. D. (2016). "A multivariate time-frequency approach for tracking QT variability changes unrelated to heart rate variability," in 2016 38*th Annual International Conference of the IEEE Engineering in Medicine and Biology Society (EMBC)* (Orlando, FL), 924–927.

Peng, C. K., Havlin, S., Stanley, H. E., and Goldberger, A. L. (1995). Quantification of scaling exponents and crossover phenomena in nonstationary heartbeat time series. *Chaos* 5, 82–87. doi: 10.1063/1.166141

Penzel, T., Kantelhardt, J. W., Grote, L., Peter, J. H., and Bunde, A. (2003). Comparison of detrended fluctuation analysis and spectral analysis for heart rate variability in sleep and sleep apnea. *IEEE Trans. Biomed. Eng.* 50, 1143–1151. doi: 10.1109/TBME.2003.817636

Phadumdeo, V. M., and Weinberg, S. H. (2018). Heart rate variability alters cardiac repolarization and electromechanical dynamics. *J. Theor. Biol.* 442, 31–43. doi: 10.1016/j.jtbi.2018.01.007

Pincus, S. M. (1991). Approximate entropy as a measure of system complexity. *Proc. Natl. Acad. Sci. U.S.A.* 88, 2297–2301. doi: 10.1073/pnas.88.6.2297

Pincus, S. M. (2001). Assessing serial irregularity and its implications for health. *Ann. N. Y. Acad. Sci.* 954, 245–267. doi: 10.1111/j.1749-6632.2001.tb02755.x

Pincus, S. M., and Goldberger, A. L. (1994). Physiological time-series analysis: what does regularity quantify? *Am. J. Physiol.* 266, H1643–H1656.

Richman, J. S., and Moorman, J. R. (2000). Physiological time-series analysis using approximate entropy and sample entropy. *Am. J. Physiol. Heart Circ. Physiol.* 278, H2039–H2049. doi: 10.1152/ajpheart.2000.278.6.H2039

Sanbe, A., James, J., Tuzcu, V., Nas, S., Martin, L., Gulick, J., et al. (2005). Transgenic rabbit model for human troponin I-based hypertrophic cardiomyopathy. *Circulation* 111, 2330–2338. doi: 10.1161/01.CIR.0000164234.24957.75

Scafetta, N., and West, B. J. (2007). Emergence of bi-fractal time series from noise via allometric filters. *EPL* 79:30003. doi: 10.1209/0295-5075/79/30003

Shaffer, F., and Ginsberg, J. P. (2017). An overview of heart rate variability metrics and norms. *Front. Pub. Health* 5:258. doi: 10.3389/fpubh.2017.00258

Shryock, J. C., Song, Y., Rajamani, S., Antzelevitch, C., and Belardinelli, L. (2013). The arrhythmogenic consequences of increasing late INa in the cardiomyocyte. *Cardiovasc. Res.* 99, 600–611. doi: 10.1093/cvr/cvt145

Sturmberg, J. P., Bennett, J. M., Picard, M., and Seely, A. J. E. (2015). The trajectory of life. Decreasing physiological network complexity through changing fractal patterns. *Front. Physiol.* 6:169. doi: 10.3389/fphys.2015.00169

Sturmberg, J. P., and West, B. J. (2013). "Fractals in physiology and medicine," in *Handbook of Systems and Complexity in Health,* eds J. P. Sturmberg and C. M. Martin (New York, NY: Springer New York), 171–192. doi: 10.1007/978-1-4614-4998-0_11

Szentandrassy, N., Kistamas, K., Hegyi, B., Horvath, B., Ruzsnavszky, F., Vaczi, K., et al. (2015). Contribution of ion currents to beat-to-beat variability of action potential duration in canine ventricular myocytes. *Pflugers Arch.* 467, 1431–1443. doi: 10.1007/s00424-014-1581-4

Thomsen, M. B., Verduyn, S. C., Stengl, M., Beekman, J. D., De Pater, G., Van Opstal, J., et al. (2004). Increased short-term variability of repolarization predicts d-sotalol-induced torsades de pointes in dogs. *Circulation* 110, 2453–2459. doi: 10.1161/01.CIR.0000145162.64183.C8

Tripathy, R. K., Deb, S., and Dandapat, S. (2017). Analysis of physiological signals using state space correlation entropy. *Healthcare Technol. Lett.* 4, 30–33. doi: 10.1049/htl.2016.0065

Tse, G., Liu, T., Li, G., Keung, W., Yeo, J. M., Fiona Chan, Y. W., et al. (2017). Effects of pharmacological gap junction and sodium channel blockade on S1S2 restitution properties in Langendorff-perfused mouse hearts. *Oncotarget* 8, 85341–85352. doi: 10.18632/oncotarget.19675

Tse, G., Sun, B., Wong, S. T., Tse, V., and Yeo, J. M. (2016a). Anti-arrhythmic effects of hypercalcemia in hyperkalemic, Langendorff-perfused mouse hearts. *Biomed. Rep.* 5, 301–310. doi: 10.3892/br.2016.735

Tse, G., Tse, V., Yeo, J. M., and Sun, B. (2016b). Atrial anti-arrhythmic effects of heptanol in langendorff-perfused mouse hearts. *PLoS ONE* 11:e0148858. doi: 10.1371/journal.pone.0148858

Tse, G., Wong, S. T., Tse, V., and Yeo, J. M. (2016c). Monophasic action potential recordings: which is the recording electrode? *J. Basic Clin. Physiol. Pharmacol.* 27, 457–462. doi: 10.1515/jbcpp-2016-0007

Tse, G., Yeo, J. M., Tse, V., Kwan, J., and Sun, B. (2016d). Gap junction inhibition by heptanol increases ventricular arrhythmogenicity by reducing conduction velocity without affecting repolarization properties or myocardial refractoriness in Langendorff-perfused mouse hearts. *Mol. Med. Rep.* 14, 4069–4074. doi: 10.3892/mmr.2016.5738

Tulppo, M. P., Kiviniemi, A. M., Hautala, A. J., Kallio, M., Seppanen, T., Makikallio, T. H., et al. (2005). Physiological background of the loss of fractal heart rate dynamics. *Circulation* 112, 314–319. doi: 10.1161/CIRCULATIONAHA.104.523712

Vikman, S., Makikallio, T. H., Yli-Mayry, S., Pikkujamsa, S., Koivisto, A. M., Reinikainen, P., et al. (1999). Altered complexity and correlation properties

of R-R interval dynamics before the spontaneous onset of paroxysmal atrial fibrillation. *Circulation* 100, 2079–2084. doi: 10.1161/01.CIR.100.20.2079

West, B. J., Geneston, E. L., and Grigolini, P. (2008). Maximizing information exchange between complex networks. *Phys. Rep.* 468, 1–99. doi: 10.1016/j.physrep.2008.06.003

Wilders, R., and Jongsma, H. J. (1993). Beating irregularity of single pacemaker cells isolated from the rabbit sinoatrial node. *Biophys. J.* 65, 2601–2613. doi: 10.1016/S0006-3495(93)81289-X

Xue, Y., and Bogdan, P. (2017). "Constructing compact causal mathematical models for complex dynamics," in *Proceedings of the 8th International Conference on Cyber-Physical Systems* (Pittsburgh, PA: ACM). doi: 10.1145/3055004.3055017

Zaniboni, M., Pollard, A. E., Yang, L., and Spitzer, K. W. (2000). Beat-to-beat repolarization variability in ventricular myocytes and its suppression by electrical coupling. *Am. J. Physiol. Heart Circ. Physiol.* 278, H677–H687. doi: 10.1152/ajpheart.2000.278.3.H677

Conflict of Interest Statement: The authors declare that the research was conducted in the absence of any commercial or financial relationships that could be construed as a potential conflict of interest.

frontiers in Physiology

ORIGINAL RESEARCH
published: 30 November 2018
doi: 10.3389/fphys.2018.01704

Multifractal Dynamic Functional Connectivity in the Resting-State Brain

*Frigyes Samuel Racz, Orestis Stylianou, Peter Mukli and Andras Eke**

Department of Physiology, Semmelweis University, Budapest, Hungary

Assessing the functional connectivity (FC) of the brain has proven valuable in enhancing our understanding of brain function. Recent developments in the field demonstrated that FC fluctuates even in the resting state, which has not been taken into account by the widely applied static approaches introduced earlier. In a recent study using functional near-infrared spectroscopy (fNIRS) global dynamic functional connectivity (DFC) has also been found to fluctuate according to scale-free i.e., fractal dynamics evidencing the true multifractal (MF) nature of DFC in the human prefrontal cortex. Expanding on these findings, we performed electroencephalography (EEG) measurements in 14 regions over the whole cortex of 24 healthy, young adult subjects in eyes open (EO) and eyes closed (EC) states. We applied dynamic graph theoretical analysis to capture DFC by computing the pairwise time-dependent synchronization between brain regions and subsequently calculating the following dynamic graph topological measures: Density, Clustering Coefficient, and Efficiency. We characterized the dynamic nature of these global network metrics as well as local individual connections in the networks using focus-based multifractal time series analysis in all traditional EEG frequency bands. Global network topological measures were found fluctuating–albeit at different extent–according to true multifractal nature in all frequency bands. Moreover, the monofractal Hurst exponent was found higher during EC than EO in the alpha and beta bands. Individual connections showed a characteristic topology in their fractal properties, with higher autocorrelation owing to short-distance connections–especially those in the frontal and pre-frontal cortex–while long-distance connections linking the occipital to the frontal and pre-frontal areas expressed lower values. The same topology was found with connection-wise multifractality in all but delta band connections, where the very opposite pattern appeared. This resulted in a positive correlation between global autocorrelation and connection-wise multifractality in the higher frequency bands, while a strong anticorrelation in the delta band. The proposed analytical tools allow for capturing the fine details of functional connectivity dynamics that are evidently present in DFC, with the presented results implying that multifractality is indeed an inherent property of both global and local DFC.

Keywords: functional connectivity, dynamic functional connectivity, multifractal analyses, brain, synchronization likelihood (SL), self-organized criticality (SOC), electroencephalography (EEG)

OPEN ACCESS

Edited by:
Plamen Ch. Ivanov,
Boston University, United States

Reviewed by:
Chengyu Huo,
Changshu Institute of Technology, China
Sebastiano Stramaglia,
Università degli Studi di Bari, Italy

****Correspondence:***
Andras Eke
eke.andras@med.semmelweis-univ.hu

Specialty section:
This article was submitted to Fractal Physiology, a section of the journal Frontiers in Physiology

Received: *19 July 2018*
Accepted: *12 November 2018*
Published: *30 November 2018*

Citation:
Racz FS, Stylianou O, Mukli P and Eke A (2018) Multifractal Dynamic Functional Connectivity in the Resting-State Brain. Front. Physiol. 9:1704. doi: 10.3389/fphys.2018.01704

INTRODUCTION

Functions of the brain emerge from dynamic interactions between the elements of its complex neuronal networks (Chialvo, 2010; Werner, 2010). This phenomenon is present across a broad range of spatial scales from the microanatomical level of individual neurons through neuronal cell assemblies to macroanatomical brain regions (Sporns, 2011). Pioneering works by Friston et al. (1993) and Biswal et al. (1995) paved the way to the emergence of a new field of neuroscience aiming at describing brain function through its anatomical and functional connectivity (FC) (Sporns et al., 2005; van den Heuvel and Hulshoff Pol, 2010; Friston, 2011). The key concept underlying the latter is assessing the statistical interdependence of neural activity registered at disparate regions of the brain, as it is assumed to be proportional to the degree of their functional cooperation (Friston et al., 1993). FC studies did not only reveal the existence of several resting-state brain networks such as the default mode network (Raichle et al., 2001; Greicius et al., 2003) or the task-positive network (Fox et al., 2005), but also showed that FC properties responded to changes in physiological conditions e.g., sleep (Horovitz et al., 2009; Liu et al., 2015) or cognitive stimulation (Esposito et al., 2006; Racz et al., 2017). In addition, altered FC was also found in pathological conditions like those in degenerative dementias (Pievani et al., 2011), schizophrenia (Liu et al., 2008), or multiple sclerosis (Cader et al., 2006).

Until recently, most studies typically considered connections in functional networks and thus FC itself, too, as being stationary despite the fact that a dynamic approach might provide a more detailed and more realistic description of brain connectivity (Hutchison et al., 2013a). Indeed it has been shown that FC dynamically fluctuates even in the resting state (Chang and Glover, 2010) and also during task modulation (Sakoglu et al., 2010). Since then, investigating dynamic functional connectivity (DFC) has become one of the most rapidly evolving fields of neuroscience with a steadily expanding body of literature (Hutchison et al., 2013a; Calhoun et al., 2014; Preti et al., 2017).

In FC studies most often functional magnetic resonance imaging (fMRI) is used to monitor brain activity with high spatial resolution and precise anatomical localization (Hutchison et al., 2013a; Preti et al., 2017). Fluctuations in FC are usually captured with a sliding-window (SW) approach, however other approaches such as point process analysis (Tagliazucchi et al., 2012a) or paradigm free mapping (Gaudes et al., 2013) have also been presented. During SW analysis, FC is calculated from a small data segment (i.e., within the actual window), then the window is advanced by a predefined time step and the process is repeated until the whole signal is covered. To assess FC within the actual window, statistical interdependence is usually estimated by bivariate statistical methods as Pearson-correlation (Hutchison et al., 2013b), but multivariate methods such as spatial independent component analysis (Allen et al., 2014) or time-frequency methods (Chang and Glover, 2010) are also often used. DFC is then described through–including but not limited to–properties such as the number of stable global states, their variability, and transition probabilities (Allen et al., 2014; Calhoun et al., 2014; Damaraju et al., 2014). As graph theory provides a useful tool in characterizing complex networks of the brain (Bullmore and Sporns, 2009) along several topological aspects (Rubinov and Sporns, 2010), dynamic graph theoretical analysis is also frequently applied (Tagliazucchi et al., 2012b; Yu et al., 2015; Du et al., 2016; Racz et al., 2018). Finally, some DFC studies focus–instead of on global network topology–only on one or a few individual connections between specific regions (Rack-Gomer and Liu, 2012) or intrinsic connectivity networks (Chang and Glover, 2010; Allen et al., 2014). The fluctuating nature of DFC is then usually captured in measures such as standard deviation (Kucyi and Davis, 2014; Falahpour et al., 2016) or coefficient of variation (Gonzalez-Castillo et al., 2014), however these descriptive measures may be insensitive to finer temporal structuring, which may well be present in DFC.

Although large-scale DFC attracted increasing attention only recently, the dynamic nature of the functional coupling between neuronal cell assemblies had been addressed earlier (Friston, 2000). In fact, functional connectivity for modalities like electroencephalography (EEG) and magnetoencephalography (MEG) was reported having non-linear characteristics (Stam and van Dijk, 2002; Stam et al., 2003). Also, it was shown that several properties of DFC did not have a characteristic time-scale, instead they showed *scale-free* (fractal) dynamics; Gong et al. (2003) presented that fluctuations in phase synchronization between brain regions were scale-free with the characterizing exponent being stable across multiple subjects. Stam and de Bruin (2004) investigated DFC in terms of global synchronization and found that in the alpha and beta bands it scaled with a higher exponent with eyes closed than open. EEG microstates—periods where EEG topography remains constant for 80–120 ms (Lehmann et al., 1987)—also exhibited fractal dynamics as reported by Van de Ville et al. (2010). While these studies evidenced fine, complex temporal structuring present in functional connectivity dynamics both on global (state) and local (individual connection) levels, to the best of our knowledge still only a few studies investigated the scale-free nature of DFC.

Global scale-free (i.e., monofractal) behavior is most commonly characterized by the Hurst exponent (H) in the time-, and by the negative power spectral slope (i.e., scaling exponent, β) in the frequency domain (Eke et al., 2000, 2002). H and β are inherently interrelated (Eke et al., 2002) as they both characterize the global long-range correlation (LRC) in a signal. This is established by the Wiener-Khinchin theorem stating that the power spectrum is equivalent to the Fourier-transform of the linear autocorrelation function (Kantz and Schreiber, 2004). Describing dynamics through only H or β implicitly assumes that frequency components of the power spectrum are independent/random, and information encoded in the phase angles is not considered. According to the definition by Schreiber and Schmitz (2000) this property holds only for linear dynamics. As mentioned above, functional connections in the brain has been shown to be non-linear, which calls for more in-depth analysis techniques capable of providing a detailed-enough description of their dynamic characteristics. At this end, *multifractal* analysis considers scaling as a local instead of a global property of the signal (Mandelbrot, 1986; Tel, 1988; Theiler,

1990), yielding a set of exponents characterizing the scaling in the signal (Kantelhardt et al., 2002; Barunik and Kristoufek, 2010). Moreover, using the method of decomposing a signal into the sign and magnitude time series of its increments (Ashkenazy et al., 2001), it has been shown that multifractal properties of a signal correlated well with its degree of non-linearity (Ashkenazy et al., 2003; Gomez-Extremera et al., 2016; Bernaola-Galvan et al., 2017). Since the seminal work of Ivanov et al. (1999), a diverse set of physiological processes were shown to exhibit multifractal dynamics such as human heart rate variability (Ivanov et al., 2001; Ashkenazy et al., 2003), motor coordination (Ihlen and Vereijken, 2013) or gait dynamics (Ashkenazy et al., 2002). Multifractal analysis of human heartbeat dynamics was also able to capture the separate effects of sympathetic and parasympathetic blockade (Nunes Amaral et al., 2001) as well as reveal the impact of congestive heart failure as the loss of multifractality, substantiating future clinical and diagnostic applications (Ivanov et al., 1999, 2001, 2004). The multifractal nature of neural dynamics was also reported using several different modalities (Shimizu et al., 2004; Wink et al., 2008; Ihlen and Vereijken, 2010), therefore a multifractal approach appears a proper choice when investigating the supposedly rich dynamic properties of functional connectivity.

A recent study using dynamic graph theoretical analysis of multichannel functional near-infrared spectroscopy (fNIRS) data demonstrated that DFC in the human pre-frontal cortex (PFC) expressed multifractal properties (Racz et al., 2018). In this paper we make an attempt on expanding some of the limitations of this previous study: firstly by investigating DFC based on whole-head measurements instead of relying on those only in the PFC, and secondly by considering not only the temporal evolution of global network properties but describing the dynamic fluctuations of individual connections in the network as well. We estimate dynamic functional connectivity based on whole-head EEG measurements using the synchronization likelihood method (Stam and van Dijk, 2002) and apply dynamic graph theoretical analysis. By doing so, we calculate the temporal evolution of three network measures—Density, Clustering Coefficient, and Efficiency—, in order to characterize separate topological aspects of the dynamic networks. Then, both global DFC (as captured in the fluctuations of these network measures) and individual dynamic connections (captured as the fluctuating synchronization levels between regions) are made subject to multifractal time series analysis to reveal their dynamic properties. We performed EEG measurements in eyes open (EO) and eyes closed (EC) states in male and female subjects, which allowed for exploring differences related to state, gender, and network measure. Furthermore, analysis of individual connections between different brain regions allowed us to show if they express not only mono- but indeed multifractal character and also if they show any particular topological pattern regarding their dynamic properties. Our findings imply that multifractal analysis of the dynamics of global functional connectivity as well as that of individual functional connections may provide a valuable tool when extracting information on the temporal structuring of DFC and carry potentials for experimental and/or clinical applications as well.

MATERIALS AND METHODS

Participants, Experimental Protocol and Data Acquisition

A total of 24 young, healthy volunteers (age: 24.25 ± 2.4 ranging from 20 to 29 years, 12 female) participated in this study. This number of subjects was determined by statistical power analysis of preliminary measurements. The study was approved by the Semmelweis University Regional and Institutional Committee of Science and Research Ethics (ethical approval number: 2017/94) and all subjects provided written informed consent. No participants had reported history of any neurological or psychiatric disorders. Test subjects were instructed not to consume any stimulant (e.g., caffeine) at least 4 h prior to participating and to have at least 6 h of sleep the night before. During the measurement, subjects were seated comfortably in an armchair in a light- and sound-attenuated, electrically sealed room, instructed to remain still, retrain from structured thinking while remaining awake. Resting-state EEG measurements were performed with eyes open (EO) while visually fixating on a dot on a computer screen, followed by another recording session with eyes closed (EC), resulting in four analysis groups: female eyes open, female eyes closed, male eyes open and male eyes closed (F_{EO}, F_{EC}, M_{EO} and M_{EC}, respectively). The recorded signals were visually inspected online, and a session was completed once an artifact-free 305 s record in both EO and EC state have been obtained, which was achieved within 20 min with all subjects.

Measurements were carried out using an Emotiv Epoc+ wireless EEG system (Emotiv Systems Inc., San Francisco, CA, USA), acquiring signals from 14 brain regions according to the 10–20 international system, including AF3, F3, F7 FC5, T7, P7, O1, O2, P8, T8, FC6, F8, F4, and AF4 with additional CMS/DRL reference electrodes at P3 and P4 positions. Data was sampled at 2,048 Hz and internally band-pass filtered between 0.2 and 45 Hz with additional notch filters at 50 and 60 Hz, then down-sampled to an effective temporal resolution of 128 Hz. Electrode impedances were kept under 20 kΩ during signal acquisition. All measurements were performed with maximal contact quality confirmed by the provided Emotiv Xavier TestBench^{TM} software (version 3.1.18).

EEG Data Pre-processing

EEG data was pre-processed off-line in Matlab 2012a (The Mathworks, Natick, MA, USA) using the freely available EEGLAB toolbox (Delorme and Makeig, 2004) along with custom scripts and functions. Independent Component Analysis (ICA) was performed (Hyvarinen and Oja, 2000) to remove signal components related to eye movement, blinking, muscle contraction and general noise. These components were identified by their power spectra, visual appearance, and spatial power distribution over the cortex and rejected from the data before performing inverse ICA. Subsequently, the ICA-pruned datasets were band-pass filtered in the traditional frequency bands used in EEG-analysis: δ, 0.5–4 Hz; θ, 4–8 Hz; α, 8–13 Hz; α, 13–30 Hz, and γ, 30–45 Hz according to Stam and de Bruin (2004). All further analyses were also performed on broadband (unfiltered), ICA-pruned signals as well. The first and last 2 s of each measurement

segment were rejected, resulting in datasets with length of 38528 data points for both states of every subject.

Synchronization Likelihood

The synchronization likelihood (SL) method (Stam and van Dijk, 2002) was used for pairwise estimation of dynamic functional connectivity. SL identifies non-linear statistical interdependencies between a pair (or in case of global SL, a larger set) of signals. It is by its nature dynamic (i.e., estimates synchronization as a function of time), normalized and seems unaffected by non-stationarities (Stam and van Dijk, 2002). These properties make SL a suitable tool in FC studies using EEG measurements, as EEG signals (and brain activity in general) are often considered non-stationary (Kaplan et al., 2005; Freeman and Quian Quiroga, 2013) and the functional coupling between different neuronal ensembles was confirmed to be non-linear by several studies (Friston, 2000; Stam et al., 2003).

SL measures the general synchronization between discretely sampled processes $x(t)$ and $y(t)$, $t = 1, 2,... T$. First, the temporal evolution of $x(t)$ and $y(t)$ is reconstructed in the state space by temporal embedding (Takens, 1981), where $x(t)$ and $y(t)$ is converted into a set of state space vectors $X(t)$ and $Y(t)$ as

$$\begin{aligned} X(t) &= x\left(t, t-m, t-2m, \ldots,\ t-\left(d-1\right)m\right), \\ Y(t) &= y\left(t, t-m, t-2m, \ldots,\ t-\left(d-1\right)m\right), \end{aligned} \tag{1}$$

where d is the embedding dimension and m is the time lag. Further, let's define the probability for every state space vector $X(t)$ [and for $Y(t)$, similarly] that the distance of a randomly selected vector $X(t+u)$ is closer than distance $r_x(t)$ as

$$\begin{aligned} C\left(r_x(t), X\right) = \frac{1}{2\left(w_2 - w_1\right)} \sum_{w_1 < |u| < w_2} \theta\left\{r_x(t) - \right. \\ \left. |X(t) - X(t+u)|\right\}, \end{aligned} \tag{2}$$

where u is the temporal distance, $|\cdot|$ is the Euclidean norm, θ is the Heaviside step function, w_1 is the Theiler correction for autocorrelation (Theiler, 1986) and w_2 is a window parameter such as $w_1 \ll w_2 \ll T$. It should be noted, that w_2 serves as the time window in a SW analysis, and as u can be negative as well, the 'window length' appears as $2w_2$, with the middle $2w_1$ segment discarded to avoid effects of autocorrelation. The distance parameters $r_x(t)$ and $r_y(t)$ are set for every time point t that $C\left(r_x(t), X\right) = C\left(r_y(t), Y\right) = p_{ref}$, with p_{ref} usually fixed at a value close to 0. Thus, p_{ref} basically serves as an internal thresholding variable. Finally, the synchronization likelihood at time point t is defined as the conditional probability that $Y(t)$ and $Y(t+u)$ are closer than $r_y(t)$ given that $X(t)$ and $X(t+u)$ are closer than $r_x(t)$ and calculates as

$$\begin{aligned} SL(t) = \frac{1}{2p_{ref}\left(w_2 - w_1\right)} \sum_{w_1 < |u| < w_2} \theta\left\{r_x(t) - |X(t)\right. \\ \left. -X(t+u)\ |\right\}\ \theta\left\{r_y(t) - |Y(t) - Y(t+u)|\right\}. \end{aligned} \tag{3}$$

$SL(t)$ is then computed for every time point t. Note, that the concept of synchronization likelihood is strongly related to the correlation integral (Grassberger and Procaccia, 1983) and can be considered as a so called "fixed-mass" or "k-nearest-neighbor" approach (Theiler, 1990).

In this study, initial parameters of SL (d, m, w_1, w_2) were set to fit the filter parameters for each frequency band, according to Montez et al. (2006). Parameter settings for each frequency band and those for broadband EEG data are shown in **Table 1**.

Dynamic Graph Theoretical Analysis

Synchronization likelihood was computed on the pruned EEG datasets for all pair-wise combination of the channels, yielding a 14×14 weighted synchronization matrix for every time point, in which the connection strength is assumed to be proportional to the level of synchronization between brain regions. Each of these matrices capture the actual topology of the underlying network, and calculating different network measures over them yield Network Metrics Time Series (NMTS) that describe the temporal evolution of network topology. Complex networks have several aspects to their topologies such as modularity or small-worldness (Rubinov and Sporns, 2010). The network is required to contain a sufficiently large number of nodes for network descriptors to make sense, i.e., there is no point in calculating for example the node degree distribution on a network with 14 nodes. It has been demonstrated however, that global network measures Density (D), Clustering Coefficient (C) and Efficiency (E) can be used effectively to describe and capture significant topological differences in smaller networks (Racz et al., 2017). We used the weighted formulas to calculate the aforementioned network measures. Weighted Density (often termed also Connectivity Strength) is the fraction of overall connectivity strength present to the maximal possible connection strength in a network (Rubinov and Sporns, 2010) and calculates as

$$D^W = \frac{1}{n(n-1)} \sum_{i=1}^{n-1} \sum_{j=i+1}^{n} c_{ij}, \tag{4}$$

where n is the total number of nodes, and c_{ij} is the connection strength–in this case, $SL(t)$ for every t–between nodes i and j. Density is a general measure of "wiring cost" of a network, and is also equal to the average normalized node degree (Rubinov and Sporns, 2010). The Clustering Coefficient of an individual

TABLE 1 | Synchronization likelihood parameters for each frequency band.

Band	Range	d	m	w_1	w_2
Delta	0.5–4 Hz	25	11	264	1264
Theta	4–8 Hz	7	5	30	1030
Alpha	8–13 Hz	6	3	15	1015
Beta	13–30 Hz	8	1	7	1007
Gamma	30–45 Hz	6	1	5	1005
Broadband	0.5–45 Hz	289	1	288	1288

node denotes the fraction of the existing triangles to the maximal possible number of triangles around a node (Rubinov and Sporns, 2010) and was generalized to weighted networks by Onnela et al. (2005). Clustering Coefficient of node i calculates as

$$C_i^W = \frac{2}{k(k-1)} \sum_{j,h}^{n} \tilde{w}_{ij}\tilde{w}_{ih}\tilde{w}_{jh}, \tag{5}$$

where k is the number of edges connected to node i and $\tilde{w}_{ih}$ is the weight of the edge between nodes i and j. Edge weights are normalized by the largest weight present in the network, therefore on binary networks the formula returns with the original definition, that is also equivalent to the fraction of a node's neighbors that are also neighbors of each other (Watts and Strogatz, 1998). The global Clustering Coefficient is the average taken over individual nodes. C is the most general measure of network segregation and related to "local" information flow in the network (Rubinov and Sporns, 2010). Finally, Efficiency is a global parameter capturing network integration, and is often associated with the speed of information processing in a complex system (Rubinov and Sporns, 2010). It is the average inverse shortest path length between all nodes of a network and computes according to

$$E^W = \frac{1}{n} \sum_{i=1}^{n} \sum_{j=1, i\neq j}^{n} \frac{\left(d_{ij}^W\right)^{-1}}{n-1}, \tag{6}$$

where d_{ij}^W is the length of the shortest weighted path between nodes i and j (Latora and Marchiori, 2001). It is strongly related to the average shortest path length, however often considered as being a superior measure to the latter in describing network integration (Achard and Bullmore, 2007). Efficiency is related to the "global" information flow in the network (Rubinov and Sporns, 2010). For the sake of simplicity, in the following we will drop the superscripts "w" and will refer by D, C, and E to their weighted forms, respectively.

Since SL has an internal step of thresholding, to avoid acquiring an overwhelming amount of results we decided not to use any additional threshold values, as in a previous study (Racz et al., 2018) the dynamic properties of DFC did not show any specific relation to the value of threshold. We calculated the time evolution of Density, Clustering Coefficient, and Efficiency [D(t), C(t), and E(t), respectively] for every subject both in EO and EC states. For the calculations of D, C, and E we used functions of the Brain Connectivity Toolbox by Rubinov and Sporns (2010).

Focus-Based Multifractal Signal Summation Conversion (FMF-SSC)

Multifractal analysis, instead of a single scaling exponent yields a set of scaling exponents, each describing scaling in fluctuations of different sizes in the signal (Kantelhardt et al., 2002). This can be achieved by characterizing scaling at several statistical moments q, where small fluctuations are amplified by the negative, while large fluctuations by the positive moments (Barunik and Kristoufek, 2010; Ihlen, 2013). We used the multifractal generalization of the Signal Summation Conversion (SSC) method (Eke et al., 2000; Mukli et al., 2015) to extensively characterize the power-law scaling of the NMTSs and the SL(t)s of individual connections. In SSC, the signal is cumulatively summed and standard deviation σ is calculated at different window sizes ranging from a minimal to a maximal scale (s_{min} and s_{max}, respectively). Within each window the local linear trend is removed before calculation to diminish effects of non-stationarity. The power-law dependence of σ on s is captured in the Hurst exponent H according to $\sigma(s) \propto s^H$ (Eke et al., 2000). The multifractal generalization of SSC (MF-SSC) consists of repeating the steps of the analysis at different statistical moments q, yielding the unified scaling function $S(q,s)$ (**Figure 1**) (Mukli et al., 2015)

$$S(q,s) = \left\{ \frac{1}{N_s} \sum_{\upsilon=1}^{N_s} \sigma(\upsilon, s)^q \right\}^{\frac{1}{q}}, \tag{7}$$

where N_s is the number of non-overlapping time windows at scale s, and υ is the index of the actual window of calculation. As σ is now dependent on s and q as well, their relationship is established via the generalized Hurst exponent $H(q)$ according to $\sigma(q,s) \propto s^{H(q)}$ and can be acquired by linear regression on the values of $S(q,s)$ (Barunik and Kristoufek, 2010). On empirical

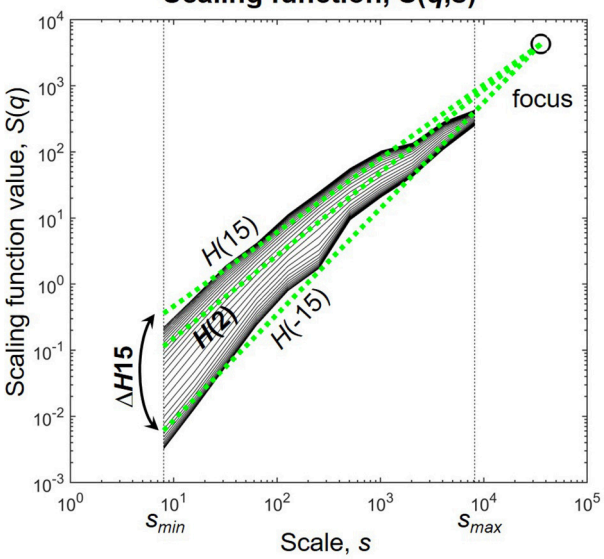

FIGURE 1 | The scaling function. $H(2)$ characterizes the global i.e., monofractal scaling, while the difference between $H(-15)$ and $H(15)$ termed $\Delta H15$ captures the degree of multifractality. The focus is used as a reference point for linear regression. Scaling function of D*(t)* of subject male 4 during eyes closed is used for illustration.

signals with finite length the regressed functions converge in one specific point termed *focus* (Mukli et al., 2015). This can be simply shown by replacing s in $S(q,s)$ with the total length of the signal as it results in the disappearance of the sum and therefore q from equation (7). The focus therefore is used as a reference point during regression, which renders the multifractal analysis of empirical time series very robust and prevents it from ending up with "inverted" or corrupted multifractal spectra (Mukli et al., 2015). Note that this way of handling of empirical signals is not unique to SSC, but can be applied also to other MF methods such as Detrended Fluctuation Analysis or Wavelet Leader methods yielding their focus-based variants (Mukli et al., 2015).

The NMTSs and SL(t)s were analyzed by FMF-SSC with the following input parameters as suggested in Mukli et al. (2015): $s_{min} = 8$ with s increasing dyadically until $s_{max} = 8192$ and q ranging from -15 to $+15$ with unit increments. The scaling range was defined between scales 2^3 and N/4, as scaling function values below and over these scales become statistically unreliable (Cannon et al., 1997; Gulich and Zunino, 2014). Scaling windows based on a dyadic scale provide efficient computation. The range of q was selected based on Grech and Pamula (2012), Mukli et al. (2015), and Nagy et al. (2017). Global (i.e., monofractal) scaling associated with the long-term memory of the signal was captured in $H(2)$, and the degree of multifractality was described by $\Delta H15 = H(-15)–H(15)$, as a measure of how much the scaling is different for small and large fluctuations (**Figure 1**). Note, that $\Delta H15$ captures the distribution of local scaling in a signal equivalently with the often used multifractal/singularity spectrum that can be acquired from $S(q,s)$ by Legendre-transformation (Frisch and Parisi, 1985; Chhabra et al., 1989).

Surrogate Data Testing

Multifractal scaling in a time series can appear as a consequence of different long-range correlations present in the signal, however multifractality can also originate in the heavy-tailed probability distribution of signal values without any correlations whatsoever (Ivanov et al., 1999; Kantelhardt et al., 2002). Also, the finite size and/or simple constant linear autocorrelation of the signal can also produce a so-called "multifractal background noise" (Grech and Pamula, 2012), that has to be distinguished from true multifractality. Thus, a proper surrogate data testing is indispensable when analyzing empirical signals. Therefore, all time series (NMTSs and SL(t)s) underwent steps of thorough tests to verify if they indeed showed true multifractality. In all of these steps, $n = 39$ surrogate datasets of equal length were generated with the null hypothesis that the investigated time series cannot be distinguished from its surrogates based on the discriminating statistical measure (Theiler et al., 1992). The null hypothesis was rejected if the discriminating statistic was found outside the mean $\pm$ 2σ range calculated from the surrogate datasets, that with $n = 39$ surrogate datasets corresponds to a 95% confidence level (Theiler et al., 1992; Kaplan and Glass, 1995).

First, we tested the presence of *global power-law scaling*. This can best be done in the frequency domain, as a signal with global power-law scaling also has a corresponding $\frac{1}{f^{\beta}}$-like spectrum (Eke et al., 2000). Hence, for every time series surrogate datasets with equal β were generated with the spectral synthesis method (Saupe, 1988), and the Kolmogorov-Smirnov distances were calculated to estimate the goodness-of-fit (GoF) of the power-law function. A time series was considered scale-free, if its GoF to a power-law function was within the mean $\pm$ 2 σ range of those calculated from surrogate data with known (identical) power-law spectra (Clauset et al., 2009; He, 2011).

Second, we tested the presence of *distribution-related multifractality* by randomly shuffling the values of the time series (Ivanov et al., 1999; Kantelhardt et al., 2002). Shuffling destroys all correlations and reduces the signal to pure random noise but has no effect on the distribution of values. Consequently, if shuffling renders $H(q) \approx 0.5$ (i.e., white noise) for all q the case of distribution-related multifractality can be excluded, otherwise presence of scaling (at least partly) could be attributed to a power-law type distribution of signal values.

Finally, we tested if the observed multifractality resulted from the presence of different *long-range correlations*. For this purpose, surrogate datasets were generated by Fourier transforming the signal with Fast Fourier Transformation, randomizing its phases and then performing inverse Fourier transformation (Theiler et al., 1992). Phase randomization leaves the amplitudes and therefore the power spectrum (hence, linear autocorrelation) unaffected (Kantz and Schreiber, 2004), while destroying all non-linear correlations in the signal (Schreiber and Schmitz, 2000). Hence it yields surrogate datasets with equal $H(2)$ i.e., *monofractal* characteristic preserved (Eke et al., 2000). As the resulting time series are monofractal signals, this step simultaneously tests for multifractal background noise/true multifractality (Grech and Pamula, 2012) and the presence of non-linearity (Ivanov et al., 1999). Multifractality was considered true and as a sign of non-linear dynamics, if the $\Delta H15$ value of a signal was significantly larger than those of surrogate datasets. In the following, we will refer those processes passing all tests as *true multifractals*.

Analysis Strategy

The flowchart of the analysis steps is shown as a summary of the methods on **Figure 2**. The first aim of this study was to show if global DFC when investigated by EEG show multifractal properties. For this purpose, the acquired D(t), C(t), and E(t) time series were made subject to surrogate data tests for power-law scaling, long-range autocorrelation and true multifractality as described above, and the fraction of subjects passing each test were computed for all measures. To explore the effect of gender (F and M), network measure (D, C, and E), and state (EO and EC) on the MF properties of global DFC, two-way repeated measures ANOVA tests were performed for each frequency band separately, with gender as grouping variable, while state and network measure as repeated measure factors. Bonferroni *post-hoc* tests were performed to identify significant differences between interactions (in the following marked by $\times$). Results will be presented in the following manner: for each frequency band, we present the significant differences considering the effect of gender, measure and state separately, along with interaction effects of gender $\times$ measure, gender $\times$ state and measure $\times$ state.

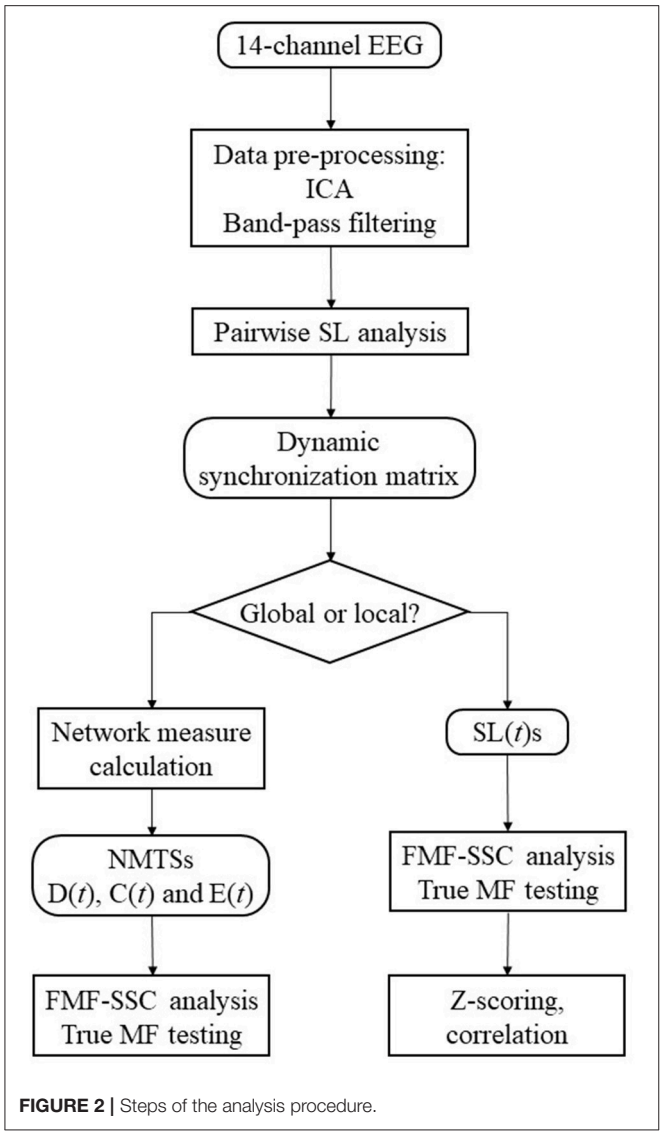

FIGURE 2 | Steps of the analysis procedure.

When they bear significance, results from the *post-hoc* tests are also discussed in detail.

Our second aim was to show if dynamic functional connections themselves—captured in SL(t) between different locations—exhibited multifractal scaling. Therefore, all SL(t)s were also processed by the same testing framework as the NMTSs. Fractions of edges in the network passing each test were calculated on the subject level and were averaged combining all four groups (F_{EO}, F_{EC}, M_{EO}, and M_{EC}) to obtain a general picture on the presence of true multifractality in functional connections. Subsequently, to reveal if functional connections express any particular topology in regards of their mono- and multifractal properties, $H(2)$ and $\Delta H15$ values of the connections were standardized (z-scored) on the subject level and averaged across subjects within all analysis groups collectively. This resulted in group-averaged networks where edge weights represent their corresponding z-scored values [z($H(2)$) and z($\Delta H15$), respectively]. Also, to investigate the possible correlation between the long-term memory and the degree of multifractality of connections, the Pearson coefficient (r) was calculated between the group averaged z($H(2)$) and z($\Delta H15$) values. In order to distinguish between a true correlation effect and pure coincidence, r was calculated on the shuffled data as well when $n = 39$ spatial surrogates (Aaria et al., 2013) were generated by randomly shuffling the z($H(2)$) and z($\Delta H15$) values [thus destroying possible correlation between $H(2)$ and $\Delta H15$]. Again, if the r of original values was outside the mean $\pm$ 2 σ range acquired from surrogate data, we regarded the correlation between $H(2)$ and $\Delta H15$ as significant.

It should be noted, that multifractality of individual connections were investigated in each group (F_{EO}, F_{EC}, M_{EO}, and M_{EC}) individually as well, however as results were comparable between analysis groups, for the sake of simplicity we decided to present the results of all groups combined. All statistical analyses were carried out in StatSoft Statistica 13.2.

RESULTS

Testing for True Multifractality

Results for surrogate data testing of NMTSs (including all groups and states) are shown in **Table 2**. In the vast majority of the cases, D(t), C(t), and E(t) were proven to have broadband power-law spectra, qualifying them as scale-free (fractal) processes. Shuffling reduced $H(q)$ approximately to 0.5 in all cases, proving again the presence of long-range correlations in the signals, while also excluding the contribution of distribution-related multifractality. True multifractality was also present in network dynamics in most of the cases for all frequency bands as well for broadband EEG data (**Table 2**).

Similar results were obtained when investigating the power-law scaling and autocorrelation properties of individual connections in the dynamic functional networks on the subject level (**Table 3**). In that most connections in the networks yielded power-law spectra, and all connections contained LRCs while distribution-related multifractality could be excluded. Although the fraction of true multifractal connections were generally high in the delta, theta and alpha bands, slightly lower values were found in functional networks of the higher (beta and gamma) frequency bands with a slightly lower amount of connections passing the true multifractality test in broadband EEG networks. Nevertheless, these results compare well with those obtained from global network dynamics (**Table 2**) implying that the multifractal nature of global network dynamics emerges from multifractally fluctuating individual connection strengths in the network. Note that values in **Table 3** refer to the fraction of connections in the functional networks of each subject, thus they are presented as mean $\pm$ σ across subjects (combining all four groups).

Multifractal Nature of Global DFC

In the following, for the $H(2)$ of D(t), C(t), and E(t) we will use the abbreviations $H_D(2)$, $H_C(2)$, and $H_E(2)$, respectively. Similarly, $\Delta H15$ of D(t), C(t), and E(t) will be referred to as ΔH_D15, ΔH_C15, and ΔH_E15. Summary of the results regarding

TABLE 2 | Fraction of NMTSs passing each surrogate data test.

	Power-law			Shuffling			Phase randomization		
Band	**D (%)**	**C (%)**	**E (%)**	**D (%)**	**C (%)**	**E (%)**	**D (%)**	**C (%)**	**E (%)**
Delta	97.9	97.9	100	100	100	100	100	100	91.7
Theta	97.9	100	95.8	100	100	100	87.5	93.8	85.4
Alpha	97.9	95.8	100	100	100	100	97.9	93.8	95.8
Beta	100	100	97.9	100	100	100	89.6	89.6	89.6
Gamma	100	100	100	100	100	100	91.7	93.8	95.8
Broadband	97.9	100	100	100	100	100	91.7	100	91.7

TABLE 3 | Fraction of functional connections in the network passing each test.

Band	**Power-law (%)**	**Shuffling (%)**	**Phase randomization (%)**
Delta	99.13 ± 9.29	100	99.47 ± 7.24
Theta	98.92 ± 10.32	100	93.77 ± 24.17
Alpha	98.86 ± 10.64	100	97.09 ± 16.80
Beta	98.99 ± 9.99	100	76.53 ± 42.38
Gamma	98.72 ± 11.25	100	81.87 ± 38.53
Broadband	98.28 ± 12.99	100	89.33 ± 30.87

$H(2)$ of global DFC is shown in **Figure 3**, while those of $\Delta H15$ are presented on **Figure 4**.

A prominent measure-related effect appeared in $H(2)$ which was present in all frequency bands, as $H_C(2)$ values were found significantly lower than those of $H_D(2)$ and $H_E(2)$. The same difference was found regarding $\Delta H15$ ($\Delta H_D15 > \Delta H_C15 < \Delta H_E15$), however in the delta band, only. Moreover, state had a significant effect in the alpha and beta bands as $H(2)$ values increased during EC compared to EO condition. Gender related effects were found sparsely with a tendency of higher $H(2)$ and $\Delta H15$ values in males. In the following, we elaborate on these results for every frequency band separately.

Delta Band

$H(2)$ values were found significantly higher in the male groups (main effect of gender, $p = 0.023$). The three network measures also showed significant difference with $H_C(2)$ being lower than those of $H_D(2)$ and $H_E(2)$ (main effect of measure, $p < 0.0001$). Interaction of measure × gender and Bonferroni *post hoc* tests showed that these differences occurred in both genders (**Figure 3A**).

Measure had a significant main effect on $\Delta H15$ as well ($p < 0.0001$). The measure × gender interaction revealed, that in females ΔH_D15 was significantly larger than ΔH_C15 andΔH_E15 with no difference between the latter two, while in males ΔH_E15 was also larger than ΔH_C15 ($p < 0.01$ in all cases). Neither gender nor state had significant effect on $\Delta H15$ in the delta band (**Figure 4A**).

Theta Band

Measure had a similar main effect on $H(2)$ as in the delta band [$H_D(2) > H_C(2) < H_E(2)$, $p < 0.001$ in all cases], however neither gender- nor state-related differences were found (**Figure 3B**).

Regarding $\Delta H15$, only measure-related differences were found (main effect of measure, $p = 0.026$). Bonferroni *post hoc* test indicated that ΔH_D15 was higher than ΔH_C15, however the interaction measure × gender showed that this was not significant in neither the male or female groups individually (**Figure 4B**).

Alpha Band

The previously observed difference in measure regarding $H(2)$ was also found in the alpha band [$H_D(2) > H_C(2) < H_E(2)$, $p < 0.001$ in all cases], however additionally in males $H_E(2)$ was slightly higher than $H_D(2)$ and $H_C(2)$ ($p = 0.043$). Also, a significant difference related to state was revealed with $H(2)$ being higher in EC than in EO state ($p = 0.035$). Interaction of measure × state verified that this difference was present in all network measures (**Figure 3C**).

Larger $\Delta H15$ values were found in the male groups (main effect of gender, $p = 0.014$). Interestingly, the interaction gender × state revealed a trend in which state had the opposite effect in the two genders, as $\Delta H15$ increased in males while decreased it in females during EC condition ($p = 0.066$) (**Figure 4C**).

Beta Band

The main effect of measure was found significant ($p < 0.0001$) with Bonferroni *post hoc* test revealing $H_C(2)$ being smaller than $H_D(2)$ and $H_E(2)$ ($p < 0.001$ in all cases). Moreover, similarly to the alpha band, state had a significant effect in increasing $H(2)$ when transitioning from EO to EC ($p < 0.001$) (**Figure 3D**).

ΔH_D15, ΔH_C15, andΔH_E15 were found increased in EC state, although the main effect of state was not significant ($p = 0.136$). The interaction of gender × state revealed that this increase was only present in the male group, while $\Delta H15$ values remained unchanged in females, although yet again only in tendency ($p = 0.093$) (**Figure 4D**).

Gamma Band

In $H(2)$, only measure-related differences appeared significant, with a similar tendency as in the alpha band, with $H_C(2)$ being lower than $H_D(2)$ and $H_E(2)$, and in males $H_E(2)$ also being higher than $H_D(2)$ too ($p < 0.001$ in all cases) (**Figure 3E**). No differences were found regarding $\Delta H15$ (**Figure 4E**).

Broadband EEG

Measure related differences were found (main effect of measure, $p < 0.0001$) with Bonferroni *post hoc* test confirming the same tendency as in most previous cases [$H_D(2) > H_C(2) < H_E(2)$, $p < 0.01$]. Also, higher $H(2)$ values were found in EC (main effect of state, $p = 0.014$) (**Figure 3F**).

The main effect of gender on $\Delta H15$ appeared significant ($p = 0.012$) with higher values in the male groups. Measure also had a significant effect on $\Delta H15$ ($p = 0.0006$) however the measure × gender interaction and Bonferroni *post hoc* test revealed that significant differences only occurred in the male group, with ΔH_D15 being significantly higher than ΔH_C15 and ΔH_E15 ($p < 0.001$ in both cases) (**Figure 4F**).

In order to keep the statistical analysis simple, frequency band was not included as a factor in the statistical analysis, however it can be clearly seen on **Figure 3** that $H(2)$ values in the delta

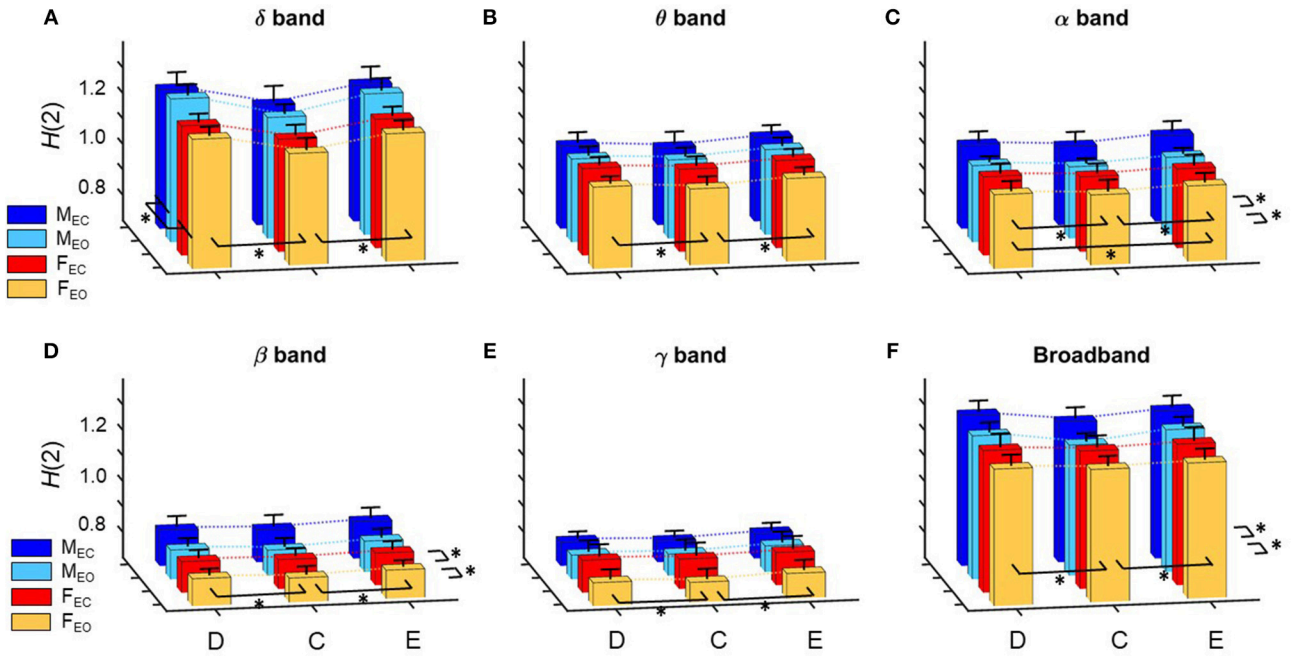

FIGURE 3 | Summary of results regarding $H(2)$ of global network metrics for the delta **(A)**, theta **(B)**, alpha **(C)**, beta **(D)**, and gamma **(E)** bands, as well as for broadband EEG **(F)**. Dotted lines connect the means of the corresponding analysis groups. Significant differences are marked by * for effects of gender, measure and state (displayed on the left, in front and right of each subplot, respectively). Note, that significant differences of interaction effects are not marked.

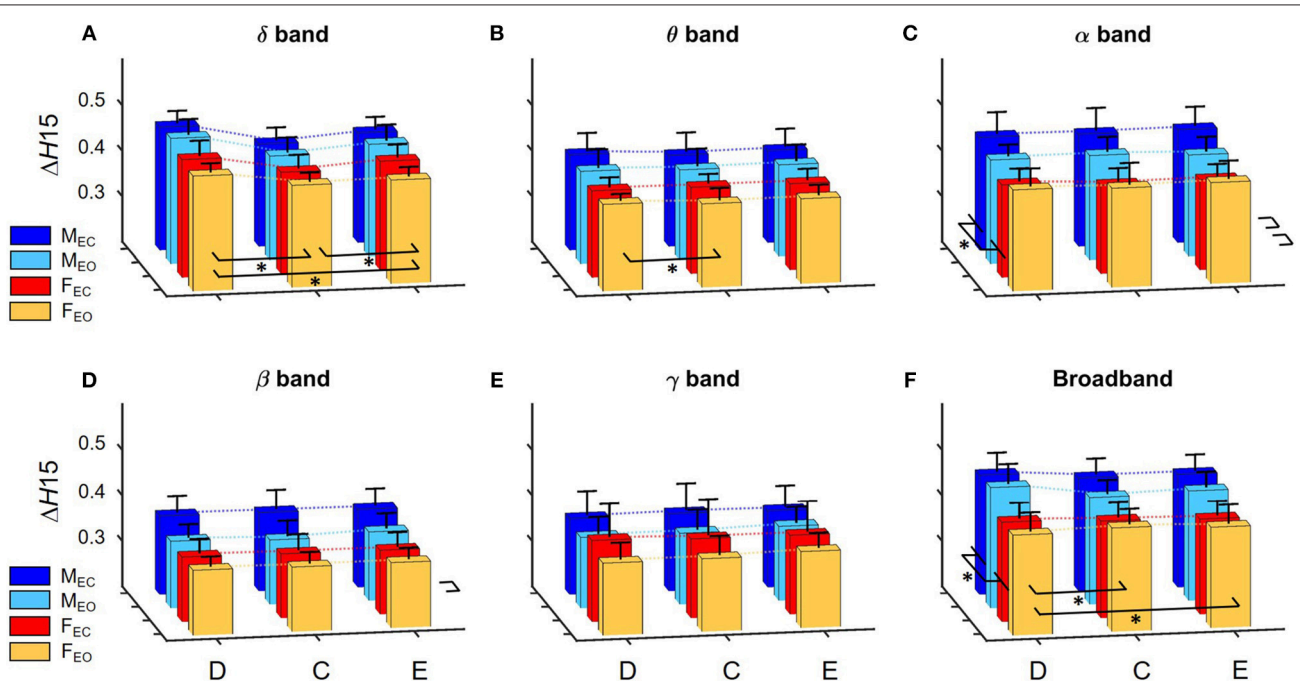

FIGURE 4 | Summary of results regarding $\Delta H15$ of global network metrics in for the delta **(A)**, theta **(B)**, alpha **(C)**, beta **(D)**, and gamma **(E)** bands, as well as for broadband EEG **(F)**. Dotted lines connect the means of the corresponding analysis groups. Significant differences are marked by * for effects of gender and measure (displayed on the left and in front of each subgraph, respectively). Again, significant differences of interaction effects are not marked.

and alpha band are considerably higher than those of the theta, beta, and gamma bands, with $H(2)$ of unfiltered signals being approximately in between. **Figure 4** shows that $\Delta H15$ values were the highest in the delta-, alpha-, and broad-band EEG, with slightly lower values in the theta, beta, and gamma bands.

Individual Connection Dynamics

Long-Range Correlation–$H(2)$

$H(2)$ of individual connections showed a characteristic topological distribution in all frequency bands as well as broadband EEG data (**Figure 5**). In that spatially proximal functional connections between ROIs expressed higher, while those between distant regions showed lower $H(2)$ values. This pattern could be observed most prominently in connections between regions of the frontal and pre-frontal cortex that had the highest $z(H(2))$ values, while in general connections linking regions of the occipital and parietal cortex to those of the frontal- and pre-frontal cortex had the lowest $z(H(2))$ values. Also, nearby connections linking contralateral regions in the frontal and pre-frontal areas expressed higher long-range correlation, however this did not hold for connections linking areas of the occipital and parietal cortex to those of the contralateral hemisphere (**Figure 5**).

Degree of Multifractality–$\Delta H15$

Topology of $\Delta H15$ of individual connections in the delta band were markedly different from those of other frequency bands (**Figure 6**). While dynamic connections in the theta, alpha, beta and gamma bands resembled a topology similar to that observed for $H(2)$ (with higher values for short- and lower-values for long-distance connections), a markedly opposite distribution appeared in the delta band. Within this range, stronger multifractality was found in connections linking the occipital and parietal regions to pre-frontal and frontal regions while lower $\Delta H15$ values appeared in connections between nearby regions. Connections estimated on broadband EEG appeared to exhibit a homogenous distribution of $\Delta H15$ without any particular topology (**Figure 6**).

Relationship Between $z(H(2))$ and $z(\Delta H15)$

The relationship between the multifractal properties of dynamic functional connections was captured in the Pearson correlation coefficient between $z(H(2))$ and $z(\Delta H15)$ values with their scatter plots shown in **Figure 7**. In the theta, alpha, beta, and gamma bands, significant positive correlations were found indicating that connections with higher long-term autocorrelation was associated with higher degree of multifractality. The opposite topology of $z(H(2))$ and $z(\Delta H15)$ in the delta band however resulted in a strong negative correlation as connections with high $H(2)$ were associated with lower $\Delta H15$ values. In broadband EEG no correlation was found concomitant with the absence of topology in $\Delta H15$ of individual connections (**Figure 5**).

DISCUSSION

Multifractal Nature of Global DFC

In this study, we reported that dynamic functional connectivity of the brain—as reconstructed from 14 channel whole-head EEG measurements and captured with dynamic graph theoretical analysis—fluctuates according to multifractal dynamics. Surrogate data tests proved that in majority, this temporal structuring was of true multifractal nature in all frequency bands as well as in broadband EEG. We also identified several significant differences in the MF characteristics of global DFC related to network measure, gender, and state.

We found that the degree of long-range temporal correlation could be attributed to specific topological aspects of the dynamic functional networks in that $H_C(2)$ was found significantly lower than $H_D(2)$ and $H_E(2)$. This pattern was present almost universally in all frequency bands as well as in broadband EEG data. A very similar pattern regarding the $H(2)$ of the same dynamic graph theoretical measures (D, C, and E) was reported previously in Racz et al. (2018), where multifractal nature of DFC in the pre-frontal cortex was investigated using fNIRS imaging. Findings of the present study and those of Racz et al. (2018) suggest therefore that this pattern is a genuine feature of FC dynamics as it can be captured in different imaging modalities across a broad range of spatio-temporal scales. In $\Delta H15$, significant differences related to network measure appeared prominently only in the delta band, where ΔH_C15 was significantly lower than ΔH_D15 and ΔH_E15. These findings are also consistent with the similar results of Racz et al. (2018), where $\Delta H15$ showed comparable differences regarding the applied network measures ($\Delta H_D15 > \Delta H_C15 < \Delta H_E15$). As in this study, this measure-related pattern was found only in the delta band with basically no significant measure-related differences in higher frequency bands. As Racz et al. (2018) investigated spontaneous brain activity in the 0.01–0.1 Hz range, these results may apply for lower-frequency brain activity, only.

Multifractal time series analysis characterizes the time-dependent scaling in a temporal process, that can emerge from intermittent periods with high variance (Ihlen and Vereijken, 2010). In this study, employing three graph theoretical measures–each capturing different aspects of network structure and topology–all were shown fluctuating in a multifractal manner, although to a different extent. The true multifractal scaling of all three network topological measures indicates that their scaling is in fact a local, time-dependent property. This implies that the temporal evolution of dynamic resting-state connection networks was interspersed with short periods of high variance in their segregation and integration, suggesting that these reorganization events leave their impact on localized and global information transfer alike (as captured in C and E, respectively). Moreover, the differences observed in the $H(2)$ and $\Delta H15$ values of these measures—at least in the delta band—imply that local and global information processing is affected differently: the lower ΔH_C15 suggesting a more "balanced" temporal structuring of localized activity, while global network integration (related to fast information transfer between distant network sites) and overall "wiring cost" is associated with larger variability in scaling.

The scale-free nature of global DFC has been demonstrated earlier by Stam and de Bruin (2004). In that study, DFC was captured in global synchronization of EEG signals (as acquired by averaging SL time series) and fractal dynamics were characterized by the monofractal Hurst exponent estimated with Detrended

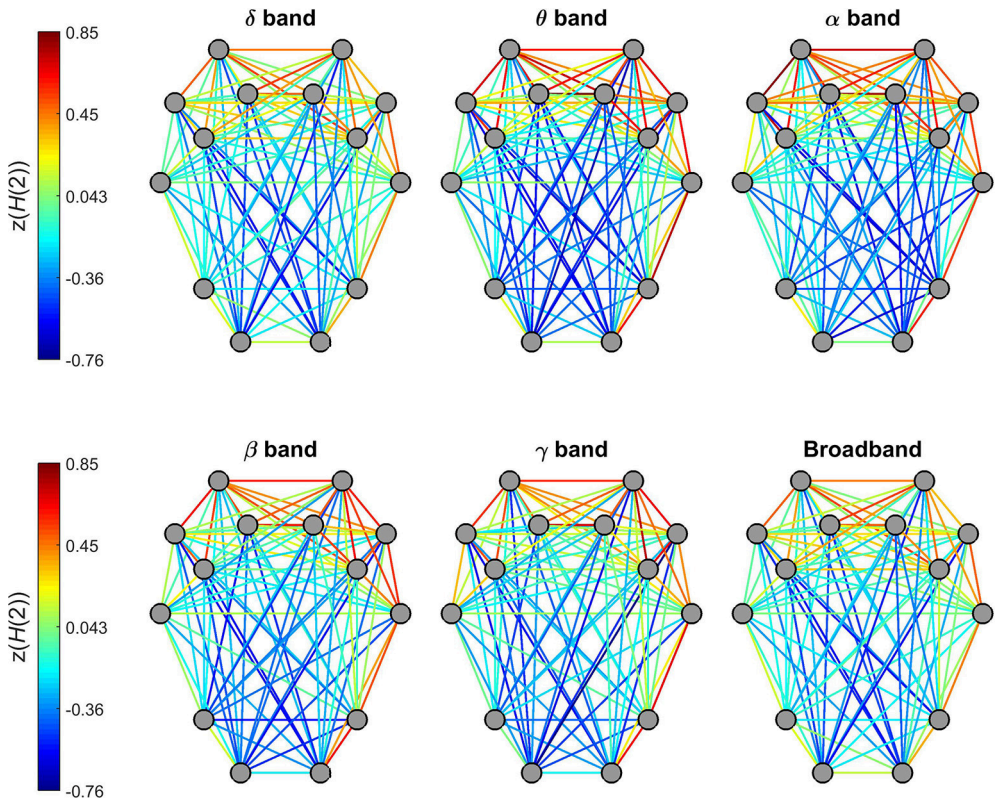

FIGURE 5 | Topology of global long-range correlations in dynamic functional connections across the brain cortex. In all frequency bands as well as in broadband EEG, connections between frontal and prefrontal regions exhibit higher, while occipito-frontal connections lower $H(2)$ values.

Fluctuation Analysis. The authors found an increased Hurst exponent in eyes closed condition in the alpha and beta bands (Stam and de Bruin, 2004). As weighted Density is in fact the averaged connectivity strength (captured in SL), our current observations regarding the same difference–i.e., increased $H(2)$ in the alpha and beta bands–are in agreement with those of Stam and de Bruin (2004) thereby extending their validity to Clustering Coefficient and Efficiency. The transition from eyes closed to eyes open state is often associated with desynchronization in cortical activity [Berger (1929), for a review see Barry et al. (2007)], with lower $H(2)$ values reflecting on the dominance of rapid fluctuations (Stam and de Bruin, 2004). The lower $H(2)$ values found in EO condition for all three network measures may indeed reflect the large-scale network reorganization affecting both local and global information flow (Rubinov and Sporns, 2010; Preti et al., 2017).

In a more recent study, Van de Ville et al. (2010) reported that EEG microstates also exhibit scale-free dynamics. Nevertheless, the authors did not find any difference in the scaling between various statistical moments as EEG microstates were found fluctuating in a strictly monofractal manner. However, this absence of MF dynamics could be the consequence of the applied analysis method. Specifically, it has been shown previously, that brain electrical activity fluctuates between only four different microstates in resting state (Lehmann et al., 1998). Van de Ville et al. (2010) used bipartitioning between these four microstates to capture microstate transitions, and confirmed fractal dynamics in all possible bipartitioning scenarios independently from the applied partition itself (Van de Ville et al., 2010). The random walk time series analyzed by Van de Ville et al. (2010) were acquired by cumulatively summing the bipartition label sequences (consisting of -1 and $+1$ values) of the EEG microstates. These are reminiscent of the sign time series obtained from an increment series (Ashkenazy et al., 2001, 2003), that can be obtained as the sign sequence of the local derivatives of a fluctuating signal. Sign time series were indeed shown to be related to the monofractal character (Gomez-Extremera et al., 2016), while scaling in the magnitude time series acquired as the absolute value sequence of local derivatives was reported to be related to multifractality of a dynamic process (Gomez-Extremera et al., 2016; Bernaola-Galvan et al., 2017). Our results show that dynamic graph theoretical analysis can capture the dynamics of FC in a more detailed fashion than EEG microstates, allowing for the unfolding of finer temporal structuring such as multifractal scaling.

Gender-related differences in DFC has also been reported previously (Yaesoubi et al., 2015a,b). Yaesoubi et al. (2015b) investigated the simultaneous occupation of different FC states (i.e., state combinations termed as "combo states") and showed that males occupy a larger fraction of all possible combo states

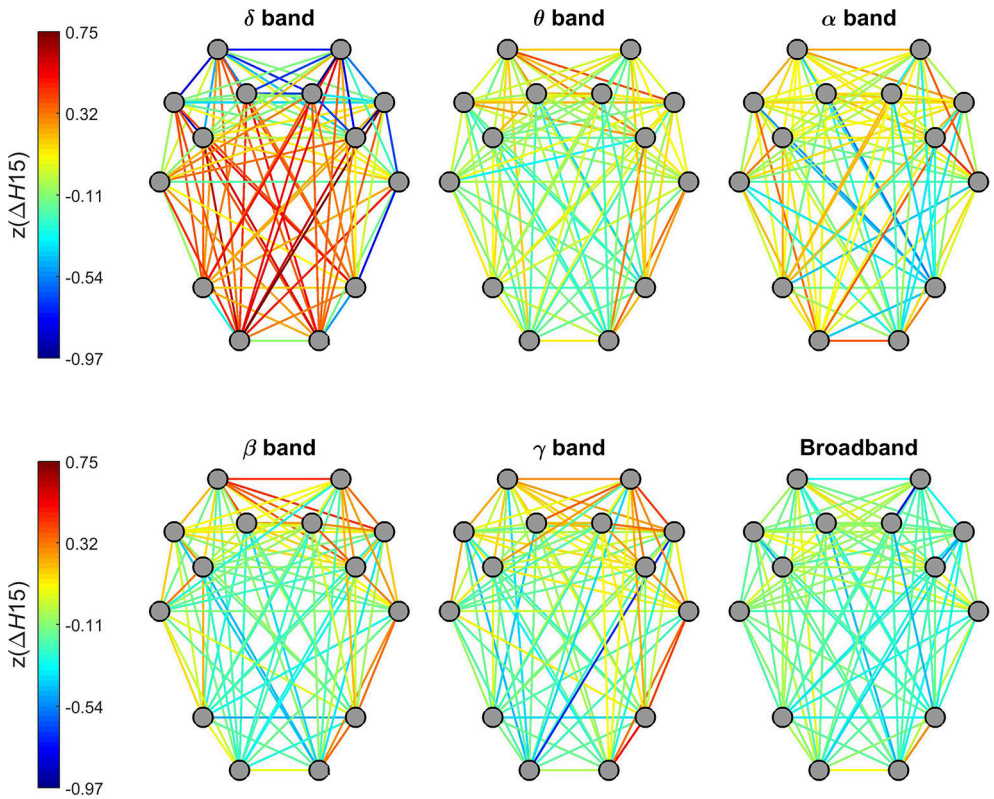

FIGURE 6 | Topology of the degree of multifractality in dynamic functional connections across the brain cortex. Connections of the delta band showed a markedly different topology from the rest of the frequency bands. Also, no particular topological pattern was apparent in connections estimated on broadband EEG.

than females. Since spatio-temporally overlapping events were suggested as a possible origin of multifractal dynamics in a complex system (Lima et al., 2017), this may indeed be the underlying reason of the higher degree of multifractality of DFC observed in males in the alpha band. We also found higher autocorrelation i.e., higher $H(2)$ values in male subjects in the delta band. It is well-known, that functional connectivity correlates well with structural (anatomical) connectivity (SC) (Greicius et al., 2009; Honey et al., 2009) even when investigated on multiple time scales (Honey et al., 2007). Our present findings showed that in some cases gender can have an influence on FC dynamics, which could well be–at least in part–to gender-related differences in brain anatomical connectivity (Ingalhalikar et al., 2014).

Finally, $1/f^{\beta}$ i.e., scale-free neurodynamics were suggested in numerous studies as an indication of an underlying self-organized critical state of the brain (Linkenkaer-Hansen et al., 2001; Stam and de Bruin, 2004; Stam, 2005; Kitzbichler et al., 2009; Chialvo, 2010; Van de Ville et al., 2010; Tagliazucchi et al., 2012a; Racz et al., 2018). Moreover, it has been reported that not only mono- but indeed multifractal scaling could also occur in a three dimensional system at a critical state (Lima et al., 2017). The concept of self-organized criticality (SOC) as introduced by Bak et al. (1987) refers to the intrinsic property of a dynamic system constantly approaching a critical state without the fine tuning of an external "control parameter." A critical state—where local perturbations are allowed to dissipate across all spatial and temporal scales in the system—usually appears near (first- or secondorder) phase transitions. Therefore, SOC is often considered as an ideal state of the brain in which fast adaptation to changes in the external or internal environment can be effectively achieved by rapid large-scale reorganization (Van de Ville et al., 2010). The scale-free–and indeed, multifractal–nature of the DFC measures reported in this study may therefore be considered evidencing yet another implication of the self-organized critical nature of resting-state brain activity.

Multifractal Dynamics of Individual Functional Connections

We showed that DFC networks exhibited multifractal dynamics not only in their global graph theoretical parameters, but in their dynamic functional connections, too, as captured in the varying connectivity strengths between the nodes. This property was most prevalent in the delta, theta and alpha band connections, while slightly lower fraction of beta and gamma band as well as broadband EEG connections was proven as true multifractals.

Given the moderate spatial resolution in this study, instead of focusing on individual differences between inter-regional connections, we rather investigated if dynamic functional connections showed any global topology in their $H(2)$ and $\Delta H15$ values and if there was a relationship between them. In all frequency bands as well as in broadband EEG data we found a

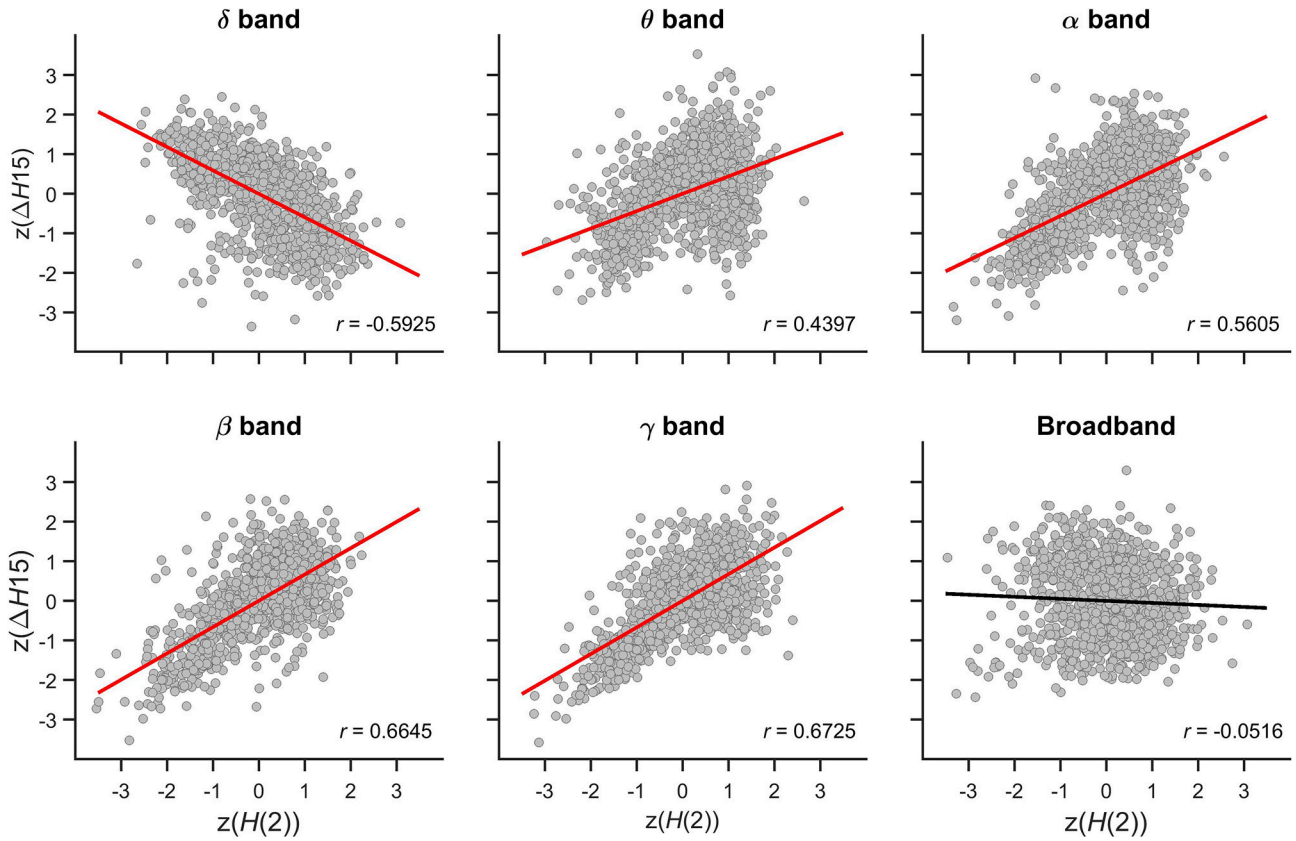

FIGURE 7 | Cross-correlation between $z(H(2))$ and $z(\Delta H15)$ of individual connections. Panels are scatter plots of all connections (14*13/2) of all subjects (48). The Pearson correlation coefficient (r) is displayed in the lower right corner of each panel. Significant correlation is indicated by red regression line, while the black regression line for broadband EEG indicates that the correlation was indistinguishable from spatial surrogates.

characteristic topology in the long-term autocorrelation of FC strength, as short-range connections between the frontal and pre-frontal areas tend to have higher $H(2)$ values than long-range connections linking the same regions to the occipital and parietal cortex. A very similar topology regarding the degree of multifractality captured in $\Delta H15$ was found in the theta, alpha, beta, and gamma bands. On the contrary, the topological pattern was the opposite in the delta band: long-range connections linking occipital regions with mostly the frontal and pre-frontal regions showed higher $\Delta H15$ values than those linking nearby regions prominently again the frontal and pre-frontal areas. This inverse relationship in the delta band could be captured in a strong negative correlation between $H(2)$ and $\Delta H15$ values. However, in the higher frequency bands the topology of $\Delta H15$ values were similar to those of $H(2)$ thus resulting in strong positive correlation between the two. No correlation was found between the two MF measures in broadband EEG connections. It should be emphasized that a relationship between $H(2)$ and $\Delta H15$ is indeed non-trivial, as these measures capture two separate properties of the multifractal spectrum (i.e., spectral center and spectral width) (Theiler, 1990; Kantelhardt et al., 2002; Kantelhardt, 2009; Mukli et al., 2015).

It has been shown in dynamic processes, that monofractal scaling [captured in $H(2)$ of the scaling function or the center of the multifractal spectrum] is attributed to linear properties, while the degree of multifractality [as assessed equivalently either by $\Delta H15$ or the multifractal spectrum width] correlates well with the degree of non-linearity (Gomez-Extremera et al., 2016; Bernaola-Galvan et al., 2017). In addition non-linearity in a power-law correlated signal can also be well estimated by the long-term autocorrelation of its magnitude time series (Ashkenazy et al., 2003; Schmitt et al., 2009). Multifractality often emerges from the presence of intermittent periods of higher variance (Ihlen and Vereijken, 2010). Accordingly, from the topological pattern observed in broadband EEG and in the lower frequency range (i.e., delta band), it is apparent that connections between nearby regions express a lower degree of non-linearity and they are more linearly autocorrelated (however in most cases still non-linear as well), while on the contrary, the opposite is true for long-distance connections where linear autocorrelation is weaker and the dynamics appear more non-linear. Therefore our results are in good agreement with—and presumably reflect the same phenomenon as—previous findings demonstrating the non-linear nature of neuronal synchronization (Stam et al., 2003) and intermittent periods of

high synchronization between neuronal cell assemblies (Friston, 2000). Also, this is in line with the fact that brain activity is generally scale-free on the large-scale level while becoming more synchronized when observed smaller spatial scales (Buzsaki, 2006).

Dynamic synchronization levels mainly capture the joint activity of neuron populations of the regions of interest. The fractal and multifractal nature of individual connections therefore may also indicate that a possible critical state of brain activity may not only be present on a global level, but also on smaller spatial scales, too. In a SOC simulation using a modified version of the classic sand pile model, Mukli et al. (2018) investigated the effect of the size and connection density of the cellular automata on the multifractal properties of their dynamics, which was captured in the total number of sand grains resident in the system at a given moment. Their results demonstrated, that with (independently) increasing system size or connection density, both $H(2)$ and $\Delta H15$ of the system dynamics increased (Mukli et al., 2018). This phenomenon is very reminiscent of the positive correlation found in this study between $H(2)$ and $\Delta H15$ of individual connections in the higher frequency bands. Therefore, higher $H(2)$ and $\Delta H15$ values of a dynamic connection may well reflect that the joint activity between the two regions involved larger and/or more densely interconnected neuronal populations. Also, the frequency range of network oscillations is constrained by the networks size because most neuronal connections are local and thus yield high-frequency oscillations (Braitenberg and Schüz, 2013). Accordingly, slower oscillations can only be produced when larger neuronal cell assemblies are involved (Buzsaki and Draguhn, 2004). Higher $H(2)$ values indicate the dominance of slow fluctuations thus suggesting the involvement of large neural populations. These considerations are well in line with the results of this study regarding that the highest $H(2)$ and $\Delta H15$ values were found in connections of the frontal and prefrontal cortex; regions that are both anatomically and functionally well connected and form a high-level association cortex with diverse functionality (Kandel, 2013). On the contrary, lower values were found between both anatomically and functionally distant regions.

Nevertheless the inverse relationship between $H(2)$ and $\Delta H15$ found in the delta band raises some questions. Delta band activity is not prominent in awake state during physiological conditions, however several studies demonstrated the critical nature of brain dynamics during sleep stages (Lo et al., 2002, 2004, 2013). It also has been shown recently (using an alternate DFC approach termed time delay stability, TDS), that different sleep stages–that are known to be dominated by specific EEG frequency bands, as α oscillations are most prominent during quiet wake and rapid eye movement, while θ and δ fluctuations usually characterize light- and deep sleep, respectively–exhibit FC topologies characteristic to sleep stage and frequency band as well (Bartsch et al., 2015; Liu et al., 2015). Therefore, sleep would probably be a better setting for further investigating the multifractal and critical nature of delta band connections—and their relation to other frequency bands—that is evidently beyond the scope of this present study.

Limitations, Future Perspectives

Multifractal analysis could reveal relevant information at the global (network) and the local (connection) levels, that otherwise may remain hidden in static and also in most dynamic functional connectivity approaches. MF analysis of DFC carries potential for future applications both in basic science and clinical fields, however one has to consider some methodological difficulties with this approach. For a reliable numerical estimation of fractal and/or multifractal parameters, a signal length of at least a few thousand data points is desired, as well as long-enough measurement time and high temporal resolution so that the signal could represent a sufficiently broad range of temporal scales (Eke et al., 2002; Ihlen, 2013). While these prerequisites can be readily met with imaging modalities such as EEG, fNIRS, or MEG, still major drawbacks remain owing to their lower spatial resolution, their lack of exact source localization and the fact that these techniques cannot access subcortical regions. These limitations can be partly overcome by using fMRI—with spatial normalization even allowing for exact comparison between separate studies—however at the expense of lower temporal resolution and limited signal length, both considerably affecting the applicability of multifractal analysis (Eke et al., 2012). As these methods–e.g., EEG and fMRI–can provide complementary information, the importance of simultaneous EEG-fMRI (and/or fNIRS-fMRI) measurements is indeed crucial in revealing the relationship between EEG-DFC and fMRI-DFC so that DFC could be investigated with high temporal resolution and exact spatial localization, alike.

Although in this study the whole brain cortex is sampled, the spatial resolution is still fairly limited. Using a higher spatial resolution method would not only benefit from a more detailed sampling of brain activity, but would also allow for calculating more complex network measures—i.e., those related with modularity, centrality or network motifs being more complex than triangles—that could reveal even more details on functional brain organization. Also, from **Table 1** it is apparent, that gamma band activity may not be well represented in the state space during SL calculation. This is a limitation brought about by the sampling frequency that calls for greater caution when results regarding the gamma band are evaluated.

DFC analyses carry great potentials not only in basic research leading to a better understanding of brain functions, but also in the clinical field, as several studies already demonstrated their applicability in neuropsychiatric diseases such as schizophrenia (SZ) (Sakoglu et al., 2010; Calhoun et al., 2014; Damaraju et al., 2014) or autism (Price et al., 2014). Thus dynamic graph theoretical analyses similar to the one presented in this study could prove a useful and potentially powerful tool when investigating DFC in clinical settings. When analyzing the DFC of the default mode network with fMRI imaging in SZ patients, the same dynamic graph theoretical measures as used in this study were found to be fluctuating around a lower average value than in healthy controls (Du et al., 2016). Moreover in a whole brain DFC study on SZ patients, in addition to the same results it was also demonstrated that $D(t)$, $C(t)$, and $E(t)$ showed less variance than in healthy controls (Yu et al., 2015). Results of the present study

clearly show, that the standard deviation (i.e., the square root of variance) of graph theory metrics depends on the observation scale and that second order statistics alone are insufficient to fully characterize the network dynamics. Multifractal analysis however is suitable to capture such features, therefore may serve as a more sensitive tool in distinguishing physiological states from pathological conditions based on their dynamic graph theoretical measures.

Finally, in a recently established field of biological systems science termed network physiology (Bashan et al., 2012; Ivanov and Bartsch, 2014), the dynamic interactions of local neural activity with several other physiological subsystems (e.g., the cardiac and respiratory system) were analyzed (Bartsch and Ivanov, 2014; Bartsch et al., 2015; Lin et al., 2016). These studies showed that during different physiological states such as sleep stages, the interactions between the elements of this physiological network change significantly. As functional connectivity was also shown to alter during different physiological conditions (Horovitz et al., 2009; Liu et al., 2015; Racz et al., 2017), a dynamic graph theoretical approach may contribute to this emerging field by providing a way for capturing coordinated states of neural activity so that its interactions with other functions of the human body could be further analyzed.

CONCLUSIONS

In this study, we showed that dynamic global functional connectivity of the brain—when investigated by EEG mapping and captured in dynamic graph theoretical measures—fluctuates according to a multifractal temporal pattern. Our results revealed that several network topological aspects exhibit different characteristics. Moreover, the dynamic functional connections assembling these networks showed multifractal dynamics themselves. We found a characteristic topology in both mono- and multi-fractal measures with a positive correlation between them in the higher frequency bands, while anticorrelation in the delta band. Our results suggest that multifractality is indeed a fundamental property of both global and local (i.e., individual) DFC with specific global and local attributes to network topology and anatomical localization, respectively. Our findings are in support of a possible self-organized critical nature of resting-state brain activity. We propose that multifractal analysis can provide a more detailed description of global and local connectivity dynamics than most methods applied in the field, and it could serve as a valuable tool for a better characterization of healthy and pathological brain functions.

AUTHOR CONTRIBUTIONS

FR carried out the EEG measurements, developed the analysis framework, performed the analysis on measured data, and wrote the manuscript. OS helped carrying out the measurements and did the data pre-processing. PM helped conducting the measurements and writing the manuscript. AE helped developing and writing the manuscript and provided conceptual guidance in the study.

REFERENCES

Aaria, A. T., Mansour, A., Huang, L., Baliki, M. N., Cecchi, G. A., Mesulam, M. M., et al. (2013). Linking human brain local activity fluctuations to structural and functional network architectures. *Neuroimage* 73, 144–155. doi: 10.1016/j.neuroimage.2013.01.072

Achard, S., and Bullmore, E. (2007). Efficiency and cost of economical brain functional networks. *PLoS Comput. Biol.* 3:e17. doi: 10.1371/journal.pcbi.0030017

Allen, E. A., Damaraju, E., Plis, S. M., Erhardt, E. B., Eichele, T., and Calhoun, V. D. (2014). Tracking whole-brain connectivity dynamics in the resting state. *Cerebral Cortex* 24, 663–676. doi: 10.1093/cercor/bhs352

Ashkenazy, Y., Hausdorff, J. M., Ivanov, P. C., and Stanley, H. (2002). A stochastic model of human gait dynamics. *Physica A* 316, 662–670. doi: 10.1016/S0378-4371(02)01453-X

Ashkenazy, Y., Havlin, S., Ivanov, P. C., Peng, C. K., Schulte-Frohlinde, V., and Stanley, H. E. (2003). Magnitude and sign scaling in power-law correlated time series. *Physica A* 323, 19–41. doi: 10.1016/S0378-4371(03)00008-6

Ashkenazy, Y., Ivanov, P. C., Havlin, S., Peng, C. K., Goldberger, A. L., and Stanley, H. E. (2001). Magnitude and sign correlations in heartbeat fluctuations. *Phys. Rev. Lett.* 86, 1900–1903. doi: 10.1103/PhysRevLett.86.1900

Bak, P., Tang, C., and Wiesenfeld, K. (1987). Self-organized criticality: an explanation of the 1/f noise. *Phys. Rev. Lett.* 59, 381–384. doi: 10.1103/PhysRevLett.59.381

Barry, R. J., Clarke, A. R., Johnstone, S. J., and Magee, C. (2007). EEG differences between eyes-closed and eyes-open resting conditions. *Clin. Neurophysiol.* 118, 2765–2773. doi: 10.1016/j.clinph.2007.07.028

Bartsch, R. P., and Ivanov, P. C. (2014). Coexisting forms of coupling and phase-transitions in physiological networks. *Nonlin. Dynam. Electron. Syst.* 438, 270–287. doi: 10.1007/978-3-319-08672-9_33

Bartsch, R. P., Liu, K. K. L., Bashan, A., and Ivanov, P. C. (2015). Network physiology: how organ systems dynamically interact. *PLoS ONE* 10:e0142143. doi: 10.1371/journal.pone.0142143

Barunik, J., and Kristoufek, L. (2010). On hurst exponent estimation under heavy-tailed distributions. *Physica A* 389, 3844–3855. doi: 10.1016/j.physa.2010.05.025

Bashan, A., Bartsch, R. P., Kantelhardt, J. W., and Havlin, S. (2012). Network physiology reveals relations between network topology and physiological function. *Nat. Commun.* 3:702. doi: 10.1038/ncomms1705

Berger, H. (1929). Über das elektrenkephalogramm des menschen. *Archiv für Psychiatrie Nervenkrankheiten* 87, 527–570.

Bernaola-Galvan, P. A., Gomez-Extremera, M., Romance, A. R., and Carpena, P. (2017). Correlations in magnitude series to assess nonlinearities: application to multifractal models and heartbeat fluctuations. *Phys. Rev. E* 96:032218. doi: 10.1103/PhysRevE.96.032218

Biswal, B. Yetkin, F. Z., Haughton, V. M., and Hyde, J. (1995). Functional connectivity in the motor cortex of resting human brain using echo-planar MRI. *Magn. Reson. Med.* 34, 537–541. doi: 10.1002/mrm.1910340409

Braitenberg, V., and Schüz, A. (2013). *Cortex: Statistics and Geometry of Neuronal Connectivity*. Berlin: Springer Science & Business Media.

Bullmore, E., and Sporns, O. (2009). Complex brain networks: graph theoretical analysis of structural and functional systems. *Nat. Rev. Neurosci.* 10, 186–198. doi: 10.1038/nrn2575

Buzsaki, G. (2006). *Rhythms of the Brain*. Oxford, NY: Oxford University Press.

Buzsaki, G., and Draguhn, A. (2004). Neuronal oscillations in cortical networks. *Science* 304, 1926–1929. doi: 10.1126/science.1099745

Cader, S., Cifelli, A., Abu-Omar, Y., Palace, J., and Matthews, P. M. (2006). Reduced brain functional reserve and altered functional connectivity in patients with multiple sclerosis. *Brain* 129, 527–537. doi: 10.1093/brain/awh670

Calhoun, V. D., Miller, R., Pearlson, G., and Adali, T., (2014). The chronnectome: time-varying connectivity networks as the next frontier

in fMRI data discovery. *Neuron* 84, 262–274. doi: 10.1016/j.neuron.2014.10.015

Cannon, M. J., Percival, D. B., Caccia, D. C., and Raymond, G. (1997). Evaluating scaled windowed variance methods for estimating the Hurst coefficient of time series. *Physica A* 241, 606–626. doi: 10.1016/S0378-4371(97)00252-5

Chang, C., and Glover, G. H. (2010). Time-frequency dynamics of resting-state brain connectivity measured with fMRI. *Neuroimage* 50, 81–98. doi: 10.1016/j.neuroimage.2009.12.011

Chhabra, A. B., Meneveau, C., Jensen, R. V., and Sreenivasan, K. R. (1989). Direct determination of the f(alpha) singularity spectrum and its application to fully developed turbulence. *Phys. Rev. A Gen. Phys.* 40, 5284–5294. doi: 10.1103/PhysRevA.40.5284

Chialvo, D. R. (2010). Emergent complex neural dynamics. *Nat. Phys.* 6, 744–750. doi: 10.1038/Nphys1803

Clauset, A., Shalizi, C. R., and Newman, M. E. J. (2009). Power-law distributions in empirical data. *Siam Rev.* 51, 661–703. doi: 10.1137/070710111

Damaraju, E., Allen, E. A., Belger, A., Ford, J. M., McEwen, S., Mathalon, D. H., et al. (2014). Dynamic functional connectivity analysis reveals transient states of dysconnectivity in schizophrenia. *Neuroimage Clin.* 5, 298–308. doi: 10.1016/j.nicl.2014.07.003

Delorme, A., and Makeig, S. (2004). EEGLAB: an open source toolbox for analysis of single-trial EEG dynamics including independent component analysis. *J. Neurosci. Methods* 134, 9–21. doi: 10.1016/j.jneumeth.2003.10.009

Du, Y., Pearlson, G. D., Yu, Q., He, H., Lin, D., Sui, J., et al. (2016). Interaction among subsystems within default mode network diminished in schizophrenia patients: a dynamic connectivity approach. *Schizophr. Res.* 170, 55–65. doi: 10.1016/j.schres.2015.11.021

Eke, A., Hermán, P., Bassingthwaighte, J. B., Raymond, G. M., Percival, D. B., Cannon, M., et al. (2000). Physiological time series: distinguishing fractal noises from motions. *Pflugers Arch.* 439, 403–415. doi: 10.1007/s004249900135

Eke, A., Herman, P., Kocsis, L., and Kozak, L. R. (2002). Fractal characterization of complexity in temporal physiological signals. *Physiol. Meas.* 23, R1–R38. doi: 10.1088/0967-3334/23/1/201

Eke, A., Herman, P., Sanganahalli, B. G., Hyder, F., Mukli, P., and Nagy, Z. (2012). Pitfalls in fractal time series analysis: fmri bold as an exemplary case. *Front. Physiol.* 3:417. doi: 10.3389/fphys.2012.00417

Esposito, F., Bertolino, A., Scarabino, T., Latorre, V., Blasi, G., Popolizio, T., et al. (2006). Independent component model of the default-mode brain function: Assessing the impact of active thinking. *Brain Res. Bull.* 70, 263–269. doi: 10.1016/j.brainresbull.2006.06.012

Falahpour, M., Thompson, W. K., Abbott, A. E., Jahedi, A., Mulvey, M. E., Datko, M., et al. (2016). Underconnected, but not broken? dynamic functional connectivity mri shows underconnectivity in autism is linked to increased intra-individual variability across time. *Brain Connect* 6, 403–414. doi: 10.1089/brain.2015.0389

Fox, M. D., Snyder, A. Z., Vincent, J. L., Corbetta, M., Van Essen, D. C., and Raichle, M. E. (2005). The human brain is intrinsically organized into dynamic, anticorrelated functional networks. *Proc. Natl. Acad. Sci. U.S.A.* 102, 9673–9678. doi: 10.1073/pnas.0504136102

Freeman, W. J., and Quian Quiroga, R. (2013). *Imaging Brain Function With EEG : Advanced Temporal and Spatial Analysis of Electroencephalographic Signals*. New York, NY: Springer.

Frisch, U., and Parisi, G. (1985). *On the Singularity Structure of Fully Developed Turbulence*. Amsterdam: Turbulence and Predictability in Geophysical Fluid Dynamics and Climate Dynamics, Elsevier.

Friston, K. J. (2000). The labile brain. I. Neuronal transients and nonlinear coupling. *Philos. Trans. R Soc. Lond. B Biol. Sci.* 355, 215–236. doi: 10.1098/rstb.2000.0560

Friston, K. J. (2011). Functional and effective connectivity: a review. *Brain Connect.* 1, 13–36. doi: 10.1089/brain.2011.0008

Friston, K. J., Frith, C. D., Liddle, P. F., and Frackowiak, R. (1993). Functional connectivity: the principal-component analysis of large (PET) data sets. *J. Cereb. Blood Flow Metab.* 13, 5–14. doi: 10.1038/jcbfm.1993.4

Gaudes, C. C., Petridou, N., Francis, S. T., and Dryden, I. L. (2013). Paradigm free mapping with sparse regression automatically detects single-trial functional magnetic resonance imaging blood oxygenation level dependent responses. *Hum. Brain Mapp.* 34, 501–518. doi: 10.1002/hbm.21452

Gomez-Extremera, M., Carpena, P., Ivanov, P., and Bernaola-Galvan, P. A. (2016). Magnitude and sign of long-range correlated time series: decomposition and surrogate signal generation. *Phys. Rev. E* 93:042201. doi: 10.1103/PhysRevE.93.042201

Gong, P., Nikolaev, A. R., and van Leeuwen, C. (2003). Scale-invariant fluctuations of the dynamical synchronization in human brain electrical activity. *Neurosci. Lett.* 336, 33–36. doi: 10.1016/S0304-3940(02)01247-8

Gonzalez-Castillo, J., Handwerker, D. A., Robinson, M. E., Hoy, C. W., Buchanan, L. C., Saad, Z. S., et al. (2014). The spatial structure of resting state connectivity stability on the scale of minutes. *Front Neurosci* 8:138. doi: 10.3389/fnins.2014.00138

Grassberger, P., and Procaccia, I. (1983). Characterization of strange attractors. *Phys. Rev. Lett.* 50, 346–349. doi: 10.1103/PhysRevLett.50.346

Grech, D., and Pamula, G. (2012). Multifractal Background Noise of Monofractal Signals. *Acta Phys Pol A* 121, B34–B39.

Greicius, M. D., Krasnow, B., Reiss, A. L., and Menon, V. (2003). Functional connectivity in the resting brain: a network analysis of the default mode hypothesis. *Proc. Natl. Acad. Sci. U.S.A.* 100, 253–258. doi: 10.1073/pnas.0135058100

Greicius, M. D., Supekar, K., Menon, V., and Dougherty, R. F. (2009). Resting-state functional connectivity reflects structural connectivity in the default mode network. *Cereb. Cortex* 19, 72–78. doi: 10.1093/cercor/bhn059

Gulich, D., and Zunino, L. (2014). A criterion for the determination of optimal scaling ranges in DFA and MF-DFA. *Phys. Stat. Mech. Appl.* 397, 17–30. doi: 10.1016/j.physa.2013.11.029

He, B. J. (2011). Scale-free properties of the functional magnetic resonance imaging signal during rest and task. *J. Neurosci.* 31, 13786–13795. doi: 10.1523/JNEUROSCI.2111-11.2011

Honey, C. J., Kotter, R., Breakspear, M., and Sporns, O. (2007). Network structure of cerebral cortex shapes functional connectivity on multiple time scales. *Proc. Natl. Acad. Sci. U.S.A.* 104, 10240–10245. doi: 10.1073/pnas.0701519104

Honey, C. J., Sporns, O., Cammoun, L., Gigandet, X., Thiran, J. P., Meuli, R., et al. (2009). Predicting human resting-state functional connectivity from structural connectivity. *Proc. Natl. Acad. Sci. U.S.A.* 106, 2035–2040. doi: 10.1073/pnas.0811168106

Horovitz, S. G., Braun, A. R., Carr, W. S., Picchioni, D., Balkin, T. J., Fukunaga, M., et al. (2009). Decoupling of the brain's default mode network during deep sleep. *Proc. Natl. Acad. Sci. U.S.A.* 106, 11376–11381. doi: 10.1073/pnas.0901435106

Hutchison, R. M., Womelsdorf, T., Allen, E. A., Bandettini, P. A., Calhoun, V. D., Corbetta, M., et al. (2013a). Dynamic functional connectivity: promise, issues, and interpretations. *Neuroimage* 80, 360–378. doi: 10.1016/j.neuroimage.2013.05.079

Hutchison, R. M., Womelsdorf, T., Gati, J. S., Everling, S., Menon, R., et al. (2013b). Resting-state networks show dynamic functional connectivity in awake humans and anesthetized macaques. *Hum. Brain Mapp.* 34, 2154–2177. doi: 10.1002/hbm.22058

Hyvarinen, A., and Oja, E. (2000). Independent component analysis: algorithms and applications. *Neural Netw.* 13, 411–430. doi: 10.1016/S0893-6080(00)00026-5

Ihlen, E. A., and Vereijken, B. (2010). Interaction-dominant dynamics in human cognition: beyond 1/f(alpha) fluctuation. *J. Exp. Psychol. Gen.* 139, 436–463. doi: 10.1037/a0019098

Ihlen, E. A., and Vereijken, B. (2013). Identifying multiplicative interactions between temporal scales of human movement variability. *Ann. Biomed. Eng.* 41, 1635–1645. doi: 10.1007/s10439-012-0724-z

Ihlen, E. A. F. (2013). Multifractal analyses of response time series: a comparative study. *Behav. Res. Methods* 45, 928–945. doi: 10.3758/s13428-013-0317-2

Ingalhalikar, M., Smith, A., Parker, D., Satterthwaite, T. D., Elliott, M. A., Ruparel, K., et al. (2014). Sex differences in the structural connectome of the human brain. *Proc. Natl. Acad. Sci. U.S.A.* 111, 823–828. doi: 10.1073/pnas.1316909110

Ivanov, P. C., Amaral, L. A., Goldberger, A. L., Havlin, S., Rosenblum, M. G., Struzik, Z. R., et al. (1999). Multifractality in human heartbeat dynamics. *Nature* 399, 461–465. doi: 10.1038/20924

Ivanov, P. C., and Bartsch, R. P. (2014). *Network Physiology: Mapping Interactions Between Networks of Physiologic Networks. Networks of Networks: the Last Frontier of Complexity*. Berlin: Springer, 203–222.

Ivanov, P. C., Chen, Z., Hu, K., and Stanley, H. E. (2004). Multiscale aspects of cardiac control. *Phys. Stat. Mech. Appl.* 344, 685–704. doi: 10.1016/j.physa.2004.08.016

Ivanov, P. C., Nunes Amaral, L. A., Goldberger, A. L., Rosenblum, M. G., Stanley, H. G., and Struzik, Z. R. (2001). From 1/f noise to multifractal cascades in heartbeat dynamics. *Chaos* 11, 641–652. doi: 10.1063/1.1395631

Kandel, E. R. (2013). *Principles of Neural Science*. New York, NY: McGraw-Hill.

Kantelhardt, J. W. (2009). *Fractal and Multifractal Time Series. Encyclopedia of Complexity and Systems Science.* Berlin: Springer, 3754–3779.

Kantelhardt, J. W., Zschiegner, S. A., Koscielny-Bunde, E., Bunde, A., Havlin, H., Stanley, H. E., et al. (2002). Multifractal detrended fluctuation analysis of nonstationary time series. *Phys. A* 316, 87–114. doi: 10.1016/S0378-4371(02)01383-3

Kantz, H., and Schreiber, T. (2004). *Nonlinear Time Series Analysis*. Cambridge, NY: Cambridge University Press.

Kaplan, A. Y., Fingelkurts, A. A., Fingelkurts, A. A., and Borisov, S. (2005). Nonstationary nature of the brain activity as revealed by EEG/MEG: Methodological, practical and conceptual challenges. *Signal Process* 85, 2190–2212. doi: 10.1016/j.sigpro.2005.07.010

Kaplan, D., and Glass, L., (1995). *Understanding Nonlinear Dynamics*. New York, NY: Springer-Verlag.

Kitzbichler, M. G., Smith, M. L., Christensen, S. R., and Bullmore, E. (2009). Broadband criticality of human brain network synchronization. *Plos Comput. Biol.* 5:e1000314. doi: 10.1371/journal.pcbi.1000314

Kucyi, A., and Davis, K. D. (2014). Dynamic functional connectivity of the default mode network tracks daydreaming. *Neuroimage* 100, 471–480. doi: 10.1016/j.neuroimage.2014.06.044

Latora, V., and Marchiori, M. (2001). Efficient behavior of small-world networks. *Phys. Rev. Lett.* 87:198701. doi: 10.1103/PhysRevLett.87.198701

Lehmann, D., Ozaki, H., and Pal, I. (1987). Eeg alpha-map series - brain micro-states by space-oriented adaptive segmentation. *Electroen. Clin. Neuro* 67, 271–288. doi: 10.1016/0013-4694(87)90025-3

Lehmann, D., Strik, W., K., Henggeler, B., Koenig, T., and Koukkou, M. (1998). Brain electric microstates and momentary conscious mind states as building blocks of spontaneous thinking: i. Visual imagery and abstract thoughts. *Int. J. Psychophysiol.* 29, 1–11.

Lima, G. Z. D. S., Corso, G., Correa, M. A., Sommer, R. L., Ivanov, P. C., and Bohn, F. (2017). Universal temporal characteristics and vanishing of multifractality in Barkhausen avalanches. *Phys. Rev. E* 96:022159. doi: 10.1103/PhysRevE.96.022159

Lin, A. J., Liu, K. K. L., Bartsch, R. P., and Ivanov, P (2016). Delay-correlation landscape reveals characteristic time delays of brain rhythms and heart interactions. *Philos. Trans. R. Soc. Math. Phys. Eng. Sci.* 374:20150182. doi: 10.1098/rsta.2015.0182

Linkenkaer-Hansen, K., Nikouline, V. V., Palva, J. M., and Ilmoniemi, R. (2001). Long-range temporal correlations and scaling behavior in human brain oscillations. *J. Neurosci.* 21, 1370–1377. doi: 10.1523/JNEUROSCI.21-04-01370.2001

Liu, K. K., Bartsch, R. P., Lin, A., and Mantegna, R. N (2015). Plasticity of brain wave network interactions and evolution across physiologic states. *Front. Neural Circuits* 9:62. doi: 10.3389/fncir.2015.00062

Liu, Y., Liang, M., Zhou, Y., He, Y., Hao, Y., Song, M., et al. (2008). Disrupted small-world networks in schizophrenia. *Brain* 131, 945–961. doi: 10.1093/brain/awn018

Lo, C.-C., Bartsch, R. P., and Ivanov, P. C. (2013). Asymmetry and basic pathways in sleep-stage transitions. *EPL* 102:10008. doi: 10.1209/0295-5075/102/10008

Lo, C.-C., Nunes Amaral, L. A.,Havlin, S., Ivanov, P. C., Penzel, T., and Peter, J.-H., et al. (2002). Dynamics of sleep-wake transitions during sleep. *EPL* 57:625. doi: 10.1209/epl/i2002-00508-7

Lo, C. C., Chou, T., Penzel, T., Scammell, T. E., Strecker, R. E., Stanley, H. E., et al. (2004). Common scale-invariant patterns of sleep–wake transitions across mammalian species. *Proc. Natl. Acad. Sci. U.S.A.* 101, 17545–17548. doi: 10.1073/pnas.0408242101

Mandelbrot, B. B. (1986). Multifractals and fractals. *Phys Today* 39, 11–18. doi: 10.1063/1.2815135

Montez, T., Linkenkaer-Hansen, K., van Dijk, B. W., and Stam, C. J. (2006). Synchronization likelihood with explicit time-frequency priors. *Neuroimage* 33, 1117–1125. doi: 10.1016/j.neuroimage.2006.06.066

Mukli, P., Nagy, Z., and Eke, A. (2015). Multifractal formalism by enforcing the universal behavior of scaling functions. *Phys. A* 417, 150–167. doi: 10.1016/j.physa.2014.09.002

Mukli, P., Nagy, Z., Racz, F. S., Herman, P., and Eke, A. (2018). Impact of healthy aging on multifractal hemodynamic fluctuations in the human prefrontal cortex. *Front Physiol.* 9:1072. doi: 10.3389/fphys.2018.01072

Nagy, Z., Mukli, P., Herman, P., and Eke, A. (2017). Decomposing multifractal crossovers. *Front. Physiol.* 8:533. doi: 10.3389/fphys.2017.00533

Nunes Amaral, L. A., Ivanov, P. C., Aoyagi, N., Hidaka, I., Tomono, S., Goldberger, A. L., et al. (2001). Behavioral-independent features of complex heartbeat dynamics. *Phys. Rev. Lett.* 86, 6026–6029. doi: 10.1103/PhysRevLett.86.6026

Onnela, J. P., Saramaki, J., Kertesz, J., and Kaski, K. (2005). Intensity and coherence of motifs in weighted complex networks. *Phys. Rev. E Stat. Nonlin. Soft Matter Phys.* 71:065103. doi: 10.1103/PhysRevE.71.065103

Pievani, M., de Haan, W., Wu, T., Seeley, W. W., and Frisoni, G. (2011). Functional network disruption in the degenerative dementias. *Lancet Neurol.* 10, 829–843. doi: 10.1016/S1474-4422(11)70158-2

Preti, M. G., Bolton, T. A., and Van De Ville, D. (2017). The dynamic functional connectome: state-of-the-art and perspectives. *Neuroimage* 160, 41–54. doi: 10.1016/j.neuroimage.2016.12.061

Price, T., Wee, C. Y., Gao, W., and Shen, D. G. (2014). Multiple-network classification of childhood autism using functional connectivity dynamics. *Lect. Notes Comput. Sci.* 8675, 177–184. doi: 10.1007/978-3-319-10443-0_23

Rack-Gomer, A. L., and Liu, T. T. (2012). Caffeine increases the temporal variability of resting-state BOLD connectivity in the motor cortex. *Neuroimage* 59, 2994–3002. doi: 10.1016/j.neuroimage.2011.10.001

Racz, F. S., Mukli, P., Nagy, Z., and Eke, A. (2017). Increased prefrontal cortex connectivity during cognitive challenge assessed by fNIRS imaging. *Biomed. Opt. Express* 8, 3842–3855. doi: 10.1364/BOE.8.003842

Racz, F. S., Mukli, P., Nagy, Z., and Eke, A. (2018). Multifractal dynamics of resting-state functional connectivity in the prefrontal cortex. *Physiol. Meas.* 39:024003. doi: 10.1088/1361-6579/aaa916

Raichle, M. E., MacLeod, A. M., Snyde, A. Z., Powers, W. J., Gusnard, D. A., Shulman, G. L., et al. (2001). A default mode of brain function. *Proc. Natl. Acad. Sci. U.S.A.* 98, 676–682. doi: 10.1073/pnas.98.2.676

Rubinov, M., and Sporns, O. (2010). Complex network measures of brain connectivity: uses and interpretations. *Neuroimage* 52, 1059–1069. doi: 10.1016/j.neuroimage.2009.10.003

Sakoglu, U., Pearlson, G. D., Kiehl, K. A., Wang, Y. M., Michael, A. M., and Calhoun, V. D. (2010). A method for evaluating dynamic functional network connectivity and task-modulation: application to schizophrenia. *Magn. Reson. Mater. Phy.* 23, 351–366. doi: 10.1007/s10334-010-0197-8

Saupe, D. (1988). "Algorithms for random fractals," in *The Science of Fractal Images*, eds H. O. Peitgen and D. Saupe (Springer), 71–136.

Schmitt, D. T., Stein, P. K., and Ivanov, P. C. (2009). Stratification pattern of static and scale-invariant dynamic measures of heartbeat fluctuations across sleep stages in young and elderly. *Ieee Trans. Biomed. Eng.* 56, 1564–1573. doi: 10.1109/Tbme.2009.2014819

Schreiber, T., and Schmitz, A. (2000). Surrogate time series. *Phys. D* 142, 346–382. doi: 10.1016/S0167-2789(00)00043-9

Shimizu, Y., Barth, M., Windischberger, C., Moser, E., and Thurner, S. (2004). Wavelet-based multifractal analysis of fMRI time series. *Neuroimage* 22, 1195–1202. doi: 10.1016/j.neuroimage.2004.03.007

Sporns, O. (2011). The human connectome: a complex network. *Ann. N. Y. Acad. Sci.* 1224, 109–125. doi: 10.1111/j.1749-6632.2010.05888.x

Sporns, O., Tononi, G., and Kotter, R. (2005). The human connectome: a structural description of the human brain. *PLoS Comput. Biol.* 1:e42. doi: 10.1371/journal.pcbi.0010042

Stam, C. J. (2005). Nonlinear dynamical analysis of EEG and MEG: review of an emerging field. *Clin. Neurophysiol.* 116, 2266–2301. doi: 10.1016/j.clinph.2005.06.011

Stam, C. J., Breakspear, M. A. M., van Cappellen, W., and van Dijk, B. W. (2003). Nonlinear synchronization in EEG and whole-head MEG recordings of healthy subjects. *Hum. Brain Mapp.* 19, 63–78. doi: 10.1002/hbm.10106

Stam, C. J., and de Bruin, E. A. (2004). Scale-free dynamics of global functional connectivity in the human brain. *Hum. Brain Mapp.* 22, 97–109. doi: 10.1002/hbm.20016

Stam, C. J., and van Dijk, B. W. (2002). Synchronization likelihood: an unbiased measure of generalized synchronization in multivariate data sets. *Phys. D* 163, 236–251. doi: 10.1016/S0167-2789(01)00386-4

Tagliazucchi, E., Balenzuela, P., Fraiman, D., and Chialvo, D. R. (2012a). Criticality in large-scale brain FMRI dynamics unveiled by a novel point process analysis. *Front. Physiol.* 3:15. doi: 10.3389/fphys.2012.00015

Tagliazucchi, E., von Wegner, F., Morzelewski, A., Brodbeck, V., and Laufs, H. (2012b). Dynamic BOLD functional connectivity in humans and its electrophysiological correlates. *Front. Hum. Neurosci.* 6:339. doi: 10.3389/fnhum.2012.00339

Takens, F. (1981). "Detecting strange attractors in turbulence," in *Dynamical Systems and Turbulence, Warwick 1980*, eds D. Rand and L.S. Young (Berlin: Springer), 366–381.

Tel, T. (1988). Fractals, multifractals, and thermodynamics - an introductory review. *Z Naturforsch A* 43, 1154–1174. doi: 10.1515/zna-1988-1221

Theiler, J. (1986). spurious dimension from correlation algorithms applied to limited time-series data. *Phys. Rev. A* 34, 2427–2432. doi: 10.1103/PhysRevA.34.2427

Theiler, J. (1990). Estimating fractal dimension. *J. Opt. Soc. Am. A* 7, 1055–1073. doi: 10.1364/Josaa.7.001055

Theiler, J., Eubank, S., Longtin, A., Galdrikian, B., and Farmer, J. D. (1992). Testing for nonlinearity in time-series - the method of surrogate data. *Phys. D* 58, 77–94. doi: 10.1016/0167-2789(92)90102-S

Van de Ville, D., Britz, J., and Michel, C. M. (2010). EEG microstate sequences in healthy humans at rest reveal scale-free dynamics. *Proc. Natl. Acad. Sci. U.S.A.* 107, 18179–18184. doi: 10.1073/pnas.1007841107

van den Heuvel, M. P., and Hulshoff Pol, H. E. (2010). Exploring the brain network: a review on resting-state fMRI functional connectivity. *Eur. Neuropsychopharmacol.* 20, 519–534. doi: 10.1016/j.euroneuro.2010.03.008

Watts, D. J., and Strogatz, S. H. (1998). Collective dynamics of 'small-world' networks. *Nature* 393, 440–442. doi: 10.1038/30918

Werner, G. (2010). Fractals in the nervous system: conceptual implications for theoretical neuroscience. *Front. Physiol.* 1:15. doi: 10.3389/Fphys.2010.00015

Wink, A. M., Bullmore, E., Barnes, A., Bernard, F., and Suckling, J. (2008). Monofractal and multifractal dynamics of low frequency endogenous brain oscillations in functional MRI. *Hum. Brain Mapp.* 29, 791–801. doi: 10.1002/hbm.20593

Yaesoubi, M., Allen, E. A., Miller, R. L., and Calhoun, V. (2015a). Dynamic coherence analysis of resting fMRI data to jointly capture state-based phase, frequency, and time-domain information. *Neuroimage* 120, 133–142. doi: 10.1016/j.neuroimage.2015.07.002

Yaesoubi, M., Miller, R. L., and Calhoun, V. D. (2015b). Mutually temporally independent connectivity patterns: A new framework to study the dynamics of brain connectivity at rest with application to explain group difference based on gender. *Neuroimage* 107, 85–94. doi: 10.1016/j.neuroimage.2014.11.054

Yu, Q., Erhardt, E. B., Sui, J., Du, Y., He, H., Hjelm, D., et al. (2015). Assessing dynamic brain graphs of time-varying connectivity in fMRI data, Application to healthy controls and patients with schizophrenia. *Neuroimage* 107, 345–355. doi: 10.1016/j.neuroimage.2014.12.020

Conflict of Interest Statement: The authors declare that the research was conducted in the absence of any commercial or financial relationships that could be construed as a potential conflict of interest.

The handling editor is currently co-organizing a Research Topic with one of the authors, AE and confirms the absence of any other collaboration.

frontiers in Physiology

METHODS
published: 10 December 2018
doi: 10.3389/fphys.2018.01767

Fractal and Multifractal Properties of Electrographic Recordings of Human Brain Activity: Toward Its Use as a Signal Feature for Machine Learning in Clinical Applications

Lucas G. Souza França[1], José G. Vivas Miranda[2], Marco Leite[1], Niraj K. Sharma[1], Matthew C. Walker[1], Louis Lemieux[1] and Yujiang Wang[1,3,4]**

[1] Department of Clinical and Experimental Epilepsy, UCL Queen Square Institute of Neurology, University College London, London, United Kingdom, [2] Institute of Physics, Federal University of Bahia, Salvador, Brazil, [3] Interdisciplinary Computing and Complex BioSystems (ICOS) Research Group, School of Computing, Newcastle University, Newcastle upon Tyne, United Kingdom, [4] Institute of Neuroscience, Newcastle University, Newcastle upon Tyne, United Kingdom

OPEN ACCESS

Edited by:
Paul Bogdan,
University of Southern California,
United States

Reviewed by:
Andras Eke,
Semmelweis University, Hungary
Yuankun Xue,
University of Southern California,
United States
Damian Kelty-Stephen,
Grinnell College, United States

***Correspondence:**
Lucas G. Souza França
lucas.franca.14@ucl.ac.uk
Yujiang Wang
yujiang.wang@newcastle.ac.uk

Specialty section:
This article was submitted to Fractal Physiology, a section of the journal Frontiers in Physiology

Received: 25 June 2018
Accepted: 22 November 2018
Published: 10 December 2018

Citation:
França LGS, Miranda JGV, Leite M, Sharma NK, Walker MC, Lemieux L and Wang Y (2018) Fractal and Multifractal Properties of Electrographic Recordings of Human Brain Activity: Toward Its Use as a Signal Feature for Machine Learning in Clinical Applications. Front. Physiol. 9:1767. doi: 10.3389/fphys.2018.01767

The quantification of brain dynamics is essential to its understanding. However, the brain is a system operating on multiple time scales, and characterization of dynamics across time scales remains a challenge. One framework to study such dynamics is that of fractal geometry; and currently there exist several methods for the study of brain dynamics using fractal geometry. We aim to highlight some of the practical challenges of applying fractal geometry to brain dynamics—and as a putative feature for machine learning applications, and propose solutions to enable its wider use in neuroscience. Using intracranially recorded electroencephalogram (EEG) and simulated data, we compared monofractal and multifractal methods with regards to their sensitivity to signal variance. We found that both monofractal and multifractal properties correlate closely with signal variance, thus not being a useful feature of the signal. However, after applying an epoch-wise standardization procedure to the signal, we found that multifractal measures could offer non-redundant information compared to signal variance, power (in different frequency bands) and other established EEG signal measures. We also compared different multifractal estimation methods to each other in terms of reliability, and we found that the Chhabra-Jensen algorithm performed best. Finally, we investigated the impact of sampling frequency and epoch length on the estimation of multifractal properties. Using epileptic seizures as an example event in the EEG, we show that there may be an optimal time scale (i.e., combination of sampling frequency and epoch length) for detecting temporal changes in multifractal properties around seizures. The practical issues we highlighted and our suggested solutions should help in developing robust methods for the application of fractal geometry in EEG signals. Our analyses and observations also aid the theoretical understanding of the multifractal properties of the brain and might provide grounds for new discoveries in the study of brain signals. These could be crucial for the understanding of neurological function and for the developments of new treatments.

Keywords: EEG, fractal, multifractal, epilepsy, variance, characteristic time, signal features, machine learning

1. INTRODUCTION

Brain dynamics are non-linear and are often considered as one of the most complex natural phenomena, involving several different and interacting temporal scales. For example, fast electric activity, slower chemical reactions, and even slower diffusive processes have been observed in the brain. Interestingly, brain dynamics have also been characterized as "scale-free" (Stam and de Bruin, 2004; Fraiman and Chialvo, 2012), meaning that certain signal properties stay preserved across different time scales. To describe and quantify such time scale invariant dynamics, the framework of fractal geometry is often applied (Werner, 2010).

Fractals have two specific properties: they consist of parts that are similar to the whole—termed self-similarity, and they have a fractional Hausdorff-Besicovitch dimension, also called fractal dimension (FD) (Mandelbrot, 1982; Feder, 1988; Falconer, 2003). Fractal geometry has been applied to the study of temporal dynamics, such as human brain dynamics in health (Lutzenberger et al., 1995; Pereda et al., 1998; Eke et al., 2000, 2002; Linkenkaer-Hansen et al., 2001; Bullmore et al., 2003, 2009; Gong et al., 2003; Acharya et al., 2005; Bassett et al., 2006, 2010; Hsu et al., 2007; Van De Ville et al., 2010; Papo et al., 2017) and disease (Esteller et al., 1999; Gómez et al., 2009; Zappasodi et al., 2014), providing intriguing results. For example, FD has been shown to vary prior to and during epileptic seizures (Esteller et al., 1999).

Objects adequately characterized by a single fractal dimension are referred to as monofractals. However, the fractal formalism has to be extended to capture certain phenomena that cannot be described by a single fractal dimension; these are called multifractals (Stanley et al., 1999). Multifractal objects can be conceived as decomposable into different subsets or parts, each characterized by its own distinct fractal dimension. The subsets are more precisely described as different statistical moments, and a multifractal is an object where the fractal dimension depends on the statistical moment being examined (Mukli et al., 2015). Thus multifractal objects are often described by a spectrum, showing the subsets/statistical moments and their corresponding fractal dimensions. Some natural phenomena exhibit multifractal patterns in space, for example, turbulence (Meneveau and Sreenivasan, 1987; Chhabra and Jensen, 1989), soil composition (Miranda et al., 2006; Zeleke and Si, 2006; Vázquez et al., 2008; Paz-Ferreiro et al., 2010a,b); and in time, for example heart beat patterns (Ivanov et al., 1999), and human physical activity (França et al., 2019).

There is also considerable evidence that brain dynamics are multifractal (Suckling et al., 2008; Ihlen and Vereijken, 2010; Ciuciu, 2012; Zorick and Mandelkern, 2013; Zhang et al., 2015; Papo et al., 2017; Xue and Bogdan, 2017; Racz et al., 2018). At the very least, additional statistical moments appear to be required, to characterize such dynamics (Fraiman and Chialvo, 2012). Furthermore, it is known that interacting processes with different time scales, similar to those observed in the brain, can generate multifractal patterns (Argoul et al., 1989; Suckling et al., 2008).

To measure the multifractal spectrum in brain dynamics, Multifractal Detrended Fluctuation Analysis (MF-DFA) (Kantelhardt et al., 2002) is currently the most used approach (Ihlen, 2012; Zhang et al., 2015). However, more advanced and potentially more stable estimation techniques have been proposed, such as the Multifractal Detrended Moving Average (Xu et al., 2017), and Chhabra-Jensen approaches (Chhabra and Jensen, 1989). These techniques, to our knowledge, however, have not yet been evaluated with brain signals. In addition, there are several parameter choices to be made for the purpose of the analysis. For example, to capture time-varying changes in multifractal properties, the epoch length and sampling frequency have to be chosen. These parameters may impact the multifractal estimation (Eke et al., 2002), but, to date, have not been studied systematically in the context of brain dynamics.

The biggest gap in the literature so far, however, is how multifractal properties relate to existing time series signal measures of brain dynamics (e.g., variance of the signal, band power, etc.). A major concern is that complex methods of analysis may not offer a significant advance over simpler, already established methods—this is crucial to a putative feature in machine learning applications, e.g., seizure prediction or detection (Mormann et al., 2007; Freestone et al., 2015; Brinkmann et al., 2016; Baldassano et al., 2017; Karoly et al., 2017; Kuhlmann et al., 2018a,b; Varatharajah et al., 2018). For example, in the analysis of the electroencephalogram of epileptic seizures, complex methods were found to actually reproduce patterns detected by simpler measures such as variance of the signal (Martinerie et al., 2003; McSharry et al., 2003). It is therefore, essential to understand how the (mono- and multi-) fractal measures relate to more traditional measures, and if new features can be obtained from the signal by applying a mono- or multi-fractal formalism.

To summarize, there is a knowledge gap in three critical areas: (1) which (multi)fractal characterization methodology is best suited for brain signals? (2) what are the optimal estimation parameters (e.g., in terms of recording epoch length) of potentially time varying multifractal properties? (3) what is the relationship between (multi)fractal properties and more traditional and established time series signal measures? To address these questions, we chose to analyse intracranially recorded human electroencephalography (icEEG) data, due to its high temporal resolution and high signal to noise ratio.

2. MATERIALS AND METHODS

To address the questions above, we will first outline four experiments. We will then provide details on monofractal and and multifractal estimation methods, and also show how time series data with known mono- and multifractal properties can be generated to test the performance of the estimation methods. To test the multifractal measures on real-life brain signals, we then applied our analysis on human intracranial EEG. Thus, finally, we will summarize the EEG datasets used in this work.

The original scripts used in this work are available in https://github.com/yujiangwang/MultiFractalEEG. In addition, the following software packages were used: MATLAB; R (R Core Team, 2017); and ggplot2, R.matlab, reshape2, PerformanceAnalytics, and RColorBrewer (Wickham, 2007, 2009; Neuwirth, 2014; Peterson and Carl, 2014; Bengtsson, 2016).

2.1. Experiments

2.1.1. Experiment 1: Monofractal Estimation With Respect to Changing Signal Variance

Estimation of monofractal properties has been applied to EEG signals in the past with varying and often contrasting results (Esteller et al., 1999; Li et al., 2005). A particular concern is that complex measures may simply reflect simple properties of the signal (Martinerie et al., 2003; McSharry et al., 2003). Hence, in our first analysis, we focus on the relationship between monofractal measures and signal variance. For this, we used a simulated monofractal time series (termed fractional Brownian motion, or short fBm) with its standard deviation modulated by a modified ramp function.

The fBm was simulated with a Hurst exponent $H = 0.7$ and a modulating function M (described in more detail later and in **Appendix A** in **Supplementary Material**) and split into 1,800 1,024-sample epochs. We estimated the monofractal dimension of this simulated signal using the Higuchi and DFA methods. To assess the impact of signal variance, we have also tested the effect of epoch-based standardization. To ensure that our effects were not simply an artifact generated by the fBm, we also repeated the analysis on one exemplary icEEG data segment.

2.1.2. Experiment 2: Multifractal Estimation Stability

In order to evaluate the stability of multifractal properties in time, we generated a time series exhibiting stable multifractal properties over time using the p-Model. The time series was then evaluated using an epoch-based approach with the three estimators: MF-DFA, MF-DMA, and Chhabra-Jensen. The stability of the estimator can then simply be assessed as the temporal variability of its output.

2.1.3. Experiment 3: Multifractal Estimation of Human EEG and Its Potential Added Value

To assess whether the chosen multifractal metrics contribute any non-redundant features about the signal in addition to more established signal metrics, we analyzed human EEG signals recorded intracranially. Again, we used an epoch-based approach, and we compared the multifractal metrics to a number of conventional signal metrics (mean, standard deviation, line length, bandpower) on each epoch. The similarity between signal features was evaluated using Pearson correlation and Mutual Information (Guyon and Elisseeff, 2003) (the code is available at https://github.com/robince/gcmi) (Ince et al., 2017). Furthermore, monofractal metrics were also included in this comparison, to further demonstrate the advantages in applying a multifractal over monofractal approaches.

2.1.4. Experiment 4: Impact of Sampling Frequency and Epoch Length on Multifractal Estimation of Human EEG

Finally, we also evaluated the impact of the multifractal estimation parameters in the characterization of a seizure. We used intracranial EEG signals recorded from four patients undergoing pre-surgical planning, the signals were originally sampled at 5,000 Hz. For this analysis, down-sampled versions were evaluated with epochs of different sizes. To assess the effect of sampling frequency, we down-sampled the signal to 4,000, 3,000, 2,500, 2,000, 1,000, 800, 750, 600, 500, 400, 300, and 250 Hz. For each sampling frequency, we evaluated different epoch sizes (1,024, 2,048, 4,096, 8,192, and 16,384 points).

We defined a difference in multifractal spectrum width ($\Delta\alpha^{\dagger}$) during the seizure compared to the background as the effect size (Cohen's D) between the ictal and interictal periods:

$$D = \frac{< \Delta\alpha^{\dagger}_{ictal} > - < \Delta\alpha^{\dagger}_{interictal} >}{s(\Delta\alpha^{\dagger}_{interictal})} \quad (1)$$

where $< \Delta\alpha^{\dagger} >$ represents the mean and s denotes standard deviation.

2.2. Fractal Dimension Estimation

To estimate the monofractal properties from a time series, we used two established estimation approaches: Higuchi method (Higuchi, 1988) and Detrended Fluctuation Analysis (Peng et al., 1994). These methods are widely applied in the literature and aim to capture the features of a time series in a single scaling exponent.

Mandelbrot (1982) defined fractals as self-similar structures with fractal dimensions (*FD*) that are between their topological and embedding dimensions T and E, and an established relationship of $FD+H = E$, where $E = T+1$, $T = 1$ in the case of a time series, and H is the Hurst exponent. When assuming this self-similarity, we can measure both *FD* and H in our EEG time series as alternative ways of estimating the fractal dimension.

However, we also note that more generally, the fractal dimension *FD* and the Hurst exponent H do not necessarily reflect the same property of the time series (see Gneiting and Schlather, 2004 for more details). Indeed, we empirically tested the relationship between our estimated *FD* and H for an example EEG time series and found that *FD* and H correlate with $\rho = -0.8$, and their empirical relationship is $FD = -0.86H + 2.74$. For our application in EEG time series, we conclude that *FD* and H measure two related, but slightly different signal properties [*FD*: a measure of roughness, H: a measure of long memory dependency (Gneiting and Schlather, 2004)]. Note that this of course also depends on how the *FD* and H are estimated exactly. Nevertheless, for our paper, we will apply these two established methods to estimate *FD* and H, respectively. We will assess the properties of both methods in the context of EEG, to demonstrate that our conclusions generalize to both types of measures.

2.2.1. Higuchi Method

The Higuchi method measures the fractal dimension FD of a time series. It consists of constructing series with elements of an original time series and measuring their lengths (Higuchi, 1988). Given a time series with N time points $X(1), X(2), ..., X(N)$, the Equation (2) shows a rule for reconstructing smaller time series with elements of the original recording. The lengths of the time series can be assessed according to Equation (3). The brackets $\lfloor \rfloor$ represent Gauss' notation, i.e., the rounded integer of the division (Higuchi, 1988). The variable d represents a down-sampling factor of the original time series.

$$X(m), X(m+d), X(m+2d), ..., X\left(m + \left\lfloor \frac{N-m}{d} \right\rfloor d\right) \quad \text{where} \quad m = 1, 2, ..., d \quad (2)$$

$$L_m(d) = \frac{\left\{ \sum_{i=1}^{\lfloor (N-m)/d \rfloor} |X(m+id) - X(m+(i-1)d)| \frac{N-1}{\lfloor (N-m)/d \rfloor d} \right\}}{d} \quad (3)$$

If the average curve length $< L_m(d) >_m$ over d sets follows a power law, according to Equation (4), the time series has scaling properties, with a fractal dimension FD_{Hig}.

$$< L(d) > \propto d^{-FD_{Hig}} \quad (4)$$

The routine used in the estimation of Higuchi fractal dimension FD is available at https://uk.mathworks.com/matlabcentral/fileexchange/50290-higuchi-and-katz-fractal-dimension-measures.

2.2.2. Detrendred Fluctuation Analysis

The Detrended Fluctuation Analysis (DFA) method is an alternative method (Peng et al., 1994, 1995), which estimates the Hurst exponent H in time series data instead of the fractal dimension.

The method consists of the following steps: Initially the time series with N time points $X(1), X(2), ..., X(N)$ is integrated as follows:

$$y(k) = \sum_{i=1}^{k} (X(i) - \langle X \rangle) \quad (5)$$

Where $X(i)$ represents the $i-th$ element of the time series and $< X >$ denotes the mean over the whole recording. The second step consists of dividing the time series into N_l windows of length l, then the mean square root of the integrated series is subtracted from the local trend, in every window (Peng et al., 1995), as shown in Equation (6).

$$F(l) = \sqrt{\frac{1}{N_l} \sum_{k=1}^{N_l} [y(k) - y_l(k)]^2} \quad (6)$$

The local trend ($y_l(k)$) is obtained from a linear regression over the time series in the window, and number N_l represents the total number of windows. In the following step, Equation (6) is obtained for several window lengths (l). The relation between $F(l)$ and l is described by a power law, according to Equation (7), where H is the Hurst exponent.

$$F(l) \propto l^H \quad (7)$$

The code used here is available in the Physionet repository (https://www.physionet.org/physiotools/dfa/) (Peng et al., 1995; Goldberger et al., 2000).

2.3. Multifractal Spectrum Estimation

In this section, we describe three multifractal spectrum estimators: Multifractal Detrended Moving Average (Gu and Zhou, 2010), Multifractal Detrended Fluctuation Analysis (Kantelhardt et al., 2002; Ihlen and Vereijken, 2010; Ihlen, 2012), and Chhabra-Jensen (Chhabra and Jensen, 1989), as these are the most established methods used in the literature.

Multifractal properties are represented as spectra (**Figure 1**), where essentially the fractal scaling properties, or more precisely Hausdorff dimensions [often noted as $f(\alpha)$], are measured over a range of different singularities (α). Formally, the singularity spectrum is a function that describes the Hausdorff dimension of subsets of the time series $X(t)$ with a specific Hölder exponent, according to:

$$f(\alpha) = D_F\{X(t_s), H(X(t_s)) = \alpha\} \quad (8)$$

Essentially, $f(\alpha)$ is the Hausdorff dimension (D_F) of the subset (t_s) of the time series $X(t_s)$ that has a the Hölder exponent α (van den Berg, 1999; Murcio et al., 2015). A definition of the Hausdorff dimension is available in **Appendix D** in **Supplementary Material**.

To characterize the function, or singularity spectrum $f(\alpha)$, usually, the width ($\Delta\alpha$) and height (Δf)—differences of maximum and minimum values of α and $f(\alpha)$, respectively—of the spectrum are used. $\Delta\alpha$ indicates the range of singularities present in a time series, this is also the most commonly used measure of how multifractal a time series is. The spectrum height Δf indicates the range of Hausdorff dimensions present in the time series. See **Figure 1** for an exemplary singularity spectrum plot.

2.3.1. MF-DMA

Multifractal Detrended Moving Average (MF-DMA) is one of the most commonly used methods for the estimation of multifractal measures. The method of calculation consists of the following steps (Gu and Zhou, 2010): Given time series $X(t)$ with time points $X(1), X(2), ..., X(N)$, the cumulative sum time series is obtained:

$$y(t) = \sum_{t=1}^{N} X(t) \quad (9)$$

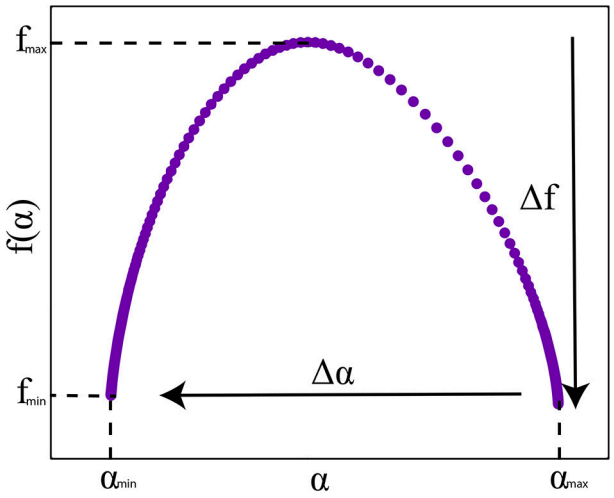

FIGURE 1 | Multifractal singularity spectrum with a characteristic parabolic shape. The spectrum width ($\Delta\alpha$) and height (Δf) measures are indicated by the arrows.

We then calculate the moving average over time windows of length l:

$$\tilde{y}(t) = \frac{1}{l}\sum_{z=0}^{l-1} y(t-z) \tag{10}$$

A detrended version of the signal is obtained by the subtraction:

$$\epsilon(i) = y(i) - \tilde{y}(i) \tag{11}$$

The resulting series is then divided in N_l disjoint sets of points of size l and a root-mean-square function is obtained for each set ν via:

$$F_\nu(l) = \left\{\frac{1}{l}\sum_{i=1}^{l}\epsilon_\nu^2(i)\right\}^{\frac{1}{2}} \tag{12}$$

A generalized qth-order overall fluctuation function can be obtained from:

$$F_q(l) = \left\{\frac{1}{N_l}\sum_{\nu=1}^{N_l} F_\nu(l)^q\right\}^{\frac{1}{q}} \quad q \neq 0 \tag{13}$$

and

$$\ln F_0(l) = \frac{1}{N_l}\sum_{\nu=1}^{N_l}\ln F_\nu(l) \quad \text{for} \quad q = 0 \tag{14}$$

It is possible to find a power-law relationship between $F^q(l)$ and the window length, or scale l by:

$$F^q(l) \propto l^{\alpha(q)} \tag{15}$$

The multifractal "mass exponent" (Biswas and Cresswell, 2012) can be defined as:

$$\tau(q) = q\alpha(q) - D_f \tag{16}$$

where D_f is the fractal dimension of the support measure. For a single-channel time series, $D_f = 1$. The spectrum, $f(\alpha)$, can be obtained with a Legendre transform (Gu and Zhou, 2010):

$$\alpha(q) = \frac{d\tau(q)}{dq} \tag{17}$$

$$f(q) = q\alpha - \tau(q) \tag{18}$$

It is important to note that the Legendre transform is known to cause problems in multifractal spectra derivations if some heterogeneities are present in the signal, as has been reported elsewhere (Chhabra and Jensen, 1989; Mukli et al., 2015).

2.3.2. MF-DFA

The Multifractal Detrended Fluctuation Analysis (MF-DFA) method is essentially a generalization of the DFA approach (Kantelhardt et al., 2002; Ihlen, 2012). The time series is first rebuilt according to Equation (5).

It is then divided into $N_l = \frac{N}{l}$ non-overlapping epochs ν of length l. The variance of the detrended series is calculated as follows:

$$F_\nu^2(l) = \frac{1}{l}\sum_{k=1}^{n}(y((\nu-1)l+1) - y_\nu(k))^2 \tag{19}$$

where y_ν represents the fitting in the epoch ν obtained via linear regression. The overall q-th order fluctuation functions can be obtained as:

$$F_q(l) = \left\{\frac{1}{N_l}\sum_{\nu=1}^{N_l}(F_\nu^2(l))^{\frac{q}{2}}\right\}^{\frac{1}{q}} \tag{20}$$

A log-log plot of $F_q(l)$ vs. l for different values of q should present a linear curve defined by the power law in Equation (15). Similarly to the MF-DMA method, the multifractal scaling exponent can be defined as in Equation (16) and the spectrum $f(\alpha)$ can be determined in the same way as in the MF-DMA approach.

2.3.3. Chhabra-Jensen

Multifractal spectra can be obtained in a more direct way, without the need for the Legendre transform using the Chhabra-Jensen (CJ) method (Chhabra and Jensen, 1989; Miranda et al., 2006; Zeleke and Si, 2006; Vázquez et al., 2008; Paz-Ferreiro et al., 2010a,b; Murcio et al., 2015; Xu et al., 2017; França et al.,

2019). Considering a time series as a distribution over time, the approach consists of calculating a family of generalized measures by covering the time series with windows. These are probabilistic measures with an emphasis factor q that accentuates different singularities depending on its value. More singular regions are emphasized by $q > 1$ whereas less singular regions will have a higher weight with $q < 1$ (Chhabra and Jensen, 1989).

First, we define:

$$\mu_i(q,l) = \frac{P_i(l)^q}{\sum_j P_j(l)^q} \tag{21}$$

where $P_i(l)$ represents the cumulative probability of a window i. l corresponds to the size of the window in which the generalized measures are obtained. The window epochs are indexed by the variables i and j. Then the multifractal spectra can be obtained directly from:

$$\alpha(q) = \lim_{l\to 0} \frac{\sum_i \mu_i(q,l)\log P_i(l)}{\log l} \tag{22}$$

and

$$f(q) = \lim_{l\to 0} \frac{\sum_i \mu_i(q,l)\log \mu_i(q,l)}{\log l} \tag{23}$$

A numerical approximation to the equations above is provided by the measures $M\alpha$ and Mf functions in Equations (24) and (25).

$$M\alpha = \sum_i \mu_i(q,l)\log P_i(l) \tag{24}$$

$$Mf = \sum_i \mu_i(q,l)\log \mu_i(q,l) \tag{25}$$

α and $f(q)$ can then be obtained as the slopes by regressing these two measures against the scales l: $M\alpha \sim l$ and $Mf \sim l$.

The algorithmic summary of the Chhabra-Jensen method consists of the following steps:

- The algorithm has as input the time series, a range of q values to which the spectrum will be evaluated, and window sizes l that vary in a dyadic scale.
- The time series is divided into non-overlapping epochs of length l and the generalized measures are estimated according to Equation (21).
- The measures $M\alpha$ and Mf are obtained from the generalized measures.
- α and $f(q)$ in Equations (22) and (23), respectively, are obtained with a linear regression procedure: $\log(M\alpha)$ is regressed against $-\log(l)$ and $log(Mf)$ is regressed against $-\log(l)$, they give α and f respectively as the slopes.
- A rejection criterion is also used, where all q exponent values with $R^2 < 0.9$ in the linear regression are not considered.

The code used in this study to calculate the multifractal spectrum is available at: https://github.com/lucasfr/chhabra-jensen. A flow-chart diagram of the algorithm is included in the repository above and in **Appendix Figure E1** in **Supplementary Material**.

2.4. Data

2.4.1. Simulating Fractal Time Series: Modulated Fractional Brownian Motion

To fully test methods of estimating the monofractal dimension from time series, we computationally produced time series that are known to be fractal (used for Experiment 1). We generated fractional Brownian motion (fBm) (Mandelbrot and Van Ness, 1968) profiles/time series using a novel modified version of the Wood-Chan or circulant embedding approach (Kroese and Botev, 2015; Shevchenko, 2015) that allow us to change the variance of the signal over time, in order to evaluate its influence on the fractal estimation. Our modulated fBM approach uses a modulating function, $M(t)$, which produces a signal that has an amplitude varying over time. The details of fBm and our Modulated fBm (ModfBm) are described in **Appendix A** in **Supplementary Material**. The fBm time series was simulated with Hurst exponent $H = 0.7$; the value was chosen due to its persistent features, i.e., it generates a time series with memory. The modulating function $M(t)$ used to modify the variance of the signal over time (see also described in **Appendix A** in **Supplementary Material**) is shown in **Figure 2C**. Using this method, we generated time series to evaluate the impact of variance change on monofractal estimators.

Note that there are alternative methods to generate monofractal time series (Davies and Harte, 1987; Eke et al., 2002; Mukli et al., 2015; Nagy et al., 2017). However, as our aim was not to compare generative models of monofractal time series, but rather simply demonstrate that the effects we observe in EEG signals could be more general. We chose the above mentioned approaches as example demonstrations.

2.4.2. Simulating Multifractal Time Series: p-Model

Similarly to the fBm, we also used a computational procedure to generate time series that are known to be multifractal (for Experiment 2) based on the *p-model*, which was developed to reproduce features observed in turbulence experiments known to have multifractal properties (Meneveau and Sreenivasan, 1987). This is a simple model, having a single fraction p_1 as its only input and is often mentioned in literature (Meneveau and Sreenivasan, 1987, 1991; Lipa and Buschbeck, 1989; She and Leveque, 1994; Consolini et al., 1996; Davis et al., 1997; Sreenivasan and Antonia, 1997; Kestener and Arneodo, 2003; Zhou, 2008; Pechlivanidis and Arheimer, 2015). Briefly the algorithm works as follows: From an interval of length L and height $\epsilon_L = c$ (is a constant), we create two segments of length $L/2$. Based on the input parameter p_1, it is possible to establish a second fraction in which a second parameter will be given by $p_2 = 1 - p_1$. The heights of each interval will thus be given by $y = 2p_1\epsilon_L$, and $y = 2p_2\epsilon_L$, respectively. This procedure is repeated for

each remaining segment, selecting left or right for p_1 randomly (Meneveau and Sreenivasan, 1987).

We employed the *p-model* in the simulation of a time series profile with multifractal properties to be evaluated by different estimation methods. It was generated with a code available at http://www2.meteo.uni-bonn.de/staff/venema/themes/surrogates/pmodel/ (Davis et al., 1997; Venema et al., 2006). Using this algorithm, we generated time series to evaluate the performance of different multifractal estimators with $p = 0.4$. The value was rounded (for simplicity) from the figure used elsewhere ($p = 0.375$) (Davis et al., 1997).

2.4.3. Human EEG Data

Intracranial EEG data segments extracted from recordings in patients undergoing evaluation for epilepsy surgery were used for Experiments 3 and 4. In order to evaluate the effect of EEG signal variance change on multifractal properties (Experiment 3), we specifically looked for one recording, where the signal variance changes dramatically over time. One such recording was found in one patient (male, 28 years old, temporal lobe epilepsy, recorded at the National Hospital for Neurology and Neurosurgery (NHNN) (UCLH NHS Foundation Trust, Queen Square, London, UK), patient ID: "NHNN1") near one seizure event. We used a 60-min recording segment around the epileptic seizure for our analysis. The seizure onset and offset were marked by expert clinicians, independent of this research project. Note that we used this segment specifically due to the dramatic change in signal variance, which actually occurred before the seizure and evolves over about 15 min. We do not make conclusions about the seizure event itself at this stage, but rather use this recording as an example to illustrate a technical point about multifractal property estimation from EEG.

To analyse the possible changes in multifractal properties during seizures (Experiment 4), we used a different dataset: Intracranial EEG from four subjects were retrieved from the ieeg.org repository (http://www.ieeg.org/) (Wagenaar et al., 2013): "I001_P005_D01," "I001_P034_D01," "I001_P010_D01," and "Study 040." These subjects were chosen due to the high sampling rate of their recordings (5 kHz), as we evaluated the impact of sampling frequency on multifractal properties. We extracted a 15-min segment around every seizure in each patient for further analysis. In Experiment 4, we performed the multifractal analysis on channels that were marked as seizure onset channels. We show the results for one patient in the main figure and the results for the remaining three patients are shown in **Appendix B** in **Supplementary Material**. Further information on the recordings is available in **Appendix F** in **Supplementary Material**.

The anonymized data analyzed in this study were recorded in patients undergoing evaluation for epilepsy surgery. iEEG.org portal provided EEG data and ethical approval for analyzing the data was provided by Mayo Clinic IRB (Brinkmann et al., 2009, 2016).

For NHNN data, the subject gave informed written consent, and the study was approved by the Joint Research Ethics Committee of the NHNN (UCLH NHS Foundation Trust) and UCL Queen Square Institute of Neurology, Queen Square, London, UK.

2.5. Pre-processing and Analysis of Time Series

Unless stated otherwise, we have applied the same pre-processing and analysis parameters to the computationally generated time series and the human EEG recordings and performed the fractal and multifractal estimations on 1,024-sample epochs. In Experiments 1 and 2, we were specifically interested in the effect of signal variance on the (multi) fractal estimation, and for comparison we also subjected the EEG signal to a standardization procedure, as follows:

$$x' = \frac{X - < X >}{s} \tag{26}$$

where $< X >$ is the epoch mean and s the epoch standard deviation of the time series X, resulting in a time series with zero mean and unit standard deviation in each epoch.

The Chhabra-Jensen method requires as input a distribution function over the domain of positive real numbers, which is incompatible with EEG data which contain positive and negative values. Hence, we propose the use of a sigmoid-transformation here (Equation 27) to map the time series onto positive values, in order to apply the Chhabra-Jensen method. Example sigmoid functions and correspondingly transformed EEG signal are shown in **Appendix Figure E2** in **Supplementary Material**.

$$\sigma(X) = \frac{1}{1 + e^{\nu X}} \tag{27}$$

The parameter ν was chosen based on its effect on the estimated multifractal width for three types of time series: icEEG (NHNN1-channel 1), surrogate EEG (temporally shuffled values of the original time series from NHNN1-channel 1) and a simulated random series (with the same mean and variance), across the range $\nu = [0.1, 2.0]$ in steps of 0.1. To find the optimal value for the parameter ν, we needed to balance the trade-off between the three series in terms of presenting the most distinct $\Delta\alpha$ values (**Appendix Figure E3A** in **Supplementary Material**), while showing minimum distortion on the recording, or maximum correlation with the original time series (**Appendix Figure E3B** in **Supplementary Material**). We chose $\nu = 1$ as an acceptable trade-off point. Finally, to compare multifractal properties to classical EEG frequency band power, we used the following definitions for the classical EEG frequency bands: δ (0.5–4 Hz), θ (4–8 Hz), α (8–15 Hz), β (15–30 Hz), and γ (30–60 Hz).

3. RESULTS

3.1. Experiment 1: Monofractal Estimation With Respect to Changing Signal Variance

We evaluated the relationship between monofractal measures and signal variance using a simulated time series based on fractional Brownian motion (fBm), where its signal variance

is modulated by a modified ramp function. The modulation function is shown in **Figure 2A** and resulting time series in **Figure 2B**. The standard deviation of the generated time series indeed tracks the shape of the modulating function (**Figure 2C**).

We estimated the monofractal dimension of this simulated signal using two standard methods: Higuchi and DFA. We observe that both methods appear to be affected by the changing signal variance (**Figures 2D,F**). Furthermore, the effect persists even after epoch-based standardization (**Figures 2E,G**): the monofractal properties and standard deviation correlate with $\rho = 1.00$ and $\rho = 0.99$ for the Higuchi and DFA methods, respectively. A similar effect was observed for a real icEEG recording that contained changes in signal variance over time (**Appendix Figure E4** in **Supplementary Material**).

In conclusion, monofractal properties derived for each epoch from DFA and Higuchi methods (with, or without signal standardization) correlate highly with the signal standard deviation of the epoch. Therefore, in epoch-based approaches (e.g., for application such as detecting or predicting epileptic seizures), the monofractal properties cannot be regarded as a new useful EEG feature of an epoch that is not redundant to standard deviation of the epoch. Thus we turn our attention to multifractal properties of the signal next.

3.2. Experiment 2: Multifractal Estimation Stability

In the following, we will denote the epoch-wise estimates of multifractal width $\Delta\alpha$ and height Δf (and $\Delta\alpha^{\dagger}$ and $\Delta f^{\dagger}$ for the measure of the epoch-based standardized time series).

This experiment was designed to assess the reliability of the different multifractal estimation methods over time. In other words, if the multifractal properties of the time series remain constant over different epochs, then we expect the multifractal estimation method to show the same output over these different epochs. Note that the accuracy of these methods (i.e., the method outputting the expected multifractal measures of a predefined multifractal object with known multifractal properties) has been demonstrated elsewhere (Chhabra and Jensen, 1989; Kantelhardt et al., 2002; Gu and Zhou, 2010).

Figure 3 shows the simulated signal by the p-model and the outputs of the three multifractal spectral estimation methods. In all cases, the magnitude of $\Delta\alpha^{\dagger}$ and $\Delta f^{\dagger}$ were clearly different from zero. The ($\Delta\alpha^{\dagger}$, $\Delta f^{\dagger}$) output variances over time for the MF-DFA, MF-DMA, and Chhabra-Jensen estimation methods were: (0.018, 0.18), (4.17e-4, 0.0028), and (2.3e-30, 6.5e-30), respectively. In addition, the MF-DFA output violated the theoretical topological limit of $\Delta f^{\dagger} = 1$, again indicating problems in the MF-DFA method, potentially due to the inversion of multifractal spectrum (Mukli et al., 2015). As the Chhabra-Jensen method shows the lowest variance over time (i.e., most reliable/stable), it will be our multifractal analysis method of choice for the remainder of this work.

3.3. Experiment 3: Multifractal Estimation of Human EEG and Its Potential Added Value

Next, we evaluated the relationship between multifractal signal properties and other widely used conventional EEG measures (such as signal variance). **Figure 4** shows the results of the multifractal spectrum and conventional measures in comparison. The pattern of multifractal spectrum width without epoch-based standardization ($\Delta\alpha$) reflects the signal variance closely, in contrast to the estimate for the epoch-based standardized signal ($\Delta\alpha^{\dagger}$). Finally, signal line length also shows a very different temporal profile from $\Delta\alpha^{\dagger}$. A similar figure showing the variation of Δf and $\Delta f^{\dagger}$ metrics is available in **Appendix Figure E5** in **Supplementary Material**.

Figure 5 shows the quantification of similarities of the signals in **Figure 4** through a correlation analysis. In summary, a high degree of correlation is present between the signal standard deviation, multifractal spectrum width ($\Delta\alpha$), and detrended fluctuation analysis (monofractal approach) both with and without epoch-based standardization. We found that standardization reduces the correlation between $\Delta\alpha$ and the standard variation from $\rho = 0.86$ (for $\Delta\alpha$) to $\rho = -0.14$ (for $\Delta\alpha^{\dagger}$). We also note that $\Delta\alpha$ is highly correlated with DFA and DFA† estimates ($\rho = 0.74$ and $\rho = 0.71$, respectively) while it is markedly reduced for $\Delta\alpha^{\dagger}$ ($|\rho| < 0.3$). The analysis based on the mutual information (Ince et al., 2017) rather than correlation showed a similar pattern (**Appendix Figure E6** in **Supplementary Material**).

The relationships of the multifractal properties and specific EEG frequency band power are shown in **Figure 6**. In summary, the correlation values between the multifractal measures $\Delta\alpha^{\dagger}$, $\Delta f^{\dagger}$, and signal power in the classical EEG bands are low ($|\rho| < 0.3$). A supplementary analysis of EEG time series data containing different sleep stages (which are known to be dominated by specific frequencies) shows similar results (see **Appendix C** in **Supplementary Material**). Based on these results, we focused on $\Delta\alpha^{\dagger}$ (using epoch-wise standardization of the time series) in the subsequent analysis.

3.4. Experiment 4: Impact of Sampling Frequency and Epoch Length on Multifractal Estimation of Human EEG

The variation of the multifractal spectrum width $\Delta\alpha^{\dagger}$ for different combinations of epoch sizes and sampling frequencies is shown in **Figure 7A**. On visual inspection, it is clear that there are some combinations of epoch size and sampling frequency that show a clear increase of $\Delta\alpha^{\dagger}$ during the ictal period (marked by the red lines). To quantify this effect, **Figure 7B** shows the Cohen's effect size D of the ictal vs. interictal $\Delta\alpha^{\dagger}$ distributions plotted against epoch duration (in seconds). In this plot, we included 15 different sampling frequencies, and also data from three different EEG channels (all in the seizure onset zone). A peak in D can be seen at about 1 s (across all sampling frequencies), indicating that the change in $\Delta\alpha^{\dagger}$ during a seizure can be best captured when using 1 s epochs (regardless of sampling frequency). This effect was not found for

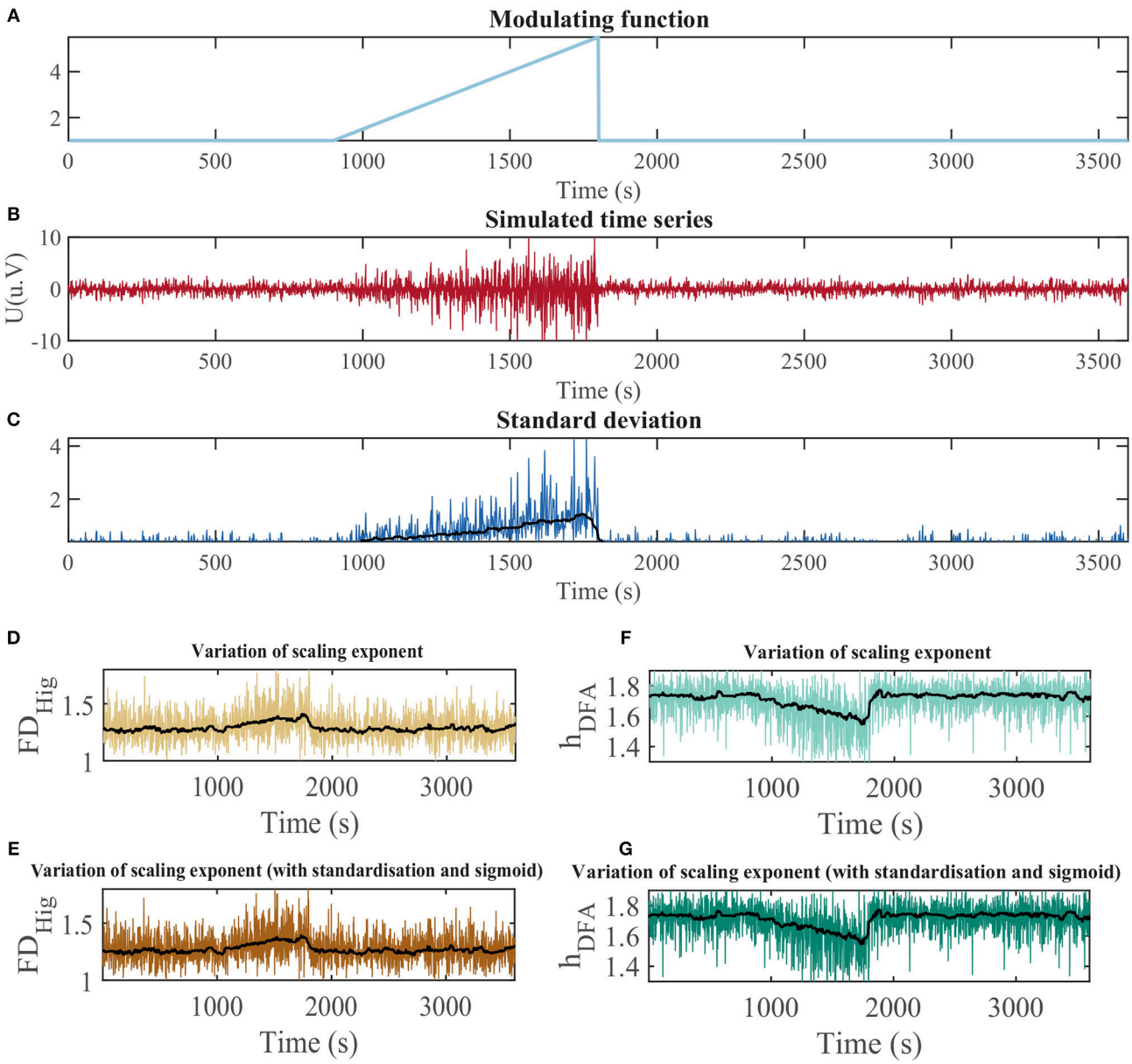

FIGURE 2 | Impact of the signal standard deviation on monofractal scaling exponent estimation. **(A)** Modulation of the standard deviation of the time series over time; **(B)** Time series simulated using fractional Brownian motion based on modulation in **(A)**; **(C)** Standard deviation of the simulated signal in **(B)**. **(D)** Monofractal dimension obtained with the Higuchi method from signal without epoch-based standardization. **(E)** Monofractal dimension obtained with the Higuchi method from epoch-based standardized signal. **(F)** Hurst exponent obtained with the DFA method from signal without epoch-based standardization. **(G)** Hurst exponent obtained with the DFA method from epoch-based standardized signal.

the sampling frequency or epoch length separately. Similar results for additional patients are shown on Supplementary materials (**Appendix B** in **Supplementary Material**).

4. DISCUSSION

In this study, we have explored the monofractal and multifractal properties of human EEG recordings and used simulated data to test the performance of fractal property estimation methods. Although mono- and multi-fractal approaches have been widely employed in the study of physiological signals in humans (Ivanov et al., 1999; Stanley et al., 1999; Hu et al., 2004, 2009; Costa et al., 2017; França et al., 2019), we have demonstrated that the monofractal dimension may be capturing a similar signal feature as the signal variance. When using standardization to remove the effect of signal variance, we demonstrated that multifractal measures (estimated by the Chhabra-Jensen method) capture information not contained in widely used conventional signal

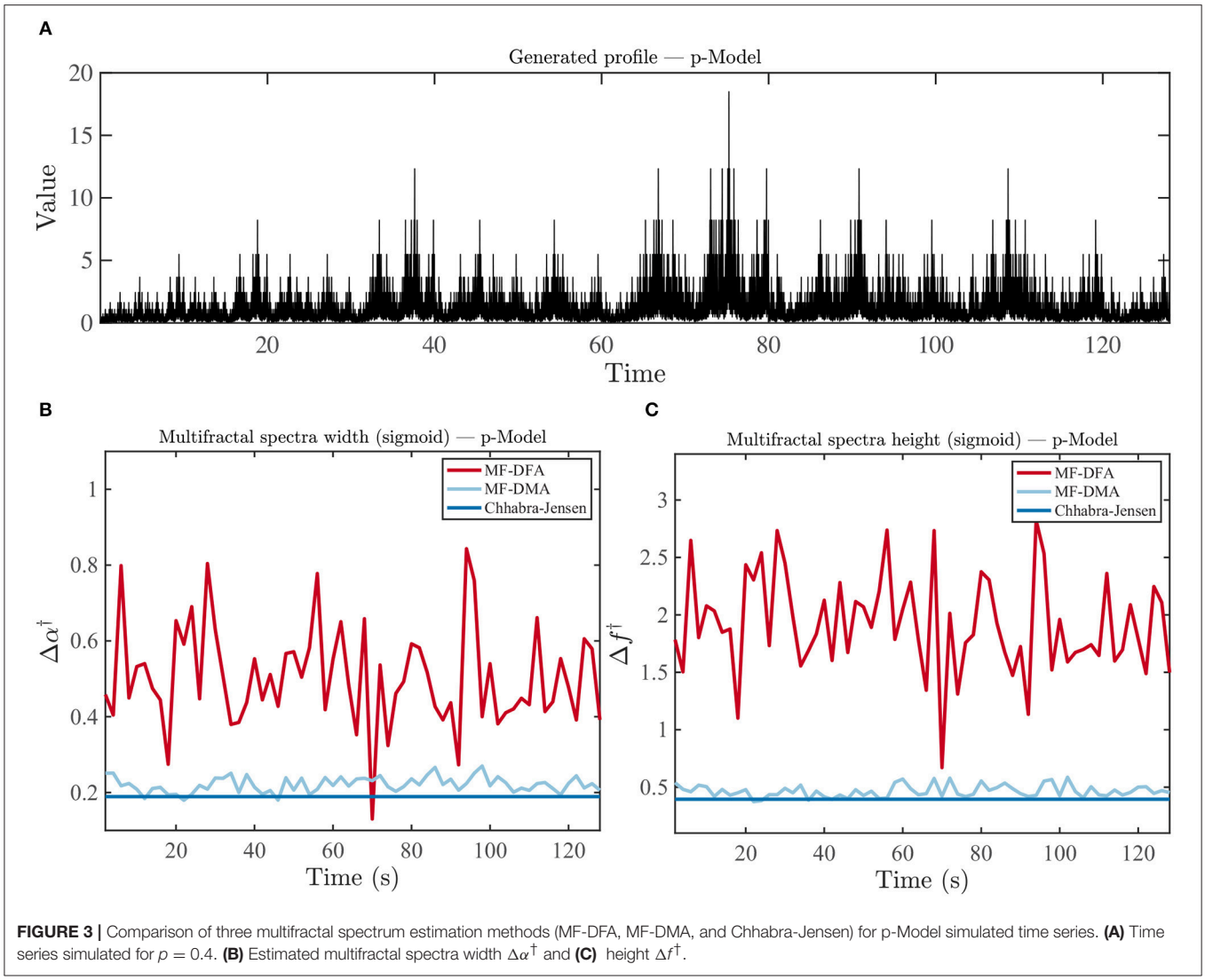

FIGURE 3 | Comparison of three multifractal spectrum estimation methods (MF-DFA, MF-DMA, and Chhabra-Jensen) for p-Model simulated time series. **(A)** Time series simulated for $p = 0.4$. **(B)** Estimated multifractal spectra width $\Delta\alpha^{\dagger}$ and **(C)** height $\Delta f^{\dagger}$.

measures, making it a viable feature for machine learning in clinical EEG applications. Finally, using epileptic seizure as an example, we showed that the epoch length can significantly impact the detection of time-varying effects in multifractal properties, suggesting the need for data- and application-specific optimization.

4.1. Methodological Considerations

One of our key observations is that monofractal estimators are tightly correlated with signal variance—even following epoch-wise standardization, whereas multifractal properties following epoch-wise standardization are no longer tightly correlated with signal variance. This may appear to be a curious and non-intuitive observation that, to our knowledge, has not been reported before.

To interpret this observation, it is worth noting the relationship between monofractal and multifractal analyses. Essentially, in multifractal analysis, at the point for which $q = 2$, the corresponding $f(\alpha)$ is the so-called correlation dimension, which is an alternative way of estimating the monofractal dimension (Murcio et al., 2015). The relationship between monofractal dimension and signal variance has been established and explained before (Cannon et al., 1997). By the same token, signal variance also affects higher statistical moments ($q > 2$ or $q < -2$). However, when analysing the exact effect of variance on the multifractal spectrum (**Appendix Figure E9** in **Supplementary Material**), we observe that the variance particularly impacts the multifractal spectrum width and height, but maintains an almost constant value of $f(\alpha)$ for $q = 2$. This explains why epoch-wise standardization does not impact monofractal dimension but does impact multifractal spectrum width and height. The mono- and multifractal properties we are investigating here are essentially describing different properties of the multifractal spectrum. Note that through our standardization procedure, we do not abolish "multifractality," but only its dependence on signal variance. Future work has to show mathematically the exact reason for this observation, although intuitively it is understandable that the standardization

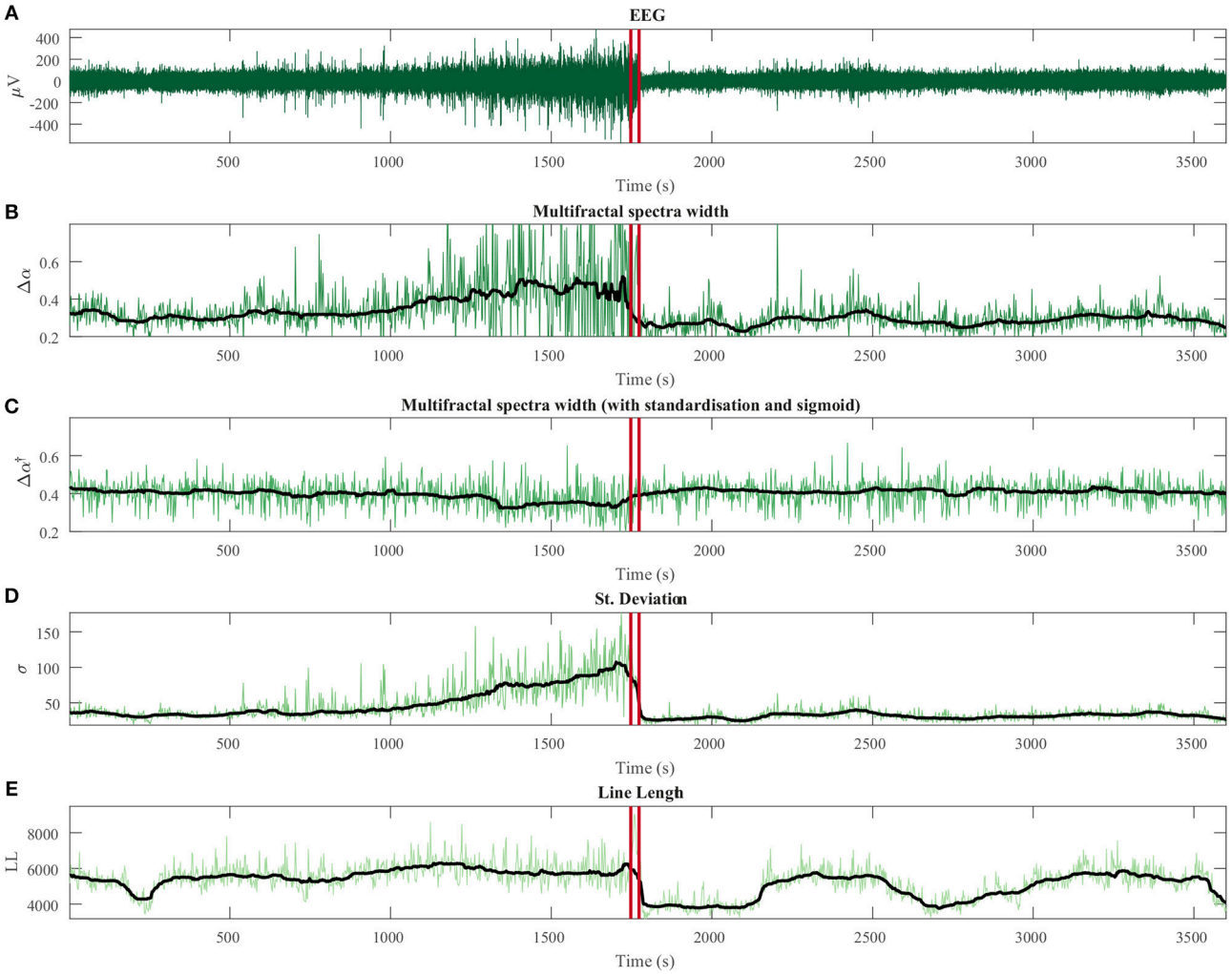

FIGURE 4 | Temporal dynamics of multifractal spectrum width compared with conventional measures for human intracranial EEG. **(A)** Intracranial EEG segment containing a seizure (onset and offset marked with red vertical lines). Note that this recording was chosen because it showed a dramatic change in signal variance during non-seizure periods, not because of any seizure related properties. **(B)** Variation of multifractal spectrum width without epoch-wise standardization ($\Delta\alpha$). **(C)** Multifractal spectrum width based on epoch-wise standardized time series ($\Delta\alpha^{\dagger}$). **(D)** Standard deviation in each epoch. **(E)** Line length in each epoch. Black line: moving average of each measure.

procedure (a linear transformation of the signal) changes the $q = 2$ moment least and affects higher moment more.

We further observed that the Chhabra-Jensen method is the most reliable out of the three multifractal estimation methods. As was pointed out in the original publication (Chhabra and Jensen, 1989), this is most likely due to the fact that the Chhabra-Jensen method avoids a Legendre transform that the other methods require. The Legendre transformation requires smoothing of the D_q curve and can lead to errors. For further advantages of the Chhabra-Jensen method, the reader is referred to the original publication (Chhabra and Jensen, 1989). A recent development, FMF method (Mukli et al., 2015; Nagy et al., 2017), may be an alternative to the approach proposed in this study.

Finally, our analysis highlighted the importance of choosing an adequate epoch size given a sampling frequency, in order to study events such as epileptic seizures. However, our study was based on the analysis of ictal vs. interictal epochs, i.e., a hard separation that may not represent continuous phenomena accurately. Future work should take into account that multifractal properties may be continuously changing over time (a striking example is shown in **Appendix Figure E7** in **Supplementary Material**), and an explicitly time based approach may be needed. Along similar lines, our finding of a optimal time scale may be due to the non-stationary nature of the multifractal properties. Further theoretical work may have to develop a temporally resolved multifractal estimator, in order to fully understand this aspect.

4.2. Implications for the Understanding of Brain Activity and Brain Generators

Previous studies reported that the brain is characterized by critical dynamics (Eguíluz et al., 2005; Chialvo, 2010, 2012; Racz

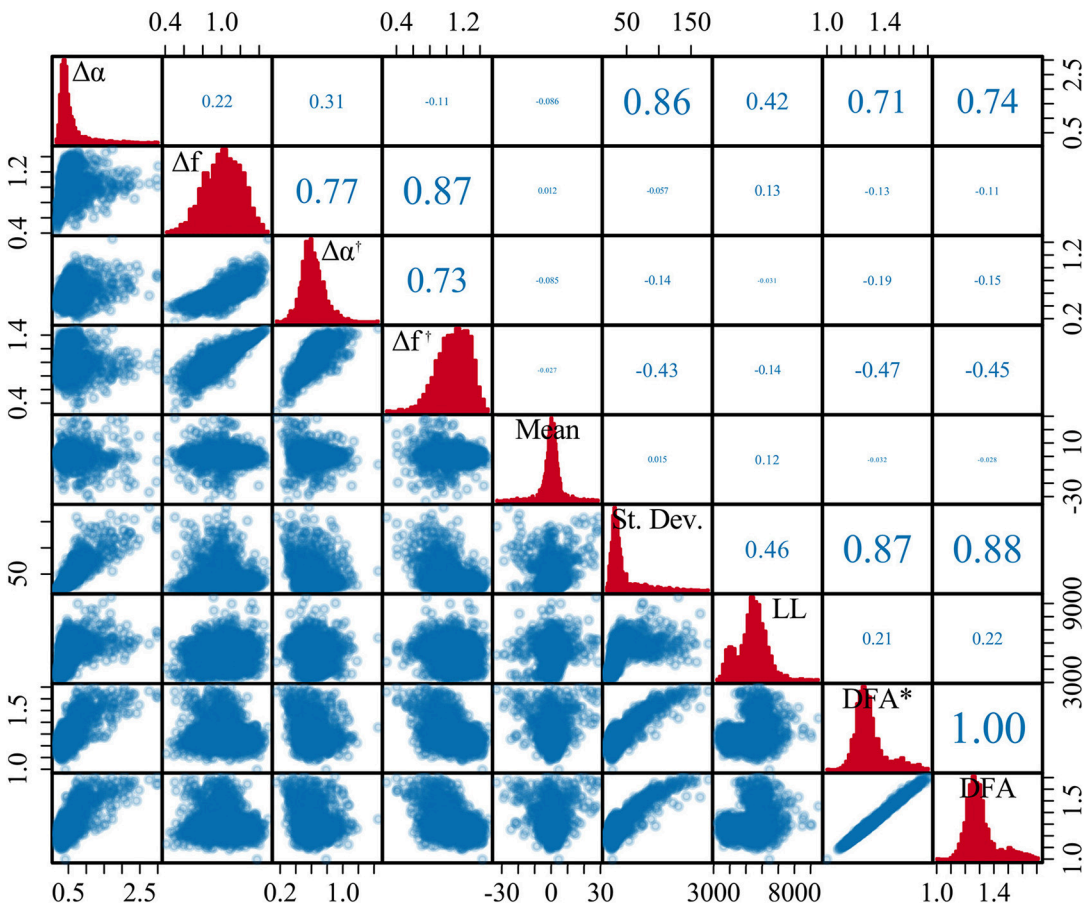

FIGURE 5 | Correlation between multifractal spectrum and conventional EEG measures for human icEEG data (from **Figure 4**). The diagonal of the matrix shows the distribution for each measure across epochs. The lower triangle contains the scatter plots for each pair of measures across epochs. The upper triangle shows the Pearson correlation value for each pair of measure, where the size of the font additionally corresponds to the correlation coefficient to provide an additional visual cue.

et al., 2018). This characteristic, found from microscopic spatial scales (such as neuronal networks) (Beggs and Plenz, 2003, 2004) to the whole-brain level (Eguíluz et al., 2005), is thought to facilitate the storage and processing of information. It has been further suggested that more than one scaling exponent would be necessary to properly characterize the brain's critical dynamics (Suckling et al., 2008; Ihlen and Vereijken, 2010; Ciuciu, 2012; Fraiman and Chialvo, 2012; Zorick and Mandelkern, 2013; Papo, 2014; Zhang et al., 2015; Papo et al., 2017; Racz et al., 2018), as departures from the power-law pattern have been frequently observed in brain signals. Hence, it has been proposed that using additional, higher-order statistical moments can better characterize such data (Fraiman and Chialvo, 2012). In this work, we contribute a complementary observation: while monofractal measures of EEG appeared to essentially follow the slow changes of signal variance, multifractal characterization is capable of revealing new information.

In terms of generative processes that can produce monofractal properties, it has been suggested that a property called Self-Organized Criticality (SOC) (Bak et al., 1987) may play an essential role. SOC describes the capacity of a system to evolve naturally into a critical state (a state in which a minimum perturbation could lead to events of all sizes). Such phenomena display power-law distributions and fractal properties as signatures (Bak and Paczuski, 1995). An example process that displays SOC is the so-called single avalanche or Bak–Tang–Wiesenfeld model (also known as Abelian sandpile model) (Bak et al., 1987). SOC behavior has been linked to physiological control mechanisms, such as in human heart rate variability (Goldberger et al., 2002). Similar to SOC, a related regime—termed non-classical SOC—is thought to give rise to multifractal properties (Lovejoy and Schertzer, 2007). The analysis and understanding of the non-classical SOC is, however, still under development.

In this context, our multifractal spectral analyses of human EEG data suggest that cerebral phenomena should not be modeled by a single avalanche model (classical SOC), in agreement with findings in a previous study (Fraiman and Chialvo, 2012). Moreover, it is hypothesized that brain dynamics are non-ergodic (Bianco et al., 2007), i.e., display preferential states and depends on previous states (Papo, 2014), which are all properties of multifractal processes (Lovejoy and Schertzer,

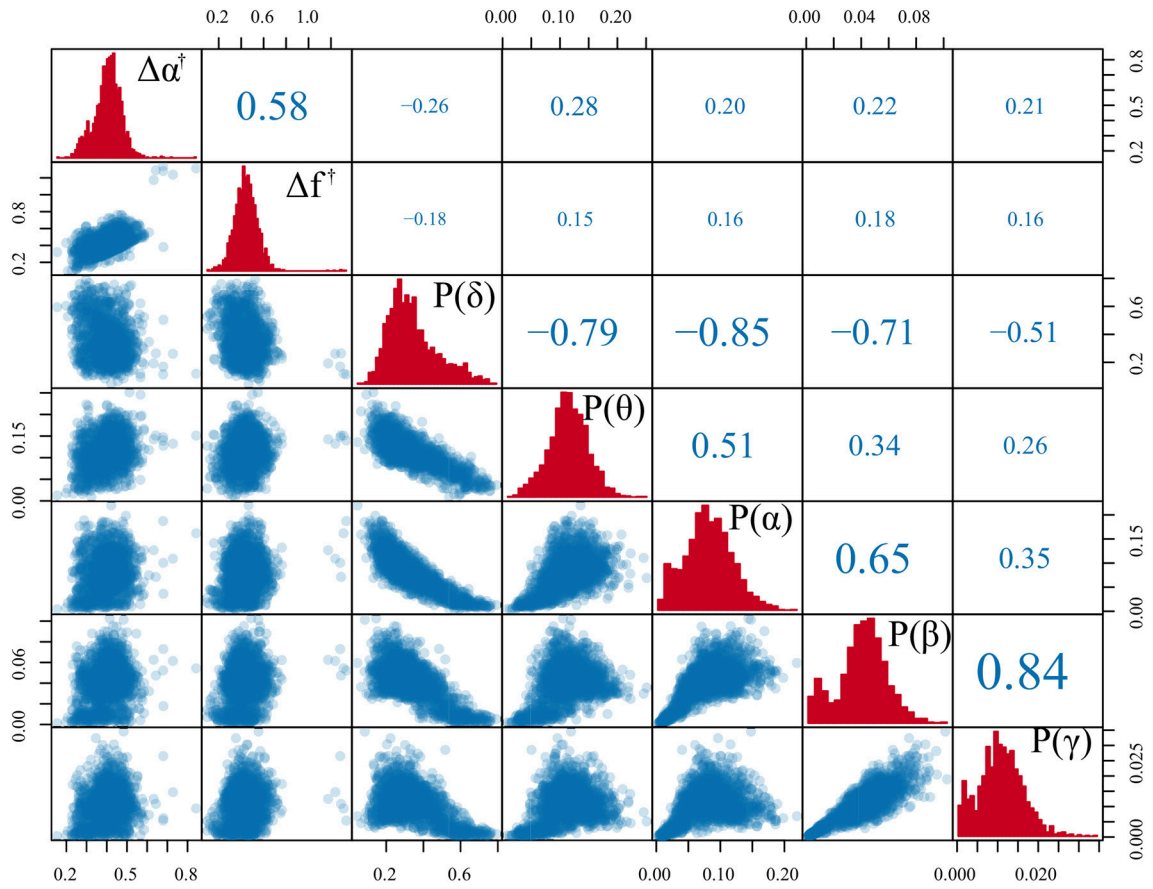

FIGURE 6 | Comparison of multifractal measures with classical spectral band power. Scatter plot matrix comparing both standardized multifractal spectrum width and height ($\Delta\alpha^{\dagger}$ and $\Delta f^{\dagger}$) with the δ, θ, α, β, and γ average band power in each epoch. Each scatter point is derived from a single epoch of the time series. The diagonal of the matrix features the histograms for each measure. The lower triangle contains the scatter plots for each pair of measures. The upper triangle shows the Pearson correlation for each pair of measure, where the size of the font additionally corresponds to the correlation coefficient to provide an additional visual cue. The icEEG data underlying this figure is shown in **Figure 4A**.

2007). Thus, multifractal analyses could provide a new paradigm for studying brain function and structure, as previously suggested in other studies of normal (Suckling et al., 2008; Ihlen and Vereijken, 2010; Ciuciu, 2012; Zorick and Mandelkern, 2013; Papo, 2014; Papo et al., 2017; Racz et al., 2018) and pathological brain activity (Zhang et al., 2015). Furthermore, generative processes displaying multifractal properties could help understanding the observed multifractal changes on a mechanistic level.

4.3. On the Detection of Brain State Transitions in Health and Disease

We want to emphasize that the conclusions from our work are drawn on the basis that slow changes in signal fractal features can be captured by using an epoch-wise feature extraction procedure. It is also from a feature redundancy perspective that we argue for the need of multifractal approaches over monofractal measures. We do not dispute the usefulness of monofractal measures in other general applications. In our work, we essentially performed a feature selection procedure using correlation and mutual information (Guyon and Elisseeff, 2003). We evaluated how different signal feature compare on an epoch-wise basis. Feature selection is crucial to obtain faster and cost effective models, and avoids overfitting of the available data. It might also help achieving a deeper insight into the nature of the studied phenomena (Blum and Langley, 1997; Liu et al., 1998; Guyon and Elisseeff, 2003; Liu and Yu, 2005; Saeys et al., 2007).

A fundamental observation in our work is that an optimal time scales may exist for specific physiological processes (such as epileptic seizures) in terms of their multifractal dynamics (**Figure 7** and **Appendix B** in **Supplementary Material**). This result suggests that, at least in an epoch-based study, for any given epileptic seizure in a given patient, the variety of scaling exponents ($\Delta\alpha$) will depend on the length of the epoch analyzed. This is further supported by similar findings in monofractal analysis (Eke et al., 2002). The implications of this observation are that certain scaling exponents will only exist in specific time scales and the diversity of scaling exponents will depend on the duration of the epoch. These results suggest the potential need for "tuning," i.e., potentially having to find the characteristic

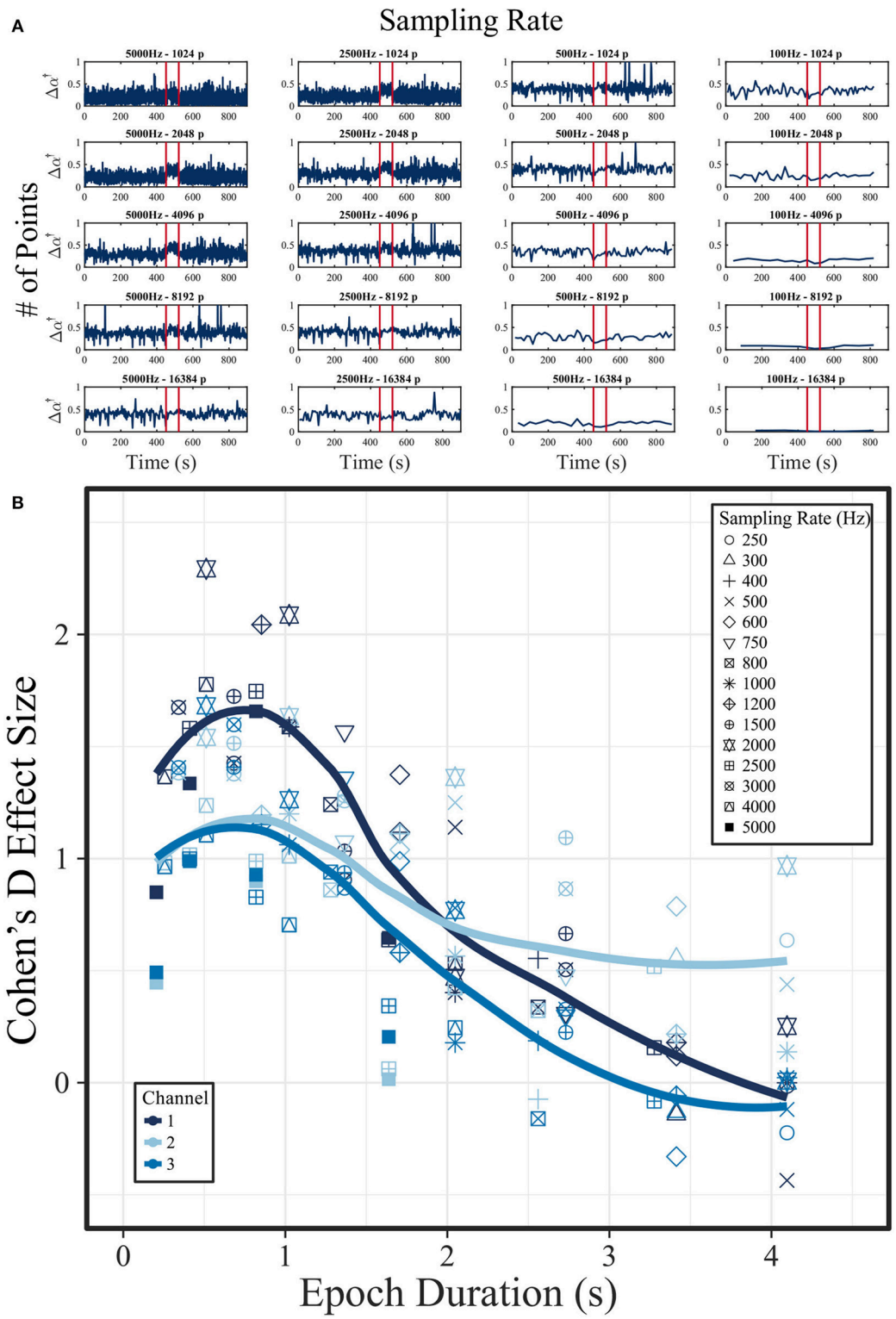

FIGURE 7 | Influence of EEG sampling frequency and epoch length on multifractal spectrum width around and during an epileptic seizure. **(A)** Multifractal spectrum width ($\Delta\alpha^{\dagger}$) in a 15-min intracranial EEG segment containing one seizure (onset and offset marked by the red lines). The signal was initially sampled at 5,000 Hz. Each column shows $\Delta\alpha^{\dagger}$ for 5,000, 2,500, 500, and 100 Hz sampling rates. Different epoch sizes were used ranging from 1,024 to 16,384 samples (in each row). **(B)** Relationship of effect size *D* (between the interictal and ictal distribution of $\Delta\alpha^{\dagger}$) and epoch duration in seconds (obtained by dividing the number of sampling points by the sampling rate of the signal). Channel 1 is the data shown in **(A)**. The solid line represents a LOESS curve fitting of the data points, with formula "y ~ x." The data used for this figure is obtained from for subject "I001_P005_D01" around seizure 1. Channel 1: ADMacro_01. Channel 2: ADMacro_02. Channel 3: ADMacro_03.

time for every studied phenomenon. If this is indeed the case, a temporally resolved (not epoch-based) multifractal method should be developed in future to adequately characterize brain dynamics.

Furthermore, the slow temporal changes in multifractal dynamics need to be characterized in a systematic way. Using epileptic seizures as an example, **Appendix Figure E**7 in **Supplementary Material** shows that dramatic changes in multifractal properties can sometimes be seen before an epileptic seizure. This observation requires further investigation to address questions such as: are all epileptic seizures characterized by pre-ictal changes in multifractal properties? Do other physiological processes, such as sleep, influence this finding? To answer these questions, we will most likely also need well-characterized experimental conditions, where seizures can be triggered in a controlled manner.

Finally, it is well-recognized that epileptic seizures are spatio-temporal processes (see e.g., Wang et al., 2014, 2017), and our current approach of only focusing in the temporal aspect in one location will need to be expanded. Data-driven unsupervised approaches, such as dimensionality reduction, may help summarize spatial aspects. Additionally, the challenge will be to develop a spatio-temporal multifractal analysis approach that can also deal with the challenges of low spatial sampling resolution in EEG recordings.

4.4. Outlook

Our work has highlighted several challenges that need to be considered when analysing multifractal properties of EEG signals; namely choice of the appropriate estimation method, estimation parameters, and the influence of the time series variance on signal features. We have suggested some solutions to these problems, such as the used of the Chhabra-Jensen approach combined with an epoch-wise standardization approach, which has shown potential capabilities as a signal feature for machine learning applications. We have also highlighted possible process-specific challenges. In terms of epileptic seizures, future work is required to analyse a larger number of patients in order to draw firmer conclusions on the potential clinical relevance of multifractal analyses. Furthermore, the study of mechanistic generative models of EEG may shed light on why those multifractal changes occur. For example, a generative process of potential interest could feature a modified version of Bak–Tang–Wiesenfeld model (Bak et al., 1987).

4.5. Summary

In this paper, we have analyzed the monofractal and multifractal properties of human EEG recordings. We have shown that monofractal estimates are influenced by the standard deviation of the time series, thus not capturing features beyond signal variance. For multifractal estimation, we have shown that the Chhabra-Jensen approach is the most stable, and we have developed a method of signal pre-processing to remove the influence caused by the variance of the signal. Using the suggested approach, the multifractal estimates do not correlate with traditional EEG measures, thus yielding additional information about the signal and being a relevant signal feature. Finally, our results also indicate a preferential time scale to identify differences in multifractal properties between ictal and interictal state recordings in patients with epilepsy.

DATA AVAILABILITY STATEMENT

The datasets analyzed for this study can be found in https://github.com/yujiangwang/MultiFractalEEG.

AUTHOR CONTRIBUTIONS

LF, LL, MW, and YW: conceptualization, project administration, resources, and writing of the original draft. LF: data curation, funding acquisition, investigation, and visualization. LF and YW: formal analysis and validation. JM, LF, LL, MW, and YW: methodology. JM, LF, and YW: software. LL, MW, and YW: supervision. JM, LF, LL, MW, ML, NS, and YW: writing of the review, and editing.

FUNDING

LF was supported by a grant from Brazilian National Council for Scientific and Technological Development (CNPq) (206907/2014-1). YW gratefully acknowledges the Wellcome Trust (208940/Z/17/Z).

ACKNOWLEDGMENTS

The authors acknowledge the use of the UCL Legion High Performance Computing Facility (Legion@UCL), and associated support services, in the completion of this work.

The authors would like to thank Benjamin H. Brinkmann, Joost Wagenaar, and Hoameng Ung from iEEG.org, and Dr. Peter Taylor for helpful comments throughout the project.

SUPPLEMENTARY MATERIAL

The Supplementary Material for this article can be found online at: https://www.frontiersin.org/articles/10.3389/fphys.2018.01767/full#supplementary-material

REFERENCES

Acharya, R., Faust, O., Kannathal, N., Chua, T., and Laxminarayan, S. (2005). Non-linear analysis of EEG signals at various sleep stages. *Comput. Methods Prog. Biomed.* 80, 37–45. doi: 10.1016/j.cmpb.2005.06.011

Argoul, F., Arnéodo, A., Grasseau, G., Gagne, Y., Hopfinger, E. J., and Frisch, U. (1989). Wavelet analysis of turbulence reveals the multifractal nature of the Richardson cascade. *Nature* 338, 51–53. doi: 10.1038/338051a0

Bak, P., and Paczuski, M. (1995). Complexity, contingency, and criticality. *Proc. Natl. Acad. Sci. U.S.A.* 92, 6689–6896. doi: 10.1073/pnas.92.15.6689

Bak, P., Tang, C., and Wiesenfeld, K. (1987). Self-organized criticality: an explanation of the 1/ f noise. *Phys. Rev. Lett.* 59, 381–384. doi: 10.1103/PhysRevLett.59.381

Baldassano, S. N., Brinkmann, B. H., Ung, H., Blevins, T., Conrad, E. C., Leyde, K., et al. (2017). Crowdsourcing seizure detection: algorithm development and validation on human implanted device recordings. *Brain* 140, 1680–1691. doi: 10.1093/brain/awx098

Bassett, D. S., Greenfield, D. L., Meyer-Lindenberg, A., Weinberger, D. R., Moore, S. W., and Bullmore, E. T. (2010). Efficient physical embedding of topologically complex information processing networks in brains and computer circuits. *PLoS Comput. Biol.* 6:e1000748. doi: 10.1371/journal.pcbi.1000748

Bassett, D. S., Meyer-Lindenberg, A., Achard, S., Duke, T., and Bullmore, E. (2006). Adaptive reconfiguration of fractal small-world human brain functional networks. *Proc. Natl. Acad. Sci. U.S.A.* 103, 19518–19523. doi: 10.1073/pnas.0606005103

Beggs, J. M., and Plenz, D. (2003). Neuronal avalanches in neocortical circuits. *J. Neurosci.* 23, 11167–11177. doi: 10.1523/JNEUROSCI.23-35-11167.2003

Beggs, J. M., and Plenz, D. (2004). Neuronal avalanches are diverse and precise activity patterns that are stable for many hours in cortical slice cultures. *J. Neurosci.* 24, 5216–5229. doi: 10.1523/JNEUROSCI.0540-04.2004

Bengtsson, H. (2016). *R.matlab: Read and Write Mat Files and Call Matlab From Within R*. R package version 3.6.1.

Bianco, S., Ignaccolo, M., Rider, M. S., Ross, M. J., Winsor, P., and Grigolini, P. (2007). Brain, music, and non-Poisson renewal processes. *Phys. Rev. E* 75:061911. doi: 10.1103/PhysRevE.75.061911

Biswas, A. P. H., and Si, C. (2012). "Application of multifractal and joint multifractal analysis in examining soil spatial variation: a review," in *Fractal Analysis and Chaos in Geosciences*, ed S.-A. Ouadfeul (InTech), 109–138. doi: 10.5772/51437

Blum, A. L., and Langley, P. (1997). Selection of relevant features and examples in machine learning. *Artif. Intell.* 97, 245–271.

Brinkmann, B. H., Bower, M. R., Stengel, K. A., Worrell, G. A., and Stead, M. (2009). Large-scale electrophysiology: acquisition, compression, encryption, and storage of big data. *J. Neurosci. Methods* 180, 185–192. doi: 10.1016/j.jneumeth.2009.03.022

Brinkmann, B. H., Wagenaar, J., Abbot, D., Adkins, P., Bosshard, S. C., Chen, M., et al. (2016). Crowdsourcing reproducible seizure forecasting in human and canine epilepsy. *Brain* 139, 1713–1722. doi: 10.1093/brain/aww045

Bullmore, E., Barnes, A., Bassett, D. S., Fornito, A., Kitzbichler, M., Meunier, D., et al. (2009). Generic aspects of complexity in brain imaging data and other biological systems. *NeuroImage* 47, 1125–1134. doi: 10.1016/j.neuroimage.2009.05.032

Bullmore, E., Fadili, J., Breakspear, M., Salvador, R., Suckling, J., and Brammer, M. (2003). Wavelets and statistical analysis of functional magnetic resonance images of the human brain. *Stat. Methods Med. Res.* 12, 375–399. doi: 10.1191/0962280203sm339ra

Cannon, M. J., Percival, D. B., Caccia, D. C., Raymond, G. M., and Bassingthwaighte, J. B. (1997). Evaluating scaled windowed variance methods for estimating the Hurst coefficient of time series. *Physica A.* 241, 606–626. doi: 10.1016/S0378-4371(97)00252-5

Chhabra, A., and Jensen, R. V. (1989). Direct determination of the f(α) singularity spectrum. *Phys. Rev. Lett.* 62, 1327–1330. doi: 10.1103/PhysRevLett.62.1327

Chialvo, D. R. (2010). Emergent complex neural dynamics. *Nat. Phys.* 6, 744–750. doi: 10.1038/nphys1803

Chialvo, D. R. (2012). Critical brain dynamics at large scale. *Crit. Neural Syst.* 2013, 1–22. doi: 10.1002/9783527651009.ch3

Ciuciu, P. (2012). Scale-free and multifractal time dynamics of fMRI signals during rest and task. *Front. Physiol.* 3:186. doi: 10.3389/fphys.2012.00186

Consolini, G., Marcucci, M. F., and Candidi, M. (1996). Multifractal structure of auroral electrojet index data. *Phys. Rev. Lett.* 76, 4082–4085. doi: 10.1103/PhysRevLett.76.4082

Costa, I. d. S., Gamundí, A., Miranda, J. G. V., França, L. G. S., De Santana, C. N., and Montoya, P. (2017). Altered functional performance in patients with fibromyalgia. *Front. Hum. Neurosci.* 11:14. doi: 10.3389/fnhum.2017.00014

Davies, R. B., and Harte, D. S. (1987). Tests for Hurst effect. *Biometrika* 74, 95–101. doi: 10.1093/biomet/74.1.95

Davis, A., Marshak, A., Cahalan, R., and Wiscombe, W. (1997). The landsat scale break in stratocumulus as a three-dimensional radiative transfer effect: implications for cloud remote sensing. *J. Atmos. Sci.* 54, 241–260. doi: 10.1175/1520-0469(1997)054<0241:TLSBIS>2.0.CO;2

Eguíluz, V. M., Chialvo, D. R., Cecchi, G. A., Baliki, M., and Apkarian, A. V. (2005). Scale-free brain functional networks. *Phys. Rev. Lett.* 94:018102. doi: 10.1103/PhysRevLett.94.018102

Eke, A., Hermán, P., Bassingthwaighte, J. B., Raymond, G., Percival, D. B., Cannon, M., et al. (2000). Physiological time series: distinguishing fractal noises from motions. *Pflügers Archiv Eur. J. Physiol.* 439, 403–415. doi: 10.1007/s004249900135

Eke, A., Herman, P., Kocsis, L., and Kozak, L. R. (2002). Fractal characterization of complexity in temporal physiological signals. *Physiol. Meas.* 23, R1–R38. doi: 10.1088/0967-3334/23/1/201

Esteller, R., Vachtsevanos, G., Echauz, J., Henry, T., Pennell, P., Epstein, C., et al. (1999). "Fractal dimension characterizes seizure onset in epileptic patients," in *1999 IEEE International Conference on Acoustics, Speech, and Signal Processing. Proceedings. ICASSP99 (Cat. No.99CH36258)*, Vol. 4, 2343–2346.

Falconer, K. (2003). *Fractal Geometry*. Chichester: John Wiley & Sons, Ltd.

Feder, J. (1988). *Fractals*. Boston, MA: Springer US.

Fraiman, D., and Chialvo, D. R. (2012). What kind of noise is brain noise: anomalous scaling behavior of the resting brain activity fluctuations. *Front. Physiol.* 3:307. doi: 10.3389/fphys.2012.00307

França, L. G. S., Montoya, P., and Miranda, J. G. V. (2019). On multifractals: a non-linear study of actigraphy data. *Phys. A* 514, 612–619. doi: 10.1016/j.physa.2018.09.122

Freestone, D. R., Karoly, P. J., Peterson, A. D. H., Kuhlmann, L., Lai, A., Goodarzy, F., et al. (2015). Seizure prediction: science fiction or soon to become reality? *Curr. Neurol. Neurosci. Rep.* 15:73. doi: 10.1007/s11910-015-0596-3

Gneiting, T., and Schlather, M. (2004). Stochastic models that separate fractal dimension and the hurst effect. *SIAM Rev.* 46, 269–282. doi: 10.1137/S0036144501394387

Goldberger, A. L., Amaral, L. A. N., Glass, L., Hausdorff, J. M., Ivanov, P. C., Mark, R. G., et al. (2000). PhysioBank, physioToolkit, and physioNet : components of a new research resource for complex physiologic signals. *Circulation* 101, e215–e220. doi: 10.1161/01.CIR.101.23.e215

Goldberger, A. L., Amaral, L. A. N., Hausdorff, J. M., Ivanov, P. C., Peng, C., and Stanley, H. E. (2002). Fractal dynamics in physiology: alterations with disease and aging. *Proc. Natl. Acad. Sci. U.S.A.* 99(Suppl. 1), 2466–2472. doi: 10.1073/pnas.012579499

Gómez, C., Mediavilla, Á., Hornero, R., Abásolo, D., and Fernández, A. (2009). Use of the Higuchi's fractal dimension for the analysis of MEG recordings from Alzheimer's disease patients. *Med. Eng. Phys.* 31, 306–313. doi: 10.1016/j.medengphy.2008.06.010

Gong, P., Nikolaev, A. R., and van Leeuwen, C. (2003). Scale-invariant fluctuations of the dynamical synchronization in human brain electrical activity. *Neurosci. Lett.* 336, 33–36. doi: 10.1016/S0304-3940(02)01247-8

Gu, G.-F., and Zhou, W.-X. (2010). Detrending moving average algorithm for multifractals. *Phys. Rev. E* 82:011136. doi: 10.1103/PhysRevE.82.011136

Guyon, I., and Elisseeff, A. (2003). An introduction to variable and feature selection. *J. Mach. Learn. Res.* 3, 1157–1182. Available online at: http://www.jmlr.org/papers/v3/guyon03a.html

Higuchi, T. (1988). Approach to an irregular time series on the basis of the fractal theory. *Phys. D* 31, 277–283. Guyon and Elisseeff, 2003

Hsu, W.-Y., Lin, C.-C., Ju, M.-S., and Sun, Y.-N. (2007). Wavelet-based fractal features with active segment selection: application to single-trial EEG data. *J. Neurosci. Methods* 163, 145–160. doi: 10.1016/j.jneumeth.2007.02.004

Hu, K., Ivanov, P. C., Chen, Z., Hilton, M. F., Stanley, H., and Shea, S. A. (2004). Non-random fluctuations and multi-scale dynamics regulation of human activity. *Phys. A Stat. Mech. Appl.* 337, 307–318. doi: 10.1016/j.physa.2004.01.042

Hu, K., Van Someren, E. J. W., Shea, S. A., and Scheer, F. A. J. L. (2009). Reduction of scale invariance of activity fluctuations with aging and Alzheimer's disease: involvement of the circadian pacemaker. *Proc. Natl. Acad. Sci. U.S.A.* 106, 2490–2494. doi: 10.1073/pnas.0806087106

Ihlen, E. A. F. (2012). Introduction to multifractal detrended fluctuation analysis in Matlab. *Front. Physiol.* 3, 1–18. doi: 10.3389/fphys.2012.00141

Ihlen, E. A. F., and Vereijken, B. (2010). Interaction-dominant dynamics in human cognition: beyond 1/fα fluctuation. *J. Exp. Psychol.* 139, 436–463. doi: 10.1037/a0019098

Ince, R. A., Giordano, B. L., Kayser, C., Rousselet, G. A., Gross, J., and Schyns, P. G. (2017). A statistical framework for neuroimaging data analysis based on mutual information estimated via a gaussian copula. *Hum. Brain Mapp.* 38, 1541–1573. doi: 10.1002/hbm.23471

Ivanov, P. C., Amaral, L. A. N., Goldberger, A. L., Havlin, S., Rosenblum, M. G., Struzik, Z. R., et al. (1999). Multifractality in human heartbeat dynamics. *Nature* 399, 461–465. doi: 10.1038/20924

Kantelhardt, J. W., Zschiegner, S. A., Koscielny-Bunde, E., Havlin, S., Bunde, A., and Stanley, H. (2002). Multifractal detrended fluctuation analysis of nonstationary time series. *Phys. A* 316, 87–114. doi: 10.1016/S0378-4371(02)01383-3

Karoly, P. J., Ung, H., Grayden, D. B., Kuhlmann, L., Leyde, K., Cook, M. J., et al. (2017). The circadian profile of epilepsy improves seizure forecasting. *Brain* 140, 2169–2182. doi: 10.1093/brain/awx173

Kestener, P., and Arneodo, A. (2003). Three-dimensional wavelet-based multifractal method: the need for revisiting the multifractal description of turbulence dissipation data. *Phys. Rev. Lett.* 91:194501. doi: 10.1103/PhysRevLett.91.194501

Kroese, D. P., and Botev, Z. I. (2015). "Spatial process simulation," *Lecture Notes in Mathematics*, ed V. Schmidt (Cham: Springer International Publishing), 369–404.

Kuhlmann, L., Karoly, P., Freestone, D. R., Brinkmann, B. H., Temko, A., Barachant, A., et al. (2018a). Epilepsyecosystem.org: crowd-sourcing reproducible seizure prediction with long-term human intracranial EEG. *Brain* 141, 2619–2630. doi: 10.1093/brain/awy210

Kuhlmann, L., Lehnertz, K., Richardson, M. P., Schelter, B., and Zaveri, H. P. (2018b). Seizure prediction-ready for a new era. *Nat. Rev. Neurol.* 14, 618–630. doi: 10.1038/s41582-018-0055-2

Li, X., Polygiannakis, J., Kapiris, P., Peratzakis, A., Eftaxias, K., and Yao, X. (2005). Fractal spectral analysis of pre-epileptic seizures in terms of criticality. *J. Neural Eng.* 2, 11–16. doi: 10.1088/1741-2560/2/2/002

Linkenkaer-Hansen, K., Nikouline, V. V., Palva, J. M., and Ilmoniemi, R. J. (2001). Long-range temporal correlations and scaling behavior in human brain oscillations. *J. Neurosci.* 21, 1370–1377. doi: 10.1523/JNEUROSCI.21-04-01370.2001

Lipa, P., and Buschbeck, B. (1989). From strong to weak intermittency. *Phys. Lett. B* 223, 465–469.

Liu, H., Motoda, H., and Dash, M. (1998). "A monotonic measure for optimal feature selection," in *European Conference on Machine Learning*, 101–106. doi: 10.1007/BFb0026678

Liu, H., and Yu, L. (2005). Toward integrating feature selection algorithms for classification and clustering. *IEEE Trans. Knowl. Data Eng.* 17, 491–502. doi: 10.1109/TKDE.2005.66

Lovejoy, S., and Schertzer, D. (2007). Scaling and multifractal fields in the solid earth and topography. *Nonlin. Process. Geophys.* 14, 465–502. doi: 10.5194/npg-14-465-2007

Lutzenberger, W., Preissl, H., and Pulvermüller, F. (1995). Fractal dimension of electroencephalographic time series and underlying brain processes. *Biol. Cybern.* 73, 477–482. doi: 10.1007/BF00201482

Mandelbrot, B. B. (1982). *The Fractal Geometry of Nature, Vol. 1*. New York, NY: WH freeman.

Mandelbrot, B. B., and Van Ness, J. W. (1968). Fractional brownian motions, fractional noises and applications. *SIAM Rev.* 10, 422–437. doi: 10.1137/1010093

Martinerie, J., Le Van Quyen, M., Baulac, M., and Renault, B. (2003). Reply to "Prediction of epileptic seizures: are nonlinear methods relevant?" *Nat. Med.* 9, 242–242. doi: 10.1038/nm0303-242

McSharry, P. E., Smith, L. A., and Tarassenko, L. (2003). Reply to "Prediction of epileptic seizures: are nonlinear methods relevant?" *Nat. Med.* 9, 241–242. doi: 10.1038/nm0303-2

Meneveau, C., and Sreenivasan, K. R. (1987). Simple multifractal cascade model for fully developed turbulence. *Phys. Rev. Lett.* 59, 1424–1427. doi: 10.1103/PhysRevLett.59.1424

Meneveau, C., and Sreenivasan, K. R. (1991). The multifractal nature of turbulent energy dissipation. *J. Fluid Mech.* 224:429. doi: 10.1017/S0022112091001830

Miranda, J., Montero, E., Alves, M., Paz González, A., and Vidal Vázquez, E. (2006). Multifractal characterization of saprolite particle-size distributions after topsoil removal. *Geoderma* 134, 373–385. doi: 10.1016/j.geoderma.2006.03.014

Mormann, F., Andrzejak, R. G., Elger, C. E., and Lehnertz, K. (2007). Seizure prediction: the long and winding road. *Brain* 130, 314–333. doi: 10.1093/brain/awl241

Mukli, P., Nagy, Z., and Eke, A. (2015). Multifractal formalism by enforcing the universal behavior of scaling functions. *Phys. A* 417, 150–167. doi: 10.1016/j.physa.2014.09.002

Murcio, R., Masucci, A. P., Arcaute, E., and Batty, M. (2015). Multifractal to monofractal evolution of the London street network. *Phys. Rev. E* 92:062130. doi: 10.1103/PhysRevE.92.062130

Nagy, Z., Mukli, P., Herman, P., and Eke, A. (2017). Decomposing multifractal crossovers. *Front. Physiol.* 8:533. doi: 10.3389/fphys.2017.00533

Neuwirth, E. (2014). *Rcolorbrewer: Colorbrewer Palettes*. R package version 1.1-2.

Papo, D. (2014). Functional significance of complex fluctuations in brain activity: from resting state to cognitive neuroscience. *Front. Syst. Neurosci.* 8:112. doi: 10.3389/fnsys.2014.00112

Papo, D., Goñi, J., and Buldú, J. M. (2017). Editorial: on the relation of dynamics and structure in brain networks. *Chaos Interdisc. J. Nonlin. Sci.* 27:047201. doi: 10.1063/1.4981391

Paz-Ferreiro, J., Miranda, J., and Vidal Vázquez, E. (2010b). Multifractal analysis of soil porosity based on mercury injection and nitrogen adsorption. *Vadose Zone J.* 9:325. doi: 10.2136/vzj2009.0090

Paz-Ferreiro, J., Vázquez, E. V., and Miranda, J. (2010a). Assessing soil particle-size distribution on experimental plots with similar texture under different management systems using multifractal parameters. *Geoderma* 160, 47–56. doi: 10.1016/j.geoderma.2010.02.002

Pechlivanidis, I. G., and Arheimer, B. (2015). Large-scale hydrological modelling by using modified PUB recommendations: the India-HYPE case. *Hydrol. Earth Syst. Sci.* 19, 4559–4579. doi: 10.5194/hess-19-4559-2015

Peng, C., Buldyrev, S. V., Havlin, S., Simons, M., Stanley, H. E., and Goldberger, A. L. (1994). Mosaic organization of DNA nucleotides. *Phys. Rev. E* 49, 1685–1689. doi: 10.1103/PhysRevE.49.1685

Peng, C., Havlin, S., Stanley, H. E., and Goldberger, A. L. (1995). Quantification of scaling exponents and crossover phenomena in nonstationary heartbeat time series. *Chaos Interdisc. J. Nonlin. Sci.* 5, 82–87. doi: 10.1063/1.166141

Pereda, E., Gamundi, A., Rial, R., and González, J. (1998). Non-linear behaviour of human EEG: fractal exponent versus correlation dimension in awake and sleep stages. *Neurosci. Lett.* 250, 91–94. doi: 10.1016/S0304-3940(98)00435-2

Peterson, B. G., and Carl, P. (2014). *Performanceanalytics: Econometric Tools for Performance and Risk Analysis*. R package version 1.4.3541.

R Core Team (2017). *R: A Language and Environment for Statistical Computing* (Vienna).

Racz, F. S., Mukli, P., Nagy, Z., and Eke, A. (2018). Multifractal dynamics of resting-state functional connectivity in the prefrontal cortex. *Physiol. Meas.* 39:024003. doi: 10.1088/1361-6579/aaa916

Saeys, Y., Inza, I., and Larranaga, P. (2007). A review of feature selection techniques in bioinformatics. *Bioinformatics* 23, 2507–2517. doi: 10.1093/bioinformatics/btm344

She, Z.-S., and Leveque, E. (1994). Universal scaling laws in fully developed turbulence. *Phys. Rev. Lett.* 72, 336–339. doi: 10.1103/PhysRevLett.72.336

Shevchenko, G. (2015). "Fractional Brownian motion in a nutshell," in *International Journal of Modern Physics: Conference Series*, Vol. 36. doi: 10.1142/S2010194515600022

Sreenivasan, K. R., and Antonia, R. A. (1997). The phenomenology of small-scale turbulence. *Annu. Rev. Fluid Mech.* 29, 435–472. doi: 10.1146/annurev.fluid.29.1.435

Stam, C. J., and de Bruin, E. A. (2004). Scale-free dynamics of global functional connectivity in the human brain. *Hum. Brain Mapp.* 22, 97–109. doi: 10.1002/hbm.20016

Stanley, H., Amaral, L., Goldberger, A., Havlin, S., Ivanov, P., and Peng, C. (1999). Statistical physics and physiology: monofractal and multifractal approaches. *Phys. A Stat. Mech. Appl.* 270, 309–324. doi: 10.1016/S0378-4371(99)00230-7

Suckling, J., Wink, A. M., Bernard, F. A., Barnes, A., and Bullmore, E. (2008). Endogenous multifractal brain dynamics are modulated by age, cholinergic blockade and cognitive performance. *J. Neurosci. Methods* 174, 292–300. doi: 10.1016/j.jneumeth.2008.06.037

Van De Ville, D., Britz, J., and Michel, C. M. (2010). EEG microstate sequences in healthy humans at rest reveal scale-free dynamics. *Proc. Natl. Acad. Sci. U.S.A.* 107, 18179–18184. doi: 10.1073/pnas.1007841107

van den Berg, J. C., (ed.). (1999). *Wavelets in Physics*. Cambridge: Cambridge University Press.

Varatharajah, Y., Berry, B., Cimbalnik, J., Kremen, V., Van Gompel, J., Stead, M., et al. (2018). Integrating artificial intelligence with real-time intracranial EEG monitoring to automate interictal identification of seizure onset zones in focal epilepsy. *J. Neural Eng.* 15:046035. doi: 10.1088/1741-2552/aac960

Vázquez, E. V., Ferreiro, J. P., Miranda, J. G. V., and González, A. P. (2008). Multifractal analysis of pore size distributions as affected by simulated rainfall. *Vadose Zone J.* 7, 500–511. doi: 10.2136/vzj2007.0011

Venema, V., Bachner, S., Rust, H. W., and Simmer, C. (2006). Statistical characteristics of surrogate data based on geophysical measurements. *Nonlin. Process. Geophys.* 13, 449–466. doi: 10.5194/npg-13-449-2006

Wagenaar, J. B., Brinkmann, B. H., Ives, Z., Worrell, G. A., and Litt, B. (2013). "A multimodal platform for cloud-based collaborative research," in *2013 6th International IEEE/EMBS Conference on Neural Engineering (NER)* (IEEE), 1386–1389. doi: 10.1109/NER.2013.6696201

Wang, Y., Goodfellow, M., Taylor, P. N., and Baier, G. (2014). Dynamic mechanisms of neocortical focal seizure onset. *PLoS Comput. Biol.* 10:e1003787. doi: 10.1371/journal.pcbi.1003787

Wang, Y., Trevelyan, A. J., Valentin, A., Alarcon, G., Taylor, P. N., and Kaiser, M. (2017). Mechanisms underlying different onset patterns of focal seizures. *PLoS Comput. Biol.* 13:e1005475. doi: 10.1371/journal.pcbi.1005475

Werner, G. (2010). Fractals in the nervous system: conceptual implications for theoretical neuroscience. *Front. Physiol.* 1:15. doi: 10.3389/fphys.2010.00015

Wickham, H. (2007). Reshaping data with the reshape package. *J. Stat. Softw.* 21, 1–20. doi: 10.18637/jss.v021.i12

Wickham, H. (2009). *ggplot2: Elegant Graphics for Data Analysis*. New York, NY: Springer-Verlag.

Xu, H. C., Gu, G. F., and Zhou, W. X. (2017). Direct determination approach for the multifractal detrending moving average analysis. *Phys. Rev. E* 96:052201. doi: 10.1103/PhysRevE.96.052201

Xue, Y., and Bogdan, P. (2017). Reliable multi-fractal characterization of weighted complex networks: algorithms and implications. *Sci. Rep.* 7:7487. doi: 10.1038/s41598-017-07209-5

Zappasodi, F., Olejarczyk, E., Marzetti, L., Assenza, G., Pizzella, V., and Tecchio, F. (2014). Fractal dimension of EEG activity senses neuronal impairment in acute stroke. *PLoS ONE* 9:e100199. doi: 10.1371/journal.pone.0100199

Zeleke, T. B., and Si, B. C. (2006). Characterizing scale-dependent spatial relationships between soil properties using multifractal techniques. *Geoderma* 134, 440–452. doi: 10.1016/j.geoderma.2006.03.013

Zhang, Y., Zhou, W., and Yuan, S. (2015). Multifractal analysis and relevance vector machine-based automatic seizure detection in intracranial EEG. *Int. J. Neural Syst.* 25:1550020. doi: 10.1142/S0129065715500203

Zhou, W.-X. (2008). Multifractal detrended cross-correlation analysis for two nonstationary signals. *Phys. Rev. E* 77:066211. doi: 10.1103/PhysRevE.77.066211

Zorick, T., and Mandelkern, M. A. (2013). Multifractal detrended fluctuation analysis of human EEG: preliminary investigation and comparison with the wavelet transform modulus maxima technique. *PLoS ONE* 8:e68360. doi: 10.1371/journal.pone.0068360

Conflict of Interest Statement: The authors declare that the research was conducted in the absence of any commercial or financial relationships that could be construed as a potential conflict of interest.

frontiers in Physiology

ORIGINAL RESEARCH
published: 28 February 2019
doi: 10.3389/fphys.2019.00113

Multi-Scale Expressions of One Optimal State Regulated by Dopamine in the Prefrontal Cortex

Guyue Hu[1,2,5], *Xuhui Huang*[1,2,3,4], *Tianzi Jiang*[1,2,4,5] *and Shan Yu*[1,2,4,5]*

[1] Brainnetome Center, Institute of Automation, Chinese Academy of Sciences, Beijing, China, [2] National Laboratory of Pattern Recognition, Institute of Automation, Chinese Academy of Sciences, Beijing, China, [3] Research Center for Brain-inspired Intelligence, Institute of Automation, Chinese Academy of Sciences, Beijing, China, [4] CAS Center for Excellence in Brain Science and Intelligence Technology, Chinese Academy of Sciences, Beijing, China, [5] University of Chinese Academy of Sciences, Beijing, China

The prefrontal cortex (PFC), which plays key roles in many higher cognitive processes, is a hierarchical system consisting of multi-scale organizations. Optimizing the working state at each scale is essential for PFC's information processing. Typical optimal working states at different scales have been separately reported, including the dopamine-mediated inverted-U profile of the working memory (WM) at the system level, critical dynamics at the network level, and detailed balance of excitatory and inhibitory currents (E/I balance) at the cellular level. However, it remains unclear whether these states are scale-specific expressions of the same optimal state and, if so, what is the underlying mechanism for its regulation traversing across scales. Here, by studying a neural network model, we show that the optimal performance of WM co-occurs with the critical dynamics at the network level and the E/I balance at the level of individual neurons, suggesting the existence of a unified, multi-scale optimal state for the PFC. Importantly, such a state could be modulated by dopamine at the synaptic level through a series of U or inverted-U profiles. These results suggest that seemingly different optimal states for specific scales are multi-scale expressions of one condition regulated by dopamine. Our work suggests a cross-scale perspective to understand the PFC function and its modulation.

Keywords: optimal states, working memory, criticality, E/I balance, dopamine, the PFC

OPEN ACCESS

Edited by:
Plamen Ch. Ivanov,
Boston University, United States

Reviewed by:
Christopher Kello,
University of California, Merced, United States
Chengyu Huo,
Changshu Institute of Technology, China

***Correspondence:**
Shan Yu
shan.yu@nlpr.ia.ac.cn

Specialty section:
This article was submitted to Fractal Physiology, a section of the journal Frontiers in Physiology

Received: *28 September 2018*
Accepted: *30 January 2019*
Published: *28 February 2019*

Citation:
Hu G, Huang X, Jiang T and Yu S (2019) Multi-Scale Expressions of One Optimal State Regulated by Dopamine in the Prefrontal Cortex. Front. Physiol. 10:113. doi: 10.3389/fphys.2019.00113

INTRODUCTION

The brain is consisting of structures at different scales that are hierarchically organized, ranging from synapses and cells all the way to networks of brain areas (Park and Friston, 2013; Betzel and Bassett, 2017). Incorporating regularities for different levels to give a coherent, cross-scale account for brain functions is a significant challenge for systems neuroscience. The prefrontal cortex (PFC), which is involved in many higher cognitive processes, such as working memory (WM), planning, and multi-tasking (Yang and Raine, 2009; Diamond, 2013), has been intensively studied at different scales, revealing diverse scale-specific optimal states that can benefit the information processing occurring at corresponding scales. Firstly, at the system level, WM, which refers to the ability to temporarily hold and manipulate information in the brain (Baddeley, 1992, 2012),

is strongly modulated by dopamine (DA) according to a well-established "inverted-U" profile. That is, too strong or too weak of dopamine D1 activation is detrimental for WM, with optimal performance achieved at an intermediate level (Zahrt et al., 1997; Vijayraghavan et al., 2007). Deficits in this modulation can lead to severe impairment in WM, which is a key symptom in various brain disorders (Austin et al., 2001; Steele et al., 2007), such as schizophrenia (Lett et al., 2014). Secondly, at the network level, it has been discovered that the state of PFC networks *in vitro* could be affected by DA. That is, intermediate dopamine D1 receptor activation led to a so-called critical state (Stewart and Plenz, 2006), which has been suggested as the optimal state for neuronal information processing (Beggs and Plenz, 2003; Kinouchi and Copelli, 2006; Levina et al., 2007; Millman et al., 2010; Yu et al., 2017). Thirdly, at the cellular level, the balance between the excitation and inhibition, reflected by the close tracking of the inhibitory inputs to the excitatory ones for individual neurons (Okun and Lampl, 2008), has been suggested as an important factor that modulates the overall working state of the network (Vogels et al., 2011). Although diverse biological and computational approaches (Cools and D'Esposito, 2011; Barak and Tsodyks, 2014) have been used to study the working state regulation in the PFC, it remains unclear whether the optimal states manifested at individual scales mentioned above are just different expressions of the same unified, cross-scale optimal state at the PFC.

In addition, if a unified optimal state indeed exists, what could be the underlying mechanism modulating it at all scales simultaneously? Anatomical studies indicated that the PFC contains many DA receptors (Goldman-Rakic, 1995) and receives diffuse projections from midbrain dopaminergic neurons (Robbins, 2000). Thus, a potential candidate for the cross-scale modulation of the optimal state is the dopamine modulation. Previous studies have shown that different degrees of dopamine D1 receptor activation act differentially on glutamatergic synapses between the excitatory and inhibitory neurons. Specifically, with low doses of DA, the inputs to both excitatory and inhibitory neurons are unaffected; with moderate doses of DA, the enhancement of glutamatergic input to excitatory neurons is more pronounced; and with high doses of DA, the inputs to both excitatory and inhibitory neurons are strongly enhanced (Muly et al., 1998; Gao et al., 2001). However, how such a mechanism could give rise to the modulation across different scales in order to adjust the working state of the PFC remains unclear.

Here we address these two issues by studying a network model. We found that the optimal performance of WM at the system level co-occurs with critical neuronal dynamics at the network level and the most balanced excitation and inhibition at the cellular level. Importantly, such a unified optimal state is obtained through an intermediate level of dopamine D1 activation at the synaptic level. These results suggest that empirically observed, seemingly different optimal states at individual scales are different expressions of one condition regulated by dopamine. These results shed new light on the multi-scale state optimization for information processing in the PFC.

RESULTS

The State Transition of Neuronal Dynamics in the Network

Our network model is adapted from a biologically plausible WM model (Mongillo et al., 2008). In this model, the external input for the network first activates one of the excitatory-selective neuronal populations (Es, cf. **Figure 1A**), whose activities form the internal representation of the input. These activities trigger short-term synaptic facilitation, resulting in the strengthening of the synaptic connections within this population. Consequently, a strongly interconnected neuronal group is temporarily formed. Through recurrent excitation, this group can maintain its activity as the internal representation of the recent input, even after the input is removed, thereby forming WM. To investigate how network's WM performance can be modulated, we examined its behavior within a 2-D parameter space (the EE–EI plane). The two dimensions represent synaptic strength among excitatory neurons (J_{EE}) and strength of synapses from excitatory to inhibitory neurons (J_{EI}), respectively. Driven by weak background noise, the average firing rate of the neuronal populations changed as a function of J_{EE} and J_{EI} (**Figure 1B**). In this EE-EI plane, we found phase transition from a low (*phase1*) to high activity regime (*phase2*). In *phase1*, the neuronal activities were very sparse, with weak responses evoked by background noise (**Figure 1C**), whereas in *phase2*, high-frequency reverberating activities within one population were maintained without external inputs (**Figure 1D**). Note that the active population in this case was stochastically chosen by the dynamics. This population activates the inhibitory group (I, cf. **Figure 1A**), resulting in the suppression of activities of other populations. Network behavior analysis within the EE-EI plane provided a clear view of how WM can be achieved. That is, in normal condition, the network resides in *phase1* at rest (i.e., without external input). When the external input triggers activities leading to short-term increases in J_{EE}, the network state moves along a trajectory parallel to the J_{EE} axis and toward the phase transition border. If the input is sufficiently strong to push the system across the transition border into *phase2*, the reverberating activities are self-maintained and WM is formed. Contrastingly, if the network resides in *phase2* at rest, the maintained reverberating activities have no corresponding sensory event ("imaginary memory"), which is reminiscent of hallucination in brains disorders, e.g., schizophrenia (Horga et al., 2014; Llorca et al., 2016).

Dopamine Modulation at the Synaptic Level in the Model

We next study how to model the dopamine modulation at the synaptic level and introduce it into the model. Previous studies have indicated that activation of the dopamine D1 receptor can have different effects on the excitatory inputs between excitatory to excitatory and excitatory to inhibitory synapses. Specifically, glutamatergic input of excitatory neurons may increase at low D1 activation and, such a strengthening effect saturates relatively early; however, glutamatergic input of inhibitory neurons is less sensitive to D1 activation, resulting

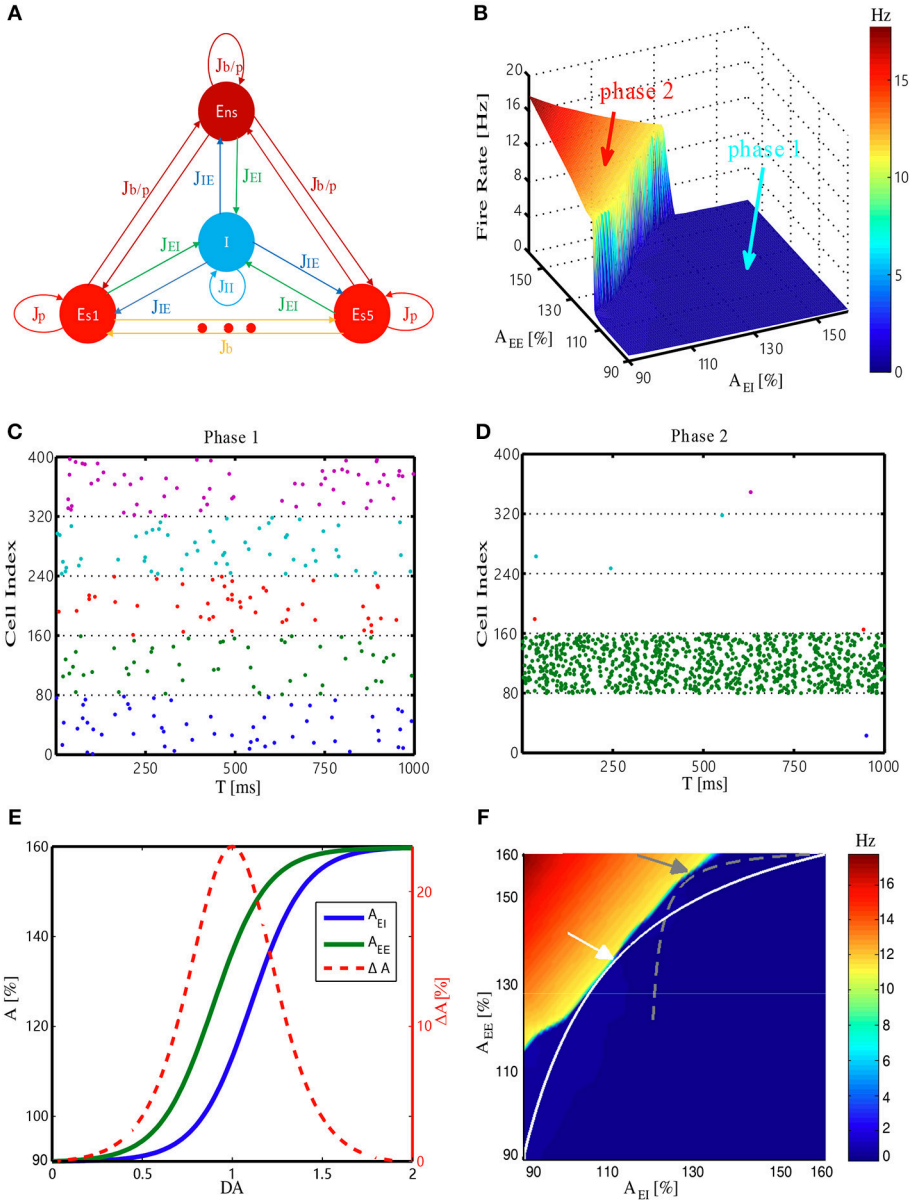

FIGURE 1 | Structure and dynamic behavior of the WM model, and its DA modulation. **(A)** Network architecture. E_{S1}, …, E_{S5}, E_{ns} and I denote five selective excitatory populations, one non-selective excitatory population, and one inhibitory population, respectively. J_{ij} (where *i*, *j* is I or E) denotes the synaptic connection from *i* population to *j* population. The E–E synapse can be a potentiated value (J_p), baseline value (J_b), or potentiated value with a certain probability ($J_{b/p}$). J_{EI} and J_{EE} (J_b, J_p, $J_{b/p}$) are modulated by DA (see Materials and Methods). **(B)** Firing rate of the most active Es population at rest (i.e., without external stimulus) changes with synaptic strength among excitatory neurons (J_{EE}) and from the excitatory to inhibitory neurons (J_{EI}). A_{EE} and A_{EI} are the scaling factors for J_{EE} and J_{EI}, respectively. **(C,D)** Spiking patterns corresponding to the two different phases (*phase1* and *phase2*) in **(B)**. Different colors represent five Es populations (only 10% neurons are shown), with each dot denoting a spike. **(E)** Scaling factors A_{EE} and A_{EI} change as a function of dopamine D1 activation level. The strength difference ($\Delta A = A_{EE} - A_{EI}$) reaches its maximum at DA = 1.0. **(F)** Trajectories represent how the corresponding system state changes with DA. The system represented by the white trajectory is analyzed in the main text. Similar results can also be obtained through the gray trajectory (with a different synaptic strength range), demonstrating the robustness of the results. Arrows mark the intermediate level of DA = 1.0.

in "delayed" onset and saturation of strengthening effects (Muly et al., 1998; Dash et al., 2007). Therefore, in our model, the effects of increasing the dopamine D1 activation level were simulated by changing the strengths of J_{EE} and J_{EI} through multiplying corresponding scaling factors A_{EE} and A_{EI}, according to the functions shown in **Figure 1E**. For each level of D1 activation, we deduced the corresponding values of J_{EE} (A_{EE}) and J_{EI} (A_{EI}), providing coordinates to pinpoint the network state in the EE-EI plane. Eventually, a continuous trajectory representing how the network state changed was obtained (**Figure 1F**, white curve).

With the increases in D1 activation level, the network initially approached and then deviated from the transition border, with the shortest distance achieved by an intermediate D1 activation level. This analysis was not sensitive to specific positions at which the trajectory met the phase transition border (determined by different strength range, see Materials and Methods), as similar results can be obtained with different trajectories (**Figure 1F**, gray curve).

WM Performance at the System Level Regulated by Dopamine

We then examined how WM performance at the system level changed along the regulation trajectory of dopamine D1 activation mentioned above. As shown in **Figure 2A**, a memory item could be *loaded* into WM when the network was in the resting state. Importantly, the content of WM could also be *updated* if another item need to be memorized. At the "behavioral" level, these two measures were applied to evaluate the performance of WM, including the sensitivity of loading items and the flexibility of updating memory. Specifically, at each level of D1 activation, stimuli with a fixed strength were applied to one item-selective excitatory population (Es) with different durations. As shown in **Figure 2B**, we found that regardless of the input strength, the shortest time (T_{sens}) needed for successfully *loading* an item into WM exhibited a U-shaped profile. As a result, the *sensitivity* of WM, defined as the reciprocal of T_{sens}, had an inverted-U profile, with the maximal sensitivity achieved with the intermediate D1 activation (**Figure 2C**). Similarly, when we defined the shortest time needed to *update* a memory item as T_{flexi} (normalized by the smallest T_{flexi} obtained in the whole DA modulation curve), and used its reciprocal as the measure of the *flexibility* of WM, we found that the flexibility of WM also exhibited an inverted-U profile (**Figure 2D**).

Next we studied the network mechanisms underlying these WM behaviors. As WM is formed by the system jumping from *phase1* to *phase2* in response to an external input, the closer the original state is to the transition border, the easier it is for the system to go through the transition. Closer examination of the system's behavior revealed that intermediate D1 activation was associated with the highest firing rates f (**Figure 2E**) and maximal neural transmitter utilization parameter u (**Figure 2F**). Accordingly, in such a state, the total amount of available transmitter in presynaptic neurons, x, was lowest (**Figure 2G**). Interestingly, as the increase in u was less pronounced compared with the decrease in x, the amount of neural transmitter released per spike (ux) reached the minimum (**Figure 2H**), reflecting a more efficient use of transmitter to produce individual spikes in the network. However, as the increase in firing rates was more pronounced under an intermediate D1 activation, the overall use of neural transmitter in the entire network (uxf) was maximized in such a state (**Figure 2I**). This observation indicates the price the system needs to pay for increased sensitivity and flexibility of WM—the accelerated pace of consuming neurotransmitter and, consequently, more energy used to refill the reservoir. Note that the U or inverted-U profiles in **Figure 2** are non-symmetrical. Although the difference of connecting strengths (ΔA) could be the same for lower and higher dopamine concentrations, the absolute connecting strengths (A_{EE}, A_{EI}) with higher D1 activations were larger than those with lower D1 activations (**Figures 1E,F**), which led to different network dynamics.

Critical State at the Network Level Regulated by Dopamine

To bridge the state modulation regularity of WM performance at the system level with the corresponding regulation processes and characteristics at the network level, we examined the relationship between the maximal WM sensitivity/flexibility and features of network's dynamics. Specifically, we analyzed two indicators of so-called critical dynamics: avalanche size distribution and branching parameter. Avalanches are activity cascades within the system and avalanche size is how many neurons are involved in the corresponding cascade (**Figure 3A**). A hallmark of the critical state is that avalanche size distribution exhibits a power-law with the exponent close to −1.5 (Beggs and Plenz, 2003). Consistently, we found the network dynamics exhibited a power-law distribution with exponent closest to −1.5 under the intermediate D1 activation (**Figures 3B,C**). Another indicator of critical dynamics is the branching parameter, which is defined as how many neurons, on average, can be activated by one active neuron. It measures how quickly the activities in a recurrent network are amplified or attenuated. Stable activity propagation of the critical state is associated with a branching parameter close to 1 (Beggs and Plenz, 2003; Shew and Plenz, 2013). Here, we found that the branching parameter estimated from the network dynamics was closest to 1 under the intermediate D1 activation (**Figure 3D**). Importantly, with too strong or too weak D1 activation, the system deviated from the critical state in the same direction. Specifically, large avalanches were formed less frequently and the branching parameter was <1, indicating a subcritical state in which the propagation of activities was over-attenuated. Such a phenomenon is in line with the previous finding that high or low D1 activation resulted in a subcritical state in brain slices (Stewart and Plenz, 2006), reflected by the deeper slopes of avalanche size distributions and branching parameters being smaller than one. Further, to provide an overview of the network state regarding the distance from criticality (**Figure 3E**), we plotted the branching parameter for all possible states within the EE-EI plane. We found a phase transition in the branching parameter corresponding to the transition in terms of network activity level, and the self-sustained activities in the top left part was associated with a branching parameter close to 1. The trajectory of DA modulation (**Figure 3E**) provides a direct assessment of how the distance from the critical state was modulated by different levels of D1 activation. Compared with **Figure 2**, it is clear that the critical state jointly emerged with the optimal WM performance when the intermediate degree of dopamine D1 activation (DA = 1.0) was set at the synaptic level.

Criticality at the Network Level Maintained by E/I Balance at the Cellular Level

We next addressed how critical dynamics at the network level could be maintained with the intermediate degree of D1 activation. Specifically, given the short-term synaptic facilitation

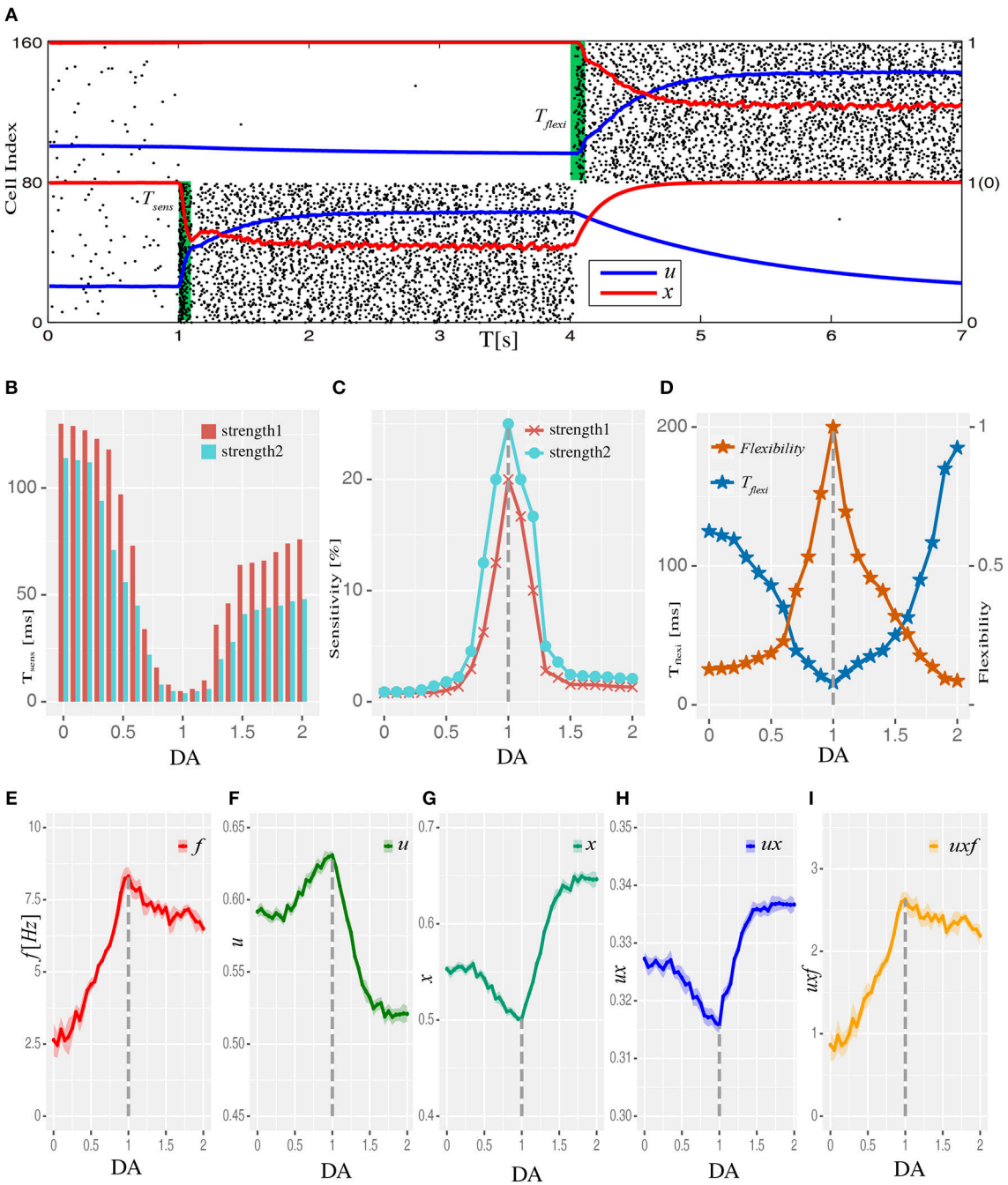

FIGURE 2 | Dopamine modulation and the optimal working memory performance. **(A)** One item is *loaded* into memory from the resting state and *updated* to another item by applying item-specific stimuli (green shading) with a durations of T_{sens} and T_{flexi}, respectively. Black dots are neural spikes (only 10% neurons are shown). *u* and *x* donates average utilization parameter and available resource in corresponding populations, respectively. **(B)** The shortest stimulation time (T_{sens}) needed for the model to load the stimulus into WM from resting state at each D1 activation level. Results for two stimulus strengths (strength1 < strength2) are shown. **(C)** Sensitivity of WM, defined as the reciprocal of T_{sens}, exhibits an inverted-U profile with dopamine D1 modulation. **(D)** The shortest time (T_{flexi}) needed to update a memory item and corresponding flexibility were also shaped by the U and inverted-U profiles, respectively. **(E–I)** Internal parameters that determine the system's dynamics change as a function of D1 activation, including firing rate *f* (average firing rate), *u* (utilization parameter), *x* (available resources), *ux* (transmitters used per spike), and *uxf* (total transmitters used) of the population receiving memory stimuli (strength1, and in total 200 ms long), which was E_{s1} for all analyses presented in this paper. Data are represented as mean ± S.D. across all the neurons in the population.

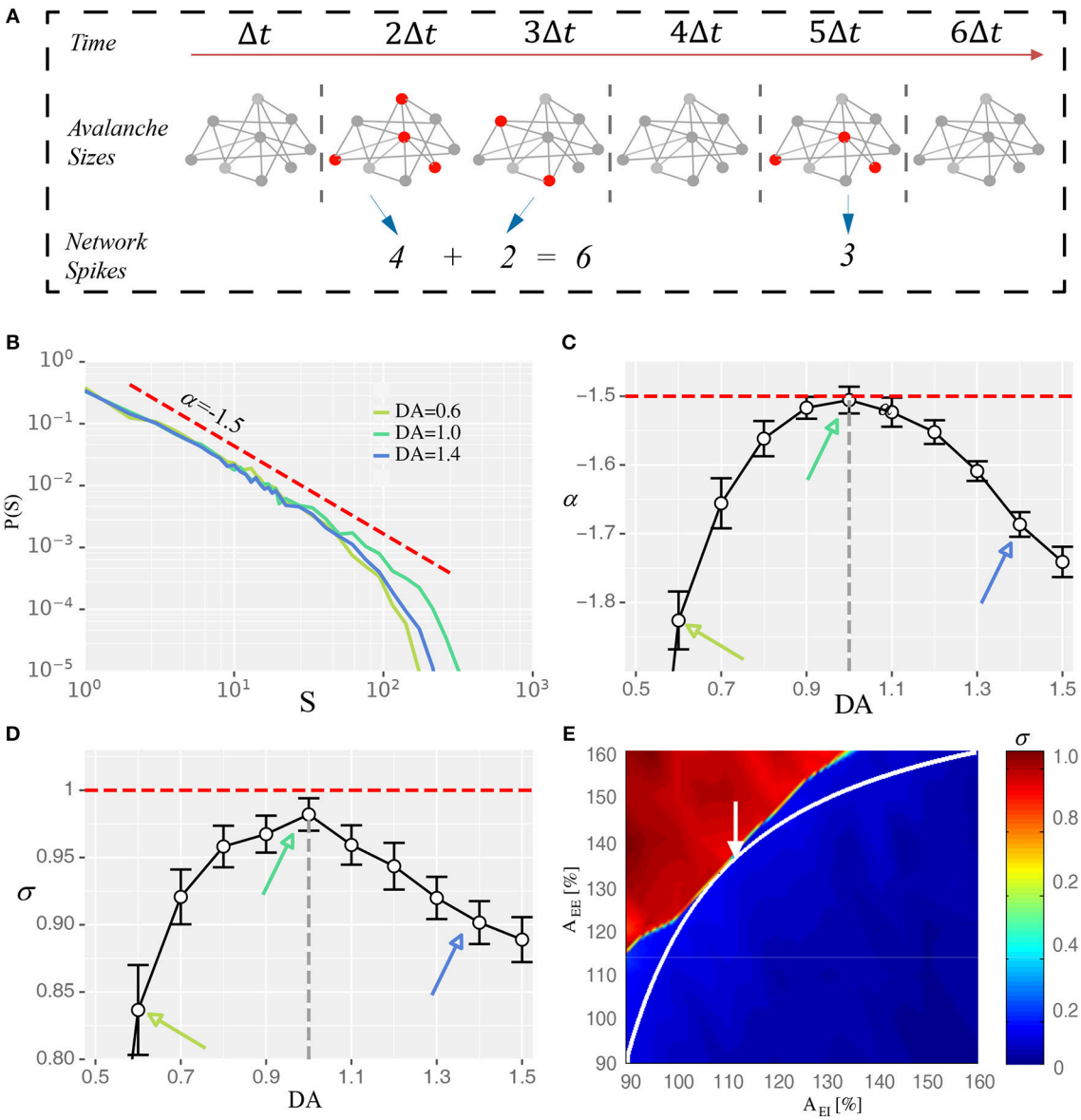

FIGURE 3 | Intermediate D1 activation corresponds to a state close to criticality. **(A)** Schematic diagram showing the identification of neuronal avalanches. Solid circles represent individual neurons, with red donating active state and gray donating quiescence. Neurons that fire in the same time bin or consecutive bins of length Δt form an activity cascade, i.e., an avalanche. Avalanche size, s, is defined as the number of active neurons in the cascade. Two avalanches ($s = 6$ and 3) are shown. **(B)** Avalanche size distribution obtained with three different levels of D1 activation, with the intermediate level (DA = 1.0) associated with distribution closest to a power-law exponent of −1.5 (red dashed line). **(C,D)** The exponent (α) and the branching parameter (σ) change as a function of the D1 activation level. Red dotted lines represent $\alpha = -1.5$ and $\sigma = 1$ in **(C,D)**, respectively. States corresponding to DA = 0.6, 1.0, and 1.4 are marked by arrows with the same color as in **(B)**. α and σ estimated with different D1 activation levels are statistically significant (one-way ANOVA, $p < 0.05$; *post-hoc* test among DA = 0.6, 1.0, and 1.4, $p < 0.05$; Data are represented as mean ± S.D. across fifteen trials at each DA level). **(E)** Branching parameter (σ) exhibits a phase transition similar to the firing rate shown in **Figure 1F**.

mechanisms built in the network, and that the intermediate D1 activation leads to the most active network state, what mechanism can prevent the system from a runaway excitation, i.e., being supercritical, under such a condition? One possible mechanism is the balance between the excitation and inhibition, i.e., E/I balance, at the cellular level. Reflected by the close tracking of the inhibitory inputs to the excitatory ones, E/I balance is well-documented (Okun and Lampl, 2008) and is suggested as an important factor modulating the overall network state (Vogels et al., 2011). This balance is essential to maintain the states of neuronal networks, demonstrated by both experimental (Shew et al., 2009) and modeling studies (Lombardi et al., 2012; Poil et al., 2012). Under the intermediate D1 activation, the correlation between the total inhibitory and excitatory currents in the network was maximized (**Figure 4**), reflecting a higher level of E/I balance. This effect was global to the entire network, as

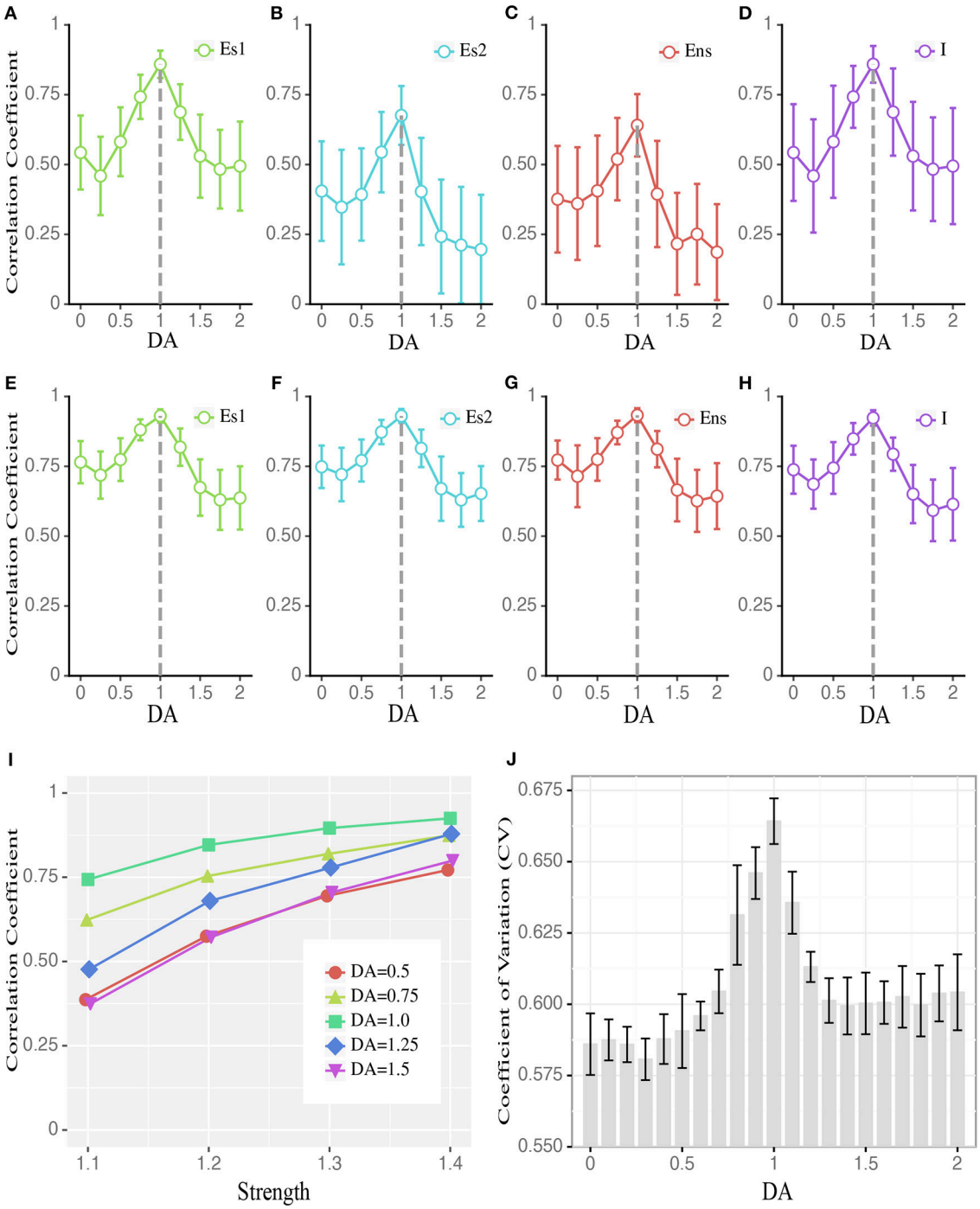

FIGURE 4 | Dopamine modulates the balance between excitatory and inhibitory currents to individual neurons. **(A–D)** The average correlation coefficient of excitatory and inhibitory currents received by individual neurons in different populations during stimulus presentation, including stimulus-targeted selective population (E_{s1}), Es population without stimulation (results for E_{s2} are shown as an example), non-selective population (E_{ns}), and inhibitory population (I). Data are means ± SD across the corresponding population. **(E–H)** Similar to **(A–D)** but the correlation coefficient is computed based on only recurrent currents, excluding external inputs and leaky currents. **(I)** The correlation coefficient of E_{s1} (to save space, E_{s2}, E_{ns}, and I are omitted.) in **(A)** increases with stronger stimulation strengths. DA = 1 is associated with the largest correlation across all strengths. For visual clarity, only the means of the correlation coefficients across the corresponding population are shown. **(J)** CV (coefficient of variation) of the inter-spike interval changes as a function of DA modulation, with DA = 1 corresponding to the highest CV (Data are represented as mean ± S.D. across fifteen trials at each DA level). The group differences between low, high, and intermediate DA in **(A–J)** are statistically significant (one-way ANOVA with multiple comparison tests under Tukey's criterion, $p < 0.05$).

it was manifested in all neuronal populations (**Figures 4A–D**). Furthermore, the correlation between the E and I currents was higher when we only analyzed the recurrent inputs (i.e., without external inputs, background inputs, and membrane leakages; see Methods) (**Figures 4E–H**), suggesting that recurrent dynamics dominated the E/I balance. To further verify this, we examined how the E/I currents correlation changed as a function of recurrent activity levels induced by external inputs with different strengths. As shown in **Figure 4I**, this correlation increased monotonically as a function of the strength of external inputs, with the intermediate D1 activation associated with the highest correlation, reconfirming the casual role of recurrent activities in determining the E/I balance. Besides the highly correlated E and I currents, a large coefficient of variation (CV) of neuronal activities is also an important indicator of the E/I balance (van Vreeswijk and Sompolinsky, 1996). Consistently, we found that the CV of network activities was maximized with the intermediate D1 activation (**Figure 4J**). These results imply that the network state under the intermediate D1 activation is associated with the highest level of E/I balance, which allows the inhibition to track the excitatory drive within the network and to avoid the supercritical state.

Multi-Scale Expressions of One Optimal State Regulated by Dopamine

Finally, based on all the results described above, we propose a framework incorporating the optimal states from the perspectives of WM, network dynamics and the E/I balance, as shown in **Figure 5**. At the synaptic level, different levels of dopamine D1 activation have different enhanced efficacy to the glutamatergic input of the excitatory and inhibitory neurons, i.e., J_{EE} and J_{EI}. This changes the relative strength of the excitation and inhibition in the system. As a result, the measures of WM, critical dynamics and the E/I balance at different scales are all shaped by a series of U or inverted-U profiles. The extrema of these U or inverted-U profiles suggest optimal working states for corresponding scales, which simultaneously obtained by the intermediate level of D1 activation. According to such a framework, the optimal states in the PFC, including the best WM performance at the system level, critical neuronal dynamics at the network level, and detailed E/I balance at the cellular level are multi-scale expressions of one state modulated by dopamine.

DISCUSSION

When interpreting the results, several limitations need to be clarified. Firstly, we did not consider the lags between the excitatory and inhibitory currents in calculating their correlations. From previous current-clamp recordings in single neurons, the inhibitory currents lag about a few milliseconds behind the excitatory currents (Okun and Lampl, 2008). Such values are smaller than the sampling interval of currents in our simulation. Therefore, neglecting the lags in calculating the correlation between excitatory and inhibitory currents would not have a strong effect on the results. Secondly, in our simulation, we chose a specific range of A_{EE} and A_{EI}, however, the main results obtained can be well-replicated by other choices of the range of A_{EE} and A_{EI}, e.g., the results (cf., **Supplementary Figure S1**) obtained from the gray modulation curve in **Figure 1F**, suggesting that our results are generalizable for different dopamine baseline and modulation range. Thirdly, many different computational models of WM have been proposed (Wang, 2002; Goldman et al., 2003; Machens, 2005; Barak and Tsodyks, 2014). Here we built our system by adapting a biophysically realistic model of WM (Mongillo et al., 2008), which is agreed well with various empirically observed electrophysiological properties (Rainer and Miller, 2002; Shafi et al., 2007). It awaits future studies to investigate if the same results can be obtained in other WM models. Fourthly, in the present model, the neural noise was modeled as stable Gaussian white noises, as in many other computational models of WM (Brunel and Wang, 2001; Mongillo et al., 2008). Recently, it was reported that the variance of neural noise is related to environmental factors, such as body temperature (Dvir et al., 2018), which has not been considered here. Our results demonstrated that it was the recurrent currents rather than the background noise primarily determined the detailed E/I balance for individual neurons (**Figures 4A–I**). Thus, as long as the noise variance level is within a normal range (i.e., the noise currents do not suppress the recurrent currents), the optimal state would not change.

In our results, the optimal working memory performance is regulated by dopamine by a typical U or inverted-U profiles, which are in line with many previous empirical (Dash et al., 2007; Vijayraghavan et al., 2007; Kroener et al., 2009; Van Snellenberg et al., 2016) and computational (Brunel and Wang, 2001; Dash et al., 2007; Lew and Tseng, 2014) studies . On top of that, our results provide a possible link between the system level characteristics and underlying synaptic mechanisms. We show that not only the measures at the system level like sensitivity and flexibility but also the measures at the synaptic level, such as available resources (x), are shaped by dopamine-mediated U or inverted-U profiles. These results indicate that the modulation of WM performance at the system level is an aggregated effect of modulations occurring at the finer scales of neural networks.

A neural network operating close to a critical state has various functional advantages in terms of information encoding, storage, transmission, and processing (Kinouchi and Copelli, 2006; Beggs, 2008; Kello, 2013). Along with the empirical evidence that biological neural networks were indeed exhibited typical behavioral hallmarks of criticality in their dynamics, it has been long expected that critical neural networks can play an essential role in various brain functions, and the deviation from such a state may lead to functional deficits as seen in many brain disorders. However, so far there is no mechanism to directly link the critical neural network and well-characterized brain functions. Our results demonstrate that the optimal performance of working memory at the system level was achieved when the neural network was operating most close to a critical state at the network level, and deviation from the critical state would impair WM performance. Because the basal dopamine levels are variable across individuals (Mattay et al., 2000; Gibbs and D'Esposito,

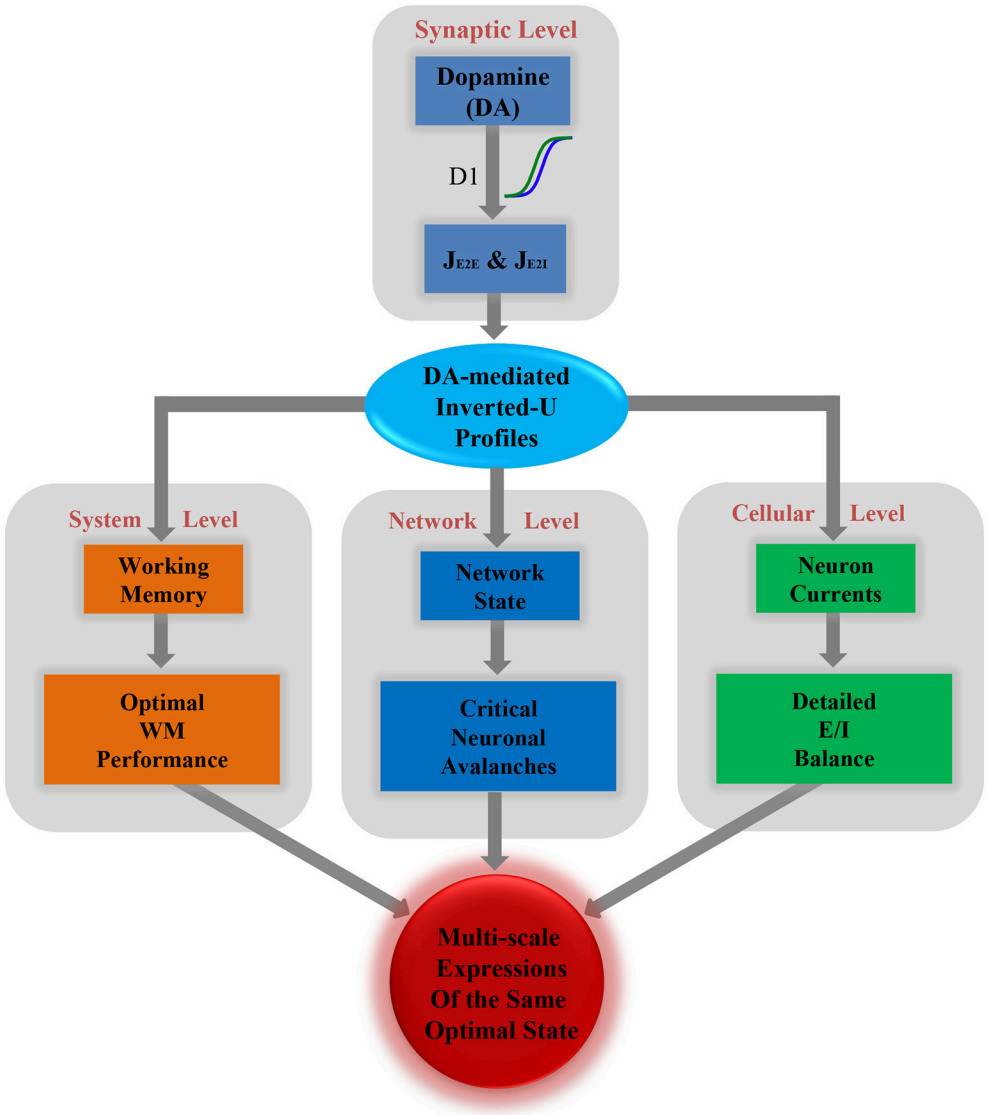

FIGURE 5 | Multi-scale expressions of the same optimal state regulated by dopamine, including detailed E/I balance at the cellular level, critical dynamics at the network level, and optimal WM performance at the system level.

2005; Cools and D'Esposito, 2011), the DA-induced inverted-U profile of WM performance is not a robust biomarker for diagnosing working memory deficits. Unlike the optimal concentration suggested by the DA-induced inverted-U profile of WM performance, which varies greatly across individuals, the critical state is a feature of network dynamics that is individual-invariant. Thus, it would be informative to study if the deviation from criticality can be used as an individual-invariant biomarker of network anomalies underlying WM deficits.

Our results quantitatively show that the excitatory currents are highly correlated with the inhibitory currents in individual neurons, indicating detailed E-I balance. The finding is consistent with the current-clamp recordings in single neurons that the excitatory and inhibitory currents of nearby cells track each other closely (Okun and Lampl, 2008). The current-clamp recording can only record the sum of the excitatory or inhibitory currents in a single neuron, so the relative contributions of sub-components of the currents, such as the recurrent currents, the external inputs, and the leaky currents of neurons, are difficult to delineate. Simulations are free from this limitation, which enables us to illustrate that the recurrent currents play a more important role in keeping the E/I balance compared to the background noise, the leaky currents, and item-targeted external inputs.

The most important finding of the present work is that optimal states at different scales in the network model are different expressions of the same underlying condition modulated by dopamine. The measures at each scale are characterized by a series of U or inverted-U profiles, and

each extremum indicates an optimal working state in the corresponding scale. Specifically, at the system level, DA-mediated WM performance profiles suggest an optimal state accompanied by the maximum sensitivity and flexibility. At the network level, the optimal state is corresponding to the critical dynamics, which hold numerous advantages in information processing, including transmission (Beggs and Plenz, 2003; Rämö et al., 2007), storage (Haldeman and Beggs, 2005; Larremore et al., 2011), computation (Bertschinger and Natschläger, 2004), stability (Beggs, 2008) and dynamic range (Hosaka et al., 2008; Shew et al., 2009; Gautam et al., 2015). At the cellular level, an optimal state means that the excitatory and inhibitory currents most closely track each other (Okun and Lampl, 2008; Cafaro and Rieke, 2010), which can optimize the coding and metabolic efficiency (Yizhar et al., 2011; Sengupta et al., 2013), and track the external input more quickly (van Vreeswijk and Sompolinsky, 1996). Importantly, all these optimal states in the PFC manifested at different scales are regulated by the same control parameter—the concentration of dopamine at the synaptic level, with an intermediate concentration corresponding to above mentioned optimal states at all levels. An interesting question is that what is the mechanism to dynamically modulate the dopamine in the PFC. Anatomical studies indicate that the PFC contains abundant DA receptors (Goldman-Rakic, 1995) and receives diffuse projections from the mesocortical and mesolimbic dopaminergic systems originating in the ventral tegmental area of the midbrain (Bannon and Roth, 1983; Cools and D'Esposito, 2011). Thus, DA release in the PFC will occur in response to a variety of events either aversive or rewarding, and this release may prepare the PFC networks running in the optimal state to deal with environmental or cognitive challenges (Seamans and Robbins, 2010).

Working memory deficits were observed in many brain disorders, such as schizophrenia (Lett et al., 2014), depression (Austin et al., 2001), epilepsy (Swartz et al., 1996), and autism (Steele et al., 2007). At the same time, abnormal regulation in dopamine has been reported in related disorders, especially in schizophrenic patients (Abi-Dargham et al., 2002). In addition, disruption in the E/I balance has been implicated in the same set of diseases (Rubenstein and Merzenich, 2003; Fritschy, 2008; Marín, 2012; Murray et al., 2014). Here we provide a cross-scale view to better understand how the changes in dopamine in the PFC might cause E/I imbalance, which can push the network away from the critical state and eventually induce WM impairments. This provides a potentially useful multi-scale framework to reveal how the effects of abnormal neuromodulation at the synaptic level can penetrate different scales and give rise to functional deficits in different pathological conditions.

Our results indicate that these optimal states in the PFC manifested at different scales are actually multi-scale expressions of the same condition modulated by dopamine. More generally, the multi-scale nature of complex biological systems are widely reported. For example, healthy heartbeat interval series have been found to exhibit multi-fractal properties (Ivanov et al., 1999, 2004). In the brain, activity measures across a wide range of spatial scales, including those based on neural spikes, the local field potential (LFP), magnetoencephalography (MEG), functional magnetic resonance imaging (fMRI), have revealed a highly similar dynamical regime close to criticality (Beggs and Plenz, 2003; Tagliazucchi et al., 2012; Shriki et al., 2013; Bellay et al., 2015). In addition, previous modeling study have also reported pervasive scaling laws at the cellular, network and behavioral levels in the critical branching neural network (Kello, 2013). The current results further highlight that incorporating the multi-scale properties with a cross-scale perspective is vital for understanding complex phenomena and processes in physiology.

In summary, based on studying a neural network model, here we demonstrate a cross-scale mechanism of dopamine modulation for state optimization in the PFC, which for the first time links several seemingly unrelated regularities at different levels into a unified, coherent framework. Our results suggest that the optimal performance of WM at the system level, critical dynamics at the network level, and E/I balance at the cellular level could be multi-scale expressions of one optimal state in the PFC. This unified framework gives a novel cross-scale understanding of state optimization in the PFC, and more generally, provide a new perspective to incorporate scale-specific regularities into a coherent, cross-scale account for brain functions.

MATERIALS AND METHODS

Network Model

Our model was adapted from a biophysically realistic model proposed by previous work (Mongillo et al., 2008), which utilizes calcium-mediated synaptic facilitation among recurrently connected excitatory neurons to form WM.

Model Architecture

The architecture of our model is shown in **Figure 1A**. The network is composed of three types of neuronal populations: (1) selective excitatory (Es) populations (from Es1 to Esp) to encode in total p memory items, each containing fN_E neurons selected from a pool of excitatory neurons (in total $N_E = 8{,}000$ excitatory neurons; f is a proportion common to all Es populations); (2) one non-selective excitatory (Ens) population formed by the remaining $(1 - pf)N_E$ excitatory neurons; and (3) one inhibitory population (I) with $N_I = 2{,}000$ inhibitory neurons.

Each neuron, regardless of which population it belongs to, randomly receives presynaptic connections from all other neurons in the network with common probability c. To mimic the long-term potentiation effect of Hebbian learning, the excitatory-to-excitatory connections (J_{EE}) within the same Es population are set to be stronger (J_p), whereas the connections between different Es populations are set to be weaker, i.e., baseline value (J_b). The synapses connecting neurons from the Es populations to neurons in the Ens population, as well as the connections within the Ens population, take the potentiated strength (Jp) with probability γ and the baseline strength (J_b) with probability $(1 - \gamma)$. These synaptic strengths are indicated by $J_{b/p}$ in **Figure 1A**.

All excitatory-to-excitatory synapses (J_{EE}) display short-term plasticity (see below), whereas the remaining synapses,

TABLE 1 | Parameters used in the model.

Dopamine modulation parameters		**Dopamine1**	**Dopamine2**
Optimal concentration of dopamine	D_0	1.0	1.0
Concentration domain	[*Dmin, Dmax*]	[0, 2.0]	[0, 2.0]
Steep parameter	K_c	0.150	0.120
Shifting parameter	D_v	0.105	0.185
Selective stimulation		**Strength1**	**Strength2**
Contrast factor	A_{cue}	1.10	1.15
Network parameters		**E**	**I**
Coding probability	f	0.10	0.10
Number of memory items	p	5	5
Probability of synaptic connection	c	0.20	0.20
Number of excitatory/inhibitory cells	N	8,000	2,000
Mean external current	μ_{ext}	23.80 mV	21.0 mV
Standard deviation of external current	σ_{ext}	1.0 mV	1.0 mV
Cell parameters		**E**	**I**
Spike emission threshold	θ	20 mV	20 mV
Reset potential	V_r	16 mV	13 mV
Membrane time constant	τ	15 ms	10 ms
Absolute refractory period	τ_{arp}	2 ms	2 ms
Synaptic parameters		**Values**	
Synaptic efficacy E to I	J_{EI}	0.135 mV	
Synaptic efficacy I to E	J_{IE}	0.25 mV	
Synaptic efficacy I to I	J_{II}	0.20 mV	
Baseline level of E to E synapses	J_b	0.10 mV	
Potentiated level of E to E synapses	J_p	0.45 mV	
Fraction of initial potentiated synapses	γ	0.10	
Synaptic delays	δ	0–1 ms	
Short-term synaptic parameters		**Values**	
Baseline utilization factor	U	0.20	
Baseline available resources	X	1.00	
Recovery time of utilization factor	τ_d	1,500 ms	
Recovery time of synaptic resources	τ_f	200 ms	

*Dopamine1 and Dopamine2 are parameters used for the white and gray modulation curve in **Figure 1F**, respectively. Some parameters are based on a previous computational working memory model (Mongillo et al., 2008).*

including the excitatory-to-inhibitory (J_{EI}), inhibitory-to-excitatory (J_{IE}), and inhibitory-to-inhibitory (J_{II}), are constant. For convenience, all parameters used in this model are listed in **Table 1**.

Dynamic Rules of the Model

Activities of individual neurons are modeled by the leaky integrate-and-fire model (LIF) with a refractory period of τ_{arp}. Below the firing threshold (θ), the membrane potential of neuron i (V_i) is governed by:

$$\tau_{\mathrm{m}}\dot{V}_i = -V_i + I_i^{(rec)}(t) + I_i^{(ext)}(t) \tag{1}$$

where τ_{m} is the membrane time constant. The external input (including background noise and memory-specific stimuli) $I_i^{(ext)}(t)$ is modeled as Gaussian white noise, with a mean of μ_{ext} and standard deviation of σ_{ext}:

$$I_i^{(ext)}(t) = \mu_{ext} + \sigma_{ext} \cdot \eta_i(t) \tag{2}$$

where $\eta_i(t)$ is the standard Gaussian white noise. Memory-specific stimuli are modeled by increasing μ_{ext} but maintaining σ_{ext}. The recurrent current $I_i^{(rec)}(t)$ is given by:

$$I_i^{(rec)}(t) = \sum_j \hat{J}_{ij}(t) \sum_k \delta(t - t_{\mathrm{k}}^{(j)} - D_{ij}) \tag{3}$$

where $t_{\mathrm{k}}^{(j)}$ refers to the firing times of presynaptic neuron j, D_{ij} is the transmission delay uniformly distributed between 0 and 1 ms, and $\hat{J}_{ij}(t)$ is the instantaneous synaptic efficacy. For excitatory-to-excitatory synapses, their strengths are dynamically adjusted according to:

$$\hat{J}_{ij}(t) = J_{ij} \cdot u_j(t - D_{ij}) x_j(t - D_{ij}) \tag{4}$$

$$\dot{u}(t) = \frac{U - u_j(t)}{\tau_f} + U\left[1 - u_j(t)\right] \sum_k \delta\left(t - t_k^{(j)}\right) \tag{5}$$

$$\dot{x}_j(t) = \frac{X - x_j(t)}{\tau_d} + u_j(t)\, x_j(t) \sum_k \delta\left(t - t_k^{(j)}\right) \tag{6}$$

where x indicates the available number of presynaptic neurotransmitters, and u refers to the portion of x that can be utilized during synaptic transmission, which reflects the influence of calcium level on release probability at the presynaptic site. U and X are the baseline values for u and x, respectively. After each spike, x and u change according to Equations (5, 6) with their corresponding time constants τ_d (depressing) and τ_f (facilitating), respectively. As mentioned above, only the excitatory-to-excitatory synapses are subjected to this form of plasticity. All remaining synapse efficacies are kept constant.

Model Dopamine Modulation

Previous studies have shown that different levels of dopamine D1 receptor activation act differently on glutamatergic input between the excitatory and inhibitory neurons. Specifically, with low doses of DA, the inputs to both excitatory and inhibitory neurons are unaffected; with moderate doses of DA, the enhancement of glutamatergic input to excitatory neurons is more pronounced; and with high doses of DA, the inputs to both excitatory and inhibitory neurons are strongly enhanced(Muly et al., 1998; Gao et al., 2001). These differential effects of D1 activation level have been widely acknowledged in computation models studying DA modulation of the prefrontal cortical networks (Durstewitz et al., 2000; Brunel and Wang, 2001; Lew and Tseng, 2014). To reflect D1 modulation in the present model, we multiplied the absolute strength of excitatory-excitatory (E-E) synapses (J_{EE}, including J_b, J_p, and $J_{b/p}$) and excitatory-inhibitory (E/I) synapses (J_{EI}) with relative strength factors A_{EE} and A_{EI}, respectively. A_{EE} and A_{EI} are both functions of DA level, and the differences between them change with DA, as indicated by the red dotted line (A) in **Figure 1E**. The range of DA was set as $D \in [0, 2]$. Accordingly,

we fixed the intermediate level of D1 activation at the center of the range, i.e., $D_0 = 1.0$. The range of the two scaling factors was set as $[A_{min}, A_{max}]$. The functions of A_{EE} and A_{EI} could then be specified as:

$$A_{EE} = \left[\frac{1}{C_{EE}} \cdot \left(1 + \frac{D_L}{1 + e^{(D_{E0}-D)/K_c}}\right) - A_{P1}\right] \cdot 100\% \quad (7)$$

$$A_{EI} = \left[\frac{1}{C_{EI}} \cdot \left(1 + \frac{D_L}{1 + e^{(D_{I0}-D)/K_c}}\right) - A_{P1}\right] \cdot 100\% \quad (8)$$

$$D_{E0} = D_0 - D_V \quad (9)$$

$$D_{I0} = D_0 + D_V \quad (10)$$

$$D_L = A_{max} - A_{min} \quad (11)$$

$$A_{P1} = 1 - A_{min} \quad (12)$$

where D refers to the level of D1 activation, and K_C and D_V are two key parameters controlling the function shape in **Figure 1E**. Steep parameter K_C controls the vertical steepness and shifting parameter D_V controls the largest efficacy difference between the two functions at D_0. C_{EE} and C_{EI} are the normalization parameters obtained by setting $D_V = 0$ in Equations (9, 10) and $D = D_0$ in the following equations:

$$C_{EE} = 1 + \frac{D_L}{1 + e^{(D_{E0}-D)/K_c}} \quad (13)$$

$$C_{EI} = 1 + \frac{D_L}{1 + e^{(D_{I0}-D)/K_c}} \quad (14)$$

Each D1 activation level uniquely determines a A_{EI}, A_{EE} pair (**Figure 1E**), which then specifies a point in the EE-EI plane. With a continuously increasing D1 activation level, a system state trajectory can be obtained. The exact shape and position of the trajectory can be controlled by tuning parameters K_C and D_V. Given (1) the objective function of obtaining the maximal sensitivity of WM and avoiding the risk of "imaginary memory" (see the main text for details), and (2) the constraints that at very low/high D1 activation both J_{EE} and J_{EI} should be weak/strong, eventually, we can obtain the trajectory as shown in **Figure 1F**. With the increase in D1 activation level, the trajectory starts from the diagonal, then approaches the transition line, before finally returning to the diagonal.

Our main conclusions are robust toward different choices of free parameters used in the model. For example, we show that similar results (**Supplementary Figure S1**) can be obtained with a different range of synaptic strengths, controlled by the scaling factor $[A_{\min}, A_{\max}]$, i.e., the gray trajectory in **Figure 1F**.

Analysis of Network Activities

Neuronal Avalanche Identification

We defined neuronal avalanches according to previous work (Beggs and Plenz, 2003) (cf. **Figure 3A**). An avalanche is a cascade of activity propagation within the network. To identify such a cascade, a small time-window Δt is used to bin a Es population activities. An inactive time bin is a bin during which no neurons have fired, whereas an active time bin is the one during which at least one neuron has fired. The cascades are then defined as neuronal activities that occur either within the same bin or within consecutive active bins (**Figure 3A**). For the present analysis, $\Delta t = 0.3$ ms, which is two times the average inter-spike interval within the population. Avalanche size is defined as the number of neurons involved in the corresponding cascade. All neuronal avalanches in the present work are obtained with 2,000 ms-long simulations with a time step of 0.1 ms.

Power-Law Fitting

In critical neural networks, avalanche size distribution follows a power law:

$$P(s) \propto s^{\alpha} \quad (15)$$

where P(s) is the probability density function (PDF) of observed avalanche size s, α is the exponent that gives the power-law slope in a log-log plot, which is close to -1.5 for critical networks measured under both *in vitro* and *in vivo* conditions (Beggs, 2004; Gireesh and Plenz, 2008). To reduce the effect of noise on distribution, a smoothing method based on geometric mean values under the log-log coordinate was applied (Christensen and Moloney, 2005), and the fit area are obtained by optimization the object of minimal the Kolmogorov–Smirnov distance between the data and fitting candidates, finally the exponent α then estimated by least-square fitting in log-log coordinates. We implemented these through a public python package Powerlaw (Alstott et al., 2014).

Branching Parameter

Branching parameter σ is defined as the average number of active units in the next time step that are triggered by one active unit at the current time step. Following previous work (Beggs and Plenz, 2003), it can be measured by:

$$\sigma = \left\langle \frac{Descendants}{Ancestors} \right\rangle \quad (16)$$

where $\langle\rangle$ refers to the operation of arithmetic average, *Ancestors* is the number of active units in the first bin of an avalanche, and *Descendants* is the number of active units in the second bin of the corresponding avalanche.

Correlation Coefficient and Coefficient of Variation

The correlation coefficient is used to measure the degree of balanced excitatory and inhibitory input to a neuron, which is calculated as:

$$\rho = \frac{\mathrm{cov}(x_1, x_2)}{\sqrt{D(x_1) + D(x_2)}} \quad (17)$$

where x_1 and x_2 refer to the excitatory and inhibitory currents, respectively, and D is the variance of the corresponding currents. Note that the correlation coefficient between excitatory and inhibitory currents is always a negative value. We always plotted its absolute value in this to facilitate visual comparison.

The coefficient of variation of distribution is defined as:

$$CV = \frac{\mu}{\sigma} \quad (18)$$

where μ and σ refer to the mean and standard deviation of distribution, respectively.

AUTHOR CONTRIBUTIONS

GH, XH, TJ, and SY planned the study. GH and XH carried out network simulations and analysis. GH and SY wrote the manuscript.

FUNDING

This study was supported by the National Key Research and Development Program of China (2017YFA0105203), Natural Science Foundation of China (Grant Nos. 81471368, 11505283), the Strategic Priority Research Program of the Chinese Academy of Sciences (CAS) (XDB32040200), Special Financial Grant from the China Postdoctoral Science Foundation funded project (2015T80154), and Hundred-Talent Program of CAS (for SY).

ACKNOWLEDGMENTS

The authors would like to thank Dr. Dietmar Plenz for helpful discussions and Dr. Gianluigi Mongillo for technical assistance.

SUPPLEMENTARY MATERIAL

The Supplementary Material for this article can be found online at: https://www.frontiersin.org/articles/10.3389/fphys.2019.00113/full#supplementary-material

REFERENCES

Abi-Dargham, A., Mawlawi, O., Lombardo, I., Gil, R., Martinez, D., Huang, Y., et al. (2002). Prefrontal dopamine D-sub-1 receptors and working memory in schizophrenia. *J. Neurosci.* 22, 3708–3719. doi: 10.1523/JNEUROSCI.22-09-03708.2002

Alstott, J., Bullmore, E., and Plenz, D. (2014). Powerlaw: a python package for analysis of heavy-tailed distributions. *PLoS ONE* 9:e0085777. doi: 10.1371/journal.pone.0085777

Austin, M.-P., Mitchell, P., and Goodwin, G. M. (2001). Cognitive deficits in depression. *Br. J. Psychiatry* 178, 200–206. doi: 10.1192/bjp.178.3.200

Baddeley, A. (1992). Working memory. *Science* 255, 556–559. doi: 10.1126/science.1736359

Baddeley, A. (2012). Working memory: theories, models, and controversies. *Annu Rev Psychol* 63, 1–29. doi: 10.1146/annurev-psych-120710-100422

Bannon, M. J., and Roth, R. H. (1983). Pharmacology of mesocortical dopamine neurons. *Pharmacol. Rev.* 35, 53–68.

Barak, O., and Tsodyks, M. (2014). Working models of working memory. *Curr. Opin. Neurobiol.* 25, 20–24. doi: 10.1016/j.conb.2013.10.008

Beggs, J. M. (2004). Neuronal avalanches are diverse and precise activity patterns that are stable for many hours in cortical slice cultures. *J. Neurosci.* 24, 5216–5229. doi: 10.1523/JNEUROSCI.0540-04.2004

Beggs, J. M. (2008). The criticality hypothesis: how local cortical networks might optimize information processing. *Philos. Trans. A Math. Phys. Eng. Sci.* 366, 329–343. doi: 10.1098/rsta.2007.2092

Beggs, J. M., and Plenz, D. (2003). Neuronal avalanches in neocortical circuits. *J. Neurosci.* 23, 11167–11177. doi: 10.1523/JNEUROSCI.23-35-11167.2003

Bellay, T., Klaus, A., Seshadri, S., and Plenz, D. (2015). Irregular spiking of pyramidal neurons organizes as scale-invariant neuronal avalanches in the awake state. *Elife* 4, 1–25. doi: 10.7554/eLife.07224

Bertschinger, N., and Natschläger, T. (2004). Real-time computation at the edge of chaos in recurrent neural networks. *Neural Comput.* 16, 1413–1436. doi: 10.1162/089976604323057443

Betzel, R. F., and Bassett, D. S. (2017). Multi-scale brain networks. *Neuroimage* 160, 73–83. doi: 10.1016/j.neuroimage.2016.11.006

Brunel, N., and Wang, X.-J. (2001). Effects of neuromodulation in a cortical network model of object working memory dominated by recurrent inhibition. *J. Comput. Neurosci.* 11, 63–85. doi: 10.1023/A:1011204814320

Cafaro, J., and Rieke, F. (2010). Noise correlations improve response fidelity and stimulus encoding. *Nature* 468, 964–967. doi: 10.1038/nature09570

Christensen, K., and Moloney, N. R. (2005). *Complexity and Criticality*. London: Imperial College Press.

Cools, R., and D'Esposito, M. (2011). Inverted-U-shaped dopamine actions on human working memory and cognitive control. *Biol Psychiatry* 69, e113–e125. doi: 10.1016/j.biopsych.2011.03.028

Dash, P. K., Moore, A. N., Kobori, N., and Runyan, J. D. (2007). Molecular activity underlying working memory. *Learn. Mem.* 14, 554–563. doi: 10.1101/lm.558707

Diamond, A. (2013). Executive functions. *Annu. Rev. Psychol.* 64, 135–168. doi: 10.1146/annurev-psych-113011-143750

Durstewitz, D., Seamans, J. K., and Sejnowski, T. J. (2000). Dopamine-mediated stabilization of delay-period activity in a network model of prefrontal cortex. *J. Neurophysiol.* 83, 1733–1750. doi: 10.1152/jn.2000.83.3.1733

Dvir, H., Elbaz, I., Havlin, S., Appelbaum, L., Ivanov, P. C., and Bartsch, R. P. (2018). Neuronal noise as an origin of sleep arousals and its role in sudden infant death syndrome. *Sci. Adv.* 4:eaar6277. doi: 10.1126/sciadv.aar6277

Fritschy, J.-M. (2008). E/I balance and GABAA receptor plasticity. *Front. Mol. Neurosci.* 1:5. doi: 10.3389/neuro.02.005.2008

Gao, W. J., Krimer, L. S., and Goldman-Rakic, P. S. (2001). Presynaptic regulation of recurrent excitation by D1 receptors in prefrontal circuits. *Proc. Natl. Acad. Sci. U.S.A.* 98, 295–300. doi: 10.1073/pnas.98.1.295

Gautam, S. H., Hoang, T. T., McClanahan, K., Grady, S. K., and Shew, W. L. (2015). Maximizing sensory dynamic range by tuning the cortical state to criticality. *PLoS Comput. Biol.* 11:e1004576. doi: 10.1371/journal.pcbi.1004576

Gibbs, S. E. B., and D'Esposito, M. (2005). Individual capacity differences predict working memory performance and prefrontal activity following dopamine receptor stimulation. *Cogn. Affect. Behav. Neurosci.* 5, 212–221. doi: 10.3758/CABN.5.2.212

Gireesh, E. D., and Plenz, D. (2008). Neuronal avalanches organize as nested theta- and beta/gamma-oscillations during development of cortical layer 2/3. *Proc. Natl. Acad. Sci. U.S.A.* 105, 7576–7581. doi: 10.1073/pnas.0800537105

Goldman, M. S., Levine, J. H., Major, G., Tank, D. W., and Seung, H. S. (2003). Robust persistent neural activity in a model integrator with multiple hysteretic dendrites per neuron. *Cereb. Cortex* 13, 1185–1195. doi: 10.1093/cercor/bhg095

Goldman-Rakic, P. S. (1995). Cellular basis of working memory. *Neuron* 14, 477–485. doi: 10.1016/0896-6273(95)90304-6

Haldeman, C., and Beggs, J. M. (2005). Critical branching captures activity in living neural networks and maximizes the number of metastable states. *Phys. Rev. Lett.* 94:58101. doi: 10.1103/PhysRevLett.94.058101

Horga, G., Schatz, K. C., Abi-Dargham, A., and Peterson, B. S. (2014). Deficits in predictive coding underlie hallucinations in schizophrenia. *J. Neurosci.* 34, 8072–8082. doi: 10.1523/JNEUROSCI.0200-14.2014

Hosaka, R., Araki, O., and Ikeguchi, T. (2008). STDP provides the substrate for igniting synfire chains by spatiotemporal input patterns. *Neural Comput.* 20, 415–435. doi: 10.1162/neco.2007.11-05-043

Ivanov, P. C., Chen, Z., Hu, K., and Eugene Stanley, H. (2004). Multiscale aspects of cardiac control. *Phys. A Stat. Mech. Appl.* 344, 685–704. doi: 10.1016/j.physa.2004.08.016

Ivanov, P. C., Nunes Amaral, L. A., Goldberger, A. L., Havlin, S., Rosenblum, M. G., Struzik, Z. R., et al. (1999). Multifractality in human heartbeat dynamics. *Nature* 399, 461–465. doi: 10.1038/20924

Kello, C. T. (2013). Critical branching neural networks. *Psychol. Rev.* 120, 230–254. doi: 10.1037/a0030970

Kinouchi, O., and Copelli, M. (2006). Optimal dynamical range of excitable networks at criticality. *Nat. Phys.* 2, 348–351. doi: 10.1038/nphys289

Kroener, S., Chandler, J. L., Phillips, P. E. M., and Seamans, J. K. (2009). Dopamine modulates persistent synaptic activity and enhances the signal-to-noise ratio in the prefrontal cortex. *PLoS ONE* 4:e6507. doi: 10.1371/journal.pone.0006507

Larremore, D. B., Shew, W. L., and Restrepo, J. G. (2011). Predicting criticality and dynamic range in complex networks: effects of topology. *Phys. Rev. Lett.* 106, 1–4. doi: 10.1103/PhysRevLett.106.058101

Lett, T. A., Voineskos, A. N., Kennedy, J. L., Levine, B., and Daskalakis, Z. J. (2014). Treating working memory deficits in schizophrenia: a review of the neurobiology. *Biol. Psychiatry* 75, 361–370. doi: 10.1016/j.biopsych.2013.07.026

Levina, A., Herrmann, J. M., and Geisel, T. (2007). Dynamical synapses causing self-organized criticality in neural networks. *Nat. Phys.* 3, 857–860. doi: 10.1038/nphys758

Lew, S. E., and Tseng, K. Y. (2014). Dopamine modulation of GABAergic function enables network stability and input selectivity for sustaining working memory in a computational model of the prefrontal cortex. *Neuropsychopharmacology* 39, 3067–3076. doi: 10.1038/npp.2014.160

Llorca, P. M., Pereira, B., Jardri, R., Chereau-Boudet, I., Brousse, G., Misdrahi, D., et al. (2016). Hallucinations in schizophrenia and Parkinson's disease: an analysis of sensory modalities involved and the repercussion on patients. *Sci. Rep.* 6:38152. doi: 10.1038/srep38152

Lombardi, F., Herrmann, H. J., Perrone-Capano, C., Plenz, D., and De Arcangelis, L. (2012). Balance between excitation and inhibition controls the temporal organization of neuronal avalanches. *Phys. Rev. Lett.* 108, 1–5. doi: 10.1103/PhysRevLett.108.228703

Machens, C. K. (2005). Flexible control of mutual inhibition: a neural model of two-interval discrimination. *Science* 307, 1121–1124. doi: 10.1126/science.1104171

Marín, O. (2012). Interneuron dysfunction in psychiatric disorders. *Nat. Rev. Neurosci.* 13, 107–120. doi: 10.1038/nrn3155

Mattay, V. S., Callicott, J. H., Bertolino, A., Heaton, I., Frank, J. A., Coppola, R., et al. (2000). Effects of dextroamphetamine on cognitive performance and cortical activation. *Neuroimage* 12, 268–275. doi: 10.1006/nimg.2000.0610

Millman, D., Mihalas, S., Kirkwood, A., and Niebur, E. (2010). Self-organized criticality occurs in non-conservative neuronal networks during up states. *Nat. Phys.* 6, 801–805. doi: 10.1038/nphys1757

Mongillo, G., Barak, O., and Tsodyks, M. (2008). Synaptic theory of working memory. *Science* 319, 1543–1546. doi: 10.1126/science.1150769

Muly, E. C., Szigeti, K., and Goldman-Rakic, P. S. (1998). D1 receptor in interneurons of macaque prefrontal cortex: distribution and subcellular localization. *J. Neurosci.* 18, 10553–10565. doi: 10.1523/JNEUROSCI.18-24-10553.1998

Murray, J. D., Anticevic, A., Gancsos, M., Ichinose, M., Corlett, P. R., Krystal, J. H., et al. (2014). Linking microcircuit dysfunction to cognitive impairment: effects of disinhibition associated with schizophrenia in a cortical working memory model. *Cereb Cortex* 24, 859–872. doi: 10.1093/cercor/bhs370

Okun, M., and Lampl, I. (2008). Instantaneous correlation of excitation and inhibition during ongoing and sensory-evoked activities. *Nat. Neurosci.* 11, 535–537. doi: 10.1038/nn.2105

Park, H.-J., and Friston, K. (2013). Structural and functional brain networks: from connections to cognition. *Science* 342:1238411. doi: 10.1126/science.1238411

Poil, S. S., Hardstone, R., Mansvelder, H. D., and Linkenkaer-Hansen, K. (2012). Critical-state dynamics of avalanches and oscillations jointly emerge from balanced excitation/inhibition in neuronal networks. *J. Neurosci.* 32, 9817–9823. doi: 10.1523/JNEUROSCI.5990-11.2012

Rainer, G., and Miller, E. K. (2002). Timecourse of object-related neural activity in the primate prefrontal cortex during a short-term memory task. *Eur. J. Neurosci.* 15, 1244–1254. doi: 10.1046/j.1460-9568.2002.01958.x

Rämö, P., Kauffman, S., Kesseli, J., and Yli-Harja, O. (2007). Measures for information propagation in boolean networks. *Phys. D* 227, 100–104. doi: 10.1016/j.physd.2006.12.005

Robbins, T. W. (2000). Chemical neuromodulation of frontal-executive functions in humans and other animals. *Exp. Brain Res.* 133, 130–138. doi: 10.1007/s002210000407

Rubenstein, J. L. R., and Merzenich, M. M. (2003). Model of autism: increased ratio of excitation/inhibition in key neural systems. *Genes Brain Behav.* 2, 255–267. doi: 10.1034/j.1601-183X.2003.00037.x

Seamans, J. K., and Robbins, T. W. (2010). *Dopamine Modulation of the Prefrontal Cortex and Cognitive Function.* Totowa, NJ: Humana Press.

Sengupta, B., Stemmler, M. B., and Friston, K. J. (2013). Information and efficiency in the nervous system–a synthesis. *PLoS Comput. Biol.* 9:e1003157. doi: 10.1371/journal.pcbi.1003157

Shafi, M., Zhou, Y., Quintana, J., Chow, C., Fuster, J., and Bodner, M. (2007). Variability in neuronal activity in primate cortex during working memory tasks. *Neuroscience* 146, 1082–1108. doi: 10.1016/j.neuroscience.2006.12.072

Shew, W. L., and Plenz, D. (2013). The functional benefits of criticality in the cortex. *Neuroscientist* 19, 88–100. doi: 10.1177/1073858412445487

Shew, W. L., Yang, H., Petermann, T., Roy, R., and Plenz, D. (2009). Neuronal avalanches imply maximum dynamic range in cortical networks at criticality. *J. Neurosci.* 29, 15595–15600. doi: 10.1523/JNEUROSCI.3864-09.2009

Shriki, O., Alstott, J., Carver, F., Holroyd, T., Henson, R. N., Smith, M. L., et al. (2013). Neuronal avalanches in the resting MEG of the human brain. *J. Neurosci.* 33, 7079–7090. doi: 10.1523/JNEUROSCI.4286-12.2013

Steele, S. D., Minshew, N. J., Luna, B., and Sweeney, J. A. (2007). Spatial working memory deficits in autism. *J. Autism Dev. Disord.* 37, 605–612. doi: 10.1007/s10803-006-0202-2

Stewart, C. V., and Plenz, D. (2006). Inverted-U profile of dopamine-NMDA-mediated spontaneous avalanche recurrence in superficial layers of rat prefrontal cortex. *J. Neurosci.* 26, 8148–8159. doi: 10.1523/JNEUROSCI.0723-06.2006

Swartz, B. E., Simpkins, F., Halgren, E., Mandelkern, M., Brown, C., Krisdakumtorn, T., et al. (1996). Visual working memory in primary generalized epilepsy: an 18FDG-PET study. *Neurology* 47, 1203–1212. doi: 10.1212/WNL.47.5.1203

Tagliazucchi, E., Balenzuela, P., Fraiman, D., and Chialvo, D. R. (2012). Criticality in large-scale brain fmri dynamics unveiled by a novel point process analysis. *Front. Physiol.* 3:15. doi: 10.3389/fphys.2012.00015

Van Snellenberg, J. X., Girgis, R. R., Horga, G., van de Giessen, E., Slifstein, M., Ojeil, N., et al. (2016). Mechanisms of working memory impairment in schizophrenia. *Biol. Psychiatry* 80, 617–626. doi: 10.1016/j.biopsych.2016.02.017

van Vreeswijk, C., and Sompolinsky, H. (1996). Chaos in neuronal networks with balanced excitatory and inhibitory activity. *Science* 274, 1724–1726. doi: 10.1126/science.274.5293.1724

Vijayraghavan, S., Wang, M., Birnbaum, S. G., Williams, G. V, and Arnsten, A. F. (2007). Inverted-U dopamine D1 receptor actions on prefrontal neurons engaged in working memory. *Nat. Neurosci.* 10, 376–384. doi: 10.1038/nn1846

Vogels, T. P., Sprekeler, H., Zenke, F., Clopath, C., and Gerstner, W. (2011). Inhibitory plasticity balances excitation and inhibition in sensory pathways and memory networks. *Science* 334, 1569–1573. doi: 10.1126/science.1211095

Wang, X.-J. (2002). Probabilistic decision making by slow reverberation in cortical circuits. *Neuron* 36, 955–968. doi: 10.1016/S0896-6273(02)01092-9

Yang, Y., and Raine, A. (2009). Prefrontal structural and functional brain imaging findings in antisocial, violent, and psychopathic individuals: a meta-analysis. *Psychiatry Res.* 174, 81–88. doi: 10.1016/j.pscychresns.2009.03.012

Yizhar, O., Fenno, L. E., Prigge, M., Schneider, F., Davidson, T. J., O'Shea, D. J., et al. (2011). Neocortical excitation/inhibition balance in information processing and social dysfunction. *Nature* 477, 171–178. doi: 10.1038/nature10360

Yu, S., Ribeiro, T. L., Meisel, C., Chou, S., Mitz, A., Saunders, R., et al. (2017). Maintained avalanche dynamics during task-induced changes of neuronal activity in nonhuman primates. *Elife* 6, 1–22. doi: 10.7554/eLife.27119

Zahrt, J., Taylor, J. R., Mathew, R. G., and Arnsten, A. F. (1997). Supranormal stimulation of D1 dopamine receptors in the rodent prefrontal cortex impairs spatial working memory performance. *J. Neurosci.* 17, 8528–8535. doi: 10.1523/JNEUROSCI.17-21-08528.1997

Conflict of Interest Statement: The authors declare that the research was conducted in the absence of any commercial or financial relationships that could be construed as a potential conflict of interest.

frontiers in Physiology

ORIGINAL RESEARCH
published: 24 April 2019
doi: 10.3389/fphys.2019.00480

Multifractal Desynchronization of the Cardiac Excitable Cell Network During Atrial Fibrillation. II. Modeling

Guillaume Attuel[1], *Evgeniya Gerasimova-Chechkina*[2], *Françoise Argoul*[3], *Hussein Yahia*[1] *and Alain Arneodo*[3]*

[1] Geometry and Statistics in Acquisition Data, Centre de Recherche INRIA, Talence, France, [2] Laboratory of Physical Foundation of Strength, Institute of Continuous Media Mechanics UB RAS, Perm, Russia, [3] Laboratoire Ondes et Matières d'Aquitaine, Université de Bordeaux, UMR 5798, CNRS, Talence, France

In a companion paper (I. Multifractal analysis of clinical data), we used a wavelet-based multiscale analysis to reveal and quantify the multifractal intermittent nature of the cardiac impulse energy in the low frequency range $\lesssim$ 2Hz during atrial fibrillation (AF). It demarcated two distinct areas within the coronary sinus (CS) with regionally stable multifractal spectra likely corresponding to different anatomical substrates. The electrical activity also showed no sign of the kind of temporal correlations typical of cascading processes across scales, thereby indicating that the multifractal scaling is carried by variations in the large amplitude oscillations of the recorded bipolar electric potential. In the present study, to account for these observations, we explore the role of the kinetics of gap junction channels (GJCs), in dynamically creating a new kind of imbalance between depolarizing and repolarizing currents. We propose a one-dimensional (1D) spatial model of a denervated myocardium, where the coupling of cardiac cells fails to synchronize the network of cardiac cells because of abnormal transjunctional capacitive charging of GJCs. We show that this non-ohmic nonlinear conduction 1D modeling accounts quantitatively well for the "multifractal random noise" dynamics of the electrical activity experimentally recorded in the left atrial posterior wall area. We further demonstrate that the multifractal properties of the numerical impulse energy are robust to changes in the model parameters.

Keywords: atrial fibrillation, modeling, excitable cell network, kinetics of gap junction channel, multifractal analysis, intermittent dynamics

OPEN ACCESS

Edited by:
Plamen Ch. Ivanov,
Boston University, United States

Reviewed by:
Chunhua Bian,
Nanjing University, China
Chengyu Huo,
Changshu Institute of Technology, China

***Correspondence:**
Alain Arneodo
alain.arneodo@u-bordeaux.fr

Specialty section:
This article was submitted to Fractal Physiology, a section of the journal Frontiers in Physiology

Received: *03 November 2018*
Accepted: *05 April 2019*
Published: *24 April 2019*

Citation:
Attuel G, Gerasimova-Chechkina E, Argoul F, Yahia H and Arneodo A (2019) Multifractal Desynchronization of the Cardiac Excitable Cell Network During Atrial Fibrillation. II. Modeling. Front. Physiol. 10:480. doi: 10.3389/fphys.2019.00480

1. INTRODUCTION

Atrial fibrillation (AF) is the most common sustained tachyarrhythmia encountered in clinical practice (Nattel and Harada, 2014). It is sometimes not diagnosed until the occurrence of a severe complication such as embolic stroke. Often associated with heart disease, clinical investigations do not always uncover any preexisting cardiovascular comorbidity (idiopathic or lone AF). Physiologically, current understanding of the onset and perpetuation of most tachyarrhythmias including AF presumes the involvement of circuit reentries. This scenario was established historically from the observation of reciprocating rhythms initiated in the atrio-ventricular node via the fast and slow pathways of impulse conduction. Atrial flutter and regular tachycardias were thus inferred to be rooted in circling conduction pathways, as going around anatomical obstacles

or scars for example. Tachyarrhythmias may also spontaneously evolve toward more irregular arrhythmias such as AF. Experiments show that AF can be induced by *in situ* injection of toxins like aconitine as well as by ectopic stimulation, i.e., under extreme conditions enforcing local functional changes of the excitable conducting substrate. AF may then persist independently of the inciting protocol (Macfarlane et al., 2011; Zipes et al., 2017). These observations paved the way to the concept of multiple circuit reentries, not necessarily linked to the anatomy but to a vulnerable atrial substrate because of functional dispersion in space and time (such as non uniform dispersion of refractoriness) (Moe and Abildskov, 1959; Moe et al., 1964; Allessie et al., 1977; Attuel et al., 1989; Winfree, 1989). But clinically, the question remained whether abnormal conducting pathways and ectopic triggers do stabilize AF. In that respect, intervention procedures were developed either to surgically create an electrical maze in the atria or, in a less invasive and safer way, to isolate abnormal ectopic activity as found in the pulmonary veins areas by radio frequency ablation. Both procedures led to high clinical success rates in stopping paroxysmal AF (Cox et al., 1991; Haïssaguerre et al., 1998). Unfortunately, the diverse procedures instigated since then remain suboptimal because the risk of relapse increases with time, and the disease often evolves toward a chronic state (Ganesan et al., 2013; Takigawa et al., 2014).

Cardiomyocytes belong to the family of excitable cells which are ubiquitous in animals and plants (Hille, 2001). They are distinguishable from non-excitable cells by their ability to reach an electrically depolarized state of their extra-cellular phospolipid bi-layer membranes. Action potentials (APs) correspond to cycle events in which the membrane reaches a depolarized state before relaxing back to the polarized rest state. In the wake of the seminal work by Hodgkin and Huxley on the giant squid axon AP (Hodgkin and Huxley, 1952a,b), a cardiac impulse is similarly described by the nonlinear coupling between a diffusing activator, the electric potential across the excitable cell membrane, and a non-diffusing inhibitor, the overall ion currents permeating through the membrane (Noble, 1962, 1965; Beeler and Reuter, 1977; Plonsey and Barr, 2007; Fenton and Cherry, 2008; Macfarlane et al., 2011). This nonlinearity underlies the fact that the AP amplitudes depend very little on the intensity of the exciting perturbation, provided they are suprathreshold. Various transmembrane proteins selectively allow some solutes to permeate. Leaking (potassium) channels are balanced by (sodium-potassium) pump exchangers forcing the cell membrane into a negatively polarized state, which compensates for the hypertonic activity of internally sequestered vital substances (Tosteson and Hoffman, 1960; Armstrong, 2003). Excitable cells take advantage of this situation to generate electrical signals. Their plasma membrane incorporates a large number of ion channels, sensitive to various other species such as e.g., calcium. They are proteins forming pores that greatly facilitate ion transport down electrochemical gradients. Ion channels act as voltage dependent gates and their reaction rates reflect the height of the free energy barrier separating the open and closed conformation states (Hille, 2001). The membrane depolarizes in a few milliseconds to a near Nernst-Planck resting equilibrium, as for instance triggered by a supra-threshold electrical stimulus. In the heart, in addition, each cardiomyocyte cycle lasts a definite amount of time, typically a few hundreds milliseconds, incorporating a refractory period during which re-excitation is impossible.

Electric pulses travel by ohmic conduction within a single cell membrane, whereas the transport of these pulses across adjacent cardiac cells is ensured by gap junction channels (GJCs). These GJCs connect adjacent cardiac cells along a preferred longitudinal direction, each via tight assemblies of hundreds to thousands of pores, themselves formed by two hemichannels of six bound proteins called connexins. Also found in nearly every connected animal tissues, and on the contrary to ion channels, GJCs are wide and open at rest, thereby prominently contributing to homeostasis, chemical messaging, and electrical permeability throughout the whole network of connected cells (Weidmann, 1966; Severs, 1990; Kumar and Gilula, 1996; Harris, 2001; Evans and Martin, 2002). The reduction of connexin genetic expression was shown to be source of conduction inhomogeneities increasing susceptibility to arrhythmias in ventricles and atria, in various animal models and in humans with diverse heart conditions, potentially causing sudden cardiac death (van der Velden et al., 2000; Dupont et al., 2001; van der Velden and Jongsma, 2002; Ausma et al., 2003; Danik et al., 2004; Severs et al., 2008). Recent studies also suggest that missense mutations in connexin encoding genes predispose to AF (Gollob et al., 2006), whereas connexin gene transfer plays a protective role in preventing sustained AF (Bikou et al., 2011; Igarashi et al., 2012).

The phenomenology of irregular arrhythmias is classically interpreted as emanating from the chaotic dynamics of excitable reaction-diffusion systems in which ohmic conduction is assumed. Typical routes to deterministic chaos with specific rhythms were theoretically identified in simple models based on cell cycle phase resetting (Glass and Mackey, 1979, 1987; Guevara et al., 1981; Guevara and Glass, 1982). In particular, period doubling bifurcations in the dynamics of excitable pulses propagating on a ring (Courtemanche et al., 1993) were put forward as a mechanism prior to the onset of AF. More complete ion channel models such as the historical Beeler-Reuter model (Beeler and Reuter, 1977), were shown to succeed in generating generic spatio-temporal patterns (Jensen et al., 1984; Chialvo et al., 1990; Fenton and Cherry, 2008). Spiral waves in 2D spatial dimensions (theoretically scroll waves in 3D) were observed experimentally during ventricular tachycardia as well as before the onset of fibrillation (Pertsov et al., 1993; Gray et al., 1995; Garfinkel et al., 1997; Zipes et al., 2017). These spiral waves can be seen as focal wave trains swirling periodically around the analog of the "leading circle" at their core (Allessie et al., 1977; Winfree, 1989). More recently, cellular automata on a two-dimensional square lattice was used to demonstrate that phase-dependent spiral attenuation could reproduce wave propagation in excitable media of myocardial cells (de la Casa et al., 2007a,b). Within this framework, fibrillation was interpreted as the break-up of unstable spiral waves spoiling rhythmic regularity (Gerhardt et al., 1990; Ito and Glass, 1991; Bär and Eiswirth, 1993; Karma, 1993; Panfilov and Hogeweg, 1993; Bär

and Brusch, 2004; Zipes et al., 2017). Other models based on nonlinear stochastic feedback mechanisms were also proposed to explain the regulation of cardiac dynamics (Ivanov et al., 1998), suggesting that it could be intrinsically random (physiological noise). To our knowledge, it has never been reported in cardiac models the existence of a multifractal intermittent dynamics of the cardiac impulse energy as observed experimentally over large time scales in our companion paper I (Attuel et al., 2017). In this study, we elaborate on a tentative interpretation of the observed intermittent dynamics during AF as the signature of synaptic plasticity. Typical individual GJC transition times between open and closed states were shown to be much longer than those of membrane polarization but compare well with membrane recovery time ($\gtrsim$ 100ms) (Spray et al., 1984; Neyton and Trautmann, 1986; Wang et al., 1992; Bukauskas and Verselis, 2004; Desplantez et al., 2007). Moreover, slow gating modulations have been evidenced due to cytoplasmic protons (low pH) and free calcium (Spray et al., 1984; Burt and Sray, 1988; Kumar and Gilula, 1996; Harris, 2001; Bukauskas and Verselis, 2004; Perrachia, 2004; Swietach et al., 2013). Thus, a perturbation of the GJC opening and closing due to electric charge may induce some time lag or advance in the activation of the cell, slowing down or boosting the propagation of the AP, even impeding or reversing it (after reexcitation), resulting in a local departure from ohmic conduction law.

Here, we propose a mathematical model of cardiac cell excitability which includes their dynamical coupling by GJC kinetics. As (i) gap junctions electrically bind cardiac cells preferentially along their elongated direction (Severs, 1990; Evans and Martin, 2002)), and (ii) in the left atrial lateral wall area, the CS has a thin surrounding muscular structure traversed by myocardial strands (Ho et al., 2012), we simply consider a one-dimensional (1D) spatial model to describe the transport of AP along and across myocardial cells via the temporal interplay of voltage-gated channels and GJCs. We show that (if probably not minimal) this 1D model robustly accounts for the intermittent modulation of cardiac pulse trains experimentally observed in the clinical data recorded in the left atrial posterior wall area of the CS (The study reported in Companion paper I (Attuel et al., 2017) was carried out with the recommendations of the International Cardiac Electrophysiological Service of public hospital CHU Haut-Lévêque, Pessac, France. The protocol for clinic research was approved by the Institutional Clinical Research and Ethics Committee: CPP (Comité de Protection des Personnes) and AFSSaPS (Agence Française de Sécurité Sanitaire des Produits de Santé). All patients involved gave written informed consent to the investigation of data. For this specific investigation of the data, the authors accessed fully anonymized and de-identified data.

2. MODEL AND NUMERICAL DATA

To reproduce the spatio-temporal multifractal intermittent dynamics of voltage signals collected from the CS of patients with chronic AF (companion paper I Attuel et al., 2017), we propose the following system of four nonlinearly coupled partial differential equations (PDEs) (Attuel et al., 2016):

$$\left\{\begin{array}{rcl} c_m\,\frac{\partial}{\partial t}\,U_m &=& \mathbf{F}(U_m,\,w_m) - \,c_g^{-1}\,\frac{\partial}{\partial x}\,\left(g\,\rho_g\right) + \,\kappa\,\frac{\partial^2}{\partial x^2}\,U_m, \\ \frac{\partial}{\partial t}\,w_m &=& \mathbf{G}(U_m,\,w_m), \\ \frac{\partial}{\partial t}\,g &=& \omega^2\,\rho_g - \,\nu_1\,g, \\ \frac{\partial}{\partial t}\,\rho_g &=& -g\,\frac{\partial}{\partial x}U_m - \,\nu_2\,\rho_g, \end{array}\right. \tag{1}$$

where $U_m(x,t)$ is the membrane electric potential drop, $w_m(x,t)$ the ionic channel gating variable, $g(x,t)$ the gap junction conductance deviation from normal, and $\rho_g(x,t)$ the gap junction capacitive charge density. $w_m(x,t)$ is generally a vector of state variables describing the generation of the APs that is related to the intracellular concentration variations of different ions (Na^+, K^+, Ca^{2+}, Cl^-). As explained in section 2.1, the kinetics of the voltage gated channels will be described by the simplified FitzHugh-Nagumo model (FitzHugh, 1962; Nagumo et al., 1962; Izhikevich and FitzHugh, 2006). Let us note that, as compared to previous modeling attempts, our model (Equation 1) lies on the assumption that the gap junction conductance is not static, and that the GJC gating is driven by both the local transmembrane field produced by the charging of the gap junction and its conductance (nonlinear coupling term). The first two equations correspond to the standard mono-domain model for cardiac AP conduction, in which an additional term for the GJC current has been introduced, responsible for an imbalance between depolarizing and repolarizing membrane currents. The last two equations describe the GJC conduction and capacitive charging.

2.1. Standard Modeling of Cardiac AP Conduction

Let us consider an idealized elongated fiber of excitable cells (**Figure 1**), along which a traveling depolarization front (AP upstroke) is classically modeled by a 1D cable equation, assuming Kirchhoff's law of conservation of currents (Plonsey and Barr, 2007; Niebur, 2008; Macfarlane et al., 2011):

$$\left\{\begin{array}{rcl} c_m\,\frac{\partial}{\partial t}\,U_m &=& \mathbf{F}(U_m,\,w_m) + \,\kappa\,\frac{\partial^2}{\partial x^2}\,U_m, \\ \frac{\partial}{\partial t}\,w_m &=& \mathbf{G}(U_m,\,w_m), \end{array}\right. \tag{2}$$

where U_m (in V) is the electric potential across the cell membrane, c_m (in F/m) is the fiber's insulating membrane capacitance per unit length, $\kappa = \sigma S$ (in $\Omega^{-1}\times$m) is an inverse resistance per unit length with σ the mono-domain conductivity[1], and S (in m^2) is the fiber cross-section. The coupling of the membrane electric potential U_m with inhibiting membrane currents responsible for repolarization by ion specific voltage-gated channels (Na^+, K^+, Ca^{2+}, Cl^-) is represented by the variable w_m (in A/m) in the nonlinear function **F**. The function **G** symbolizes the kinetics of the repolarizing voltage gated ion channels. One example of a boundary condition consists in imposing an external current stimulus I_{ext} (in A), possibly time dependent, at the $x = 0$ extremity of the cell array:

$$\kappa\,\frac{\partial}{\partial x}U_m\,(x=0) \;=\; -\,I_{ext}. \tag{3}$$

[1] $\sigma^{-1} = \sigma_i^{-1} + \sigma_e^{-1}$, where σ_i and σ_e are the internal and external medium conductivities in bi-domain models.

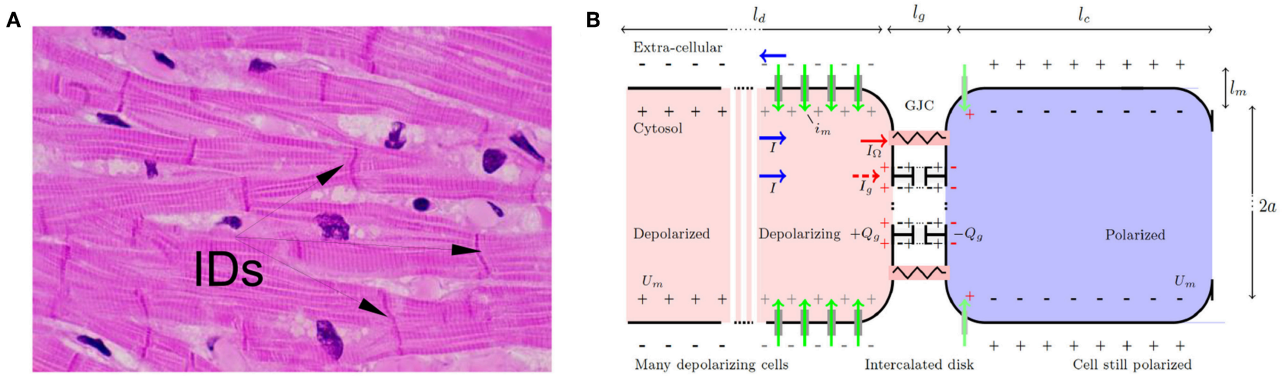

FIGURE 1 | (A) Microscopic view of cardiac muscle cells (longitudinal section) stained with hematoxylin (nuclei) and eosin (cytoplasm). The myocardial cells can be recognized by their elongated aspect (50–100 μm long, with sections $\sim 10\mu$m), a longitudinal striated organization, multiple branchings and connections at their extremities via intercalated disks (IDs). **(B)** Schematic GJCs at the onset of depolarization. Depolarizing (resp. polarized) cells are stained in red (resp. blue). Surface charges are depicted with $\pm$ symbols, on the inner and outer side of the depolarizing (gray) and polarized (black) membranes and on the dysfunctional GJCs (red) with capacitive charge loading Q_g such that $\langle Q_g \rangle = \int \rho_g \, dx$. Voltage-gated channel ionic flows are marked with green vertical arrows. Normal GJCs: red resistor symbol, dysfunctional GJCs: gray capacitor symbol. Total currents I (blue horizontal arrow) circulate in opposite directions inside and outside the cell, splitting into the normally flowing ohmic current I_Ω (red), and residual closed GJCs current I_g (dashed red) building up charge. Typical membrane and intercalated disk dimensions are $l_m \approx l_g \sim 5$ nm.

A popular model for the nonlinear function $\mathbf{F}(U_m, w_m)$ in Equation 2 is the so-called FitzHugh-Nagumo (FHN) model (FitzHugh, 1962; Nagumo et al., 1962; Izhikevich and FitzHugh, 2006), which was constructed from a damped van der Pol oscillator model (named the Bonhoeffer-van der Pol model by Fitzhugh). Indeed, the FHN model was introduced as a nerve model to simplify the Hodgkin-Huxley model (Hodgkin and Huxley, 1952a,b) and to facilitate analytic calculations:

$$\mathbf{F}(U_m, w_m) \; = \; \mu \, U_m \, (A - U_m) \, (U_m - B) \; - \; \gamma^2 w_m, \quad (4)$$

where μ, A, B and γ are real parameters. Note that $c_m / (A \, B \, \mu) \approx \tau_d$ corresponds to a depolarization time scale, A and B are coefficients establishing the magnitude of the saturating "plateau" potential while the sign of A tells whether the portion of fiber is excitable ($A > 0$) or self-sustained oscillating ($A < 0$), and $\gamma^2 > 0$ is the coupling rate between U_m and w_m. The coupling to membrane currents is described by the following form of the function $\mathbf{G}$ in Equation (2):

$$\mathbf{G}(U_m, w_m) \; = \; \alpha^2 U_m \; - \; \nu_0 w_m \; + \; \lambda \, , \quad (5)$$

where $\alpha^2 > 0$ (real positive) is an inverse inductance per unit length, λ is a leaking current parameter that will be put to zero for simplicity, and ν_0^{-1} a relaxation time scale for voltage gated channel inactivation. Since Equation (2) is a RLC circuit analog, it is straightforward to show that the saturating plateau potential lasts for a typical refractory period RP $\approx (\alpha\gamma)^{-1}$, similarly to the damped van der Pol oscillator (Van der Pol and Van der Mark, 1928; Takashi, 2007).

It takes a time $\tau_d \sim 1$ to 10 ms to depolarize one cell membrane. Actually, τ_d acts as a cut-off time scale for continuous models as Equation (2). For a linear capacitance $c_m \lesssim 10^{-6}$ F/m, and a linear conductivity $\kappa \lesssim 10^{-10}$ $\Omega^{-1}\times$m, an upstroke (ion channels releasing the electric energy stored by conversion of chemical bond energy) is estimated to travel at a typical velocity $c \sim \sqrt{\kappa \, (c_m \, \tau_d)^{-1}} \gtrsim 0.1$ m/s. This is consistent with the conduction velocity measured in the atria under various conditions $c \sim 0.1$ to 1 m/s (Zipes et al., 2017). The upstroke spans a typical membrane length of order $l_d \approx c \, \tau_d \sim 0.1$ to 10 mm (**Figure 1B**), which acts as a spatial cut-off scale in such continuous models. Note that for very slow conduction velocity and rapid upstroke, the upstroke length scale can decrease down to the longitudinal size of one cell. Mathematically, a single boundary stimulus gives rise to a unique traveling upstroke: $U_m(x, t) = U_m(x - c \, t)$. Immediately following depolarization, other voltage gated ion channels start contributing in a way as to set the membrane potential back to its original negative value. The resting polarized state is then restored back in a typical time of order $\tau_r \gtrsim 100$ ms in the heart (Hille, 2001; Plonsey and Barr, 2007; Macfarlane et al., 2011). Time history dependencies of channel activation define the absolute refractory period RP of duration $\gtrsim 100$ ms in the heart.

A traveling pulse solution of the partial differential (Equation 2) indeed corresponds to a homoclinic cycle in the FHN model biasymptotic to the resting electric potential stable fixed point (Beuter et al., 2003; Izhikevich, 2007; Fenton and Cherry, 2008; Guckenheimer and Kuehn, 2009). Homoclinic cycles are triggered locally by the advancing foot of the depolarizing front or by an external stimulus. To reproduce the observed variety of physiological properties of an excitable myocardium, nonlinear modifications or extra membrane currents were added to the coupling functions $\mathbf{F}$ and $\mathbf{G}$ as for instance in Bär and Eiswirth (1993), Karma (1993), Panfilov and Hogeweg (1993), Fenton and Karma (1998), Fenton et al. (2002), Fenton and Cherry (2008), and Zipes et al. (2017). However, in their FHN type, Equations (2), (4), and (5) are quite adapted to simulate the homoclinic orbits underlying AP cycles and cardiac pulse trains. The dynamical complexity of the original FHN model

has attracted a lot of mathematical and numerical attention (Glass and Mackey, 1987; Izhikevich, 2007). Under periodic stimulation, period doubling bifurcations were shown to precede a transition to deterministic chaos (Nolasco and Dahlen, 1968; Glass and Mackey, 1979, 1987; Guevara et al., 1981; Chialvo et al., 1990; Fenton and Cherry, 2008). Interestingly, along the line of the diffusely coupled Fitzhugh-Nagumo (Equations 2–5), the generation of higher-dimensional hyperchaotic spatio-temporal dynamics was suggested as a possible explanation of the dynamic transition to fibrillatory states in cardiac tissue (Baier and Müller, 2004).

2.2. Inter-cellular Ion Conduction and GJC Dynamics

The cardiac cell-cell contacts, where electrical signal conduction occurs, are found at intercalated discs located mostly at the narrow end of elongated cardiomyocytes. On their lateral side, the cardiomyocytes are ensheathed by cell-matrix contacts (**Figure 1**) with weaker electrical coupling. This organization favors a synchronized unidirectional propagation of electrical signals through serial strands of cardiomyocytes. When this synchronization is compromised, life-threatening arrhythmias can develop, and ultimately can become an obstacle for the regeneration of damaged heart tissues. The cardiac intercalated discs (IDs) must therefore be resilient to both mechanical and electrical disturbances to ensure a fast and reproducible propagation of the electrical signal that initiates contraction throughout the heart. ID includes three main structures: (i) the desmosome and (ii) the adherens junction (AJ) that provide the mechanical strength and continuity of the cell-cell contact, and that are both connected to the cytoskeleton, and (iii) the gap junction (GJ) which couples the cells electrically and metabolically. Other proteins which are not directly involved in the cell-cell contact also reside in the ID, including ion channels. The close contact and communication between cardiac myocytes is therefore essential for proper heart functioning as a syncytium, for both electrical and mechanical signal conductions. The GJCs (type I) which are found in cardiac muscles are organized in hexagonal arrays (connexins), with 8–9 center-to-center spacing, and overall thickness $\sim$ 15-16 nm. Despite their negligible size, as compared to the myocyte length, these junctions were soon recognized as discontinuous conduction zones of the myocardium (Spach, 1983), and they were suspected to offer a low resistance to the transfer of electrical signals and more surprisingly to enhance this transfer nonlinearly (Cole et al., 1988).

Several numerical and theoretical attempts have tried to reconcile the difference of scales (from membrane and GJCs thickness to cell length) in a continuous or quasi-continuous treatment of cardiac fiber excitability (Diaz et al., 1983; Joyner et al., 1984; Cole et al., 1988; Keener, 1990; Bub et al., 2005; Pumir et al., 2005; Hand and Griffith, 2010; Hand and Peskin, 2010; Lin and Keener, 2010, 2013). At the heart tissue level, it appears at first legitimate to discard the GJC discontinuities, except maybe for radical instances of static or permanent alterations of GJCs due e.g., to connexin expression depletion (Cole et al., 1988) or gap junction blocker like α-glycerrhetinic acid (Bub et al., 2005) over large areas. As the longitudinal electric field generated by repeatedly passing APs drives the GJCs, we propose in this study to consider the spatio-temporal dynamics of the GJC conductances especially at cardiac intercalated discs where most GJCs reside. Indeed, we do not explicitly account for the discreteness of the GJCs spatially, considering instead an average behavior, but we introduce a nonlinear coupling term in the conduction current mono-domain cable (Equation 2) to mark the distinct propagation and polarization dynamics of GJCs and channel-gated ion channels.

Transjunctional voltage gated inactivation and recovery rates are comparable to repolarization rates (Neyton and Trautmann, 1986; Wang et al., 1992; Desplantez et al., 2007). This is a clue that we regard as pivotal for the behavior of ion transport along the direction of propagation at the locations of GJCs, especially during rapidly beating electrical activity (AP). As compared to previous AP propagation models involving GJCs (Burt and Sray, 1988; Kumar and Gilula, 1996; Harris, 2001; Bukauskas and Verselis, 2004; Danik et al., 2004; Perrachia, 2004), we put more attention on the dynamical implication of GJC (slow) kinetics in response to positive charge accumulation (capacitive charging). By considering that the capacitive charging of closed GJCs is proportional to the voltage drop across the interstitial space, we show that the GJC slow kinetics can enhance the effect thereby amplifying fluctuations around a stationary conductance. The whole AP propagation can therefore be strongly affected because small initial fluctuations of the GJC conductance may be amplified to non negligible values corresponding to a sort of nonlinear resonance of the GJC dynamics.

Averaging over typical depolarization time and length scales, corresponding to several thousands of intercalated discs, allows to derive a continuous mathematical model of inter-cellular ion condition and GJC dynamics. When combined with the well controlled FHN mono-domain mode, we get the following 1D system of nonlinearly coupled PDEs:

$$\begin{cases} c_m \frac{\partial}{\partial t} U_m = \mu\, U_m\,(A - U_m)\,(U_m - B) \\ \qquad\qquad - \gamma^2 w_m - c_g^{-1} \frac{\partial}{\partial x}\left(g\,\rho_g\right) + \kappa\, \frac{\partial^2}{\partial x^2} U_m, & \text{(6a)} \\ \frac{\partial}{\partial t} w_m = \alpha^2 U_m - \nu_0 w_m + \lambda, & \text{(6b)} \\ \frac{\partial}{\partial t} g = + \omega^2\, \rho_g - \nu_1\, g, & \text{(6c)} \\ \frac{\partial}{\partial t} \rho_g = - g\, \frac{\partial}{\partial x} U_m - \nu_2\, \rho_g, & \text{(6d)} \end{cases}$$

with the same boundary conditions as defined in Equation (3). The new dynamical variables are: (i) the GJC conductance fluctuations g (around its mean value accounted for in κ) (in $S \equiv \Omega^{-1}$), which can be interpreted as the non zero gradient part $g \equiv \frac{\partial}{\partial x}\kappa \neq 0$, and (ii) the average capacitive charge linear density ρ_g. The new parameters are c_g: an average linear capacitance analog to c_m but for the intercalated disks, ω^2: a reaction rate for the zeroth-order kinetic Equation (6c), and ν_1 a relaxation rate ($\nu_2 \to 0$). Note that the zeroth-order (independent of g) reaction rate is justified because only a small fraction of abnormally closing GJCs have to grow from zero initially, while a majority of others remain conducting. At the same time, capacitive charges act on all nearby hexamers. In addition, current conservation modifies Equation (2) so as to include a current term coming

TABLE 1 | Parameters used in the simulations of Equations (6)–(8).

Param	L	c_m	c_g	κ	μ	A	B	ν_0	ν_1	ν_2	γ^2	α^2	ω^2	λ
Simul #1	210	1	1	0.01	3	0.1	1	0.02	0.01	0.0001	3	0.008	10^5	0
Simul #2	150	1	1	0.01	3	0.1	1	0.02	0.01	0.0001	3	0.008	10^5	0
Simul #3	90	1	1	0.01	3	0.1	1	0.02	0.01	0.0001	3	0.008	10^5	0
Simul #4	30	1	1	0.01	3	0.1	1	0.02	0.01	0.0001	3	0.008	10^5	0
Simul #5	150	1	1	0.005	6	0.1	1	0.01	0.005	0.0001	6	0.004	5.10^4	0
Simul #6	150	1	1	0.04	3	0.1	1	0.02	0.01	0.0001	3	0.008	10^5	0
Simul #7	150	1	1	0.08	3	0.1	1	0.02	0.01	0.0001	3	0.008	10^5	0

The spatial size is L in $\delta x = 0.3$ mm units (section 2.3). The parameter dimensions are: c_m ($ms \times mm^{-1} \times \Omega^{-1}$), c_g ($ms \times mm^{-1} \times \Omega^{-1}$), κ ($mm \times \Omega^{-1}$), ω^2 ($mm \times ms^{-2} \times mV^{-1}$), ν_i (ms^{-1}) for $0 \leq i \leq 2$; α^2 (ms^{-2}), γ (no unit), μ ($mm^{-1} \times \Omega^{-1} \times mV^{-2}$), A, B (mV).

from the capacitive charging of GJCs. Precisely, the local ohmic current flowing through open GJCs experiences losses due to closed GJCs. Thus, adding the GJC current as $I_g = c_g^{-1}\, g\rho_g$, to the unpertubed conduction current $I_\Omega = -\kappa \frac{\partial}{\partial x} U_m$, gives a total longitudinal current $I = I_\Omega + I_g$ (**Figure 1B**). From charge conservation hypothesis, taking the divergence of I yields Equation (6a). Equation (6d) is obtained by considering that the net capacitive charging current density $\frac{\partial}{\partial t}\rho_g$ is non zero as soon as the GJCs start closing massively. This current density is written as the product of the GJC conductance and the local electric field produced by the AP wave ($-\frac{\partial}{\partial x} U_m$). Finally, ν_1 accounts for the GJC relaxation rate while ν_2 (with $\nu_2 \ll \nu_1$) accounts for other charge leakages. We refer the reader to **Table 1** for more details on units and numerical values.

The boundary conditions are defined such that the value of A is chosen opposite ($A \to -A$) for $x = 0$, making this fiber end self-sustained oscillating, and unconstrained for $x = L$ with null electric field $-\frac{\partial}{\partial x} U_m\,(x = L) = 0$, while no external current is added $I_{ext} = 0$. Thus, we set :

$$c_m \frac{\partial}{\partial t} U_m = \mu\, U_m\,(-A - U_m)\,(U_m - B) - \gamma^2 w_m - c_g^{-1}\, g\, \rho_g \quad \text{for } x = 0, \tag{7}$$

and

$$\frac{\partial}{\partial t}\rho_g = -\nu_2\, \rho_g \quad \text{for } x = L. \tag{8}$$

2.3. Numerical Scheme

We use standard finite difference techniques to integrate numerically the system of partial differential Equation (6) with boundary conditions defined in Equations (7) and (8). The linear Laplacian operator is handled with the standard "Crank-Nicholson" scheme using tri-diagonalization. But, one notable unusual trait, as compared to other cardiac models, is that by construction here, the spatial operator is no longer elliptic because of the divergence term. This calls for a special treatment of the gap junction fluctuating quantities.

One way to find out a stable scheme is by considering the following heuristic. For the sake of exposition simplicity, the mean membrane potential is assumed adiabatically constant $\frac{\partial}{\partial t} U_m = 0$. Equation (6d) possesses an important mirror antisymmetry upon changing $U_m \to -U_m$ and $x \to -x$, which distinguishes flow directions of GJ charging or discharging, for a given fluctuating conductance. Consistently, Equations (6b, c) are invariant under the change $\rho_g \to -\rho_g$ and $g \to -g$. Hence, the fluctuating vector $W = \begin{bmatrix} \rho_g \\ g \end{bmatrix}$ obeys the following temporal evolution equation:

$$\frac{\partial}{\partial t} W = \mathrm{M}\, W, \tag{9}$$

where the matrix local evolution operator is

$$\mathrm{M} = \begin{bmatrix} -\nu_2 & -\frac{\partial}{\partial x} U_m \\ \omega^2 & -\nu_1 \end{bmatrix}, \tag{10}$$

which shows ($\nu_2 \to 0$) that the quantity $\theta = \omega\sqrt{\left|\frac{\partial}{\partial x} U_m\right|}$ can act, for some fluctuation, as a typical growth rate (as in the case of a right moving depolarizing front for which the gradient is negative) or as a typical pulsation frequency otherwise. To handle this particular linear, (temporal) evolution, the so-called "leap-frog" method is usually well adapted and was found numerically stable.

When fluctuations can be assumed as happening over a local spatial distance $\delta\ell$ such that a positive variation from zero is $W \simeq -\delta\ell \frac{\partial}{\partial x} W$, one can rewrite dimensionally the temporal evolution operator (Equation 10) into a spatial transfer operator: $\mathrm{M}\, W \to -\mathrm{M}' \frac{\partial}{\partial x} W - \nu W$ where

$$\mathrm{M}' = \begin{bmatrix} 0 & \delta\ell \frac{\partial}{\partial x} U_m \\ -\delta\ell\omega^2 & 0 \end{bmatrix}, \tag{11}$$

and $\nu = \begin{bmatrix} \nu_2 \\ \nu_1 \end{bmatrix}$. Thus, an advection velocity appears of magnitude $v = \delta\ell\theta$, directed in one or the other way depending on the sign of the fluctuating variables. If not further driven, these fluctuating variables are damped over a spatial distance (along a characteristic) $\Delta x = \pm v \Delta t$, in a time $\Delta t \sim \nu_1^{-1}$. A standard "upwind" scheme takes good care of the numerical stability of advection, with sufficient precision, but favors a particular direction of propagation for positive fluctuations, here in agreement with the mirror antisymmetry. This also explains why we choose to place on the outer left side of our 1D

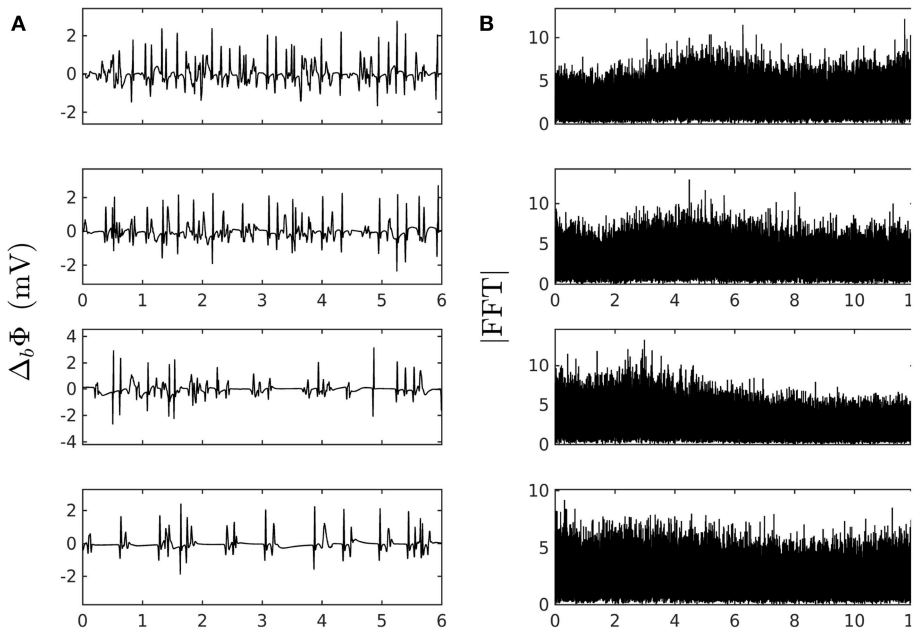

FIGURE 2 | Numerically simulated pseudo bipolar potential. **(A)** 6 s time-series $\Delta_b\Phi$ (Equation 12) are generated at positions x (in $\delta x = 0.3$ mm units) = 8, 18, 75 and 134 (from top to bottom) with our model defined in Equations (6)–(8) with parameter values defined in Simul #2 (**Table 1**), $L = 150$ (in $\delta x = 0.3$ mm units). **(B)** Corresponding Fourier transform power spectra. No attempt was made to reproduce the high and low pass filtering used in real bipolar catheter acquisitions. The natural point source frequency at the boundary is $\sim \alpha\,\gamma \approx 5$ Hz. Rarefaction of pulses occurs as one moves away from the source which is a hint at some randomly back-scattered pulses that collide and annihilate up-following pulses without reexciting new pulses.

system a rapidly beating cell (Equation 7) mimicking an ectopic source, whereas the dynamics is monitored only on its right, at different spatial positions. The outer right boundary is chosen non-excitable in the present study, which mimics any kind of connection to non-conducting tissues. Numerical integration values of time step $\delta t = 0.4$ ms for all simulations in **Table 1** (except Simul #5 for which $\delta t = 0.25$ ms), and spatial step $\delta x = 0.3$ mm are chosen to abide by the Courant-Friedrichs-Lewy condition $v\,\delta t/\delta x < 1$, for which an upper bound estimate of the conduction velocity is $c \simeq 0.1$ m/s.

2.4. Software and Documentation

The numerical integration code can be downloaded directly from the following link: https://geostat.bordeaux.inria.fr/images/fwd-matlab-code.zip or through Geostat team software page: https://geostat.bordeaux.inria.fr/index.php/downloads.html (last item).

2.5. From the Formal Model Variables to Experimentally Recorded Potential Values

We simulated the external electric potential recorded by a bipolar electrode $\Delta_b\Phi$ by use of the dipole layer approximation. Within the mono-domain framework, the electric potential felt just outside a cardiac fiber of thickness $e \sim 2$ mm is evaluated as (Plonsey and Barr, 2007; Macfarlane et al., 2011):

$$\Delta_b\Phi(x,t) = \Pi_p \star i_d(x,t) = \int \Pi_p(x-x';\,e) \left(\kappa\frac{\partial^2}{\partial x^2}U_m(x',t) - i_g(x',t)\right)\mathrm{d}x', \qquad (12)$$

where Π_p is the convolution function for the bipolar probe, $i_d(x,t) = \kappa\frac{\partial^2}{\partial x^2}U_m(x,t) - i_g(x,t)$ the total dipole layer current divergence (or flux across a fiber section), and $i_g(x,t) = \frac{\partial}{\partial x}I_g(x,t)$ the new contribution coming from GJC losses. Since we are interested in variations over distances greater than the depolarization length scale, a good approximation is to compute $\Pi_p(x) = \frac{\partial}{\partial x}\Pi(x,e)$, where $\Pi(x,e) = 2\pi\left(\frac{x}{|x|} - \frac{x}{\sqrt{x^2+e^2}}\right) \approx \int |r|^{-3}\ \vec{r}\cdot\vec{\mathrm{d}S}$ is the solid angle spanning the fiber section at a distance $\vec{r} = (x,e)$ of the depolarization front from the probe. **Figure 2** shows typical pseudo bipolar potential time series numerically simulated with our 1D system of PDEs (Equation 6) with, as boundary condition at $x = 0$ (Equation 7), an automatically beating source of frequency $\alpha\gamma \sim 5$ Hz so as to match the cardiac pulse trains observed experimentally. Tuning the newly introduced parameters ω^2 and ν_1 in Equation (6), we have found quite easily paths leading from a phase of coherent propagation of AP pulses to a phase of quite incoherent and intermittent electrical activity (**Figure 2**) that strongly reminds the very irregular behavior of electric potential time series recorded during AF (see for comparison **Figure 1** in our companion paper I Attuel et al., 2017). Besides the obvious interest of analyzing the succession of bifurcations and transition events encountered along these paths in parameter space, we will focus in this paper on a comparative study of the complex and highly intermittent modulation of cardiac pulse trains simulated numerically with our model of cardiac AP conduction and GJC dynamics and the one observed experimentally in the coronary sinus during episodes of AF (Attuel et al., 2017).

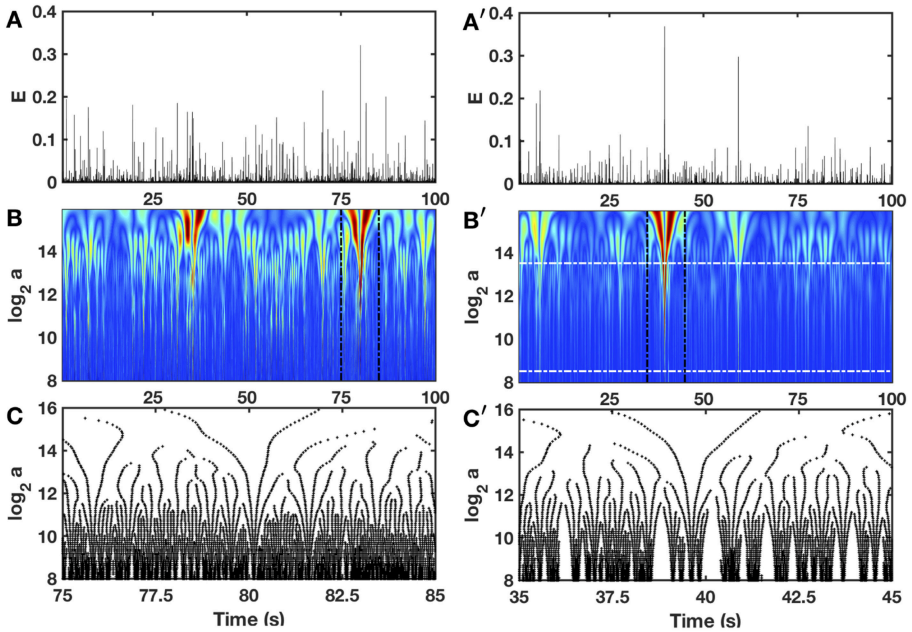

FIGURE 3 | Wavelet transform of local impulse energy time-series. **(A)** A 100 s portion of $E(t)$ recorded at the electrode Pt3 (Companion paper I Attuel et al., 2017). **(B)** Time-scale WT representation of $E(t)$ with the third-order analyzing wavelet $g^{(3)}$ (Equation 16). The modulus of the WT is coded, independently at each scale a, using 256 colors from black ($|T_{g^{(3)}}(t,a)| = 0$) to red ($\max_t |T_{g^{(3)}}(t,a)|$). **(C)** WT skeleton defined by the maxima lines of a 10 s portion of $E(t)$. The scale $a = \alpha \Delta t/\delta t$, where α is an analyzing wavelet dependent constant ($\alpha = 8.6\ 10^{-2}$ for $g^{(3)}$ with the lastwave software), and $\delta t = 0.4$ ms. **(A′–C′)** same as **(A–C)** for a numerical time series $E(x,t)$ generated at position $x = 75$ (in $\delta x = 0.3$ mm units) with our model defined in Equations (6)–(8) with the set of parameter values used in Simul #2 (**Table 1**), and a total system length $L = 150$ (in $\delta x = 0.3$ mm units). In **(B′)** the white horizontal dashed-dotted lines delimit the range of time scales ($2^{8.5} \leq a \leq 2^{13.5}$) used to perform linear regression fit estimates of the $\tau(q)$ and $D(h)$ multifractal spectra.

3. METHODS OF ANALYSIS

3.1. Local Impulse Energy

With the same convention as in the companion paper I (Attuel et al., 2017), the local 1D impulse electric energy traveling with scarcely any alteration at velocity c over a depolarization time period τ_d, is evaluated from Equation (12) as:

$$E(x,t) = \left(\frac{\partial \Delta\phi_b(x,t)}{\partial t} \right)^2 , \tag{13}$$

after dropping some constant prefactors. To practically derive $E(x,t)$ from the numerically simulated $\Delta_b \phi(x,t)$, we used the same order 4 finite difference scheme as in the companion paper I (Attuel et al., 2017).

3.2. Zooming on the Local Impulse Energy With the Wavelet Transform Microscope

In **Figure 3** is shown in a comparative time-scale decomposition of two 100 s long local (x fixed) impulse energy time-series, the first one was experimentally recorded at the electrode Pt3 in a patient with chronic AF (companion paper I, Attuel et al., 2017) and the second ones was numerically simulated with Equations (6)–(8) with model parameters defined in Simul #2 (**Table 1**). The continuous wavelet transform (WT) consists in expanding signals in terms of wavelet constructed from a single function, the "analyzing wavelet" ψ, by means of translations and dilations (Grossmann and Morlet, 1984; Daubechies, 1992; Meyer, 1992; Mallat, 1998):

$$T_\psi[E](t_0,a) = \frac{1}{a} \int_{-\infty}^{+\infty} E(t)\, \psi\left(\frac{t-t_0}{a}\right) dt\ , \tag{14}$$

where t_0 is a time parameter and a (> 0) a scale parameter (inverse of frequency). Interestingly, by choosing a wavelet ψ which has its first n_ψ moments null [$\int t^m \psi(t) dt = 0, 0 \leq m < n_\psi$], it can be proven (Arneodo et al., 1988, 1995b, 2008; Jaffard, 1989; Muzy et al., 1991, 1994; Mallat and Hwang, 1992) that:

$$T_\psi[E](t_0,a) \sim a^{h(t_0)},\ a \to 0^+, \tag{15}$$

provided $n_\psi > h(t_0)$, where $h(t_0)$ is the point-wise Hölder exponent that characterizes the maximum regularity of the signal E at point t_0. As experienced in the companion paper I (Attuel et al., 2017) for experimental local impulse energy time-series, we will use in this work the third derivative of a Gaussian function as analyzing wavelet with $n_\psi = 3$ (Muzy et al., 1994; Arneodo et al., 1995b) (Figure S1 in the companion paper I):

$$g^{(3)}(t) = \frac{d^3}{dt^3} \left(e^{-t^2/2} \right). \tag{16}$$

Interestingly, to track cusp singularities (for oscillating singularities like chirps see Arneodo et al., 1995a, 1997),

the WT skeleton defined by the so-called maxima lines of local WT modulus maxima (WTMM) (**Figures 3C,C'**), was proved to be of practical use since along these maxima lines, Equation (15) was shown to apply (Mallat and Hwang, 1992).

3.3. A Wavelet-Based Multifractal Formalism

The wavelet transform modulus maxima (WTMM) method (Muzy et al., 1991, 1994; Bacry et al., 1993; Arneodo et al., 1995b, 2008) was originally developed to generalize box-counting techniques (Arneodo et al., 1987) and to remedy the limitations of the structure functions method (Muzy et al., 1993) in performing multifractal analysis of one-dimensional (1D) velocity signals in fully-developed turbulence. It has proved very efficient to estimate scaling exponents and multifractal spectra (Muzy et al., 1994; Audit et al., 2002; Arneodo et al., 2008; Ivanov et al., 2009). The WTMM method has been extensively applied in different domains of fundamental and applied science, including the analysis of complex time-series found in genomics (Nicolay et al., 2007; Arneodo et al., 2011; Audit et al., 2013) and physiological systems (Ivanov et al., 1999, 2001, 2009; Nunes Amaral et al., 2001; Goldberger et al., 2002; Ciuciu et al., 2012; Chudácek et al., 2014; Gerasimova et al., 2014; Richard et al., 2015; Gerasimova-Chechkina et al., 2016). The WTMM method and its wavelet leaders discrete generalization (Jaffard et al., 2007; Wendt et al., 2007) have already been applied to cardiac signals but mainly to characterize the fluctuations of inter-beat intervals (Ivanov et al., 1999, 2001; West et al., 2004; Leonarduzzi et al., 2010; Wendt et al., 2014; Gadhoumi et al., 2018). As for the analysis of experimental local impulse energy time-series in the companion paper I (Attuel et al., 2017), we will use here two declinations of the WTMM method, the moment (partition function) method and the magnitude cumulant method (Muzy et al., 1994; Arneodo et al., 2008).

The method of moments consists in investigating the scaling behavior of partition functions defined in term of WTMM:

$$Z(q,a) = \sum_{l \in \mathcal{L}(a)} |T_\psi[E](t,a)|^q \sim a^{\tau(q)},\ a \to 0^+, \qquad (17)$$

where $q \in \mathbb{R}$, $\mathcal{L}(a)$ is the set of the maxima lines l that defines the WT skeleton and the exponents q and $\tau(q)$ play, respectively, the role of an inverse temperature and a free energy in the analogy that links the multifractal formalism and thermodynamics (Bohr and Tél, 1988; Arneodo et al., 1995b). Then, from the Legendre transform of $\tau(q)$:

$$D(h) = \min_q [qh - \tau(q)], \qquad (18)$$

we get as equivalent of entropy, the so-called $D(h)$ singularity spectrum defined as the fractal (Hausdorff) dimension of the set of points t where the Hölder exponent (equivalent of energy) $h(t) = h$ (Bacry et al., 1993; Muzy et al., 1993, 1994; Arneodo et al., 1995b; Jaffard, 1997a,b).

In practice, to avoid instabilities in performing the Legendre transform, we instead compute the following expectation values (Muzy et al., 1994; Arneodo et al., 1995b), analogous to the fundamental thermodynamic relations, by inversion of Equation (18):

$$h(q,a) = \frac{\partial}{\partial q} \ln(Z(q,a)) = \sum_{l \in \mathcal{L}(a)} \ln\left(|T_\psi[E](l,a)|\right) \cdot W_\psi[E](q,l,a), \qquad (19)$$

and

$$\begin{aligned} D(q,a) &= q \frac{\partial}{\partial q} \ln(Z(q,a)) - \ln(Z(q,a)) \\ &= \sum_{l \in \mathcal{L}(a)} W_\psi[E](q,l,a) \cdot \ln\left(W_\psi[E](q,l,a)\right), \end{aligned} \qquad (20)$$

where $W_\psi[E](q,l,a) = |T_\psi[E](l,a)|^q / Z(q,a)$ corresponds to the Bolzmann weight (Arneodo et al., 1995b). Then, from the slopes of $h(q,a)$ and $D(q,a)$ vs. $\ln a$, we get $h(q)$ and $D(q)$, and therefore the $D(h)$ singularity spectrum as a curve parametrized by q.

An alternative method that can be used as a double check of the predictions of the method of moments is the so-called method of magnitude cumulants (Delour et al., 2001). This method consists in computing the cumulants $C_n(a)$ of the magnitude $\ln|T_a|$. Then from the behavior of the cumulants:

$$\begin{aligned} &C_1(a) \equiv \langle \ln|T_a| \rangle \sim c_1 \ln(a), \\ &C_2(a) \equiv \langle \ln^2|T_a| \rangle - \langle \ln|T_a| \rangle^2 \sim -c_2 \ln a, \\ &C_3(a) \equiv \langle \ln^3|T_a| \rangle - 3\langle \ln^2|T_a| \rangle + 2\langle \ln|T_a| \rangle^3 \sim c_3 \ln a, \\ &\cdots \end{aligned} \qquad (21)$$

we get the following expansion formula for $\tau(q)$:

$$\tau(q) - c_0 + c_1 q - c_2 q^2/2! + c_3 q^3/3! \cdots \qquad (22)$$

where the coefficients $c_n > 0$ are estimated as the slope of $C_n(a)$ vs. $\ln a$ ($n = 1,\ 2,\ 3,\ , \cdots$), and $c_0 = D_F$ as the fractal dimension of the support of singularities of $E(t)$.

Multifractal analysis allows us to distinguish monofractal signals of unique Hölder exponent H. Their $\tau(q)$ spectrum is a linear function of q with slope $c_1 = H$, all the other $c_i = 0$, $i \geq 2$. The corresponding $D(h)$ singularity spectrum reduces to a single point $D(h = c_1) = D_F$. In contrast, a nonlinear $\tau(q)$ is the signature of multifractal signals with Hölder exponent $h(t)$ fluctuating over time (Muzy et al., 1991, 1994; Bacry et al., 1993; Arneodo et al., 1995b, 2002, 2008). As in the companion paper I (Attuel et al., 2017), in this study we will fit the numerical data by so-called log-normal quadratic approximation

$$\tau(q) = -c_0 + c_1 q - c_2 q^2/2, \qquad (23)$$

leading to a quadratic single hump shaped $D(h)$ singularity spectrum

$$D(h) = c_0 - (h - c_1)^2/2c_2, \qquad (24)$$

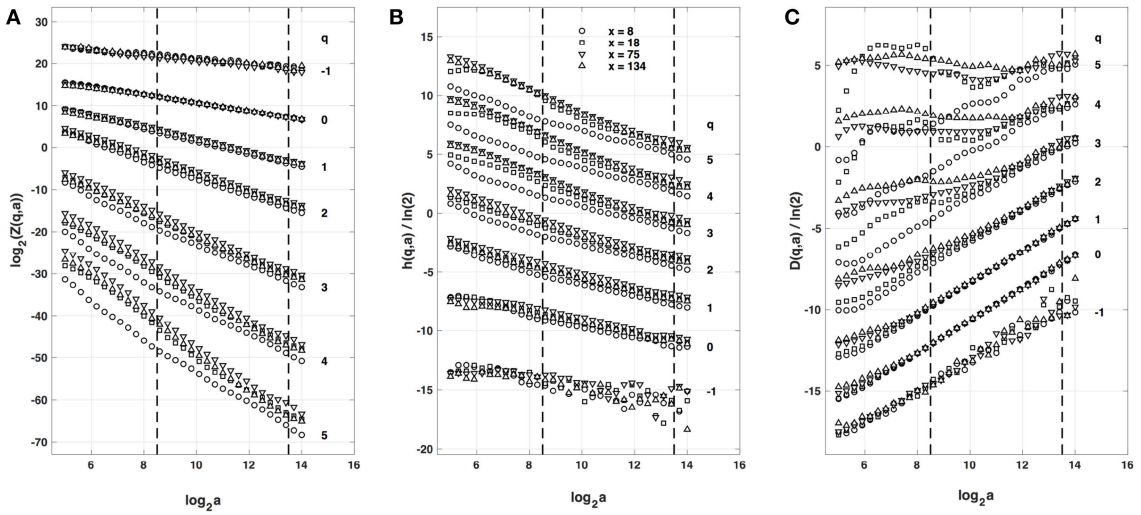

FIGURE 4 | Multifractal analysis of local impulse energy time-series $E(x,t)$ generated with our model defined in Equations (6)–(8) with the parameter values defined in Simul #2 (**Table 1**), $L = 150$ (in $\delta x = 0.3$ mm units). **(A)** $\log_2 Z(q,a)$ vs. $\log_2 a$ (Equation 17). **(B)** $h(q,a)/\ln 2$ *vs* $\log_2 a$ (Equation 19). **(C)** $D(q,a)/\ln 2$ vs. $\log_2 a$ (Equation 20). The computation were performed with the WTMM method (Paper I, Methods of Analysis Attuel et al., 2017) for different values from $q = -1$ to 5 with the analyzing wavelet $g^{(3)}$ (Equation 16). The vertical dashed lines delimit the range of scales ($2^{8.5} \leq a \leq 2^{13.5}$) used for the linear regression estimate of $\tau(q)$, $h(q)$ and $D(q)$ in **Figure 5**. The symbols correspond to the time-series $E(x,t)$ computed at the spatial positions $x = 8$ (○), 18 (□), 75 (▽) and 134 (△) (in $\delta x = 0.3$ mm units).

where $c_0 = -\tau(0) = D_f$ is the fractal dimension of the support of singularities of $E(t)$, c_1 is the value of h that maximizes $D(h)$, and the intermittency coefficient c_2 characterizes the width of the $D(h)$ spectrum (Delour et al., 2001).

3.4. Beyond One-Point Statistics: The Two-Point Magnitude Correlation Method

Many studies have misleadingly extrapolated a multifractal diagnosis to the existence of an underlying multiplicative cascade process. To address this issue, we indeed need to investigate two-point statistics. The two-point magnitude correlation method amounts to investigate how the two-point magnitude correlation function (Arneodo et al., 1998a)

$$C(a,\Delta t) = \langle \big(\ln|T_a(t)| - \langle \ln|T_a(t)|\rangle\big) \cdot \big(\ln|T_a(t+\Delta t)| - \langle \ln|T_a(t)|\rangle\big)\rangle \qquad (25)$$

changes as a function of Δt at scale a. As demonstrated by Arneodo et al. (1998a,b) for random multiplicative cascades on wavelet dyadic trees (see also Meneveau and Sreenivasan, 1991):

$$C(a,\Delta t) \sim -c_2 \ln \Delta t, \qquad \Delta t > a, \qquad (26)$$

where the proportionality coefficient c_2 is the intermittency coefficient defined in Equations (21) and (22) [Note that $C(a,\Delta t = 0) \equiv C_2(a) \sim -c_2 \ln a$]. Thus, by computing $C(a,\Delta t)$ from Equation (25) and plotting it as a function of $\ln \Delta t$, inferences can be made about long-range dependence and consistency with a multiplicative cascading process (Arneodo et al., 1998a,b). Applications of the two-point magnitude correlation method have already provided insight into a wide variety of problems, e.g., the validation of the log-normal cascade phenomenology of fully developed turbulence (Arneodo et al., 1998a,c, 1999) and of high resolution temporal rainfall (Venugopal et al., 2006; Roux et al., 2009), and the demonstration of the existence of a causal cascade of information from large to small scales in financial time series (Arneodo et al., 1998d; Muzy et al., 2001). In the companion paper I (Attuel et al., 2017), we have applied this method to experimental local impulse energy time-series during episodes of AF. Surprisingly, this study has revealed the absence of an underlying multiplicative time-scale structure that will be used in this work as a multifractal random noise numerical test of the pertinence of our cardiac excitable network modeling (section 2) during AF.

4. RESULTS

4.1. One-Point Multi-Fractal Analysis of Local Impulse Energy Numerical Data

4.1.1. Multifractal Analysis of the Simulated Impulse Energy Time-Series With the WTMM Method of Moments

When applying the WTMM method to the impulse energy time-series $E(x,t)$ obtained by numerically integrating Equation 6 with periodically driven boundary condition (Equation 7) at $x = 0$ (**Figure 3A'**), we confirmed that the partition function $Z(q,a)$ (Equation 17) obtained from the WT computed with the analysing wavelet $g^{(3)}$ (**Figure 3B'**) and its skeleton (**Figure 3C'**), displays scaling properties for $q = -1$ up to $\lesssim 5$ over a range of time-scales larger than the typical interbeat ~ 0.2 s (**Figure 2B**). We strictly limited this range to (1.7, 54 s) for

linear regression fit estimates in a logarithmic representation (**Figure 4A**). The $\tau(q)$ spectrum so-obtained at different spatial positions $x = 8, 18, 75$ and 134 for a 1D system of total length $L = 150$ (x and L expressed in $\delta x = 0.3$ mm units) is robustly well approximated by a quadratic spectrum (Equation 23) with parameter values that do not change much when moving away from the periodic beating source at $x = 0$ (**Table 2**). The support of singularities of $E(x,t)$ has a fractal dimension $c_0 = D_F \sim 1$, independently of x. The singularities of Hölder $h = c_1 \sim 0.45 - 0.48$ that maximizes $D(h)$ are also consistently observed all along our 1D spatial system. Interestingly, the intermittency coefficient c_2 is significantly different from zero (the hallmark of multifractal signals) and increases from values $c_2 \sim 0.03$ close to the source up to values $c_2 \sim 0.1$ far away from the source. Overall the values of c_0, c_1 and c_2 parameters reported in **Table 2** are very similar to the ones obtained in **Table 1** of the companion paper I (Attuel et al., 2017) for electrodes Pt3 and Pt5 located in the left atrial posterior wall. Our numerical simulations thus reveals some increased intermittency of $E(x,t)$, when moving away from the periodic beating source, rather rapidly converging to a $\tau(q)$ spectrum in quantitative agreement with the one observed experimentally (**Figure 5A**). This is confirmed when, respectively, plotting $h(q,a)/\ln 2$ (Equation 19) and $D(q,a)/\ln 2$ (Equation 20) vs. $\log_2 a$ (**Figures 4B,C**). Despite some deterioration of scaling for large $q \gtrsim 4$ values, from the estimate of the slopes $h(q)$ and $D(q)$, we get the single humped $D(h)$ spectra shown in **Figure 5B** and which clearly widen when moving away from the source to ultimately match the $D(h)$ spectra observed experimentally (**Figure 5B**). As a check of the reliability of the so-obtained $D(h)$ spectra, they are found quite well approximated by the quadratic spectra defined in Equation 24 with the parameter values obtained from a polynomial fitting of the $\tau(q)$ data (**Table 2**, **Figure 5**).

TABLE 2 | Results of the WTMM multifractal analysis of local impulse energy time-series $E(x,t)$ numerically simulated with our model defined in Equations (6)–(8) with the set of parameter values defined in Simul #2 (**Table 1**), $L = 150$ (in $\delta x = 0.3$ mm units).

	$x = 8$	$x = 18$	$x = 75$	$x = 134$
c_0	1.004 ± 0.001	1.005 ± 0.001	1.013 ± 0.001	0.989 ± 0.002
c_1	−0.449 ± 0.003	−0.435 ± 0.005	−0.481 ± 0.002	−0.460 ± 0.007
c^*_1	−0.448 ± 0.007	−0.443 ± 0.007	−0.486 ± 0.008	−0.462 ± 0.009
c_2	0.028 ± 0.006	0.060 ± 0.009	0.070 ± 0.003	0.097 ± 0.013
c^*_2	0.042 ± 0.013	0.051 ± 0.014	0.074 ± 0.011	0.063 ± 0.013

c_0, c_1, c_2 are the coefficients of the quadratic log-normal approximation of $\tau(q)$ (Equation 23) obtained at spatial positions $x = 8, 18, 75$ and 134 (in $\delta x = 0.3$ mm units), with the WTMM method of moments when using the analysing wavelet $g^{(3)}$ (Equation 16). c^*_1 and c^*_2 are the corresponding coefficients obtained with the magnitude cumulant method (Equation 21).

4.1.2. Multifractal Analysis of the Impulse Energy Data With the Method of Magnitude Cumulants

As previously performed in our companion paper I (Attuel et al., 2017) for the analysis of experimental impulse energy data, we have reproduced our multifractal analysis of numerical time-series using the alternate magnitude cumulant methodology. The first-, second- and third-order cumulants where computed using Equation (21) and are plotted vs. the logarithm of the scale in **Figure 6**. As expected, $C_1(a)$, $C_2(a)$ and $C_3(a)$ display consistent scaling behavior over the same range of scales ($2^{8.5} \leq a \leq 2^{13.5}$). The results obtained for $C_3(a)$ (**Figure 6C**) confirm that with limited 422 s long time series as recorded in experiments, there is no way to conclude about the possible departure from a log-normal quadratic $\tau(q)$ spectrum ($c_3 \equiv 0$). Interestingly, the quadratic $\tau(q)$ spectra with parameter values c^*_1 and c^*_2 listed in **Table 2**, are found in good agreement with the ones previously estimated

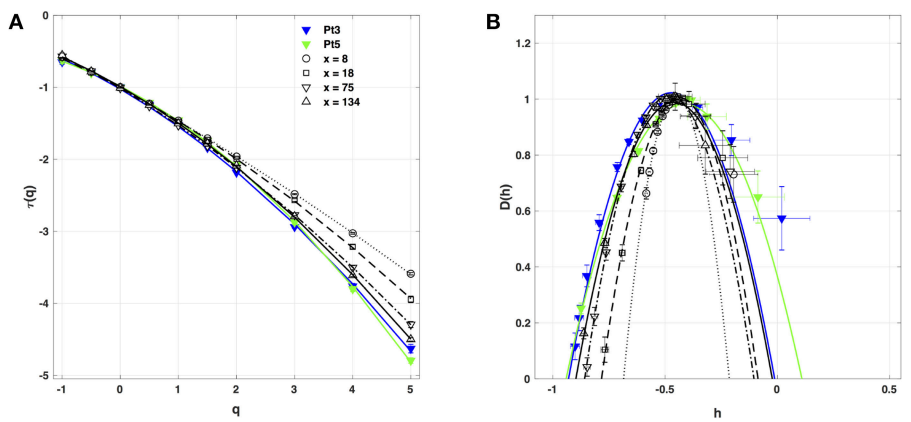

FIGURE 5 | Multifractal spectra of local impulse energy time-series $E(x,t)$ generated with our model defined in Equations (6)–(8) with the set of parameter values defined in Simul #2 (**Table 1**), $L = 150$ (in $\delta x = 0.3$ mm units). **(A)** $\tau(q)$ vs. q estimated by linear regression fit of $\log_2 Z(q,a)$ vs. $\log_2 a$ (**Figure 4A**). **(B)** $D(h)$ vs. h obtained from linear regression fits of $h(q,a)$ (**Figure 4B**) and $D(q,a)$ (**Figure 4C**) vs. $\log_2 a$. The symbols have the same meaning as in **Figure 4**. The curves correspond to quadratic spectra Equations (23) and (24) with parameters $[c_0, c_1, c_2]$ reported in **Table 2** for time-series $E(x,t)$ computed at the spatial positions $x = 8$ (○), 18 (□), 75 (▽) and 134 (△) (in $\delta x = 0.3$ mm units). For comparison are reported the spectra previously obtained for the experimental time-series recorded at the electrodes Pt3 (blue ▼) and Pt5 (green ▼) in the left atrial posterior wall (Companion paper I Attuel et al., 2017).

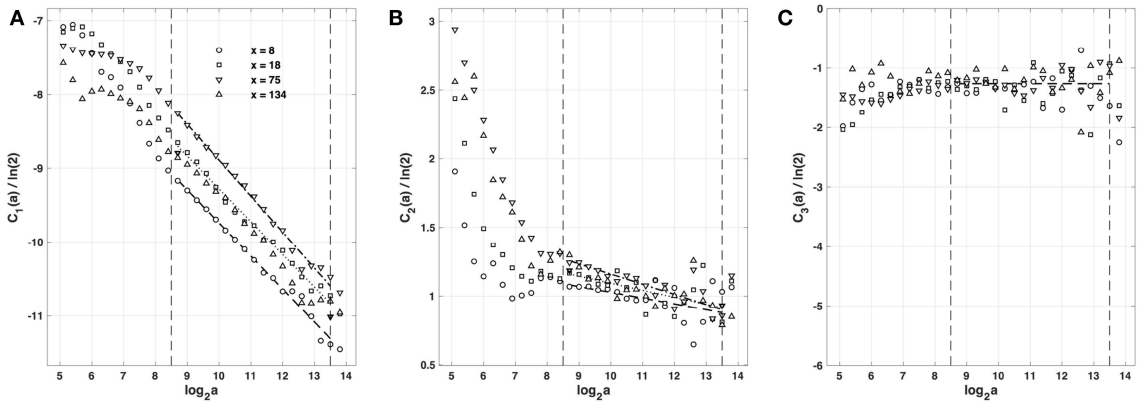

FIGURE 6 | Magnitude cumulant analysis of local impulse energy time-series $E(x, t)$ generated with our model defined in Equations (6)–(8) with the set of parameter values defined in Simul #2 (**Table 1**), $L = 150$ (in $\delta x = 0.3$ mm units). **(A)** $C_1(a)/\ln 2$ vs. $\log_2 a$. **(B)** $C_2(a)/\ln 2$ vs. $\log_2 a$. **(C)** $C_3(a)/\ln 2$ vs. $\log_2 a$. The computation of the $C_n(a)$ (Equation 21) was performed with the third-order analyzing wavelet $g^{(3)}$ (Equation 16). The vertical dashed lines delimit the range of scales ($2^{8.5} \leq a \leq 2^{13.5}$) used for the linear regression estimate of coefficients c_1^*, c_2^* and c_3^* of $\tau(q)$ (Equation 22) reported in **Table 1**. The symbols have the same meaning as in **Figures 4**, **5**.

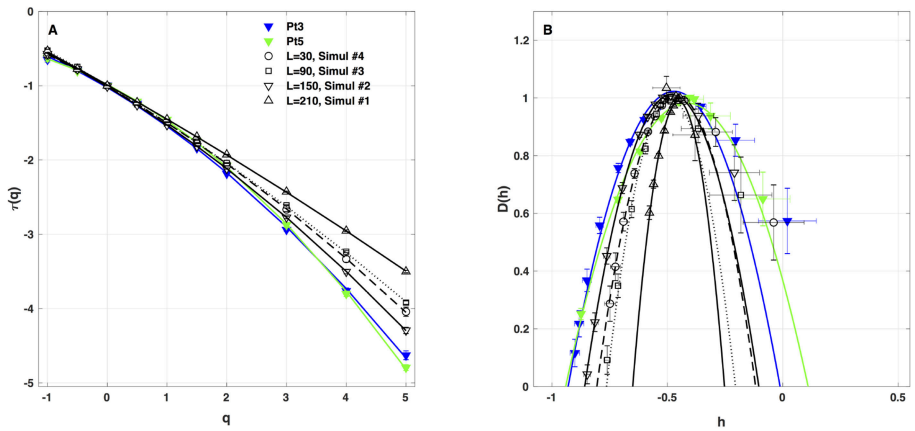

FIGURE 7 | Multifractal spectra of local impulse energy time-series $E(x, t)$ generated with our model defined in Equations (6)–(8) with the sets of parameter values defined in **Table 1**. **(A)** $\tau(q)$ vs. q. **(B)** $D(h)$ vs. h. These spectra were computed at the same relative spatial position $x = L/2$ for different lengths $L = 30$ (Simul #4, ○, ···), 90 (Simul #3, □, – – – – – –), 150 (Simul #2, ▽, ————), and 210 (Simul #1, △, ————) (in $\delta x = 0.3$ mm units). The curves correspond to quadratic spectra (Equations 23 and 24) with parameters $[c_0, c_1, c_2]$ reported in **Table 3**. For comparison are reported the spectra previously obtained from the experimental time-series recorded at the electrodes Pt3 (blue ▼) and Pt5 (green ▼) in the left atrial posterior wall (Companion paper I Attuel et al., 2017).

with the method of moments. This not only strengthens the multifractal diagnosis of the local impulse energy at low frequencies but it further confirms that farther from the source, larger the intermittency coefficient c_2, and closer to the experimental multifractal spectra obtained in the companion paper I (Attuel et al., 2017).

4.2. Robustness of the Multifractal Properties of Local Impulse Energy Under Model Parameter Changes

4.2.1. 1D Spatial System Length L

As a first test of the robustness of the computed multifractal properties of local impulse energy time series, we have performed additional simulations of our 1D PDE system (Equations 6–8) for the same parameter values as before but changing the total length (in $\delta x = 0.3$ mm units) of our cellular array $L = 210$ (Simul #1), 150 (Simul #2), 90 (Simul #3) and 30 (Simul #4). As shown in **Figure 7** and **Table 3**, when using both the methods

TABLE 3 | Results of the WTMM multifractal analysis of local impulse energy time-series $E(x = L/2, t)$ numerically simulated with our model defined in Equations (6)–(8) with the set of parameter values defined in **Table 1** for different lengths: $L = 30$ (Simul #4), $L = 90$ (Simul #3), $L = 150$ (Simul #2), and $L = 210$ (Simul #1) (in $\delta x = 0.3$ mm units).

	$L = 30$	$L = 90$	$L = 150$	$L = 210$
c_0	1.004 ± 0.001	1.003 ± 0.000	1.013 ± 0.000	0.994 ± 0.001
c_1	−0.506 ± 0.003	−0.476 ± 0.002	−0.481 ± 0.002	−0.452 ± 0.003
c_1^*	−0.504 ± 0.003	−0.481 ± 0.004	−0.486 ± 0.008	−0.453 ± 0.008
c_2	0.012 ± 0.005	0.068 ± 0.004	0.070 ± 0.003	0.088 ± 0.005
c_2^*	0.024 ± 0.009	0.051 ± 0.012	0.074 ± 0.011	0.075 ± 0.009

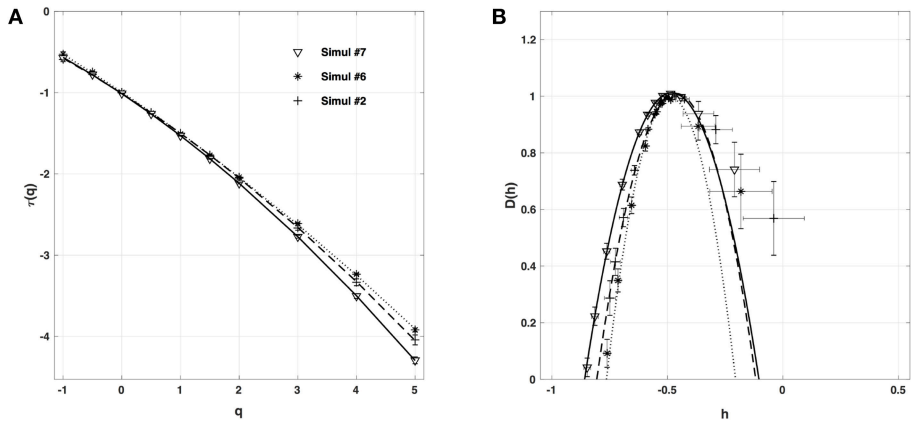

FIGURE 8 | Multifractal spectra of local impulse energy time-series $E(x, t)$ generated with our model defined in Equations (6)–(8) with the sets of parameter values defined in Simul #6 (**Table 1**) and $L = 150$ (in $\delta x = 0.3$ mm units). **(A)** $\tau(q)$ vs. q. **(B)** $D(h)$ vs. h. The spectra were computed at the same relative spatial position $x = L/2 = 75$ for different conductivities of the fiber: Simul #2 ($\triangledown$, ———), Simul #6 ($+$, – – – – –) and Simul #7 ($*$, $\cdots$). The curves correspond to quadratic spectra (Equations 23 and 24) with parameters $[c_0, c_1, c_2]$ reported in **Table 4**.

TABLE 4 | Results of the WTMM multifractal analysis of local impulse energy time-series $E(x = L/2, t)$ numerically simulated with our model defined in Equations (6)–(8) for different values of the conductivity parameter κ defined in Simul #2, Simul #6 and Simul #7 (**Table 1**), $L = 150$ (in $\delta x = 0.3$ mm units).

	$\kappa = 0.01$ mm.Ω^{-1}	$\kappa = 0.04$ mm.Ω^{-1}	$\kappa = 0.08$ mm.Ω^{-1}
c_0	1.013 ± 0.001	1.010 ± 0.001	0.994 ± 0.001
c_1	−0.481 ± 0.003	−0.462 ± 0.004	−0.484 ± 0.005
c_1^*	−0.486 ± 0.008	−0.468 ± 0.010	−0.509 ± 0.009
c_2	0.070 ± 0.003	0.059 ± 0.07	0.039 ± 0.009
c_2^*	0.074 ± 0.011	0.058 ± 0.013	0.022 ± 0.016

of moments and of magnitude cumulants to compute the $\tau(q)$ and $D(h)$ spectra of $E(x = L/2, t)$ at the midpoint of the array, we recover qualitatively similar multifractal spectra with $c_0 = D_F = 1$, $c_1 \sim 0.45$–0.50 and an intermittency coefficient c_2 that increases when increasing L. This is nothing but a confirmation that $E(x, t)$ becomes more and more intermittent when moving the spatial position $X = L/2$ away from the periodically beating source at $x = 0$. For 1D arrays as small as $L = 30$, $c_2 \sim 0.015$ corresponding to a very narrow $D(h)$ spectrum (**Figure 7B**). When increasing L, this $D(h)$ spectrum widens progressively to become comparable to the ones obtained experimentally ($c_2 \sim 0.1$) in **Table 1** of the companion paper I (Attuel et al., 2017) for the electrodes Pt3 and Pt5 located in the left atrial posterior wall.

4.2.2. Fiber Conductivity κ

When changing the fiber conductivity parameter κ that accounts for the diffusive coupling of the cells in our 1D cell array (Equation 6a), not much modification of the $\tau(q)$ and $D(h)$ spectra is observed (**Figure 8**). Some weak narrowing of $D(h)$ is obtained when increasing κ corresponding to a small but systematic decrease of the intermittency coefficient from $c_2 \sim 0.07$ for $\kappa = 0.01$ mm.Ω^{-1} to $c_2 \sim 0.04$ for $\kappa = 0.08$ mm.Ω^{-1} (**Table 4**). This is an indication that when strengthening the inter-cell conduction coupling, keeping all the other model parameters fixed, one somehow reduces the multifractal (intermittent) desynchronization of our 1D excitable cell network.

4.2.3. New Set of Parameters

We have also reproduced the one-point multifractal analysis reported in section 4.1.1 (Simul #2) to local impulse energy numerical time-series generated with the parameter set defined in Simul #5 (**Table 1**) and the same 1D system spatial size $L = 150$ (in $\delta x = 0.3$ mm units). Many parameters were changed, including κ, μ, ν_0, ν_1, γ^2, α^2 and ω^2 (**Table 1**). As shown in **Figure 9**, the $\tau(q)$ and $D(h)$ spectra obtained at different spatial positions $x = 8, 18, 75$, and 134 are quite similar to the ones previously obtained in **Figure 5**. They are robustly approximated by quadratic spectra (Equations 23 and 24, respectively) with comparable c_0, c_1, and c_2 parameter values (**Table 5**).

4.3. Two-Point Magnitude Analysis of Local Impulse Energy Data

The results of the two-point magnitude correlation analysis of the local impulse energy time series numerically generated with our 1D PDE system (Equations 6–8) with the set of parameter values defined in Simul #2 are shown in **Figure 10**. $C(a, \Delta t)/C(a, 0)$ (Equation 25) computed with the third-order analyzing wavelet $g^{(3)}$ (Equation 16) is represented vs. $\ln(\Delta t)$ for two scales $a = 2^9$ and 2^{10} in the scaling range. Strikingly, for the four numerical time-series corresponding to different spatial positions $x = 8$ (**Figure 10A**), 18 (**Figure 10B**), 75 (**Figure 10C**), and 134 (**Figure 10D**), for time-lag $\Delta t \gtrsim a$, $C(a, \Delta)/C(a, 0)$ drops to zero as a clear indication that the magnitudes are uncorrelated. As a reference, we put in each panel in **Figure 10**, a dashed straight line of slope $-c_2$ as predicted by Equation (26) for multifractal signals exhibiting a cascading multiplicative structure along a time-scale tree (Arneodo et al., 1998a,b). The slow decay predicted by the "multiplicative" log-normal model with intermittency coefficient c_2 is definitely

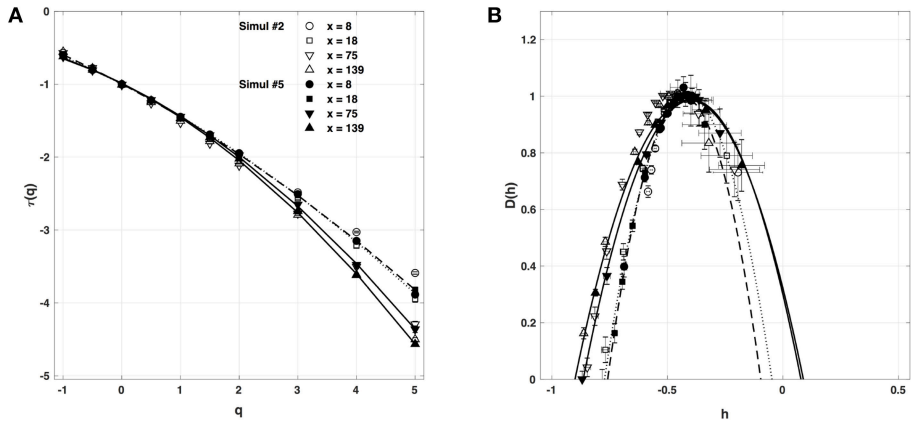

FIGURE 9 | Multifractal spectra of local impulse energy time-series $E(x,t)$ generated with our model defined in Equations (6)–(8) with the set of parameter values defined in Simul #5 (**Table 1**) and $L = 150$ (in $\delta x = 0.3$ mm units). **(A)** $\tau(q)$ vs. q. **(B)** $D(h)$ vs. h. The spectra were computed with the WTMM method with the third-order analyzing wavelet $g^{(3)}$ (Equation 16). The symbols correspond to the spatial positions $x = 8$ (●, ⋯), 18 (■, – – – – –), 75 (▼, ————), and 139 (▲, ————) (in $\delta x = 0.3$ mm units). The curves correspond to quadratic spectra (Equations 23 and 24) with parameters $[c_0, c_1, c_2]$ reported in **Table 5**. For comparison are reported in open symbols (○, □, ▽ △), the corresponding spectra previously obtained with the set of parameter values defined in Simul #2 (**Table 1**) and $L = 150$ in **Figure 5**.

TABLE 5 | Results of the WTMM multifractal analysis of local impulse energy time-series $E(x,t)$ numerically simulated with our model defined in Equations (6)–(8) with the parameters defined in Simul #6 (**Table 1**), $L = 150$ (in $\delta x = 0.3$ mm units).

	$x = 8$	$x = 18$	$x = 75$	$x = 134$
c_0	0.996 ± 0.001	0.994 ± 0.001	0.986 ± 0.002	0.986 ± 0.002
c_1	−0.410 ± 0.006	−0.427 ± 0.002	−0.393 ± 0.008	−0.406 ± 0.009
c_1^*	−0.412 ± 0.006	−0.422 ± 0.007	−0.406 ± 0.003	−0.425 ± 0.005
c_2	0.066 ± 0.011	0.055 ± 0.004	0.112 ± 0.016	0.124 ± 0.017
c_2^*	0.056 ± 0.011	0.046 ± 0.010	0.067 ± 0.010	0.070 ± 0.008

not observed. Thus, the numerical local impulse energy time series look much more like what has been called log-normal multifractal random noise in pioneering works to distinguish "uncorrelated" and "multiplicative" log-normal models (Arneodo et al., 1998a). Importantly, a similar absence of magnitude correlation was observed with the experimental time-series recorded at the electrodes located in the left atrial posterior wall in our companion paper I (Attuel et al., 2017). This is a strong evidence that our cardiac excitable cell network model indeed accounts for both one-point and two-point statistics of local impulse energy time-series during AF.

5. CONCLUSIONS

To summarize, we proposed a model of cardiac excitable cell network which accounts for the transport of AP along and across myocardial cells via the spatio-temporal interplay of voltage-gated and gap junction channels kinetics. We demonstrated that this model robustly reproduces the multifractal intermittent nature of the cardiac impulse energy experimentally recorded in the left atrial posterior wall area over times ($\gtrsim 0.5$ s) longer that the mean interbeat ($\simeq 10^{-1}$ s) during AF (companion paper I, Attuel et al., 2017). In particular, this model gives full account of the experimental observation of the absence of a multiplicative time-scale structure underlying multifractal scaling. To our knowledge, our combined experimental and numerical studies are the first to report the observation, quantification and modeling of such multifractal dynamics which is found more complex than previously suspected. Preliminary exploration of the model bifurcation diagram suggests that it shares with other models a good reproducibility of the spectrum of rhythmic and AP disorders, such as early after depolarizations (EADs) or salvos of premature beats, found experimentally prior to the onset of AF. This stems here from the membrane current imbalance between depolarization and repolarization, originating in the capacitive currents building up at the GJs. In the model, the nonlinearity of the GJC temporal response was proposed to be due to a nonlinear coupling of the local electric field with the GJC charging during AP propagation. However, the nature of our studies was exploratory, with a data set limited to a few patients, and although it was performed on time-series rather long for clinical practice (422 s), they were not so long regarding the range of time scales [0.6, 10 s] where scaling was observed. The relevance of our modeling would definitely benefit of the analysis of new data over a large set of patients at different stages of AF development and to be explored in different areas of the atria. Recording electric potential time series during AF concomitantly to non intrusive Cardiovascular Magnetic Resonance (CMR) imaging could help further the assessment of atrial remodeling features such as increased expression of intercellular gap junction and conduction velocity shortening, in addition to sinus node dysfunction. Even more instructive, the comparative analysis of different types of rhythms as atrial flutter, AV junctional rhythm and various other annotated rhythms (Gadhoumi et al., 2018) would allow us to evaluate the practicality of multifractal cardiac impulse energy in the discrimination of AF from other rhythms. Also, by combining our wavelet-based multifractal analysis (low frequency) to a more classical dynamical system

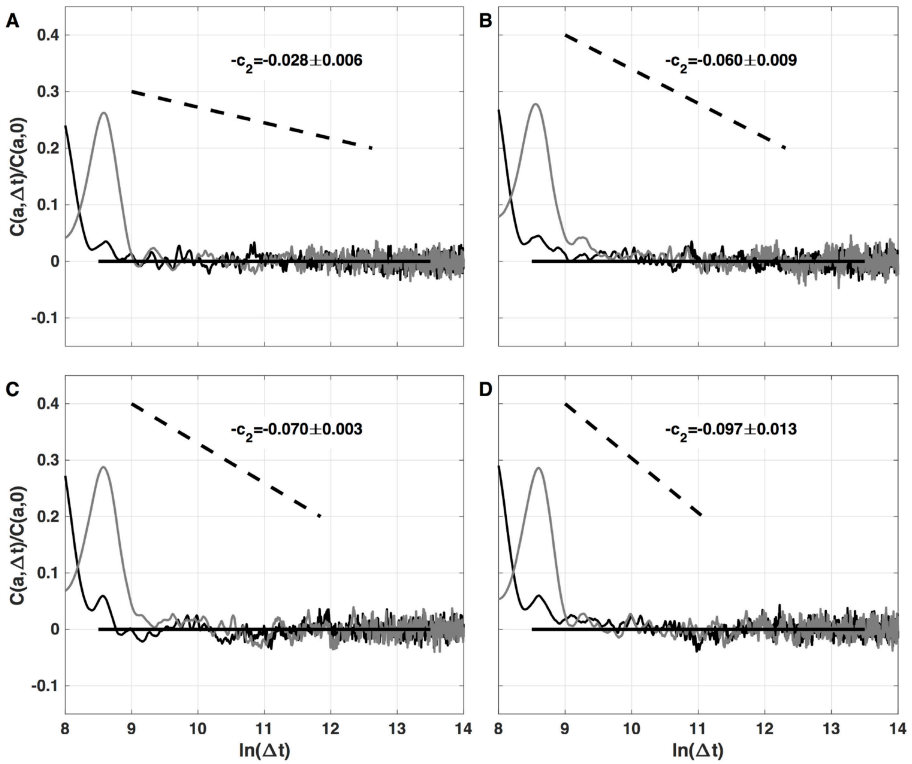

FIGURE 10 | Two-point magnitude analysis of local impulse energy time-series $E(x, t)$ generated with our model defined in Equations (6)–(8) with the sets of parameter values defined in Simul #2 (**Table 1**), $L = 150$ (in $\delta x = 0.3$ mm units). Two-point correlation function $C(a, \Delta t)/C(a, 0)$ vs. $\ln(\Delta t)$ (Equation 25) computed with the third-order analyzing wavelet $g^{(3)}$ (Equation 16). The two curves correspond to scales $a = 2^9$ (black) and 2^{10} (gray) within the scaling range. The different panels correspond to different spatial positions $x = 8$ **(A)**, 18 **(B)**, 75 **(C)**, and 134 **(D)** (in $\delta x = 0.3$ mm units).

analysis including bifurcation diagrams, Lyapunov exponent computations, we should be in position to improve and refine our physiological heart tissue modeling and to open new perspectives toward the understanding of mechanisms of AF perpetuation.

AUTHOR CONTRIBUTIONS

GA, FA, HY, and AA: conception and design; GA, FA, and AA: development and methodology; GA, EG-C, FA, and AA: analysis and interpretation of data; GA, EG-C, FA, HY, and AA: writing, review, and/or revision of the manuscript; GA, EG-C, and FA: administrative, technical or material support (i.e., requiring and organizing data, constructing databases).

FUNDING

This work was partially supported by Contrat Conseil Région Aquitaine CAVERNOM Cardiac Arrhythmia Complexity and Variability by means of Robust Nonlinear Methods (Grant N° 2014-1R60212-00003295), by the President of Russian for the young scientists (Grant N° 14.W01.17.2674-MK), and by the Metchnikov Program (EG-C visit to LOMA).

ACKNOWLEDGMENTS

The data used in this study have been provided by IHU Liryc, Hôpital Xavier Arnozan, Avenue du Haut Lévêque, 33604 Pessac cedex.

REFERENCES

Allessie, M. A., Bonke, F. I., and Schopman, F. J. (1977). Circus movement in rabbit atrial muscle as a mechanism of tachycardia. *Circ. Res.* 41, 9–18. doi: 10.1161/01.RES.41.1.9

Armstrong, C. M. (2003). The Na/K pump, Cl ion, and osmotic stabilization of cells. *Proc. Natl. Acad. Sci. U.S.A.* 100, 6257–6262. doi: 10.1073/pnas.0931278100

Arneodo, A., Audit, B., Decoster, N., Muzy, J.-F., and Vaillant, C. (2002). "A wavelet based multifractal formalism: application to DNA sequences, satellite images of the cloud structure and stock market data," in *The Science of Disasters: Climate Disruptions, Heart Attacks, and Market Crashes*, eds A. Bunde, J. Kropp, and H. J. Schellnhuber (Berlin: Springer Verlag), 26–102.

Arneodo, A., Audit, B., Kestener, P., and Roux, S. G. (2008). Wavelet-based multifractal analysis. *Scholarpedia* 3:4103. doi: 10.4249/scholarpedia.4103

Arneodo, A., Bacry, E., Jaffard, S., and Muzy, J.-F. (1997). Oscillating singularities on Cantor sets: a grand-canonical multifractal formalism. *J. Stat. Phys.* 87, 179–209. doi: 10.1007/BF02181485

Arneodo, A., Bacry, E., Manneville, S., and Muzy, J.-F. (1998a). Analysis of random cascades using space-scale correlation functions. *Phys. Rev. Lett.* 80, 708–711. doi: 10.1103/PhysRevLett.80.708

Arneodo, A., Bacry, E., and Muzy, J.-F. (1995a). Oscillating singularities in locally self-similar functions. *Phys. Rev. Lett.* 74, 4823–4826. doi: 10.1103/PhysRevLett.74.4823

Arneodo, A., Bacry, E., and Muzy, J.-F. (1995b). The thermodynamics of fractals revisited with wavelets. *Physica A* 213, 232–275. doi: 10.1016/0378-4371(94)00163-N

Arneodo, A., Bacry, E., and Muzy, J.-F. (1998b). Random cascades on wavelet dyadic trees. *J. Math. Phys.* 39, 4142–4164. doi: 10.1063/1.532489

Arneodo, A., Grasseau, G., and Holschneider, M. (1988). Wavelet transform of multifractals. *Phys. Rev. Lett.* 61, 2281–2284. doi: 10.1103/PhysRevLett.61.2281

Arneodo, A., Grasseau, G., and Kostelich, E. J. (1987). Fractal dimensions and $f(\alpha)$ spectrum of the Hénon attractor. *Phys. Lett. A* 124, 426–432. doi: 10.1016/0375-9601(87)90546-9

Arneodo, A., Manneville, S., and Muzy, J.-F. (1998c). Towards log-normal statistics in high Reynolds number turbulence. *Eur. Phys. J. B* 1, 129–140. doi: 10.1007/s100510050162

Arneodo, A., Manneville, S., Muzy, J.-F., and Roux, S. G. (1999). Revealing a lognormal cascading process in turbulent velocity statistics with wavelet analysis. *Philos. Trans. R. S. London Ser. A* 357, 2415–2438. doi: 10.1098/rsta.1999.0440

Arneodo, A., Muzy, J.-F., and Sornette, D. (1998d). "Direct" causal cascade in the stock market. *Eur. Phys. J. B* 2, 277–282. doi: 10.1007/s100510050250

Arneodo, A., Vaillant, C., Audit, B., Argoul, F., d'Aubenton-Carafa, Y., and Thermes, C. (2011). Multi-scale coding of genomic information: from DNA sequence to genome structure and function. *Phys. Rep.* 498, 45–188. doi: 10.1016/j.physrep.2010.10.001

Attuel, G., Gerasimova-Chechkina, E., Argoul, F., Yahia, H., and Arneodo, A. (2017). Multifractal desynchronization of the cardiac excitable cell network during atrial fibrillation. I. Multifractal analysis of clinical data. *Front. Physiol.* 8:01139. doi: 10.3389/fphys.2017.01139

Attuel, G., Pont, O., Xu, B., and Yahia, H. (2016). "Sudden cardiac death and turbulence," in *The Foundations of Chaos Revisited: From Poincaré to Recent Advancements*, ed C. Skiadas (Switzerland: Springer), 235–248.

Attuel, P., Pellerin, D., and Gaston, J. (1989). "Latent atrial vulnerability: new means of electrophysiologic investigations in paroxysmal atrial arrhythmias," in *The Atrium in Health and Disease*, eds P. Attuel, P. Coumel, and M. Janse (Mont Kisco, NY: Mount KiscoFutura Publishing Co., Inc), 159–200.

Audit, B., Bacry, E., Muzy, J.-F., and Arneodo, A. (2002). Wavelet-based estimators of scaling behavior. *IEEE Trans. Info. Theory* 48, 2938–2954. doi: 10.1109/TIT.2002.802631

Audit, B., Baker, A., Chen, C.-L., Rappailles, A., Guilbaud, G., Julienne, H., et al. (2013). Multiscale analysis of genome-wide replication timing profiles using a wavelet-based signal-processing algorithm. *Nat. Protoc.* 8, 98–110. doi: 10.1038/nprot.2012.145

Ausma, J., van der Velden, H. M. W., Lenders, M.-H., van Ankeren, E. P., Jongsma, H. J., Ramaekers, F. C. S., et al. (2003). Reverse structural and gap-junctional remodeling after prolonged atrial fibrillation in the goat. *Circulation* 107, 2051–2058. doi: 10.1161/01.CIR.0000062689.04037.3F

Bacry, E., Muzy, J.-F., and Arneodo, A. (1993). Singularity spectrum of fractal signals from wavelet analysis: exact results. *J. Stat. Phys.* 70, 635–674. doi: 10.1007/BF01053588

Baier, G., and Müller, M. (2004). Excitable chaos in diffusively coupled FitzHugh-Nagumo equations. *Rev. Mex. Fis.* 50, 422–426.

Bär, M., and Brusch, L. (2004). Breakup of spiral waves caused by radial dynamics: eckhaus and finite wavenumber instabilities. *New J. Phys.* 6:5. doi: 10.1088/1367-2630/6/1/005

Bär, M., and Eiswirth, M. (1993). Turbulence due to spiral breakup in a continuous excitable medium. *Phys. Rev. E* 48:R1635. doi: 10.1103/PhysRevE.48.R1635

Beeler, G. W., and Reuter, H. (1977). Reconstruction of the action potential of ventricular myocardial fibres. *J. Physiol.* 268, 177–210. doi: 10.1113/jphysiol.1977.sp011853

Beuter, A., Glass, L., Mackey, M. C., and Titcombe, M. S. (2003). *Nonlinear Dynamics in Physiology and Medicine*. New York, NY: Springer Science+Business Media.

Bikou, O., Thomas, D., Trappe, K., Lugenbiel, P., Kelemen, K., Koch, M., et al. (2011). Connexin 43 gene therapy prevents persistent atrial fibrillation in a porcine model. *Cardiovasc. Res.* 92, 218–225. doi: 10.1093/cvr/cvr209

Bohr, T., and Tél, T. (1988). "The thermodynamics of fractals," in *Directions in Chaos*, Vol. 2, ed B.-L. Hao (Singapore: World Scientific Publishing Co), 194–237.

Bub, G., Shrier, A., and Glass, L. (2005). Global organization of dynamics in oscillatory heterogeneous excitable media. *Phys. Rev. Lett.* 94:028105. doi: 10.1103/PhysRevLett.94.028105

Bukauskas, F. F., and Verselis, V. K. (2004). Gap junction channel gating. *Biochim. Biophys. Acta* 1662, 42–60. doi: 10.1016/j.bbamem.2004.01.008

Burt, J. M., and Sray, D. C. (1988). Single-channel events and gating behavior of the cardiac gap junction channel. *Proc. Natl. Acad. Sci. U.S.A.* 85, 3431–3434. doi: 10.1073/pnas.85.10.3431

Chialvo, D. R., Gilmour, R. J., and Jalife, J. (1990). Low dimensional chaos in cardiac tissue. *Nature* 343, 653–657. doi: 10.1038/343653a0

Chudácek, V., Andén, J., Mallat, S., Abry, P., and Doret, M. (2014). Scattering transform for intrapartum fetal heart rate variability fractal analysis: a case-control study. *IEEE Trans. Biomed. Eng.* 61, 1100–1108. doi: 10.1109/TBME.2013.2294324

Ciuciu, P., Varoquaux, G., Abry, P., Sadaghiani, S., and Kleinschmidt, A. (2012). Scale-free and multifractal time dynamics of fMRI signals during rest and task. *Front. Physiol.* 3:186. doi: 10.3389/fphys.2012.00186

Cole, W. C., Picone, J. B., and Sperelakis, N. (1988). Gap junction uncoupling and discontinuous propagation in the heart. *Biophys. J.* 53, 809–818. doi: 10.1016/S0006-3495(88)83160-6

Courtemanche, M., Glass, L., and Keener, J. P. (1993). Instabilities of a propagating pulse in a ring of excitable media. *Phys. Rev. Lett.* 70, 2182–2185. doi: 10.1103/PhysRevLett.70.2182

Cox, J. L., Schuessler, R. B., D'Agostino, H. J. J., Stone, C. M., Chang, B. C., Cain, M. E., et al. (1991). The surgical treatment of atrial fibrillation. III. Development of a definitive surgical procedure. *J. Thorac. Cardiovasc. Surg.* 101, 569–583.

Danik, S. B., Liu, F., Zhang, J., Suk, H. J., Morley, G. E., Fishman, G. I., et al. (2004). Modulation of cardiac gap junction expression and arrhythmic susceptibility. *Circ. Res.* 95, 1035–1041. doi: 10.1161/01.RES.0000148664.33695.2a

Daubechies, I. (1992). *Ten Lectures on Wavelets*. CBMS-NSF Reg. Conf. Ser. Appl. Math. Vol 61. Philadelphia, PA: SIAM.

de la Casa, M. A., de la Rubia, F. J., and Ivanov, P. C. (2007a). Patterns of phase-dependent spiral wave attenuation in excitable media. *Phys. Rev. E* 75:051923. doi: 10.1103/PhysRevE.75.051923

de la Casa, M. A., de la Rubia, F. J., and Ivanov, P. C. (2007b). Patterns of spiral wave attenuation by low-frequency periodic planar fronts. *Chaos* 17:015109. doi: 10.1063/1.2404640

Delour, J., Muzy, J.-F., and Arneodo, A. (2001). Intermittency of 1D velocity spatial profiles in turbulence: a magnitude cumulant analysis. *Eur. Phys. J. B* 23, 243–248. doi: 10.1007/s100510170074

Desplantez, T., Dupont, E., Severs, N. J., and Weingart, R. (2007). Gap junction channels and cardiac impulse propagation. *J. Membr. Biol.* 218, 13–28. doi: 10.1007/s00232-007-9046-8

Diaz, P. J., Rudy, Y., and Plonsey, R. (1983). Intercalated discs as a cause for discontinuous propagation in cardiac muscle: a theoretical simulation. *Ann. Biomed. Eng.* 11, 177–189. doi: 10.1007/BF02363285

Dupont, E., Matsushita, T., Kaba, R. A., Vozzi, C., Coppen, S. R., Khan, N., et al. (2001). Altered connexin expression in human congestive heart failure. *J. Mol. Cell. Cardiol.* 33, 353–371. doi: 10.1006/jmcc.2000.1308

Evans, W. H., and Martin, P. E. M. (2002). Gap junctions: structure and function (review). *Mol. Membr. Biol.* 19, 121–136. doi: 10.1080/09687680210139839

Fenton, F. H., and Cherry, E. M. (2008). Models of cardiac cell. *Scholarpedia* 3:1868. doi: 10.4249/scholarpedia.1868

Fenton, F. H., Cherry, E. M., Hasting, H. M., and Evans, S. J. (2002). Multiple mechanisms of spiral wave breakup in a model of cardiac electrical activity. *Chaos* 12, 852–892. doi: 10.1063/1.1504242

Fenton, F. H., and Karma, A. (1998). Vortex dynamics in three-dimensional continuous myocardium with fiber rotation: filament instability and fibrillation. *Chaos* 8, 20–47. doi: 10.1063/1.166311

FitzHugh, R. (1962). *Mathematical Models of Excitation and Propagation in Nerve*. New York, NY: McGraw-Hill, Biological Engineering.

Gadhoumi, K., Do, D., Badilini, F., Pelter, M. M., and Hu, X. (2018). Wavelet leader multifractal analysis of heart rate variability in atrial fibrillation. *J. Electrocardiol.* 51, S83–S87 doi: 10.1016/j.jelectrocard.2018.08.030

Ganesan, A. N., Shipp, N. J., Brooks, A. G., Kuklik, P., Lau, D. H., Lim, H. S., et al. (2013). Long-term outcomes of catheter ablation of atrial fibrillation: a systematic review and meta-analysis. *J. Am. Heart Assoc.* 2:e004549. doi: 10.1161/JAHA.112.004549

Garfinkel, A., Chen, P.-S., Walter, D. O., Karagueuzian, H. S., Kogan, B., Evans, S. J., et al. (1997). Quasiperiodicity and chaos in cardiac fibrillation. *J. Clin. Invest.* 99, 305–314. doi: 10.1172/JCI119159

Gerasimova, E., Audit, B., Roux, S. G., Khalil, A., Gileva, O., Argoul, F., et al. (2014). Wavelet-based multifractal analysis of dynamic infrared thermograms to assist in early breast cancer diagnosis. *Front. Physiol.* 5:176. doi: 10.3389/fphys.2014.00176

Gerasimova-Chechkina, E., Toner, B., Marin, Z., Audit, B., Roux, S. G., Argoul, F., et al. (2016). Comparative multifractal analysis of dynamic infrared thermograms and X-ray mammograms enlightens changes in the environment of malignant tumors. *Front. Physiol.* 7:336. doi: 10.3389/fphys.2016.00336

Gerhardt, M., Schuster, M., and Tyson, J. J. (1990). A cellular automaton model of excitable media including curvature and dispersion. *Science* 247, 1563–1566. doi: 10.1126/science.2321017

Glass, L., and Mackey, M. C. (1979). A simple model for phase locking of biological oscillations. *J. Math. Biol.* 6, 207–223. doi: 10.1007/BF02547797

Glass, L., and Mackey, M. C. (1987). *From Clocks to Chaos: The Rhythms of Life*. Princeton, NJ: Princeton University Press.

Goldberger, A. L., Amaral, L. A. N., Hausdorff, J. M., Ivanov, P. C., Peng, C.-K., and Stanley, H. E. (2002). Fractal dynamics in physiology: alterations with disease and aging. *Proc. Natl. Acad. Sci. U.S.A.* 99, 2466–2472. doi: 10.1073/pnas.012579499

Gollob, M. H., Jones, D. L., Krahn, A. D., Danis, L., Gong, X.-Q., Shao, Q., et al. (2006). Somatic mutations in the connexin 40 gene (gja5) in atrial fibrillation. *N. Eng. J. Med.* 354, 2677–2688. doi: 10.1056/NEJMoa052800

Gray, R. A., Jalife, J., Panfilov, A. V., Baxter, W. T., Cabo, C., Davidenko, J. M., et al. (1995). Mechanisms of cardiac fibrillation. *Science* 270, 1222–1225. doi: 10.1126/science.270.5239.1222

Grossmann, A., and Morlet, J. (1984). Decomposition of Hardy functions into square integrable wavelets of constant shape. *SIAM J. Math. Anal.* 15, 723–736. doi: 10.1137/0515056

Guckenheimer, J., and Kuehn, C. (2009). Homoclinic orbits of the Fitzhugh Nagumo equation: the singular-limit. *Discrete Contin. Dyn. Syst.* 2, 851–872. doi: 10.3934/dcdss.2009.2.851

Guevara, M. R., and Glass, L. (1982). Phase locking, period-doubling bifurcations, and chaos in a mathematical model of a periodically driven oscillator: a theory for the entrainement of biological oscillators and the generation of cardiac dysrhythmias. *J. Math. Biol.* 14, 1–23. doi: 10.1007/BF02154750

Guevara, M. R., Glass, L., and Shrier, A. (1981). Phase locking, period-doubling bifurcations, and irregular dynamics in periodically stimulated cardiac cells. *Science* 214, 1350–1353. doi: 10.1126/science.7313693

Haïssaguerre, M., Jaïs, P., Shah, D. C., Takahashi, A., Hocini, M., Quiniou, G., et al. (1998). Spontaneous initiation of atrial fibrillation by ectopic beats originating in the pulmonary veins. *N. Engl. J. Med.* 339, 659–666. doi: 10.1056/NEJM199809033391003

Hand, P. E., and Griffith, B. E. (2010). Adaptive multiscale model for simulating cardiac conduction. *Proc. Natl. Acad. Sci. U.S.A.* 107, 14603–14608. doi: 10.1073/pnas.1008443107

Hand, P. E., and Peskin, C. S. (2010). Homogenization of an electrophysiological model for a strand of cardiac myocytes with gap-junctional and electric-field coupling. *Bull. Math. Biol.* 72, 1408–1424. doi: 10.1007/s11538-009-9499-2

Harris, A. L. (2001). Emerging issues of connexin channels: biophysics fills the gap. *Q. Rev. Biophys.* 34, 325–472. doi: 10.1017/S0033583501003705

Hille, B. (2001). *Ion Channels of Excitable Membranes, 3rd Edn.* Sunderland: Sinauer Associates, Inc.

Ho, S. Y., Cabrera, J. A., and Sanchez-Quintana, D. (20012). Left atrial anatomy revisited. *Circ. Arrhythm. Electrophysiol.* 5, 220–228. doi: 10.1161/CIRCEP.111.962720

Hodgkin, A. L., and Huxley, A. F. (1952a). Currents carried by sodium and potassium ions through the membrane of the giant axon of Loligo. *J. Physiol.* 116, 449–472. doi: 10.1113/jphysiol.1952.sp004717

Hodgkin, A. L., and Huxley, A. F. (1952b). A quantitative description of membrane current and its application to conduction and excitation in nerve. *J. Physiol.* 117, 500–544. doi: 10.1113/jphysiol.1952.sp004764

Igarashi, T., Finet, J. E., Takeuchi, A., Fujino, Y., Strom, M., Greener, I. D., et al. (2012). Connexin gene transfer preserves conduction velocity and prevents atrial fibrillation. *Circulation* 125, 216–225. doi: 10.1161/CIRCULATIONAHA.111.053272

Ito, H., and Glass, L. (1991). Spiral breakup in a new model of discrete excitable media. *Phys. Rev. Lett.* 66, 671–674. doi: 10.1103/PhysRevLett.66.671

Ivanov, P. C., Amaral, L. A. N., Goldberger, A. L., Havlin, S., Rosenblum, M. G., Stanley, H. E., et al. (2001). From 1/f noise to multifractal cascades in heartbeat dynamics. *Chaos* 11, 641–652. doi: 10.1063/1.1395631

Ivanov, P. C., Amaral, L. A. N., Goldberger, A. L., Havlin, S., Rosenblum, M. G., Struzik, Z. R., et al. (1999). Multifractality in human heartbeat dynamics. *Nature* 399, 461–465. doi: 10.1038/20924

Ivanov, P. C., Amaral, L. A. N., Goldberger, A. L., and Stanley, H. E. (1998). Stochastic feedback and the regulation of biological rhythms. *Europhys. Lett.* 43, 363–368. doi: 10.1209/epl/i1998-00366-3

Ivanov, P. C., Ma, Q. D. Y., Bartsch, R. P., Hausdorff, J. M., Nunes Amaral, L. A., Schulte-Frohlinde, V., et al. (2009). Levels of complexity in scale-invariant neural signals. *Phys. Rev. E* 79:041920. doi: 10.1103/PhysRevE.79.041920

Izhikevich, E. M. (2007). *Dynamical Systems in Neuroscience: The Geometry of Excitability and Bursting*. Cambridge: MIT Press.

Izhikevich, E. M., and FitzHugh, R. (2006). FitzHugh Nagumo model. *Scholarpedia* 1:1349. doi: 10.4249/scholarpedia.1349

Jaffard, S. (1989). Hölder exponents at given points and wavelet coefficients. *C. R. Acad. Sci. Paris Ser. I* 308, 79–81.

Jaffard, S. (1997a). Multifractal formalism for functions part I: results valid for all functions. *SIAM J. Math. Anal.* 28, 944–970. doi: 10.1137/S0036141095282991

Jaffard, S. (1997b). Multifractal formalism for functions part II: self-similar functions. *SIAM J. Math. Anal.* 28, 971–998. doi: 10.1137/S0036141095283005

Jaffard, S., Lashermes, B., and Abry, P. (2007). "Wavelet leaders in multifractal analysis," in *Wavelet Analysis and Applications*, eds T. Qian, M. I. Vai, and Y. Xu (Basel: Birkhäuser Basel), 201–246.

Jensen, J. H., Christiansen, P. L., and Scott, A. C. (1984). Chaos in the Beeler-Reuter system for the action potential of ventricular myocardial fibres. *Physica D* 13, 269–277. doi: 10.1016/0167-2789(84)90283-5

Joyner, R. W., Veenstra, R., Rawling, D., and Chorro, A. (1984). Propagation through electrically coupled cells. Effects of a resistive barrier. *Biophys. J.* 45, 1017–1025. doi: 10.1016/S0006-3495(84)84247-2

Karma, A. (1993). Spiral breakup in model equations of action potential propagation in cardiac tissue. *Phys. Rev. Lett.* 71, 1103–1106. doi: 10.1103/PhysRevLett.71.1103

Keener, J. P. (1990). The effects of gap junctions on propagation in myocardium: a modified cable theory. *Ann. N. Y. Acad. Sci.* 591, 257–277. doi: 10.1111/j.1749-6632.1990.tb15094.x

Kumar, N. M., and Gilula, N. B. (1996). The gap junction communication channel. *Cell* 84, 381–388. doi: 10.1016/S0092-8674(00)81282-9

Leonarduzzi, R. F., Schlotthauer, G., and Torres, M. E. (2010). "Wavelet leader based multifractal analysis of heart rate variability during myocardial ischaemia," in *Annual International Conference of the IEEE Engineering in Medicine and Biology* (Buenos Aires), 110–113.

Lin, J., and Keener, J. P. (2010). Ephaptic coupling in cardiac myocytes. *IEEE Trans. Biomed. Circuits Syst.* 60, 576–582.

Lin, J., and Keener, J. P. (2013). Modeling electrical activity of myocardial cells incorporating the effects of ephaptic coupling. *Proc. Natl. Acad. Sci. U.S.A.* 107, 20935–20940. doi: 10.1073/pnas.1010154107

Macfarlane, P. W., van Oosterom, A., Kligfield, P., Pahlm, O., Janse, M., and Camm, J. (eds.) (2011). *Comprehensive Electrocardiography*. London: Springer.

Mallat, S. (1998). *A Wavelet Tour of Signal Processing*. New York, NY: Academic Press.

Mallat, S., and Hwang, W. L. (1992). Singularity detection and processing with wavelets. *IEEE Trans. Inf. Theory* 38, 617–643. doi: 10.1109/18.119727

Meneveau, C., and Sreenivasan, K. (1991). The multifractal nature of turbulent energy dissipation. *J. Fluid Mech.* 224, 429–484. doi: 10.1017/S0022112091001830

Meyer, Y. (1992). *Wavelets and Operators*. Cambridge: Cambridge University Press.

Moe, G. K., and Abildskov, J. A. (1959). Atrial fibrillation as a self-sustaining arrhythmia independent of focal discharge. *Am. Heart J.* 58, 59–70. doi: 10.1016/0002-8703(59)90274-1

Moe, G. K., Rheinboldt, W. C., and Abildskov, J. A. (1964). A computer model of atrial fibrillation. *Am. Heart J.* 67, 200–220. doi: 10.1016/0002-8703(64)90371-0

Muzy, J.-F., Bacry, E., and Arneodo, A. (1991). Wavelets and multifractal formalism for singular signals: application to turbulence data. *Phys. Rev. Lett.* 67, 3515–3518. doi: 10.1103/PhysRevLett.67.3515

Muzy, J.-F., Bacry, E., and Arneodo, A. (1993). Multifractal formalism for fractal signals: the structure-function approach versus the wavelet-transform modulus-maxima methods. *Phys. Rev. E* 47, 875–884. doi: 10.1103/PhysRevE.47.875

Muzy, J.-F., Bacry, E., and Arneodo, A. (1994). The multifractal formalism revisited with wavelets. *Int. J. Bifurc. Chaos* 4, 245–302. doi: 10.1142/S0218127494000204

Muzy, J.-F., Sornette, D., Delour, J., and Arneodo, A. (2001). Multifractal returns and hierarchical portfolio theory. *Quant. Finance* 1, 131–148. doi: 10.1080/713665541

Nagumo, J., Arimoto, S., and Yoshizawa, S. (1962). An active pulse transmission line simulating nerve axon. *Proceedings of the IRE* 50, 2061–2070. doi: 10.1109/JRPROC.1962.288235

Nattel, S., and Harada, M. (2014). Atrial remodeling and atrial fibrillation: recent advances and translational perspectives. *J. Am. Coll. Cardiol.* 63, 2335–2345. doi: 10.1016/j.jacc.2014.02.555

Neyton, J., and Trautmann, A. (1986). Physiological modulation of gap junction permeability. *J. Exp. Biol.* 124, 93–114.

Nicolay, S., Brodie of Brodie, E. B., Touchon, M., Audit, B., d'Aubenton Carafa, Y., Thermes, C., et al. (2007). Bifractality of human DNA strand-asymmetry profiles results from transcription. *Phys. Rev. E* 75:032902. doi: 10.1103/PhysRevE.75.032902

Niebur, E. (2008). Neuronal cable theory. *Scholarpedia* 3:2674. doi: 10.4249/scholarpedia.2674

Noble, D. (1962). A modification of the Hodgkin-Huxley equations applicable to Purkinje fibre action and pacemaker potentials. *J. Physiol.* 160, 317–352. doi: 10.1113/jphysiol.1962.sp006849

Noble, D. (1965). Electrical properties of cardiac muscle attributable to inward-going (anomalous) rectification. *J. Cell Comp. Physiol.* 66, 127–136. doi: 10.1002/jcp.1030660520

Nolasco, J. B., and Dahlen, R. W. (1968). Graphic method for the study of alternation in cardiac action potential. *J. Appl. Physiol.* 5, 191–196. doi: 10.1152/jappl.1968.25.2.191

Nunes Amaral, L. A., Ivanov, P. C., Aoyagi, N., Hidaka, I., Tomono, S., Goldberger, A. L., et al. (2001). Behavioral-independent features of complex heartbeat dynamics. *Phys. Rev. Lett.* 86, 6026–6029. doi: 10.1103/PhysRevLett.86.6026

Panfilov, A., and Hogeweg, P. (1993). Spiral breakup in a modified FitzHugh-Nagumo model. *Phys. Lett. A* 176, 295–299. doi: 10.1016/0375-9601(93)90921-L

Perrachia, C. (2004). Chemical gating of gap junction channels Roles of calcium, pH and calmodulin. *Biochim. Biophys. Acta* 1662, 61–80. doi: 10.1016/j.bbamem.2003.10.020

Pertsov, A. M., Davidenko, J. M., Salomonsz, R., Baxter, W. T., and Jalife, J. (1993). Spiral waves of excitation underlie reentrant activity in isolated cardiac muscle. *Circ. Res.* 72, 631–650. doi: 10.1161/01.RES.72.3.631

Plonsey, R., and Barr, R. C. (2007). *Bioelectricity: A Quantitative Approach. 3rd Edn.* London: Springer.

Pumir, A., Arutunyan, A., Krinsky, V., and Sarvazyan, N. (2005). Genesis of ectopic waves: role of coupling, automaticity, and heterogeneity. *Biophys. J.* 89, 2332–2349. doi: 10.1529/biophysj.105.061820

Richard, C. D., Tanenbaum, A., Audit, B., Arneodo, A., Khalil, A., and Frankel, W. N. (2015). Swdreader: a wavelet-based algorithm using spectral phase to characterize spike-wave morphological variation in genetic models of absence epilepsy. *J. Neurosci. Methods* 242, 127–140. doi: 10.1016/j.jneumeth.2014.12.016

Roux, S. G., Venugopal, V., Fienberg, K., Arneodo, A., and Foufoula-Georgiou, E. (2009). Evidence for inherent nonlinearity in temporal rainfall. *Adv. Water Resourc.* 32, 41–48. doi: 10.1016/j.advwatres.2008.09.007

Severs, N. J. (1990). The cardiac gap junction and intercalated disc. *Int. J. Cardiol.* 26, 137–173. doi: 10.1016/0167-5273(90)90030-9

Severs, N. J., Bruce, A. F., Dupont, E., and Rothery, S. (2008). Remodelling of gap junctions and connexin expression in diseased myocardium. *Cardiovasc. Res.* 80, 9–19. doi: 10.1093/cvr/cvn133

Spach, M. S. (1983). The discontinuous nature of electrical propagation in cardiac muscle. *Ann. Biomed. Eng.* 2, 209–261. doi: 10.1007/BF02363287

Spray, D. C., White, R. L., Campos De Carvalho, A., Harris, A. L., and Bennet, M. V. L. (1984). Gating of gap junction channels. *Biophys. J.* 45, 219–230. doi: 10.1016/S0006-3495(84)84150-8

Swietach, P., Youm, J.-B., Saegusa, N., Leem, C.-H., Spitzer, K. W., and Vaughan-Jones, R. D. (2013). Coupled Ca^{2+}/H^{+} transport by cytoplasmic buffers regulates local Ca^{2+} and H^{+} ion signaling. *Proc. Natl. Acad. Sci. U.S.A.*, 110, E2064–E2073. doi: 10.1073/pnas.1222433110

Takashi, K. (2007). Van der Pol oscillator. *Scholarpedia* 2:2202. doi: 10.4249/scholarpedia.2202

Takigawa, M., Takahashi, A., Kuwahara, T., Okubo, K., Takahashi, Y., Watari, Y., et al. (2014). Long-term follow-up after catheter ablation of paroxysmal atrial fibrillation: the incidence of recurrence and progression of atrial fibrillation. *Circ. Arrhythm. Electrophysiol.* 7, 267–273. doi: 10.1161/CIRCEP.113.000471

Tosteson, D. C., and Hoffman, J. F. (1960). Regulation of cell volume by active cation transport in high and low potassium sheep red cells. *J. Gen. Physiol.* 44, 169–194. doi: 10.1085/jgp.44.1.169

Van der Pol, B., and Van der Mark, J. (1928). The heartbeat considered as a relaxation oscillation and an electrical model of the heart. *Philos. Mag.* 7, 763–775. doi: 10.1080/14786441108564652

van der Velden, H. M. W., Ausma, J., Rook, M. B., Hellemons, A. J. C. G. M., van Veen, T. A. A. B., Allessie, M. A., et al. (2000). Gap junctional remodeling in relation to stabilization of atrial fibrillation in the goat. *Cardiovasc. Res.* 46, 476–486. doi: 10.1016/S0008-6363(00)00026-2

van der Velden, H. M. W., and Jongsma, H. J. (2002). Cardiac gap junctions and connexins: their role in atrial fibrillation and potential as therapeutic targets. *Cardiovasc. Res.* 54, 270–279. doi: 10.1016/S0008-6363(01)00557-0

Venugopal, V., Roux, S. G., Foufoula-Georgiou, E., and Arneodo, A. (2006). Revisiting multifractality of high-resolution temporal rainfall using a wavelet-based formalism. *Water Resour. Res.* 42:W06D14. doi: 10.1029/2005WR004489

Wang, H.-Z., Jian, J. L., Lemanski, F. L., and Veenstra, R. D. (1992). Gating of mammalian cardiac gap junction channels by transjunctional voltage. *Biophys. J.* 63, 139–151. doi: 10.1016/S0006-3495(92)81573-4

Weidmann, S. (1966). The diffusion of radiopotassium across intercalated disks of mammalian cardiac muscle. *J. Physiol.* 187, 323–342. doi: 10.1113/jphysiol.1966.sp008092

Wendt, H., Abry, P., and Jaffard, S. (2007). Bootstrap for empirical multifractal analysis. *IEEE Signal Process. Mag.* 24, 38–48. doi: 10.1109/MSP.2007.4286563

Wendt, H., Kiyono, K., Abry, P., Hayano, J., Watanabe, E., and Yamamoto, Y. (2014). Multiscale wavelet p-leader based heart rate variability analysis for survival probability assessment in CHF patients. *Proceedings of the International Conference of the IEEE Engineering in Medicine and Biology Society* (Piscataway, NJ), 2809–2812. doi: 10.1109/EMBC.2014.6944207

West, B. J., Scafetta, N., Cooke, W. H., and Balocchi, R. (2004). Influence of progressive central hypovolemia on Hölder exponent distributions of cardiac interbeat intervals. *Ann. Biomed. Eng.* 32, 1077–1087. doi: 10.1114/B:ABME.0000036644.69559.ad

Winfree, A. T. (1989). Electrical instability in cardiac muscle: phase singularities and rotors. *J. Theor. Biol.* 138, 353–405. doi: 10.1016/S0022-5193(89)80200-0

Zipes, D. P., Jalife, J., and Stevenson, W. G. (eds.) (2017). *Cardiac Electrophysiology: From Cell to Bedside*. Philadelphia, PA: Elsevier Saunders.

Conflict of Interest Statement: The authors declare that the research was conducted in the absence of any commercial or financial relationships that could be construed as a potential conflict of interest.

frontiers in Physiology

ORIGINAL RESEARCH
published: 14 May 2019
doi: 10.3389/fphys.2019.00570

Differentiation of Heart Failure Patients by the Ratio of the Scaling Exponents of Cardiac Interbeat Intervals

Mirjana M. Platiša[1], Nikola N. Radovanović[2], Aleksandar Kalauzi[3], Goran Milašinović[2,4] and Siniša U. Pavlović[2,4]*

[1] Institute of Biophysics, Faculty of Medicine, University of Belgrade, Belgrade, Serbia, [2] Pacemaker Center, Clinical Center of Serbia, Belgrade, Serbia, [3] Department for Life Sciences, Institute for Multidisciplinary Research, University of Belgrade, Belgrade, Serbia, [4] Faculty of Medicine, University of Belgrade, Belgrade, Serbia

Heart failure (HF) is one of the most frequent heart diseases. It is usually characterized with structural and functional cardiac abnormalities followed by dysfunction of autonomic cardiac control. Current methods of heartbeat interval analysis are not capable to differentiate HF patients and some new differentiation of HF patients could be useful in the determination of the direction of their treatment. In this study, we examined potential of the ratio of the short-term and long-term scaling exponents (α_1 and α_2) to separate HF patients with similar level of reduced cardiac autonomic nervous system control and with no significant difference in age, left ventricular ejection fraction (LVEF) and NYHA class. Thirty-five healthy control subjects and 46 HF patients underwent 20 min of continuous supine resting ECG recording. The interbeat interval time series were analyzed using standardized power spectrum analysis, detrended fluctuation analysis method and standard Poincaré plot (PP) analysis with measures of asymmetry of the PP. Compared with healthy control group, in HF patients linear measures of autonomic cardiac control were statistically significantly reduced ($p < 0.05$), heart rate asymmetry was preserved ($C_{up} > C_{down}$, $p < 0.01$), and long-term scaling exponent α_2 was significantly higher. Cluster analysis of the ratio of short- and long-term scaling exponents showed capability of this parameter to separate four clusters of HF patients. Clusters were determined by interplay of presence of short-term and long-term correlations in interbeat intervals. Complementary measure, commonly accepted ratio of the PP descriptors, SD2/SD1, showed tendency toward statistical significance to separate HF patients in obtained clusters. Also, heart rate asymmetry was preserved only in two clusters. Finally, a multiple regression analysis showed that the ratio α_1/α_2 could be used as an integrated measure of cardiac dynamic with complex physiological background which, besides spectral components as measures of autonomic cardiac control, also involves breathing frequency and mechanical cardiac parameter, left ventricular ejection fraction.

Keywords: heart failure, scaling exponents, detrended fluctuation analysis, Poincaré plot, autonomic cardiac control, asymmetry

OPEN ACCESS

Edited by:
Paul Bogdan,
University of Southern California,
United States

Reviewed by:
Ronny P. Bartsch,
Bar-Ilan University, Israel
Danuta Makowiec,
University of Gdańsk, Poland

****Correspondence:***
Mirjana M. Platiša
mirjana.platisa@gmail.com;
mirjana.platisa@med.bg.ac.rs

Specialty section:
This article was submitted to Fractal Physiology, a section of the journal Frontiers in Physiology

Received: *31 January 2019*
Accepted: *24 April 2019*
Published: *14 May 2019*

Citation:
Platiša MM, Radovanović NN, Kalauzi A, Milašinović G and Pavlović SU (2019) Differentiation of Heart Failure Patients by the Ratio of the Scaling Exponents of Cardiac Interbeat Intervals. Front. Physiol. 10:570. doi: 10.3389/fphys.2019.00570

INTRODUCTION

Real-life experience warns us that patients do not have the same clinical response to a single treatment regimen and that traditionally accepted clinical parameters are not good enough predictors of the success of the performed therapy. This is also the case in various areas of the heart failure (HF) treatment. For instance, despite the availability of advanced imaging techniques and strict clinical, echocardiographic and electrocardiographic criteria for the selection of patients with HF and an indication for cardiac resynchronization therapy device implantation, still 20–40% of these patients do not have positive response to this therapy (Dhesi et al., 2017). Therefore, in this field it is necessary to find new ways of separating HF patients, with the intent of defining a group of them who would benefit most from the cardiac resynchronization therapy.

Both intrinsic heart rate and its modulation are primarily determined by alterations in the autonomic tone. The autonomic tone is the general activity rate of the autonomic nervous system (ANS) and it is considered to refer to its long-term activity. It is accepted that measurements of linear time domain and frequency domain variables of heart rate variability (HRV) are simple and practical tools to assess autonomic function (Akselrod et al., 1981; Task Force of the ESC and the NASPE, 1996). However, introduction of methods derived from non-linear dynamics for analyzing HRV have shown new complementary insights into dynamic and structural nature of HRV signals (Eke et al., 2002, 2012; Sassi et al., 2015; Platiša et al., 2016). Since multiple regulatory mechanisms of cardiac control operate across different time scales and have shown scaling behavior, classical linear signal analysis methods are often unsuitable to quantify complex HRV content which is far from simple periodicity. One of the featured groups of non-linear measures in quantifying complex physiological dynamics is a group of fractal measures which are used to assess self-affinity of heartbeat fluctuations over multiple time scales. Fractal organization of healthy sinus rhythm dynamics represents complex output from linear and non-linear processes, usually with non-stationary properties. Long-term scaling properties of interbeat time series was first quantified by the scaling exponent (β) as a slope of the regression line of the power versus frequency relation on log-log graph (Kobayashi and Musha, 1982; Saul et al., 1987). In general, the power law scaling exponent is typically calculated in the frequency domain as the β or in the time domain as the Hurst exponent (H) (Bassingthwaighte et al., 1994; Eke et al., 2000). The technique of detrended fluctuation analysis (DFA), based on modified root mean square analysis of a random walk, was proposed to assess the intrinsic correlation properties of a complex cardiac system where scaling exponent (α) of approximately 1 indicates fractal-like behavior of healthy heart rate dynamics (Peng et al., 1995). The obtained exponent is similar to the Hurst exponent, except that DFA may also be applied to non-stationary signals. With this method, the presence of correlations in the fluctuations of heartbeat intervals can be quantified by short- and long-term scaling exponents (α_1 and α_2) in two distinct linear regions that determine range of the short- and long-term correlation properties.

Beside monofractal complexity, multifractal analysis introduced by Ivanov et al. (1999) revealed new informations about physiological complexity of HRV signals. Multifractal complexity arises from a large number of local scaling exponents which physiological background was explained with involvement of coupled cascades of feedback loops in healthy cardiac system. More, Amaral et al. (2001) showed significant impact of parasympathetic control on the multifractal properties on HRV where atropine administration resulted with a marked loss of multifractality. Reduced multifractality also was found in pathological state, in patients with congestive HF (Ivanov et al., 1999). Further, Silva et al. (2014) found that loss of multifractality may indicate an impairment of the left ventricular ejection fraction (LVEF) in patients after acute myocardial infarction. One of the later papers of Ivanov et al. (2009) showed that physiological or physical systems with similar $1/f$ scaling behavior can differ in various levels of complexity which depend on the nature of control mechanisms. The necessity for developing new methods to detect the network between individual organ systems as well as between network of coupled control mechanisms, in response to changes in (patho)physiological conditions, has been recognized in the proposed interdisciplinary area known as a Network Physiology (Lin et al., 2016; Ivanov et al., 2017). This new field focuses on understanding physiological functions with new theoretical framework and analytic formalism.

Fractal view of physiology has become the basis in understanding and controlling physiological networks where both homeostatic and allometric control mechanisms existed (West, 2009). Homeostatic control has a negative feedback character which is local and rapid while allometric control can take into account long-range interactions in complex phenomena (West, 2010). Hence, in recent modeling the dynamics and control of complex physiological phenomena the fractional calculus is more frequently applied (Bogdan et al., 2013). Furthermore, there have been efforts of reconstructing the network between physiological processes when some physiological signals are not observed yet capturing their fractional behavior through fractional order derivatives (Gupta et al., 2018).

In this study, we analyzed heterogeneity of HF patients through application of various methods of HRV analysis. More, we examined potential of the ratio of short- and long-term scaling exponents to differentiate subgroups of HF patients with different short-term and long-term correlation properties. We also calculated standard linear HRV measures with twofold aim. The first one was to show that our data are in line with previously reported results (their reduction and alterations in HF patients) and the second one was to help us to reveal the physiological background of the obtained results.

MATERIALS AND METHODS

Subjects

The group of HF patients comprised 46 patients (nine females) with a mean age of 59 ± 2 years (range 37–78 years). All patients had HF with reduced LVEF, on average below 30%. They all

had sinus rhythm without any supraventricular or ventricular rhythm disorders, including supraventricular and ventricular extrasystoles. Most of them were in functional class NYHA II (36 patients) and 10 patients had worse functional capacity (NYHA III). Majority of HF patients in this study were receiving optimal therapy for HF, including β-blockers, angiotensin-converting enzyme (ACE) inhibitors, and aldosterone blockers. An individual therapeutic approach had always been applied to the patients, which means that patients were not exclusively receiving in the guidelines recommended, but maximum tolerated doses of drugs, and rarely, in the presence of certain contraindications, some of previously mentioned group of drugs was left out of therapy. Control healthy group was formed from 35 volunteers (17 females) with a mean age 44 ± 2 years (range 35–59 years). All subjects were non-smokers, without medical history. Ethic Committee of the Faculty of Medicine, Belgrade University approved this study (Ref. Numb. 29/III-5).

Experimental Protocol and Data Acquisition

Experiments were performed in the morning between 7:00 and 10:00 a.m. in a quiet setting at the Pacemaker Center of the Clinical Center of Serbia and at the Laboratory for Biosignals, Institute of Biophysics, Faculty of Medicine, Belgrade University. Twenty minutes electrocardiogram (ECG) and respiratory signal data were recorded with sampling rate 1 kHz using Biopac and AcqKnowledge 3.9.1 software (BIOPAC System, Inc., Santa Barbara, CA, United States). The ECG data were collected using the ECG 100C electrocardiogram amplifier module. The classic 1 channel ECG for the measurement of Lead I based on three electrodes placed on left and right shoulder and the right leg was used. The RSP 100C respiratory pneumogram amplifier module with TSD 201 transducer attached to the belt (adjustable nylon strap) was used to measure abdominal expansion and contraction. Transducer was placed on the abdomen, at the point of minimum circumference (maximum expiration). Subjects were relaxed before measurement, and they were supine and breathed with spontaneous breathing frequency. Interbeat (RR) intervals and interbreath intervals were extracted from recorded signals using the Pick Peaks tool from Origin 6.0 (Microcal Origin, Northampton, MA, United States). Breathing frequency (BF) was obtained as a reciprocal value of the mean interbreath interval.

HRV Analysis in Time Domain

A few standard HRV parameters in time domain were determined from time series of RR intervals with our Matlab program: (1) standard deviation of the RR intervals (SDNN), (2) root mean square difference between successive RR intervals, and (3) the percent of RR intervals which were longer by more than 50 ms than the immediately following RR interval (pNN50) (Task Force of the ESC and the NASPE, 1996).

Frequency Domain Analysis

Heart rate variability analysis in frequency domain was performed using Origin 6.0 (Microcal Origin, Northampton, MA, United States) (Platiša and Gal, 2006; Kapidžić et al., 2014). RR interval series were resampled using the mean RR-value for each subject. Power spectrum densities were obtained using FFT with Hanning window (Microcal Origin, Northampton, MA, United States). Absolute values of spectral components were determined carrying out an integration of the power spectrum in the range of total power (TP, 0.0033–0.4 Hz), very low frequency (VLF, 0.0033–0.04 Hz), low frequency (LF, 0.04–0.15 Hz) and high frequency (HF, 0.15–0.4 Hz) (Task Force of the ESC and the NASPE, 1996). The power of RR variability in VLF range is related to long-term regulation mechanisms related to the thermoregulation, to the renin-angiotensin system and to other humoral factors (Task Force of the ESC and the NASPE, 1996). The physiological interpretation of LF spectral component is still controversial because both sympathetic and parasympathetic contributions are involved in this measure (Task Force of the ESC and the NASPE, 1996; Billman, 2011), while HF spectral power is generally accepted as a marker of parasympathetic activation (Akselrod et al., 1981; Billman, 2011). In order to achieve a normal distribution of the data, natural logarithm of spectral powers in absolute units was taken. Relative units of spectral powers were calculated by dividing each spectral component with the sum of all three spectral powers.

Detrended Fluctuation Analysis (DFA)

A modification of the random walk model analysis has been used to quantify the fractal-like scaling properties of RR interval time series (Peng et al., 1995). The root-mean-square fluctuations of the integrated and linear detrended data $F(n)$ were measured in observation windows of varying sizes n and then plotted against the size of window on a log–log scale. The power-law behavior was quantified as the slope of the linear regression line, $\log F(n) \sim \alpha \log n$. This slope is defined as the scaling exponent α. In this study detrended fluctuation function $F(n)$ was calculated by using algorithm from PhysioNet[1] (Goldberger et al., 2000). The short-term scaling exponent α_1 was calculated over the window size n = (4–16) and the long-term scaling exponent α_2 was calculated over the window size $n \geq 16$. Scaling exponents were estimated with standard errors and the coefficient of determination (R^2) was calculated in OriginPro 8 (OriginLab Corporation, Northampton, MA, United States). An $\alpha < 0.5$ characterizes signal with anticorrelations (with stronger anticorrelations when α is closer to 0). If $\alpha = 0.5$ there are no correlations and signal represents (Gaussian) white noise; if $\alpha \approx 1$ represents $1/f$ noise and if $\alpha = 1.5$ the signal is random walk (Brownian motion) (Peng et al., 1995; Bashan et al., 2008).

Asymmetry of the Poincaré Plot

A typical HRV Poincaré plot (PP) represents scatter graph of $RR_{i+1} = f(RR_i)$. The two standard parameters SD1 and SD2, called the PP descriptors, describe distribution of points around two diagonals. It is accepted that SD1 describes instant heartbeat intervals variability and quantifies short-term HRV, while SD2 quantifies long-term HRV. Pearson correlation coefficient of PP, noted as r, measured the association between

[1] https://physionet.org/physiotools/dfa/

all pairs (RR_i, RR_{i+1}) in the time series of RR intervals of one subject. Beside excellent visualization capability and short- and long-term HRV information quantification, the standard PP technique revealed asymmetry as one of unexploited physiological phenomena in resting healthy people (Piskorski and Guzik, 2007). Guzik et al. (2006) extended standard descriptor SD1 (dispersion of the PP across the line of identity, $y = x$) to two new finer descriptors $SD1_{up}$ and $SD1_{down}$. Shortly, pattern of heart rate during acceleration is different to the pattern of deceleration, i.e., in deceleration contribution of the points above the line of identity ($RR_i < RR_{i+1}$) is higher than that of the points below the line ($RR_i > RR_{i+1}$). They introduced two variables C_{up} and C_{down}:

$$C_{up} = \frac{SD1_{up}^2}{SD1^2} \quad (1)$$

$$C_{down} = \frac{SD1_{down}^2}{SD1^2} \quad (2)$$

which determine the relative contribution of $SD1_{up}$ and $SD1_{down}$ to SD1. Analysis of the PP of RR intervals was done with our Matlab program (The MathWorks Inc., United States). Relation between C_{up} (C_{down}) and Bauer's deceleration (acceleration) capacity (Bauer et al., 2006) is explained in the **Supplementary Material**.

Statistics

Normal distribution of data was examined by the Shapiro–Wilk test (appropriate for a small sample size of up to 50 subjects). We used natural logarithm of the spectral powers to obtain their normalized values. The K-means cluster analysis with Euclidean distance measure was performed for continuous variable – the ratio of the scaling exponents α_1/α_2. One-way ANOVA was applied to find significant difference in mean values of each variable or parameter: (1) between control and HF group; (2) between four clusters in HF group with Bonferroni *post hoc* test; and (3) between control and each cluster of HF with Bonferroni *post hoc* test. Multiple regression analysis was applied to find which variables and parameters predict the ratio of the scaling exponents in HF patients. Statistical analyses were performed using IBM Statistical Package for the Social Sciences (SPSS) version 19.0. Data are presented as mean ± standard errors. $P < 0.05$ was used as statistically significant.

RESULTS

Table 1 shows clinically relevant data of HF subjects and descriptive statistic results for all linear and non-linear HRV measures in healthy control group and HF patients. It can be observed that, as it was expected, patients with HF had statistically significantly reduced values of linear measures of autonomic cardiac control compared with healthy control group. However, some quantifiers of HRV properties were not statistically different between groups (C_{up} and C_{down}, as well as short-term scaling exponent α_1). Also, younger control subjects had higher heart rate than HF patients ($p < 0.01$).

TABLE 1 | Anthropometric data, clinical parameters, and linear and non-linear parameters of heart interbeat intervals in healthy control subjects and heart failure patients.

	Control, *N* = 35 (17 F)	Heart failure, *N* = 46 (9 F)	*p*
Age (years)	44 ± 2	59 ± 2	< 0.01
NYHA		2.22 ± 0.10	
LVEF (%)		27.52 ± 0.93	
SDNN (ms)	46.3 ± 2.6	34.1 ± 2.4	< 0.01
RMSSD (ms)	31.6 ± 2.8	18.4 ± 1.5	< 0.01
pNN50 (%)	11.2 ± 2.1	3.02 ± 0.67	< 0.01
SD1 (ms)	16.4 ± 1.4	11.8 ± 1.1	0.013
SD2 (ms)	43 ± 2.4	32.0 ± 2.3	< 0.01
r, Pearson PP	0.735 ± 0.028	0.727 ± 0.035	0.86
SD2/SD1	2.94 ± 0.16	3.42 ± 0.27	0.16
C_{up}	55.3 ± 1.0**	54.27 ± 0.96**	0.47
C_{down}	44.7 ± 1.0	45.72 ± 0.96	0.46
RR (s)	0.873 ± 0.018	0.938 ± 0.023	< 0.01
ln[VLF (ms^2)]	5.68 ± 0.15	5.08 ± 0.19	0.04
ln[LF (ms^2)]	5.59 ± 0.15	3.97 ± 0.18	< 0.01
ln[HF (ms^2)]	5.27 ± 0.17	3.86 ± 0.19	< 0.01
ln[TP (ms^2)]	6.72 ± 0.14	5.70 ± 0.17	< 0.01
BF (Hz)	0.239 ± 0.10	0.258 ± 0.089	0.49
α_1	0.895 ± 0.029	1.000 ± 0.035	0.22
α_2	0.830 ± 0.022	0.932 ± 0.020	< 0.01
α_1/α_2	1.111 ± 0.052	1.099 ± 0.047	0.44

***$p < 0.01$ (C_{up} vs. C_{down}). Data are presented as mean values ± standard errors. LVEF, left ventricular ejection fraction; SDNN, standard deviation of RR intervals; RMSSD, root mean square of successive differences of RR intervals; pNN50, percentage of consecutive RR intervals that deviate from one another by more than 50 ms. SD1, SD2, and r (Pearson PP), C_{up}, and C_{down} are parameters of Poincaré plot. RR, mean interbeat interval; VLF, very low frequency spectral component; LF, low frequency spectral component; HF, high frequency spectra component; TP, total power of spectral power density; BF, breathing frequency; α_1, short-term scaling exponent; α_2, long-term scaling exponent.*

By applied cluster analysis we found that the ratio of the short- and the long-term scaling exponents, α_1/α_2, was significantly capable to differentiate four clusters of HF subjects. All curves of detrended fluctuation functions $F(n)$ plotted versus segment size n on the log-log graph are presented on **Figure 1** for healthy subjects and on **Figure 2** for the four clusters of HF patients. Values of estimated scaling exponents for each patient in each cluster of HF group could be found in the **Tables 2–5**.

Table 6 reports results of cluster analysis, with the mean and standard errors of all linear and non-linear HRV indexes for each cluster. Averaged values of short-term scaling exponent (α_1), long-term scaling exponent (α_2), as well as their ratio for each cluster and control group of healthy subjects are shown on **Figure 3**. It can be seen that in HF patients with reduced autonomic cardiac control, interplay of different correlation properties in heart rhythm over short-term and long-term scales determines four independent subgroups. In comparison of clusters with control group we found that there is no significant difference in α_1 neither in the ratio α_1/α_2 between control and 2nd cluster, while α_2 was significantly lower in control group than in the first two clusters (**Figure 3**).

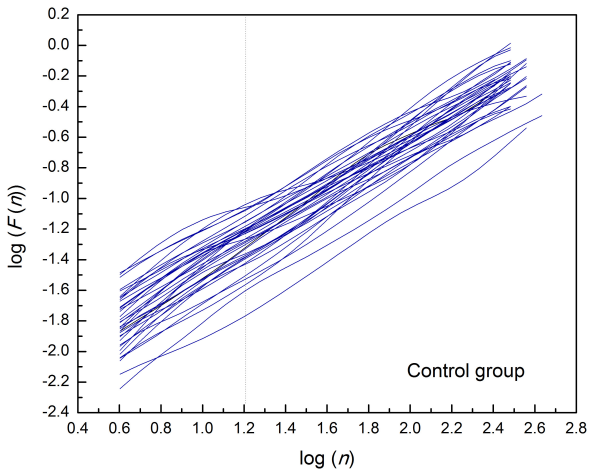

FIGURE 1 | Detrended fluctuation functions $F(n)$ for time series of interbeat intervals (approximately N = 1,200 samples) versus segment size n on the log-log graph, in the control group of healthy subjects. Dashed line separates the two ranges in which the scaling exponents have been determined (n = 16).

Comparison of heart rate dynamics indices between patients with HF showed that there is no significant difference between time HRV measures neither between absolute values of spectral components. However, we found significant difference between subgroups in relative values of spectral powers as well as in their comparison with control group (**Figure 4**). Results of statistical analysis could be found in the legend of the **Figure 4**. Also, there is no significant difference with respect to age, NYHA, LVEF, or breathing frequency between clusters patients (**Table 6**).

Poincaré plot descriptors SD1 and SD2 showed that they were not able to separate patients in obtained clusters, but there was a tendency toward statistical significance for their ratio SD2/SD1 (**Table 6** and **Figure 5**). Asymmetry variables C_{up} and C_{down}, determined from the Poincaré plots, indicated that HF patients could be separated only into two subgroups: one with dominant deceleration mechanism and the second one, where there was no statistical difference between deceleration and acceleration pattern of regulatory mechanisms (**Figure 6**). We also found that there is no statistical difference between control group and each cluster in C_{up} and C_{down}.

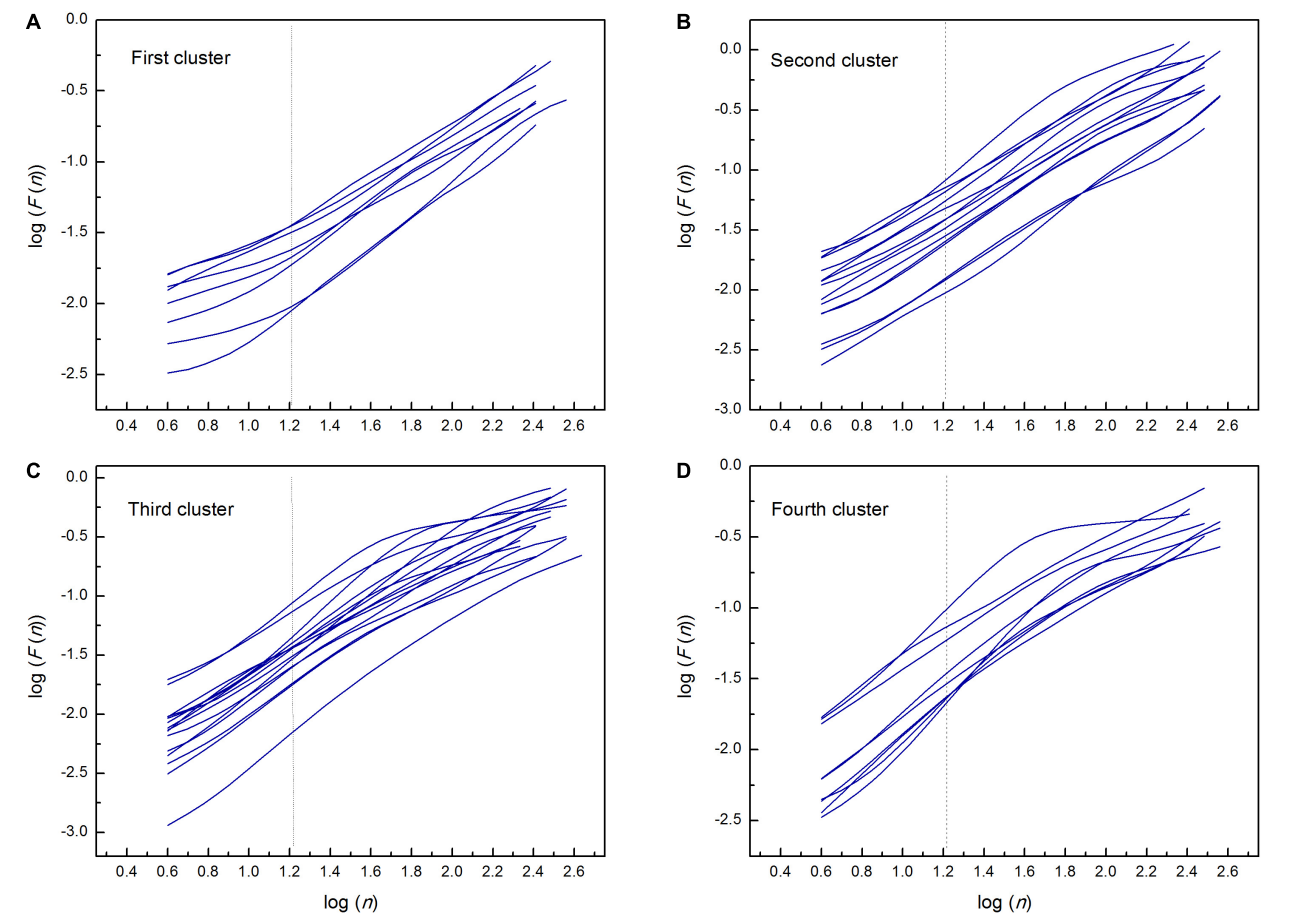

FIGURE 2 | Detrended fluctuation functions $F(n)$ for time series of interbeat intervals versus segment size n on the log-log graph; in the first **(A)**, second **(B)**, third **(C)**, and fourth **(D)** cluster of heart failure patients. Dashed lines separate the two ranges in which the scaling exponents have been determined (n = 16). Estimated scaling exponents with the coefficient of determination for every patient in each cluster are given in **Tables 2–5**.

TABLE 2 | Estimated values of short-term (α_1) and long-term (α_2) scaling exponents in the first cluster of heart failure patients.

Patient	α_1	R^2	α_2	R^2
1	0.728 ± 0.060	0.95	1.143 ± 0.012	0.99
2	0.661 ± 0.011	0.99	1.001 ± 0.014	0.99
3	0.661 ± 0.038	0.98	0.937 ± 0.021	0.99
4	0.536 ± 0.027	0.98	0.8971 ± 0.0037	0.99
5	0.420 ± 0.028	0.97	1.0636 ± 0.0077	0.99
6	0.550 ± 0.012	0.99	0.831 ± 0.051	0.99
7	0.414 ± 0.013	0.99	0.863 ± 0.012	0.99
8	0.512 ± 0.017	0.99	0.940 ± 0.016	0.99

Values are mean ± standard error. R^2, coefficient of determination (the goodness of linear fit).

TABLE 3 | Estimated values of short-term (α_1) and long-term (α_2) scaling exponents in the second cluster of heart failure patients.

Patient	α_1	R^2	α_2	R^2
1	1.015 ± 0.041	0.99	1.035 ± 0.027	0.99
2	0.956 ± 0.016	0.99	0.904 ± 0.018	0.99
3	0.948 ± 0.018	0.99	0.954 ± 0.015	0.99
4	0.830 ± 0.022	0.99	1.0147 ± 0.0069	0.99
5	0.964 ± 0.028	0.98	1.1064 ± 0.0094	0.99
6	0.827 ± 0.036	0.99	0.999 ± 0.012	0.99
7	0.898 ± 0.044	0.99	0.929 ± 0.015	0.99
8	1.060 ± 0.043	0.99	1.0073 ± 0.050	0.97
9	0.967 ± 0.033	0.99	1.033 ± 0.038	0.98
10	0.963 ± 0.016	0.99	0.929 ± 0.032	0.99
11	0.992 ± 0.014	0.99	0.9549 ± 0.0059	0.99
12	0.901 ± 0.0.37	0.99	1.021 ± 0.044	0.97
13	0.862 ± 0.044	0.99	0.988 ± 0.020	0.99
14	1.0029 ± 0.0088	0.99	1.227 ± 0.012	0.99

Values are mean ± standard error. R^2, coefficient of determination.

TABLE 4 | Estimated values of short-term (α_1) and long-term (α_2) scaling exponents in the third cluster of heart failure patients.

Patient	α_1	R^2	α_2	R^2
1	1.301 ± 0.033	0.99	1.065 ± 0.025	0.99
2	1.238 ± 0.016	0.99	0.950 ± 0.018	0.99
3	1.187 ± 0.037	0.99	1.031 ± 0.015	0.99
4	1.119 ± 0.029	0.99	0.853 ± 0.019	0.99
5	0.965 ± 0.050	0.98	0.771 ± 0.038	0.97
6	0.978 ± 0.037	0.99	0.778 ± 0.017	0.99
7	0.959 ± 0.018	0.99	0.8275 ± 0.0086	0.99
8	1.104 ± 0.062	0.98	0.892 ± 0.066	0.92
9	1.137 ± 0.038	0.98	0.557 ± 0.051	0.88
10	1.339 ± 0.018	0.99	1.189 ± 0.040	0.99
11	1.162 ± 0.041	0.99	0.909 ± 0.016	0.99
12	1.088 ± 0.020	0.99	0.865 ± 0.035	0.97
13	0.944 ± 0.032	0.99	0.697 ± 0.022	0.98
14	1.017 ± 0.016	0.99	0.841 ± 0.029	0.99
15	1.1356 ± 0.0083	0.99	0.968 ± 0.024	0.98

Values are mean ± standard error. R^2, coefficient of determination.

TABLE 5 | Estimated values of short-term (α_1) and long-term (α_2) scaling exponents in the fourth cluster of heart failure patients.

Patient	α_1	R^2	α_2	R^2
1	1.060 ± 0.025	0.99	0.7804 ± 0.0081	0.99
2	1.235 ± 0.018	0.99	0.847 ± 0.030	0.99
3	1.179 ± 0.058	0.99	0.828 ± 0.037	0.98
4	0.9603 ± 0.0018	0.99	0.739 ± 0.020	0.99
5	1.3185 ± 0.052	0.99	0.869 ± 0.065	0.91
6	1.1010 ± 0.0046	0.99	0.729 ± 0.029	0.97
7	1.3314 ± 0.0092	0.99	0.8894 ± 0.019	0.99
8	1.412 ± 0.011	0.99	0.504 ± 0.062	0.81
9	1.2142 ± 0.0089	0.99	0.863 ± 0.011	0.99

Values are mean ± standard error. R^2, coefficient of determination.

A multiple regression analysis was performed to determine predictors of the ratio α_1/α_2. We found that relative spectral powers (rHF and rVLF), the LVEF, normalized total spectral power, and breathing frequency statistically significantly predicted α_1/α_2 in HF subjects, $F(5,40) = 20.966$, $p < 0.01$, $R^2 = 0.724$ (**Table 7**). This result indicates complex physiological background of the ratio of scaling exponents which comprised relative cardiac vagal and central autonomic control, mechanical efficiency of the left ventricle, total variability as well as modulatory effect of the breathing process.

DISCUSSION

In the last few decades DFA method, i.e., short-term and long-term scaling exponents separately, showed a greater prediction potential in several cardiac diseases than any parameter from HRV analyses. In this study, we found that in HF patients short- and long-term correlation properties quantified by scaling exponents could gradually change in the opposite directions. We introduced new parameter, the ratio of short- and long-term correlation properties of heart interbeat fluctuations, which could be used as an integrative parameter of regulatory cardiac mechanisms in HF patients. This parameter is capable to differentiate four clusters which could not be simply classified by some clinical parameters (LVEF or NYHA) or solely by linear and non-linear measures of autonomic cardiac control.

The finding for the first cluster could be a good example of previously recognized interactions between short-term and long-term cardiovascular control mechanisms under specific pathological conditions (Hoyer et al., 2007). Namely, Hoyer et al. (2007) showed that cardiovascular system incorporates dominant short- and long-term control mechanisms which are in optimal adjustment in normal healthy conditions. Under pathological conditions, realized with increased collapse of the short feedback loop, the inverse association between their randomness has been recognized. As a system inherent type of readjustment, short-term randomness increased and long-term randomness decreased. We found in the first cluster of HF patients that the ratio of the scaling exponents had the lowest value; α_1 was

TABLE 6 | Comparison of clinical data, and linear and non-linear HRV measures between four clusters of heart failure patients.

	First (*N* = 8)	Second (*N* = 14)	Third (*N* = 15)	Fourth (*N* = 9)	*p*
Age (years)	62.1 ± 2.7	55.4 ± 2.5	61.1 ± 2.3	59.2 ± 3.2	0.85
NYHA	2.25 ± 0.16	2.21 ± 0.11	2.27 ± 0.12	2.11 ± 0.11	0.28
LVEF (%)	28.1 ± 2.7	25.8 ± 1.7	28.9 ± 1.7	27.3 ± 1.7	0.61
SDNN (ms)	26,6 ± 4.4	41.8 ± 4.8	31.0 ± 3.5	34.0 ± 6.5	0.15
RMSSD (ms)	20.4 ± 3.0	21.9 ± 3.1	16.4 ± 2.1	14.8 ± 3.5	0.29
pNN50 (%)	2.3 ± 1.2	4.9 ± 1.7	2.19 ± 0.82	2.1 ± 1.1	0.34
SD1 (ms)	14.8 ± 2.6	10.7 ± 1.6	13.0 ± 2.5	8.83 ± 6.4	0.37
SD2 (ms)	25.6 ± 4.2	36.2 ± 4.8	30.9 ± 3.5	33.1 ± 6.4	0.50
r, Pearson PP	0.44 ± 0.10	0.818 ± 0.029	0.707 ± 0.061	0.872 ± 0.018	< 0.01
SD2/SD1	2.06 ± 0.48	3.95 ± 0.62	3.25 ± 0.43	4.10 ± 0.33	0.07
RR (s)	1.027 ± 0.043	0.932 ± 0.041	0.910 ± 0.047	0.916 ± 0.044	0.24
ln[VLF (ms^2)]	4.10 ± 0.43	5.40 ± 0.37	5.16 ± 0.31	5.31 ± 0.30	0.36
ln[LF (ms^2)]	2.88 ± 0.43	4.04 ± 0.34	3.93 ± 0.26	4.88 ± 0.28	0.06
ln[HF (ms^2)]	4.12 ± 0.35	4.10 ± 0.34	3.47 ± 0.35	3.89 ± 0.47	0.46
ln[TP (ms^2)]	5.06 ± 0.35	5.88 ± 0.36	5.66 ± 0.28	6.07 ± 0.31	0.79
rVLF (%)	43.4 ± 7.3	63.5 ± 3.6	63.1 ± 4.7	53.8 ± 6.5	0.045
rLF (%)	12.6 ± 2.4	17.8 ± 2.0	21.9 ± 3.4	32.1 ± 3.2	0.002
rHF (%)	44.0 ± 7.5	18.6 ± 2.2	15.0 ± 3.0	14.1 ± 4.1	0.001
BF (Hz)	0.247 ± 0.022	0.252 ± 0.017	0.265 ± 0.016	0.266 ± 0.020	0.74

Data are presented as mean values ± standard errors. LVEF, left ventricular ejection fraction; SDNN, standard deviation of RR intervals; RMSSD, root mean square of successive differences of RR intervals; pNN50, percentage of consecutive RR intervals that deviate from one another by more than 50 ms. SD1, SD2, and r (Pearson PP), C_{up}, and C_{down} are parameters of Poincaré plot. RR, mean interbeat interval. Absolute and relative values of VLF, very low frequency spectral component; LF, low frequency spectral component; HF, high frequency spectral component; TP, total power of spectral power density; BF, breathing frequency.

significantly reduced and significantly lower than α_2. The short-term scaling exponent has shown greater clinical discrimination of various cardiac diseases. A reduced α_1 indicates loss of fractal organization in cardiac interbeat intervals and it is a good predictor of mortality in post-infarction patients (Huikuri et al., 2000; Tapanainen et al., 2002), specific risk factor for cardiac death in the elderly and it has been proposed as a strong predictor for HF patients (Ho et al., 1997; Mäkikallio et al., 2001). In this state of cardiac system with reduced ANS activity, loss of short-term correlations in heartbeat intervals could result from reduced capacity for cardiovascular adaptation, vagal tone (high percentage of rHF) and/or alterations in breathing pattern independent on the breathing frequency. This is an interesting finding because there are plenty of data on factors that affect the breathing frequency in HF, such as the effects of some drugs like sedatives, or LVEF, NYHA, some lung diseases, but we have not found out enough about alterations in breathing patterns so far (Forleo et al., 2015). In our earlier papers we showed that fractal organization of interbeat intervals dynamic could also be altered with some physiological processes like standing, exercise, and recovery (Platiša and Gal, 2008). Additionally, in our study with voluntary breathing at different breathing frequencies we found reduction of α_1 with increase in breathing frequency (Platiša and Gal, 2010). Perakakis et al. (2009) also showed that breathing frequencies may bias evaluation of short-term fractal scaling properties.

Compared with control, in patients from this cluster fractal long-term correlations become stronger (α_2 increased). Some previous studies have reported change of fractal scaling behavior with aging, where both scaling exponents increased with aging (Ryan et al., 1994; Lipsitz, 1995; Pikkujämsä et al., 1999). That type of correlations is usually related to the rigidness of regulatory mechanisms with reduced control ability. According Guzik's variables of asymmetry these patients also preserved asymmetry in short HRV, as it is observed in healthy subjects, which indicates that dominant deceleration mechanism had a different pattern from acceleration mechanism/s (Guzik et al., 2006). Relative spectral powers of very low frequency (rVLF) and of high frequency (rHF) regions had similar percentage values and we assumed that regulatory mechanisms in this range of frequencies are equally involved in the state of reduced autonomic cardiac control as the result of readjustment in system control mechanisms.

In the second cluster we did not find statistically significant crossover between scaling exponents (fractal correlations are very similar in both ranges). This cluster is very similar to the control group, but with significantly higher long-term scaling exponent α_2. However, comparison of distributions of relative spectral powers revealed similar rHF, but with a significant reorganization of rLF and rVLF and with domination of slower regulatory mechanism from domain of very low frequencies in these HF patients. More, asymmetry was not reached, and the pattern of short-term deceleration and acceleration mechanisms was not different. We only may speculate that patients from second cluster were in state with some developed compensatory mechanisms of cardiac control.

Regarding relationship between scaling exponents, the third and fourth cluster were similar, i.e., short-term scaling exponent is significantly higher than long-term. Compared with control group, α_1 gradually increased while α_2 remained statistically

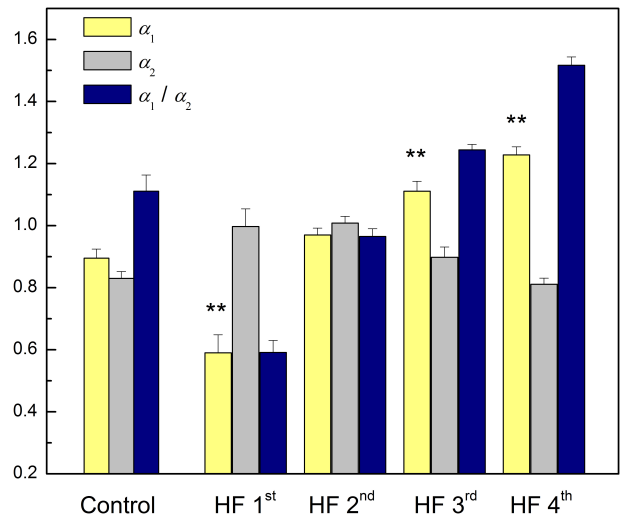

FIGURE 3 | Mean values plus standard errors of short-term scaling exponent (α_1), long-term scaling exponent (α_2) and their ratio α_1/α_2 in control group and four clusters of heart failure patients. $^{**}p < 0.01$ (α_1 vs. α_2). Short-term scaling exponent (α_1) values were significantly different between control group and three clusters (1st, 3rd, and 4th), $p < 0.01$. Long-term scaling exponent (α_2) values were significantly different between control group and two clusters (1st and 2nd), $p < 0.01$. The ratio α_1/α_2 was significantly different between control group and two clusters (1st and 4th), $p < 0.01$, and with tendency toward statistical significance with the 3rd cluster ($p = 0.07$). After comparisons only between clusters for α_1 we obtained following significances: (1st vs. 2nd, 1st vs. 3rd, and 1st vs. 4th, $p < 0.01$) and (2nd vs. 3rd, and 2nd vs. 4th, $p \leq 0.01$). For α_2 we obtained: (1st vs. 4th, $p < 0.01$) and (2nd vs. 3rd, $p = 0.06$ and for 2nd vs. 4th, $p < 0.01$). For the ratio α_1/α_2 all comparisons were statistically significant ($p < 0.01$).

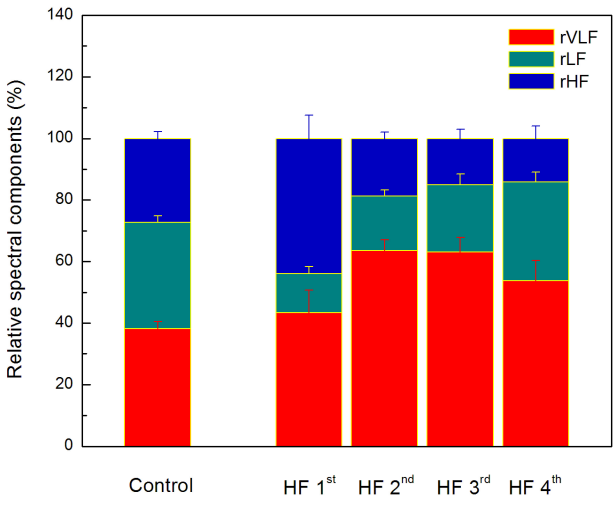

FIGURE 4 | The distribution of relative spectral components in clusters determined by the ratio of the scaling exponents. Values are given as mean plus standard errors. Relative VLF spectral component (rVLF) was significantly different between control group and two clusters (2nd and 3rd), $p < 0.01$. Relative LF spectral component (rLF) was significantly different between control group and three clusters (1st, 2nd, and 3rd), $p < 0.01$. Relative HF spectral component (rHF) was significantly different between control group and two clusters (1st and 3rd), $p < 0.05$, and with tendency toward statistical significance with the 4th cluster ($p = 0.08$). Significant and toward significant differences of comparison between clusters of heart failure patients are for rVLF (1st vs. 2nd, $p = 0.07$ and 1st vs. 3rd, $p = 0.08$), for rLF (1st vs. 4th, $p < 0.01$, and 2nd vs. 4th, $p = 0.01$), and for rHF (1st vs. 2nd, 1st vs. 3rd, and 1st vs. 4th, $p < 0.01$).

unchanged. This type of interactions between short-term and long-term randomness under HF as pathological condition, also may be another type of system inherent readjustment, here in the opposite direction compared with the first cluster. In the literature, it can be found that the increase in α_1 is usually related to vagal withdrawal (Tulppo et al., 2001; Castiglioni et al., 2011) but in this HF states probably with preserved feedback loops of regulatory mechanisms. Tendency to decreased α_2 in the fourth cluster may be related to sinus node dysfunction (Shin et al., 2011) or the β-receptor blockade (Castiglioni et al., 2011). It is believed that complexity of interbeat interval fluctuations is generated solely by ANS activity and that quantified linear and non-linear parameters of HRV are quantifiers of modulatory mechanisms of ANS. However, recently published data revealed that interbeat intervals reflect intrinsic complexity with origin in sinoatrial node cells (Ponard et al., 2007; Yaniv et al., 2013) which usually is integrated in the whole complexity of the heart rhythm. Hence, Yaniv et al. (2013) concluded that HRV is determined by the intrinsic properties of cells in the sinoatrial node and the competing influences of the two branches of the autonomic neural input. With these findings, the importance of assessments of long- term scaling exponent has increased. Hotta et al. (2005) showed that α_2 is a more powerful measure for predicting cardiac morbidity and mortality. In the study of Shin et al. (2011) long-term scaling exponent was the only parameter which was capable of discriminating differences in heart rate dynamics between patients with sinus node dysfunction. They concluded that reduced value of α_2 is a robust measure and could be an adjunctive tool for improvement of diagnostic performance in detection of sinus node dysfunction. The question is whether this finding can be applied to our patients, because they were mostly treated with highly selective beta blockers, whereas in the previously mentioned study, non-selective propranolol was used in blocking the beta receptors. Also, in healthy subjects in a much lesser extent, such alterations of scaling exponents are characterized as age-related degradation of integrated physiological regulatory systems (Iyengar et al., 1996). Our patients probably had superposition of both effects which are more pronounced in the fourth cluster. The reason for decrease of α_2 may be related to some other physiological background (**Figure 2D**). In the sixth and eighth patient, even with statistically approved linear regression analysis, a new scaling regime which is probably related to some slower regulatory mechanism could be identified. Unfortunately, our time series of 20 min length with approximately 2^{10} points was not long enough to detect this regime in all patients of the fourth cluster.

It can be observed that the third and fourth cluster are different with respect to the distribution of asymmetry variables. While there was asymmetry in the third cluster, in the fourth cluster short-term asymmetry has ceased to exist. In order to

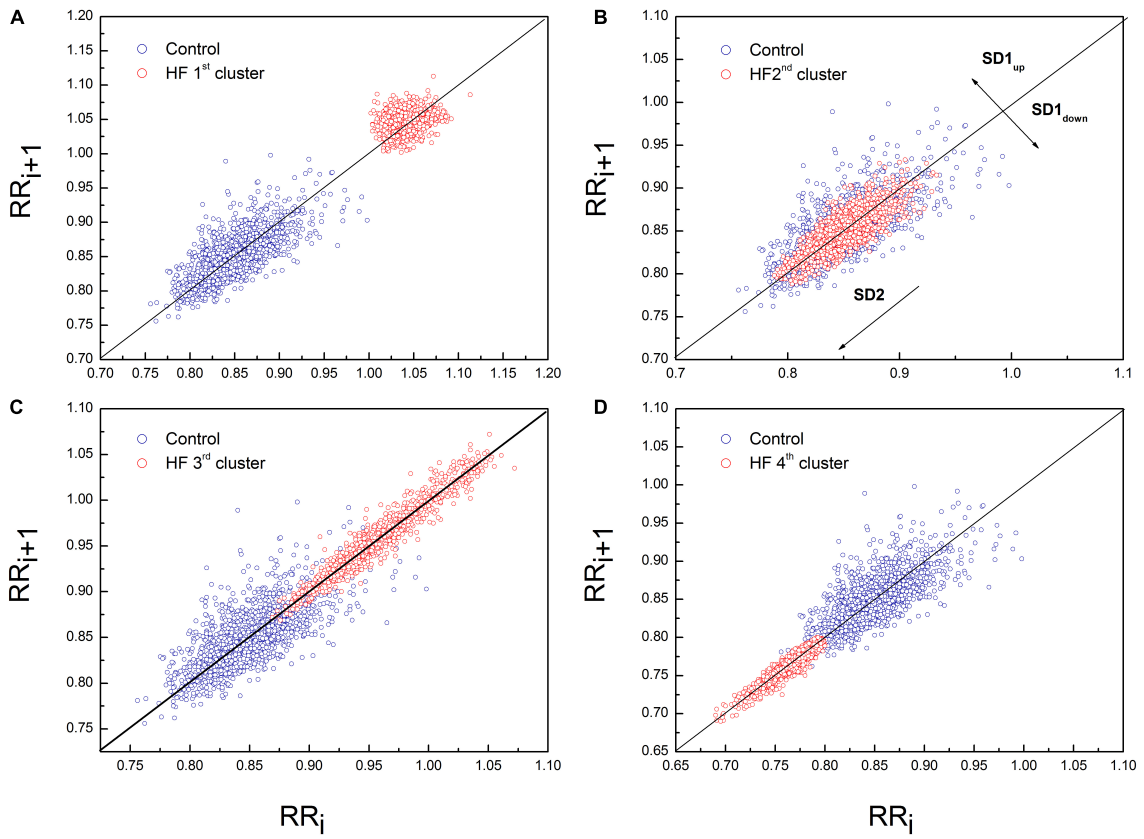

FIGURE 5 | Representative example of Poincaré plot in the first **(A)**, second **(B)**, third **(C)**, and fourth **(D)** cluster of heart failure patients with PP for one healthy subject. Patient from the first cluster had SD1 = 10.10 ms, SD2 = 12.80 ms, C_{up} = 62.72% and C_{down} = 37.28%. Patient from the second cluster had SD1 = 7.50 ms, SD2 = 22.30 ms, C_{up} = 47.42% and C_{down} = 52.58%. Patient from the third cluster had SD1 = 4.90 ms, SD2 = 35.30 ms, C_{up} = 53.8% and C_{down} = 46.2%. Patient from the fourth cluster had SD1 = 3.1 ms, SD2 = 17.7 ms, C_{up} = 42.63% and C_{down} = 57.37%. Control subject had SD1 = 13 ms, SD2 = 32 ms, C_{up} = 57.42% and C_{down} = 42.76%.

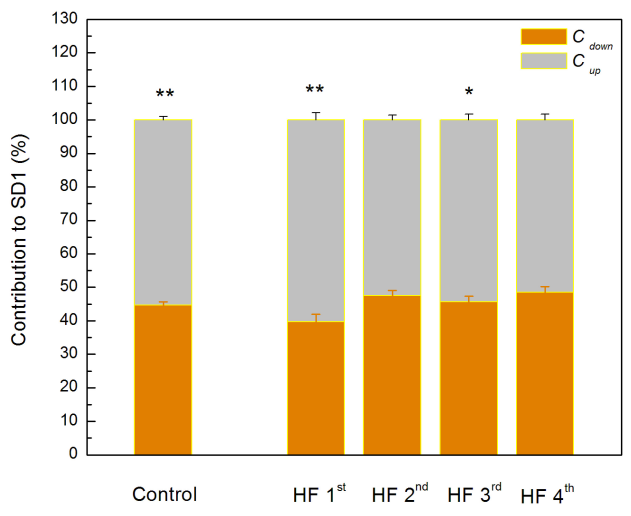

FIGURE 6 | Guzik's variables of asymmetry in clusters of heart failure patients. Data are presented as mean values plus standard errors. $^{**}p < 0.01$, $^{*}p < 0.05$ (C_{up} vs. C_{down}). There is no significant difference between control group and each of clusters with heart failure patients.

clarify all these findings, future studies with longer recordings and/or pharmacological recognition need to be done.

We also noticed that even younger control subjects had higher heart rate than HF patients. If it is known that the main pathophysiological feature of HF is the imbalance of ANS with increased sympathetic activity, then it is expected that patients with HF will have faster resting rate than control subjects (Hori and Okamoto, 2012). However, all patients with HF in this study were receiving β-blockers, and some of them were treated with additional antiarrhythmics, such as amiodarone or digoxin. Thus, in all these patients there was iatrogenic decrease of heart rate. Also, in previous study we found that HF patients with sinus rhythm and without ventricular extrasystoles have a significantly lower heart rate compared to HF patients with arrhythmias, either ventricular or supraventricular (Radovanović et al., 2018). Finally, it should be added that some researchers suggest the existence of selectivity of effects of aging on autonomic function in healthy subjects; more precisely, they believe that sympathetic function remains unchanged with increasing age (Parashar et al., 2016).

Results of multiple regression analysis showed that the ratio of the scaling exponents was significantly predicted with the small

TABLE 7 | Multiple regression analysis with predictors for the ratio of short-term to long-term scaling exponents.

	b	S.E. *b*	β	*t*	*p*
Constant	1.493	0.259		5.772	0.000
rHF (%)	−2.518	0.272	−1.318	−9.245	0.000
rVLF (%)	−1.468	0.245	−0.863	−6.004	0.000
LVEF (%)	0.014	0.005	0.273	3.023	0.004
ln[TP (ms^2)]	0.064	0.024	0.230	2.632	0.012
BF (Hz)	0.932	0.459	0.177	2.031	0.049

rHF, relative spectral component of high frequency domain; rVLF, relative spectral component of very low frequency domain; LVEF, left ventricular ejection fraction; ln TP, natural logarithm of total power; BF, breathing frequency. b, unstandardized regression coefficient; S.E.b, standard error of b; β, standardized regression coefficient.

alterations in five independent measures which determined four clusters of HF patients. Comparison of standardized regression coefficient β values showed that relative spectral components, rHF and rVLF, had strong negative relationship with the ratio of the scaling exponents. Relative strength of relationships of LVEF and lnTP with this ratio was much weaker, while with BF it was the weakest.

Recognized heterogeneity in HF patients points to the necessity of introducing new approaches in the analysis of cardiac dynamics which will comprise the interactions with the other coupled physiological systems (Ivanov et al., 2017; Kuhnhold et al., 2017). In this pathological condition, analyses of the heart–brain interactions are of special importance because of recognition and quantification of neuroplasticity changes in the dynamics of the brain stem integrators.

Limitations

The significant limitation of this study is a statistically significant age difference between healthy controls and HF patients. It is known that aging, as well as diseases, is accompanied by significant cardiovascular modifications, both structural and functional, although there are studies that indicate that fractal temporal organization of cardiac dynamics does not break down with healthy aging (Ferrari, 2002; Schmitt et al., 2009). What is sure is that with aging the sympathetic activity increases, the renin-angiotensin-aldosterone system activity decreases, respiratory sinus arrhythmia and HRV are reduced, as well as effectiveness of cardiovascular and cardiopulmonary reflexes (Ferrari, 2002; Voss et al., 2015). Some of these changes are also a characteristic of HF and, therefore, a large problem is separating truly HF dependent alterations from those arising from aging. However, we could not age-match our HF patients and healthy controls, because it was not feasible to select subjects without any medical history, even without any risk factor for cardiovascular disease development, among those who were closer in age to the HF patients. In our study, patients were treated with a combination of medications from groups of drugs recommended for the treatment of HF. The differences among patients in doses of given drugs remain an inevitable limitation of this research, since the prescribed dose of the drug was determined by the patient's comorbidities, which were numerous in our patients.

After this study it is necessary to examine the clinical potential of the ratio of short- and long-term scaling exponents, which was the basis for separating of HF patients. We want to determine whether patients of one of these clusters have greater benefit from the cardiac resynchronization therapy. Results of a multiple regression analysis, more precisely, the fact that the examined ratio is at the center of neural, cardiac and respiratory influences, encourages us that this parameter could contribute to a better selection of candidates for this therapy and also be the parameter on which we will rely on in the course of device programming optimization during follow-up period. In the future, this ratio could potentially be used by a device algorithm that would automatically optimize its function. This will surely be the topic of our next research.

CONCLUSION

Our findings showed that in the integral cardiac control quantified by the ratio of short-term and long-term scaling exponents, beside neural cardiac control, mechanical properties of the heart and the modulatory effect of the breathing frequency are significantly involved. This ratio is able of differentiating four clusters of HF patients in sinus rhythm which do not differ in cardiac autonomic control, age, LVEF and NYHA class.

ETHICS STATEMENT

This study was carried out in accordance with the recommendations of the Declaration of Helsinki. The protocol was approved by the Ethic Committee of the Faculty of Medicine, Belgrade University (Ref. Numb. 29/III-5). All subjects gave written informed consent in accordance with the Declaration of Helsinki.

AUTHOR CONTRIBUTIONS

MP, NR, and SP conceptualized the study. MP and NR designed the experiments, performed the study, wrote the manuscript, and collected and analyzed the data. AK developed program for calculation Poincaré plot descriptors and variables of asymmetry. GM and SP conducted clinical examination and recruitment of patients. All authors discussed, edited, and approved the final and revised version of the manuscript.

SUPPLEMENTARY MATERIAL

The Supplementary Material for this article can be found online at: https://www.frontiersin.org/articles/10.3389/fphys.2019.00570/full#supplementary-material

REFERENCES

Akselrod, S., Gordon, D., Ubel, F. A., Shannon, D. C., Barger, A. C., and Cohen, R. J. (1981). Power spectrum analysis of heart rate fluctuation: a quantitative probe of beat-to-beat cardiovascular control. *Science* 213, 220–222.

Amaral, L. A. N., Ivanov, P. C., Aoyagi, N., Hidaka, I., Tomono, S., Goldberger, A. L., et al. (2001). Behavioral-independent features of complex heartbeat dynamics. *Phys. Rev. Lett.* 86:6026.

Bashan, A., Bartsch, R., Kantelhardt, J. W., and Havlin, S. (2008). Comparison of detrending methods for fluctuation analysis. *Physica A* 387, 5080–5090.

Bassingthwaighte, J. B., Liebovitch, L. S., and West, B. J. (1994). *Fractal Physiology*. Oxford: Oxford University Press.

Bauer, A., Kantelhardt, J. W., Barthel, P., Schneider, R., Makikallio, T., Ulm, K., et al. (2006). Deceleration capacity of heart rate as a predictor of mortality after myocardial infarction: cohort study. *Lancet* 367, 1674–1681.

Billman, G. E. (2011). Heart rate variability – a historical perspective. *Front. Physiol.* 2:86. doi: 10.3389/fphys.2011.00086

Bogdan, P., Jain, S., and Marculescu, R. (2013). Pacemaker control of heart rate variability: a cyber physical system perspective. *ACM Trans. Embedd. Comput. Syst.* 12:50. doi: 10.1145/2435227.2435246

Castiglioni, P., Parati, G., Di Rienzo, M., Carabalona, R., Cividijan, A., Quintin, L., et al. (2011). Scale exponents and heart rate during autonomic blockade as assessed by detrended fluctuation analysis. *J. Physiol.* 589, 355–369. doi: 10.1113/jphysiol.2010.196428

Dhesi, S., Lockwood, E., and Sandhu, R. K. (2017). Troubleshooting cardiac resynchronization therapy in nonresponders. *Can. J. Cardiol.* 33, 1060–1065. doi: 10.1016/j.cjca.2017.04.007

Eke, A., Hermán, P., Bassingthwaighte, J., Raymond, G., Percival, D. B., Cannon, M. J., et al. (2000). Physiological time series: distinguishing fractal noises from motions. *Pflüg. Arch.* 439, 403–415. doi: 10.107/s004249900135

Eke, A., Herman, P., Kocsis, L., and Kozak, L. R. (2002). Fractal characterization of complexity in temporal physiological signals. *Physiol. Meas.* 23, R1–R38.

Eke, A., Herman, P., Sanganahalli, B. G., Hyder, F., Mukli, P., and Nagy, Z. (2012). Pitfalls in fractal time series analysis: fMRI BOLD as an exemplary case. *Front. Physiol.* 3:417. doi: 10.3389/fphys.2012.00417

Ferrari, A. U. (2002). Modification of the cardiovascular system with aging. *Am. J. Geriatr. Cardiol.* 11, 30–33.

Forleo, G. B., Santini, L., Campoli, M., Malavasi, M., Scaccia, A., Menichelli, M., et al. (2015). Long-term monitoring of respiratory rate in patients with heart failure: the multiparametric heart failure evaluation in implantable cardioverter-defibrillator patients (MULTITUDE-HF) study. *J. Interv. Card. Electrophysiol.* 43, 135–144. doi: 10.1007/s10840-015-0007-3

Goldberger, A. L., Amaral, L. A. N., Glass, L., Hausdorff, J. M., Ivanov, P. C., Mark, R. G., et al. (2000). PhysioBank, physiotoolkit, and physionet. components of a new research resource for complex physiologic signals. *Circulation* 101, e215–e220.

Gupta, G., Pequito, S., and Bogdan, P. (2018). Dealing with unknown unknowns: identification and selection of minimal sensing for fractional dynamics with unknown inputs. *arxiv*

Guzik, P., Piskorski, J., Krauze, T., Wykretowicz, A., and Wysocki, H. (2006). Heart rate asymetry by poincare plots of RR intervals. *Biomed. Tech.* 51, 272–275.

Ho, K. K., Moody, G. B., Peng, C. K., Mietus, J. E., Larson, M. G., Levy, D., et al. (1997). Predicting survival in heart failure case and control subjects by use of fully automated methods for deriving nonlinear and conventional indices of heart rate dynamics. *Circulation* 96, 842–848.

Hori, M., and Okamoto, H. (2012). Heart rate as a target of treatment of chronic heart failure. *J. Cardiol.* 60, 86–90. doi: 10.1016/j.jjcc.2012.06.013

Hotta, N., Otsuka, K., Murakami, S., Yamanaka, G., Kubo, Y., Matsuoka, O., et al. (2005). Fractal analysis of heart rate variability and mortality in elderly community-dwelling people: longitudinal Investigation for Longevity and Aging in Hokkaido County (LILAC) study. *Biomed. Pharmacother.* 59, S45–S48.

Hoyer, D., Frank, B., Götze, C., Stein, P. K., Żebrowski, J., Baranowski, R., et al. (2007). Interactions between short-term and long-term cardiovascular control mechanisms. *Chaos* 17:015110.

Huikuri, H. V., Mäkikallio, T. H., Peng, C. K., Goldberger, A. L., Hintze, U., and Moller, M. (2000). Fractal correlation properties of R-R interval dynamics and mortality in patients with depressed left ventricular function after an acute myocardial infaction. *Circulation* 101, 47–53.

Ivanov, P. C., Amaral, L. A. N., Goldberger, A. L., Havlin, S., Rosenblum, M. G., Struzik, Z., et al. (1999). Multifractality in human heartbeat dynamics. *Nature* 6, 461–465.

Ivanov, P. C., Liu, K. K. L., Lin, A., and Bartsch, R. P. (2017). "Network physiology: From neural plasticity to organ network interactions," in *Emergent Complexity from Nonlinearity, in Physics, Engineering and the Life Sciences*, eds G. Mantica, R. Stoop, and S. Stramaglia (Cham: Springer), 145–165.

Ivanov, P. C., Ma, Q. D. Y., Bartsch, R. P., Hausdorff, J. M., Amaral, L. A. N., Schulte-Frohlinde, V., et al. (2009). Levels of complexity in scale invariant neural signals. *Phys. Rev. E* 79:041920.

Iyengar, N., Peng, C.-K., Morin, R., Goldberger, A. L., and Lipsitz, L. A. (1996). Age-related alteraions in the fractal scaling of cardiac interbeat interval dynamics. *Am. J. Physiol.* 271, R1078–R1084.

Kapidžić, A., Platiša, M. M., Bojić, T., and Kalauzi, A. (2014). Nonlinear properties of cardiac rhythm and respiratory signal under paced breathing in young and middle-aged healthy subjects. *Med. Eng. Phys.* 36, 1577–1584. doi: 10.1016/j.medengphy.2014.08.007

Kobayashi, M., and Musha, T. (1982). 1/f fluctuation of heartbeat period. *IEEE Trans. Biomed. Eng.* 29, 456–457.

Kuhnhold, A., Schumann, A., Bartsch, R., Ubrich, R., Barthel, P., Schmidt, G., et al. (2017). Quantifying cardio-respiratory phase synchronization–a comparison of five methods using ECGs of post-infarction patients. *Physiol. Meas.* 38, 925–939. doi: 10.1088/1361-6579/aa5dd3

Lin, A., Liu, K. K. L., Bartsch, R., and Ivanov, P. C. (2016). Delay-correlation landscape reveals characteristic time delays of brain rhythms and heart interactions. *Phil. Trans. R. Soc. A* 374:20150182. doi: 10.1098/rsta.2015.0182

Lipsitz, L. A. (1995). Age- related changes in the "complexity" of cardiovascular dynamics: a potential marker of volunerability to disease. *Chaos.* 5:1995.

Mäkikallio, T. H., Huikuri, H. V., Hintze, U., Videbaek, J., Mitrani, R. D., Castellanos, A., et al. (2001). Fractal analysis and time- and frequency-domain measures of heart rate variability as predictors of mortality in patients with heart failure. *Am. J. Cardiol.* 87, 178–182.

Parashar, R., Amir, M., Pakhare, A., Rathi, P., and Chaudhary, L. (2016). Age related changes in autonomic functions. *J. Clin. Diagn. Res.* 10, CC11–CC15. doi: 10.7860/JCDR/2016/16889.7497

Peng, C.-K., Havlin, S., Stanley, H. E., and Goldberger, A. L. (1995). Quantification of scaling exponents and crossover phenomena in nonstationary heartbeat time series. *Chaos* 5, 82–87.

Perakakis, P., Taylor, M., Martinez-Nieto, E., Revithi, I., and Vila, J. (2009). Breathing frequency bias in fractal analysis of heart rate variability. *Biol. Physiol.* 82, 82–88. doi: 10.1016/j.biopsycho.2009.06.004

Pikkujämsä, S. M., Mäkikallio, T. H., Sourander, L. B., Räihä, I. J., Puukka, P., Skyttä, J., et al. (1999). Cardiac interbeat interval dynamics from childhood to senescence. *Circulation* 100, 393–399.

Piskorski, J., and Guzik, P. (2007). Geometry of the Poincaré plot of RR intervals and its asymmetry in healthy adults. *Physiol. Meas.* 28, 287–300.

Platiša, M. M., Bojić, T., Pavlović, S. U., Radovanović, N. N., and Kalauzi, A. (2016). Generalized Poincaré plots - a new method for evaluation of regimes in cardiac neural control in atrial fibrillation and healthy subjects. *Front. Neurosci.* 10:38.

Platiša, M. M., and Gal, V. (2006). Reflection of heart rate regulation on linear and nonlinear heart rate variability measures. *Physiol. Meas.* 27, 145–154.

Platiša, M. M., and Gal, V. (2008). Correlation properties of heartbeat dynamics. *Eur. Biophys. J.* 37, 1247–1252. doi: 10.1007/s00249-007-0254-z

Platiša, M. M., and Gal, V. (2010). "Influence of breathing frequency on short-term scaling exponent and spectral powers of RR interval series," in *Proceedings of the 6th Conference of the European Study Group on Cardiovascular Oscillations*, Berlin.

Ponard, J. G., Kondratyev, A. A., and Kucera, J. P. (2007). Mechanisms of intrinsic beating variability in cardiac cell cultures and model pacemaker networks. *Biophys. J.* 92, 3734–3752.

Radovanović, N. N., Pavlović, S. U., Milašinović, G., Kirćanski, B., and Platiša, M. M. (2018). Bidirectional cardio-respiratoryinteractions in heart failure. *Front. Physiol.* 9:165. doi: 10.3389/fphys.2018.00165

Ryan, S. M., Goldberger, A. L., Pincus, S. M., Mietus, J., and Lipsitz, L. A. (1994). Gender- and age-related differences in heart rate dynamics: are women more complex thanmen? *J. Am. Coll. Cardiol.* 24, 1700–1707.

Sassi, R., Cerutti, S., Lombardi, F., Malik, M., Huikuri, H., Peng, C.-K., et al. (2015). Advances in heart rate variability signal analysis: joint position statement by the e-Cardiology ESC Working group and the European heart Rhythm Association co-endorsed by the Asia Pacific Heart Rhythm Society. *Europace* 17, 1341–1353. doi: 10.1093/europace/euv015

Saul, J. P., Albrecht, P., Berger, R. D., and Cohen, R. J. (1987). Analysis of long term heart rate variability: methods, 1/f scaling and implications. *Comput. Cardiol.* 14, 419–422.

Schmitt, D. T., Stein, P. K., and Ivanov, P. C. (2009). Stratification pattern of static and scale-invariant dynamic measures of heartbeat fluctuations across sleep stages in young and elderly. *IEEE Trans. Biomed. Eng.* 56, 1564–1573. doi: 10.1109/TBME.2009.2014819

Shin, D. G., Lee, S. H., Yi, S. H., Yoo, C. S., Hong, G. R., Kim, U., et al. (2011). Breakdown of the intermediate-term fractal scaling exponent in sinus node dysfunction. *Circ. J.* 75, 2775–2780.

Silva, F. M. H. S. P., Silva Filho, A. C., Crescencio, J. C., Papa, V., and Junior, L. G. (2014). The loss of multifractality as evidence of impaired left ventricular ejection fraction in patients after acute myocardial infraction. *Comput. Cardiol.* 41, 413–416.

Tapanainen, J. M., Thomsen, P. E., Køber, L., Torp-Pedersen, C., Mäkikallio, T. H., Still, A. M., et al. (2002). Fractal analysis of heart rate variability and mortality after an acute myocardial infarction. *Am. J. Cardiol.* 90, 347–352.

Task Force of the ESC and the NASPE (1996). Standards of heart rate variability. *Eur. Heart J.* 17, 354–381.

Tulppo, M. P., Mäkikallio, T. H., Seppänen, T., Shoemaker, K., Tutungi, E., Hughson, R. L., et al. (2001). Effects ofpharmacological adrenergic and vagal modulation on fractal heart rate dynamics. *Clin. Physiol.* 21, 515–523.

Voss, A., Schroeder, R., Heitmann, A., Peters, A., and Perz, S. (2015). Short-term heart rate variability—influence of gender and age in healthy subjects. *PLoS One* 10:e0118308. doi: 10.1371/journal.pone.0118308

West, B. J. (2009). "Control from an allometric perspective," in *Progress in Motor Control: A Multidisciplinary Perspective (Advances in Experimental Medicine and Biology)*, Vol. 629, ed. D. Sternad (New York: Springer), 57–82.

West, B. J. (2010). Fractal physiology and the fractional calculus: a perspective. *Front. Physiol.* 14:12. doi: 10.3389/fphys.2010.00012

Yaniv, Y., Lyashkov, A., and Lakatta, E. G. (2013). The fractal-like complexity of heart rate variability beyond neurotransmitters and autonomic receptors: signaling intrinsic to sinoatrial node pacemaker cells. *Cardiovasc. Pharm. Open Access.* 2:111.

Conflict of Interest Statement: The authors declare that the research was conducted in the absence of any commercial or financial relationships that could be construed as a potential conflict of interest.

frontiers in Physiology

ORIGINAL RESEARCH
published: 19 November 2019
doi: 10.3389/fphys.2019.01390

Low Frequency Forced Oscillation Lung Function Test Can Distinguish Dynamic Tissue Non-linearity in COPD Patients

Maria Ghita[1,2], *Dana Copot*[1,2]*, *Mihaela Ghita*[1,2], *Eric Derom*[3] and *Clara Ionescu*[1,2,4]

[1] Dynamical Systems and Control Research Group, Ghent University, Ghent, Belgium, [2] EEDT Core Lab on Decision and Control, Flanders Make Consortium, Ghent, Belgium, [3] Department of Respiratory Diseases, Ghent University Hospital, Ghent, Belgium, [4] Department of Automation, Technical University of Cluj-Napoca, Cluj-Napoca, Romania

This paper introduces the use of low frequencies forced oscillation technique (FOT) in the presence of breathing signal. The hypothesis tested is to evaluate the sensitivity of FOT to various degrees of obstruction in COPD patients. The measurements were performed in the frequency range 0–2 Hz. The use of FOT to evaluate respiratory impedance has been broadly recognized and its complementary use next to standardized method as spirometry and body plethysmography has been well-documented. Typical use of FOT uses frequencies between 4–32 Hz and above. However, interesting information at frequencies below 4 Hz is related to viscoelastic properties of parenchyma. Structural changes in COPD affect viscoelastic properties and we propose to investigate the use of FOT at low frequencies with a fourth generation fan-based FOT device. The generator non-linearity introduced by the device is separated from the linear approximation of the impedance before evaluating the results on patients. Three groups of COPD obstruction, GOLD II, III, and IV are evaluated. We found significant differences in mechanical parameters (tissue damping, tissue elasticity, hysteresivity) and increased degrees of non-linear dynamic contributions in the impedance data with increasing degree of obstruction ($p < 0.01$). The results obtained suggest that the non-linear index correlates better with degrees of heterogeneity linked to COPD GOLD stages, than the currently used hysteresivity index. The protocol and method may prove useful to improve current diagnosis percentages for various COPD phenotypes.

Keywords: forced oscillation technique, respiratory impedance, COPD, viscoelastic properties, small airways, remodeling

OPEN ACCESS

Edited by:
Paul Bogdan,
University of Southern California,
United States

Reviewed by:
Stefan Mihaicuta,
Victor Babes University of Medicine and Pharmacy, Romania
Siddharth Jain,
California Institute of Technology,
United States

***Correspondence:**
Dana Copot
dana.copot@ugent.be

Specialty section:
This article was submitted to Fractal and Network Physiology, a section of the journal Frontiers in Physiology

Received: *01 February 2019*
Accepted: *25 October 2019*
Published: *19 November 2019*

Citation:
Ghita M, Copot D, Ghita M, Derom E and Ionescu C (2019) Low Frequency Forced Oscillation Lung Function Test Can Distinguish Dynamic Tissue Non-linearity in COPD Patients. Front. Physiol. 10:1390. doi: 10.3389/fphys.2019.01390

1. INTRODUCTION

Standardized, clinical practice requires specific maneuvers from the subject (e.g., spirometry), i.e., maximal inspiratory and expiratory effort are required. For example, in order to differentiate between patients with asthma and chronic obstructive disease (COPD) spirometry in combination with other techniques (e.g., broncho-dilation) is employed. Therefore, measurement and estimation of impedance by means of forced oscillation technique (FOT) have been widely investigated for several years to show its added value and complementarity (Kaczka and Dellaca, 2011; Oostveen et al., 2013; Kamada et al., 2017, 2018). This is a non-invasive procedure

which does not require any special maneuvers from the patient and it requires minimal effort which makes this method an ideal lung function test, especially for the limit ages (children and elderly). FOT can be briefly described as an oscillatory air flow superimposed on the breathing of the patient (Ionescu, 2013). FOT has been broadly used for screening purposes, e.g., upper airway obstruction, small airway disease in COPD (Ionescu, 2013), respiratory mechanics in obstructive sleep apnea.

The non-invasive FOT is used to measure the respiratory mechanics at low frequencies (i.e., 0.1–2 Hz) in two groups of volunteers (i.e., adults and children). FOT is a non-standardized lung function test based on the action-reaction principle applied to the lungs during normal breathing in a non-invasive manner. The patient is advised to breath normally, i.e., no force maneuvers are required, a non-condition which enlarges significantly the applicability scope to marginal groups such as infants, children, and the elderly. Developed half century ago, FOT implies the generation of a signal $U_g(t)$ (sinusoidal, or combination hereof) within 0.3 kPa peak to peak amplitude. Signal generation has varied in the past decades from loudspeakers, mechanical pistons, to fan-based ventilators, depending on the envisaged range of frequencies and power to be applied to the patient's lungs (Olarte et al., 2015). For instance, loudspeaker based mechanisms are commonly used for frequencies well above the breathing frequency; 5–250 Hz, revealing properties of the proximal airways and useful for aerosol deposition studies. Mechanical actuators and ventilators works at lower frequencies (<5 Hz) enabling information on lung tissue properties such as viscoelasticity.

For the measurements performed in this paper, the device described in Olarte et al. (2015) has been employed. A more detailed description of the system can be found in Olarte et al. (2015). As mentioned above, when measuring at low frequencies interference between the breathing signal and excitation signal occurs. For this, a non-linear estimator has been employed to eliminate the disturbance signal (i.e., breathing) without losing the information about the respiratory response. However, the mathematical details have been described elsewhere (Ionescu et al., 2011a; Ionescu, 2013; Olarte et al., 2015; Copot et al., 2017a,b).

In the current study, we propose to evaluate low frequencies FOT in the presence of breathing signal and in a fourth generation custom-made lung function FOT device. The objective is to evaluate the sensitivity of FOT to various degrees of obstruction in COPD patients and to separate from the recorded information the linear and non-linear components of the respiratory impedance. To this purpose, three COPD groups are evaluated: GOLD II, GOLD III, and GOLD IV diagnosed patients. In this paper the hypothesis whether changes in tissue distribution in COPD will induce changes in the non-linear dynamic response has been investigated. A method and protocol is proposed to determine the amount of degree and correlate it to the GOLD classification of COPD.

The paper is structured as follows. The next section presents the biometric and spirometric details for the subjects and patients evaluated in this work. The measurement device and method for estimating respiratory impedance is also described. The third section illustrates the results, followed by a discussion section. A conclusion section summarizes the main ideas of this study.

TABLE 1 | Biometric characteristics and baseline lung function data for the patients included in the study.

–	GOLD II	GOLD III	GOLD IV	Baseline
# Patients	21	22	20	20
Age (years)	60–71	65–73	70–74	33–36
Height (m)	1.68 –1.74	1.69–1.73	1.54–1.63	1.73–1.78
Weight (kg)	58–68	68–77	75–85	74–77
FEV1%pred	67–72	42–48	27–31	98–105

2. MATERIALS AND METHODS

2.1. Patients

In this paper a total number of 63 patients with COPD with an average age of 60 years old have been evaluated using the FOT device. The patients were coming for periodic lung evaluation at the pneumology department at Ghent University Hospital, Belgium. Biometric and spirometric parameters are shown in **Table 1**. Each patient signed the inform consent form and the protocol has been approved by the local ethical committee, registered under the number B670201526182.

2.2. Measurement Device

The measurement device presented in this paper is a fourth generation prototype of the device detailed in Ionescu et al. (2014) and Maes et al. (2014). The measurement device consist in two sets of three fans, one on each side of the main pipe as shown in **Figure 1**. The aim of these fans is to move the air into the tube on one side and to extract the air at the other side. A pneumotachograph and two pressure sensors deliver the flow and pressure measured at the mouth during tidal breathing. The pressure signal generated by the device is a multisine within the 0.05–2 Hz frequency interval. The device has been described in detail in Olarte et al. (2015) and Copot et al. (2017a) and includes compensation of deadspace effects (Tang et al., 2005) through closed loop control of fan speed.

2.3. Identification Method

The most identification approaches of non-linear dynamic systems is to have small amplitude variations and a good SNR, to avoid non-linear distortions. In this paper, we propose to make use of this information in a systematic analysis.

In general, for multi-harmonic periodic signals, the quadratic non-linear effect is present at combinations of $f_i - f_j$, while the cubic non-linear effect is identified for the triple combination $f_i - f_j - f_k$ (with f_i, f_j, and f_k the frequencies present in the excitation signal).

Consequently, exciting the system with periodic signals with only odd harmonics will prevent the even non-linear distortions. This allows discriminating between even and odd non-linear contributions, while providing a best linear approximation (BLA) of the system (Pintelon and Schoukens, 2012). This

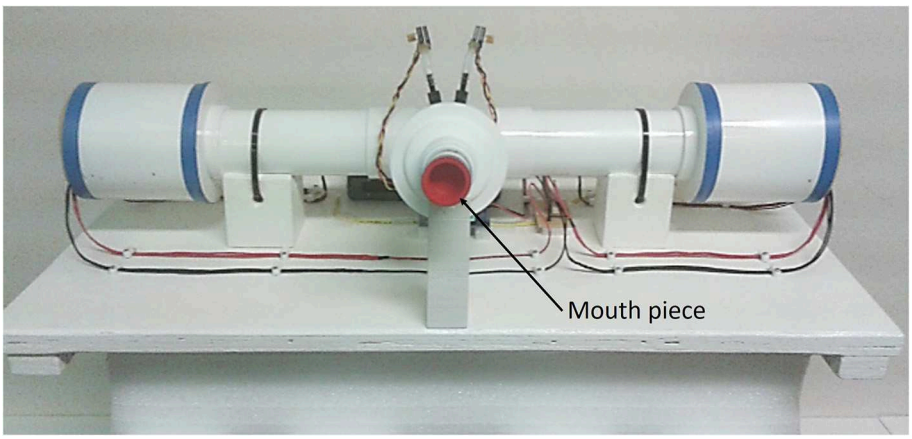

FIGURE 1 | Photo of the device used for measurements. The patient is using the mouth piece to connect to the device and the flow is directed toward the patient while he breaths using straws. PWM stands for pulse wave modulated signal.

concept has been successfully applied to respiratory impedance in loudspeaker based device and a motor-driven piston based device (Ionescu et al., 2011a, 2014).

The influence of non-linear distortions on the frequency response of measurements are quantified by using identification methods given in Schoukens et al. (2002) and Pintelon and Schoukens (2012). A brief description of the essential steps is given hereafter.

$$u(t) = \frac{1}{\sqrt{N}} \sum_{k=1}^{N} A_k \sin(\omega_k t + \phi_k) \tag{1}$$

with the phases ϕ_k random uniformly distributed in the interval $[0; 2\pi]$, $\omega_k = 2\pi k F_s$ the excited frequencies of the multisine, with F_s the frequency resolution of the signal, N the number of excited harmonics and A_k the spectrum amplitude.

Consider an input signal defined as a random phase multisine with A_k the non-zero amplitude for odd k values, $\omega_0 = 2\pi f_0$ and $f_0 = 0.1$ Hz, ϕ_k the phase uniformly and independently distributed in the $[0; 2\pi]$ interval and N the number of sinusoids. The best linear approximation (BLA) of a non-linear system can be viewed as a minimization of the mean squared error between the true output of the non-linear system and the output of an approximated linear model. The estimated BLA $\hat{G}_{BLA}(j\omega_k)$ of a wide class of non-linear systems, obtained using (1) can be written as:

$$\hat{G}_{BLA}(j\omega_k) = G_{BLA}(j\omega_k) + G_S(j\omega_k) + N_G(j\omega_k) \tag{2}$$

with $G_{BLA}(j\omega_k)$ the true best linear approximation (BLA) of the non-linear system, $G_S(j\omega_k)$ the zero mean stochastic non-linear contributions and $N_G(j\omega_k)$ the measurement noise (Schoukens et al., 2002). The stochastic non-linear contributions $G_S(j\omega_k)$ can be extracted by averaging from a manifold of experiments M containing different phase realizations in the excitation signal from (1).

The basic principles for detecting non-linearities are shown in **Figure 2**. The output of a linear system,which is excited with a multi-frequency input signal,is given on the first row. Only amplitude variations on the excited (odd) frequencies are observed (red). However, when this input signal is applied on a non-linear system (e.g., the respiratory tissue), non-linear dynamics become visible and can be measured as additional detection lines (second and third row in blue and green). These distortions are in fact superimposed to the linear output signal and contribute to the signal measured at the output (last row). The resulting out-put signal contains extra information via phase differences. The non-linear contributions can be determined via the identification of the even and odd harmonics(blue and green). A detailed description of the method can be found in Schoukens et al. (2002) and Pintelon and Schoukens (2012). In order to reduce the non-linear effect over the FRF and distinguish between even and odd non-linearities, only odd frequencies are excited in the system. In this context, the even non-linearities do not contribute to $G_B(j\omega_k)$. The presence and the level of even non-linearities can be detected at the

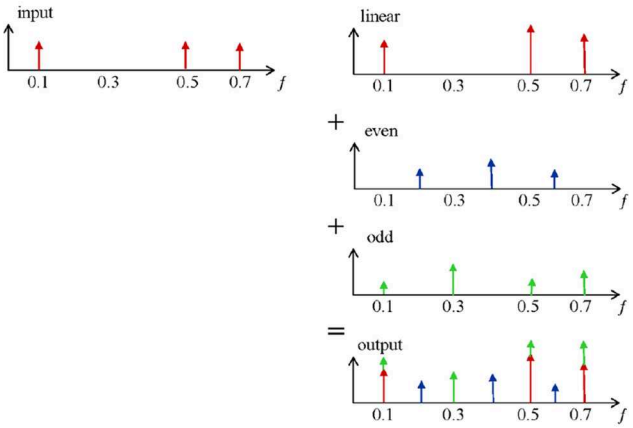

FIGURE 2 | A schematic representation of the input-output contributions.

even non-excited harmonics of the response spectrum signal. Additionally, detection of odd non-linear distortions can be identified by omitting some of the odd harmonics in the excitation (Pintelon and Schoukens, 2012).

A convenient excitation signal that allows controlling easily the excitation lines and maintains the advantages of periodic excitation is designed as in (1), where the even harmonics are not excited, and per group of three odd harmonics one is randomly omitted. To avoid that the random phase realizations affect the amplitude of the designed signal, a crest factor lower than 2.2 has been used in (1).

An in-depth systematic analysis of the device has been performed for detecting its non-linear contributions and its sensitivity to various respiratory tube calibers and lengths, along with a calibration validation, as given in Olarte et al. (2015). The respiratory impedance data from the patients presented in the current paper implies calibration and correction of non-linear contributions of the device.

In order to quantify these non-linear contributions, the following index has been introduced in Ionescu (2013) and it has been used in this paper to evaluate the degree of heterogeneity in patients with different degrees of COPD.

$$T = \frac{P_{even} + P_{odd}}{P_{exc}} \cdot \frac{U_{exc}}{U_{even} + U_{odd}} \tag{3}$$

where P represents the pressure and U is the input signal (1). Each variable is the sum of the absolute values of all the contributions in pressure signal and input flow signal respectively, at the even non-excited frequencies, the odd non-excited harmonics and the excited odd harmonics as schematically depicted in **Figure 3**. Only the corrected output pressure has been taken into account when calculating (3), i.e., the linear contribution has been estimated and subtracted. The principle of detecting the non-linear contributions has been described elsewhere (Pintelon and Schoukens, 2012). A brief description of the method is given in the **Appendix**.

The index from (3) expresses a relative ratio of the contributions at the non-excited frequency points, with respect to the contributions at the excited frequency points. Furthermore, it gives a relative measure of the gain between contributions in the input and in the output of the system. Since this is a non-linear system whose output depends on the input, the choice for this relative measure is technically sound if one aims to extract the degree of non-linearity existent in lung tissue.

2.4. Estimating Impedance and Related Parameters

After the signals are recorded, they undergo a pre-conditioning step. The purpose is to eliminate the non-linear harmonics unavoidable by the interference with the low breathing frequency. For this, we employ the method proposed in Markovsky (2012) and Markovsky et al. (2014). This pre-conditioning leaves the data ready for estimation of respiratory impedance as real-imaginary parts as a function of frequency, with minimized effect from breathing dynamics. As the algorithm is not our contribution, is not listed here.

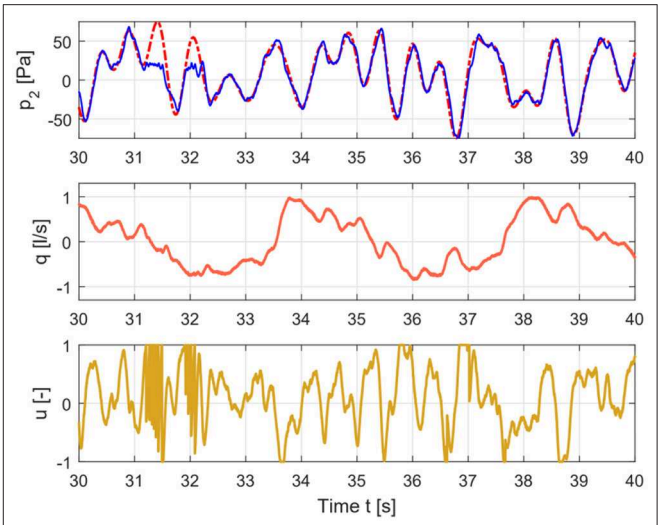

FIGURE 3 | Time signals for healthy case depicting the input signal (lower graph), flow signal (middle graph), and pressure signal (upper graph).

The subjects were asked to breath freely in normal sitting position for 30 s, i.e., about 5 periods of multisine excitation. The pressure (kPa) and flow (L) time based signals were sampled at 500 Hz frequency. The non-parametric estimation of the impedance was performed by employing the tools detailed in Daroczy and Hantos (1982), Oostveen et al. (2013), and Ionescu et al. (2014) based on spectral analysis techniques:

$$\hat{Z}_{BLA}(j\omega_k) = \frac{S_{PU}(j\omega_k)}{S_{QU}(j\omega_k)} \tag{4}$$

where S_{PU}, S_{QU} denotes the cross spectral density function between the output pressure measured at the mouth of the patient and the excitation signal, and the output flow and the excitation signal respectively, evaluated at the excited frequency lines ω_k (rad/s) corrected by the effect of non-linear contributions from the device. The result is a graphical evaluation of the respiratory properties and it is usually represented by its real and imaginary parts as a function of frequency.

To this data, non-linear least square identification algorithm can be applied to fit the parametric model:

$$Z_{CP}(j\omega_k) = R + I(j\omega_k) + \frac{1}{C(j\omega_k)^{\beta}} \tag{5}$$

where R (kPa s/L) and I (kPa s^2/L) represent the main airway resistance and inheritance, while the last term consists of a constant-phase element which can be quantified in term of imaginary and real part which will represent the tissue elastance and damping respectively, and are described by the following equations:

$$\begin{aligned} G &= \frac{1}{C\omega_k^{\beta}} \cos(\beta\pi/2) \\ H &= \frac{1}{C\omega_k^{\beta}} \sin(\beta\pi/2) \end{aligned} \tag{6}$$

The ratio between the elastance and damping represents tissue heterogeneity. When the changes in R are small then any changes in G (kPa $s^{(1-\beta)}$/L) will depict changes in parenchyma or in very small airways (Ionescu et al., 2017). Significant changes in H (kPa $s^{(1-\beta)}$/L) changes in the intrinsic mechanical properties of the parenchyma (Hantos et al., 1993; Thamrin et al., 2004).

This parametric model has been shown to reliably estimate airway and tissue properties (Ionescu, 2013). The accuracy of model parameters estimates by means of model fitting to experimental data indicates that the resistance and inheritance contain a high degree of uncertainty. The phase constancy parameter provides a reliable estimation of the peripheral tissue characteristics. The outcome of this study also indicates a dependency on frequency at low frequencies in the real part of impedance is consistently fitted by the constant-phase model from (5) when compared to other models from literature.

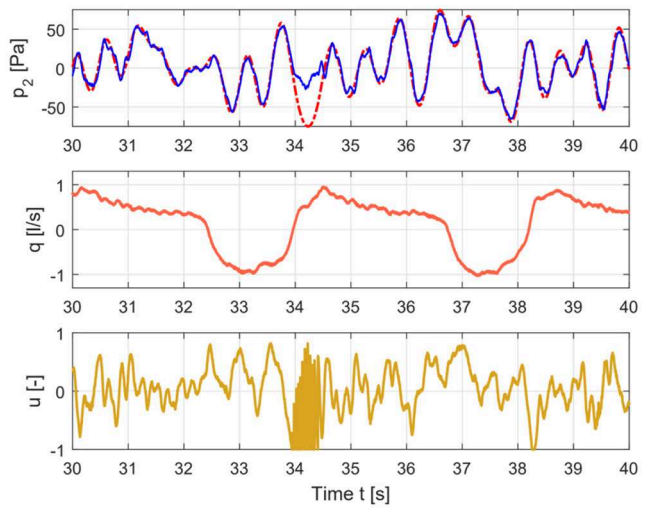

FIGURE 4 | Time signals for COPD case depicting the input signal **(lower graph)**, flow signal **(middle graph)**, and pressure signal **(upper graph)**.

We have also previously showed that FOT measurements with both (4) and (5) are useful to characterize differences between healthy subjects and COPD patients (Ionescu et al., 2010a). We have shown in the past that the proposed models, method and device can be used to differentiate between healthy and disease subjects. However, we did not employ the non-linear index to evaluate the differences between the different degrees of COPD (i.e., COPD II, COPD III, and COPD IV). Hence, the aim of this study is to investigate whether or not the non-linear index can be used to distinguish between various degrees of obstruction in COPD. We have shown that the term in fractional order frequency arises naturally from the structure and mechanical properties of the lungs, as described in Bates et al. (1994, 2007), Suki et al. (1994), and Ionescu et al. (2010b, 2011b).

The measured pressure and flow and the input signal for healthy and COPD case are shown in **Figures 3**, **4**.

Figure 5 depicts a pre-conditioned pressure and flow signal used for the estimation of the respiratory impedance.

The BLA of the respiratory impedance modulus evaluated in healthy and in COPD GOLD3 are depicted in **Figure 6** upper and lower, respectively. One may conclude the non-linear distortions tend to be more significant in patients with COPD than in healthy subjects as it can be seen in **Figure 7**. From clinical insight, this is indeed a valid conclusion, more details regarding the clinical interpretation can be found in Ionescu (2013) chapter 2. The respiratory system affected by the COPD disease changes its structure and this will also change the heterogeneous appearance of the tissues and will introduce non-linear effects such as: inflammation, clogged airways, viscoelasticity, etc. This paper presents a preliminary study on the further development of tools and methods for low-frequency measurement in a non-invasive manner. Although this evaluation is performed on a limited number of patients it indicates that measuring the non-linear contributions is beneficial to gather insight into evolution of respiratory diseases. Development of algorithms for canceling the interference with the breathing signal of the patient is motivated by the fact that the respiratory mechanics have

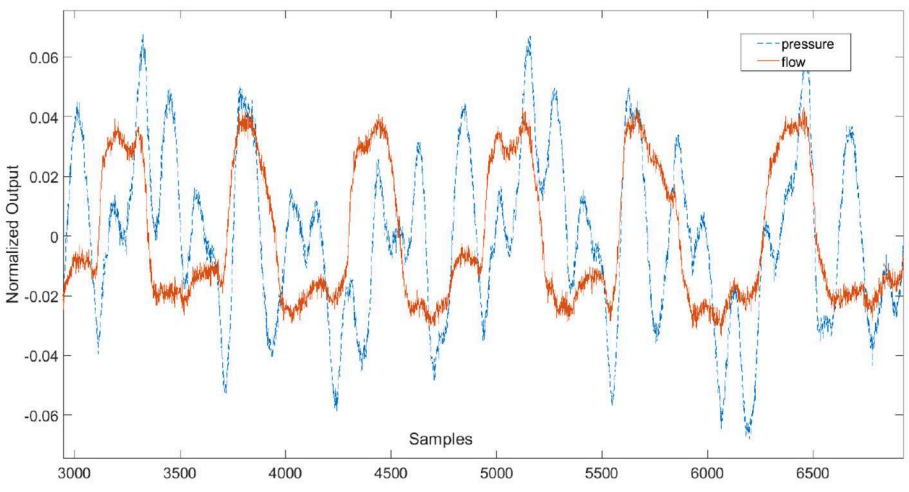

FIGURE 5 | Example of pre-conditioned time signals used for the estimation of the respiratory impedance.

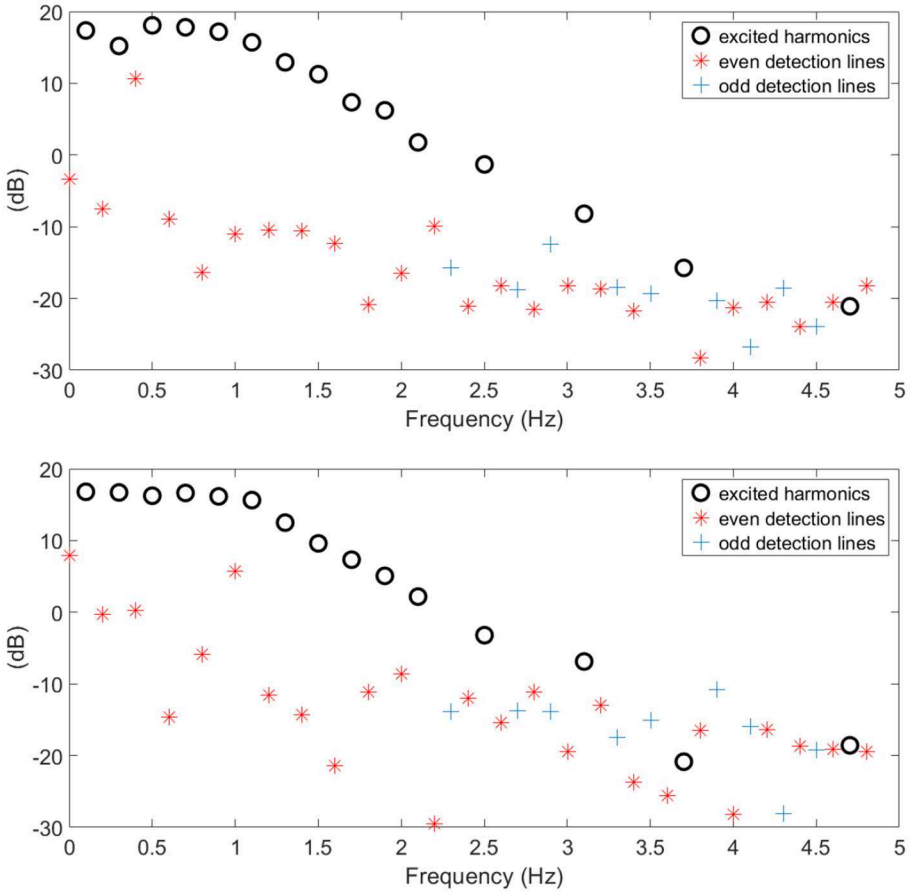

FIGURE 6 | Example of healthy **(upper)** and COPD **(lower)** estimated BLA impedance modulus along with non-linear contributions used to calculate index T.

inherent information on the viscoelastic properties of airways and tissue.

This fact is also supported by the values obtained for the T index depicted in **Figure 8** by means of Anova analysis plot (Matlab). More details about the non-linear index can be found in Copot et al. (2017a). Given that the number of subjects evaluated in each group is not very high one may conclude that at this stage a statistical measure cannot be performed, however a trend may be observed which corresponds to the expected result: heterogeneity in small airways will induce higher amount of non-linear effects in respiratory mechanics properties.

Statistical analysis was performed using the Anova plot in Matlab. With respect to airway resistance R and airway inheritance I these were not used to perform any further analysis since there was no normal distribution of the estimated parameters. The values estimated at each frequency point according to (6) and for all subjects in group are depicted as one column in the Anova plot, indicating that statistical difference exists, with $p \ll 0.001$.

Our results suggest that the proposed non-linear dynamic index for the respiratory function T is better correlated to heterogeneity in the COPD GOLD stages than the broadly used heterogeneity index η.

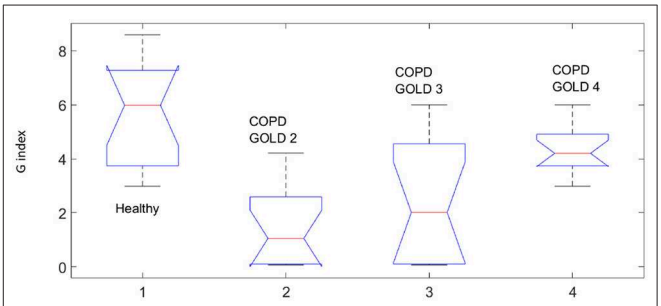

FIGURE 7 | Evolution of the index G per group ($p \ll 0.001$).

The values estimated at each frequency point and for all subjects in group are depicted as one column in the Anova plot, indicating that statistical difference exists, with $p \ll 0.001$.

3. DISCUSSION

The presence of non-linear contributions in the respiratory system increased steadily with every group, indicating a more pronounced linear behavior in healthy lungs, depicted in **Figure 8**. This does not imply a perfect linear system, but rather

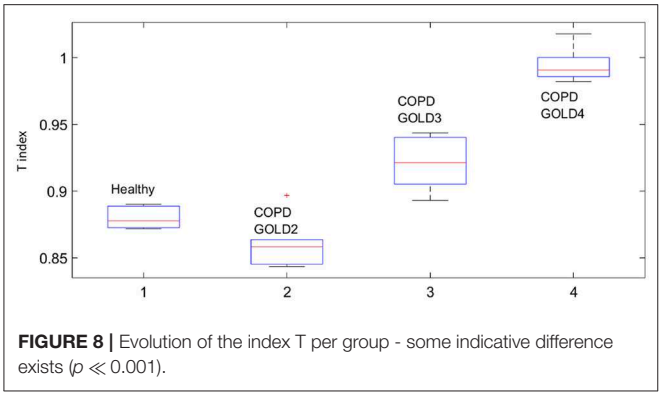

FIGURE 8 | Evolution of the index T per group - some indicative difference exists ($p \ll 0.001$).

a *less non-linear* one. Pathological changes in COPD affecting structure and viscoelastic properties introduce dynamical effects, which may move away from Newtonian rheological framework. In the remodeling framework associated with the evolution of COPD (Hogg et al., 2004; Bergeron and Boulet, 2006), thickening of the airway wall and accumulation of inflammatory exudates in the lumen will enhance turbulent airflow conditions which will enable significant non-linear contributions in the dynamical system under analysis (Ionescu et al., 2011a). In patients with GOLD III and GOLD IV, severe increase in lymphocytes and presence of lymphoid follicles will determine a drastic change in the energy balance distribution for enabling airflow in small airways (Williamson et al., 2011). This accounts for significantly higher degree of non-linearity in these groups than in GOLD II.

The degree heterogeneity in the small airways is related to the presence of non-linear contributions. In Bates and Allen (2006), a detailed description on the interpretation of the index with changes in elastance and resistance is given. With respect to η For η to increase by heterogeneity at low frequencies (i.e., f = 0.16 Hz), the resistive and elastic properties must have appropriate relative values. The regional increase/decrease in heterogeneity does not automatically lead to an increase in η (Bates and Allen, 2006). This specific aspect is reflected in COPD GOLD III data, where the hysteresivity factor has a high variability interval compared to the other groups. The relative high heterogeneity factor in healthy subjects may be due to the high variability present in the healthy respiratory system to allow high flexibility to changing environmental and operating conditions. This variability is also the backbone for adaptation and remodeling with disease. Our respiratory tree is rather robustly designed and heterogeneity in healthy does not have the same underlying principles as the structural changes due to disease.

Significant changes in G or H parameters indicate enhanced or altered secretions that cause dysfunction in small airways (Hantos et al., 1993). Changes in H will induce changes in tissue elastance. Our values of H were slightly lower than in Lorx et al. (2009) for COPD patients, but this may be due to the fact that Lorx and colleagues evaluate H at specific transrespiratory pressures. They indicated that at frequencies below 2 Hz, the elastance values in COPD may be similar or even smaller than those in healthy respiratory system, indicating the decreased elasticity resulting from emphysematous changes. This is in accordance with out results in H values for COPD GOLD III and GOLD IV.

It has been concluded in Lutchen and Gillis (1997) that lung resistance and lung elastance are extremely sensitive to mild inhomogeneous constriction in which a few highly constricted or nearly closed airway are present in peripheral zones. Strong dependencies with frequencies have been observed at breathing rates. This conclusion from their simulation studies can be well-verified with the results obtained for COPD GOLD II group, where markedly increased values for E_{ti} have been found. This indicated mild inhomogeneous constriction. By contrast, severe homogeneous constriction would not increase E_{ti} at the lower breathing frequencies, supported by our results for COPD GOLD III and GOLD IV groups. However, it seems that our proposed non-linear dynamic index T outperforms the relevance of η in degrees of heterogeneity assigned to various stages of COPD GOLD.

In Dailey and Ghadiali (2010), the very same power law formulation from (6) has been used to characterize microrheological properties of materials in the context of cell-injury during specific loads. This may be relevant for instance in analyzing lung injury during mechanical ventilation and preset positive end-expiratory pressures (Wheeler and Bernard, 2007). However, the frequency dependency allows a dynamic characterization of viscoelastic properties in lungs or in similar materials (e.g., polymers). In Freed and Einstein (2012), a model for lung parenchyma has been developed where stress-strain properties are characterized for lung lobes, similar to a pressure/volume curve model for inflation/deflation. We also showed previously that mechanical models of lungs preserving properties and structure imply the presence of a power law term in time domain, or equivalently a fractional order term in frequency as in (5) (Ionescu et al., 2010c; Ionescu, 2013). However, simple impedance models as (5) are more accessible and easier for evaluation in a clinical context than complex theoretical models which are useful for understanding underlying mechanisms of lung recruitment and may be useful when individualized treatment and follow up of COPD patients are envisaged (Derom et al., 2007). This individualized treatment could very well be paired with a wearable monitoring system for respiratory impedance as that presented in Ionescu and Copot (2017).

4. CONCLUSIONS

In this paper we have shown that forced oscillation technique is a complementary tool in evaluating tissue heterogeneity and dynamic non-linearity in respiratory impedance data. The proposed non-linear index provides valuable additional information to the classical constant-phase parameter model. The protocol enables separating linear from non-linear effects, whereas changes in tissue parameters from constant-phase model are highly sensitive to changes in peripheral airways. The non-linear dynamics index proved to be better correlated to various stages of COPD GOLD than the currently used index for histeresivity. There is no doubt that FOT, in combination

with reliable measurements at breathing frequencies, can deliver information about small airways and thus help in accurate diagnosis of various COPD phenotypes.

ETHICS STATEMENT

All subjects gave their written informed consent and the protocol was approved by the local ethical committee, registered under the number B670201526182.

AUTHOR CONTRIBUTIONS

All authors listed have made a substantial, direct and intellectual contribution to the work, and approved it for publication.

FUNDING

MaG acknowledges the BOF Grant No. 01D15919. MiG acknowledges the FWO Grant No. 1184220N. DC was the grant holder of the prestigious scholarship from the Flanders Research Centre, FWO Grant No. 12X6819N.

SUPPLEMENTARY MATERIAL

The Supplementary Material for this article can be found online at: https://www.frontiersin.org/articles/10.3389/fphys.2019.01390/full#supplementary-material

REFERENCES

Bates, J. (2007). A recruitment model of quasi-linear power-law stress adaptation in lung tissue. *Ann. Biomed. Eng.* 35, 1165–1174. doi: 10.1007/s10439-007-9291-0

Bates, J., and Allen, G. (2006). The estimation of lung mechanics parameters in the presence of pathology: a theoretical analysis. *Ann. Biomed. Eng.* 3493, 384–392. doi: 10.1007/s10439-005-9056-6

Bates, J. H., Maksym, G. N., Navajas, D., and Suki, B. (1994). Lung tissue rheology and 1/f noise. *Ann. Biomed. Eng.* 22, 674–681. doi: 10.1007/BF02368292

Bergeron, C., and Boulet, L.-P. (2006). Structural changes in airway diseases. *Chest* 129, 1068–1087. doi: 10.1378/chest.129.4.1068

Copot, D., De Keyser, R., Derom, E., and Ionescu, C. (2017a). Structural changes in the COPD lung and related heterogeneity. *PLoS ONE* 12:e0177969. doi: 10.1371/journal.pone.0177969

Copot, D., De Keyser, R., Derom, E., Ortigueira, M., and Ionescu, C. (2017b). Reducing bias in fractional order impedance estimation for lung function evaluation. *Biomed. Signal Process. Control* 39, 74–80. doi: 10.1016/j.bspc.2017.07.009

Dailey, H. L., and Ghadiali, S. N. (2010). Influence of power-law rheology on cell injury during microbubble flows. *Biomech. Model. Mechanobiol.* 9, 263–279. doi: 10.1007/s10237-009-0175-0

Daroczy, B., and Hantos, Z. (1982). An improved forced oscillatory estimation of respiratory impedance. *Int. J. Biol. Med. Res.* 13, 221–235. doi: 10.1016/0020-7101(82)90041-1

Derom, E., Strandgården, K., Schelfhout, V., Borgström, L., and Pauwels, R. (2007). Lung deposition and efficacy of inhaled formoterol in patients with moderate to severe COPD. *Respir. Med.* 101, 1931–1941. doi: 10.1016/j.rmed.2007.04.013

Freed, A. D., and Einstein, D. R. (2012). Hypo-elastic model for lung parenchyma. *Biomech. Model. Mechanobiol.* 11, 557–573. doi: 10.1007/s10237-011-0333-z

Hantos, Z., Daróczy, B., Suki, B., Nagy, S., and Fredberg, J. J. (1993). Input impedance and peripheral inhomogeneity of dog lungs. *J. Appl. Physiol.* 72, 168–179. doi: 10.1152/jappl.1992.72.1.168

Hogg, J. C., Chu, F., Utokaparch, S., Woods, R., Elliott, W. M., Buzatu, L., et al. (2004). The nature of small-airway obstruction in chronic obstructive pulmonary disease. *New Engl. J. Med.* 350, 2645–2653. doi: 10.1056/NEJMoa032158

Ionescu C. (2013). *The Human Respiratory System. An Analysis of the Interplay Between Anatomy, Structure, Breathing and Fractal Dynamics*. London: Springer-Verlag.

Ionescu, C., and Copot, D. (2017). Monitoring respiratory impedance by wearable sensor device; protocol and methodology. *Biomed. Signal Process. Control* 36, 57–62. doi: 10.1016/j.bspc.2017.03.018

Ionescu, C., De Keyser, R., Sabatier, J., Oustaloup, A., and Levron, F. (2011b). Low frequency constant-phase behaviour in the respiratory impedance. *Biomed. Signal Process. Control* 6, 197–208. doi: 10.1016/j.bspc.2010.10.005

Ionescu, C., Derom, E., and De Keyser, R. (2010a). Assessment of respiratory mechanical properties with constant-phase models in healthy and COPD lungs. *Comput. Methods Programs Biomed.* 9, 78–85. doi: 10.1016/j.cmpb.2009.06.006

Ionescu, C., Kosinsky, W., and De Keyser, R. (2010c). Viscoelasticity and fractal structure in a model of human lungs. *Arch. Mech.* 62, 21–48.

Ionescu, C., Lopes, A., Copot, D., Machado, J. A. T., and Bates, J. H. T. (2017). The role of fractional calculus in modeling biological phenomena: a review. *Commun. Nonlinear Sci. Numer. Simul.* 51, 141–159. doi: 10.1016/j.cnsns.2017.04.001

Ionescu, C., Schoukens, J., and De Keyser, R. (2011a). "Detecting and analyzing non-linear effects in respiratory impedance measurements," in *Proceedings of the American Control Conference* (San Francisco, CA), 5412–5417.

Ionescu, C., Vandersteen, G., Schoukens, J., Desager, K., and De Keyser, R. (2014). Measuring nonlinear effects in respiratory mechanics: a proof of concept for prototype device and method. *IEEE Trans. Instr. Meas.* 63, 124–134. doi: 10.1109/TIM.2013.2277519

Ionescu, C. M., Muntean, I., Tenreiro Machado, J. A., De Keyser, R., and Abrudean, M. (2010b). A theoretical study on modeling the respiratory tract with ladder networks by means of intrinsic fractal geometry. *IEEE Trans. Biomed. Eng.* 57, 246–253. doi: 10.1109/TBME.2009.2030496

Kaczka, D. W., and Dellacá, R. L. (2011). Oscillation mechanics of the respiratory system: applications to lung disease. *Crit. Rev. Biomed. Eng.* 39, 337–359. doi: 10.1615/CritRevBiomedEng.v39.i4.60

Kamada, T., Haneko, M., and Tomioka, H. (2017). Impact of exacerbations on respiratory system impedance measured by a forced oscilaltion technique in COPD: a prospective observational study. *Int. J. COPD* 12, 509–516. doi: 10.2147/COPD.S124828

Kamada, T., Haneko, M., and Tomioka, H. (2018). Comparison of respiratory system impedance in astham and COPD: a prospective observational study. *Respirology* 23, 478–484. doi: 10.1111/resp.13240

Lorx, A., Szabó, B., Hercsuth, M., Pénzes, I., and Hantos, Z. (2009). Low-frequency assessment of airway and tissue mechanics in ventilated COPD patients. *J. Appl. Physiol.* 107, 1884–1892. doi: 10.1152/japplphysiol.00151.2009

Lutchen, K., and Gillis, H. (1997). Relationship between heterogeneous changes in airway morphometry and lung resistance and elastance. *J. Appl. Physiol.* 83, 1192–1201. doi: 10.1152/jappl.1997.83.4.1192

Maes, H., Vandersteen, G., Muehlebach, M., and Ionescu, C. (2014). A fan-based, low-frequent, forced oscillation technique apparatus. *IEEE Trans. Instr. Meas.* 63, 603–611. doi: 10.1109/TIM.2013.2282188

Markovsky, I. (2012). *Low Rank Approximation: Algorithms, Implementation, Applications, Springer Series in Communications and Control Engineering*. London: Springer-Verlag.

Markovsky, I., Goos, J., Usevich, K., Pintelon, R. (2014). Realization and identification of autonomous linear periodically time-varying systems. *Automatica* 50, 1632–1640. doi: 10.1016/j.automatica.2014.04.003

Olarte, O., De Keyser, R., and Ionescu, C. (2015). Second generation fan-based device for non-invasive measurement of respiratory impedance: identification, calibration and analysis. *Biomed. Signal Process. Control* 30, 127–133. doi: 10.1016/j.bspc.2016.06.004

Oostveen, E., Boda, K., van der Grinten, C. P., James, A. L., Young, S., Nieland, H., et al. (2013). Respiratory impedance in healthy subjects:

baseline values and bronchodilator response. *Eur. Respir. J.* 42, 1513–1523. doi: 10.1183/09031936.00126212

Pintelon, R., and Schoukens, J. (2012). *System Identification, a Frequency Domain Approach*. Hoboken, NJ: John Wiley & Sons Inc.

Schoukens, J., Pintelon, R., and Dobrowiecki, T. (2002). Linear modelling in the presence of nonlinear distortions. *IEEE Trans. Instr. Meas.* 51, 786–792. doi: 10.1109/TIM.2002.803298

Suki, B., Barabási, A. L., and Lutchen, K. R. (1994). Lung tissue viscoelasticity: a mathematical framework and its molecular basis. *J. Appl. Physiol.* 76, 2749–2759. doi: 10.1152/jappl.1994.76.6.2749

Tang, Y., Turner, M. J., and Baker, A. B. (2005). Effects of alveolar dead-space, shunt and $\dot{V}/\dot{Q}$ distribution on respiratory dead-space measurements. *Br. J. Anesth.* 95, 538–548. doi: 10.1093/bja/aei212

Thamrin, C., Janosi, T. Z., Collins, R. A., Sly, P. D., and Hantos, Z. (2004). Sensitivity analysis of respiratory parameter estimates in the constant-phase model. *Ann. Biomed. Eng.* 32, 815–822. doi: 10.1023/B:ABME.0000030257.88945.81

Wheeler, A., and Bernard, G. (2007). Acute lung injury and the acute respiratory distress syndrome: a clinical review. *Lancet* 369, 1553–1564. doi: 10.1016/S0140-6736(07)60604-7

Williamson, P., Clearie, K., Menzies, D., Vaidyanathan, S., and Lipworth, B. (2011). Assessment of small-airway disease using alveolar nitric oxide and impulse oscillometry in asthma and COPD. *Lung* 189, 121–129. doi: 10.1007/s00408-010-9275-y

Conflict of Interest: The authors declare that the research was conducted in the absence of any commercial or financial relationships that could be construed as a potential conflict of interest.

Advantages of publishing in Frontiers

OPEN ACCESS
Articles are free to read for greatest visibility and readership

FAST PUBLICATION
Around 90 days from submission to decision

HIGH QUALITY PEER-REVIEW
Rigorous, collaborative, and constructive peer-review

TRANSPARENT PEER-REVIEW
Editors and reviewers acknowledged by name on published articles

Frontiers
Avenue du Tribunal-Fédéral 34
1005 Lausanne | Switzerland

Visit us: www.frontiersin.org
Contact us: info@frontiersin.org | +41 21 510 17 00

REPRODUCIBILITY OF RESEARCH
Support open data and methods to enhance research reproducibility

DIGITAL PUBLISHING
Articles designed for optimal readership across devices

FOLLOW US
@frontiersin

IMPACT METRICS
Advanced article metrics track visibility across digital media

EXTENSIVE PROMOTION
Marketing and promotion of impactful research

LOOP RESEARCH NETWORK
Our network increases your article's readership